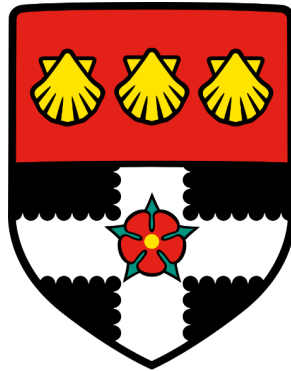


UNIVERSITY OF READING
Department of Meteorology



Effects of meteorological conditions
on building natural ventilation in
idealised urban settings

Hannah Gough

A thesis submitted for the degree of Doctor of Philosophy
2017

Declaration

I confirm that this is my own work and the use of all material from other sources has been properly and fully acknowledged.

Hannah L. Gough

Abstract

With 50 % of the worlds population dwelling in urban environments and over 70 % of people's time is spent indoors (at home, work or in vehicles). It is important to understand how the urban area effects the internal-external air exchange for buildings and how this may impact on the occupants, though this will differ depending on location. The urban area is complex, requiring multidisciplinary expertise in order to understand the driving features.

Urban areas may be simplified down for study to reduce some of the complexity. The study undertaken at Silsoe, UK, used a full-scale staggered array of nine 6 m³ cubes to gain an understanding of the effects of meteorological variables on the natural ventilation rate and pressure coefficient. After 6 months 8 cubes were removed, leaving the instrumented cube isolated for 2 months. All equipment logged constantly, creating a dataset which covers a wide range of wind directions, wind speeds, temperature differences and atmospheric stabilities making the dataset unique from previous work.

Changes in wind direction cause changes in the pressure coefficient for both isolated and array cases. However defining wind direction is difficult for the array due to the complex interaction of obstacle wakes. The relation between reference and local wind directions is non-linear. The flow within the array was dominated by mechanical turbulence generated by the wakes of the array elements, with the local turbulence intensity being 7 to 10 times greater than for an isolated cube. The presence of an opening had no effect on the pressure coefficient when acting as an inlet. Stability was found to have no effect due to the building being low-rise and the effects of turbulence could not be discerned from 30 minute averages for both pressure coefficient and ventilation measurements.

The full-scale data were compared to a wind tunnel model of the site. This allowed for increased array sizes to be used. It was found that the length and size of the rows have a non-linear effect on the pressure coefficient of a cube within the array, with a limited array reducing the pressure coefficient by 10 to 50 % \pm 5 % depending on measurement location. Pre-existing models predict the pressure coefficient for an isolated cube well, but do not accurately predict the pressure coefficient for a limited array due to the lack of wind direction and shielding terms. This is also true for the full-scale data.

The three methods used to predict ventilation rate (tracer gas decay, pressure difference and the volumetric method) were all affected by different variables such as the

presence of thermally driven ventilation, wind direction, location of the wind speed measurement and amount of turbulence within the flow. The difference in the volumetric flow methods depended on the wind speed measurement used, highlighting the difficulty in gaining an accurate representation of ventilation rate using wind speed alone, especially in an urban area. All three methods show more agreement for the array cases than for the isolated cube cases.

Pre-existing empirical models of urban wind speed (CIBSE), pressure coefficient (ASHRAE and AIVC) and ventilation rate do not capture the dual behaviour of the ratio of local and reference wind speeds found for the array. This dual behaviour is demonstrated for 1, 5, 10, 30 and 60 minute averaging periods. This behaviour is not correlated to changes in wind direction, the turbulence or speed of the oncoming flow or internal-external temperature differences. A combination of frontal area density, sheltering factor, wind speed, wind direction, opening location and temperature differences within a ventilation model is required to accurately predict ventilation rate.

Acknowledgements

Firstly I express great thanks to my supervisors Professor Janet Barlow and Doctor Vincent (Zhiwen) Luo who have offered invaluable guidance, great support, endless enthusiasm and considerable patience throughout this PhD. Great thanks are also due to Professor Sue Grimmond who stepped in as a third supervisor when everything went downhill. Thanks also to Professor Giles Harrison.

The practical part of this project was carried out in conjunction with the University of Birmingham and I have to thank Adam Robertson, Andrew Quinn and Roger Hoxey for sharing their knowledge of everything to do with the Silsoe site and the equipment. This project wouldn't have been possible without the small army of technicians that were involved in the full-scale field campaign, thanks go to: John Lally, Rosy Wilson, Ian Read, Andy Lomas and Mike Stroud from the University of Reading and Pete and John Richards from Solutions for Research. Thanks to Dr Paul Hayden, Allan Wells and Dr Paul Nathan from the University of Surrey for all their help with the wind tunnel experiments.

I am grateful to everyone involved in the REFRESH project for their contagious enthusiasm and dedication, notably Dr Marco-Felipe King and Professor Cath Noakes from the University of Leeds for the CFD modelling of the cube and invaluable input, Dr Steve Snow from the University of Southampton for his work on the social hierarchy of office environments and Dr Christos Halios for managing the data and help with coding. Thanks to Dr Dan Drew for helping with structuring and keeping an eye on me. Thanks to Professor Alan Robins from the University of Surrey for his expert guidance in analysing the wind tunnel results and to Tsuyoshi Sato from Kyushu University for help on researching the effect of wind direction on pressure coefficients. Thanks to all those involved in the ACTUAL project in helping me get my PhD off the ground.

Thanks to my friends and family, who gave me endless support, questions and encouragement along the way. Particular thanks to my parents for instilling the belief in me that your best is always good enough and Sam for discussing PhD woes at ungodly hours. Finally, thanks to the PhD students in the Department of Meteorology for their unwavering spirit and the sense of community that exists within the offices. My office mates of 2u08 were responsible for much needed entertainment and cake throughout the thick and thin.

Finally thanks to the ESPRC and the University of Reading for funding this project.

'If you fell down yesterday, stand up today.'
- H. G. Wells

Symbols Used

Table 0.1:: Symbols used throughout this thesis

Symbol	Meaning	Units
A	Area	m ²
a	Coefficient for equation 5.3	None
A_{eff}	Effective area	m ²
A_{fi}	Frontal area of a building	m ²
A_{in}	Inlet area	m ²
A_{pi}	Plan area of a building	m ²
A_r	Room area	m ²
A_{Ti}	Total area of an array	m ²
b	Crack length or width	m
c_d	Drag coefficient	None
C_a	External tracer gas concentration	ppm
C_d	Discharge coefficient	None
C_i	Indoor tracer gas concentration	ppm
C_p	Pressure coefficient	None
C_1	Coefficient	None
d	Displacement height	m
d_x	Depth	m
δp	Pressure difference	Pa
Δq_∞	free-stream dynamic pressure	Pa
δT	Temperature difference	°C
ΔT	External-internal temperature difference	°C
ΔT_h	Horizontal temperature difference	°C
ΔT_{iv}	Vertical temperature difference	°C
E	Tracer gas source	ppm
F	Ventilation parameter/ flow number	None
F_{Arch}	Archimedes number	None
Fr	Froude number	None

g	gravitational acceleration	$m\ s^{-2}$
Gr	Grashof number	None
H	Height	m
H_b	Height of bottom window	m
H_c	Height of crack	m
H_d	Height between two openings	m
H_m	Average building Height	m
H_o	Height of opening	m
H_t	Height of top window	m
k	Von Karman constant	None
k_c	Coefficient for equation 5.3	None
L	Obukhov length	m
L	Characteristic length	m
L_c	canopy drag length	m
L_R	Recirculation length	m
L_x	length	m
λ	Air changes per hour	h^{-1}
λ_f	Frontal area density	%
λ_p	Plan area density	%
λ_{WT}	Air changes per hour in wind tunnel	h^{-1}
μ	absolute viscosity	$N\ s\ m^{-2}$
n	Coefficient	None
N	Number of samples	None
ν	kinematic viscosity	$m^2\ s^{-1}$
p	pressure	Pa
p_0	Stagnation pressure	Pa
p_∞	Free stream station pressure	Pa
p_s	Static pressure	Pa
P_t	Stack pressure	Pa
ϕ	Monin Obukhov stability function for momentum	None
Φ_f	Wind tunnel blockage ratio	%
Q	Flow rate	$m^3\ s^{-1}$
Q_{all}	Total ventilation rate	$m^3\ s^{-1}$
Q_{cac}	Ventilation rate predicted by Caciolo (2010)	$m^3\ s^{-1}$
Q_{DP}	Ventilation rate predicted by De Gids and Phaff (1982)	$m^3\ s^{-1}$
Q_E	Full-scale ventilation rate	$m^3\ s^{-1}$
Q_f	Ventilation rate calculated by volumetric methods	$m^3\ s^{-1}$

Q_i	Infiltration rate	$\text{m}^3 \text{s}^{-1}$
Q_{iN}	Normalised infiltration rate	None
Q_{LH}	Ventilation rate predicted by Larsen and Heiselberg (2008)	$\text{m}^3 \text{s}^{-1}$
Q_N	Normalised flow rate	None
Q_{NF}	Normalised flow rate measured with flow techniques	None
Q_{NP}	Normalised flow rate measured with pressure techniques	None
Q_{NT}	Normalised flow rate measured with tracer techniques	None
Q_{N^w}	Normalised wind tunnel ventilation rate	None
$Q_{thermal}$	Thermal ventilation rate	$\text{m}^3 \text{s}^{-1}$
Q_w	Wind tunnel ventilation rate	$\text{m}^3 \text{s}^{-1}$
Q_{Wlocal}	Ventilation rate using the Warren and Parkins (1985) model (U_{local})	$\text{m}^3 \text{s}^{-1}$
Q_{Wref}	Ventilation rate using by the Warren and Parkins (1985) model (U_{ref})	$\text{m}^3 \text{s}^{-1}$
R	Specific gas constant	$\text{kg m}^{-2} \text{mol}^{-1} \text{K}^{-1} \text{s}^2$.
R^2	Coefficient of determination	None
Re	Reynolds number	None
ρ	Air Density	kg m^{-3}
Ri	Richardson number	None
σ_X	Error in X	Variable
t	Time	s
T	Wind tunnel air temperature	$^{\circ}\text{C}$
T^*	Ratio of the effective temperature at the opening to ΔT	None
T_e	External temperature	$^{\circ}\text{C}$
T_e	External temperature	$^{\circ}\text{C}$
T_i	Mean internal temperature	$^{\circ}\text{C}$
\bar{T}	Mean air temperature	$^{\circ}\text{C}$
θ_i	Incident wind direction	$^{\circ}$
θ_{local}	Wind direction in front of the cube	$^{\circ}$
θ_{ref}	Wind direction at 6 m	$^{\circ}$
TI	Turbulence intensity	None
U	Wind speed	m s^{-1}
u' or v'	Horizontal velocity fluctuations	m s^{-1}
u_*	Friction velocity	m s^{-1}

U_{10}	Reference wind speed at 10 m	m s^{-1}
$U_{channelling}$	Wind speed measured at the channelling mast	m s^{-1}
U_{intb}	Back internal wind speed	m s^{-1}
U_{intf}	Front internal wind speed	m s^{-1}
$U_{wind,lim}$	Wind speed threshold used by Caciolo (2010).	m s^{-1}
U_{local}	Wind speed in front of the cube at 3.5 m	m s^{-1}
U_m	Wind speed in the opening	m s^{-1}
U_{ref}	Reference wind speed at 6 m	m s^{-1}
U_b	Wind speed behind the cube at 3.5 m	m s^{-1}
U_L	Local wind speed	m s^{-1}
U_R	Reference wind speed	m s^{-1}
U_Z	Speed at height Z	m s^{-1}
v	Wind speed	m s^{-1}
V_R	Room volume	m^3
w'	Vertical velocity fluctuations	m s^{-1}
W	Width of a street canyon	m
W_x	Width	m
z	Height	m
z_H	Building height	m
z_0	Roughness length	m

Table 0.2:: Acronyms used throughout this thesis.

Acronym	Meaning
ACTUAL	Advanced climate technology: urban atmospheric laboratory
AIVC	Air Infiltration and Ventilation Centre
ASHRAE	American Society of Heating, Refrigerating and Air-Conditioning Engineers
BRE	Building research establishment
BRECSU	Building Research Establishment Conservation Support Unit
BUBBLE	Basel UrBan Boundary Layer Experiment
CFD	Computer Fluid dynamics
CIBSE	Chartered Institution of Building Service Engineers
COSMO	Comprehensive Outdoor Scale Model
DAPPLE	Dispersion of Air Pollution and Penetration into the Local Environment
DNS	Direct numerical simulation
LES	Large eddy simulation
MUST	Mock urban setting test
RANS	Reynolds Averaged Navier-Stokes
Refresh Project	Remodelling building design sustainability from a human centred approach
RSL	Roughness sub-layer
SBS	Sick Building Syndrome
UCL	Urban canopy layer
UHI	Urban heat island

Contents

1	Introduction	1
1.1	Aims	3
1.2	Structure of the thesis	5
2	Literature Review	6
2.1	Urban areas	6
2.1.1	Neighbourhood flow	7
2.1.1.1	Flow around a street canyon	7
2.1.1.2	Intersection	9
2.2	Simplification of urban areas	10
2.2.1	Flow around a simplified isolated building	12
2.2.2	Simplified urban arrays	14
2.2.2.1	Uniform cube arrays	14
2.2.2.2	Non-uniform cube arrays	17
2.3	Natural ventilation	18
2.3.1	Challenges of Natural ventilation	20
2.3.2	Natural ventilation in the urban environment	21
2.3.2.1	Case study of a naturally ventilated building in an urban environment	23
2.3.3	Measurement methods	23
2.3.3.1	Full-scale or in-situ measurements	24
2.3.3.2	Scale model	24
2.3.3.3	Computer fluid dynamics (CFD)	26
2.3.4	Buoyancy driven ventilation	27
2.3.5	Wind driven ventilation	30
2.3.6	Thermal and wind driven ventilation	31
2.3.7	Infiltration	32
2.3.8	Single sided ventilation	33
2.3.9	Empirical models for single sided ventilation	34
2.3.9.1	Warren and Parkins (1985)	34
2.3.9.2	Caciolo <i>et al.</i> (2011)	35
2.3.9.3	De Gids and Phaff (1982)	36
2.3.9.4	Larsen and Heiselberg (2008)	37
2.3.10	Cross ventilation	40
2.3.11	Pressure Coefficient (C_p)	43
2.3.11.1	Pressure coefficient within an array	46
2.3.11.2	Pressure coefficient databases	47
2.4	Conclusions	49
3	Full-scale field observations	51
3.1	Introduction	51

3.2	The site	51
3.2.1	Limitations of the site	53
3.3	The instrumented cube	54
3.3.1	Ventilation configurations	55
3.4	The Array	56
3.5	Experimental Configuration	58
3.5.1	Summary of Instruments	58
3.5.2	Wind and turbulence measurements using sonic anemometers	61
3.5.3	Background Meteorological measurements	62
3.5.4	Internal temperature measurements	63
3.5.4.1	Calibration and errors of the temperature measurements	65
3.6	Cube surface pressure measurements	66
3.6.1	Calibration and errors of the surface pressure measurements	69
3.7	CO ₂ concentration measurements	69
3.7.1	Internal measurements: K30 sensors	69
3.7.2	K30 calibration	71
3.7.3	LI-COR 7500 calibration	74
3.7.4	LI-COR 7500 and K30 comparisons	74
3.8	Ventilation measurement methodology	78
3.8.1	Tracer gas decay methodology	78
3.8.2	Choice of tracer gas	80
3.8.2.1	Errors in the tracer gas methods	81
3.8.2.2	Errors in tracer gas decay data processing	81
3.8.3	CO ₂ distribution for tracer gas releases	81
3.8.4	Tracer gas measurement procedure	82
3.8.4.1	Tracer gas release schedule	83
3.8.5	Pressure difference method	83
3.8.5.1	Errors in the pressure difference method	84
3.8.6	Flow through an opening	84
3.9	Treatment of data	85
3.9.1	Defining near-neutral stability	85
4	Wind tunnel simulations of the Silsoe array and exploration of the impacts of a limited array	87
4.1	Introduction	87
4.1.1	Motivations for wind tunnel work	87
4.2	Wind Tunnel methodology	88
4.2.1	Pressure measurements	90
4.2.2	Flow measurement	93
4.2.3	Flow uniformity	94
4.2.3.1	Logarithmic layer	95
4.2.3.2	Roughness length (z_0)	95
4.2.3.3	Turbulence intensity at building height	96
4.2.3.4	Comparison of the generated boundary layer to previous work	97
4.3	Sources of error in the wind tunnel	98
4.3.1	Wind Angle	98

4.3.2	Measurement errors	100
4.4	Overview of the arrays	101
4.4.1	Limitations of the wind tunnel model	105
4.5	Comparison of pressure coefficient results	106
4.5.1	Comparison to previous results for the isolated cube	106
4.5.2	Comparison to previously studied arrays	109
4.6	Effect of wind direction on the pressure coefficient	113
4.6.1	Isolated cube	114
4.6.2	Silsoe Array	119
4.7	Effect of the array on the measured pressure coefficient	126
4.8	Effect of the storage shed on pressure distribution	129
4.9	Differences between staggered and aligned nine-block arrays	131
4.10	Effect of increasing array size on C_p	136
4.10.1	Effect of extra rows behind the Silsoe array on the pressure coefficient	136
4.10.2	Symmetrical arrays	138
4.10.3	Comparison of the Silsoe array to the small symmetrical array	140
4.11	Wind tunnel data comparison to the AIVC model	141
4.12	Estimating ventilation rate	143
4.12.1	Results	145
4.13	Conclusions	146
5	Flow structure and wind pressure for a full-scale idealised building within an array	149
5.1	Introduction	149
5.2	External flow characteristics	150
5.2.1	Displacement height and roughness length	150
5.2.1.1	Turbulence intensity and the Isolated cube	153
5.2.1.2	Turbulence intensity within the array	154
5.2.2	Ratio of local wind speed to the 6 m reference wind speed	156
5.2.3	CIBSE wind prediction	164
5.2.4	Comparing local wind directions to reference wind directions	166
5.3	Influence of wind speed on pressure coefficient (C_p)	170
5.4	The effect of stability on C_p	175
5.4.1	Isolated cases	175
5.4.2	Array cases	179
5.5	Influence of wind direction on C_p	182
5.5.1	Isolated case	182
5.5.2	Low C_p values on the front face	183
5.6	Comparison of isolated and array C_p values	183
5.6.1	C_p differences between array and isolated cases for a range of wind directions in near-neutral conditions	185
5.7	Comparisons to published C_p values	188
5.7.1	ASHRAE	188
5.7.2	AIVC	189
5.7.3	ASHRAE and AIVC for the isolated cube	189
5.7.4	CIBSE	192
5.7.4.1	Isolated	193

5.7.4.2	Array	195
5.7.5	Conclusion	199
5.8	Full-scale comparisons to the scale model	199
5.8.1	Isolated cube	200
5.8.2	Array	205
5.9	Conclusions	209
5.9.1	Flow	210
5.9.2	Dual Behaviour	211
5.9.3	Pressure coefficient	211
5.9.4	Regulation Models	212
6	The effect of an array on natural ventilation rates	213
6.1	Introduction	213
6.2	Overview of the ventilation rate data	213
6.2.1	Thermal effects in the Silsoe cube	213
6.2.2	Buoyancy driven ventilation	218
6.2.3	Infiltration rates	223
6.3	Choice of wind speed for the volumetric flow method	225
6.3.1	Internal wind speed (U_{int})	227
6.4	Effect of different variables on ventilation rate	233
6.4.1	Comparison of tracer gas and pressure difference methods	233
6.4.2	Effect of wind direction on ventilation rate	234
6.4.3	Effect of wind speed on ventilation rate	237
6.4.4	Effect of turbulence intensity on mean ventilation rate	240
6.4.5	Effect of stability on ventilation rate	242
6.4.6	Effect of the array on ventilation rate	242
6.4.6.1	Single sided	243
6.4.6.2	Cross ventilated	243
6.4.6.3	Frontal area density and ventilation rate	245
6.4.7	Summary	247
6.5	Comparisons to the wind tunnel dataset	248
6.5.1	Comparison to all full-scale ventilation measurement methods	249
6.6	Comparisons to numerical models and pre-existing data	252
6.6.1	Comparisons to data from Straw (2000)	252
6.6.2	Comparison to Warren and Parkins (1985)	253
6.6.3	Creating a wind speed model for the Silsoe array data	255
6.6.4	Comparison to work by Caciolo <i>et al.</i> (2013)	256
6.6.5	Flow number and Archimedes number	257
6.6.6	Inter-comparisons with the Silsoe full-scale data	260
6.6.6.1	Isolated cube	261
6.6.6.2	Array	262
6.7	Conclusions	266
7	Conclusions and Future Work	269
7.1	Implications for industry	270
7.2	The wind tunnel dataset	271
7.2.1	Future wind tunnel work	272
7.3	The full-scale dataset	272

7.3.1	Future work with the full-scale dataset	273
7.3.2	Work beyond this dataset	273
A	Appendices	275
A	Structure of the Urban Boundary layer	275
B	Flow across large openings for equation 2.7	277
C	Coefficient of discharge (C_d)	279
D	Thermocouple image	281
E	Thermocouple Calibrations	281
F	Calibration of WXT520 temperature measurements	284
G	Pressure tap calibrations	286
H	K30 temperature tests	286
I	LI-COR calibration procedure	287
J	K30 fits to LI-COR data for background conditions	287
K	K30 fits to LI-COR data for decay calibration	288
L	CFD modelling	288
M	F-test and T-Test	289
	References	290

Chapter 1

Introduction

In 2014, 54 % of the world resided in an urban area and this is projected to rise to 66 % by 2050 (United Nations, 2014). Coupled with this, it is commonly estimated that 90 % of people's time in developed countries is spent indoors, either at home, at work, or travelling between the two (Klepeis *et al.*, 2001). The quality and range of frequented indoor environments play an important role in the physical as well as mental health and well-being of their occupants (Vardoulakis and Heaviside, 2012). Increased ventilation is said to improve occupant happiness and productivity (Mishra and Ramgopal, 2015), especially when inhabitants have a perceived degree of control over their environment (Raw *et al.*, 1990). However, the quality of the internal environment is strongly linked to the external environment, which for many is an urban area.

A single building will modify the surrounding environment by changing the moisture levels through decreased drainage and a lack of vegetation, change the temperature via the thermal storage properties of the construction materials and will alter the wind flow though the effects are dependent on the building's location, orientation and construction materials (Ng *et al.*, 2011). A city concentrates these properties, with an urban environment being generally warmer, drier and more sheltered from the wind at ground level (Grimmond and Oke, 1999). An example of this is the Urban Heat Island (UHI) effect, where the temperature in an urban environment is greater than that in the surrounding rural area (Arnfield, 2003).

Ventilation systems are designed to meet two key criteria: to maintain adequate indoor air quality and to ensure the thermal comfort of the occupants with the most effective type of ventilation system being dependent on the building's purpose, occupants and external conditions (CIBSE, 2005). Thermal comfort and air quality are also linked to lighting comfort and acoustic comfort, though conflicts between the differing requirements for each category are likely. To ensure an adequate flow of fresh air (assuming external air is 'fresher' than indoor air) a rate of 4-5 l s⁻¹ per person is suggested (CIBSE, 2005; Olesen, 2015). However, ventilation requirements vary depending on the type, function and occupants of the building, with fragile persons such as the young and elderly requiring a higher ventilation rate (Olesen, 2015). Natural ventilation, such as opening windows and doors, is considered a more sustainable option than mechanical ventilation but is not without flaws. Natural ventilation, the focus of this thesis, works best when there is reasonable exposure to the wind and a temperature difference be-

tween the internal and external environments exists.

However, the effects of an urban area on the local wind flow and internal and external temperature differences are, as a whole, not well understood. This is further complicated by the urban area being formed of a variety of types of areas, all of which will have differing effects on the environment. This complexity makes it difficult to predict the urban wind flows in the early design stages of a building, reducing the uptake of natural ventilation measures in favour of mechanical ventilation, which is less effected by the external environment (Belleri *et al.*, 2014). As conditions change, the building's ventilation rate will also change, with flow potentially reversing under extreme conditions (CIBSE, 2005).

Other things to consider are occupant behaviour, building materials, street furniture and the locations of the openings (Figure 1.1). Historically, studies of indoor and outdoor air movement have been undertaken separately and only in recent years have the two been considered in a dynamic equilibrium within an urban area.

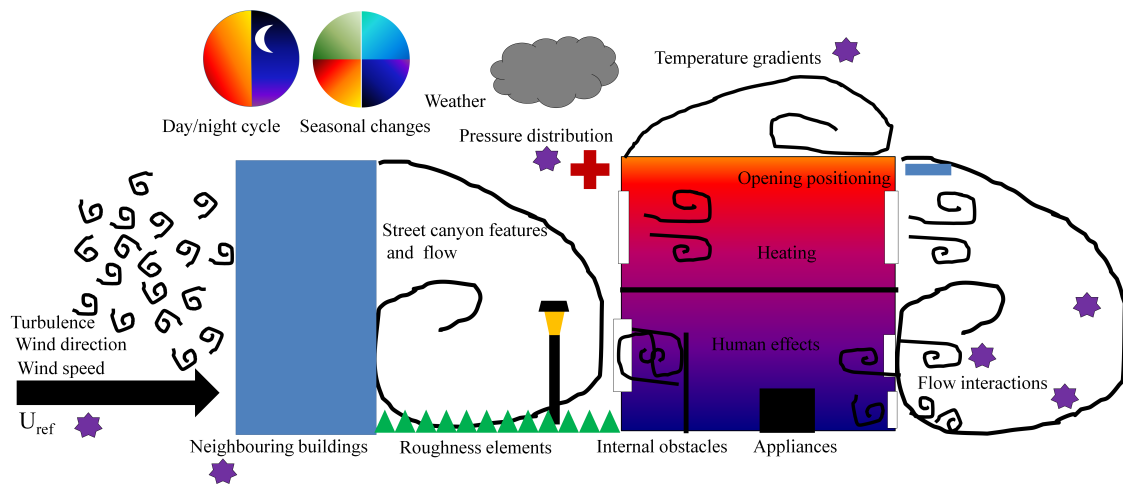


Figure 1.1: Schematic of some of the considerations required for natural ventilation with average flow features denoted by black lines. Purple stars denote variables discussed in this thesis.

UK buildings are built to strict government enforced regulations, which set minimum amounts of ventilation requirements dependent on building type. New builds make up a small proportion of the building stock with 62 % of English housing stock being built before 1965 and 35 % built before the Second World War (Allen and Hicks, 1999). Houses designed for earlier time periods may have negative effects on their current occupants, due to a change of building surroundings and as such may not meet current guidelines on ventilation (Allen and Hicks, 1999).

Traditionally, residential buildings in the UK have been naturally ventilated, with the habits and behaviours (such as opening the windows or heating their homes) of the occupants reflecting the fact that they have control over their ventilation (Etheridge, 2015). The drive towards energy efficiency during the 1990's in the UK led to the increased use

of natural ventilation in non-residential buildings, with the construction methods being improved in order to reduce the previously high levels of infiltration: unwanted airflow through cracks and joins (Etheridge, 2015). The design and location of a building's ventilation will also have an effect on the airflow both in and around the building and potentially on other buildings meaning the building's environment should be considered at all design phases.

As most of people's lives are spent indoors in buildings which are likely to have not been built for external urban conditions, it is of paramount importance to gain an understanding of the coupling between internal air and the building's surrounding environment. Though substantial research of urban areas has been undertaken, they are far from being fully understood due to the diversity of the characteristics (Arnfield, 2003).

1.1 Aims

The aim of this thesis is to understand how a simplified urban area may affect the natural ventilation of a simplified building over a wide range of atmospheric conditions. Engineering and meteorology methodologies are combined to obtain an improved understanding of how atmospheric stability, wind speed, temperature and wind direction effect the surface pressure field and the ventilation rate of a simplified building (Figure 1.1).

The use of a simplified building, in this case a cube of 6 m^3 (Chapter 3), allows comparison with similar arrays created in wind tunnel and CFD studies and reduces some of the complexities of working with real buildings in an urban environment. The openings within the cube are themselves simplified, with the internal environment being free from obstacles commonly found in true buildings. Three ventilation layouts are tested: infiltration, single sided ventilation and cross ventilation (Section 2.3). These are influenced by different conditions allowing for an understanding as to how the surroundings of a building influence the different driving mechanisms of ventilation and how this affects the internal environment and the external environment itself, as external flow will be influenced by internal flow exiting the cube.

For comparison to previous studies, a staggered array is created with a packing density of approximately 25 %. A wind tunnel study of the array is undertaken to allow for comparisons between the scales and to expand the array, to further the understanding of the effects of the size of the array on the pressure coefficient of a building.

The focus of this thesis is below the neighbourhood scale, with a focus on one simplified building, its ventilation and effect of the simplified neighbouring buildings (Figure 1.2). The neighbouring buildings will be arranged in such a way that the flow around the elements will interact. The literature review (Chapter 2) will cover studies undertaken in both ventilation and in urban areas for this scale range and for both simplified and

realistic buildings. The structure of the urban boundary layer is described in Appendix A.

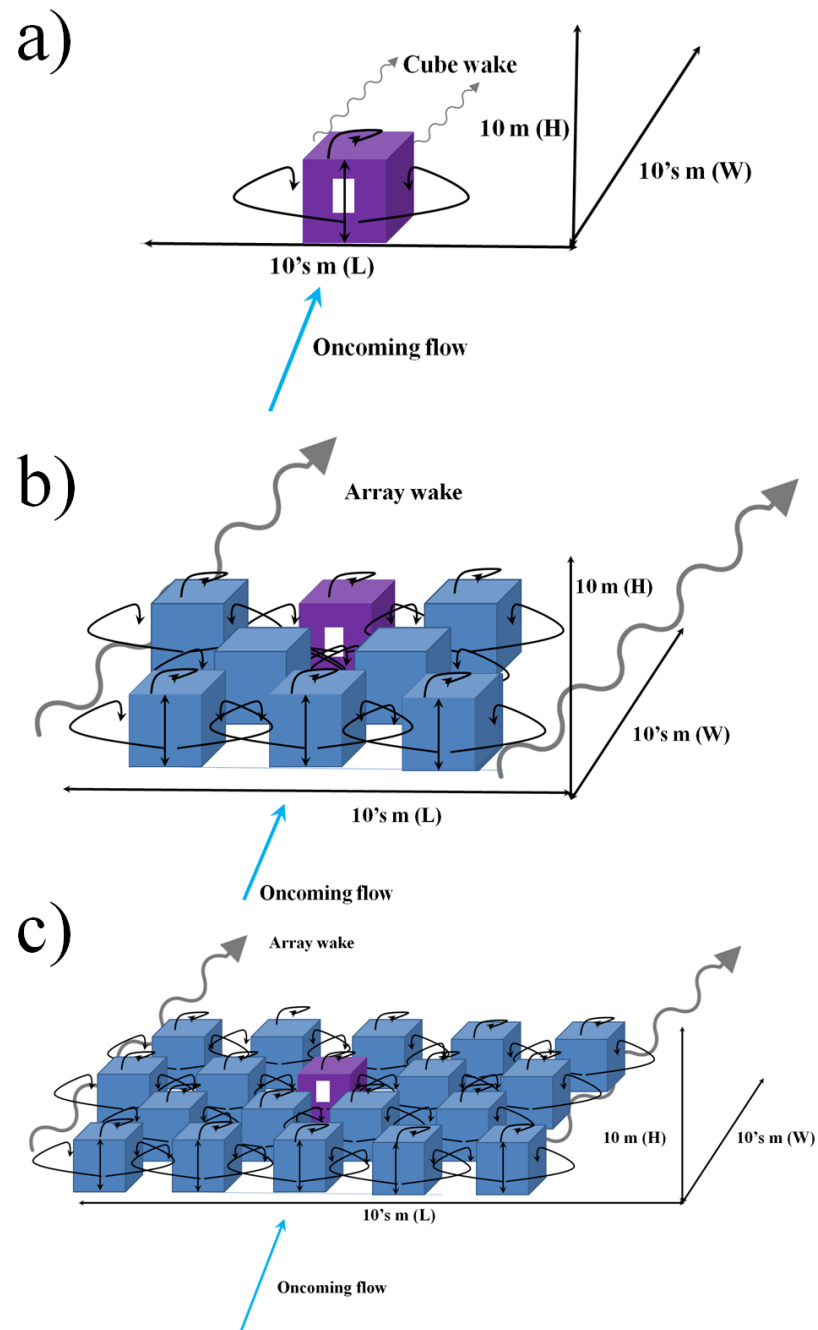


Figure 1.2: Simplified representation of a) an isolated building with ventilation b) a limited array surrounding the building of interest and c) an expansive array surrounding the building of interest. Black arrows represent simplified flow patterns caused by the buildings.

1.2 Structure of the thesis

First the extent of previous research into natural ventilation is reviewed (Chapter 2). The methodology and instrumentation used in the field campaign are described (Chapter 3) along with the wind tunnel (Chapter 4). The effects of an expanding array in a more controlled environment are also discussed in Chapter 4. Chapter 5 focuses on the pressure coefficient results, comparing them to previous models, the wind tunnel model and inter-comparing the array and isolated cube cases.

Chapter 6 follows a similar structure to Chapter 5 but focuses on the ventilation rate, the methods used to measure and calculate the ventilation rate and how the results of different empirical models compare to the measured values for the larger, more varied field campaign data set. The conclusions drawn from the work and suggestions for further work (Chapter 7) complete the thesis, with symbols and acronyms used being listed in Chapter .

Chapter 2

Literature Review

2.1 Urban areas

The study of atmospheric processes is traditionally split into different horizontal scales from the human scale to a global scale (Figure 2.1).

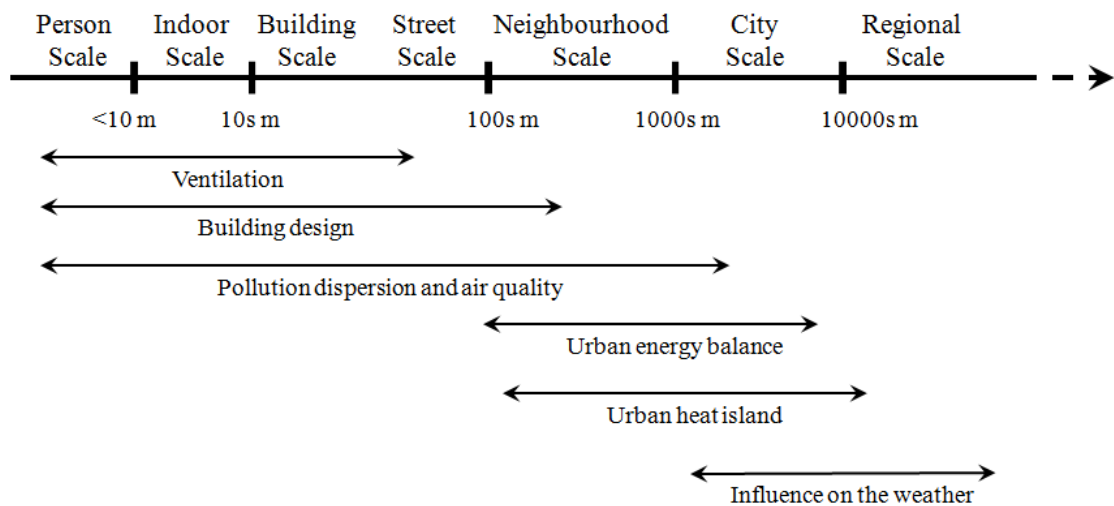


Figure 2.1: Schematic of the different horizontal scales within a city, and the scale span of some urban meteorology fields of study. Adapted from Kaimal and Finnigan (1993).

The urban area may perturb regional flow, causing deceleration and deflection of the oncoming flow. Urban areas also alter the surface-energy budget due to having relatively large obstacles made of different materials and often less vegetation when compared to the surroundings. The variations in flow and dispersion around individual buildings or groups of similar buildings are mostly averaged out at the city scale (Britter and Hanna, 2003).

A city is likely to encompass a large variety of different land uses, building types and spacing. Numerous field campaigns e.g. DAPPLE (Arnold *et al.*, 2004), ACTUAL (Drew *et al.*, 2013) and BUBBLE (Rotach *et al.*, 2005) have been performed in different cities, however research within cities is expensive. The results obtained are often difficult to interpret due to a lack of basic understanding of the turbulent flow characteristics over groups of buildings or even for simplified buildings (Coceal *et al.*, 2007b). Urban areas are complex due to the large amount of factors which may influence flow behaviour as

well as the variation in the design and layout of cities across the globe.

Urban areas are formed of neighbourhoods, made up of different buildings, making it extremely difficult to generalise the findings for an urban area due to the large amount of variables which can potentially affect the flow. These include: the relative position of one building to the next, building geometry, building density, traffic, regional settings and the statistics of the approaching flow (Figure 1.1). There is also little research into how air from within buildings influences the local flow patterns around the building and its surroundings.

The flow field downwind of an urban area relies heavily on the geometry and positioning of the buildings within the array. The wake downwind is made up of two parts: flow that has travelled through the array, often referred to as the bleed flow and flow displaced by the array (Robins and Macdonald, 2001). Unless the bleed flow is very weak, either due to extremely tight obstacle spacing and flow skimming (Section 2.1.1.1), the recirculation directly behind the array is a complex combination of recirculation directly behind the obstacles and the bleed flow leaving the array (Robins and Macdonald, 2001). Over enough distance, a wake similar to that seen for an isolated obstacle is formed (Figures 2.2, 2.5).

To remove some of the complexity, the urban area is often simplified, either in layout or building form. Often one scale is researched in detail and is commonly parametrized to assist interpretation at the above scale (Britter and Hanna, 2003).

2.1.1 Neighbourhood flow

The neighbourhood scale (1000 m to 10^4 m) has a varied urban geometry and high-detail computational and wind-tunnel studies are feasible (Xie, 2011). The flow features for an isolated building (Section 2.2.1) are also largely present for a group of buildings, though interactions between flow around individual buildings effect the significance of the features, which is dependent on building spacing (Robins and Macdonald, 2001). The separation distance required in order for the different behaviours to be observed is dependent on the geometry and orientation of the buildings as well as the approaching flow (Robins and Macdonald, 2001). For stable conditions these thresholds are likely to be larger and for unstable conditions, smaller (Section 3.9.1) (Robins and Macdonald, 2001). Neighbourhood areas can be broken down into units such as ‘street canyons’ and ‘intersections’.

2.1.1.1 Flow around a street canyon

One of the repeated elements within an urban area is the urban street canyon: an area that consists of two parallel buildings with a gap between them (Nakamura and Oke, 1988). A street canyon can be characterised by the dimensionless height to width ratio

H_m/W , where W is the building spacing and H_m is the average building height (Figure 2.2, Chapter). The dynamics within street canyons are controlled by the recirculating wakes of the upstream buildings caused by flow separation. The behaviour of the flow is relative to the direction of the oncoming wind.

If local flow is perpendicular to the street, three flow regimes can be identified (Figure 2.2). For large height to width ratios ($H_m/W > 0.65$) there is a single recirculation within the street and little exchange with the air above, known as a skimming flow. For $H_m/W < 0.3$, each building and its effects can be considered separately as an isolated roughness element. For $0.3 < H_m/W < 0.65$, the wake of one building interferes with the flow over the next (wake interference flows). The canyon vortex structure is controlled by the aspect ratio of the canyon and is strongly influenced by the geometry of the surrounding buildings (Offerle *et al.*, 2007).

For wider canyons, a ventilation region may develop against the leeward wall, whilst in narrower canyons a counter-rotating vortex may form at street level (Liu *et al.*, 2004). The flow within street canyons is asymmetric and unsteady, with a stronger, more concentrated downward flow on the downwind wall and a weaker, more extensive upward flow on the leeward wall (Britter and Hanna, 2003). Within the street canyon, even within the most stable conditions, flow within the central vortex of a street canyon changes rapidly, with the vortex existing for wind angles $\pm 60^\circ$ to the perpendicular flow of the canyon (Eliasson *et al.*, 2006).

When buoyant forces are included within a street canyon, significant changes to the flow fields occur if there are high surface temperatures and low Reynolds numbers (Re , the ratio of inertial forces to viscous forces, Section 5.8) for wind tunnel measurements (Allegrini *et al.*, 2013). Linked to temperature, the central eddy of a street canyon becomes stronger in unstable conditions and weaker in stable atmospheric conditions (Section 3.9.1) (Uehara *et al.*, 2000).

The pressure pattern around a building is linked to the local flow structure, meaning it is to be expected that ventilation rates will be sensitive to the surrounding building morphology, wind and buoyancy forces. This suggests that the stability of the atmosphere (Section 3.9.1) needs to be considered when positioning the openings of buildings in order to fully understand the local flow.

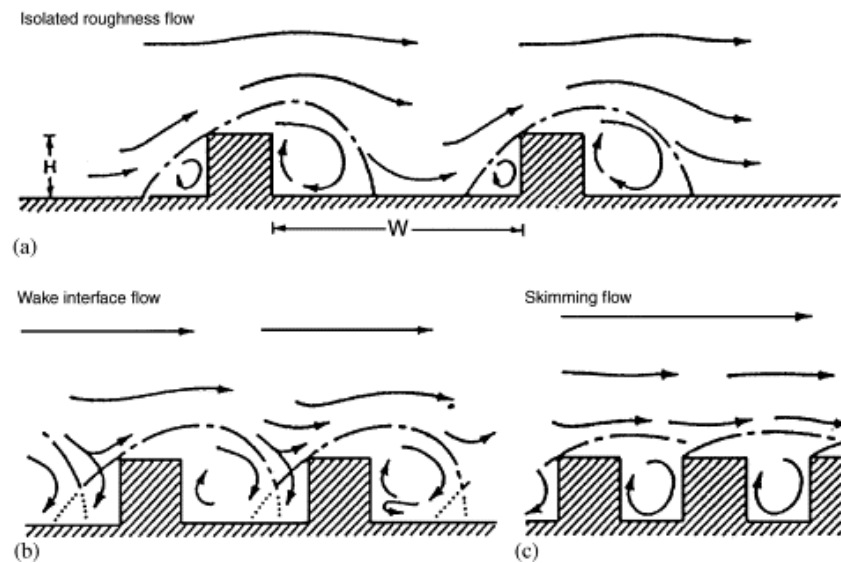


Figure 2.2: Flow regimes associated with different urban geometries. a) Isolated roughness flow, b) Wake interface flow c) Skimming flow. Source: Oke (1988). Notation described in the text above.

2.1.1.2 Intersection

An intersection, like a street canyon, can be treated as an ‘urban unit’ and modelled in similar ways: by simplifying the complex urban geometry down into blocks (Section 2.2). The geometry of real street intersections is a combination of the geometrical characteristics of the street, size and shape of the intersection, roof types and building wall shapes. For an irregular array, or a real urban area, there will be regions where the flow is displaced, accelerated, channelled, diffused, deflected, stagnated or recirculated, dependent on the shape and size of the buildings.

When the flow is not parallel to either street there are flow exchanges between the streets, helical street canyon vortices, mixing due to building wakes and flows due to the horseshoe vortex around the largest building (Figure 2.3). The flows created by the taller building mix the external air into the lower canopy and draw air from the canopy, especially up the tall building’s rear face (Robins and Macdonald, 2001).. The offset wind then modifies the street canyon vortex by disturbing the recirculation vortex, leading to a change in flow patterns (Longley *et al.*, 2004).

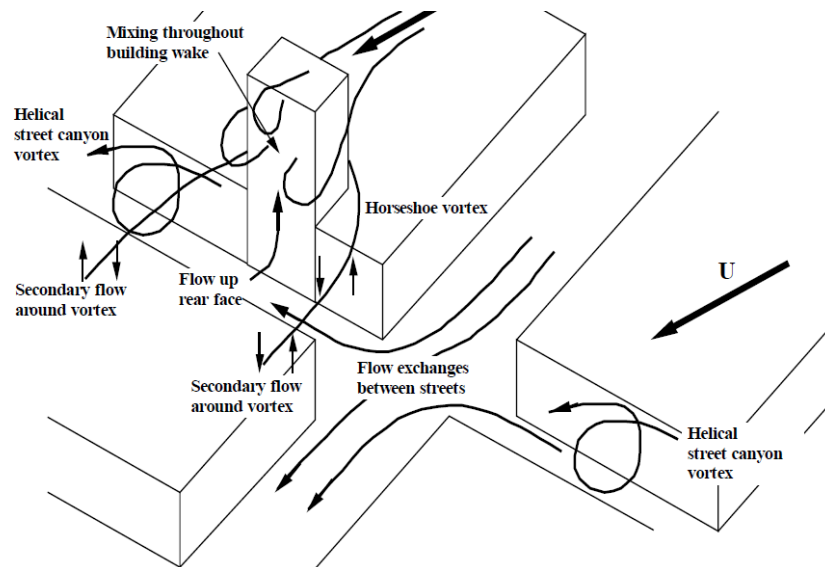


Figure 2.3: Flow field at a simplified street intersection with a tall building illustrating changes between the streets and additional mixing processes caused by the tall building. Arrows represent average flow patterns around the intersection. Source: Robins and Macdonald (2001).

Another source of complexity is the positioning of buildings relative to each other. The air exchanges at intersections are not confined to the immediate vicinity of the intersection and spread down the streets, influencing the flow in other intersections and street canyons (Robins *et al.*, 2002).

Measurements taken at a real intersection (Marylebone Road and Gloucester Place) in London, UK as part of the DAPPLE project highlight that despite complex building geometry in the vicinity of the intersection, measurements taken in the adjoining streets show that the behaviour of flow is similar to that observed in idealised two-dimensional street canyons (Figure 2.2) (Dobre *et al.*, 2005). The main large-scale features were an across-street recirculating vortex and along-street channelling. Asymmetries in the local building geometry around the intersection coupled with small changes in the background wind direction (changes in the 15 minute mean of 5° to 10°) have a profound influence on the behaviour of intersection flow patterns (Balogun *et al.*, 2010).

2.2 Simplification of urban areas

Simplified models lack the finer detail of an urban area such as presence of small architectural features, foliage, street furniture and structures (e.g. bridges). Urban areas can be simplified into arrays of rectangular buildings described by a set of morphological parameters detailing the building size and spacing (Figure 2.4) (Barlow and Coceal, 2009).

Arrays of buildings are often simplified down into arrays of cubes or cuboids, which

whilst making the basic mechanisms more obvious, neglect the effect of the smaller components of the urban area, such as vegetation or street furniture. Arrays of cubes are also used in much larger scales of meteorological models to represent the urban area in order to model the boundary layer adjusting to a new surface and can also be used at these smaller scales (Macdonald *et al.*, 1998).

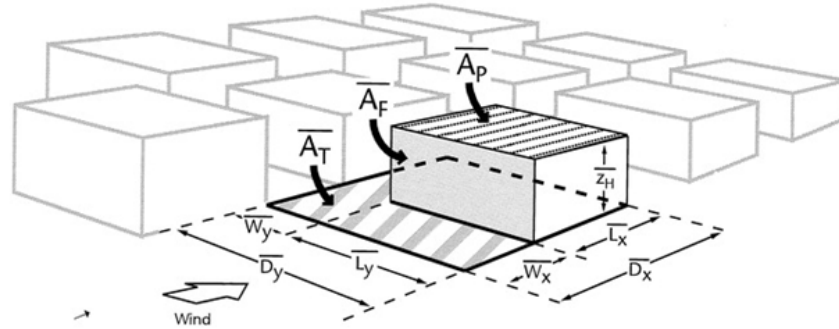


Figure 2.4: Schematic of the morphological parameters used for describing and characterising an urban area. Notation is described in the text. Source: Grimmond and Oke (1999).

Each building has a height H (shown as z_H), a stream wise (along wind) and span wise (cross wind) dimension labelled L_x and L_y respectively, with the spacing values between the buildings being W_x and W_y (Figure 2.4). Two parameters used to describe the area covered by buildings are the plan area density (λ_p) and the frontal area density (λ_f). λ_p is the ratio of the total area covered by roughness elements, in this case buildings, compared to the total plan area whereas frontal area density is the ratio of the total frontal area of the roughness elements compared to the total plan area that they occupy. λ_f is directionally dependent due to the cross section of a building varying with azimuth angle.

λ_p is given by:

$$\lambda_p = \frac{\sum_i A_{pi}}{\sum_i A_{Ti}} \quad (2.1)$$

where A_{pi} is the plan area for each individual building, and A_{Ti} is the total plan area per roughness element. These are calculated using:

$$A_{pi} = L_{xi}L_{yi} \quad (2.2)$$

$$A_{Ti} = (W_{xi} + L_{xi})(W_{yi} + L_{yi}) \quad (2.3)$$

λ_f is given by:

$$\lambda_f = \frac{\sum_i A_{fi}}{\sum_i A_{Ti}} \quad (2.4)$$

with A_{fi} being the frontal area of each building being given by its length perpendicular to the field of view from that building direction multiplied by H .

λ_f becomes difficult to calculate when the oncoming flow is not perpendicular to the obstacles, or if A_{fi} is not easy to measure (Millward-Hopkins *et al.*, 2011). Padhra (2010) describes in detail the derivation of a set of formulae describing the frontal area density as a function of the wind direction for a set of randomly-arranged cuboid-shaped obstacles.

2.2.1 Flow around a simplified isolated building

At the building scale, wind velocity becomes dominated by the morphology of local features, such as street layout and street furniture. As wind flows around structures, pockets of stagnant air may develop alongside areas of intensified wind-speeds (Ng *et al.*, 2011). Flow patterns depend on the building's surroundings, the direction of the wind and the shape of the building. Whilst detailed elements of the building's design will have small impacts on the flow around the building, the building's form is often simplified down to a cuboid devoid of small features (Figures 1.2, 2.5).

For an isolated cuboid in perpendicular flow air approaching the front is slowed, and is brought to rest at approximately two thirds of the building height, known as the stagnation point (Figure 2.5). Flow above this point is pushed over the roof. The flow separates from the edge of the roof, but depending on the length of the roof, may reattach further downstream (Robins and Macdonald, 2001). Flow below the stagnation point streamline is forced to move down the front face until it reaches the ground, causing an upstream recirculation to form. The turbulence caused by an obstacle is large scale dominated and not very dependent on the small scale viscous forces on the body surfaces (Xie and Castro, 2006).

Behind the building, a complex recirculation region forms due to the separation of flow from multiple cube edges (Figure 2.5). The size of this recirculation region is dependent on the size and orientation of the obstacle. There are also vortices present due to re-circulations at each corner of the leeward face.

If the approach flow is not oblique to the front wall e.g. at 45° (Figure 2.5c), two roof vortices may be generated. This roof vortex system mainly occurs when the upwind face is nearly normal to the wind, but reduces if the flow is skewed more than 15° (Robins and Macdonald, 2001). The flow begins to split around the upwind corner and a strong trailing vortex is shed, creating low local surface pressures: a common cause of roof damage in strong winds (Hall and Spanton, 2012). This also modifies the surrounding airflow and affects the separation regions. Changing the corner shape or roof shape can largely eliminate the trailing vortex (Robins and Macdonald, 2001).

The horseshoe vortex is enhanced or diminished by upwind structures, though this

depends on their relative size to the building (Hall and Spanton, 2012). A horseshoe vortex around wide structures often shows some instability in turbulent shear flows, with trailing vortices occasionally shedding from the main vortex and passing over the obstacle (Hall and Spanton, 2012).

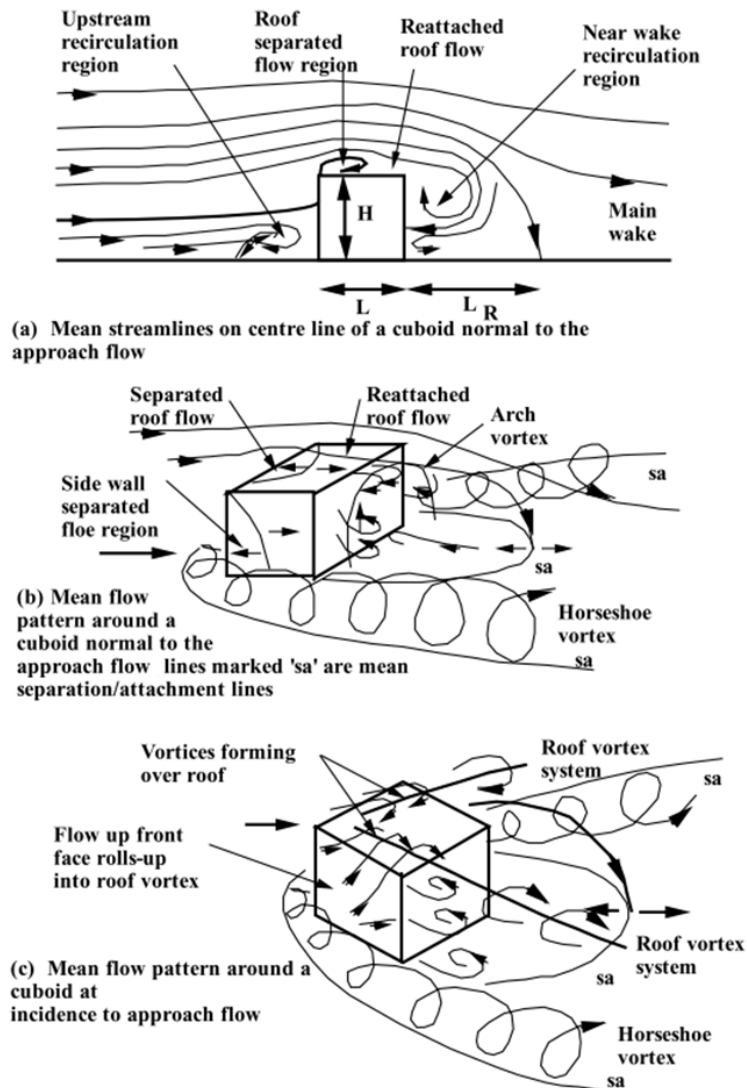


Figure 2.5: Flow around an isolated cube, showing flow (black arrows) approaching both perpendicular and at 45° to the front wall. Source: Robins and Macdonald (2001).

A building which is naturally ventilated is likely to have openings, leading to the structure of the flow being altered due to the difference between the internal flow and the external flow. However, there is little research into the effect of openings on the external flow.

2.2.2 Simplified urban arrays

Model experiments, both scale and full-scale (Sections 2.3.3.1, 2.3.3.2), are free of many of the uncertainties found in real cities related to spatial variations in material, geometry, and land use, but include realistic synoptic conditions. The use of cubes creates a simplified model of an urban environment and allows for the results obtained to be adaptable, rather than for a specific location. Cube arrays allow the physical processes within and above the roughness sub-layer to be studied with relative ease. By working with a uniform area, the results are easier to interpret.

For widely spaced cuboid arrays (a separation of $> 10 H_m$) in a neutral flow each building is effectively isolated, effectively experiencing the undisturbed boundary conditions, similar to the behaviour of street canyon flows for a $H_m/W < 0.3$ (Section 2.1.1.1). For separations of $5 H_m < x < 10 H_m$, the flow conditions are perturbed by buildings upstream. For separations $< 5 H_m$, the wakes will directly interact (Jia *et al.*, 1998). Flow will also begin to skim over densely packed buildings of similar height (Cheng *et al.*, 2007).

Work using non-uniform cube arrays is less common than uniform cube arrays, though the topic is rapidly expanding, partially driven by the need to know when the presence of a large building within an urban array overrides all other processes. The dynamics over homogeneous and heterogeneous urban canopies differ substantially (Belcher *et al.*, 2012).

2.2.2.1 Uniform cube arrays

Uniform cube arrays are arrays of cubes with the same dimensions, organised into aligned or staggered arrays (Figure 2.6). Staggered cube arrays (Figure 2.6b) provide greater drag to the flow than the aligned cube arrays (Figure 2.6a) under the same flow conditions (Zaki *et al.*, 2012).

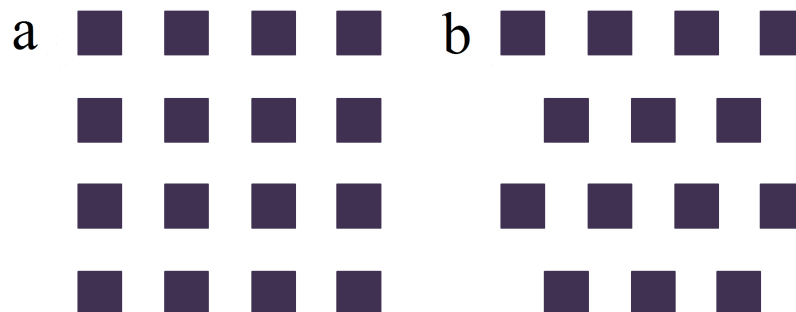


Figure 2.6: Schematic of a) an aligned array b) a staggered array of cubes.

The effect of staggered arrays with different packing densities (6.25 % to 25 %) on the urban boundary layer was researched by Cheng *et al.* (2007) using a wind tunnel

model using sharp edged wooden cubes of side 20 mm as roughness elements. For an area with a sufficiently low coverage of buildings ($\lambda_p = 6.25\%$), the roughness sub-layer can extend over a large portion of the total boundary layer depth, though this depth is dependent on wind direction (Cheng *et al.*, 2007).

DNS and LES simulations (Section 2.3.3.3) by Claus *et al.* (2012) of an aligned and staggered array respectively, show that changing the wind direction over an array can increase the drag force imposed by the surface by up to 300%. A change in wind direction will also change the variables used to characterise the wind profile e.g. the roughness length (z_0) can be altered by up to a factor of four for a 45° wind rotation (Claus *et al.*, 2012).

For a staggered array, the flow becomes a lot more complex than an aligned array of equivalent λ_p due to interacting wakes (Coceal *et al.*, 2006). For the aligned array fast flow is seen in the unobstructed regions or streets, with a strong reverse flow seen in the region in between successive cubes between rows. Due to the larger distance between cubes in the staggered array (Figure 2.6b) the flow behaves differently, with a notable absence of an instantaneous recirculation behind the cubes and large differences in the structure of the flow at different heights (Coceal *et al.*, 2006).

DNS (Section 2.3.3.3) simulations of flow around a staggered array highlight large local variations in flow statistics near corners or on the edges of streets, caused by the distortion of the mean flow due to the enhanced turbulence levels around a building (Coceal *et al.*, 2007a). The instantaneous flow was found to be much more complex than the mean flow, with a strong inhomogeneous wind field (Coceal *et al.*, 2006). The findings of Coceal *et al.* (2006) highlight the need to consider the 3D behaviour of the flow and that the mean picture of the flow is not always accurate, especially in wake regions.

Macdonald *et al.* (1998) created a 1:10 scale aligned array of approximate cubes ($\lambda_p = 16\%$). The cubes were made of galvanised steel with a height of 1.12 m and were compared to a 1:100 scale wind-tunnel model to research plume dispersion around urban buildings. Compared to the wind tunnel, there was more scatter in the plume size in the field results and larger scales of turbulence were observed (Macdonald *et al.*, 1998). Overall the dispersion patterns (flow field and concentration measurements) were qualitatively and in most cases quantitatively the similar to those from the wind tunnel (Macdonald *et al.*, 1998).

Other large scale arrays of cubes include the COSMO (Comprehensive Outdoor Scale Model) facility (Figure 2.7): an aligned array of 512 1.5 m concrete cubes (Inagaki and Kanda, 2008) and the MUST (Mock Urban Setting Test) facility made of shipping containers in Utah, USA (Yee and Biltoft, 2004).

The COSMO cubes (Figure 2.7) are hollow, with thin concrete shells making them similar in thermal properties to urban areas positioned on a $50 \times 100 \text{ m}^2$ flat concrete base and are located in Saitama, Japan. The area density and alignment of the concrete blocks

are variable. Coherent structures were observed over the COSMO array, suggesting that air exchange over a city might be controlled by both the local environment (location and roughness of buildings) and by the much larger scale motions developed above the canopy layer (Inagaki and Kanda, 2010). Adding vegetation to a street canyon within the COSMO array reduced the canyon wind speed, with increasing levels of vegetation having a larger effect, especially if trees were planted normal to the prevailing wind direction (Park *et al.*, 2012). This reduction in wind speed due to vegetation will likely reduce the ventilation rate of nearby buildings and will also create seasonal variance, depending on the type of vegetation.



Figure 2.7: Photograph of the COSMO site taken from the northwest side. The cubes are 1.5 m high. Source: Inagaki and Kanda (2008).

The work at the COSMO facility highlights a need for all scales of flow to be considered when researching within the urban area. Not including vegetation in models of an urban area may lead to an overestimation of the wind speed within a street canyon and thus an over estimation of the ventilation potential of buildings. This effect may extend to other types of street furniture, which are often neglected in simplified models of the urban area.

The MUST experiment was a 12 by 10 aligned array of shipping containers (each 12.2 m in length, 2.42 m in width and 2.54 m high) were spaced to establish a wake interference flow regime typical of some U.S. and European urban areas (Figure 2.8) (Brown *et al.*, 2006). The clear skies and weak synoptic conditions that prevailed resulted in a dataset with largely stably-stratified atmospheric conditions outside of the building array, setting the MUST dataset apart from scale models where neutral conditions are mostly used (Pardyjak *et al.*, 2002). A persistent warm thermal plume in the wake of the building and a well-mixed wake with strong stable stratification above the building height associated with the upstream flow were identified (Pardyjak *et al.*, 2002).

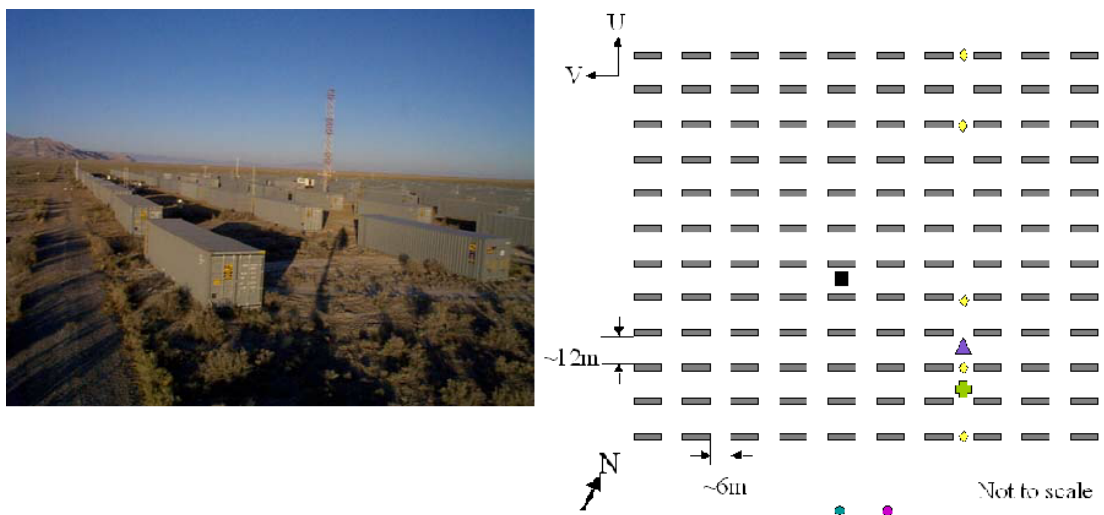


Figure 2.8: Photograph of the MUST array taken from the SE corner of the array and the plan view of the MUST array. Source: Brown *et al.* (2006).

More work into unsteady flow, the effect of λ_p , effect of wind direction and the effects of building height is required in order to fully understand the differences and similarities between uniform and realistic urban arrays. The uniform array is a strong starting point, allowing for flexibility and benchmarking against pre-existing results and being applicable to larger scale models, such as numerical weather prediction. However, though wind tunnel and scale models of uniform arrays have strong similarities, the effect of the larger scales of turbulence from wind tunnel models and CFD (Sections 2.3.3.2 and 2.3.3.3) can cause some features of the flow to be misrepresented (Macdonald *et al.*, 1998).

2.2.2.2 Non-uniform cube arrays

The non-uniformity of the urban area causes a large, uneven exchange of energy, momentum and material within the atmosphere over the area. Comparing vertical wind profiles taken from 107 LES runs of different districts in Tokyo and Nagoya with profiles 23 for conventional, simplified arrays of buildings highlight that real urban surfaces present differences in the bulk flow properties compared to simplified arrays (Kanda *et al.*, 2013). Simplified street networks were found to enhance flow near ground level and interference of wakes from individual buildings on the overall flow pattern was reduced (Kanda *et al.*, 2013). Varying the building heights, even in simple arrays, produced results that were closer to those for real urban surfaces, suggesting that the variability of the building heights is more relevant than the complexity of the streets for parametrizing the urban roughness for the log layer above the buildings (Kanda *et al.*, 2013).

Xie and Castro (2006) modelled the same staggered array as Coceal *et al.* (2007a) and Cheng and Castro (2002) using LES, only with varied building heights, finding little difference in the spatial averages and spatial variances for the flow in the region below

mean building height when compared to the uniform array. An array with a variable building height enhances vertical momentum exchange and increases turbulence in the canopy, leading to efficient mixing (Pascheke *et al.*, 2008). The wakes of the taller individual roughness elements increase upwards movement of the flow, with the larger building having an effect on the flow around other nearby roughness elements (Pascheke *et al.*, 2008).

For an array with a high vertical randomness the drag coefficient increases with increasing λ_p (7.7 % to 48.1 %) due to the taller buildings being separated by larger distances (Zaki *et al.*, 2010). This makes it difficult for a skimming flow regime to form over urban areas of variable heights. This suggests that vertical randomness leads to a thicker roughness sub-layer and that the inertial sub-layer may not exist over these arrays if the boundary layer is shallow or the fetch is short (Cheng and Castro, 2002) (Rotach, 1999). For an array with horizontal variability in the positioning of the buildings, the peak values of the drag coefficient and the λ_f condition for the peak drag coefficient value increase in the order of staggered arrays, horizontally random arrays and 45 ° rotated square arrays (Zaki *et al.*, 2010). The horizontally random array could be more streamlined than a standard staggered array (Figure 2.6b) and buffer than a 45 ° rotated square array (Figure 2.6a).

The study of non-uniform cube arrays requires more randomisation in terms of the positioning of the buildings, size of the array and rotation of the buildings (Cheng and Castro, 2002). Non-uniform arrays highlight the greater effects of taller buildings on the transfer of momentum and flow patterns and enable a unique insight into the effects of individual buildings on the overall flow pattern (Pascheke *et al.*, 2008). As for uniform arrays, the effect of changing the wind direction should also be considered. Due to the large number of variables already present within a non-uniform array, the experiments are often isothermal and thus neglect the effect of buoyancy on the turbulence of the flow and the effect of the buildings on the local temperature.

2.3 Natural ventilation

From a technological point of view, natural ventilation can be classified into ‘simple’ and ‘high-tech’. The latter are computer controlled and may be coupled with mechanical ventilation systems, known as hybrid or mixed mode systems. ‘High-tech’ natural ventilation may have the same limitations as mechanical ventilation systems, but have the benefits of both mechanical and naturally ventilated systems (Atkinson *et al.*, 2009). The focus of this thesis is ‘simple’ naturally ventilated buildings: i.e. openings only and as this work is undertaken in the UK, these will be the focus of this review.

Natural ventilation design is influenced by the wind speed, wind direction, the internal and external temperature difference, characteristics of the opening and the number

of openings on a building. When the Building Research Establishment Conservation Support Unit (BRECSU) compared naturally ventilated office buildings to mechanically ventilated (air conditioned) offices in the UK, naturally ventilated buildings offset 14 kWh m⁻² to 41 kWh m⁻² of the required cooling energy annually and, depending on the type of building, resulted in an annual saving of 0.77 £ m⁻² to 2.05 £ m⁻² in energy costs, which is likely to have risen since this study was undertaken (BRECSU, 2000). Operating, maintenance and lighting costs were also reduced, due to the penetration of daylight into the building (BRECSU, 2000).

When used effectively, ventilation reduces internal odour and indoor pollutants (e.g. CO₂, dust) by replacing internal air with external air. Ventilation can also be used to reduce humidity in a building, decreasing the risk of mould. In general, day-time natural ventilation in mild climates and night time ventilation in hot climates have been proven to be effective (Allard and Ghiaus, 2012). In mild climates design often relies only on the natural porosity of the building, combining with the purpose built openings (Liddament, 1996).

Within ventilation studies the influence of the internal structure of a building is often simplified, with rooms being assumed to be empty. Ventilation rate is influenced by obstacles within the room (Chu and Chiang, 2013). Obstacles within the internal flow are likely to alter the course of the jet which may form in cross ventilated cases (Section 2.3.10), leading to a change in ventilation rates (Chu and Chiang, 2013). Obstacles may also be heat sources, complicating the internal flow further (Chu and Chiang, 2013).

Natural ventilation gives the occupants of a room more control over their environment, allowing them to adapt immediately to their own personal perception of comfort, leading to a more productive work-force and increased happiness (Raw *et al.*, 1990). Natural ventilation can be used to prevent Sick Building Syndrome (SBS), which although there is no official definition can cause symptoms such as lethargy, headaches and other symptoms to be reported (Burge, 2004). Low rates of ventilation in a primary school negatively affected pupil's cognitive performance and attention spans due to poor air quality and low thermal comfort (Bakó-Biró and Clements-Croome, 2012). This is also true for residential and office environments (Suk *et al.*, 2003). Social hierarchies can exist within offices and houses, which may lead to increased discomfort with natural ventilation due to differences in personal thermal comfort between occupants (Snow *et al.*, 2016).

The behaviour of occupants may not always be perfectly aligned with the idealised energy modelling of the building and that occupants may undertake counter-productive actions, such as opening windows when the outdoor air temperature is higher, in an attempt to improve air quality and ventilation rates (Schakib-Ekbatan *et al.*, 2015). There is a strong relationship between a ventilation system and the building occupants and as such consideration into their behaviour and needs must occur at all stages of design, including small adjustments in the post occupancy stage (CIBSE, 2005).

Natural ventilation is best suited to narrow buildings with minimal external air and noise pollution (Shetabivash, 2015). Open plan layouts allow for effective flow through a building, whereas individual rooms reduce the efficiency of the natural ventilation (Shetabivash, 2015). Natural ventilation rates are quoted in several forms: volumetric flow rate, per occupant airflow rate, unit area flow rate, air change rate and mass flow rates (Liddament, 1996).

2.3.1 Challenges of Natural ventilation

Problems with natural ventilation arise from a lack of control over the driving forces and difficulty in filtering the incoming air, e.g. within an urban environment, where incoming air may be more polluted than the internal air and where the external environment may be louder than the internal environment, leading to unwanted noise pollution (Shetabivash, 2015). The security of open windows, especially on low levels may be of concern (Shetabivash, 2015). Retro-fitting natural ventilation systems is more difficult than installing mechanical ventilation due to the structural alterations needed and the difficulty in obtaining planning permission for listed buildings in the UK (BRECSU, 2000). Ventilation methods that are suitable for one building may not be relevant to another due to the variation in design and age of the building stock (BRECSU, 2000).

For new buildings, it is often difficult to predict the air-flow rate accurately at the design stage due to the many geometrical and physical variables that govern or influence the flow (Park and Baik, 2013). Often the positioning of openings at the design stage is based on dimensional analysis or numerical models designed for a building envelope (Etheridge, 2002). These may not take into account positioning for night-time cooling, occupant control and adequate internal air movement (Etheridge, 2002).

In the UK there is not a complete database of UK building ventilation properties, so not all of the findings from research are being utilised to improve design (Hall and Spanton, 2012). Ventilation design is primarily concerned with meeting the design objective of getting the specified amount of air into a building under the specified conditions, though these specified conditions may be based on inaccurate climatological data (Etheridge, 2000). A designer is faced with many conflicting requirements when designing a ventilation system, due to having to meet a wide variety of criteria set by building regulations, client needs and planning for maintenance of the system (Liddament, 1996). Often, studies of ventilation are undertaken using simplified models of buildings or on specific buildings due to limitations on research funding.

A natural ventilation design must be flexible so it can respond to variability in the climate in the UK and provide the required ventilation rates for the specific building type regardless of the conditions. CIBSE (2006) (Chartered Institution of Building Services Engineers) state that if an annual temperature span of $-10\text{ }^{\circ}\text{C}$ to $30\text{ }^{\circ}\text{C}$ is considered, combined with wind speeds of 0 to 10 m s^{-1} and eight different wind directions, a system

could be subjected to over 3000 different sets of driving conditions a year. The range of wind speeds and wind directions is low, suggesting the real number of combinations could be more, however this range may be reduced by the micro-climate of a site and the prevailing wind.

2.3.2 Natural ventilation in the urban environment

The urban environment has challenges for the application of natural ventilation: lower wind speed, greater temperatures due to the effect of urban heat island, noise, reduced wind speeds and pollution. 70 % - 80 % of European cities with a population of over 500,000 breach WHO (World health organisation) air quality standards at least once a year (Wackernagel *et al.*, 1999). This has likely increased in recent years, making it difficult to successfully implement natural ventilation in rapidly expanding urban areas. However, natural ventilation is a low carbon alternative to air conditioning which would stress electricity distribution systems and is worth exploring in order to work towards sustainable cities. CIBSE suggest that the predicted values of natural ventilation listed for an isolated building may be reduced by 33 % by an urban area (CIBSE, 2006). Prevailing wind direction and velocity in an urban area with a greater density of high rise buildings change seemingly randomly, resulting in large errors due to fluctuations in the wind-component if ventilation rates are being calculated under the steady state assumption (Park, 2013).

Lower wind velocities in an urban area means reduced wind pressure on the building façade and less effective cross ventilation (Section 2.3.10) (Ghiaus *et al.*, 2006). An example of the urban effects on natural ventilation can be seen in Hong Kong, where natural ventilation rates in buildings are affected by the increased mean-building height as well as channelling and sheltering effects caused by neighbouring buildings (Ng *et al.*, 2011). The “tall and bulky high-rise building blocks with very limited open spaces in-between, uniform building heights and large podium structures” caused the mean wind speeds recorded in the urban area to decrease by 40 % between 1990-2010 (Ng *et al.*, 2011). The stagnation of the air increased pollution levels, reduced outdoor thermal comfort and has also potentially caused a reduction in indoor air quality in lower storeys due to decreased ventilation potential (Ng *et al.*, 2011).

Van Hooff and Blocken (2010) used an isothermal RANS model (Section 2.3.3.3) of a stadium in Amsterdam which resolved the indoor and outdoor flow simultaneously. The stadium could be modelled within the same conditions as both an isolated building and in-situ. The CFD model was verified against full-scale 3D velocity measurements on the site and displayed a good agreement with the overall results, highlighting that for an isolated building or one in a rural environment, using a small sample of wind directions is sufficient, but will cause errors in the estimation of the ventilation rate for an urban area due to the effects of surrounding buildings (Figure 2.9).

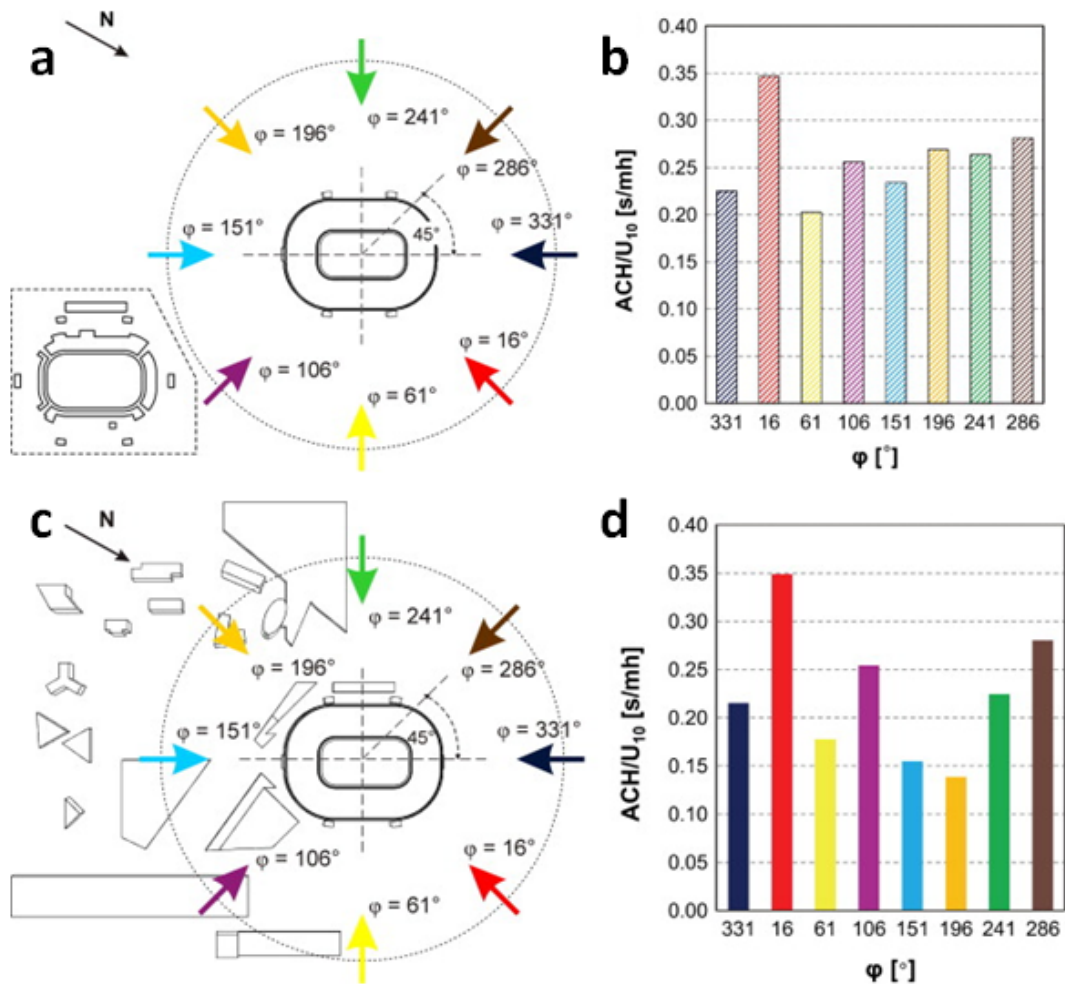


Figure 2.9: a) Top view of stadium without surrounding buildings, with indication of wind directions for the CFD simulations. The figure in the left bottom corner is a horizontal cross-section indicating the asymmetry of the stadium. b) Ratio of air change rate (ACH) to reference wind speed (U_{10}) in ($s\ m^{-1}\ h^{-1}$) for the selected wind directions. c) and d) are in a similar to a) and b), but include the surrounding buildings. Source: Van Hooff and Blocken (2010).

Eight wind directions of interest were studied, with the differences in air change rate between two different wind directions for the isolated stadium being up to 75 %. For a surrounded stadium this increased to 152 %, suggesting that excluding the urban surroundings can lead to an overestimation in air changes per hour of 96 % (Van Hooff and Blocken, 2010). Realistic flow is not likely to experience such steady wind directions and is likely to fluctuate rapidly, adding another source of error onto ventilation rate calculations. Santamouris *et al.* (2001) also reported a 90 % difference between predicted and measured airflow within a naturally ventilated building due to fluctuations in conditions.

The work by Van Hooff and Blocken (2010) clearly highlights the need to include the urban area accurately in simulations in order to estimate the natural ventilation air

change rate effectively. For individual buildings, the wall porosity must be considered as well as the shape and size of the opening and the presence of internal obstacles. Changes in the pressure coefficient on a building due to fluctuations (changes in wind direction at turbulent time-scales) in wind direction has clear implications for the predicted ventilation rate of the building (Jiang and Chen, 2002). These factors coupled with an urban area are rarely researched due to the complexity of the problem.

2.3.2.1 Case study of a naturally ventilated building in an urban environment

The School of Slavonic and East European Studies (SSEES), London, UK, is an example of how the urban area can make sustainable building design using natural ventilation challenging. Full design specifics are detailed in Short *et al.* (2004) and Short *et al.* (2009). Mechanical ventilation could not be utilised (Short *et al.*, 2004). The building was designed using CIBSE Design Summer Year Data as the climate file for computation simulations, using the thermal criteria of CIBSE: internal temperatures should not exceed 25 °C for more than 5 % of occupied hours (150 hours). This recommendation is somewhat less than the recorded temperature data for Heathrow airport, which is located outside of the main urban heat island (UHI) for London.

It also discounted the considerable uplift in summer night temperatures due to the UHI (Watkins *et al.*, 2002). Coupled with the fact that the SSEES was located within the expected peak of the UHI (night time temperatures can be up to 6 °C warmer than surrounding rural areas), the natural ventilation at night was ineffective and had to be modified post occupancy (Short *et al.*, 2009). The SSEES building and others of a similar design, highlight the difficulty in utilising natural ventilation alone to cool a building within an urban area. The use of unadjusted weather data may result in overestimation of the air infiltration and natural ventilation rates (CIBSE, 2006).

Large long-term meteorological data sets and climate projections for urban sites would provide planners with a more realistic idea of the ‘worst case scenarios’ expected and would allow for buildings to be future proofed. Understanding the interactions between temperature differences, wind speeds, wind direction and building occupants would also allow for a deeper understanding of how a building will behave in the long term at a particular urban location.

2.3.3 Measurement methods

Three main approaches are used to investigate natural ventilation within the urban environment: Full-scale observations (Section 2.3.3.1), either within or around the building itself, scaled models or full-scale idealised models, such as wind tunnel models (Section 2.3.3.2) and CFD (computer fluid dynamics) (Section 2.3.3.3). Similar methods are used to model flow around urban areas and ventilation of a building, although there is

little research linking local urban flows to an individual buildings ventilation rate. Recently there has been a move towards the use of multiple methods, such as the work by Van Hooff and Blocken (2010) and Belleri *et al.* (2014).

2.3.3.1 Full-scale or in-situ measurements

Whilst on-site measurements of ventilation are possible for constructed buildings, they will have limited use for planned buildings, due to the building altering its local environment. Often, research is undertaken into a specific building's ventilation mechanisms or building envelope, e.g. work on schools (Bakó-Biró and Clements-Croome, 2012), supermarkets (Kolokotroni *et al.*, 2015), hotels (Farrou *et al.*, 2016) and hospitals (Gilkeson *et al.*, 2013). This is due to the limited funding, specific research interests of the authors and may be due to the results not getting into academic literature. It is also difficult to undertake full-scale studies of ventilation in occupied buildings as occupant behaviour must be carefully monitored alongside all other variables throughout the observation period. Occupant requirements and behaviour should be considered during the design phase of a building.

Obtaining a range of wind directions is difficult at full-scale due to seasonal trends, meaning some wind directions occur infrequently. Until recently, most studies into ventilation were only concerned with the perpendicular wind direction due to interest in the wind load on a building and experimental limitations, though this behaviour is not representative of a realistic flow, especially in an urban area. The improvements made in CFD development (Section 2.3.3.3) and knowledge of the urban areas effects have meant that wind directions other than perpendicular or prevailing are now being actively studied (Van Hooff and Blocken, 2010).

In order to capture the full variability of environmental conditions, measurements have to be undertaken at full-scale at the expense of repeatability due to variable conditions. The specialist equipment and multidisciplinary personnel needed for full-scale observations are expensive, meaning measurements are only performed at a limited number of sampling positions. Work at full-scale often requires a team from multiple research disciplines and specialist equipment.

2.3.3.2 Scale model

Scale models can range from being almost full-scale (Larsen and Heiselberg, 2008) to smaller scaled models of buildings such as the 1:30 (Irtaza *et al.*, 2013) and 1:40 (Richards *et al.*, 2007) scale models used in wind tunnels. More commonly used scales are buildings of the order of 10 mm e.g. Robins and Macdonald (2001), though the chosen scale is often dependent on tunnel size and research objectives.

Two common methods used are wind tunnel and salt bath experiments as these allow

direct control of the driving variables. Measurements can be taken at more points than at full-scale. The cost and manpower required for scaled model experiments are both significantly lower than that required for full-scale and repeatability of the experiment is possible (Blocken *et al.*, 2016). Wind tunnel models typically include the surroundings of a building and allow for the impact of altered conditions, such as a new building to be studied. Effects of changes to the test building itself can also be studied for a range of wind directions (Stathopoulos, 2006). Blocken *et al.* (2016) provide a comprehensive review of many different wind tunnel techniques, with a focus on pedestrian level winds.

Wind tunnel models can be used to aid the design full-scale field campaigns where positioning of the sensors is of utmost importance due to limited resources and are often used for verifying CFD models (Blocken *et al.*, 2016). However, due to the spatial and temporal scaling of a wind tunnel model, it is representative of a long time scale at full-scale (e.g. for a model at the scale of 1:300, three minutes tunnel time is equivalent to 900 minutes at full-scale).

Generally, wind tunnel measurements occur under neutral stability due to neutral boundary layer simulation being a well-established procedure (Counihan (1969), Irwin (1981)). Exceptions include Robins *et al.* (2001) modelling dense gas dispersion over a rough surface in a stable boundary layer and Fedorovich and Kaiser (1998) who used a sheared atmospheric convective, unstable boundary layer. Both were undertaken within a thermally stratified wind tunnel.

Wind tunnel models which take into account both flow and thermal affects are rare, due to a lack of suitable facilities and the increased complexity of the problem (Robins and Macdonald, 2001). Flow visualisation is possible through the use of smoke or more rarely soap bubble trails e.g. Hoydysh and Dabberdt (1988).

Purely thermal driven flows are often modelled using salt baths, using different densities of water to simulate warm and cold air, as due to scaling effects, temperature differences between environments would have to be incredibly large, of the order of 100 °C, limiting the materials used for the model as well as the flexibility. When investigating ventilation due to wind and buoyancy forces using scale modelling it is necessary to achieve full-scale values of the Archimedes number (the ratio of external forces to internal viscous forces, F_{Arch} , Section 6.6.5) and this requires operating with high temperatures in the model and the use of the Boussinesq approximation: for an almost incompressible fluid, it assumed that variations of density are small and that density can be set at a constant value (Etheridge, 2015). Salt bath models have the disadvantage of having constant heat sources, which are unrealistic for a true building as the heating and cooling inputs change with time (Etheridge, 2002).

Scale modelling provides a flexibility not available in full-scale models, with some control of the test environment at a reduced cost. However, it is limited by the amount of detail that can be recreated on a scale model and does not represent all scales of tur-

bulence found in the full-scale environment (Richards *et al.*, 2007). Other methods of measuring flow rate may include sheet light and laser methods to visualise airflow patterns and flume models to predict ventilation performance (Liddament, 1996). Kanda (2006) reviews the progress made in the scale modelling of the urban environment and covers 40 different experiments undertaken with a variety of focuses.

2.3.3.3 Computer fluid dynamics (CFD)

Three different CFD methods; Direct numerical simulation (DNS), Large Eddy Simulation (LES) and Reynolds Averaged Navier-Stokes (RANS) are used to solve the Navier-Stokes equations using different approximations for the turbulence closure, depending on the requirements of the research. The use of CFD modelling has been increasing due to readily available software, price reductions and a rapid increase in computing power (Cóstola *et al.*, 2009).

DNS studies solve Navier-Stokes equations without approximation, but require large amounts of memory and can capture unsteady flow processes (Coceal *et al.*, 2006). It allows the study of smaller scale structures when run at a sufficiently high resolution.

LES and RANS methods have less memory requirements as LES resolves only the large-scale fluid motions and models the subgrid-scale motions through filtering the Navier-Stokes equations (Xie and Castro, 2006). However LES models may miss some small scale features of the flow, even at very high resolutions (Letzel *et al.*, 2008).

Xie and Castro (2006) studied DNS, LES and RANS and found that LES may be reliably able to simulate turbulent flow over urban areas at realistic Reynolds numbers (Section 5.8) with only a medium scale mesh ($16 \times 16 \times 16$ points per cube of varying height) being required to simulate large scale flow patterns and drag coefficients. LES can provide 'good' results for pressure coefficient (C_p) (Section 2.3.11) and for related natural ventilation problems, while RANS simulations provide less accurate results (Cóstola *et al.*, 2009).

RANS modelling is the most widely used in ventilation industrial applications, due to its lower cost and lower run time, though this is dependent on the computing power available (Jiang and Chen, 2002). The RANS equations are derived by averaging the Navier-Stokes equations by time-averaging if the flow is statistically steady or ensemble-averaging for time-dependent flows (Blocken *et al.*, 2016). With RANS equations, only the mean flow is solved whilst all other scales of the turbulence are approximated. RANS models may over-predict the recirculation region behind a building and may not accurately capture the separation region on the roof of a building, whereas LES models do not encounter these problems (Lakehal and Rodi, 1997). When using RANS models it is implicitly assumed that there is a fair degree of scale separation between the larger time scale of the unsteady flow features, such as wakes and the time scale of the genuine

turbulence (Castro, 2003).

CFD models are informative and require relatively low labour and equipment costs in order to achieve results that are easily interpreted. High speed models are achieved through simplification of flow processes, though the increase in computing power is allowing for more detailed models to run in an equivalent amount of time (Shetabivash, 2015).

However, CFD models are entirely dependent on set up; such as the turbulence closure model used, the boundary layer conditions imposed and assumed amongst other parameters. The coarseness of the mesh used in CFD modelling may cause differences between models and wind tunnel or full-scale measurements (Jiang *et al.*, 2003). Another disadvantage is the lack of validation for all CFD models, which still require wind tunnel and/or full-scale work in order to ensure that the model is representative of the flow. CFD solution verification and validation as well as complete reporting of the followed procedure are essential components of quality assurance for CFD models (Blocken *et al.*, 2016).

2.3.4 Buoyancy driven ventilation

Differences in the density between internal and external air, mostly due to temperature differences, cause buoyancy driven ventilation. The hotter air will have a lower density and will rise, displacing the cooler, denser air. This mechanism causes flow through openings and also effects the temperature distribution of the indoor environment. Depending on the type of ventilation used, there is a tendency for the internal flow to become stratified (Linden, 1999). Openings are positioned at low levels and high levels, the warmer air rises upwards and escapes out of the top vent, being displaced by the colder denser air from the low level openings. This is referred to as upwards displacement or stack ventilation (Figure 2.10a). This is caused by the greater internal pressure on the top opening and lower internal pressure on the bottom opening, with a neutral level: a height at which the internal pressure is equal to the external pressure.

Above the neutral level the air will flow out of the upper opening and below air is being drawn into the space by the lower opening. The jet at the inlet is positively buoyant, with the outlet jet being negatively buoyant and the temperature difference between the interior and exterior is reduced if the height between the inlet and outlet is increased (Subudhi *et al.*, 2013).

The stack pressure (P_t) is given by:

$$P_t = \rho g H_d \frac{T_i - T_e}{T_i} \quad (2.5)$$

where H_d (m) is the height difference between the lower and upper openings, T_i (K) is

the internal temperature, T_e (K) is the external temperature, g (m s^{-2}) is gravitational acceleration and ρ (kg m^{-3}) is the air density.

The buoyancy driven flow rate $Q_{thermal}$ ($\text{m}^3 \text{s}^{-1}$) for a 'small' (< 10 mm) opening is (Awbi, 2003):

$$Q_{thermal} = C_d A \sqrt{2gH_o \frac{T_i - T_e}{T_i}} \quad (2.6)$$

where C_d is the discharge coefficient of the opening which depends on the opening's size and shape, though 0.61 is normally used for sharp edged openings. A (m^2) is the area of the opening and H_o (m) is the height of the opening. Whereas for a 'large' (> 10 mm) opening (Awbi, 2003):

$$Q_{thermal} = \frac{C_d A}{3} \sqrt{2gH_o \frac{T_i - T_e}{T_i}} \quad (2.7)$$

The difference in the coefficients is due to the integration of equation 2.6 as the wind profile varies over the height of the opening (Awbi, 1996) (for the derivation of equation 2.7, see Appendix B).

One upper level opening creates mixing ventilation (Figure 2.10b), where the warm air rises out the opening and the cooler air sinks down through the same opening into the internal space, creating a turbulent plume which mixes with the internal air (Linden, 1999). Mixing ventilation results in a less stratified and more well mixed room when compared to displacement ventilation. Displacement ventilation is the more rapid of the two. As the external temperature drops at night, a building can be cooled by partially opening ventilation mechanisms around the building, often referred to as night-cooling or night-purging (e.g. Figure 2.10c).

Buoyancy driven ventilation is not reliant on the outdoor wind speed, meaning that ventilation will occur when there is a high risk of over-heating: little wind but high temperatures. A larger gradient between internal and external temperatures is likely to increase the flow rate. Buoyancy driven flow is often smaller than wind driven flow on windy days and only works if there is an internal-external temperature difference. The inclusion of stacks and chimneys for stack ventilation also limits the design of the building (Short *et al.*, 2004).

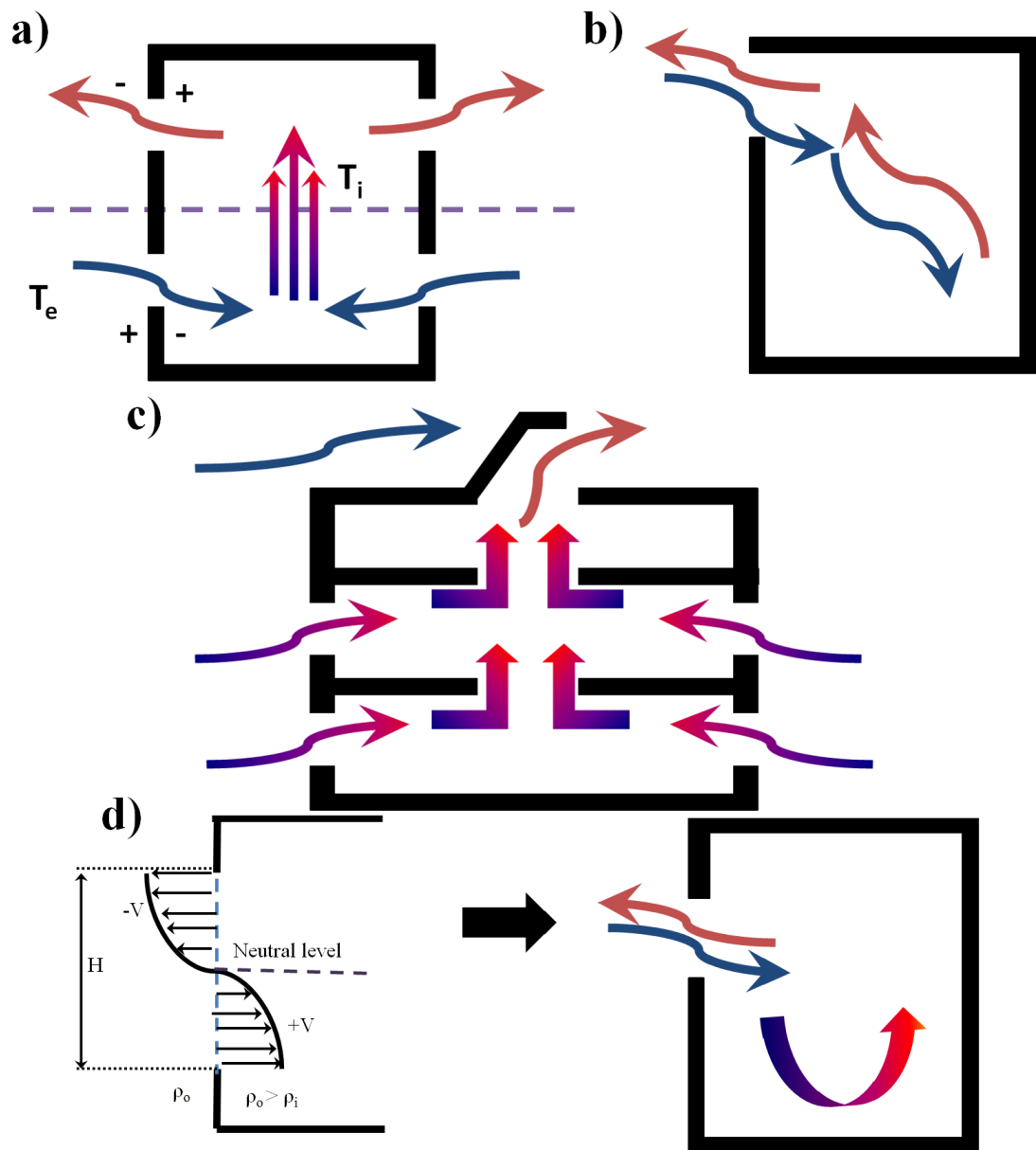


Figure 2.10: Three examples of buoyancy driven ventilation. Warmer air (red arrows), cooler air (blue arrows), pressure anomalies (+,-), neutral level (purple dashed line). For this case it is assumed $T_i > T_e$. a) the stack effect. b) Mixing ventilation. Warm air flows up and out whilst cool air flows in and sinks. c) Atrium design used to ventilate a building at night. d) Single sided ventilation, highlighting the neutral plane and the velocity across the vertical extent of the opening.

As it is difficult to recreate buoyancy driven ventilation in scaled models due to the high temperatures needed, full-scale, or near full-scale observations are much more frequent (Linden, 1999). Buoyancy and wind driven ventilation are often studied separately, with very few studies looking at the interactions between the two, which could lead to inaccurate estimates of the potential ventilation rate.

2.3.5 Wind driven ventilation

Wind driven ventilation is caused by a pressure difference across a building and depends on the wind speed, wind direction, the shape of a building, the number of openings and the proximity to other buildings. If pressures are greater on the windward side of the building and lower on the leeward side, flow travels from the windward vents to the leeward vents. These pressure differences vary with building shape, wind direction and wind speed making it incredibly difficult to compare two buildings or two locations.

Wind speed plays only a minor part compared to the other factors (e.g. wind direction) in influencing the flow pattern around a building, due to sharp edges and flow close to the building being governed by inviscid dynamics, meaning it is assumed that the flow has no viscosity and behaves similarly to an ideal fluid (Linden, 1999).

It is generally assumed that flows around wall-mounted sharp-edged bluff bodies submerged in thick turbulent boundary layers are essentially independent of the Reynolds number, meaning the flow through a purpose-provided opening has features which are independent of the Reynolds number (Lim *et al.*, 2007). This Reynolds number independence allows for scaled models suitable for use in the wind tunnel to be built (Chapter 4).

If the mean flow is of interest, this assumption of Reynolds independence is adequate for use, but research suggests the fluctuating components of the flow have some dependence on the Reynolds number (Lim *et al.*, 2007). However, should the flows around the building be dominated by vortices, even the mean components of the flow may demonstrate Reynolds dependence, a concern if full-scale implications are being derived from wind tunnel results (Section 5.8) (Lim *et al.*, 2007). Models which take into account only the mean flow are known as steady state models.

With a ‘large’ opening (> 10 mm), flow tends to be approximately turbulent under normal pressures, with the flow rate (Q_{wind}) through that opening being calculated using the standard orifice equation (Awbi, 2003):

$$Q_{wind} = C_d A \sqrt{\frac{2\Delta p}{\rho_0}} \quad (2.8)$$

where Δp is the pressure difference across the opening and ρ_0 (kg m^{-3}) is the density of the flow. The effective area (A_{eff}) of an opening is $C_d A$, which changes depending on the number of openings and their relative positions to each other. For openings in series (e.g. two windows next to each other on the same flat wall), the effective area is equivalent to:

$$A_{eff} = C_d A = C_{d1} A_1 + C_{d2} A_2 \quad (2.9)$$

where A_x is the area of the numbered window and C_{dx} is the discharge coefficient of the

numbered window. For openings in parallel, (e.g. an opening at either end of a corridor);

$$\frac{1}{A_{eff}^2} = \frac{1}{(C_d A)^2} = \frac{1}{(C_{d1} A_1)^2} + \frac{1}{(C_{d2} A_2)^2} \quad (2.10)$$

Both equations can be applied to an infinite number of openings (Awbi, 2003). Note that equation 2.8 does not include any terms which are affected by the wind direction.

2.3.6 Thermal and wind driven ventilation

In reality, natural ventilation is a combination of thermal and wind driven mechanisms. Often one mechanism dominates, which depends on the design of the building and the atmospheric conditions. Generally the wind driven and thermal driven pressure differences are added to create a total pressure difference (Δp_{total}) across the opening. The total flow through an opening (Q) is proportional to the total pressure:

$$Q \propto \Delta p_{total}^n \quad (2.11)$$

where n is dependent on the flow characteristics. Values for n are usually found from fan pressurization tests of a building. For a typical residential building, n has a value of 0.67, which is midway in its range from $n = 0.50$ for turbulent flow to $n = 1.0$ for fully developed laminar flow (Walker *et al.*, 1998). This power law pressure-flow relation was found through fan pressurisation tests, amongst others, to be more representative of infiltration rates than the orifice equation (equation 2.8) (Warren and Webb, 1980).

It is possible to combine the flow rate for each component (buoyancy and wind):

$$Q_{all} = (Q_{thermal}^{\frac{1}{n}} + Q_{wind}^{\frac{1}{n}})^n \quad (2.12)$$

Turbulence and random fluctuations in the oncoming wind speed can influence the ventilation rate of a building (CIBSE, 2006). This is more likely to occur in low wind speed conditions and when the stack effect is minimal. Turbulence in the oncoming flow will cause intermittent changes in direction of the flow across an opening. The turbulent effect is not considered in design, as the turbulence effects will be smaller than the other driving mechanisms (wind and buoyancy) (CIBSE, 2006). Whether this assumption holds for a building within an urban area is not clear. The balance between buoyancy driven and wind driven flow is dependent on the type of ventilation used.

2.3.7 Infiltration

Infiltration is the unintentional flow into a building envelope due to cracks or gaps left during the construction of the building and it is driven by the pressure difference across the gaps (Figure 2.11). A high infiltration rate can affect the efficiency of the main ventilation system, or provides unexpected ventilation if left unaccounted for.

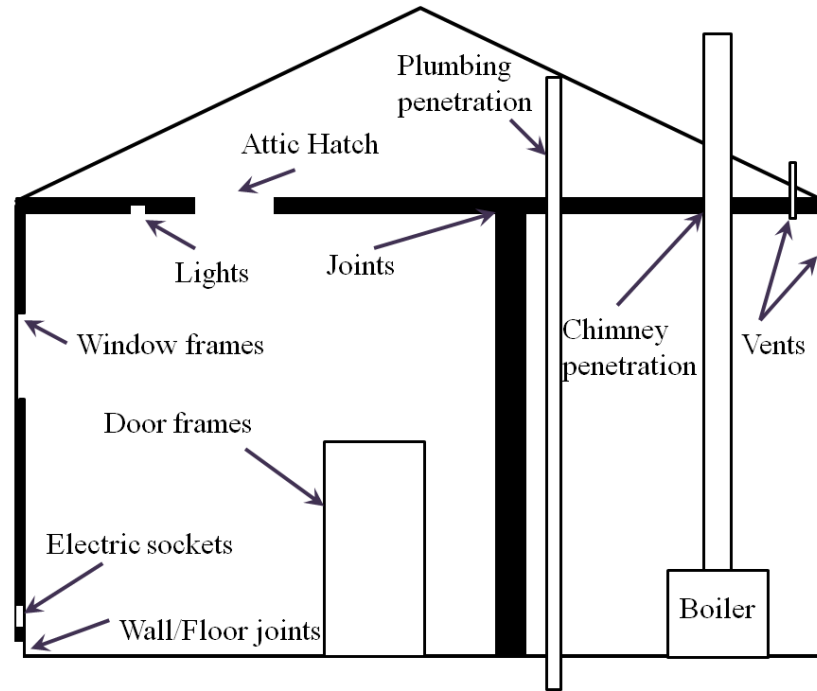


Figure 2.11: Typical air leakage paths in a house. These are likely to be similar for office buildings. Adapted from Awbi (2003).

Due to the reduced size of the potential openings, equations to calculate the flow rate via infiltration (Q_i) differ from those for larger, intentional openings. For narrow openings, with deep flow paths (e.g. mortar joints), the flow within the openings is assumed to be essentially laminar. For this the Couette flow equation is used (Awbi, 2003):

$$Q_i = \Delta p \left(\frac{bH_c^3}{12\mu d_x} \right) \quad (2.13)$$

where b (m) is the length of the crack, H_c (m) is the height of the crack and d_x (m) is the depth of the crack in the flow direction. μ (Pa s) is the absolute viscosity of the air. However, for wider cracks the flow is not fully turbulent, meaning this equation does not yet apply, as the flow is transitioning between laminar and fully turbulent flow.

One of the problems of estimating infiltration rate is the difficulty in defining the size and location of the cracks. Infiltration, like other forms of ventilation, is strongly directionally dependent (Brocklehurst, 2015). Infiltration in buildings due to wind-induced pressure is complex and is highly influenced by the turbulent nature of the wind, with

models excluding the turbulent effect of buoyancy on infiltration (Haghighat *et al.*, 2000). Haghighat *et al.* (2000) review the different models for infiltration under fluctuating wind conditions, stating that a lack of well-reported full-scale data makes it difficult to test model effectiveness and that whilst some models could be accurately used by industry, others require far too much specific knowledge to be utilised.

2.3.8 Single sided ventilation

Single sided ventilation occurs when there is only one opening, acting as an inlet, outlet or as a combination of both (Figure 2.10d). When openings act as both an inlet and an outlet, there is the potential for recirculation and air mixing. For purely buoyant flows, cooler, outdoor air flows into the building through the bottom of the opening, with warmer indoor air flowing out of the top. There will be a neutral zone where the direction of the flow changes in the opening (Larsen and Heiselberg, 2008). Equation 2.7 can be used to calculate the flow rate for single opening in this case.

Single sided ventilation is less efficient than cross ventilation per unit area of window, due to incoming and outgoing flow occurring over the same opening. Single sided ventilation fits easily into most office building layouts (Caciolo *et al.*, 2013). The rule of thumb for single sided ventilation is that windows with an opening area of 1/20th of the floor area can ventilate spaces to 2.5 times the height of the room (Kukadia *et al.*, 1998). The origins of this rule of thumb and the conditions under which it was to apply are not explicitly defined, though this rule and a similar rule for cross ventilation are widely quoted in the literature (Edwards, 1998).

The CFD model by Caciolo *et al.* (2013) suggests that for a windward facing opening, the stack effect is dominant at speeds lower than 1.5 m s^{-1} . CFD modelling by Allocca *et al.* (2003) also found that the two mechanisms may counteract and that this appeared to depend on the wind speed: with buoyancy dominating at wind speeds of $< 2 \text{ m s}^{-1}$, the two being approximately equal at 4 m s^{-1} , leading to a diminished ventilation rate. At wind speeds $> 8 \text{ m s}^{-1}$, wind driven ventilation dominates.

Net flow rates decrease significantly at greater wind speeds due to an increase in wind induced ambient turbulence, especially if the difference between internal and external temperature is small (Wilson and Kiel, 1990). This greater level of turbulence caused increased cross-stream mixing which entrained some of the outgoing air back into the incoming stream, reducing the net volume exchanged. A combination of thermal and wind-driven flow for single sided ventilation means that the flow path is characterised by a strong unsteadiness and air mixing due to turbulence diffusion (Caciolo *et al.*, 2011). This influence of the turbulence of the wind and variation in the pressure gradients induced by wind gusts on the air-flow is what makes single sided ventilation difficult to model (Freire *et al.*, 2013).

Ji *et al.* (2011) highlight that little research has been done on the effect of fluctuating wind direction due to the complexity and cost of measuring full-scale flows and the difficulty of modelling fluctuating direction within a wind tunnel. One simplification is to use a wind tunnel model with no roughness elements present, as it would be difficult to recreate the boundary layer conditions and create horizontal fluctuation in the wind direction (Ji *et al.*, 2011). However, this is still not representative of real atmospheric conditions. A full-scale data set of ventilation rates as a function of wind direction and as a function of the fluctuation in wind direction is required in order to fully understand the effects of wind direction on cross ventilation and how the behaviour of the internal flow may change in response to changes in the external flow.

Little full-scale research has been done on the interaction of temperature, wind direction and wind speed coupled with the location of the opening and the effect of the surrounding urban area on ventilation rate (Section 6.6).

2.3.9 Empirical models for single sided ventilation

Empirical models suggested for single sided ventilation which include both buoyant and wind driven forces, have only been tested against the original data-set and not for general applicability to other data (Caciolo *et al.*, 2011) (Section 6.6). The flow path produced by a combination of buoyancy and wind mechanisms is highly turbulent and unsteady, with the effect of the combination changing depending on the wind direction (Caciolo *et al.*, 2011). For a leeward opening, increased turbulent diffusion reduced the temperature difference across the opening, reducing the stack effect, leading to an air change rate that was lower than the one measured in the absence of wind. For the windward opening, the stack effect is also reduced by turbulent diffusion, though the increased size of the mixing layer within the opening led to a higher air flow rate (Caciolo *et al.*, 2011).

2.3.9.1 Warren and Parkins (1985)

Warren and Parkins (1985) suggested two expressions for flow rate for a single sided opening for an isolated building, which predict only the wind driven ventilation rate and not buoyancy effects based on full-scale measurements:

$$Q_{Wlocal} = 0.1AU_{Local} \quad (2.14)$$

$$Q_{Wref} = 0.025AU_{Ref} \quad (2.15)$$

where A is the opening area (m²). The total ventilation rate can be calculated by taking the larger of the wind driven or thermal components, as for some conditions the two

mechanisms may conflict and combining the two may lead to an overestimation (Warren, 1977).

2.3.9.2 Caciolo *et al.* (2011)

Caciolo (2010), Caciolo *et al.* (2011) and Caciolo *et al.* (2013) compare different ways of predicting the single sided ventilation rate for windward conditions. Caciolo *et al.* (2013) use a CFD model and build upon the fieldwork of Caciolo *et al.* (2011), which considers different types of opening and compares the methods suggested by Warren and Parkins (1985), Larsen and Heiselberg (2008), De Gids and Phaff (1982) and Dascalaki (1996) against their data, which was gathered using three different methods: flow visualisation, thermal anemometry and tracer gas decay.

The model designed by Caciolo (2010) takes into account θ_{ref} , using the parallel wind directions ($\theta_{ref} = \pm 90^\circ$) as the dividing line between thermally dominated ventilation (Q_{stack}) and wind dominated ventilation (Q_{wind}).

$$Q_{cac} = Q_{thermal} + Q_{wind} = \frac{1}{3} C_d A_{eff} \left(\frac{g \Delta T \Delta T^* H}{\bar{T}} \right)^{0.5} \quad (2.16)$$

where ΔT^* varies for wind speed and wind direction and is the ratio of the effective temperature difference at the opening to ΔT (the internal-external temperature difference) \bar{T} is the mean air temperature. A_{eff} is the effective area of the opening. All wind direction notation has been converted to that of this thesis. For $\theta_{ref} > 90^\circ$ and $\theta_{ref} < -90^\circ$, ΔT^* is:

$$\Delta T^* = 1.17 - 0.16 U_{wind} \quad (2.17)$$

And the Q_{wind} component is 0, as the thermal effects dominate behind the building.

For $-90^\circ < \theta_{ref} < 90^\circ$, ΔT^* depends on wind speed. For $U_{wind} < 5 \text{ m s}^{-1}$ ΔT^* is:

$$\Delta T^* = 1.17 - 0.046 U_{wind}^2 - 0.46 U_{wind} \quad (2.18)$$

and for $U_{wind} > 5 \text{ m s}^{-1}$, ΔT^* is set to 0. For $-90^\circ < \theta_{ref} < 90^\circ$, Q_{wind} is calculated using:

$$Q_{wind} = 0.037 A_{eff} (U_{wind} - U_{wind,lim}) \quad (2.19)$$

The increase in the air change rate due to the mixing layer is linear with the wind speed and that a threshold appears for wind speed below around 1.2 m s^{-1} ($U_{wind,lim}$) (Caciolo *et al.*, 2013). Below this wind speed limit, the mixing layer effect is negligible and only the stack effect contributes to the air change in the room (Caciolo *et al.*, 2013).

Caciolo *et al.* (2013) do not mention the type or depth of boundary layer included in

the CFD model, nor the height at which U_{wind} is taken from, suggesting that the building is within a uniform flow field making it difficult to compare to the Silsoe data. Other sources of difficulty include the limited number of temperature measurements in the full-scale, as the CFD looks at the temperature difference between the top and bottom of the opening, something which is not measured in the full-scale data. Using the closest thermocouples (approximately 0.5 m away) is also likely to introduce error, as there is no guarantee that the cube is well mixed, which will lead to differing flow behaviour.

Caciolo *et al.* (2013) also use wall temperature instead of internal air temperature, which was not measured in the Silsoe observations, due to the cube being made of metal and thus being more sensitive to temperature changes than a typical brick building. The test building used by Caciolo *et al.* (2013) has a slanted roof and is modelled in the full-scale, with the opening being set to one side. No errors are given by Caciolo *et al.* (2013).

2.3.9.3 De Gids and Phaff (1982)

De Gids and Phaff (1982) create an empirical expression for ventilation rate based on measurements on a full-scale building:

$$Q_{DP} = 0.5A_{eff}U_m \quad (2.20)$$

where

$$U_m = \sqrt{C_1U_{wind}^2 + C_2H|\Delta T| + C_3} \quad (2.21)$$

and C_1 , C_2 and C_3 are empirical coefficients, calculated from their full-scale observations. C_1 is a coefficient linked to the wind effect, C_2 is a coefficient linked to stack effect and C_3 is a turbulence constant. The 0.5 is based on the assumption that for a single sided opening, only half of the opening is acting as an inlet at any given time (De Gids and Phaff, 1982). It is difficult to define shape of the velocity profile in the opening, as this depends on which parameter (wind or buoyancy) dominates (De Gids and Phaff, 1982).

Equation 2.21 is used to calculate the velocity at the opening (U_m) from a wind speed (U_{wind}) taken at 10 m (De Gids and Phaff, 1982). They do not state the distance between the 10 m measurement and the location of the building. The experiments undertaken were carried out at three different locations on buildings in an urban environment with surrounding buildings up to four floors high, with all measurements being made on the first floor of the test building (De Gids and Phaff, 1982). Wind speeds, window and room air velocities, air change rates, opening area and temperature were measured, with 33 measurement cases being taken.

This correlation is used in the French Thermal Regulation for buildings and the European standard to predict the impact of window opening in buildings (Stabat *et al.*, 2012). The average error in the predictions by the De Gids and Phaff model was 29 % (Larsen

and Heiselberg, 2008).

2.3.9.4 Larsen and Heiselberg (2008)

Larsen and Heiselberg's (2008) empirical model includes the effect of wind direction on the ventilation (Section 2.3.8). The turbulence intensity of the flow was 5 % with no roughness elements being included (Larsen and Heiselberg, 2008). The wind profile of the wind tunnel was uniform, hence differing from real outdoor conditions. The pressure distribution measured on the test building in the wind tunnel was compared to that of a similar outdoor building (Larsen and Heiselberg, 2008). The distribution close to the opening had similar characteristics, the measurements in the wind tunnel are assumed represent outdoor conditions (Larsen and Heiselberg, 2008).

The model used by Larsen and Heiselberg (2008) was nearly full-scale (5.56 m x 5.56 m x 3 m), meaning that scale effects did not have to be considered, reducing the need for large temperature differences. The pressure coefficient (Section 2.3.11) was measured on the test building and was found to be similar to values expected for a building in realistic conditions. Due to the inclusion of temperature differences, it was found that for a changing wind direction, the mechanism which predominately drives the ventilation (thermal or wind driven, Sections 2.3.4, 2.3.5) is dependent on the wind angle, shown by the variation of the velocity profiles within the opening (Figures 2.12, 2.13). Due to wind tunnel models neglecting some scales of turbulence and buoyancy effects, it is likely that natural ventilation, especially single sided ventilation may be underestimated when compared to full-scale data (Jiang *et al.*, 2003).

Tunnel wind speed was varied between 0, 3 and 5 m s⁻¹ and the temperate difference between 0 °C, 5 °C and 10 °C (Larsen and Heiselberg, 2008). All 159 ventilation rate measurements used the tracer gas decay method, with the velocity of the opening being measured at 10 Hz by 24 3D ultrasonic anemometers split into 3 columns, with only one column being measured at a time to reduce flow blocking.

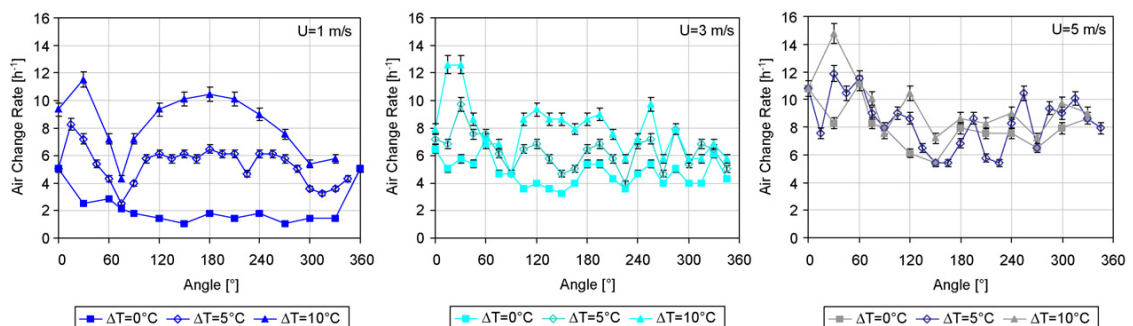


Figure 2.12: Effect on the air-change rate from changing the temperature difference (ΔT) at different incidence angles and wind velocities. Source: Larsen and Heiselberg (2008).

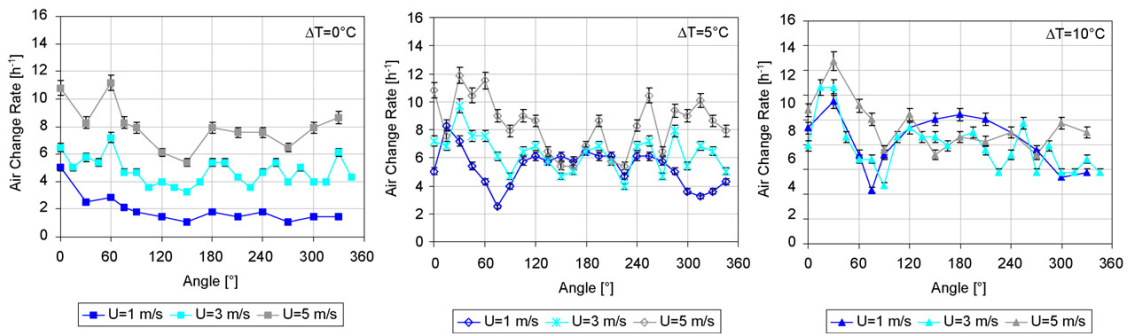


Figure 2.13: Effect on the air-change rate from changing the wind speed at different incidence angles and temperature differences (ΔT). Source: Larsen and Heiselberg (2008).

Additionally, their equation (equation 2.22) is specific to the location of the opening in their experiment, leading to errors if openings are not in a similar location. The opening was 0.86 m x 1.4 m (w x h) and positioned 0.54 m away from the right edge of the building (Larsen and Heiselberg, 2008). To generate a function dependent on wind direction only some directions are included, which means that comparisons across the entire wind direction range become difficult. Where this is required, averages of the two nearest wind direction coefficients are taken (Table 2.1). Larsen and Heiselberg (2008) state that there is a 5 % margin of error on their measurements, due to the uncertainties included in the tracer gas methods utilised. However, Larsen and Heiselberg (2008) also remark that the mixing might be uneven for lower wind velocities within the wind tunnel.

$$Q_{LH} = A_{eff} \sqrt{C_1 f(\beta_v)^2 |C_p| U_{wind}^2 + C_2 H \Delta T + (\Delta C_{p,open}(\beta_v) \Delta T) / U_{wind}^2} \quad (2.22)$$

where $f(\beta_v)$ is a function of the incidence angle (Table 2.1). Using work from Warren (1977), Larsen and Heiselberg (2008) calculated $f(\beta_v)$ by plotting the absolute face averaged C_p values for a building with a height to width ratio of 2:1:

$$\frac{U_{local}}{U_{Ref}} \approx f(\beta) \sqrt{|C_p|} \quad (2.23)$$

The function of $f(\beta)$ was found by fitting a fourth order curve to the equation by plotting $(U_{local} / U_{ref}) / \sqrt{|C_p|}$ against incident wind angle (Larsen and Heiselberg, 2008). Larsen and Heiselberg (2008) use wind directions from 0° to 360°. For comparison to the Silsoe data, the angles have been converted to -180° to 180°.

The estimated values of U_{local} / U_{ref} from equation 2.23 are then used to form an equation for the local velocity:

$$U_{local} = f(\beta) \sqrt{|C_p|} U_{ref} \quad (2.24)$$

This can be used to estimate the wind driven pressure on the building (Larsen and Heiselberg, 2008). To estimate the thermal driven flow rate (Warren, 1977):

$$Q_{thermal} = \frac{1}{3} C_d A \sqrt{\frac{(T_i - T_e) g (H_t - H_b)}{\bar{T}}} \quad (2.25)$$

where C_d is the discharge coefficient, A is the area of the opening T_i is the internal temperature, T_e is the external temperature, \bar{T} is the average temperature, g is the gravitational acceleration, H_t and H_b are the height of the top and bottom of the opening respectively.

Assuming that the flow is fully thermal driven equation 2.25 becomes equivalent to:

$$\frac{1}{3} C_d A \sqrt{\frac{(T_i - T_e) g (H_t - H_b)}{\bar{T}}} = C_d A \sqrt{\frac{2 |\Delta P|}{\rho}} \quad (2.26)$$

where the thermally driven pressure is calculated from:

$$\frac{(T_i - T_e) g (H_t - H_b) \rho}{\bar{T} 2} \quad (2.27)$$

One of the main sources of airflow in single sided ventilation is the fluctuating air movement in the opening, caused by the combination of turbulence levels in the wind, temperature differences across the opening, the wind speed and the pressure difference across the opening (Larsen and Heiselberg, 2008). This fluctuating component can be described by using ΔC_p , or the largest pressure difference in the opening (Larsen and Heiselberg, 2008). Whilst this is possible in wind tunnel models, measuring the pressure difference across an opening without altering the flow in the full-scale is difficult.

Larsen and Heiselberg (2008) calculate the function of ΔC_p with changing θ_{ref} . The type of fit is not stated in the paper. For this function and the forth order curve used to calculate $f(\beta)$, the original plot has been digitised and a curve fit obtained from the data using Matlab's 2010 manual curve fitting toolbox. The function for ΔC_p with θ_{ref} was found to be a cubic polynomial. These values might differ depending on the type of opening and the depth of opening used (Larsen and Heiselberg, 2008).

Combining the wind driven, thermal driven and fluctuating components of Δp creates a complex equation, which Larsen and Heiselberg (2008) simplify using three constant weight factors: C_1 , C_2 and C_3 in equation 2.22. These constants were found by the use of the least squares regression using equation 2.22, fitting it to 159 wind tunnel measurements (Larsen and Heiselberg, 2008).

The wind effects were most dominating when the opening was on the windward side of the building, with temperature effects being dominant when it was on the lee-

ward side of the building, likely due to the thermal structures not being disturbed by the oncoming flow (Larsen and Heiselberg, 2008). Due to this change in behaviour the constants have different values for different θ_{ref} ranges (Table 2.1).

Table 2.1: Coefficients for equation 2.22 (Larsen and Heiselberg, 2008).

Direction	Incidence angle (β)	C_1	C_2	C_3
Windward	0 ° to 75 °, 285 ° to 360 °	0.0015	0.0009	-0.0005
Leeward	105 ° to 255 °	0.0050	0.0009	0.0160
Parallel flow	90 °, 270 °	0.0010	0.0005	0.0111

Some θ_{ref} values are not included in the coefficients, likely due to the limited measurement points and the difficulty in understanding whether the thermal or wind driven component dominates. The largest deviations between modelled and measured results occurred when the modelled values are smaller than the measured values. Larsen and Heiselberg (2008) suggest this is an advantage, as from a design perspective, it is easier to close an opening than it is to extend an opening.

2.3.10 Cross ventilation

Cross ventilation occurs when there are two or more openings on opposite walls and is commonly used in open plan areas. The effectiveness of cross ventilation is dependent on the depth of the building. A rule of thumb indicates that, spaces can be ventilated using cross ventilation to a depth of around five times the room height, although any obstacles in the path may ‘short-circuit’ the flow and reduce the effectiveness of the ventilation (Kukadia *et al.*, 1998). Other forms of cross ventilation can be achieved by ‘wrapping’ a building around an open courtyard (CIBSE, 2005).

Cross ventilation is often used for night cooling, or in scenarios where a high ventilation rate is desired (Da Graga and Linden, 2003). Uptake of cross ventilation is limited as there is no simplified design procedure for utilizing it, because of the complex interaction of the internal flow with the envelope flow (Carey and Etheridge, 1999). Due to security concerns, fire regulations and privacy concerns, cross ventilation can be difficult to implement into a building (Allocca *et al.*, 2003). Effective landscaping of the area surrounding a building (where possible), allows for greater implementation of cross ventilation, as tree canopies can be used to alter the approaching flow (Mochida *et al.*, 2005). However, cross ventilation can also act as a means of transfer for pollutants, causing external pollutants to penetrate deeper into the building, potentially reducing air quality (Allard and Ghiaus, 2012).

A commonly made assumption for cross ventilation is that the effect of buoyancy forces can be neglected due to the strength of the wind driven ventilation. Another

assumption is that internal airflow is negligible, known as the simplified macroscopic approach. With sufficiently large openings, the mean kinetic energy is not lost when the airflow approaches the opening, making the flow through the openings similar to the airflow through a duct.

Flow rates for cross ventilation are calculated using equation 2.8, the equation for 'large openings' with A_{eff} calculated using equation 2.10 for parallel openings. It is assumed that pressure coefficients calculated for a sealed building can be directly applied to a cross ventilated building with no correction (Straw, 2000).

Whilst the macroscopic assumption can be used to estimate ventilation rate, in reality internal flows can be considerable and complex. Flow within a room ventilated by cross ventilation is turbulent due to the interruption of jets, flow over and around furniture, buoyant effects due to heat sources and flow in the room corners. Chu and Chiang (2013), using LES and wind tunnel models demonstrate that internal obstacles can be neglected for wall porosities (ratio of opening to total wall area) $< 3\%$ but must be included above that value, otherwise the ventilation rate of a building will be overestimated.

Da Graga and Linden (2003) describe three main types of flow pattern for a cross ventilated building based on the ratio of the area of the inlet opening, A_{in} (width \times height) to the cross sectional area, A_r (width \times height) of the room (A_r / A_{in}) (Figure 2.14). When this ratio is ~ 1 , the flow is attached to the room surfaces and is similar to turbulent flow in a channel, as seen in and is often referred to as the 'simple case'. This is commonly seen in long corridors, with the flow occupying the full cross section of the room.

When this ratio is > 1 , the flow can be divided into two regions: a jet region which connects the inlet and outlet and a recirculation region, which is composed of the return flow that occurs over the cross flow perimeter of the room. The jet in the core of the room entrains air from adjacent areas, forming recirculation areas to ensure mass conservation. The maximum velocity in the recirculation region is predicted to occur close to the internal surfaces, making the flow similar to that of a wall jet (Figure 2.14) (Da Graga and Linden, 2003). When the ratio is ~ 2 , a combination of the behaviours seen from the other two flow patterns are predicted. The jet flow attaches to part of the room perimeter, but in most cases the recirculation flow still occupies the majority of the room volume.

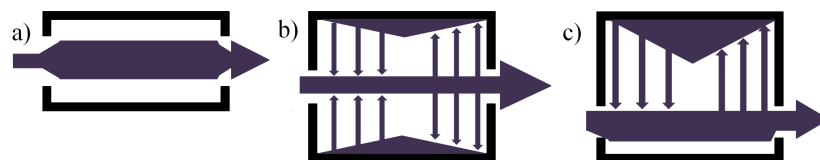


Figure 2.14: Plan view schematic showing three simplified main air flow patterns of cross ventilation from a top down perspective when the a) inlet to cross sectional area is ~ 1 , b) the ratio is much greater than 1, c) is when the ratio is ~ 2 , (a combination of a) and b)). The main channel of flow (large arrow), recirculation regions (triangles) and the interaction between the main flow and the recirculation regions (small arrows) are marked. The width of the main arrow highlights flow size. Adapted from Da Graga and Linden (2003).

The recirculating flow has been observed in many CFD studies and can often be seen in full-scale observations through the use of smoke or other tracers (Shetabivash, 2015). Openings are often around one order of magnitude smaller than the room cross section, resulting in a flow pattern that will be closer to Figure 2.14b or c (Shetabivash, 2015). The openings shape and position have a large effect on the internal air stream pattern altering the recirculation patterns, especially if there are multiple zones. Because of the complexity of the flow, many models make approximations on the system geometry by neglecting the effects of furniture and variations in outlet geometry (Linden and Carrilho da Graca, 2003).

Tominaga and Blocken (2015) used wind tunnel measurements to generate a database for CFD evaluating simulations for a cross ventilated simplified building in an atmospheric boundary layer. They measured mean and turbulent fluctuations of the velocity and compared the simplified isolated building to a case where it was sheltered by an array. The measurements obtained for the unsheltered building were similar to those obtained by Karava *et al.* (2011) using a 1:200 scale model, who found that the orifice equation predicted the ventilation flow rate with reasonable accuracy (value not stated) when openings are located in the middle or upper section of a building façade and when the wall porosity is lower than 10 %. However the flow rate is underestimated if any of the inlet or outlet openings cover more than 10 % of the wall area due to the internal flow pattern having an effect on the ventilation rate. For configurations with openings below the mid-height of the building, the orifice model overestimates the ventilation flow rate, except for configurations with large inlets and outlets (e.g. 20 % wall porosity) (Karava *et al.*, 2011).

Without changes in wind direction, opening position or size, a test building surrounded by a nine cube aligned array caused the ventilation rate to drop by 70 % compared to the isolated values (Tominaga and Blocken, 2015). The patterns of internal dispersion completely changed once the cube was sheltered probably caused by large scale flow patterns inside the room and not driven by external patterns (Tominaga and Blocken, 2015).

With a combination of wind tunnel and CFD measurements to model the effects of wind direction on cross ventilation, Ohba *et al.* (2001) found that often the eddy formed at the front of an isolated building (Figure 2.5) caused flow through the inlet to decline at a steep angle towards the building floor, reducing the penetration of the jet and the effectiveness of the ventilation. A change in the mean incident wind angle also led to changes in the cross ventilation rate due to changes in the structure of the external flow. For incident angles 40 ° to 60 °, the dynamic pressure at the outlet increased due to the change of the flow patterns around the model causing an increase in the ventilation rate (Ohba *et al.*, 2001).

An LES model of cross-ventilation, verified using full-scale on-site data and wind tunnel data was used by Jiang and Chen (2002) to explore changing the inlet boundary

conditions. The buildings were identical five-storey apartment blocks. A fixed wind direction simulated the wind tunnel model and varied for the full-scale measurements. There were differences between the two LES models. The natural wind could destroy the large recirculation regions behind a building, with only small eddies being present due to the steady wind direction not being able to ‘reach’ into all regions of a building façade (Jiang and Chen, 2002). The gradient of the pressure coefficient difference (Section 2.3.11) across the building was more uniform for a fluctuating wind direction model than for the fixed wind direction (Jiang and Chen, 2002). The indoor airflow through cross ventilation also had a thinner and faster core for a constant wind direction when compared to the results of a fluctuating wind direction (Jiang and Chen, 2002).

Gilkeson *et al.* (2013) used tracer gas releases in a naturally cross-ventilated hospital ward in order to relate ventilation rates to the risk of cross-contamination and external conditions. They found that for low wind speed cases and cases where the windows are purposely closed, the risk of infection can be increased four-fold, highlighting the importance of considering the seasonal conditions in ventilation design. Gilkeson *et al.* (2013) noted that it was not easy to characterise flow patterns caused by natural ventilation due to the variability and uncertainty of local outdoor winds due to the hospital being in an urban area, highlighting the need for long-term urban ventilation measurements which cover a range of conditions in all seasons, in order to gain an understanding as to the variability of a buildings response to the external conditions.

2.3.11 Pressure Coefficient (C_p)

The pressure coefficient (C_p) is a dimensionless quantity commonly used to describe the pressure at one point compared to a reference pressure. Negative values indicate reduced pressure on leeward surfaces, flow separation and flow reattachment. C_p is the difference between local static pressure (p_s) and free-stream static pressure (p_∞), non-dimensionalized by the free-stream dynamic pressure (Δq_∞):

$$C_p = \frac{\Delta P_{wind}}{\frac{1}{2}\rho_\infty U^2} \quad (2.28)$$

$$\Delta q_\infty = \frac{1}{2}\rho_\infty U^2 \quad (2.29)$$

C_p for an incompressible flow can be derived from Bernoulli’s equation and expressed in terms of velocity (U). Consider the flow over an aerodynamic body immersed in a free-stream with pressure p_∞ and velocity U_∞ . Using an arbitrary point in the flow Anderson Jr (2010):

$$p_\infty + \frac{1}{2}\rho U_\infty^2 = p_s + \frac{1}{2}\rho U^2 \quad (2.30)$$

or

$$p_s - p_\infty = \frac{1}{2}\rho(U_\infty^2 - U^2) \quad (2.31)$$

Substituting equation 2.31 into equation 2.30 gives:

$$C_p = \frac{p_s - p_\infty}{q_\infty} = \frac{\frac{1}{2}\rho(U_\infty^2 - U^2)}{\frac{1}{2}\rho U_\infty^2} \quad (2.32)$$

or

$$C_p = 1 - \left(\frac{U}{U_\infty}\right)^2 \quad (2.33)$$

Equation 2.33 holds for incompressible flow only (Anderson Jr, 2010). At a stagnation point ($U = 0$) in an incompressible flow the pressure coefficient is always equal to 1, the maximum value of C_p anywhere in the flow field. However, this does not hold true for compressible flows. In regions of the flow where $U > U_\infty$ or $p < p_\infty$, C_p will be a negative value.

Errors in C_p are calculated using :

$$\sigma C_p = C_p \sqrt{\left(\frac{\sigma_{\Delta P}}{\Delta P}\right)^2 + \left(\frac{\sigma_\rho}{\rho}\right)^2 + 4\left(\frac{\sigma_U}{U}\right)^2} \quad (2.34)$$

where σ_X represents the error in X and can be a combination of measurement and instrument error.

As the wind is non-uniform within atmospheric boundary layer flows, the height at which the free stream pressure (for Δp) is obtained will affect the measurement (Anderson Jr, 2010). There is no formal standard for the height at which the reference pressure should be measured but it is most often 'at the height of the building a little way upwind' though this should be confirmed for each individual case (Hall and Spanton, 2012). There is no set method for the measurement of p_0 but instead it is assumed to be approximately constant over height in the undisturbed upwind flow (Hall and Spanton, 2012). The directional fluctuation in the wind speed combined with fluctuations of wind speed itself can strongly influence the pressure coefficient (Park, 2013).

On-site full-scale measurements of real buildings provide the most representative description of C_p . The definition of proper boundary conditions is a main constraint in using full-scale C_p observations for verification purposes and that defining a reference point, especially within an urban environment is difficult (Cóstola *et al.*, 2009). Many of the existing datasets cannot be used for verification purposes due to the lack of information on the approaching wind flow (Reinhold, 1982). For ventilation and infiltration studies, the effects of turbulence on the temporal variation of C_p are often neglected (Etheridge, 2000).

Cóstola *et al.* (2009) discusses the common assumption that C_p is independent of U

which is considered to be true when flow around a building is Reynolds number (Re) independent (Section 5.8) and is not significantly influenced by thermal processes. For bluff bodies with sharp edges, the assumption that C_p is Reynolds number independent is generally valid for all velocities because of the high Reynolds numbers in building aerodynamics (Cóstola *et al.*, 2009). However, for low wind speeds, it is likely that the flow will be influenced by thermal processes such as solar radiation as well as related small scale and large scale thermal processes such as stratification and atmospheric stability (Stull, 1988).

The uncertainty in C_p is subject to the error on the measurements of the pressure on the façade, reference pressure, reference wind speed, air temperature and atmospheric pressure. Statistical variabilities of the data themselves, errors on measurement equipment, physical variability of the flow due to different simulation methods, different time and geometric scales imposed by a given wind-tunnel flow, imperfections of the model, imperfections of the software used for the data analysis and human error all also have an effect (Hölscher and Niemann, 1998). Measurement protocol and instrument positioning will also effect the results (Cóstola *et al.*, 2009). The lack of stated uncertainty in C_p limits how full-scale measurements can be inter-compared and also affects how scale models and CFD simulations can be validated, though uncertainty values are not commonly quoted in the literature.

Whilst the error on C_p is likely to be larger for full-scale observations when compared to wind tunnel experiments, there has also been considerable variation in the estimates of C_p for the ‘classic wind tunnel case’: an isolated cube. Hölscher and Niemann (1998) compared the wind-tunnel results for C_p of an isolated cube, for three wind directions measured by 12 institutions. All institutions were given the same instructions: Measure the mean surface pressures on a floor-mounted cube, at a scale which corresponds to 50 m height at the full-scale. Re , based on the cube height and the velocity at 50 m above ground, must be $> 5 \times 10^5$. The area blockage ratio was to be smaller than 5%. The results (Figure 2.15) alongside wind tunnel measurements made by Richards *et al.* (2007) highlight the large range of C_p values caused by the use of differing equipment and methods. C_p values from different data sources, for the same set-up and same building can differ (Cóstola *et al.*, 2009). For an isolated building which is completely exposed, differences of 0.4 are noted, comparable to the range seen in Figure 2.15 (Cóstola *et al.*, 2009). This range increases for sheltered buildings, especially at façade corners which can be considerably greater, with differences of up to 1.0 (Cóstola *et al.*, 2009).

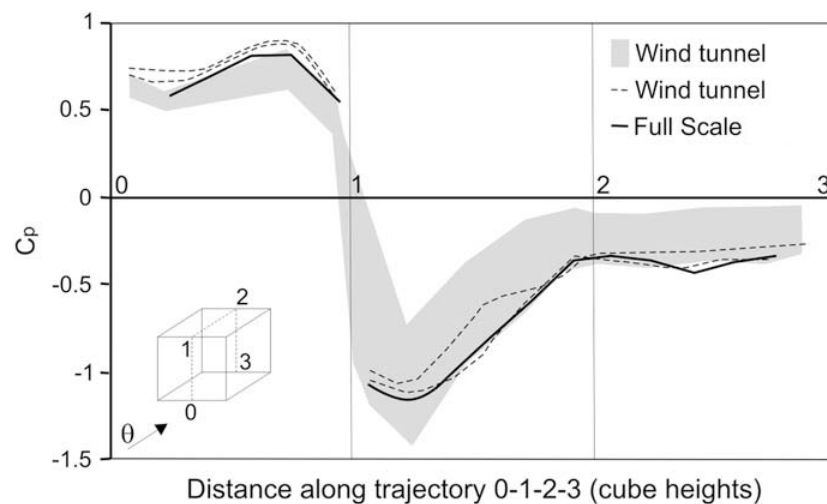


Figure 2.15: Results of the study by Hölscher and Niemann (1998). The dashed lines are the results from Richards *et al.* (2007) and the solid black line is the full-scale results. Adapted from Hölscher and Niemann (1998).

2.3.11.1 Pressure coefficient within an array

Ahmad *et al.* (2012) used pressure taps to calculate the drag force on a cube surrounded within square, staggered and diamond uniform arrays of cubes, with several different packing densities used for the staggered array (7.7 % to 39.1%). The results, without direct ventilation rate measurements of the test cube (located at the centre of the array), show the overall pressure drag of a rectangular building decreases as surrounding building density increases from (4 % to 40 %). The sheltering of the pressure tapped cube caused an overall decrease in the C_p values recorded, with the magnitude being dependent on the height of the reference wind velocity, from 9 % using a velocity taken at 20 H to 24 % using building height velocity compared to the C_p values measured for least dense array.

The pressure pattern of a building varies depending on its height ratio to the surrounding buildings (Figure 2.3) (Hall and Spanton, 2012). If a building is shorter or the same height as its surroundings, it will experience a sheltered flow pressure pattern. If the building is taller than its surroundings, the bottom half will experience a 'sheltered affect', though the pressure pattern will change towards an isolated flow as other buildings no longer impede the flow (Hall and Spanton, 2012).

Park (2013) found that the directional fluctuations are independent of the mean wind speed and that directional fluctuations may strongly influence C_p , especially when they combine with wind speed fluctuations. Selectively choosing data which neglects the effect of either wind or temperature is a common methodology in full-scale ventilation research, due to the complexities of combining the two. However, this is not representative of the most conditions but is, at times, a necessary simplification.

2.3.11.2 Pressure coefficient databases

Databases of C_p values are available which are compilations from one or more sources, classified according to parameters such as building shape, roof type and orientation to the incident wind. These are most commonly used to calculate the wind load on structures.

Two databases are used for infiltration and ventilation of simple structures: the AIVC database (Liddament (1986), Air Infiltration and Ventilation Centre) and the ASHRAE handbook (2001) (American Society of Heating, Refrigerating and Air-Conditioning Engineers). The AIVC database contains values of C_p for low rise buildings (> 3 storeys) and high rise buildings.

The C_p database for low-rise buildings consists of tables with surface-averaged data, for rectangular floor plans and for three shielding levels: exposed, semi-sheltered (surrounding obstacles with half of the building height) and sheltered (surrounding obstacles with the same height as the building). The data are provided for wind direction sectors of 45° for the wall of a square floor plan building and for the long and short walls of a rectangular (1:2) floor plan building. Unfortunately the method used to convert the wind-tunnel data to the database is not stated (Cóstola *et al.*, 2009). Building height and the H/W ratio are not given and only the averaged value over the whole surface provided for the façades, despite it being known that the behaviour of C_p varies with location (Cóstola *et al.*, 2009).

For the sheltered cases, the spacing between the obstacles, λ_p and wind profile used in the wind-tunnel tests are not provided. This is of concern and makes inter-comparison difficult. The effect of packing density and array type on C_p is shown in Figure 2.16 (Cheng *et al.*, 2007).

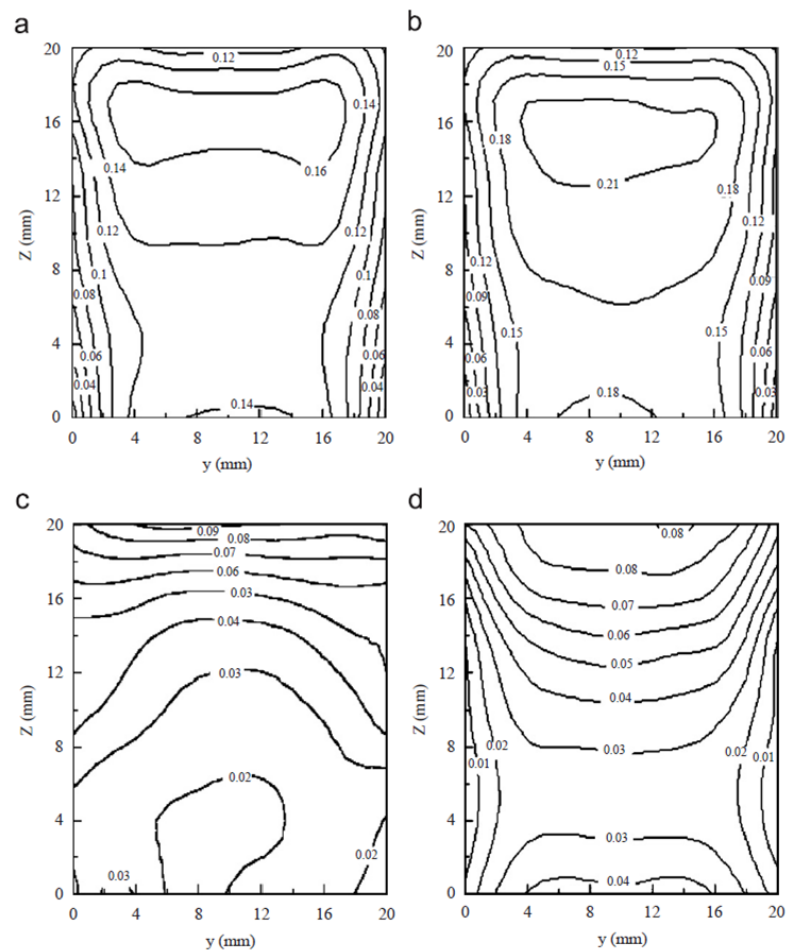


Figure 2.16: Pressure coefficients for a cube within a) an aligned array of packing density 6.25 % b) a staggered array of $\lambda_p = 6.25\%$ c) an aligned array with $\lambda_p = 25\%$ and d) a staggered array with $\lambda_p = 25\%$. All arrays contained 20 cubes and all arrays were measured at a reference wind speed of 10 m s^{-1} . Source: Cheng *et al.* (2007).

However the AIVC database gives several warnings: “the intention of these data sets is to provide the user with an indication of the range of C_p values which might be anticipated for various building orientations and for various degrees of shielding” and “Caution: Approximate data only. No responsibility can be accepted for the use of data presented in this publication” (Liddament, 1986). Despite these warnings, the data have been reproduced in research for building performance, (e.g. Santamouris and Allard (1998), Orme and Leksmono (2002)) and is currently in use by the scientific community (Cóstola *et al.*, 2009).

The ASHRAE handbook reproduces data from primary sources for low rise and high rise buildings, it presents both surface averaged C_p values and examples of expected distribution across the surface. The building geometries used are simple rectangular prisms with four different floor plan aspect ratios with data available over wind angles of 0° to 180° . The ASHRAE database provides correction factors for the reference wind

speed based on sheltering factors, though does not give the basis of the wind profiles used. For both databases no uncertainty values are given. Sawachi *et al.* (2004) questions the validity of a fixed C_p value for wind directions which are at an oblique angle to the opening, though no other guidance is available (CIBSE, 2006).

2.4 Conclusions

This literature review has broadly covered research into flow around urban areas and the effects on ventilation, however, it is by no means conclusive.

Simplifying an urban area down into an array of uniform cubes allows for an understanding as to how the packing density effects flow and drag, how array shape alters drag and how flow adjusts over the urban area. Using a horizontally non-uniform array is rare, but vertically non-uniform arrays are of interest due to the increasing number of high-rise buildings being built. Varying building height prevents flow from skimming over the top of an array, causing it to continually adjust to the changes in the canopy height (Cheng and Castro, 2002). Taller buildings also appear to have a larger influence on the surrounding flow when surrounded by smaller buildings (Zaki *et al.*, 2010). Internal and external flows need to be more frequently coupled to allow for an understanding of how different surroundings effect the internal environment and occupant satisfaction. The effect of neighbouring buildings on the ventilation rate of a building which may or may not be the same size also needs to be considered.

Little consideration is often given to the larger scale driving forces in studies of ventilation, with the worst case scenarios (low winds, high temperatures or maximum expected gusts) often being the driving forces of design. Most research has been undertaken in near neutral conditions for both ventilation and flow in urban areas and little work has been done on the effect of stable and unstable atmospheric conditions on ventilation, especially on single sided ventilation, due to the buoyant component. All ventilation models need to be tested against full-scale data with modifications made to quantify the affects of local topography on the ventilation rate as sheltering effects can reduce the ventilation rate as shown by Tominaga and Blocken (2015) and Van Hooff and Blocken (2010).

Changes in wind direction will influence the flow around a building and the ventilation rate, with differences between steady directions being up to 152 % (Van Hooff and Blocken, 2010). This is due to changes in the sheltering due to surrounding buildings. A way of relating the sheltering factor of a building to the local canopy characteristics is required, as the effect of wind direction will be dependent on the location of the building of interest. Both long term changes in wind direction and short term fluctuations in wind direction both in the reference wind and local wind profile need to be considered in order to be able to quantify a realistic atmospheric flow.

The local wind speed within the urban area will determine the dominating ventilation mechanism, especially for single sided ventilation. A low reference wind speed suggests thermal mechanisms dominate, with wind driven and thermal being roughly equivalent at 4 m s^{-1} and wind driven fully dominating at 8 m s^{-1} (Allocca *et al.*, 2003). The dominating mechanism also alters as a function of wind direction, with the effect of changing the mean incident wind direction being similar for purely thermal driven and purely wind driven (Larsen and Heiselberg, 2008). For a city, air exchange might be controlled by both the local environment (location and roughness of buildings) and by the much larger scale motions developed above the canopy layer, which will in turn effect the ventilation rates (Inagaki and Kanda, 2010). Small irregularities within a regular array are shown by Santiago *et al.* (2010) to have an effect on the flow in the micro-scale.

Combining the changes in speed, with changes in the wind direction with fluctuations in wind direction and with changes in internal and external temperature difference has not been done before and as such, no guidelines are available to planners and architects. Research into natural ventilation of buildings is selective and is unique to the chosen building, with no standard practise and no standard way of recording the experimental set-up, making it difficult to inter-compare results and improve methodology. A multi-model approach is required. Full-scale data, though being expensive, is the key to evaluating scale models which in turn aids in the verification of CFD approaches. Wind tunnel results can allow for the full-scale data set to be expanded upon for a relatively low cost.

Prior research illustrates the need for a range of conditions to be studied in order to understand how ventilation of a specific building may change over time, allowing for more realistic predictions of energy usage and ventilation performance. Combining the methodologies of engineering and urban meteorology will allow for a large, varied dataset which contains variations in stability, temperature, wind speed, wind direction and wind direction fluctuation for a range of ventilation layouts. Data measured for a simplified urban area should allow for the results to be applicable across a broad range of circumstances with all methodology, positioning and uncertainties quantified, in order to allow easier comparison to other datasets and modelling methods. Ventilation models are tested against realistic full-scale data in order to more fully understand their shortcomings and strengths.

Chapter 3

Full-scale field observations

3.1 Introduction

Full-scale, natural ventilation observations were undertaken between September 2014 and July 2015 at Wrest Park, Silsoe, Bedfordshire, England (Figure 3.1) with an isolated instrumented cube (Figure 3.3) and with an instrumented cube surrounded by an array (Figure 3.5). The instruments used are summarised in Table 3.2.

Observations are used to investigate how an array of surrounding buildings of similar size influences the distribution of the pressure coefficient and ventilation rate of a building over a range of atmospheric conditions. The full-scale, idealised representation of an urban area, is free from anthropogenic influence. Buildings are simplified into cubes to allow comparisons with wind tunnel and CFD studies e.g. Cheng *et al.* (2007). Due to the space limitations on site, a staggered array was chosen to provide maximum blockage of the flow at the test building for the prevailing wind direction (Ahmad *et al.*, 2012).

By measuring both the isolated cube and the array, the effect of the array on the flow around the instrumented cube could be determined. Three different ventilation set ups were used: sealed, single-sided and cross ventilated (Sections 2.3.7, 2.3.8, 2.3.10). Three different methods of measuring ventilation rate were used to permit evaluation of the current models for natural ventilation rate and to investigate how different ventilation types may be affected by changes in wind direction (θ_{ref}), atmospheric stability, reference wind speed (U_{ref}) and the presence of the array. The data are used to consider the combined effects of θ_{ref} , the presence of an array and atmospheric stability on pressure coefficients (C_p) (Section 2.3.11, Chapter 5) and ventilation rate (Chapter 6).

3.2 The site

The site was chosen due to the presence of an *in-situ* test structure (Section 3.3) and due to the large amount of research already undertaken on the test structure and surroundings. The site has few obstructions (Figure 3.2). It is anticipated that the wake of the wind break trees (estimated height 3 m) to the South-West does not extend to the site (Figure 3.2).

The Silsoe research site wind characteristics for the site have been studied with detailed measurements up to 100 m above ground with measurements being well matched by a simple logarithmic profile with a roughness length (z_0) of 0.006 to 0.03 m, depending on wind direction (Hoxey and Baker, 2012).

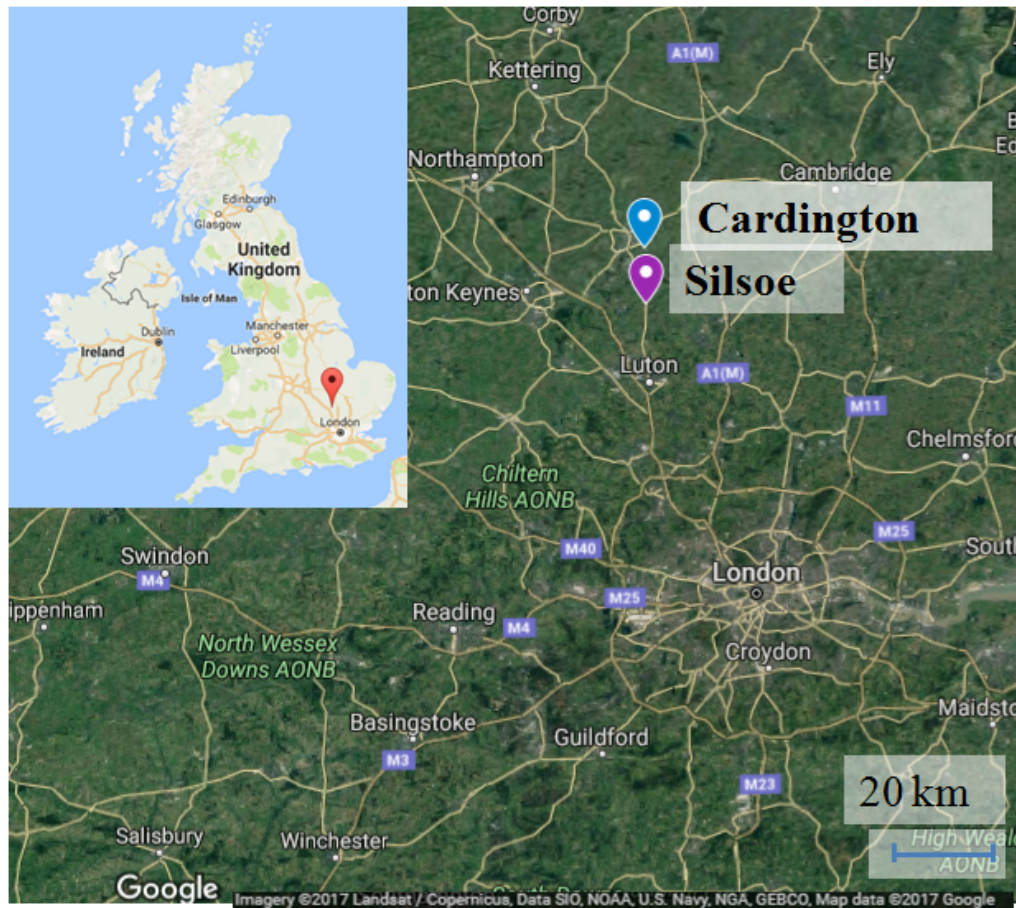


Figure 3.1: Test site (Silsoe, Latitude 52.01088 ° N on Longitude -0.410979 ° W) and the location of Cardington, the nearest Met Office meteorological station 10 km away Both maps Copyright 2017 Google and Landsat.

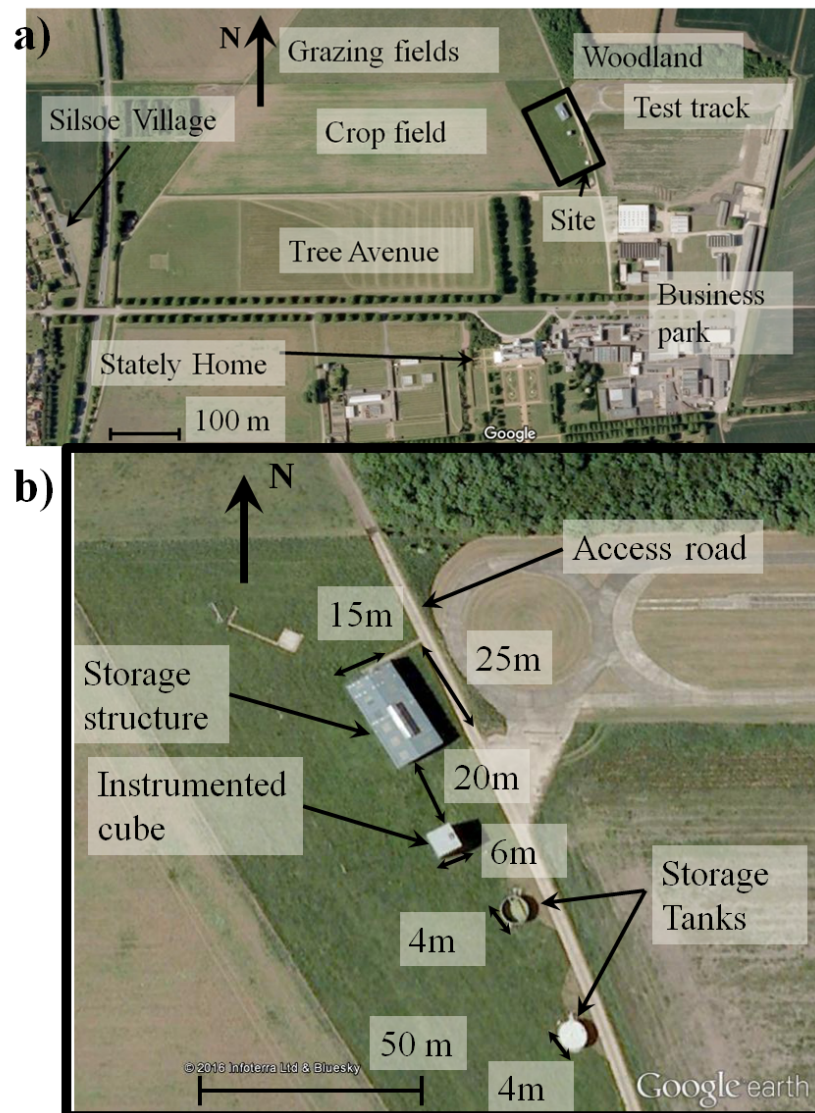


Figure 3.2: Silsoe site and a) surroundings and b) in detail. No features of the site have changed since 2009. Copyright 2016 Infoterra, Blue Sky Limited and Google Earth.

3.2.1 Limitations of the site

The site is located next to an English Heritage property, so visual impact had to be kept to a minimum. With the site open to the public a risk of theft or tampering was present but fortunately this did not occur. The access road to the local farms (Figure 3.2b) limited the extent of the array and therefore the array choice (Section 3.4). The reference flow measurements (Section 3.5.2) show excellent agreement to the flow measurements taken from the Cardington Met Office site (Figure 3.1).

The two storage tanks (2 m high and 4 m wide) and the storage shed (height 6 m with a sloping roof and is 15 m wide and 25 m long) could not be removed (Figure 3.2). During storms or heavy rain the site would lose power, requiring a full-reboot of

most/all logging systems, which could be delayed due to accessibility problems, leading to a loss of data. To the west of the site (Figure 3.2) the crop height varied during the year. The observations began just after harvesting, with crop stumps ~ 0.1 m tall present.

3.3 The instrumented cube

The test-structure was a metal cube (Figure 3.3) with external dimensions $6 \times 6 \times 6$ m³, constructed on a large turntable and secured by four metal adjustable legs located within the cube. The cube remained stationary for the duration of the experiments, with the front of the cube positioned facing the direction with the longest fetch (approximately 240°). The West wall will be referred to as the Front wall, with the East wall being the Back wall. The exterior of the cube is clad with flat, steel sheets to ensure uniform external surfaces. Each wall had the capability of having a horizontal and vertical array of pressure taps mounted externally, internally or a mixture of both (Section 3.6).

Removable panels were located on the front and back faces, allowing the cube to be tested as both a sealed and a ventilated structure. The removable panels used were 0.4 m wide by 1 m high with the centre point being 3.5 m from the ground (Figure 3.3). The discharge coefficient (C_d) defined as the ratio of true flow to theoretical flow, was confirmed to be 0.616 ± 0.016 for both openings (Appendix C) when acting as an inlet (Hoxey and Robertson, personal communication, 2015). When the opening acted as an outlet, the discharge coefficient was 0.658 ± 0.022 (Hoxey and Robertson, personal communication, 2015). Access to the cube was through a door in the North side, which was closed for all ventilation experiments.

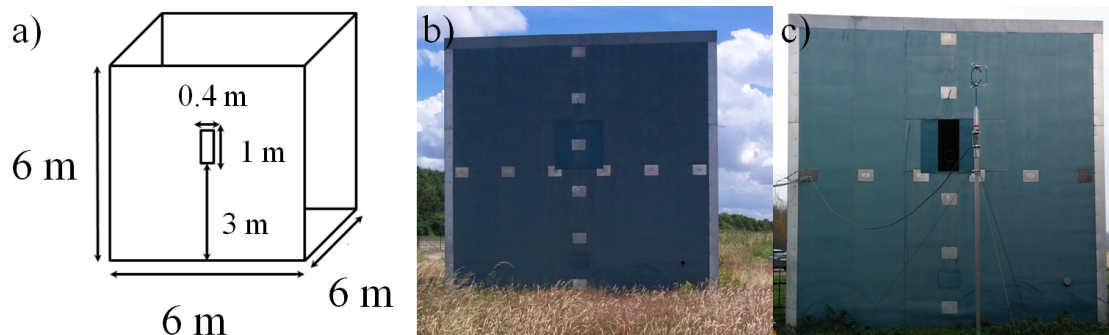


Figure 3.3: The Silsoe cube a) Dimensions b) photograph of the Front (west) face. c) Front face of the cube with the vent open and the front (local) mast visible (Section 3.5.2). Silver panels are surface pressure taps (Section 3.5).

The Silsoe cube is a simplified representation of a building in the full-scale allowing it to be directly compared to wind tunnel models formed of cubes. Work using the 6 m ‘test’ building has been undertaken by Yang (2004), Straw (2000), Knapp (2007) and Richards and Hoxey (2008). Richards and Hoxey have undertaken research with the structure

for approximately 25 years. The test building has been modelled in the wind tunnel by Richards *et al.* (2007) and using various CFD methods (Irtaza *et al.*, 2013).

Ventilation studies include using used 1 m^2 openings for both single sided and cross ventilation for $\theta_{ref} = 0^\circ$, 90° and at 45° to the openings (Straw, 2000). The pressure difference and constant injection tracer gas methods using carbon monoxide were used to measure the ventilation rate (Straw, 2000). Tracer gas releases similar to Straw (2000) are not possible due to increased health and safety guidelines. Velocities were measured upwind of the structure and inside the cube.

Standard $k-\epsilon$ and RNG (Renormalisation Group Theory) $k-\epsilon$ turbulence models have been used to simulate the wind induced ventilation of the Silsoe cube and the results compared to full-scale data (Straw, 2000).

Ventilation experiments and CFD modelling of the Silsoe cube using smaller windows ($0.35 \text{ m} \times 0.25 \text{ m}$) located 1 m and 5 m above the ground has been undertaken by Yang (2004). The ratio of opening area to wall area was 0.24 % and the small openings chosen effected the building surface pressure distribution close to the openings (Yang, 2004).

The vast amount of research undertaken on the Silsoe cube make it a unique facility with a well studied site profile. Research techniques have been refined through time to accommodate the characteristics of the site and cube. The site allows for ventilation of a building to be studied without the influence of an urban area, which reduces the complexity of the problem. The design of the cube allows for internal and external measurements, allowing the coupling of the environments to be studied. This set-up (Section 3.5) has been influenced by the findings of Yang (2004) and Straw (2000), with the opening size reduced (Figure 3.3) in order to reduce the ventilation rate of the cube to allow for a more accurate measurement when using tracer gas methods.

3.3.1 Ventilation configurations

Six different natural ventilation configurations were tested (Table 3.1). In single-sided ventilation only the front panel is removed whereas for cross ventilation the back and front panels were removed. The sealed cube tests were used to gain an understanding of the infiltration rate of the cube and required no panels to be removed. For the single sided ventilation, the opening to wall ratio was 0.22.

The cube was on uneven ground causing a gap around the base that varied between 0.05 m to 0.15 m on the North West corner. During preliminary array tests it was noted that this gap was responsible for 10 % to 50 % of the measured ventilation. Packing foam (Figure 3.4) was used to fill the gaps in order to obtain a level of infiltration similar to that of Yang (2004) ($0.5 - 1 \text{ h}^{-1}$) where the base was filled with sand. This packing foam remained in place for both the array and isolated cube studies (Table 3.1).



Figure 3.4: External Back (east) cube face with the packing foam clearly visible.

Table 3.1:: Array set up and period of observations. The site was decommissioned in April 2016.

Type	Opening	Foam	Start date	End date
Array	Sealed	N	01/10/14	18/11/14
Array	Single sided	N	18/11/14	12/12/14
Array	Cross	N	12/12/14	22/12/14
Array	Sealed	Y	22/12/14	13/02/15
Array	Single sided	Y	13/02/15	19/03/15
Array	Cross	Y	20/03/15	09/04/15
Isolated	Sealed	Y	25/06/15	07/07/15
Isolated	Single sided	Y	09/06/15	25/06/15
Isolated	Cross	Y	21/05/15	09/06/15

3.4 The Array

A temporary staggered array of eight approximately $6 \times 6 \times 6 \text{ m}^3$ straw cubes was built around the instrumented cube (Figure 3.5) at the beginning of the observation period. The total area of the array was 1260 m^2 , with a plan area density (λ_p) of 25.7%. The array was positioned so that it was facing into the prevailing wind direction of approximately 240° (Figure 3.5). Prevailing winds will be referred to as $\theta_{ref} = 0^\circ$, with clockwise angles being positive values and anticlockwise angles being negative values (Figure 3.5).

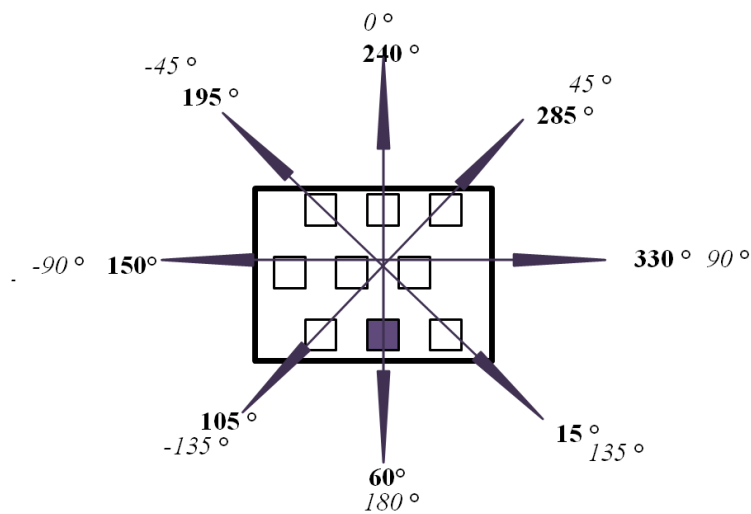


Figure 3.5: Silsoe cube array. Camera is facing to the West. The black box denotes the total area of the array used to calculate λ_p and λ_f . Meteorological angles are in bold and notation angles are in italics.

Straw was chosen to minimise the visual impact and to create a temporary a structure robust enough to safely withstand several months exposure to strong winds. However the nature of this material means the sides and tops of the cubes were not completely smooth and over time began to tilt and buckle. The array of eight extra cubes created a layout that represented a simplified residential area, free from irregular building arrangements, trees and the effect of human activities.

Ideally a row of cubes would be positioned behind the instrumented cube, in keeping with wind tunnel and modelling experiments, however both access and health and safety constraints meant that this was not possible (Figure 3.3).

Between 10/04/2015 and 21/05/2015 the array was removed from the site, and observations were carried out on the isolated cube using instruments which remained in the same locations until 08/07/2015 (Table 3.1).

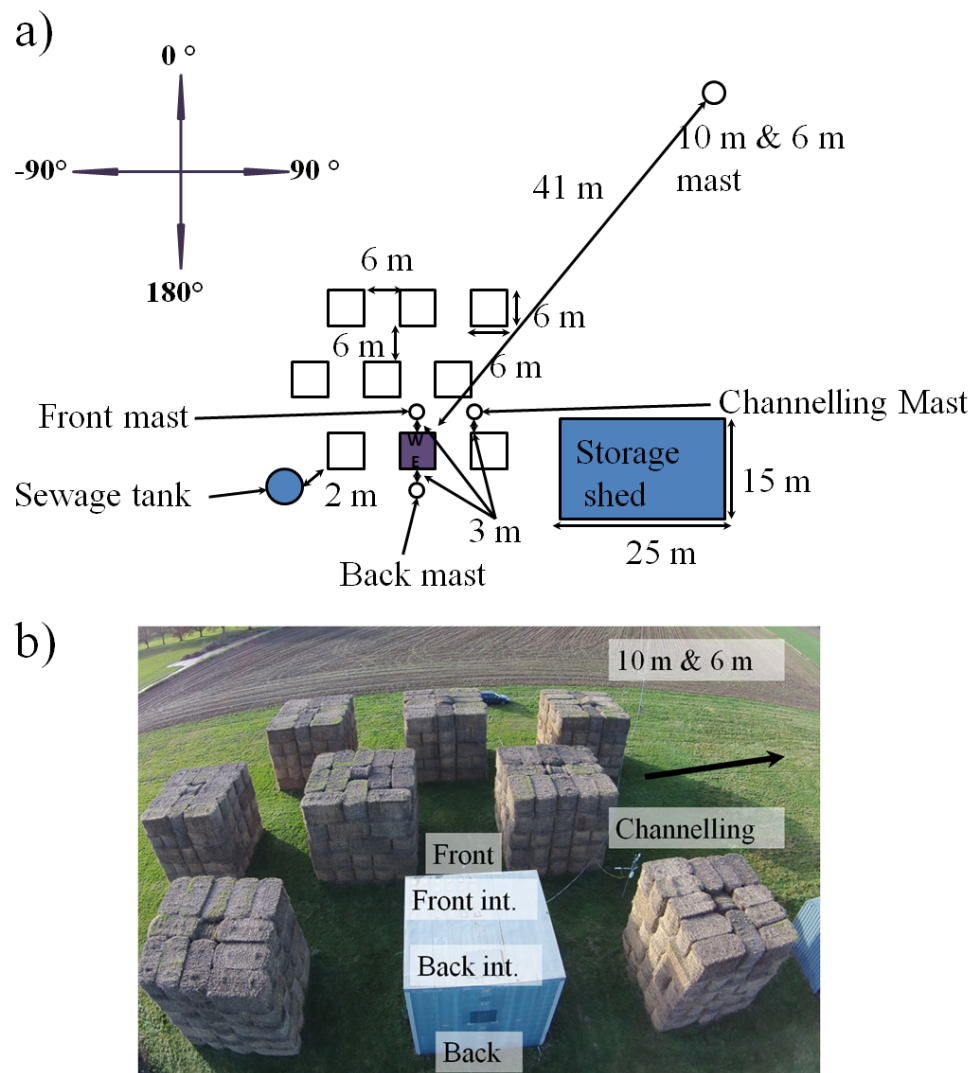


Figure 3.6: a) Plan of the cube array with dimensions and distances marked. b) Overview of the external mast locations within the array. These remained in place from 01/10/14 to 08/07/2015 through the isolated and array configurations.

3.5 Experimental Configuration

Given the aim of capturing a wide range of atmospheric conditions, simultaneous measurements of wind speed, wind direction, stability, temperature, rainfall, turbulence, radiation, CO_2 and pressure were needed (Table 3.2).

3.5.1 Summary of Instruments

Table 3.2.: Summary of equipment used for the full-scale observations at Silsoe, including instrument type, model and errors.

Instrument type	Number	Reference material	Specifications
Gill Windmaster R3-50 Sonic Anemometer	7	Table 3.3	<p>Velocity Range: 0 - 45 m s⁻¹ Resolution: 0.01 m s⁻¹ Accuracy: less than 1.5 % RMS at 12 m s⁻¹</p> <p>Direction Range: 0 - 359 ° Resolution: 0.1 ° Accuracy: 2 ° at 12 m s⁻¹</p>
LI-COR LI-7500 Infra-red hygrometer	1	Figure 3.8	<p>Range CO₂: 0-3000 ppm Accuracy CO₂: 1 % of reading</p> <p>Range H₂O: 0-60 ppt Accuracy H₂O: 2 % of reading</p>
K30 FR 2 Hz 1 % non-dispersive infra-red (NDIR) CO ₂ Sensor	3	Section 3.7.1	<p>Range: 0 - 10000 ppm Error on Measurements: ± 20 ppm ± 1 % of measured value Accuracy: ± 30 ppm ± 3 % of measured value Response time: 2 s at 0.5 L min⁻¹ flow 20 s diffusion time</p>

Honeywell Analogue Pressure taps	32	Section 3.6	<p>1:16 Range: -2.5 to 2.5 Inches of H_2O Honeywell 163PC01D75</p> <p>17:32 Range: 5 to 5 Inches of H_2O Honeywell 163PC01D76</p> <p>Response time (all): 1 ms</p> <p>Drift (all) 0.5 % of the measurement span per year</p>
Type-K thermocouples	24	Section 3.5.4	<p>Range: -100 to 250 °C</p> <p>Error on Measurements ± 1.5 °C ± 0.25 %</p> <p>Time response in moving air: 0.1 s</p> <p>Diameter: 0.2 mm</p>
Vaisala WXT520 Weather Station	1	Figure 3.8	<p>Wind Speed Accuracy: $\pm 3\%$ at 10 m s^{-1}</p> <p>Wind direction Accuracy: $\pm 3^\circ$</p> <p>Wind Response time: 250 ms</p> <p>Air temperature accuracy at 20 °C : ± 0.3 °C</p> <p>Humidity 0-90 % accuracy: ± 3 %</p> <p>Pressure accuracy at 0 - 30°C: ± 5 hPa</p> <p>Precipitation accuracy: 5%</p>
Kipp and Zonen CNR4	1	Figure 3.8	<p>Response time: < 18 s</p> <p>Non-Linearity: < 1 %</p> <p>Sensitivity: 5 to 20 $\mu \text{ V/W} / \text{m}^2$</p>

3.5.2 Wind and turbulence measurements using sonic anemometers

Seven sonic anemometers were deployed; two within the cube and five outside (Figure 3.6) in order to monitor internal and external flow (Tables 3.2, 3.3). The internal and external sonic anemometers were positioned so that the instrument head centres were in line with the middle of the opening. This position was chosen to avoid the effects of window edges on the flow and was in keeping with the methodology of Straw (2000). The 6 m reference sonic anemometer was logged with the cube surface pressures (Section 3.6), with the remainder of the sonic anemometers logged through a MOXA UC 7410 Plus fan-less computer for synchronised time stamps. Post processing of the sonic anemometer data used methods outlined by Barlow *et al.* (2014) and Wood *et al.* (2010).

Table 3.3: Names, heights, locations and sampling frequencies (SF) of the seven sonic anemometers deployed at Silsoe.

Name	Height (m)	Location	SF (Hz)
Reference	6	Upstream of cube	10
10 m reference	10	Upstream of cube	10
Front (Local)	3.5	3 m in front of west opening	10
Back	3.5	3 m in front of east opening	10
Channelling	2.9	41.5 m North of cube (bearing 270° , $\theta_{ref} = 30^\circ$, Figure 3.5).	20
Front internal	3.5	0.3 m away from the inside of front (west) opening	10
Back external	3.5	0.3 m away from the of back (east) opening	10

The 6 m (building height) sonic anemometer was chosen as the reference mast for the wind speed (U_{ref}) and wind direction (θ_{ref}), due to concerns about the wind direction measurements obtained from the 10 m mast (Figure 3.6). Data were split into three categories by wind speed: high ($> 6 \text{ m s}^{-1}$), medium (3 to 6 m s^{-1}) and low ($< 3 \text{ m s}^{-1}$). The low windspeed threshold (3 m s^{-1}) is in line with the methodology being used by Richards and Hoxey (2012) (Section 5.3). For some wind directions, such as North-East sector, there are little to no data after low wind speeds ($< 3 \text{ m s}^{-1}$) are discarded (Figure 3.7).

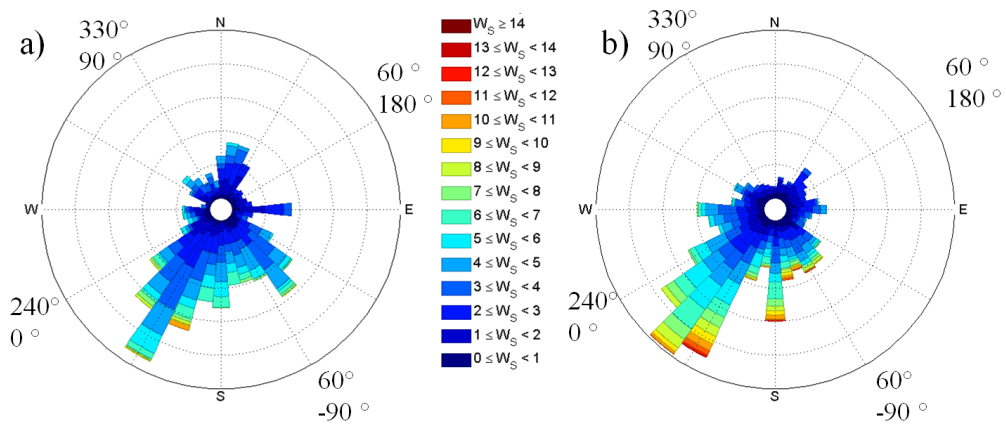


Figure 3.7: Wind rose of the 6 m reference mast data for the a) isolated cube and b) array. Colours represent U_{ref} (m s^{-1}) with the length of the bars representing the frequency of that θ_{ref} . Inner labels are meteorological θ_{ref} values and outer labels are with respect to the cube. All values are half hour averages and taken from the 6 m mast, with the prevailing south-westerly winds evident.

3.5.3 Background Meteorological measurements

The background meteorological measurements provide information on the atmospheric conditions at the site, and allow data to be filtered for different weather conditions. The WXT520 weather station provides a measurement of outdoor temperature positioned to minimise solar gains (Table 3.2, Figure 3.8).

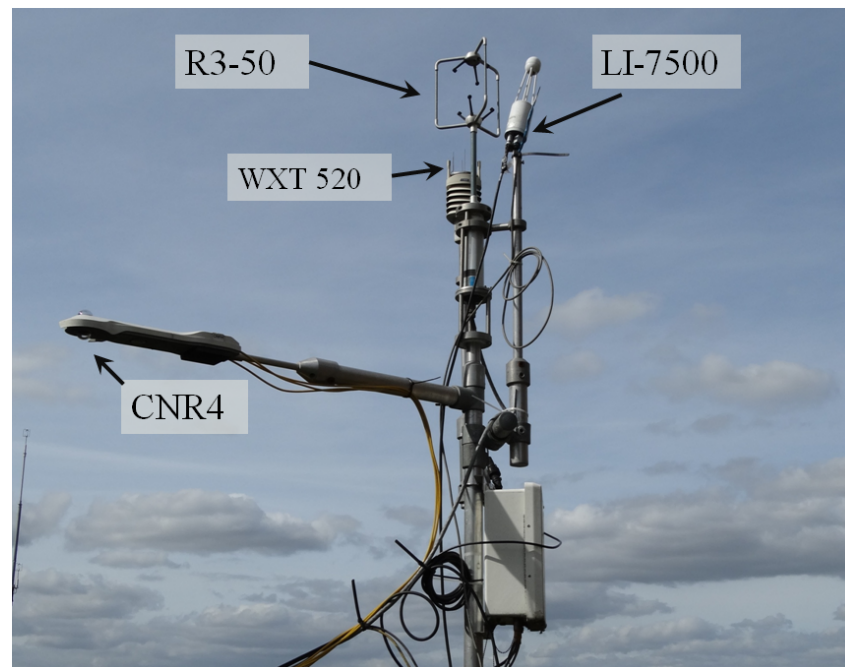


Figure 3.8: Overview of the instruments on the Channelling mast. Vaisala WXT520 weather station, Gill R3-50 sonic anemometer, Kipp and Zonen CNR4 net radiometer and LI-COR LI-7500 CO_2 and H_2O analyser all logged to a CR1000 Campbell logger located within the cube, with all instruments sampling at 20 Hz (Table 3.2). The centre of the sonic anemometer head, LI-COR LI-7500 head and the WXT sonic anemometer transducers were mounted at 2.9 m.

3.5.4 Internal temperature measurements

To gain an understanding of the incoming air temperature and how the horizontal and vertical thermal gradients of the cube change with different atmospheric conditions, 16 RS components type-K thermocouples were used (Figure 3.9, Table 3.2). These formed four arrays of four thermocouples over heights ranging from 0.5 m to 4 m above ground (Table 3.4, Figure 3.9). A further eight thermocouples created a horizontal array 3 m off the ground, strung between both openings (Table 3.4).

The temperature measurements allow a comparison between the volumetric averaged internal temperature and the external air temperature, used for determining whether the flow is thermally or wind driven. It also aids in determining the mixing state of the room. A well mixed room is likely to have little difference across the horizontal and vertical temperature gradients, whereas a temperature stratification may suggest that the room is not well mixed (Section 3.8).

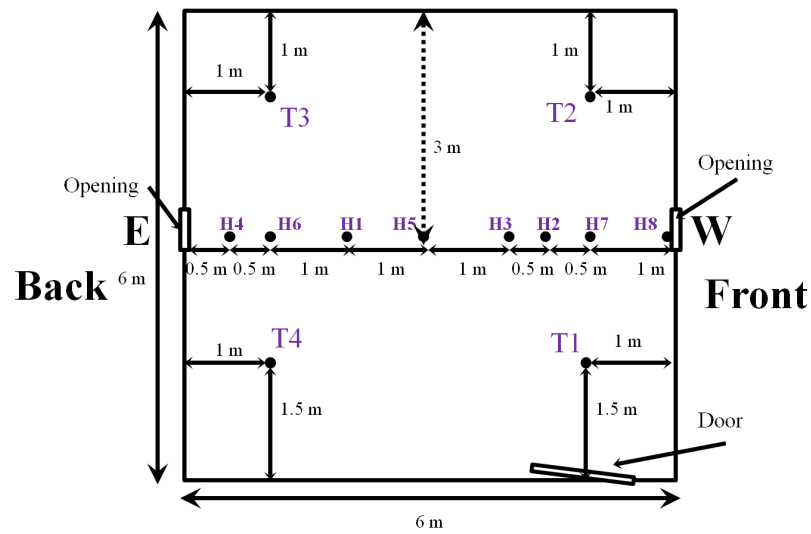


Figure 3.9: Plan view of the inside of the cube detailing the location of the horizontal array of thermocouples (H1-H8) all 3 m off the ground and the four vertical arrays (T1-T4, Table 3.4).

Table 3.4.: Height and position of the 16 thermocouples creating four vertical profiles within the instrumented cube. Numbers are the thermocouple numbers (Figure 3.9). All heights are taken above the floor

T1 #	Height (m)	T2 #	Height (m)	T3 #	Height (m)	T4 #	Height (m)
13	1	14	1.5	15	3	16	2
9	1.5	10	2.75	11	2.5	12	2.5
5	2.5	6	3.5	7	1	8	3.5
1	3	2	4	3	0.75	4	4
H #	Distance from Front Sonic (m)						
1	4	2	1.5	3	2	4	5.5
5	3	6	5	7	1	8	0

The locations (Figure 3.9) were chosen based on areas of interest: the horizontal array was aligned with the expected stream flow for cross ventilation and the vertical arrays were positioned away from the sides of the cube to minimise heating effects. The vertical arrays of thermocouples did not cover the entire depth of the cube due to restrictions with the positioning of the sensors. Internal humidity was not measured.

The mean temperature range for the internal temperature was $-0.1\text{ }^{\circ}\text{C}$ to $38.6\text{ }^{\circ}\text{C} \pm 3\text{ }^{\circ}\text{C}$. The range of internal and external temperature differences (internal-external temperature) was $-11\text{ }^{\circ}\text{C}$ to $19\text{ }^{\circ}\text{C}$ with the $-11\text{ }^{\circ}\text{C}$ occurring on a warm day (external temperature $13.1\text{ }^{\circ}\text{C}$) on 22nd November 2014.

Type-K thermocouples (Appendix D) were chosen due to their ease of use, low price and fast response time (manufacturer stated 0.1 s). The resolution of the thermocouples was $0.01\text{ }^{\circ}\text{C}$ with an accuracy of $\pm 1.5\text{ }^{\circ}\text{C} \pm 0.25\%$. The thermocouples were logged in groups of 8 at 10 Hz to Picolog TC-08 junction boxes, with synchronised logging to the same laptop using Picolog software. The thermocouples were extended using connecting cable and compatible plugs, which provided negligible resistance (Section 3.5.4.1). All Picolog TC-08 junction boxes were calibrated by the manufacturer before deployment, and were used in the calibration procedure of the thermocouples (Section 3.5.4.1).

The TC-08 junction boxes have a 0.1 s response time (equivalent to the thermocouples) and have built-in cold junction compensation. The cold junction provides the reference temperature required by the thermocouples to determine the measured temperature. This, combined with the manufacturer stated type-K thermocouple error of 0.25 % of the temperature reading $\pm 1.5\text{ }^{\circ}\text{C}$ gives a total error on each temperature reading of $\pm 0.45\% \pm 2\text{ }^{\circ}\text{C}$. The magnitude of this error suggests that the temperature measurements are not suitable for measuring instantaneous fluctuations in temperature (Kaimal and Finnigan, 1993). Besides instrumentation error, errors may also be caused by condensation forming on the sensor due to the rapid temperature changes within the cube and leakage through the openings.

3.5.4.1 Calibration and errors of the temperature measurements

After deployment, all 24 thermocouples were tested in a Design Environmental Delta 190H environmental chamber to ensure that all sensors responded in a similar way to controlled temperature changes over a range of conditions larger than that experienced during the field campaign. Calibrating all thermocouples against a known standard allows for the full-scale data to be corrected for any instrument biases. The calibration procedure consisted of two parts: testing whether the extension cabling had an effect on thermocouple performance and testing for hysteresis effects. For all experiments, the thermocouples are tested over a temperature range of $-20\text{ }^{\circ}\text{C}$ to $60\text{ }^{\circ}\text{C}$.

As the differences of the wired and non-wired runs were within the errors of the fit, it is assumed the cabling did not have an effect on the behaviour or response times of the thermocouples. The second phase of the thermocouple calibrations were undertaken with the thermocouples plugged directly into their respective junction boxes, set to log at 10 Hz.

Runs over the range of $-20\text{ }^{\circ}\text{C}$ to $60\text{ }^{\circ}\text{C}$ with $10\text{ }^{\circ}\text{C}$ increments from low to high (Run

1) and high to low (Run 2) were repeated twice to check for hysteresis effects. After each run the chamber was returned to ambient temperature. The chamber was set to remain at the set temperature for ten minutes before changing to the next stage within ten minutes, within the chambers maximum 1.6 °C per minute heating/cooling rate. Humidity was allowed to vary between 25 % - 75 % but was not set. The error on the chamber temperature reading was stated in the calibration log to be ± 0.35 °C. The chamber was set to log at 1 Hz and all thermocouple data were averaged to 1 Hz. The thermocouples remained in the same positions for all calibration observations: all thermocouples were 0.15 m away from all walls and 0.15 m above the chamber floor.

Each sensor had a weighted total least squares fit assessment of linearity, which considers total measurement uncertainties in both coordinates, using the chamber temperature as the reference (Appendix E). An equation of the form $y = mx + c$ is calculated for each thermocouple for each calibration, providing that both the chamber and thermocouples have linear responses. The gradient of the line represents the sensitivity of the instrument, and the y-intercept the bias or offset of the instrument. The uncertainty of the fit is calculated using Matlab's 2011 statistical package (polyfit), producing the standard errors with 95 % confidence intervals on the gradient and intercept (Appendix E).

The differences in the observed fits for Runs 1 and 2 and their repeats were smaller than the errors on the fitted coefficients, which suggests that the thermocouples display no hysteresis effects and respond linearly to changes in temperature. It is assumed that the bias of the thermocouples remained stable over the entire observation period. For all sensors a 2 °C gradient in internal temperatures is detectable. Anything smaller than 2 °C is masked by the error of the instrument. For looking at internal to external temperature differences using the WXT520 temperature sensor as the external sensor (Table 3.2), a 2.1 °C difference is distinguishable, influenced by the large error on the internal thermocouple measurements (Appendix F).

3.6 Cube surface pressure measurements

The surface pressure taps on the cube measured the external surface pressure distribution and aid understanding into how the flow, induced by the array, alters the surface pressure of a building. The pressures on the surface of the cube were measured using pressure taps (Figure 3.10): 7 mm holes located centrally on 0.6 m² steel panels, which were mounted flush onto the cube cladding to minimise their effect on the pressures measured. Pressure signals were transmitted pneumatically, using 6 mm internal diameter plastic tubes to transducers located within the cube. Each pressure tap had its own transducer which converted the pneumatic pressure into a voltage signal, which was then converted to a pressure (Pa). The transducers contains a silicon diaphragm that de-

flects when a pressure is applied to it and provide an output voltage that is proportional to the applied pressure. The individual transducers meant that the pressure tap measurements occurred simultaneously at a frequency of 10 Hz with the transducers being split into two sets of 16 in an upgrade to the original 16 tap set-up used by Straw (2000).

30 external pressure taps were used with 2 internal pressure taps as the latter also varies over time (Straw, 2000). The internal pressure is not constant for a cross ventilated building with large openings and can be used to suggest flow leakage or infiltration (Karava *et al.*, 2006). The external pressure taps were open to the environment, with drains fitted to ensure that any moisture in the openings would not adversely affect the data. The drain was in the form of a Y-shaped connector. One branch was attached to the back of the pressure tap, another to the pressure transducer and the third branch (pointed vertically downwards), was sealed using a porous bung through which moisture drained.

The 30 external pressure taps were split across the four faces, four on the roof, four in a horizontal array on the centre line across the North and South faces and 9 on the front and back faces, with five of those in a vertical array and four in a horizontal array (Figure 3.10). This configuration remained for all six observational set-ups (Section 3.3.1) with the locations of the pressure taps being chosen as a compromise between coverage and detail. A reference pressure was measured using a static pressure probe, with a reference dynamic pressure measured using a directional pitot tube at 6 m (building height) alongside the 6 m reference wind speed (Figure 3.6).

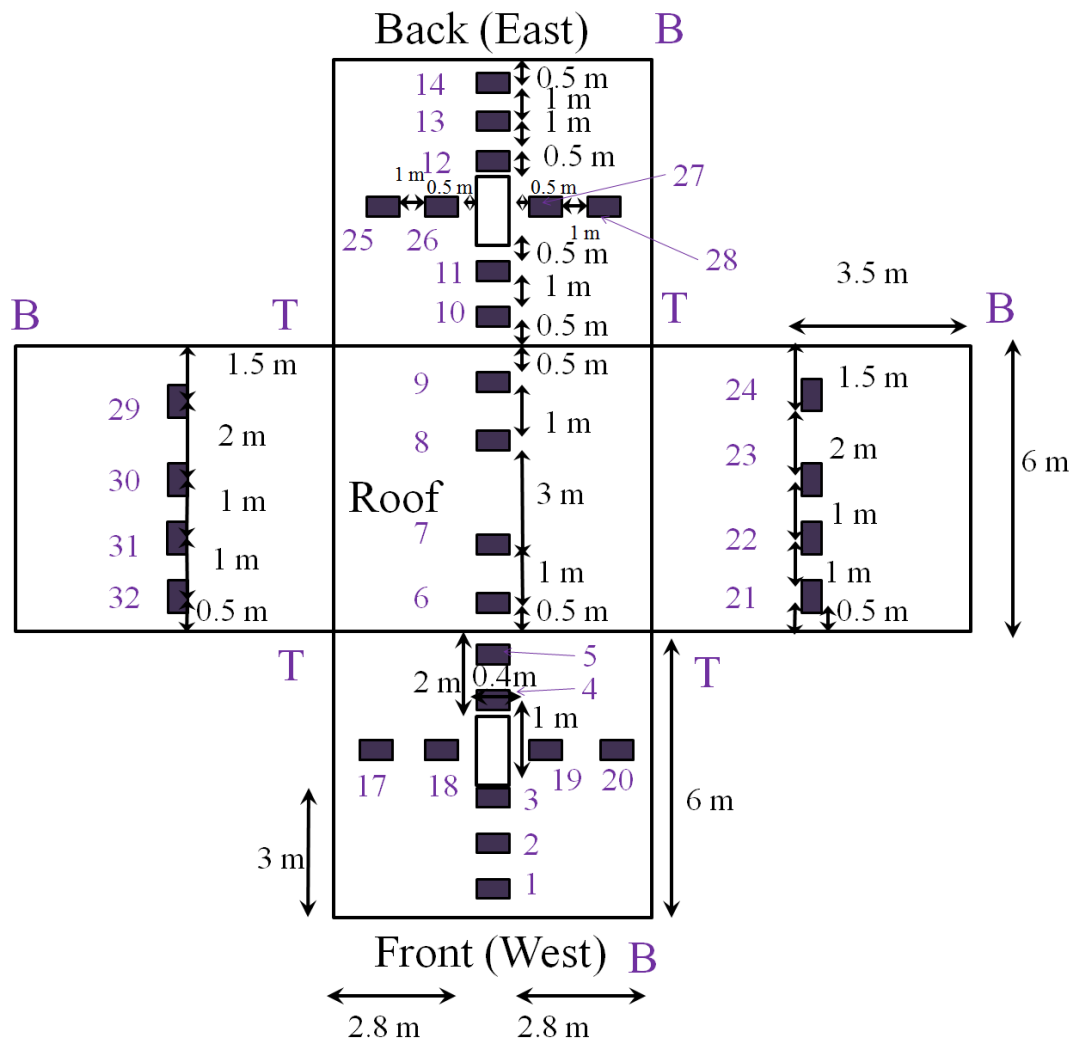


Figure 3.10: Plan of the pressure taps (purple) and distances between taps (black) on each face of the cube as seen when looking directly at the cube. 15 and 16 were the internal taps and are not shown, but were positioned just underneath the openings on the Front and Back faces in the same positions as 3 and 13 respectively. Drawing not to scale. T indicates the top of a face and B the base.

The pressure tap system was left to log continuously, with a new file generated every half an hour to combat instrument drift. The routine was:

1. 60 seconds of zero measurements based on a reference pressure
2. 60 seconds of calibration of the pressure transducers to the zero measurements
3. 24 minutes of pressure measurements
4. 60 seconds of calibration of the pressure transducers to the zero measurements
5. 60 seconds of zero measurements based on a reference pressure

The last ten readings (the last second of data) of each section were not analysed due to the valves switching to the reference pressure instead of surface pressure.

3.6.1 Calibration and errors of the surface pressure measurements

All zeroing and calibration sections (Section 3.6) were removed from the final data set, along with any time periods where a complete cycle did not occur. Pressure tap 9 (located on the roof) became water-logged and is not included in any analysis. The mean instrumentation error for the pressure tap system is estimated at 0.1 Pa (Hoxey, personal communication 2016).

The method of calibration of each pressure tap is similar to Straw's (2000): Initial and final zero values are taken as an average from each zeroing stage and the drift (of the order 0.001 Pa) is found. This is due to the pressure transducers being made from multiple materials which respond to changes in pressure and temperature. For each pressure measurement, an appropriate value of zero is calculated from linear interpolation between the static start zero and end zero. The interpolated value of zero was subtracted from each pressure measurement. The final pressure measurement in pascals was calculated as the zeroed pressure divided by the calibration value. The calibration factors (voltage to pressure conversion values) obtained during laboratory calibrations undertaken by Solutions for Research are listed in Appendix G.

3.7 CO₂ concentration measurements

CO₂ concentrations were measured inside the cube and outside the cube for the tracer gas releases (Table 3.2). Three internal (Section 3.7.1) instruments and one external instrument (LI-COR 7500) were used, to calculate the difference between internal and external CO₂ levels. Three internal instruments were used due to the size of the cube and to test the validity of the assumption that the cube is well mixed. The LI-COR 7500 was located on the Channelling mast (Figures 3.6, 3.8) and logged the external CO₂ concentration.

3.7.1 Internal measurements: K30 sensors

Three Senseair K30 FR CO₂ (hereafter K30) non-dispersive Infra-red sensors (NDIR) were used internally (Table 3.2, Figure 3.11). The K30 sensors were within a case made from a waterproof electronic junction box to provide some protection from water and spiders but were not electronically shielded (Figure 3.11). Through testing the cases were found to not restrict airflow to the sensor. The K30 sensors were chosen for their fast manufacturer stated response time (2 s in moving air and 20 s for stagnant air), 2

Hz frequency, low price, ease of use and smaller error than other sensors available at the time.



Figure 3.11: A K30 FR 2 Hz CO₂ sensor, on the base of the custom built casing and the complete casing, designed to provide the K30 sensors with some protection from water damage whilst still allowing adequate airflow around the sensor.

The K30 sensors were logged via USB port into the same laptop using the program ‘Gaslab’, meaning all readings of the CO₂ concentration were synchronised in time. The sensors will be referred to as the ‘East’, ‘Low’ and ‘Middle’ CO₂ sensors (Figure 3.12). The location of the sensors did not change unless high levels of moisture were recorded. In these circumstances the instruments may have been repositioned (to within 1 m of the original position) to avoid water damage until conditions improved.

- The ‘East’ sensor was positioned just under the east opening, 1 m away from the east wall and 2.75 m above the ground.
- The ‘Low’ sensor was hung under the steel girder of the east wall, 1 m away from the North-East corner of the cube and 0.3 m above the ground. This sensor was positioned to capture any possible flow through the blocked gap under the cube.
- The ‘Middle’ sensor was positioned 3 m above the ground at the centre-point of the Northern wall, roughly 0.5 m away from the wall itself. This sensor was moved to be 0.7 m away from the wall if high levels of water were noted within the cube.

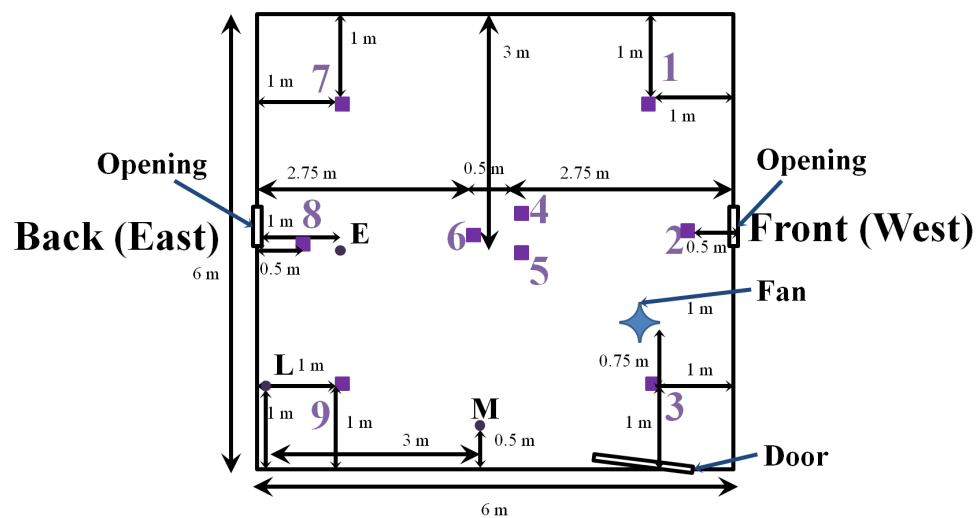


Figure 3.12: Location of the tracer gas inlet pipes (purple numbers and squares). Pipes 1-5 and 7-9 are positioned at 3 m above floor level with pipe 6 being at ground level (Section 3.8). The K30 Sensors are marked (to within 0.1 m, purple circles): low sensor (L), east sensor (E) and middle sensor (M), with photos of the positions provided. The door, openings and the position of the mixing fan (Section 3.8.1) are also marked.

During low temperatures ($< 5\text{ }^{\circ}\text{C}$), the sampling frequency of measurements became more sporadic with this behaviour being seen during testing in the environmental chamber (Section 3.7.2). To prevent loss of data, the ‘Gaslab’ logging program was restarted before every tracer gas release to ensure that the sensors were stable and logging at 2 Hz. For measurements requiring a long period of time (> 2 hours) due to low ventilation rates, some data was lost at the end of the observation period due to the reduced sampling frequency. This effect of low temperatures could not be fixed without altering the thermal environment of the cube.

3.7.2 K30 calibration

The K30 sensors were tested for hysteresis effects and sensor drift over time. The K30 sensors were calibrated by the manufacturer (Senseair) before the study was undertaken. Calibration of the instruments can also be done manually by zeroing the device by flooding the sensor with Nitrogen or a similar gas in a sealed environment. The K30 sensors also required a background calibration by calibrating the sensor in an environment with exactly 400 ppm of CO_2 , achieved using pure CO_2 (Senseair).

During the initial testing, the three K30 sensors displayed varying readings of background CO_2 levels (Figure 3.13), even when in the same sealed environment, possibly due to different calibrated background levels. For tracer gas releases, the offset was corrected for each individual sensor, as the focus is on the change in CO_2 , rather than the absolute value (Section 3.8.1).

To check for sensors drift, the K30 dataset was compared to the LI-COR dataset, for half hour averages, for internal ambient conditions (Figure 3.14). The difference between the LI-COR and East sensor is uniform across the whole study, with some negative difference outliers probably being caused by human presence in the cube.

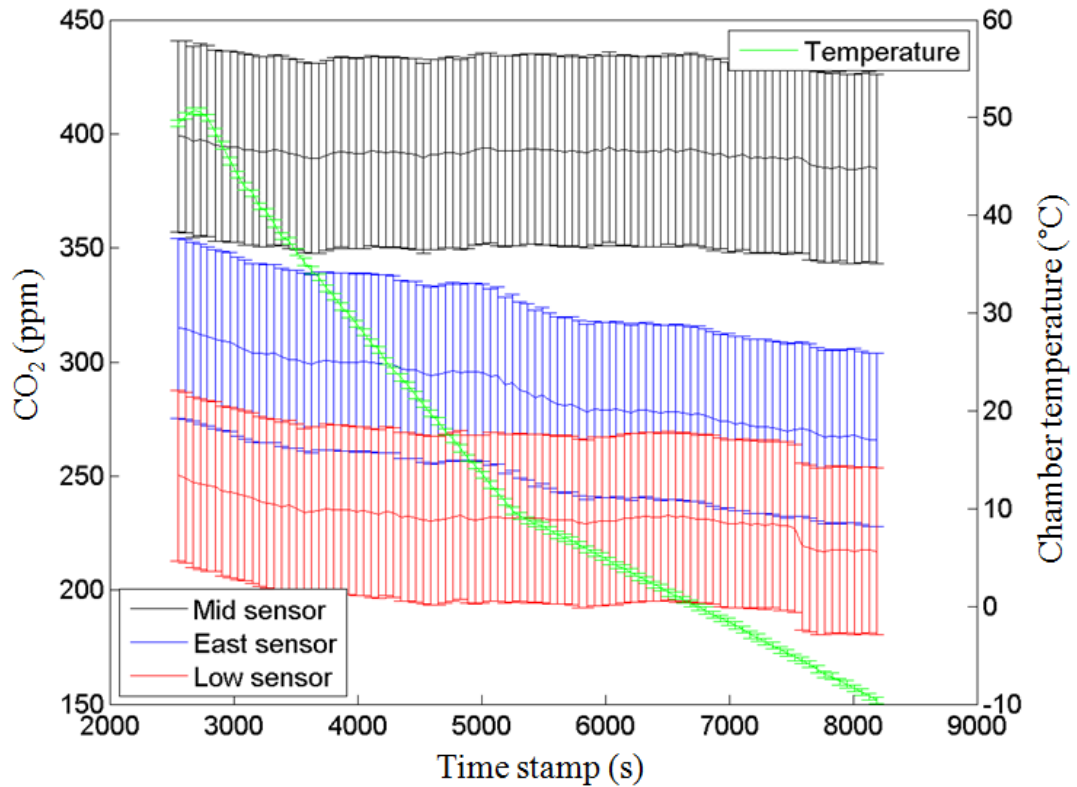


Figure 3.13: Behaviour of the K30 sensors during a varied temperature test. Right axis is temperature change (green line). Left axis is CO₂ concentration. The CO₂ level was the background level in the room, with no gas release. The room was left undisturbed for the duration of the release.

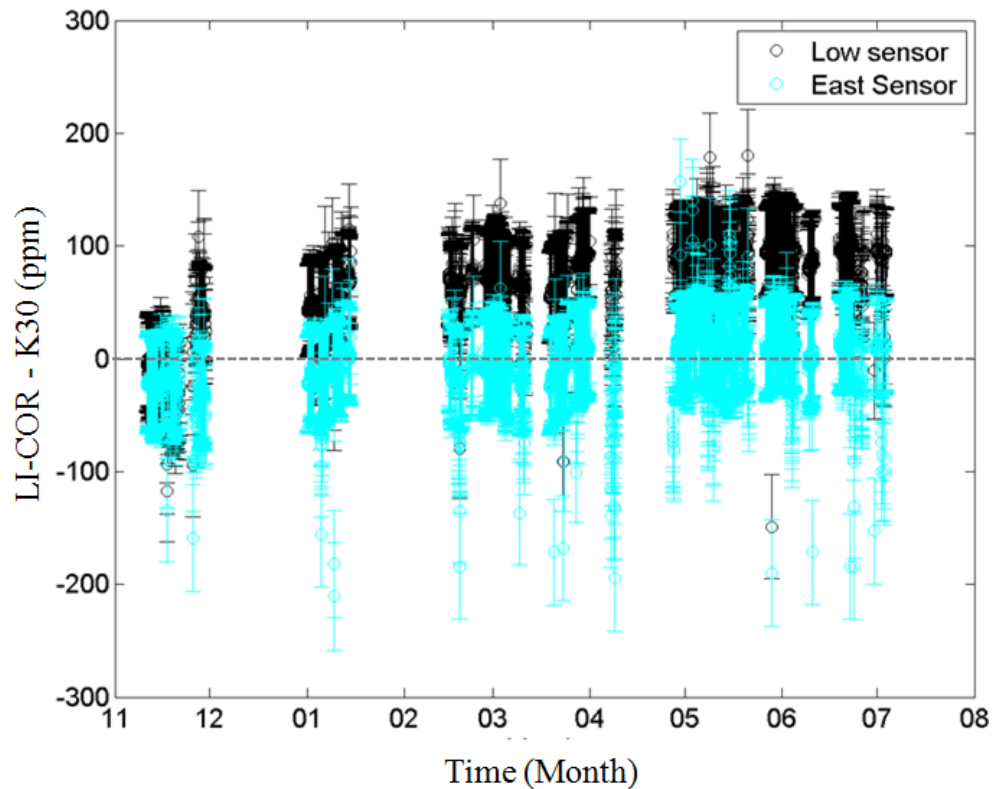


Figure 3.14: Difference in the recorded background levels of CO_2 : difference between the LI-COR and the low sensor (black) and the difference between the LI-COR and the East sensor (cyan). Error bars are the measurement error. The Mid sensor is not included due to it not being in place for the entire study. The difference between the LI-COR and the Low sensor clearly changes in December to January, due to the Low sensor malfunctioning. Gaps in the data set are due to one or both systems not operating.

To test for the influence of temperature on the K30 sensors, a Design Environmental Delta 190H environmental chamber (Section 3.5.4.1) was set to vary over a larger range of temperatures (55 to 10 °C), than recorded in the field. For these tests, the CO_2 concentration in the chamber was ambient, with all personnel being absent from the surrounding room. The initial phase of the experiment brought the chamber from room temperature to 55 °C, which gave time for any CO_2 in the room from human activity to decay down to normal background levels.

The results of the temperature sensitivity test (Appendix H), suggest that there is no dependence on temperature. As any drift due to differing temperatures is within the range of the instrument error, the effect of temperature on the K30 CO_2 reading is not a concern in the field.

3.7.3 LI-COR 7500 calibration

The LI-COR LI-7500 was used as the benchmark instrument for the K30 sensors, due to its low error, stable calibration and common use in meteorological applications. The two types of instruments were tested against each other to ensure a similar response style to fluctuations in CO_2 .

The LI-COR 7500 underwent a two-part calibration; the values of the calibration coefficients are determined by the manufacturer during factory testing. Adjustments to the zero and span values are undertaken by the user in order to bring the instruments response back to its factory calibration. The LI-COR was calibrated with CO_2 (Appendix I) at the start and end of the field-work in order to check for drift over the nine months. The calibration remained stable with no change to the span or zero values (± 0.0001) of the instrument.

3.7.4 LI-COR 7500 and K30 comparisons

At the end of the campaign the LI-COR 7500 and K30 were compared in three ways:

1. K30 sensors were mounted alongside the LI-COR 7500 on the Channelling mast for direct comparison in realistic background conditions on 10th July 2015.
2. K30 sensor and LI-COR 7500 were tested at background levels of CO_2 for a range of temperatures (45 °C to -20 °C) in a Design Environmental Delta 190H environmental chamber.
3. All sensors were placed in a sealed box (dimensions 0.6 m x 0.6 m x 0.3 m) which was flooded with CO_2 above the limits of both sensors before being left to decay naturally.

For case 1, undertaken immediately after completion of the full-scale data set, little difference, besides the offset of the different K30s can be noted between the behaviour of the LI-COR and K30s in real neutral atmospheric conditions. Results were similar for case 2, undertaken at a range of temperatures in background CO_2 conditions.

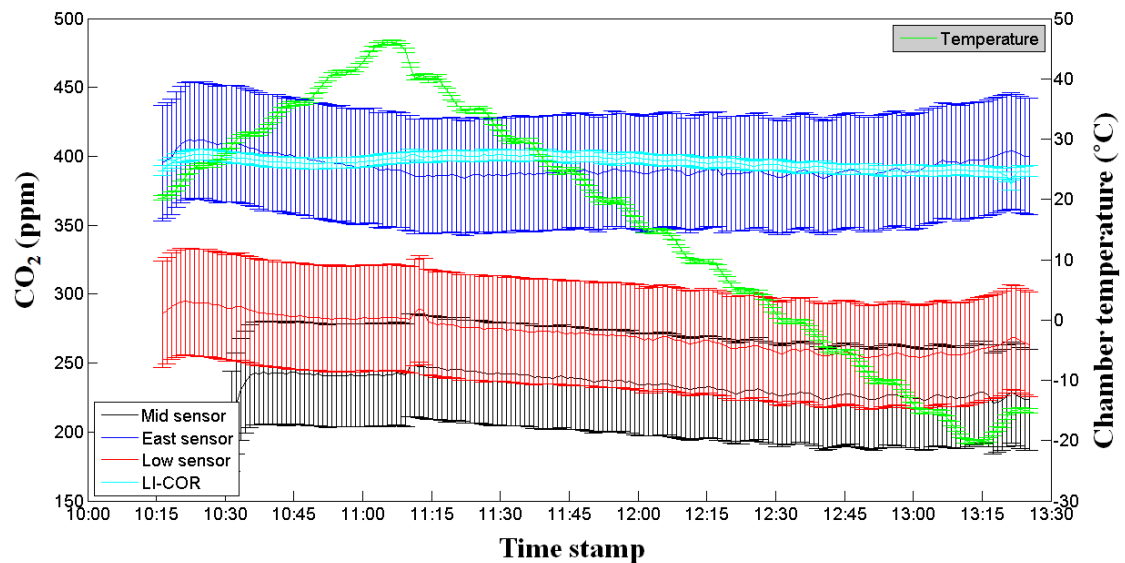


Figure 3.15: K30 sensors with the LI-COR at background conditions over a range of temperatures. The left axis: concentration (ppm) the right axis is temperature ($^{\circ}\text{C}$, green line). Error bars are the instrument error. Data are 1 minute averaged to prevent the response time of the K30s affecting the results.

The East sensor was closest within the recorded values of the LI-COR. The Low and Mid sensors (Figure 3.16) are in agreement with each other and have moderately strong linear fits (Appendix J). This calibration also highlighted that the Mid sensor in particular was highly sensitive to cold temperatures.

The relation between K30 readings and temperature suggest a moderately strong correlation between concentration recorded and temperature (Appendix J). It is difficult to understand if the temperature of the chamber did have an effect on the readings taken by the K30 sensors, as it was difficult to keep the CO_2 concentration in the chamber stable due to a loose seal on the side. This would also lead to incomplete mixing within the chamber. The difference in temperature between ambient air and the injected CO_2 may also be related to this.

Thirdly, to test the response of the LI-COR and K30s to a rapid change in CO_2 concentration to ensure they all responded in the same way, all instruments were placed in a sealed plastic box, then CO_2 gas was pumped in to above the sensor limits (Table 3.2). An 0.02 m by 0.04 m opening allowed the concentration left to decay undisturbed. The sensors were positioned as close as possible to ensure no biases due to the proximity to the opening. To ensure that the response time of the K30 sensors was not influencing the experimental results, 1 minute averages were calculated (Figure 3.16). All K30 sensors, regardless of offset display the same response to the CO_2 decay.

Due to the rapid decay, and the 3000 ppm limit on the LI-COR, there are few data points available for higher concentrations (Figure 3.16, Appendix K). The error on the

intercept (Figure 3.16b) for the East sensor is of similar magnitude to the value itself, suggesting that there is some variation in the offset of the East sensor over large concentration ranges. However, of all the K30 sensors, the East sensor displays very similar tendencies to the LI-COR, ($R^2 = 0.995$).

The Low sensor constantly underestimates the CO_2 concentration, due in part to its lower 400 ppm calibration. The Low sensor's response to changes in CO_2 is approximately linear, displaying a shallower gradient when compared to the East sensor.

The Mid sensor displays a linear relation with increasing CO_2 concentration, similar to that seen for the East and Low sensors but only for concentrations under 1000 ppm. After this the gradient increases and the mid sensor over estimates the CO_2 concentration when compared to the LI-COR. This was not an effect of the averaging time.

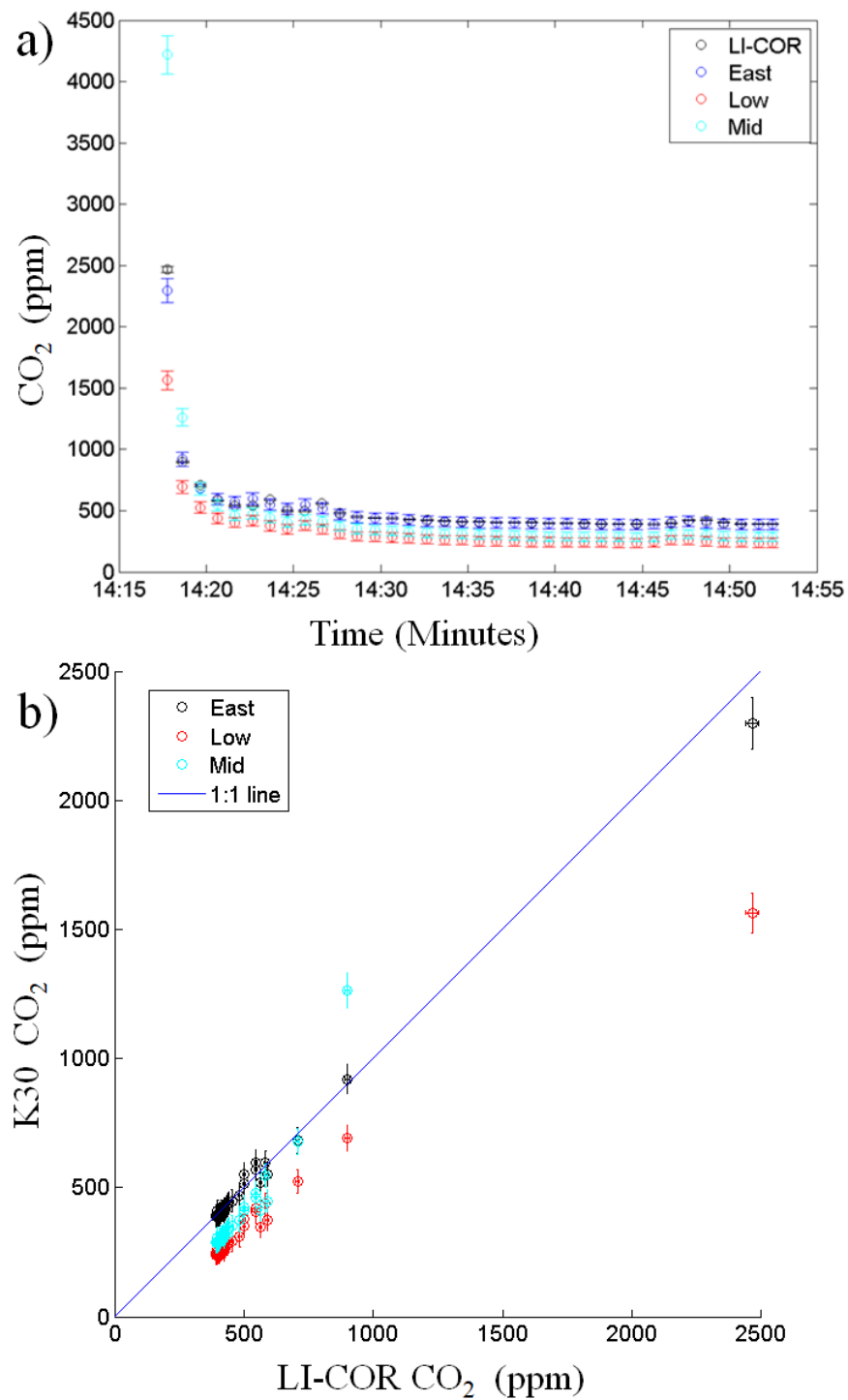


Figure 3.16: a) Decay curve for LI-COR and K30 sensors. The LI-COR reading remained consistent at 3000 ppm until the concentration dropped below this level. b) 1 minute averaged LI-COR concentrations against K30 concentrations for the decay test with a 1:1 line (dark blue), the east sensor (black), low (red) and mid (cyan). Error is based on instrument error.

3.8 Ventilation measurement methodology

Three methods were used to calculate ventilation rate: the tracer gas decay technique (Section 3.8.1), based on wind speed (Section 3.8.6) and using the pressure difference across the opening (Section 3.8.5). A combination of direct and indirect measurements are used in order to gain an understanding of how each responds under different atmospheric conditions and differences between the methods.

3.8.1 Tracer gas decay methodology

The direct measurement of the flow rate using tracer gases is best suited to a single-zone building or when sub-sections of a building can be isolated (Sherman, 1990). There are a lack of guidelines for the positioning of sensors, even for mechanically ventilated rooms, where errors can be up to 85 % (Van Buggenhout *et al.*, 2009). Overall, the best position for a sensor is at the outlet, with a 10 % difference from the reference measurement (Van Buggenhout *et al.*, 2009). However, for a building within a realistic flow the location of the outlet is likely to change depending on the wind direction, especially if it is in cross ventilated flow (Van Buggenhout *et al.*, 2009).

With no clear set of guidelines, it is difficult to inter-compare results. Persily and Levin (2011) suggest that the measurement method employed and details on its application, instrumentation used, calibrations, the time over which the measurement was made, total number of measurements, meteorological conditions and building conditions should be noted.

Three main tracer gas techniques are regularly used to calculate the flow rate and thus the Air Change Rate, normally quoted in air changes per hour (λ) (Etheridge and Sandberg, 1996):

- Constant injection. A defined volume of gas is injected at a constant rate whilst the concentration response is recorded. Depending on the room conditions and the air change rate, an equilibrium concentration will be reached
- Constant Concentration. Gas is injected into a room with the aim of maintaining a set concentration for a set amount of time
- Tracer gas decay. Gas is pumped into a room and then shut off, before being left to decay. The rate of the decay is dependent on the ventilation rate of the room

One air change per hour is defined as the one complete replacement of the internal air with external air (Awbi, 2003). In this study the tracer gas decay method was used given the large volume of the instrumented cube and therefore cost. Unlike other methods, it does not require an accurate measurement of the input rate of the gas. A summary of the experiments undertaken is given in Table 3.5.

All tracer gas techniques stem from a mass balance equation, assuming that the concentration of a tracer gas can only change when either more tracer gas is added or is removed by ventilation processes (Laussmann and Helm, 2011):

$$V_R \frac{dC_i(t)}{dt} = (C_a - C_i(t))Q + E \quad (3.1)$$

where V_R (m^3) is the room volume, Q ($\text{m}^3 \text{s}^{-1}$) is the volumetric flow rate between the room and outside, C_i (kg m^{-3}) is the indoor concentration of tracer gas, C_a (kg m^{-3}) is the external concentration of tracer gas, E (kg s^{-1}) is the amount of tracer gas emitted from a tracer gas source and t (s) is time. $C_i Q$ is the transport of tracer gas from the room air to the outside air through any openings or cracks, $C_a Q$ is the transport of tracer gas from the outside air into the room air.

Dividing both sides of equation 3.1 by V_R (Laussmann and Helm, 2011):

$$\frac{dC_i(t)}{dt} = -(C_i - C_a) \frac{Q}{V_R} + \frac{E}{V_R} \quad (3.2)$$

Q/V_R is defined as the air change rate λ . When the units of time are hours (the engineering convention) this is quoted in ACH. Substituting λ into equation 3.2 and integrating gives:

$$C_i(t) = (C_0 - C_a) \exp(-\lambda t_i) + C_a + \frac{E}{(\lambda V_R)} (1 - \exp(-\lambda t_i)) \quad (3.3)$$

where C_0 is the initial amount of tracer gas released into the room. If there are no new internal emissions ($E=0$), equation (3.3) can be simplified to (Laussmann and Helm, 2011):

$$C_i(t) = (C_0 - C_a) \exp(-\lambda t_i) + C_a \quad (3.4)$$

This is often rearranged to a $y = mx + c$ form. With a steady ventilation rate, the air change rate is given by the slope λ :

$$\ln(C_i(t)C_a) = \ln(C_0 - C_a)\lambda t \quad (3.5)$$

Equation 3.1 is subject to several assumptions (Laussmann and Helm, 2011):

- There are no chemical reactions which alter the tracer gas concentration (i.e. chemically inert)
- The furnishings of the room do not absorb or release the tracer gas
- The room is well mixed and thus C_i is spatially uniform within the room

- The exchange of tracer gas-containing air and external air only occurs in places in direct contact with the outside, such as windows
- The room in which the tracer gas is released is considered a single-zone system

Often, the well-mixed assumption may not hold, and this is most easily seen through differences in ACH rate calculated using data from individual sensors. Li *et al.* (2014) used multiple CO_2 sensors in student accommodation in order to confirm that the room was well mixed, before the CO_2 concentration in the room was measured at only one measurement point. If a well-mixed state is not confirmed, the local ventilation rate is calculated at a sensor and is representative of the ventilation at that point only. As real buildings fluctuate between being well-mixed and having some stratification, or 'dead zones' within the rooms, a 10-15 % error occurs when using tracer gas releases to measure natural ventilation (Van Buggenhout *et al.*, 2009).

In this study if the fitted decay line (equation 3.5) has an R^2 value of less than 0.75 the data are not used in the analysis. All line fits have an error in the fitted coefficients which takes into account the instrument errors.

3.8.2 Choice of tracer gas

Sherman (1990) suggested that an ideal tracer gas must be:

- Non-hazardous to humans and the objects of the test zone
- Non-reactive and passive
- Must be detectable and measurable
- Should also be distinguishable from all other constituents of the atmospheric air

However, practical considerations such as cost, availability and instrumentation should also be considered. CO_2 is often used to measure air flow within indoor spaces, as the equipment is cheap and easily available to suit a variety of experimental designs. However, at high concentrations CO_2 can be hazardous to humans causing dizziness, nausea, drowsiness and confusion at concentrations of between 20000-100000 ppm (2-5 %), at over 100000 ppm (10 %) hearing and vision become impaired with loss of consciousness occurring with prolonged exposure (Cable, 2004). Levels of over 20000 ppm were not required for this field campaign.

As CO_2 is present in air (400-500 ppm), a concentration of CO_2 that is distinguishable from the background levels is needed. Whilst the background concentration level of CO_2 could be described as stable. For this site, there may be an identifiable diurnal cycle due to the photosynthesis of the surrounding plants. CO_2 is also not likely to react on release.

The tracer gas chosen was CO_2 for its ease of use, availability, wide range of equipment and low cost.

3.8.2.1 Errors in the tracer gas methods

In addition to instrument errors (Section 3.7) weighted linear regression analysis will be used to minimise the effect of the proportional errors on the resulting air change rate. However, other errors occur as a result of the set-up. Due to the slight temperature difference between the CO_2 gas and the ambient air (depending on the air temperature), even with the use of a fan it is difficult to ensure that the cube remains well-mixed for the duration of the measurement.

3.8.2.2 Errors in tracer gas decay data processing

Each tracer gas release is considered independently to address concerns about mixing and flow within the cube. The start of the decay is from field note time logs. The end of the decay curve depended on the specific tracer gas release, but was always taken when the CO_2 concentration was still greater than the combination of external concentration and instrument error (Table 3.2).

Where possible, ventilation rates are the average of the three sensors unless there are concerns about the mixing within the cube, (highlighted by the release of smoke to check for stratification) individual sensors may be taken as a representation of a ‘local ventilation rate’ instead of a cube wide ventilation rate.

Over the nine months, the external CO_2 sensor recorded background levels of 375 ppm to 450 ppm (95 % within 371 ppm to 403 ppm), with odd instances of 500-550 ppm, but these were attributed to people working on the mast through the experimental logs. This results in an error on the outdoor concentration of 3.75 to 4 ppm, which is comparatively small compared to the errors on the K30 sensors.

When the outdoor concentration data were unavailable (e.g. instrument malfunction), 387 ppm is used. The external measurements varied on average by 3-4 ppm over the course of each tracer gas release. The difference in the calculated λ between using the actual LI-COR data and a constant value for the background or ambient concentration is 0.01 h^{-1} . Using 400 ppm instead of 387 ppm gives a difference of 0.025 h^{-1} , with 350 ppm giving a difference of 0.11 h^{-1} when compared to the 400 ppm. This suggests that even if the background levels of CO_2 varied by 50 ppm over the course of a release, the effect on the calculated air change rate would be of the order of magnitude of 0.1 h^{-1} . This variation is less than the instrument error on the K30 sensors (which, when averaged, was roughly 10 % of the magnitude of the calculated λ).

3.8.3 CO_2 distribution for tracer gas releases

The cube had nine gas outlets to release the tracer and a large desk fan (effective range of 4 m horizontally, and 2 m vertically) to improve mixing (Figure 3.12); eight of these

outlets were at 3 m above floor level, with one being at floor level in the centre of the room. The floor level pipe had a length (outlet to regulator) of 2.2 m, with all others being 3.1 m in length. The CO_2 was heated by the regulator to approximately 10 °C in order to prevent the outlet freezing during release and to reduce the temperature difference between the tracer gas and the ambient air. The cube was not disturbed during decay measurements, with the gas input being stopped from outside the cube.

3.8.4 Tracer gas measurement procedure

When a change of opening type occurred, measurements did not start until one hour after modifications to allow the cube to return to ambient concentrations of CO_2 . The methodology for undertaking tracer gas measurements was as follows:

1. The front opening (if being used) was blocked from the outside with a temporary, easily removable panel. Blocking both the front and back openings for cross ventilated cases was impractical, though would have been ideal. The small fan used to aid mixing was turned on
2. The K30 sensors (Section 3.7) and the logging program were reset
3. Sensors were checked for any signs of water damage or loose connections before logging was restarted. Distribution pipes were also checked for damage along with the regulator and flow-meter on the CO_2 cannister
4. All personnel on site were warned of the pending tracer gas release and left the instrumented cube
5. The door was shut and the CO_2 released from the cannister at a rate of 40 L min⁻¹
6. The CO_2 was released for 10-15 minutes. The maximum concentration achieved was always between 3000-10000 ppm
7. After 10-15 minutes, the blocking panels were removed and the gas switched off
8. The building was left undisturbed for at least 20 minutes. Infiltration tests were often left to decay over-night due to λ being 0.5 to 5 h⁻¹, with isolated cross ventilated cases having a range of λ of 3 to 35 h⁻¹
9. Unless the safety sensor was sounding (CO_2 levels above 15000 ppm), the door was opened briefly to allow for the logging system to be checked

λ is calculated from the data obtained for each sensor using equation 3.5.

3.8.4.1 Tracer gas release schedule

All tracer gas releases (Table 3.5) were undertaken when personnel were on site, meaning all releases occurred during the day.

Table 3.5:: Summary of tracer gas releases undertaken between September 2014 and July 2015. Unsealed cases refer to the tracer gas releases undertaken when the gap in the bottom of the cube was not blocked (Section 3.3). Sealed cases refer to when the cube gap was blocked with packing foam.

Set-up	Array cases	Isolated cases
Infiltration (unsealed)	14	4
Single sided (unsealed)	16	0
Cross ventilated (unsealed)	11	0
Infiltration (sealed)	9	15
Single Sided (sealed)	15	26
Cross ventilated (sealed)	18	26
Single sided (Sealed) East window	2	0
Total:	85	71

3.8.5 Pressure difference method

If a pressure difference between the internal and external environments or between the front and back of a building can be deduced, the flow rate through the opening, Q_p , can be calculated under the assumption that the flow is approximately turbulent under normal pressures (Section 2.3.11).

The largest source of error for the pressure difference method arises from the use of the mean, rather than instantaneous pressure differences (Choinière *et al.*, 1992). However to allow for correlation with the measured background variables half hour averages are used in this study. Looking into the instantaneous pressure differences and the correlation with instantaneous atmospheric data is beyond the scope of this thesis and will be considered as part of the Refresh project.

The pressure difference across an opening (Δp) can be defined as: the difference can be across the opening (external pressure- internal pressure) or the pressure difference between the front and back face averages. The external pressure is calculated from the average of the pressure measurements located around the opening: Taps 3, 4, 18 and 19 for the front face and Taps 11, 12, 26 and 27 for the back face (Figure 3.10).

For infiltration measurements, this method is not used as there are no set openings. In all cases, the average of the external taps is calculated, before the difference is calcu-

lated between the external and internal for each reading of data. This difference is then averaged over the averaging time.

3.8.5.1 Errors in the pressure difference method

The error on flow rate calculated using the standard orifice equation (equation 2.8, Section 2.3.5) can be calculated through error propagation:

$$\delta Q_p = Q_p \sqrt{\left(\frac{\delta C_d}{C_d}\right)^2 + \left(\frac{\delta A}{A}\right)^2 + \left(\frac{\delta \Delta p}{\Delta p}\right)^2 + \left(\frac{\delta \rho_0}{\rho_0}\right)^2} \quad (3.6)$$

where δ is the error in the measured value. The error in C_d based on experiments to be ± 0.1 (Appendix C), the error on the window area has been estimated at $\pm 10\%$. The error in ρ_0 is obtained by calculating ρ for the maximum and minimum external temperatures measured on the site and a reference pressure (101 hPa).

The error in Δp is calculated from the instrumentation error and the standard error over the averaging time. The standard error (SE) of a measurement over a measurement period:

$$SE = \frac{\sigma_s X}{\sqrt{N}} \quad (3.7)$$

where σ_s is the standard deviation of X and N is the number of samples. This is calculated based on the averaging time over which the pressure difference is calculated i.e. 14400 samples. Equation 3.7 is used for standard errors of all instruments. This gives the error on each individual pressure measurement as:

$$\delta P_{tap} = \frac{\sigma_s X}{\sqrt{N}} + 0.1 \quad (3.8)$$

The error in Δp becomes

$$\delta \Delta p = \sqrt{\delta p_{int} + \delta p_{ext}} \quad (3.9)$$

which is used in equation 3.6. The errors for the individual taps are then combined for each face during averaging and divided by the number of taps, giving the error in the mean external measurement. Equation 3.8 is also used to calculate the error on the internal pressure.

3.8.6 Flow through an opening

The simplest method assumes that the window is acting as either an inlet or an outlet at any point in time and that the flow is wind driven (Section 2.3).

$$Q_f = UA \quad (3.10)$$

The flow rate, Q_f ($\text{m}^3 \text{s}^{-1}$) is calculated by multiplying the mean wind speed, U (m s^{-1}) by the opening area, A (m^2). This velocity can either be directly measured, or obtained from reference wind speed measurements using the methodology outlined in CIBSE (2006) (Chapter 6). The errors depend on the velocity used and where it is measured. Too close to the opening, and the flow through the opening is disturbed, and too far from the opening, it may not be representative of the flow through the opening.

Equation 3.10 does account for wind direction and will not be representative of the wind experienced by the cube, especially in the array case. However, in CFD modelling this method is often used, as the wind speed is easily calculated, but care must be taken to ensure that the point chosen is representative of the local flow and not heavily influenced by the presence of the studied building itself.

3.9 Treatment of data

Periods of time (a total of seven days of data) where the reliability of the sensors was questionable were removed. Calibrations (Chapter 3) have been applied to the pressure data, temperature data, CO_2 data and wind data. Data are sorted into categories depending on the time stamp (GMT). 30 minute averages were chosen due to the common use in meteorological studies (Barlow and Coceal, 2009).

The focus of this thesis is on the mean pressure coefficients and ventilation rates and not on the instantaneous values. These will be considered as part of the Refresh project (<http://www.refresh-project.org.uk/>).

3.9.1 Defining near-neutral stability

The boundary layer stability is defined using z/L , where L is the Obukhov length and z is the height at which the measurement is taken (6 m). The atmosphere at this height can be defined as stable, neutral, near-neutral or unstable and is dependent on the presence of a buoyancy flux caused by heating from the surface.

The local stability is considered near-neutral if $|z/L| < 0.1$ (Högström, 1988). The boundary layer is considered stable if $z/L > 0.1$ and unstable if $z/L < -0.1 \pm 0.015$ was used by Richards and Hoxey (2002). The observations are predominately near-neutral and there are no cases of high wind stable cases recorded (Table 3.6). 1712 half hour periods were recorded for the isolated case and 6102 for the array case.

Table 3.6: Number of half hour averages for stability and wind speed thresholds.

Stability and wind speed	Array	Isolated
Near Neutral ($-0.1 < z/L < 0.1$) High wind ($> 6 \text{ m s}^{-1}$)	653	107
Near Neutral ($-0.1 < z/L < 0.1$) Low wind ($< 3 \text{ m s}^{-1}$)	2170	485
Near Neutral ($-0.1 < z/L < 0.1$) Med wind (3 to 6 m s^{-1})	2032	578
Stable ($z/L > 0.1$) High wind ($> 6 \text{ m s}^{-1}$)	0	0
Stable ($z/L > 0.1$) Low wind ($< 3 \text{ m s}^{-1}$)	846	190
Stable ($z/L > 0.1$) Med wind (3 to 6 m s^{-1})	49	8
Unstable ($z/L < -0.1$) High wind ($> 6 \text{ m s}^{-1}$)	0	6
Unstable ($z/L < -0.1$) Low wind ($< 3 \text{ m s}^{-1}$)	314	185
Unstable ($z/L < -0.1$) Med wind (3 to 6 m s^{-1})	38	153

Chapter 4

Wind tunnel simulations of the Silsoe array and exploration of the impacts of a limited array

4.1 Introduction

Wind tunnel studies are less time intensive than full-scale studies into ventilation and pressure coefficients (C_p) of a building (Section 2.3.3.2). Wind tunnel models allow for some control of the wind speed (U), wind direction (θ) and experimental set-up. They require specialist facilities and knowledge to ensure that the results are representative of the full-scale flow (Section 2.3). Although changes to the test building itself and a range of wind directions can be controlled and studied, Stathopoulos (2006) the amount of detail which can be recreated on a scale model is limited meaning all scales of turbulence found in the full-scale environment are not captured (Richards *et al.*, 2007).

This chapter describes wind tunnel work using a 1:300 scale model of the full-scale Silsoe site (Chapter 3). The scaled model and controlled conditions of the wind-tunnel allow for the impacts of a limited array and a more extensive array to be explored (Section 4.10).

4.1.1 Motivations for wind tunnel work

Wind tunnels have been used for a variety of research purposes; dispersion (Macdonald *et al.*, 1998), flow within urban canyons (Kastner-Klein *et al.*, 2001), the effect of fluctuating wind direction (θ) on natural ventilation and can be used to estimate C_p (Ji *et al.*, 2011).

The wind tunnel allows the Silsoe array to be expanded beyond what was possible for the full-scale site (Chapter 3). Thus, larger and symmetrical arrays can be studied to assess whether the size of an array has an impact on the pressure drop felt by a building within the array. This impact can be quantified and potentially applied to the full-scale data. A range of wind directions that were not measured in the full-scale can be eval-

uated (Figure 3.7). The flow behaviour around the array for a steady wind speed and direction is also captured, removing the complexity of varying wind speeds and directions. The effect of specific site features on C_p can also be tested.

4.2 Wind Tunnel methodology

Experiments were conducted in the 'A' wind tunnel (Figure 4.1) at the Environmental Flow Research Centre (EnFlo) at the University of Surrey, UK (Table 4.1). The 'A' wind tunnel is a low speed open-circuit wind tunnel with a 0.6 m high, 0.9 m wide and 4.5 m long test section constructed of wood and metal with glass side panels. The roof of the working section was constructed from a combination of wood and a movable acetate sheet and was weighted down for the duration of the experiment to maintain its position and to ensure a proper seal.

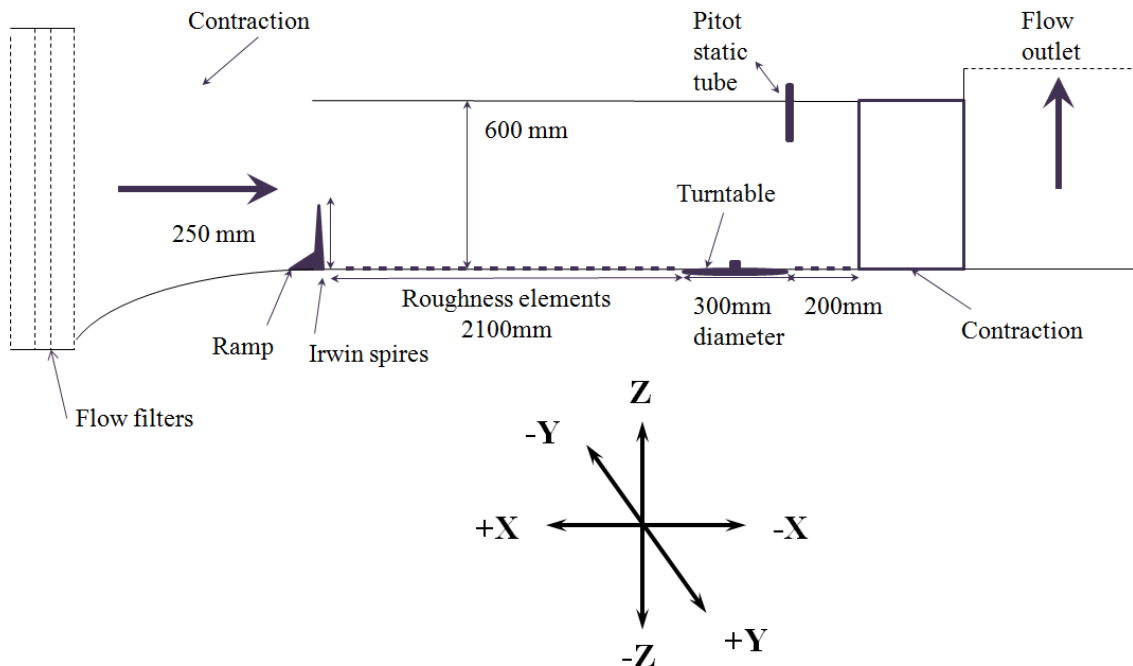


Figure 4.1: Schematic of the 'A' wind tunnel used in the experiment and the coordinate system of the tunnel. $z=0$ is the base of the tunnel, $x=0$, $y=0$ is the centre of the turntable. A positive x value means that the location is upstream of the centre of the turntable i.e. located closer to the inlet. A positive y means that the location is to the right of the centre of the turntable and a positive z position means that the location is within the bounds of the tunnel. $\theta_{ref} = 0^\circ$ within the wind tunnel refers to flow that is perpendicular to the objects front face and a 10° clockwise rotation corresponds to $\theta_{ref} = -10^\circ$, in line with the notation used throughout this thesis (Figure 3.5). The diagram is not to scale.

The entire floor of the working section was lined with 6 mm boards covered in a staggered pattern of small right-angled brackets, 8 mm wide (in the spanwise direction) and 2 mm high (Figure 4.2a). This had previously been used by Snyder and Castro

(2002), to create a rough surface similar to that of the full-scale field. A perspex turntable of radius 0.15 m, centred 2.1 m from the flow inlet was set into the roughness boards. The boards were screwed into place to minimise the difference in height between each board and the turn-table.

Seven 0.25 m Irwin spires (Irwin, 1981) were used to generate a boundary layer in the tunnel, with a small ramp leading from the inlet to the spires to minimise the height difference between the tunnel floor and the spires (Figure 4.2a).

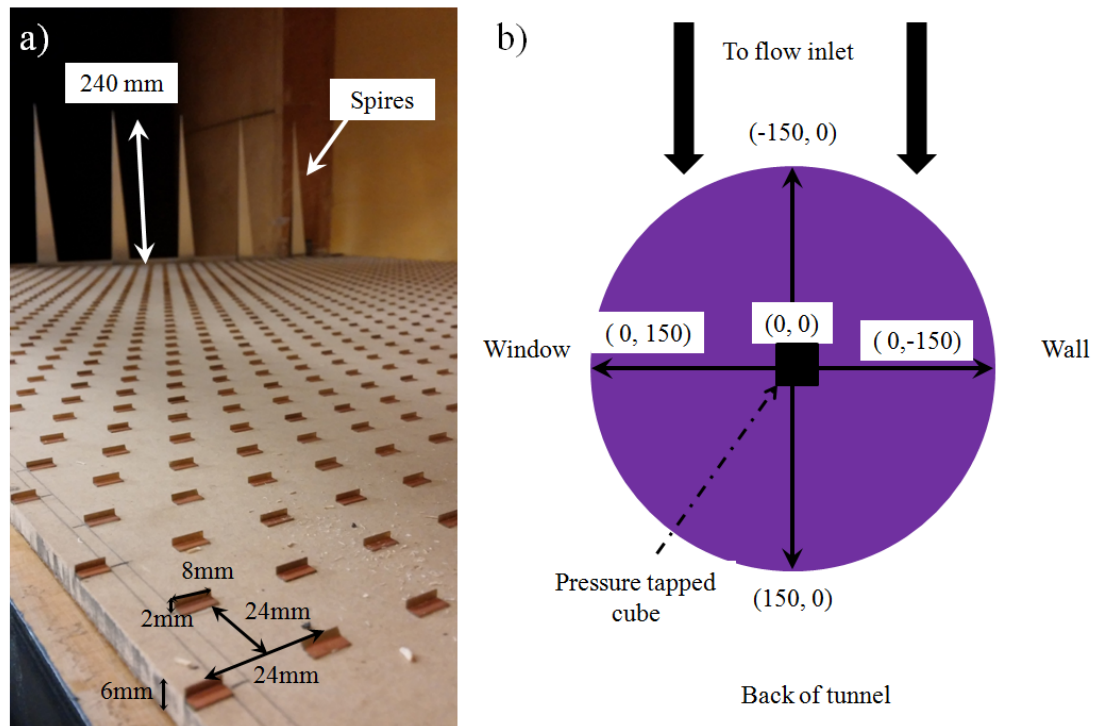


Figure 4.2: a) Irwin spires and roughness elements in the wind tunnel as seen from the side of the tunnel, looking towards the flow inlet, with the dimensions of the roughness elements annotated. b) schematic of the turntable with coordinates marked. Coordinates are given in mm.

Table 4.1:: Summary of wind tunnel experiment

Variable	Specifications
Tunnel used	Enflo 'A' low speed open-circuit tunnel (Figure 4.1)
Aim	Investigate the effect of increasing array size on C_p with wind direction
Boundary layer type	Atmospheric, based on full-scale data (Section 4.2.3), Seven 0.25 m Irwin spires used (Figure 4.2)
Instrument errors	< 5 %Combination of pressure and wind speed errors
Reference measurement location	Pressure and wind speed in line with centre of array
Roughness elements	8 mm wide (spanwise direction), 2 mm high (Figure 4.2), 20 mm wooden cubes (Figure 4.9)
Turbulence intensity	Free-stream: < 0.6 % Building height: 19 % \pm 1 %
Variables changed	Wind direction, array size
Variables measured	Wind speed, wind direction, surface pressure
Wind speed	10 m s ⁻¹

4.2.1 Pressure measurements

The cube representing the instrumented cube from the full-scale experiment is a 20 mm brass cube previously used for drag experimentation by Cheng *et al.* (2007). The brass cube had 42 pressure taps on two opposing sides, referred to as 'front' and 'back', with each side having 3 rows of 7 pressure taps. The height of these rows is different for the front and back faces, meaning the cube can be rotated by 180 ° in order to have 42 pressure measurements on each face (Figure 4.3). Rotating the cube by 90 ° allows for the pressure data to be captured for the cube sides, called 'north' and 'south' in line with the full-scale experiment (Figure 4.3).

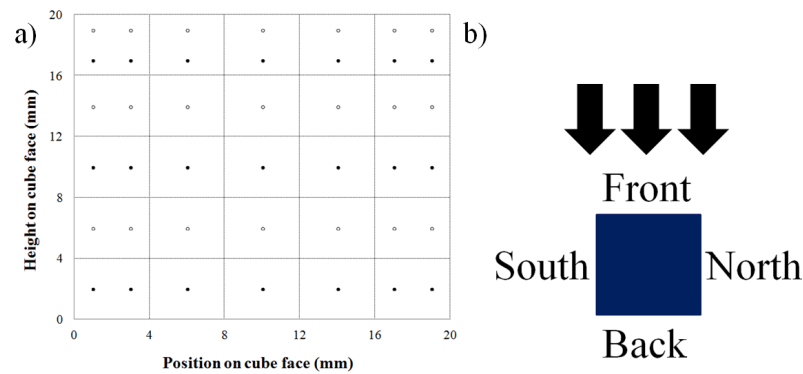


Figure 4.3: a) Schematic showing locations of all pressure tap measurements on opposite cube faces. Front face (open); back face (filled). Note that for a given wind direction the cube is rotated in order to achieve forty-two measurements on all four faces b) Naming of the cube faces when at a 0° rotation (flow perpendicular to the front face).

The pressure measurements were taken at 200 Hz with a one minute averaging period in order to reduce averaging errors. The reference static pressure was measured at $x = 55$ mm, $y = 95$ mm and $z = 300$ mm to ensure that it did not disrupt the flow around the array and provided a local reference pressure measurement.

The method utilised allows for simultaneous sampling of all pressure taps at frequencies lower than 2 kHz, reducing the run time and reducing the effect of wind speed variation on the measurements. A digital simultaneous pressure acquisition, based on the methodology of the Honeywell true stability system (<http://sensing.honeywell.com/>) is used. The hardware and software were designed in house at EnFlo laboratory at the University of Surrey and consists of 8 cards, each with 8 sensors. The set-up (Figure 4.4) consists of 48 Honeywell pressure transducers, each with a range of ± 160 Pa, a maximum measurement frequency of 2 kHz and a response time of 0.5 ms. The minimum step change in pressures the sensors could sense was 0.019 Pa. The sensors have a manufacturer stated accuracy of $\pm 0.25\%$ FSS BFSL (Full Scale Span Best Fit Straight Line) which reduces the software needed to correct system inaccuracies. The system measures the differential pressure, with all sensors being connected to the same reference pressure via the same length of connecting Silicon tubing (3 mm external diameter and 1 mm internal diameter). The sensors correct for temperature variation in the surroundings automatically. The system is connected to the brass cube via a tubing system (Figure 4.4).

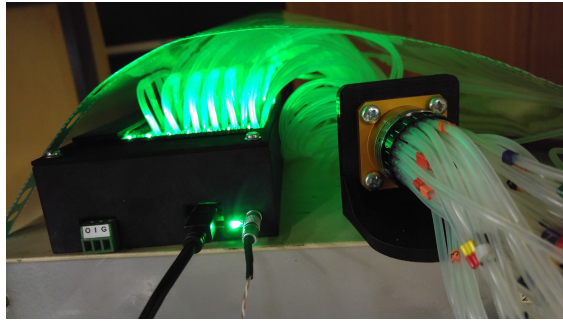


Figure 4.4: Photograph of the simultaneous pressure acquisition system. The cards are the Honeywell pressure transducers, which are connected to the static pressure from the reference pitot tube and to the pressure taps on the cube. The adapter on the right is the connection between the pressure tapped cube and the system, with all pipes being labelled.

Data were transferred to the PC via a USB connection with National Instruments Labview software. The USB cable was kept away from all sources of electrical interference where possible, such as laptops, power cables and extension leads, to avoid erroneous pressure recordings. A pitot-static tube measures the flow velocity by measuring the difference (Δp in Pa) between the stagnation (p_0 in Pa) and static pressures (p_s in Pa) of the oncoming flow:

$$p_0 - p_s = \Delta p \quad (4.1)$$

$$U = \sqrt{\frac{2RT(p_0 - p_s)}{p_a}} \quad (4.2)$$

where p_a is the atmospheric pressure in Pa, R is the specific gas constant ($287 \text{ J kg}^{-1} \text{ K}^{-1}$) and T is the temperature of the air (K). A thermocouple was positioned in the inlet of the working section, with p_a being measured using an accurate electronic pressure transducer, located 12 km from the wind tunnel laboratory at the National Physical Laboratory in Teddington (Padhra, 2010). The measurement uncertainty of the pressure transducer was $\pm 30 \text{ Pa}$, resulting in the uncertainty of the flow velocity of $\pm 0.02 \text{ m s}^{-1}$ (0.2 % of the set speed 10 m s^{-1}).

The program sequence was as follows:

1. Wind tunnel speed was set to 0 m s^{-1}
2. A zero value is taken simultaneously for all taps at 0 m s^{-1}
3. Wind tunnel speed was set to 10 m s^{-1} and allowed to settle for two minutes
4. Pressure tap measurements were taken for the front and back faces. All 42 measurements were taken simultaneously and with an averaging time of one minute
5. After a set of measurements was completed, the program paused with the wind

tunnel set to 10 m s^{-1} . The access hatch closest to the turn table was opened and the cube rotated 180° clockwise by hand and aligned by eye (Section 4.3)

6. The hatch was closed and the program resumed. The wind tunnel speed was allowed to settle for thirty seconds at 10 m s^{-1} to ensure that the flow remained steady
7. Pressure tap measurements for the cube at 180° were taken. This was the same procedure as for the 0° case. This completed the front and back measurements
8. The program was paused with the wind tunnel set to 10 m s^{-1} , the hatch opened and the cube was rotated 90° anti-clockwise to begin the start of the side measurements
9. The hatch was closed and the program resumed. The wind tunnel speed was allowed to settle for thirty seconds at 10 m s^{-1}
10. Pressure tap measurements for the cube at 270° were taken. This was the same procedure as for the 0° case
11. The program was paused with the wind tunnel set to 10 m s^{-1} , the hatch opened and the cube was rotated 180° to complete the second stage of the side measurements
12. The hatch was closed and the program resumed. The wind tunnel speed was settled for one minute at 10 m s^{-1}
13. Pressure tap measurements for the cube at 90° were taken. This was the same procedure as for the 0° case
14. Tunnel speed was set to 0 m s^{-1} and allowed to settle
15. Another set of zero measurements were taken
16. Wind tunnel speed was set to 0 m s^{-1} in preparation for the next run. All runs followed this procedure

4.2.2 Flow measurement

For all experimental runs, the free stream velocity, U_∞ , was set to 10 m s^{-1} and was measured by a Pitot static tube connected to the pressure measurement system (Section 4.2.1). The wind tunnel speed was allowed to settle for about two minutes at the start of each session to ensure that the flow speed was stable. The flow had a free-stream turbulence intensity of $< 0.6 \%$. Turbulence intensity (TI) was calculated using (Kaimal and Finnigan, 1993):

$$TI = \frac{\sigma_{u'}}{U} \quad (4.3)$$

Where $\sigma_{u'}$ is defined as the root mean square (RMS) or standard deviation of the turbulent velocity fluctuations at a particular location over a period of time and U is the average velocity measured at the same location for the same period of time as u' . $\sigma_{u'}$ can be used to suggest the spread of the gust sizes in the oncoming flow. A $TI > 1$ suggests that the range of the speed of the gusts is greater than the mean flow speed, meaning that the flow is dominated by turbulence caused by the gusts rather than the mean flow (Kaimal and Finnigan, 1993).

The free-stream turbulence intensity profiles were taken in the wind tunnel without any obstacles and was measured at the centre point of the turntable (0,0).

4.2.3 Flow uniformity

To ensure that the wind tunnel sides were not affecting the uniformity of the flow around the turntable, the vertical wind profile was measured at five points (Figure 4.2b): (0,0) the centre point of the turntable, (-150,0) and (150,0) the front and back of the turntable, (0,150) and (0,-150), the far left and right hand sides of the turntable, named 'Window' and 'Wall' respectively. These wind profiles were taken with the roughness elements present and with the turntable in place, with the central measurement being taken above the pressure tapped cube. A pitot-static tube (made in-house) was used to measure the flow velocity at ten heights between 10 mm and 350 mm. All profiles except the central profile sampled at 10 mm as the first point. The central profile sampled at 20 mm as the first point; the location of the top of the cube.

At each height, U was sampled for 60 s at 200 Hz and an average taken to reduce the sampling error. Ten seconds were left between each measurement to allow the traverse to move and become stable.

The profiles along the x-axis of the turntable are within the error limits of each other, with slight differences occurring for the central (0,0) measurement, due to it being taken above the isolated cube (Figure 4.5). Of all the profiles, the 'Window' profile shows the greatest variation from the other profiles possibly due to slight gaps in the joins of the tunnel, leading to flow leakage. All boundary layer winds fall within error bars once normalised by the reference free stream flow speed (U_{inf}). The average of the boundary layers is used throughout this section.

The speed at each height was compared to U_{inf} measured 0.1 m away from the working section inlet towards the window of the tunnel, in order to determine boundary layer depth. The standard wind tunnel definition of boundary layer depth is the height at which the wind speed becomes 99 % of the reference wind-speed (U_{ref}) (Cheng and Castro, 2002). For all individual profiles, and the average profile, the boundary layer

thickness was 150 mm (i.e. 7.5 cube heights) over the turntable.

4.2.3.1 Logarithmic layer

There are three different layers to the average wind tunnel generated boundary layer (Figure 4.5). A logarithmic layer exists above the wind tunnel surface, between 1.5 and 2 cube heights up to $36 \text{ mm} \pm 2 \text{ mm}$. The logarithmic fit is given in the form $y = mx + c$ for the test average:

$$\ln(z) = 1.45U - 6.94 \quad (4.4)$$

where z (m) denotes height above the tunnel surface and U (m s^{-1}) is the wind speed at that height. The coefficient of determination (R^2) for the fit was 0.98.

Above the logarithmic layer, there is the outer layer where the flow is slightly influenced by the roughness below, but not by the individual buildings (Figure 4.5). The top layer (190 mm onwards) is the free stream velocity. There will be a shallow ceiling boundary layer at the very top of the tunnel (Figure 4.5).

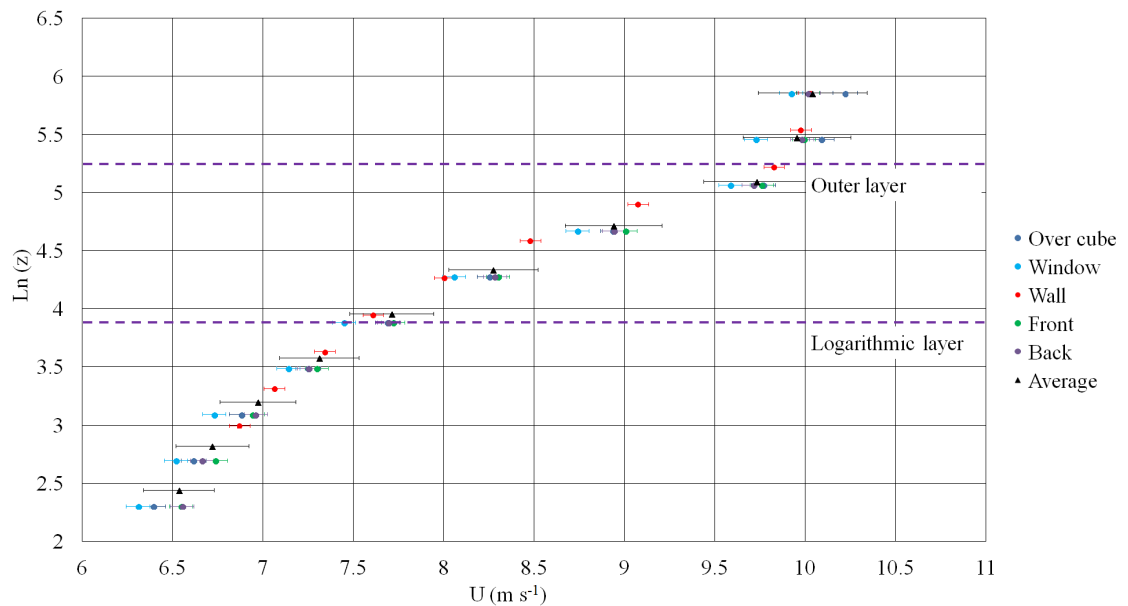


Figure 4.5: Five boundary layer mean velocity profiles and the average profile (black triangles) measured around the turntable (Figure 4.2b) in the wind tunnel against the logarithmic height (note axes). Error bars denote the standard error. Height error bars are too small to be seen.

4.2.3.2 Roughness length (z_0)

To determine the roughness length (z_0) of the wind tunnel model, flow is assumed to be of near-neutral stability, two points of data at different heights are chosen from within the logarithmic layer:

$$U_{z1} = \frac{u_*}{\kappa} \ln\left(\frac{z_1 - d}{z_0}\right) \quad (4.5)$$

$$U_{z2} = \frac{u_*}{\kappa} \ln\left(\frac{z_2 - d}{z_0}\right) \quad (4.6)$$

where U_{z1} (m s^{-1}) is the flow speed at the lowest chosen height (z_1), U_{z2} (m s^{-1}) is the flow speed at the upper chosen height (z_2), u_* is the friction velocity (m s^{-1}), κ is the von Karman constant (0.4), d is the zero plane displacement, defined as the height (m) at which the mean velocity is zero due to relative large obstacles; d can be assumed to be zero for the roughness elements used here due to the small scale of the model. Dividing U_{z2} by U_{z1} gives:

$$\frac{U_{z2}}{U_{z1}} = \frac{\ln(z_2) - \ln(z_0)}{\ln(z_1) - \ln(z_0)} \quad (4.7)$$

Rearranging equation 4.7 for z_0 :

$$\frac{\frac{U_{z2}}{U_{z1}} (\ln(z_1) - \ln(z_2))}{\frac{U_{z2}}{U_{z1}} - 1} = \ln(z_0) \quad (4.8)$$

The average z_0 calculated within the logarithmic layer was $3.3 \times 10^{-5} \text{ m} \pm 1 \times 10^{-6} \text{ m}$ ($0.033 \pm 0.001 \text{ mm}$), approximately one sixth of the roughness of the array elements. The equivalent full-scale terrain can be described as open and flat with a few isolated obstacles and a combination of grass and low crops (Stull, 1988). The full-scale site is described as having a surface roughness length of $0.006 - 0.01 \text{ m}$, meaning the wind tunnel is representative of the surrounding surface of the full-scale site (Richards and Hoxey, 2012). The wind tunnel simulation does not account for the effects of the tree avenue, nearby buildings and the woodland at the full-scale site (Figure 3.2). z_0 is higher for arrays with a higher plan area density, but changing the direction of the oncoming flow leads to changes in z_0 and the friction velocity regardless of the plan area density (Yang *et al.*, 2016).

4.2.3.3 Turbulence intensity at building height

The average turbulence intensity generated at building height by the roughness elements and boundary layer generators for the wind tunnel model was $19 \% \pm 1 \%$, with all tests being consistent at building height (Figure 4.6). The longitudinal turbulence intensity is typically 20% at building height for the full-scale cube in near-neutral conditions, though no uncertainty is stated (Richards *et al.*, 2001). This suggests that the wind tunnel model experiences similar turbulence intensities to that of the full-scale. However, as the data set of Richards *et al.* (2001) only considers selected wind conditions, the value of turbu-

lence intensity will differ depending on the wind direction for the full-scale site, due to other obstacles (Sections 5.2.1.1, 5.2.1.2).

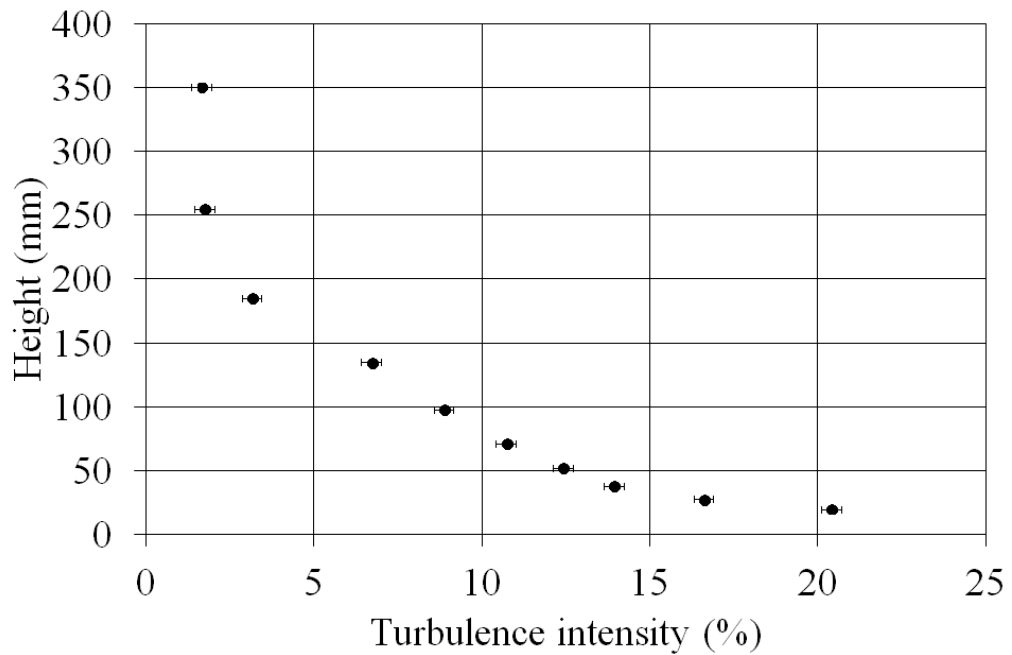


Figure 4.6: Average longitudinal turbulence intensity profile for the wind tunnel boundary layer (equation 4.3). Height error bars not visible.

4.2.3.4 Comparison of the generated boundary layer to previous work

The Silsoe cube has been previously modelled at a 1:40 scale by Richards *et al.* (2007), using the full-scale Silsoe data from Richards *et al.* (2001) as a reference. There is good agreement between the mean velocity profiles of previous results and this experiment in the logarithmic layer (below heights of two cube heights), with deviation occurring above the logarithmic layer between the two wind tunnel boundary layers, due to the differing characteristics of the wind tunnels used (Figure 4.7). The full-scale data were only available up to two cube heights due to limitations with mast height in the full-scale experiment (Richards *et al.*, 2001).

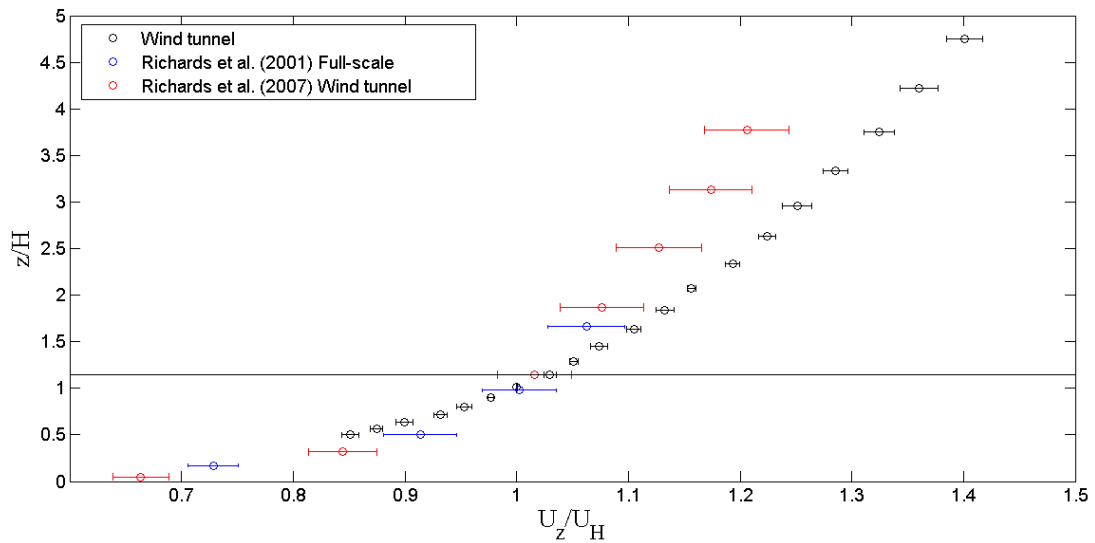


Figure 4.7: Comparison of the generated boundary layer (black points) to the full-scale measurements by Richards *et al.* (2001) (blue) and the wind tunnel experiment simulating the full-scale experiment by (Richards *et al.*, 2007) (black). Line denotes where the boundary layer behaviours begin to deviate. Data from Richards *et al.* (2007) have been digitised, so carries a processing error.

With the logarithmic boundary layer showing good agreement to previous wind tunnel and full-scale measurements, and the roughness lengths and turbulence intensities being similar to previous full-scale measurements (Richards *et al.*, 2001), it can be assumed that the boundary layer generated during these experiments is representative of the logarithmic layer of the full-scale boundary layer and that direct comparisons can be made between full-scale and wind tunnel experiments.

4.3 Sources of error in the wind tunnel

Though not commonly reported, all measurements within a wind tunnel environment will likely carry some form of error.

4.3.1 Wind Angle

One source of error for these wind tunnel experiments is the human error involved in positioning the cube. Three test runs were undertaken: Run 1 was an isolated cube lined up to $\theta_{ref} = 0^\circ$ through the use of rulers and spirit levels, Run 2 was an isolated cube aligned to $\theta_{ref} = 4^\circ$ in a similar manner and Run 3 was an isolated cube lined up by eye to $\theta_{ref} = 0^\circ$. Run 1 was assumed to be the most accurate ($\pm 1^\circ$). The human error within the tests was assumed to be systematic, as the same person was involved in each experiment.

For each of the three tests, measurements were taken at 200 Hz and averaged over 30 seconds. The cube was not rotated during this experiment, meaning only 21 pressure measurements were taken on the front and back cube faces. The side faces were not tested as the effects were assumed to be the same for each face.

Comparisons of the pressure measured on different runs were made for each individual tap (Figure 4.8). The deliberate misalignment of 4° (Test 2) caused up to a $76\% \pm 2\%$ drop in the recorded pressure compared to the results of Test 1 for the back face, with the largest differences (range of $-76 - 14\% \pm 2\%$) being located on one side of the face ($y < 0$ from the centre of the cube) (Figure 4.8a). In Test 3 (human alignment to $\theta_{ref} = 0^\circ$), this trend towards the $-y$ side having large differences on the back face is not seen, with the range of pressure differences between Test 1 and Test 3 being $-11.6\% - 10.6\% \pm 2\%$, considerably lower than the differences between Test 1 and Test 2, (Figure 4.8b).

The percentage differences across the front face (Figure 4.8c, d), were smaller than those for the back face. For the comparison between Test 1 and Test 2, the percentage difference varied between $-33\% - 18\% \pm 5\%$. By rotating the cube $4^\circ \pm 1^\circ$, the point of impact was shifted from the centre of the cube towards the $-y$ side of the cube, resulting in an increase in pressure measured by those pressure taps. For Test 1 and Test 3 this difference was $0.84\% - 33\% \pm 5\%$ with no change in sign present. This larger increase in pressure on the $-y$ side of the front face for Test 2, leads to a larger negative pressure on the $-y$ side of the back face. For the $+y$ side, the decrease in recorded values on the front face leads to a slight increase in recorded pressure on the back face. This trend was also present in the differences between Test 3 and Test 1, though the overall percentage difference is lower.

The pressure differences recorded in Test 3 are lower for both faces than those recorded in Test 2, when both were compared to Test 1. This suggests that the human error involved in aligning the cubes by eye is $< 4^\circ$ and was assumed to be $\pm 2^\circ$ for all experiments. The taps most affected by a misalignment are located on the cube edges.

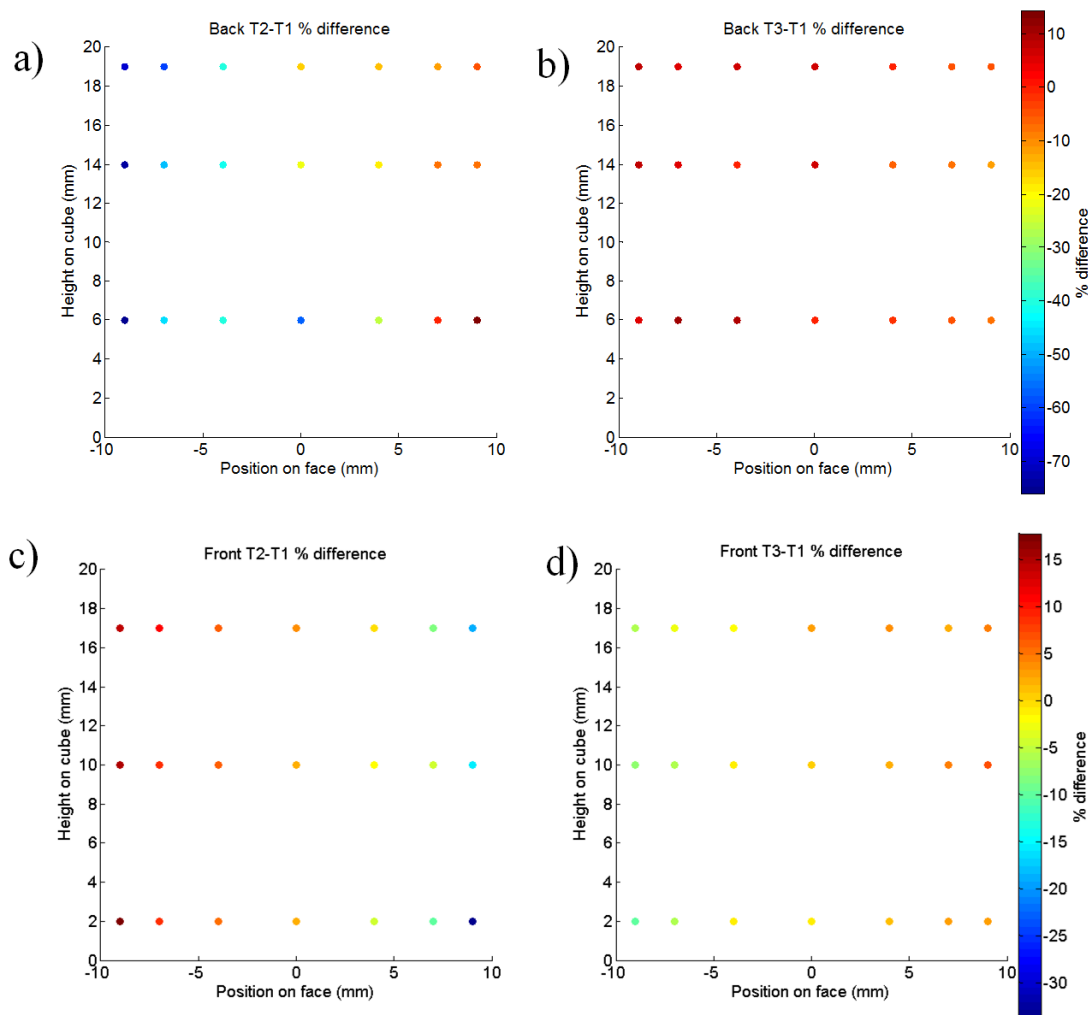


Figure 4.8: Percentage pressure differences (colour) between a) Test 1 and Test 2 for the back face b) Test 1 and Test 3 for back face c) as a) but for the front face d) as b) but for the front face. The errors on the values plotted range from 2 % to 4 %. See text for definitions of tests.

The cubes used to create the arrays may also be misaligned when placed within the array, though it is assumed that a slight misalignment (of $\pm 2^\circ$) of an array element is likely to have less of an effect on the overall pressure patterns on the instrumented cube than a misalignment of the instrumented cube itself. All array elements were aligned using a ruler and grid pattern to minimise errors of this type.

4.3.2 Measurement errors

Each measurement has an instrument error associated with it. It is combined with the standard error of the average over the selected time period in order to form an error estimate for each measurement. In order to ensure that the wind tunnel was operating at the correct speed, all measurements are taken after a brief settling period, and if the tunnel speed was altered a lengthy spin-up period (2 minutes) was allowed. Each set of

pressure measurements has a zero measurement to check for drift at the start and end of the set.

4.4 Overview of the arrays

The array elements surrounding the test cube were 20 mm sharp-edged wooden cubes, previously used by Cheng *et al.* (2007). These were sanded smooth before use to remove any imperfections and were attached to the turntable using a small amount of silicon sealant, minimising the height variation to ± 1 mm (5 % of the cube height). All arrays were built around the instrumented brass cube, which remained located in the centre of the turntable (0,0) for all runs. The same spacing (one cube height or 20 mm) was used for all arrays, with all arrays being staggered for a wind direction $\theta_{ref} = 0^\circ$ and aligned with a model rotation of $\pm 90^\circ$ (Table 4.2).

The wind tunnel blockage ratio (Φ_f) the ratio of the array frontal cross-sectional area to the wind tunnel cross sectional area is calculated using:

$$\Phi_f = \frac{W_c H_c}{W_t H_t} \quad (4.9)$$

where W_c is the width of the cube in metres, H_c is the height of the cube in metres, W_t is the width of the tunnel in metres and H_t is the height of the tunnel in metres.

Table 4.2:: Five wind tunnel set-ups used.

Array	Number of cubes	λ_p	Φ_f	Model rotation	θ_{ref}
A) Isolated cube	1	N/A	0.074 %	0 °, 45 °	0 °, 315 °
B) Silsoe Array	9	25 %	0.44 %	0 °, 10 °, 45 °, 80 °, 90 °, 100 °, 170 °, 180 °, 190 °, 260 °, 270 °, 280 °, 350 °	0 °, 350 °, 315 °, 280 °, 270 °, 260 °, 190 °, 180 °, 170 °, 100 °, 90 °, 80 °, 10 °
				0 °, 10 °, 45 °, 80 °, 90 °, 100 °, 170 °, 180 °, 190 °, 260 °, 270 °, 280 °, 350 °	0 °, 350 °, 280 °, 270 °, 260 °, 190 °, 180 °, 170 °, 100 °, 90 °, 80 °, 10 °
C) Silsoe array (extended)	15	24 %	0.44 %	0 °, 10 °, 45 °, 80 °, 90 °, 100 °, 170 °, 180 °, 190 °, 260 °, 270 °, 280 °, 350 °	0 °, 350 °, 280 °, 270 °, 260 °, 190 °, 180 °, 170 °, 100 °, 90 °, 80 °, 10 °
D) Small symmetrical array	23	25.5 %	0.66 %	0 °, 45 °, 90 °	0 °, 315 °, 270 °
E) Large symmetrical array	45	26 %	0.96 %	0 °, 45 °, 90 °	0 °, 315 °, 270 °
F) Silsoe array with storage shed	9	N/A	N/A	0 °, 260 °, 270 °, 280 °	0 °, 80 °, 90 °, 100 °
G) Isolated cube with storage shed	9	N/A	N/A	0 °, 260 °, 270 °, 280 °	0 °, 80 °, 90 °, 100 °
H) Aligned array	9	25 %	0.44 %	0 °, 10 °, 45 °, 90 °, 180 °	0 °, -10 °, -45 °, -90 °, 180 °

The isolated, surface mounted cube (Table 4.2A) is a classic case within the wind tunnel literature (Castro and Robins, 1977). Here it represents the full-scale isolated cube. It was used to determine whether the wind tunnel model was comparable to other set-ups, such as Richards *et al.* (2007) and Castro and Robins (1977) (Section 4.5.1).

The nine cube array (Figure 4.9a) is a 1:300 scaled version of the full-scale experiment (Chapter 3) and is referred to as the Silsoe array. By recreating the array pattern within the wind tunnel, wind angles which were uncommon in the full-scale data set could be explored. The wind-tunnel array allows for a comparison with the scaled isolated cube, in order to understand the combined effect of wind direction and the shielding from the array and whether it is similar for both full-scale and scaled models. Due to the Silsoe array being the main focus of the wind tunnel work, a larger range of rotation angles (Table 4.2B) were chosen to allow for comparison to the full-scale, to aid understanding of the influence of wind direction changes on the flow pattern and thus the pressure distribution across the instrumented cube.

The limited extent of the Silsoe array is explored by extending to a 15 cube array, referred to as the extended Silsoe array (Figure 4.9b). Like for the Silsoe array (Figure 4.9a) a large range of rotation angles were tested (Table 4.2C).

A small symmetrical staggered array (e.g. used by Hanna *et al.* (2002); Ahmad *et al.* (2012); Cheng *et al.* (2007); Coceal *et al.* (2006)) is formed of 23 cubes (Figure 4.9c, Table 4.2D) reduces the variation seen due to θ when compared to asymmetric arrays (Coceal *et al.*, 2006).

The largest symmetrical array (45 cubes, Figure 4.9d, Table 4.2E) allows for an understanding as to how array size influences changes in pressure patterns and C_p like research undertaken by Hall and Spanton (2012). The large symmetrical array (Figure 4.9d) is compared directly to the small symmetrical array (Figure 4.9c).

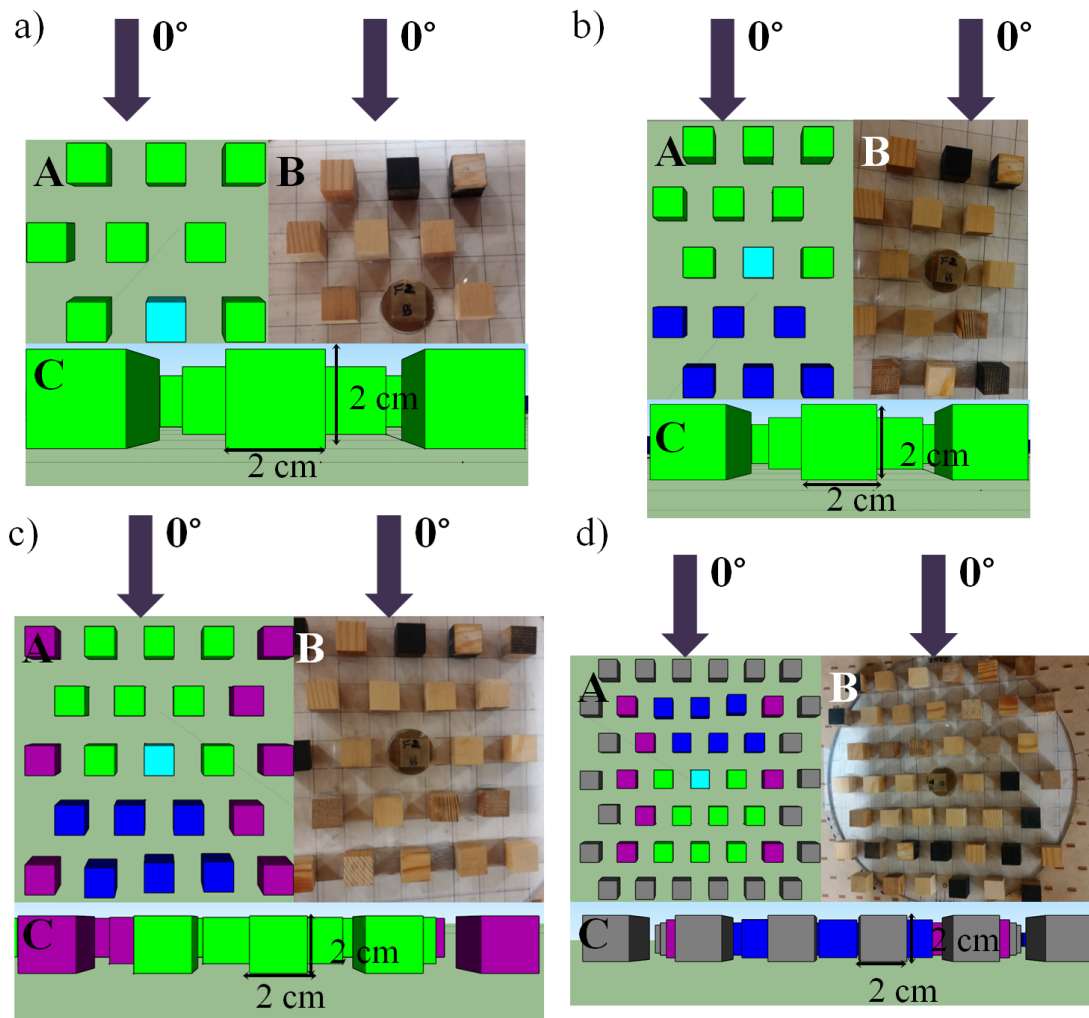


Figure 4.9: A is the plan view of the array, drawn in Google Sketchup, B is the model used in the wind tunnel and C is the frontal view of the array for the a) Silsoe array b) extended Silsoe array c) small symmetrical array and d) large symmetrical array. Colours represent the additional cubes added at each stage. Instrumented cube (light blue), Silsoe array (green), extended (dark blue), small symmetrical (purple) and large symmetrical (grey).

To check the extent of flow adjustment to the large symmetrical array's surface, the canopy drag length scale (L_c) was calculated. The canopy drag length scale is determined by the layout and geometry of the obstacles (Coceal and Belcher, 2004):

$$L_c = \frac{2H}{c_d(z)} \frac{1 - \lambda_p}{\lambda_f} \quad (4.10)$$

where H is the mean height of the obstacles, c_d is the sectional drag coefficient which relates the wind speed at height z to the average drag at z , λ_p is the plan area density and λ_f is the frontal area density. Following the method outlined by Coceal and Belcher (2004) and based on data taken from similar staggered arrays ($\lambda_p = 25\%$) by Cheng and Castro (2002), a mean value of c_d for all heights is determined as 2.6, suitable for

modelling turbulent shear flow over cubes (Coceal and Belcher, 2004). This value takes into account that within the array the vertical velocity profile is not logarithmic. No uncertainty estimates are given for the drag coefficient in Coceal and Belcher (2004). The length taken by a flow to adjust to a new canopy is equivalent to $3L_c$ (Barlow, 2014). This suggests that due to the limited size of the arrays studied, the flow is continually adjusting the surface below.

4.4.1 Limitations of the wind tunnel model

The storage shed located close to the array (Figure 3.5) was modelled in the wind tunnel (Figure 4.10), using the Richardson and Blackmore (1995) measurements. Details such as the fencing on the roof could not be modelled due to the scale of the model (Figure 4.10).

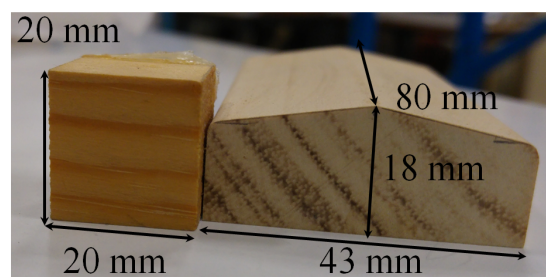


Figure 4.10: Photo of the scaled model of the storage shed with all dimensions marked: a 20 mm cube is included for comparison.

Obstacles not modelled in the wind tunnel include an avenue of trees and the surrounding buildings to the far south of the array (Figure 3.2). These would be expensive to model in the wind tunnel due to scale and limitations in tunnel width. Representing the crop field at the 1:300 scale was not feasible (Figure 3.2). The sewage tanks were also not modelled, due to the wind direction where they would effect the array being rare, and the exact dimensions being unknown (Figure 3.2).

The positioning of the reference pressure will affect the overall results. The choice to place the reference pressure adjacent and above the pressure tapped cube and arrays means that compared to previous work, the pressure coefficients obtained are likely to be more negative and thus not match exactly with previous results. This is due to other studies positioning the reference pressure at the inlet of the wind tunnel. The current pressure position in this experiment ensures that any fluctuations caused by entry into the tunnel have been smoothed out by the flow, making the results more representative of the oncoming flow experienced by the pressure tapped cube.

4.5 Comparison of pressure coefficient results

C_p (equation 2.28) is plotted for front to back cases by starting at the pressure taps at the middle-base of the front face, working up to the roof, over the roof and down the back face to the cube base (Figure 4.11A). For the side cases, the taps at height $z = 10$ mm are used (Figure 4.11B).

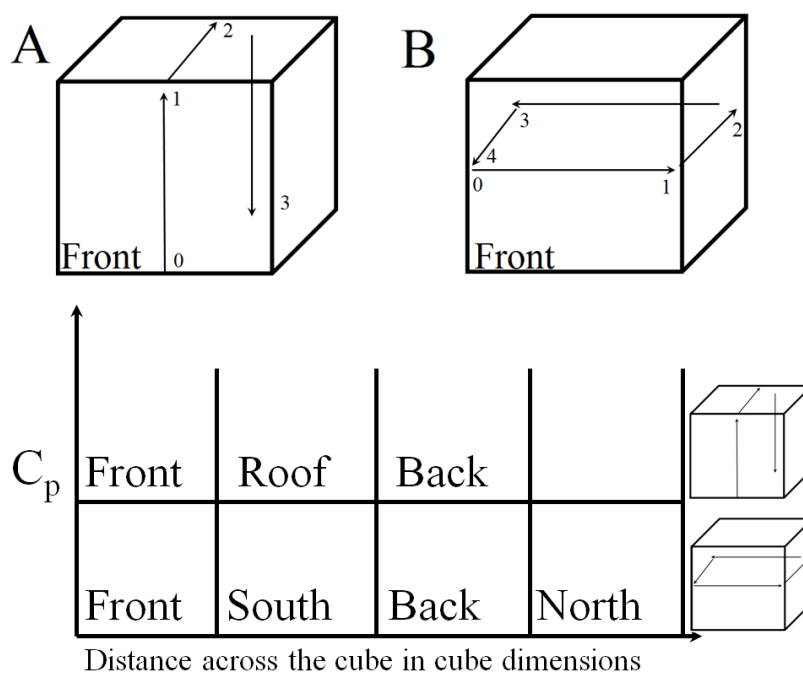


Figure 4.11: Schematic of the methodology used to plot C_p across the cube. A is the front to back C_p path and B is the C_p path which includes the sides. The front face of the cube is marked. Lower: The formatting style of the graphs used to display the change in C_p across the instrumented cube. The top layer demonstrates the layout for the vertical path (at mid-face), up the front, over the roof and down the back face. The lower layer shows the path around the cube (at half-height), beginning at the front and moving in an anticlockwise direction.

C_p contours are drawn from 42 points on each face, meaning that small details on the faces are likely to be lost. Each contour plot is set to have a maximum of 20 contours.

4.5.1 Comparison to previous results for the isolated cube

The 1:40 wind tunnel study by Richards *et al.* (2007) focused on flow re-attachment on the cube roof. The Castro and Robins (1977) dataset is extensively used as a reference for evaluation. All tests had a scaled atmospheric boundary layer instead of uniform flow, but varied in the level of turbulence intensity and in the model scale (Section 4.2.3).

The measured C_p for the wind tunnel scale isolated Silsoe cube for $\theta_{ref} = 0^\circ$ is compared against tests conducted by Richards *et al.* (2007) and Castro and Robins (1977) (Figure 4.12). Differences in the models may be related to the Richards *et al.* (2007) model

having a high Jensen number: the ratio between building height and roughness length (H/z_0). Their recorded Jensen number was between 600-1000 to match full-scale estimates, compared to approximately 80 for this experiment and 50 for Castro and Robins (1977).

The results (Figure 4.12) show good agreement on the front face between all the models. The Castro and Robins (1977) results are 0.1 higher for pressure taps near the roof of the cube. For the vertical back pressure taps, the current results are 0.1 higher (i.e. less negative) than Richards *et al.* (2007) results and around 0.25 less (more negative) than the Castro and Robins (1977) measurements.

This is also true for the horizontal pressure taps on the back face. The results for the horizontal path around the cube are similar with the front face being within error bars of tests by Richards *et al.* (2007). There is almost a 0.8 difference on the sides of the isolated cube, though this is likely to be caused by differences in positioning within the wind tunnel. For example, the isolated cube used in these tests was positioned with the small 'L' shaped roughness elements surrounding it, whereas in other tests it may have been smooth board either side. Another cause for the differences between the models is the location of the reference pressure measurement, with a pressure being taken upstream of the isolated cube would lead to a drop in measured C_p and vice versa for downstream measurements. Castro and Robins (1977) had the highest turbulence intensity out of those compared, which resulted in flow reattaching to the roof and sides, which in turn effected the base pressure.

Richards *et al.* (2001) compared several studies, over a range of roughness types and Jensen numbers. There was a spread in front face C_p of 0.2 and a spread of back face C_p of 0.4 between models, suggesting this difference is caused by Reynolds number and relative roughness effects, but turbulence intensity differences should also be considered (Castro and Robins, 1977).

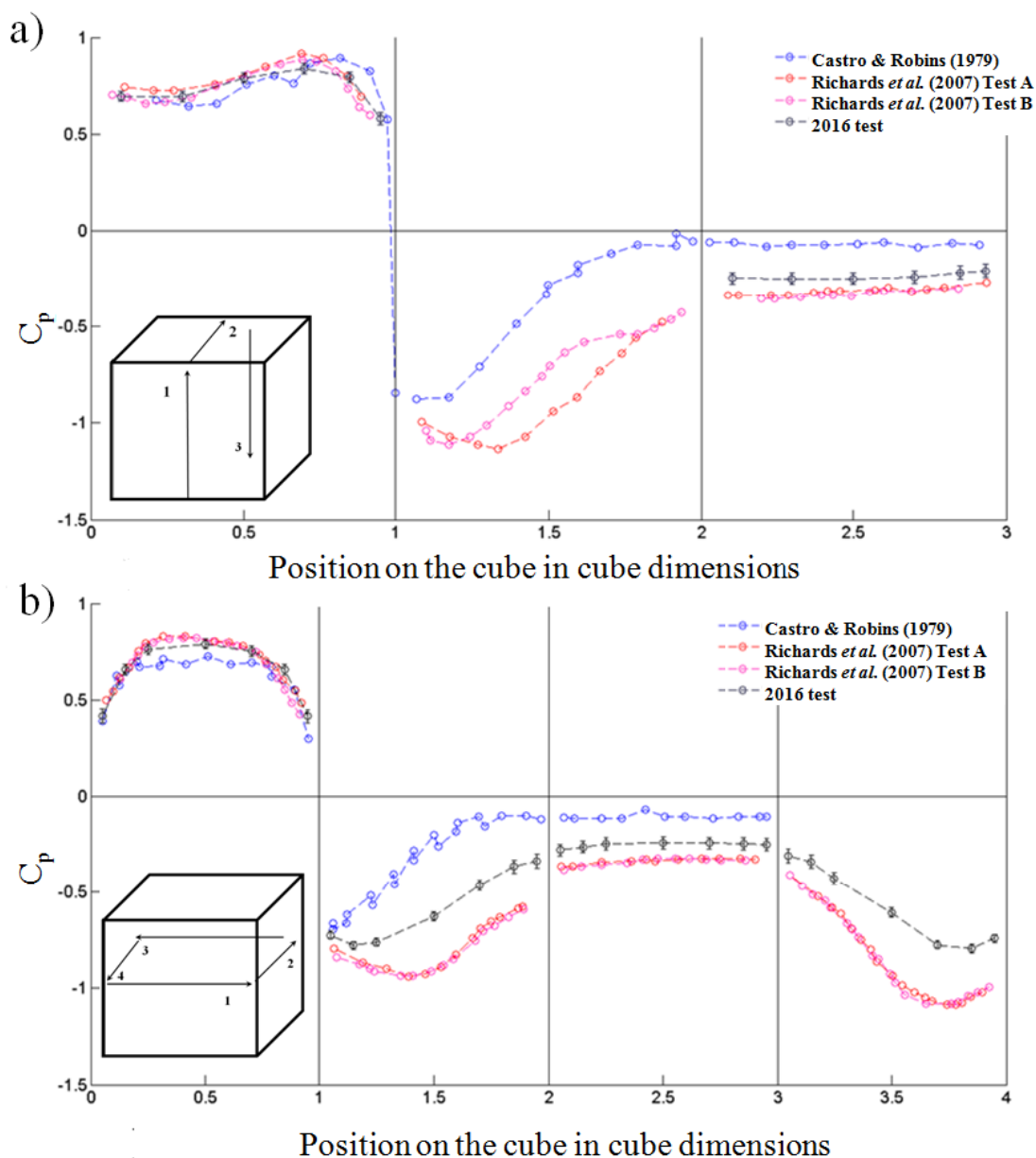


Figure 4.12: C_p results from this experiment (black) across the a) front and back and b) around the sides, of an isolated cube for $\theta_{ref} = 0^\circ$ with the digitised results of Castro and Robins (1977) (60 mm cube, blue) and the digitised results of the 1:40 Silsoe model in the University of Auckland Wind tunnel (pink and red) (Richards *et al.*, 2007). No error estimates are available for these data sets.

Overall, given the adequate agreement with Castro and Robins (1977) and Richards *et al.* (2001), the isolated cube wind-tunnel model is likely to be representative of the full-scale experiments and in-line with expected results for a model of this scale. Differences may be explained by differing techniques and flow conditions.

4.5.2 Comparison to previously studied arrays

No 'classic' case exists for arrays, with a wide range of layouts (staggered and aligned), sizes, packing densities, element numbers and model building height occur in the literature. In this section, the closest matches to this experiment are compared.

Ahmad *et al.* (2012) studied cube arrays of different packing densities (7.7 %, 30.9 % and 39.1 %) using a pressure tapped cube to assess impacts of urban area effects on wind induced ventilation, assuming the opening itself has no effect on the measured C_p . The pressure tapped cube had 25 pressure taps on the face and was 25 mm in height and width. Following the style of Ahmad *et al.* (2012) the bulk C_p is used: the average C_p along a row of pressure taps at a certain height are plotted against the location of the row, normalised by the height of the cube.

As Ahmad *et al.* (2012) measured the reference pressure behind the array (at 20H), an offset is expected within C_p due to differing placements of reference pitot tube. No errors are mentioned, though measurements were zeroed (unstated frequency) and the system allowed to warm up before use to reduce inconsistencies. The boundary layer profile is also not presented, with differing turbulence intensities and roughness levels also being a likely cause of discrepancies between data sets.

As expected, most values, aside from the large symmetrical array are between the 7.7 % and the 30.9 % arrays measured by Ahmad *et al.* (2012) (Figure 4.13). The increase in C_p with the small symmetrical array is discussed in Section 4.10.3. The Silsoe array and extended Silsoe array show a decrease in C_p above $z/H = 0.8$, which may be due to the roof recirculation, though the measurements by Ahmad *et al.* (2012) do not extend far enough up the front face to allow for comparisons. This trend decreases once the array becomes wider and could be related to slight misalignments of array elements having a greater effect for a smaller array, compared to a larger array. The C_p values of the large symmetrical array are lower than those for the 39.1 % array, though the lack of error estimates for data from Ahmad *et al.* (2012) and the small C_p values mean that this is not a conclusive result. Discrepancies with Ahmad *et al.* (2012) and this Silsoe work could be due to differences in the height of the array elements, differences in boundary layers and the flow conditions.

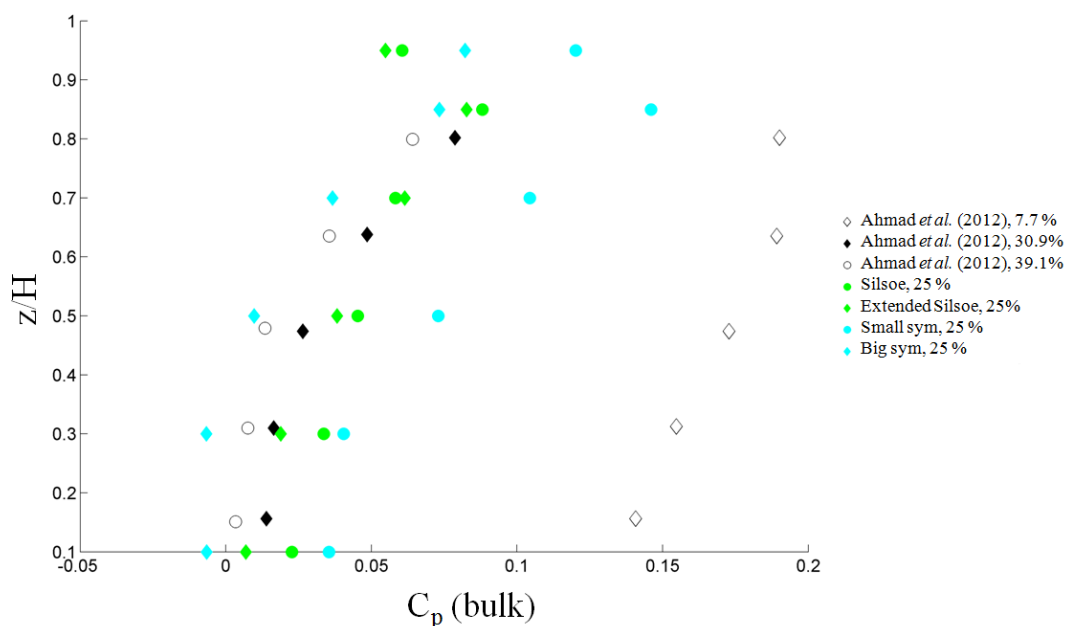


Figure 4.13: Different packing densities measured by Ahmad *et al.* (2012) (black) compared to the wind tunnel results for the Silsoe array (green), extended Silsoe array (green diamond) and the two symmetrical arrays (cyan) (Table 4.2, Figure 4.9).

Cheng *et al.* (2007) studied the effect of packing density (6.25 % and 25 %) and array type (staggered or aligned) on the drag and C_p , using the same equipment and tunnel as this experiment. Their arrays covered the entire working section of the wind tunnel (0.9 m \times 5 m) and spanned 4 m. Five separate square baseboards (each 880 mm \times 880 mm \times 9 mm) were covered in wooden cubes arranged in a staggered pattern (Cheng and Castro, 2002). Most measurements were taken around the tunnel centre line, about 3 m downstream of the ramp, 3 m into the array (Cheng and Castro, 2002). Like this experiment, the reference pressure was located above the pressure tapped cube in the free stream flow.

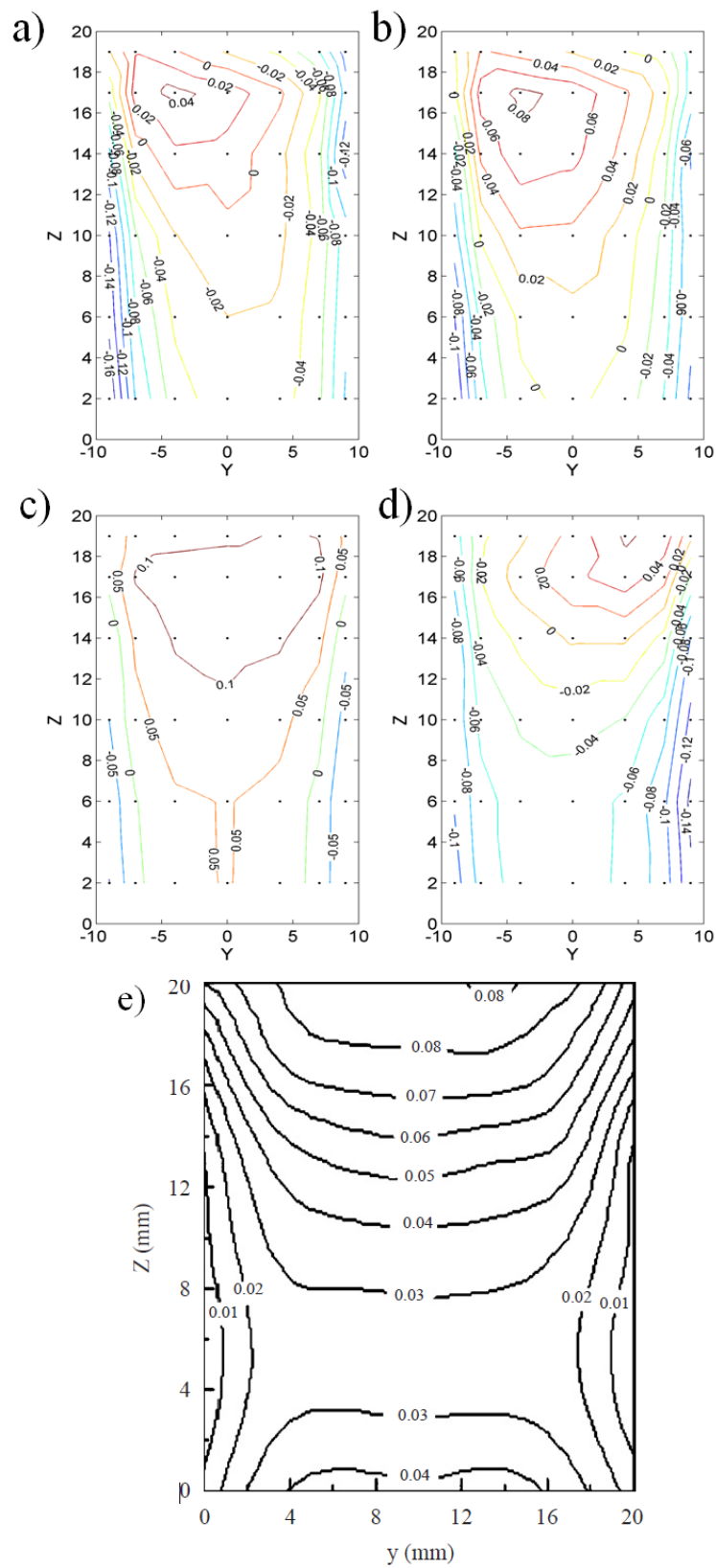


Figure 4.14: Front face C_p contours of the a) Silsoe array (Figure 4.9a) b) extended Silsoe array (Figure 4.9b) c) small symmetrical array (Figure 4.9c) and d) large symmetrical array (Figure 4.9d). e) Extensive array of 25% packing density from Cheng *et al.* (2007).

The Cheng *et al.* (2007) results are broadly symmetrical in the y direction (Figure 4.14e), in the current work the peak pressure occurs off-centre towards y in the case of the Silsoe (Figure 4.14a) and extended Silsoe arrays (Figure 4.14b) and $+y$ in the large symmetrical array (Figures 4.14c, d). The most similar contour pattern to Cheng *et al.* (2007) is the small symmetrical array (Figure 4.14c), though the C_p for the small symmetrical array are higher.

The symmetry in Cheng *et al.*'s (2007) results is caused by the pressure tapped cube being deep within the array ($> 7 H$), so the flow is fully adapted to the array geometry (Figure 4.15b). For a cube deep within the array, the features of the wakes are smeared through interactions through multiple rows, leading to a reduction of speed and ultimately a more uniform, yet chaotic flow (Figure 4.15). The arrays in this work are shallow and not extensive (Figure 4.15a), so the flow is not fully adjusted to the array and the wakes of the adjacent array elements have a direct effect on the instrumented cube. However, this also means that the wind speed around the instrumented cube is likely to be higher, as it is less shielded.

Comparison of array results is difficult due to differences in boundary layer type, array width and length and building height. This demonstrates the difficulty in utilising research findings in design, as there is no clear and precise comparison of all the different variables and their effect on C_p .

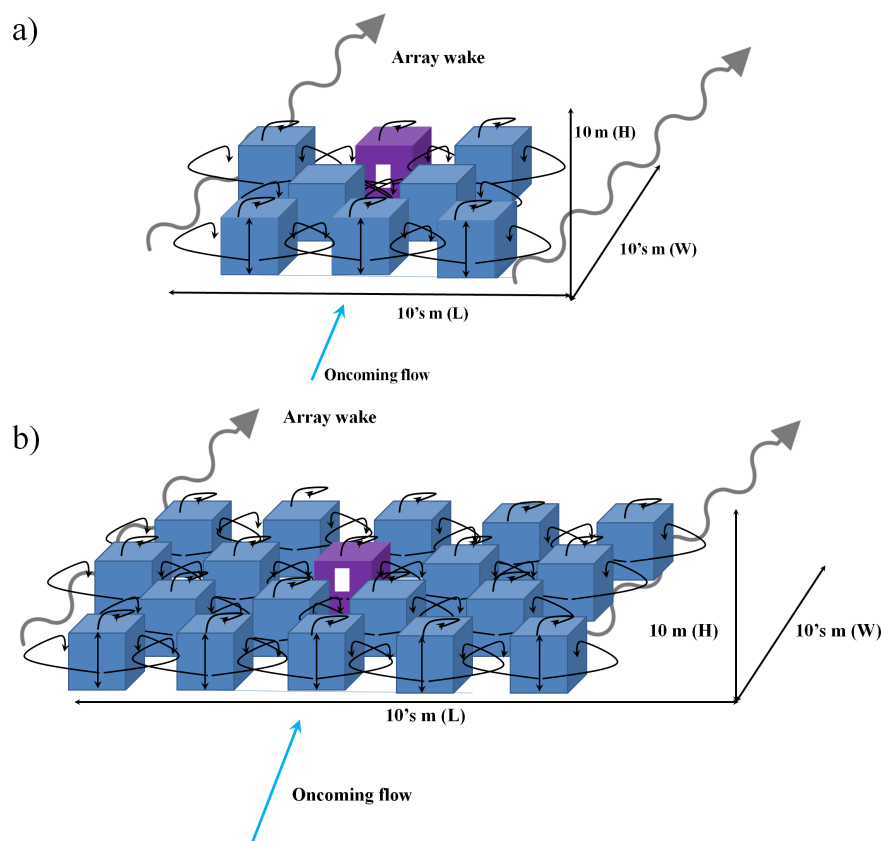


Figure 4.15: Schematic of the simplified wake regions of a) a limited array and b) an extensive array

4.6 Effect of wind direction on the pressure coefficient

To allow for comparisons of the full-scale, all angles are reported in the same system (Table 4.3), Figure 4.16).

Table 4.3:: Conversion of model rotation into reference wind direction suitable for comparing to the full-scale case (Table 4.2).

Model Rotation (°)	Full-scale angle θ_{ref} (°)
0	0
10	-10
45	-45
90	-90
135	-135
180	180
225	135
270	90
350	10

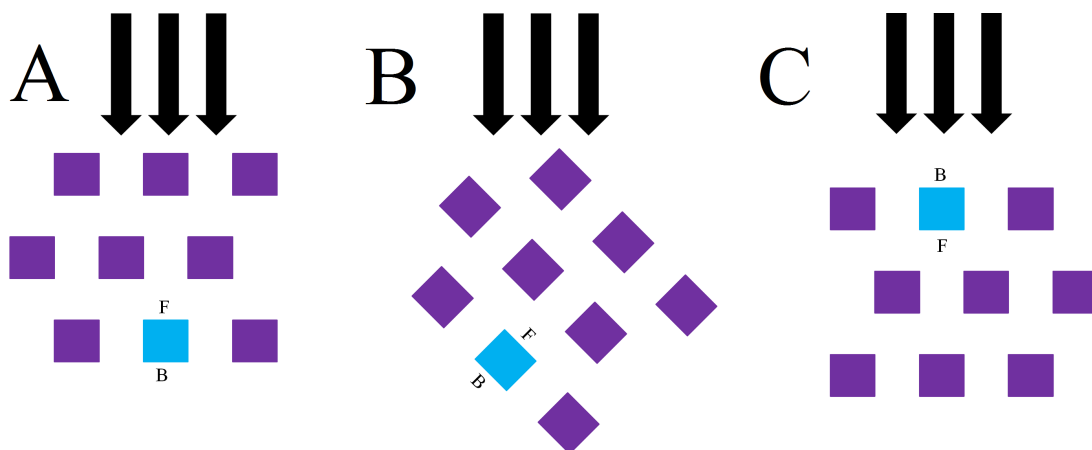


Figure 4.16: Notation to describe the positioning of the instrumented cube (blue) for three different Silsoe model rotations. Case A is a 0° model rotation, Case B is a 45° model rotation ($\theta_{ref} = -45^\circ$) and Case C is a 180° ($\theta_{ref} = 180^\circ$) model rotation. The black arrows denote the direction of flow within the wind tunnel. F and B indicate the front and back of the instrumented cube

4.6.1 Isolated cube

For a 10° change in θ_{ref} on the measured C_p for an isolated cube there is little difference for the vertical taps on the front face, with all values having overlapping error bars, due to the flow impacting on the centre of the front face (Figures 4.17, 4.18). The horizontal band of pressure taps at half building height (Figure 4.17b) show that for the 10° rotations, there is an equal but opposite effect, as the point of maximum pressure shifts depending on wind direction and there is a difference at the central vertical point

For the 10° case the maximum front face pressure moves towards the $+y$ direction, with the minimum pressure on the back moving towards the $-y$ direction. The 0° case shows no such trend, with a uniform pressure distribution on the back face.

A 5° rotation is almost exactly (± 0.001) equal to $\theta_{ref} = 0^\circ$ though this could be due to the error in alignment of the model (Section 4.3). The horizontal trace of the back face shows, like the vertical trace, that there are larger differences present on the back face than on the front face, with a range of 0.2 between all angles (Figure 4.17). These small changes in θ_{ref} change the reattachment behaviour of the flow, and alter the location of prominent vortices.

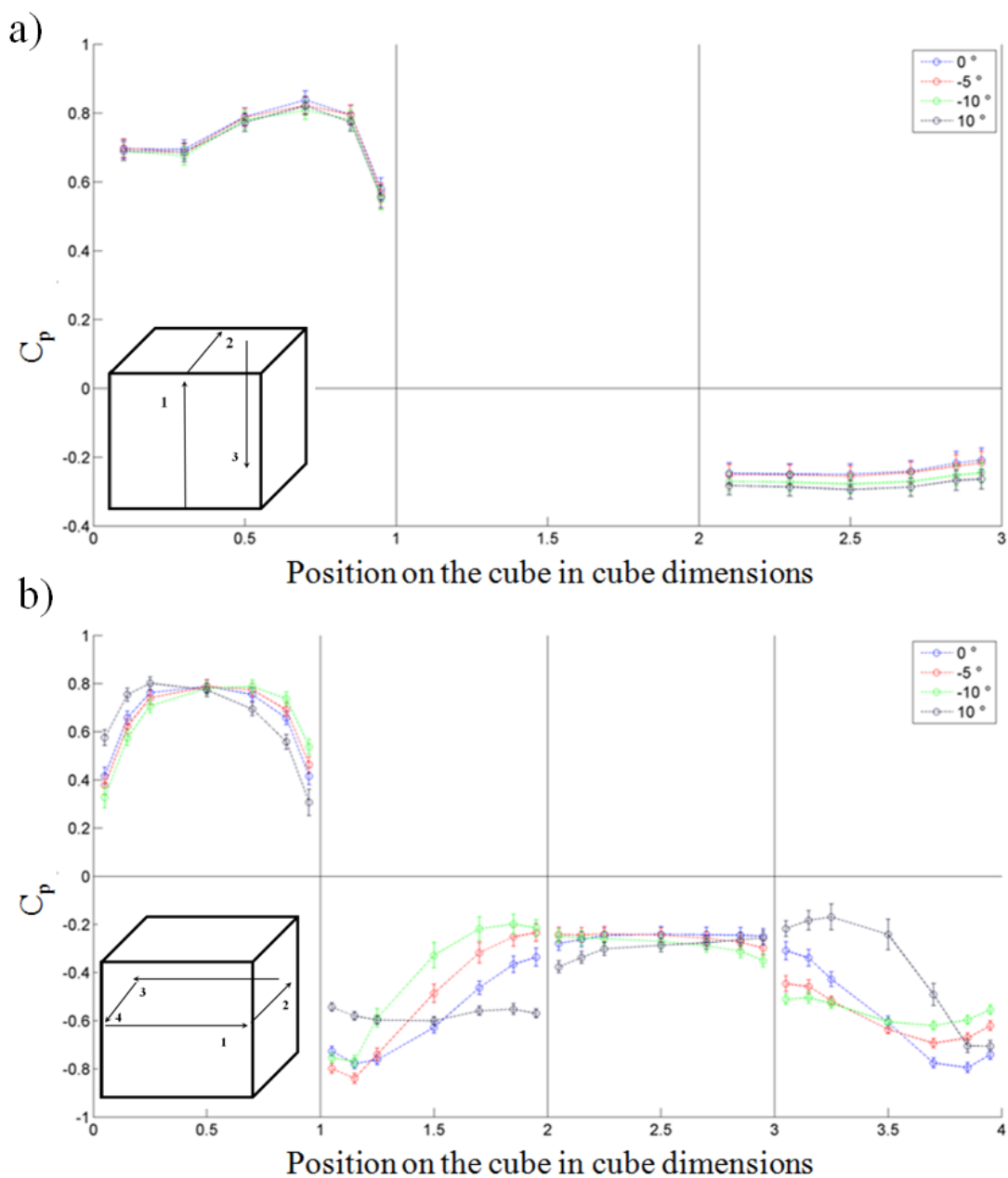


Figure 4.17: C_p for the a) vertical taps and b) horizontal central taps for an isolated cube (Table 4.2A) at $\theta_{ref} = -10^\circ$ to 10° (see key for different rotation angles).

The $\theta_{ref} = -5^\circ$ contour plots (Figure 4.18), coupled with the error analysis of model positioning (Section 4.3) suggest that a 5° rotation has an effect on the location of the maximum pressure point on an isolated cube, though it has only a 0.05 ± 0.005 effect on the front face averaged C_p when compared to $\theta_{ref} = 0^\circ$. This shift in the location of maximum pressure may cause the ventilation rate estimated from $\theta_{ref} = 0^\circ$ data to over-predict the air exchange, leading to an inefficient building design.

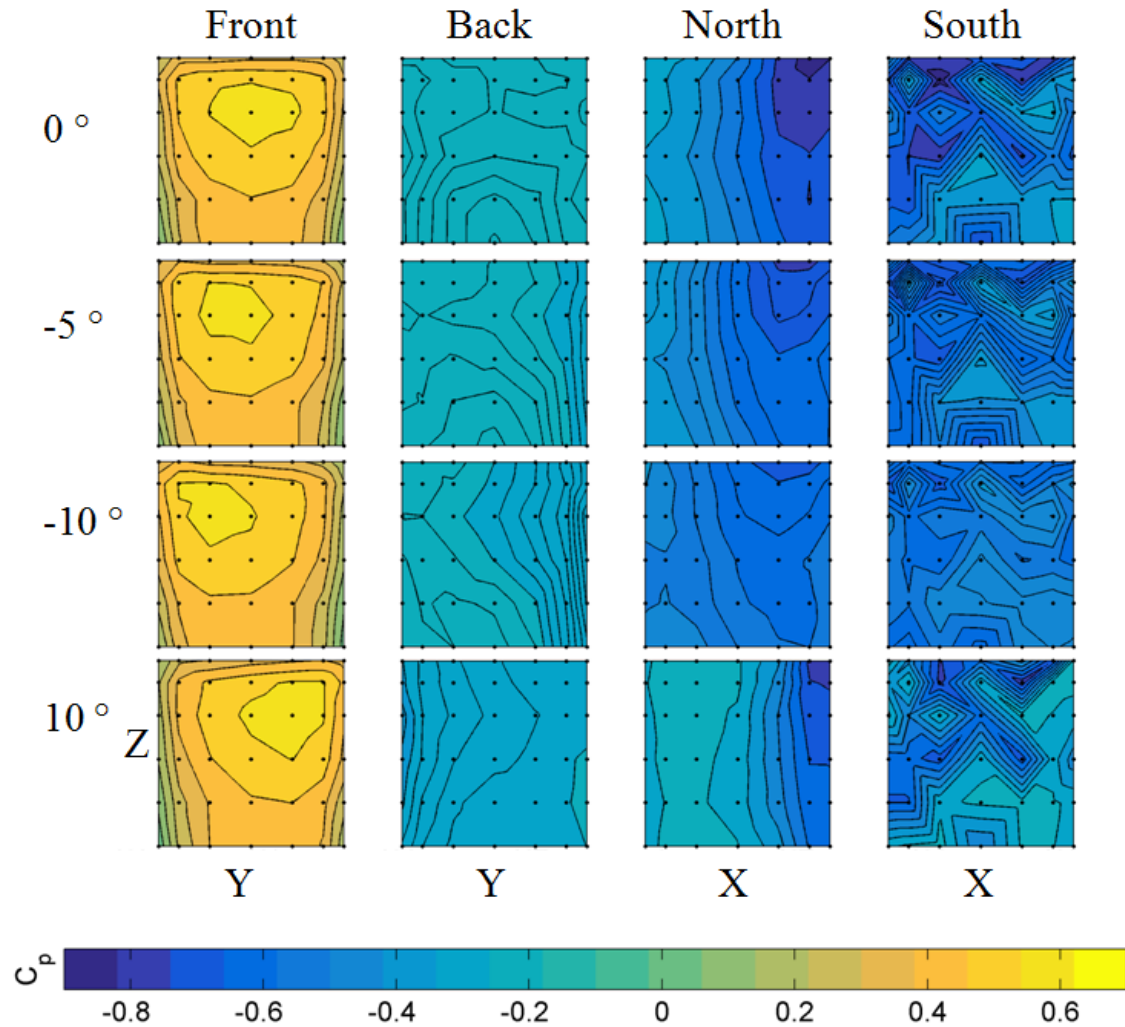


Figure 4.18: Contour plots of C_p for the isolated cube (Table 4.2A) for Figure 4.17. Black dots denote measurement locations, different cube faces (columns) and θ_{ref} (rows).

$\theta_{ref} = -90^\circ$ and $\theta_{ref} = 180^\circ$ cause negative pressure on the front face, with $\theta_{ref} = 0^\circ$ showing positive values of around 0.7 for the front face vertical trace (Figures 4.19, 4.20). It is assumed that $\theta_{ref} = 90^\circ$ C_p values will be similar to $\theta_{ref} = -90^\circ$ values, only effecting opposite faces. $\theta_{ref} = -90^\circ$ shows a peak on the south face as this is where the flow is impacting (for $\theta_{ref} = 90^\circ$ this would be the north face).

The front and back C_p values are reversed for $\theta_{ref} = 180^\circ$ in comparison to $\theta_{ref} = 0^\circ$, with negative values of around -0.1 occurring on the front face and values of 0.8 occurring on the back for the vertical pressure taps. The horizontal trace is also reversed when compared to the $\theta_{ref} = 0^\circ$ C_p (Figure 4.20). The behaviour of all four sides for the $\theta_{ref} = 0^\circ$, -90° and 180° cases are all similar with the location shifting depending on the rotation. This suggests that $\theta_{ref} = 90^\circ$, -90° and 180° C_p values can be predicted with reasonable accuracy from the $\theta_{ref} = 0^\circ$ results.

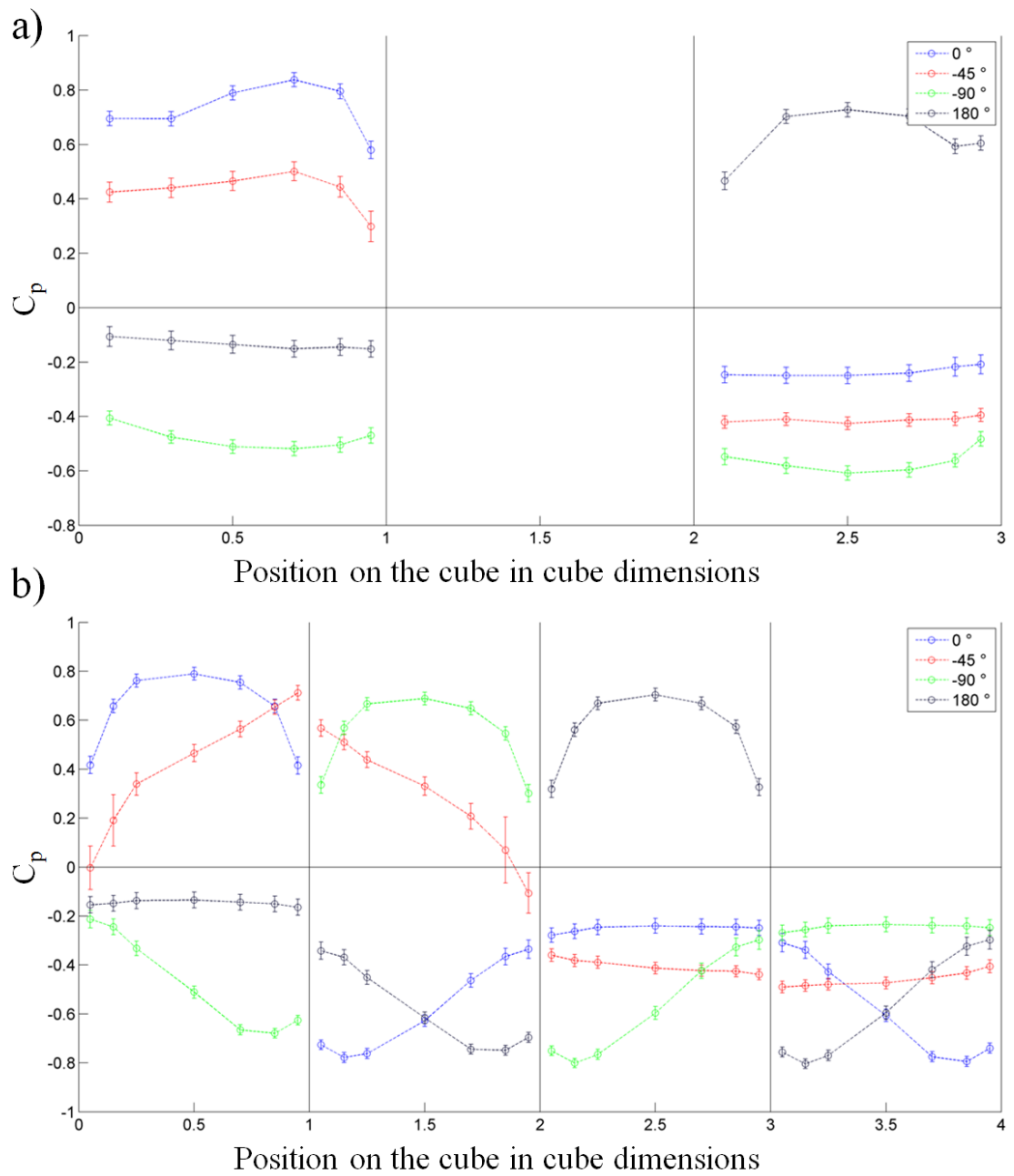


Figure 4.19: C_p for the a) vertical taps and b) horizontal central taps for an isolated cube (Table 4.2A) at $\theta_{ref} = -90^\circ, 45^\circ, 180^\circ$ and 0° .

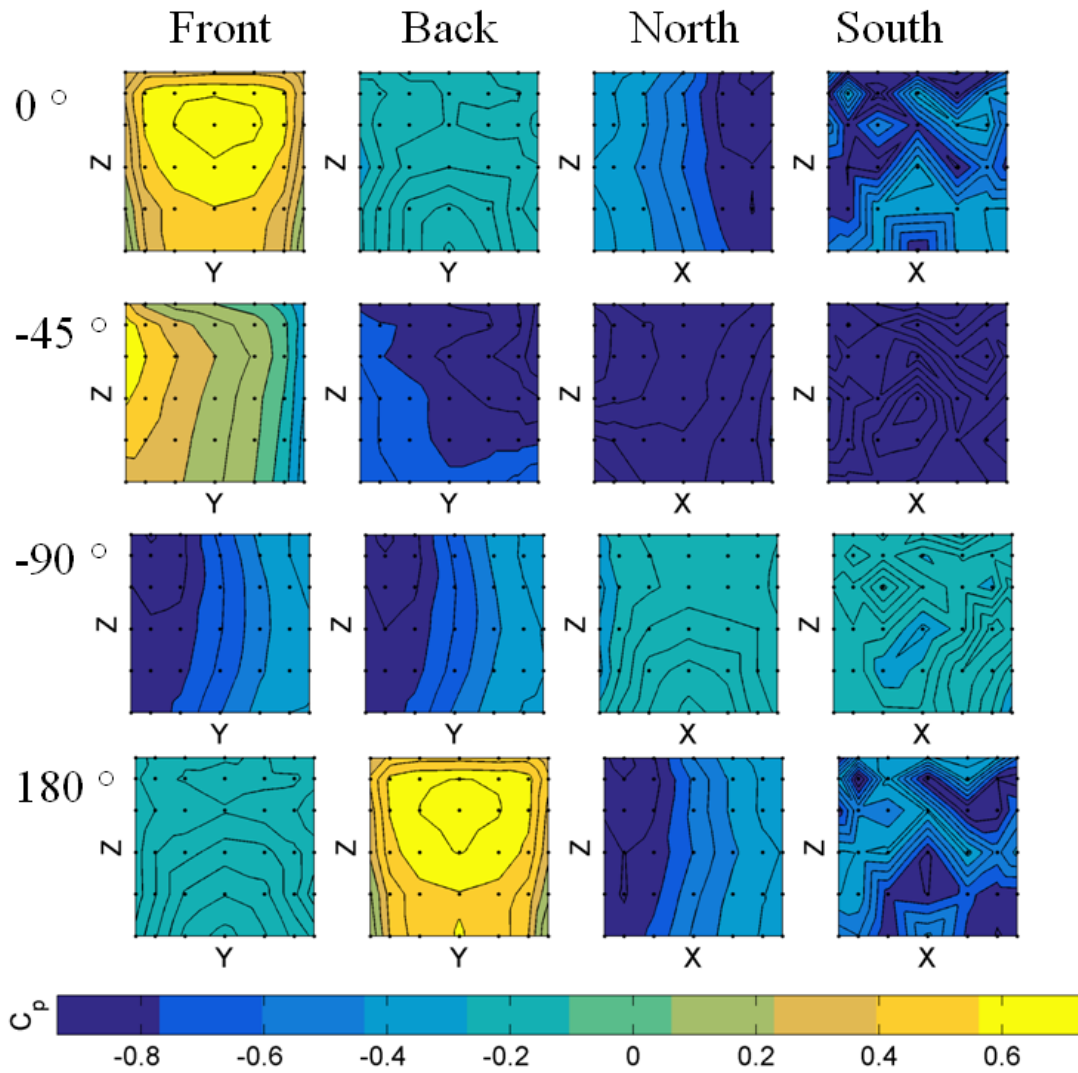


Figure 4.20: C_p contour plots for the isolated cube for Figure 4.19.

A rotation of -45° reduces the C_p for the vertical taps by 0.3, due to the wind impacting on the corner. This can also be seen in the horizontal trace (Figure 4.19) as the C_p measured is larger for taps closer to the corner of impact, with the C_p increasing from 0 to 0.8 horizontally. C_p then decreases along the next side (1 to 2 on the x-axis) as the distance from the impact increases. For the back face, the -45° rotation is more negative than the 0° rotation by 0.1 and 0.2 for the final face. The point of impact can be seen in the second row of contour plots in Figure 4.20, though the lack of symmetry between the front and south faces suggests a slight misalignment of the cube.

The contour plots show that a large change in θ_{ref} causes the patterns expected on each face to shift (Figure 4.20). For example the front face contours seen for $\theta_{ref} = 0^\circ$ can be found on the back face for a $\theta_{ref} = 180^\circ$ case. A 5° shift in θ_{ref} is detectable, with the maximum pressure point shifting to the edge of the front face. This shift in maximum pressure point occurs for $\theta_{ref} = 0^\circ$ to 45° .

4.6.2 Silsoe Array

Unlike the case of a single cube, rotating the model Silsoe array by 10° leads to an asymmetrical response due to the distribution of the array elements. Due to the array being asymmetric, the $\theta_{ref} = \pm 10^\circ$ vertical C_p profiles on the front face differ, caused by the geometrical asymmetry of the array (Figure 4.21).

The $\theta_{ref} = -10^\circ$ front face pressure coefficients are lower in both the horizontal and the vertical profiles compared to $\theta_{ref} = 0^\circ$. It is difficult to discern any trends due to the small C_p values (0.05-0.1) on the front face. More variation is noted for the front face, though all angles are within standard error. The point of impact can also be seen to shift with a change in θ_{ref} of 10° (Figure 4.21), though repeated testing for $\theta_{ref} = 0^\circ$ Silsoe array demonstrates that due to the asymmetry, the point of maximum pressure tends towards the +y direction. This shift is strengthened when $\theta_{ref} = 10^\circ$ with $\theta_{ref} = -10^\circ$ having a weakened effect on the position of the point of maximum pressure due to the natural tendency of the array acting against the main flow effects. The lack of variation on the back face suggests that the array has little effect.

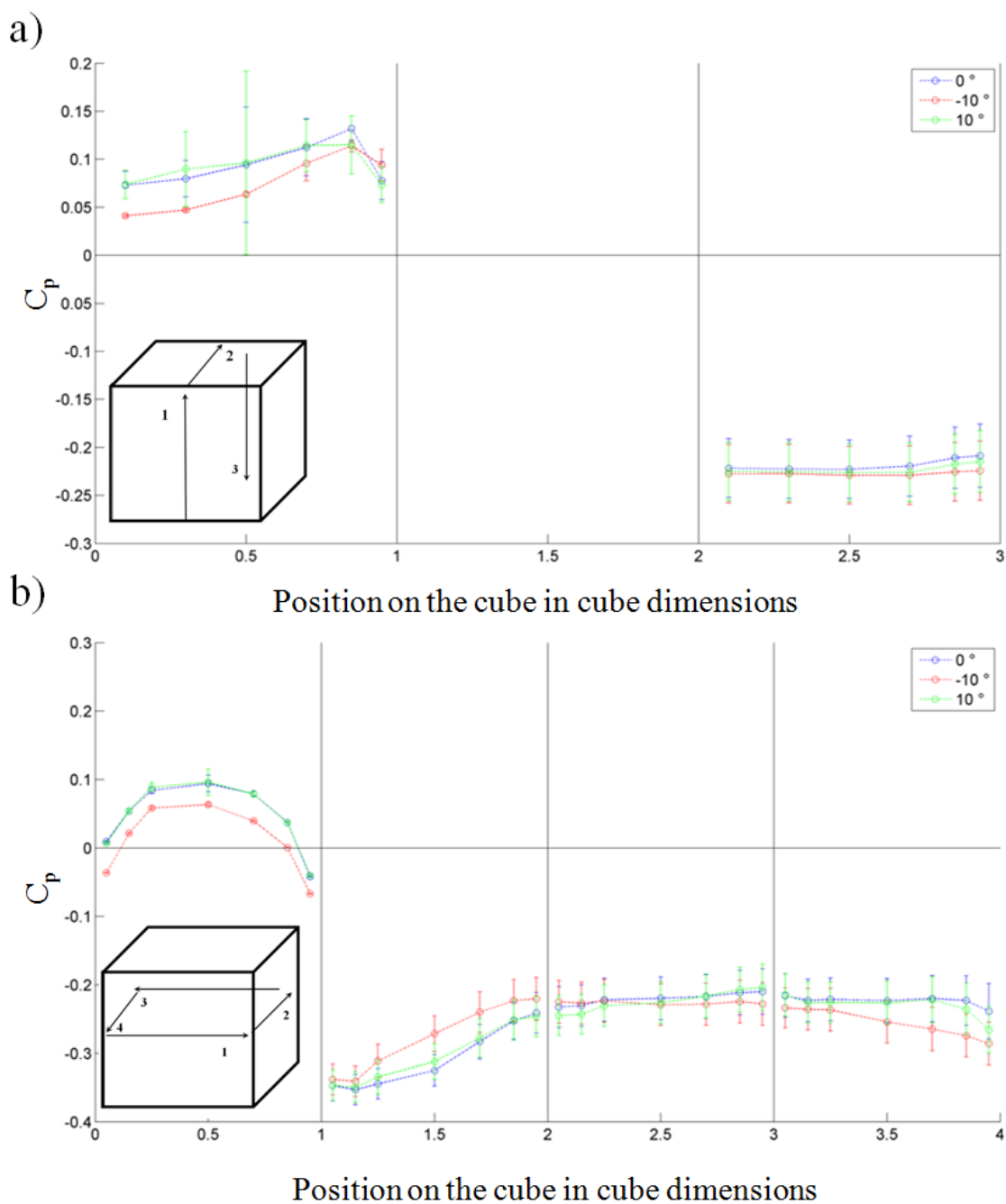


Figure 4.21: C_p for the a) vertical taps and b) horizontal central taps for the Silsoe array (Figure 4.9a) at angles between $\theta_{ref} = -10^\circ$ to 10° .

A region of positive pressure is present at the $+x$ corner of the north face for $\theta_{ref} = 0^\circ, \pm 10^\circ$ (Figure 4.24). This could be due to a slight height misalignment in the closet array elements, but could also be caused by the vortex from the front corner reattaching at this point. The south face contours (Figure 4.24) highlight a point of high pressure in the centre of the face, which could also be due to a corner vortex.

The shift in the C_p pattern for a 10° change in θ_{ref} is less obvious for the $\theta_{ref} = \pm$

$90^\circ \pm 10^\circ$ cases, due to the flow being channelled along the streets of the array (not shown). However, the trend is visible for $\theta_{ref} = 180^\circ \pm 10^\circ$ (Figure 4.22), where the back face behaves similarly to an isolated cube being rotated by $\pm 10^\circ$. Note the symmetrical pressure distribution on the back face in an unobstructed flow.

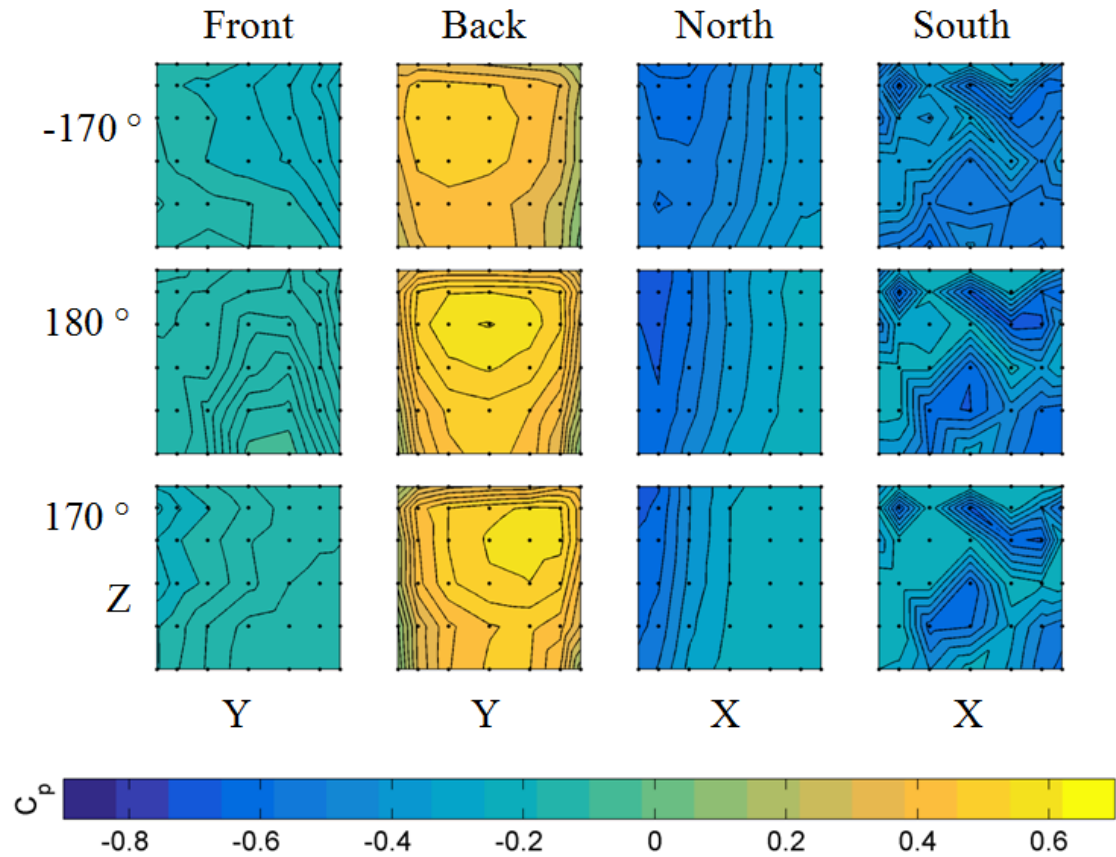


Figure 4.22: C_p contour plots of the instrumented cube in the Silsoe array (Figure 4.9a). Black dots denote measurement locations.

The pressure on the front face horizontal and vertical taps is only positive for $\theta_{ref} = 0^\circ \pm 10^\circ$ cases, after which the face pressure tends to negative values, as shown by the $\theta_{ref} = -45^\circ$ C_p values (Figure 4.24).

A difference of 0.1 C_p is measured between the $\theta_{ref} = -45^\circ$ case and the $\theta_{ref} = 0^\circ$ C_p values. The point of maximum pressure for the -45° case is shifted to the bottom +y corner, due to the oncoming flow being aligned with the diagonal channels within the array. This may reduce the amount of displacement the oncoming flow experiences. For $\theta_{ref} = 45^\circ$ the oncoming flow is channelled through the array, being strengthened by the wake of the first row and the side vortices of the second row (Claus *et al.*, 2011).

The $\theta_{ref} = 180^\circ$ case back face shows equivalent C_p values, as it faces unobstructed flow: the array appears not to have any effect here. A significant effect would be one which reduces the C_p values by 25 % or more. This may not be the case if the adja-

cent surrounding elements have varying heights. The front face of the $\theta_{ref} = 180^\circ$ case matches that of the $\theta_{ref} = 0^\circ$ back face, which strengthens the conclusion that only objects upwind of the pressure tapped cube have a large effect on the pressure field, though this may hold only for arrays where building height is uniform (Figure 4.24). For the 180° case, the potential re-impact of the corner vortices on the north face is not visible, suggesting that the array disrupts the circulations, which leads to them not always impacting on the sides of the cube.

Comparing $\theta_{ref} = 180^\circ$ for the isolated cube (Table 4.2A) to $\theta_{ref} = 180^\circ$ for the Silsoe array (Figure 4.9a) leads to the conclusion that the north and south sides are also largely unaffected by the array, possibly due to the spacing between buildings being equivalent to one cube height, meaning that the effects of neighbouring buildings do not reach the instrumented cube.

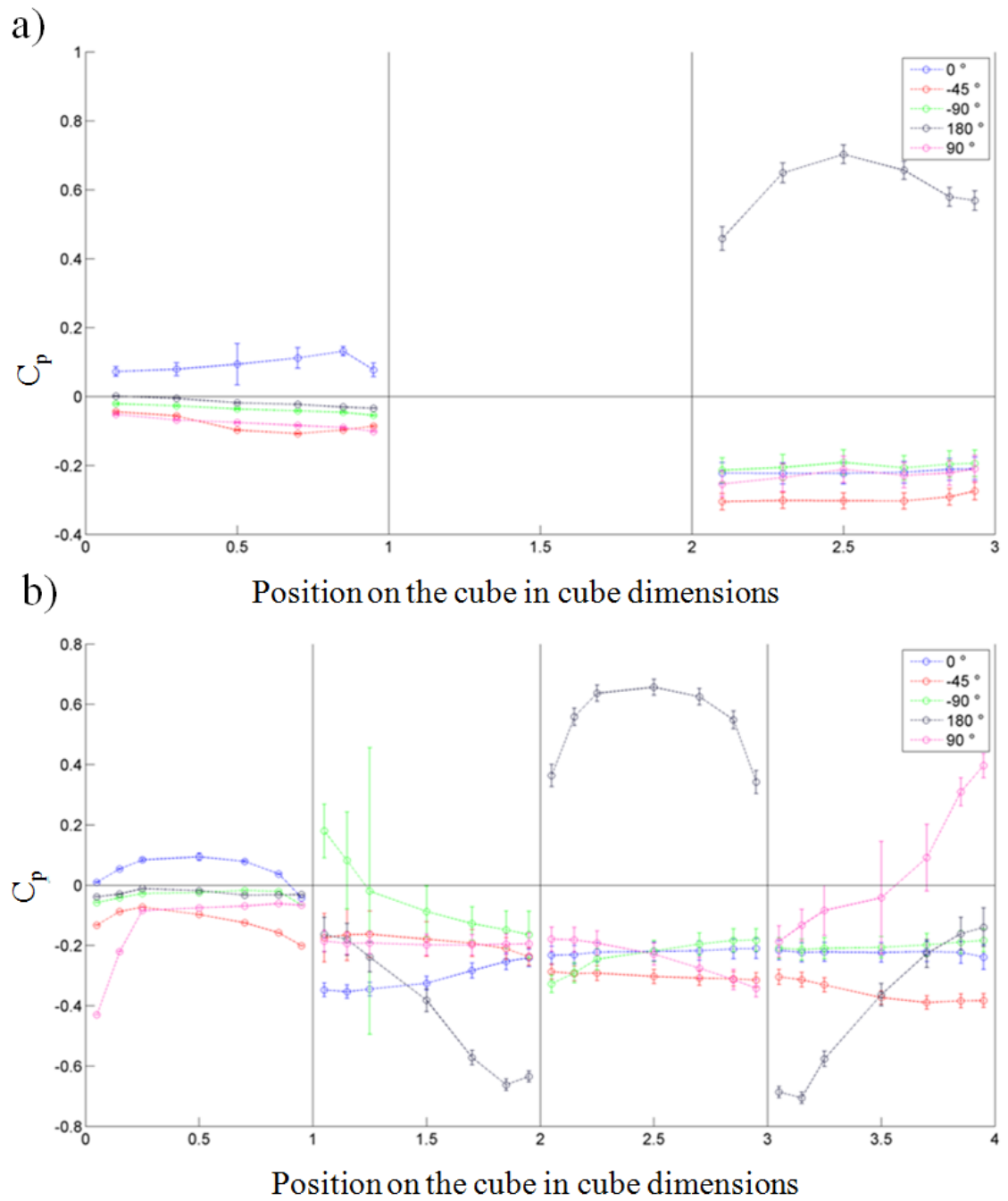


Figure 4.23: C_p for the a) vertical taps and b) horizontal central taps for the Silsoe array (Figure 4.9a) for $\theta_{ref} = -90^\circ, 90^\circ, -45^\circ, 180^\circ$ and 0° .

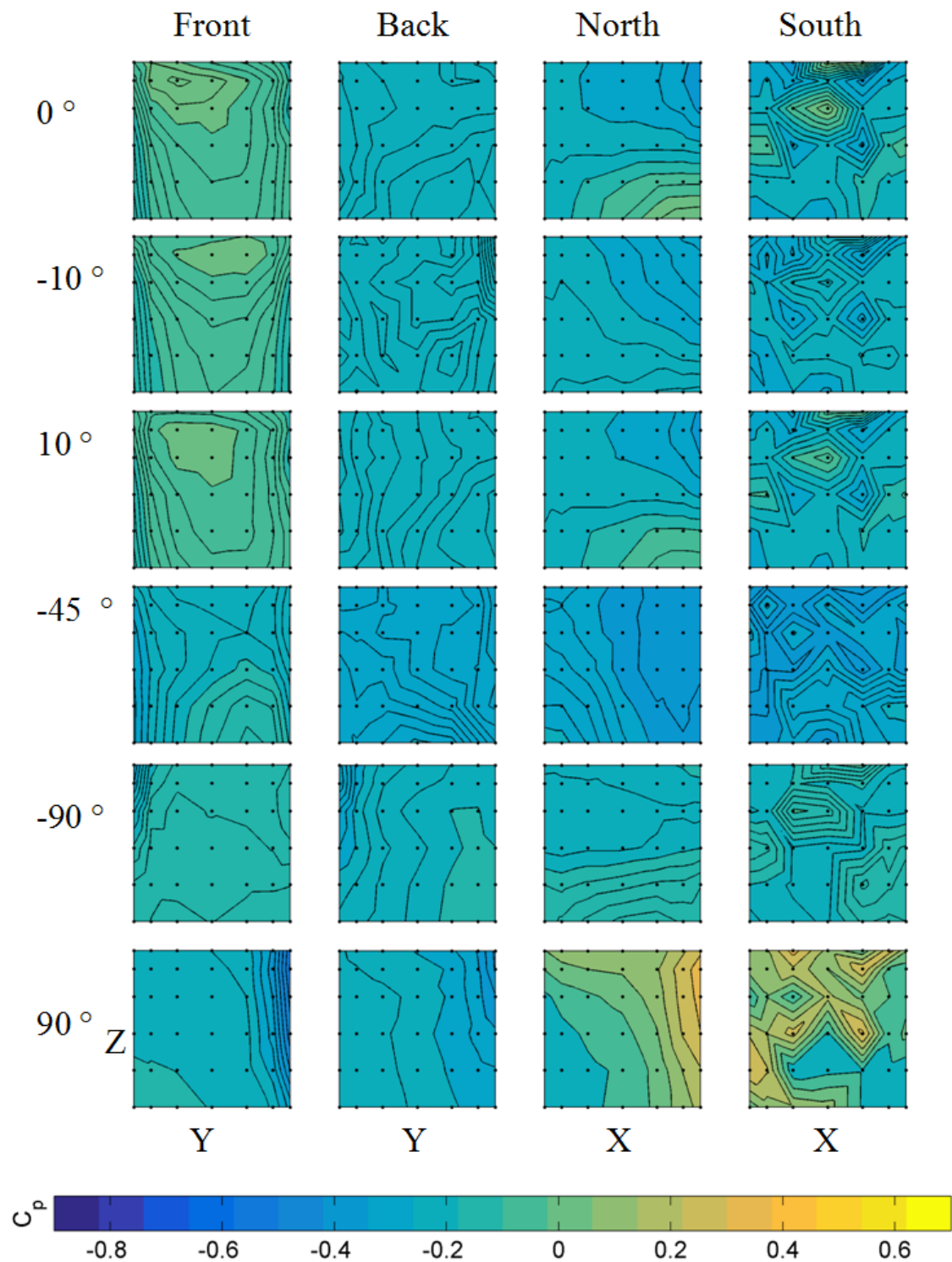


Figure 4.24: C_p contour plots for Figure 4.21 and Figure 4.23.

For the $\theta_{ref} = \pm 90^\circ$ (Figure 4.24) cases differences occur due to the asymmetry of the Silsoe array and due to the external flow being parallel to the streets. The -90° rotation means that the central row has an extra cube facing into the oncoming flow

in comparison to the 90° rotation (Figure 4.25), where there is one less cube upwind, leading to positive pressures on the north and south faces. The front and back faces remain similar due to the array acting as an aligned array and flow being channelled down the spacing between the rows. The north and south faces display similar trends to those seen on the front and back faces in an aligned flow, due to the wake of the cube in front effecting the local flow.

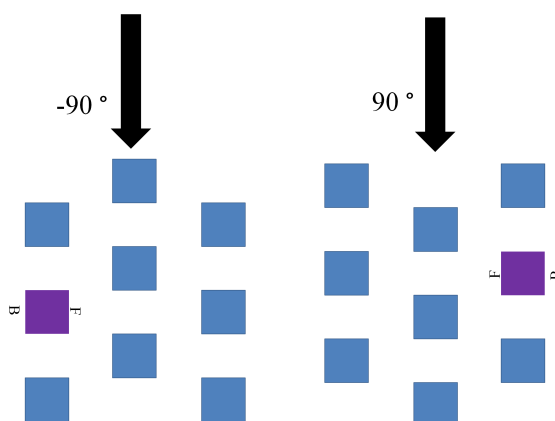


Figure 4.25: Schematic of $\theta_{ref} = -90^\circ$ and 90° for the Silsoe array.

For a staggered array the two rows upwind of the instrumented cube influence the local flow, with the wake of the first row interacting with the side vortices of the second row for $\theta_{ref} = 0^\circ$ (Claus *et al.*, 2011). Claus *et al.* (2011) state that this occurs for $\theta_{ref} = 27^\circ$, though the wake of the first row is no longer symmetrical and the interaction with the side vortices is biased towards one side, which will change depending on the wind direction. The structure of the local flow is also height dependent (Claus *et al.*, 2011).

Surrounding the pressure tapped cube with an asymmetrical array makes predicting the effect of θ_{ref} on the C_p more complicated due to the interacting wakes of all the array elements and the varying levels of shielding provided as the wind direction changes. Additionally the reduced pressure coefficients ($C_p < 0.1$) and associated uncertainties in the presence of the surrounding array elements make it difficult to discern the changes in C_p due to wind direction. A rotation of 180° means that the pressure tapped cube is exposed to an unobstructed oncoming flow and the C_p recorded for the back (i.e. flow-facing) face are similar to those seen on the front face of isolated cube, suggesting that the elements either side of the pressure tapped cube do not have an effect on the C_p of the back face. This changes as the flow is shifted $\pm 10^\circ$ from $\theta_{ref} = 180^\circ$ as the elements on the edge of the array begin to shield the pressure tapped cube.

$\theta_{ref} = \pm 90^\circ$ cases lead to the staggered Silsoe array (Figure 4.9a) acting as an aligned array, due to the orientation of the array with respect to θ_{ref} . The results of the wind tunnel work suggest that there are no angles for which the flow fully penetrates into the array meaning that there is always some degree of shielding ($\theta_{ref} = 170^\circ$ to 190° to -170° to -190°).

°) aside from the parallel cases ($\theta_{ref} = 90^\circ$ and -90°). This suggests that the C_p of the Silsoe array (Figure 4.9a) can be expected to always be lower than that of an isolated cube (Table 4.2A), which for ventilation means that a lower ventilation rate within the array should be expected.

4.7 Effect of the array on the measured pressure coefficient

The peak C_p on the front face of the isolated cube (Table 4.2A) is at $z = 14$ mm at around $C_p = 0.7 \pm 0.0004$, with large variation ($C_p = 0.1$ to 0.6) occurring around the edges of the front cube face (Figure 4.27). The variation near the edges of the face is still present in the Silsoe array case (Figure 4.9a) but is reduced in magnitude (0.1 to 0.2) due to the shielding by the array in front of the instrumented cube. Within the array, the C_p values are reduced by $60\text{-}90\% \pm 5\%$ (dependent on the tap of interest) for the front face, with the peak in C_p (magnitude 0.15 ± 0.002) shifting into the upper -y corner (Figure 4.28).

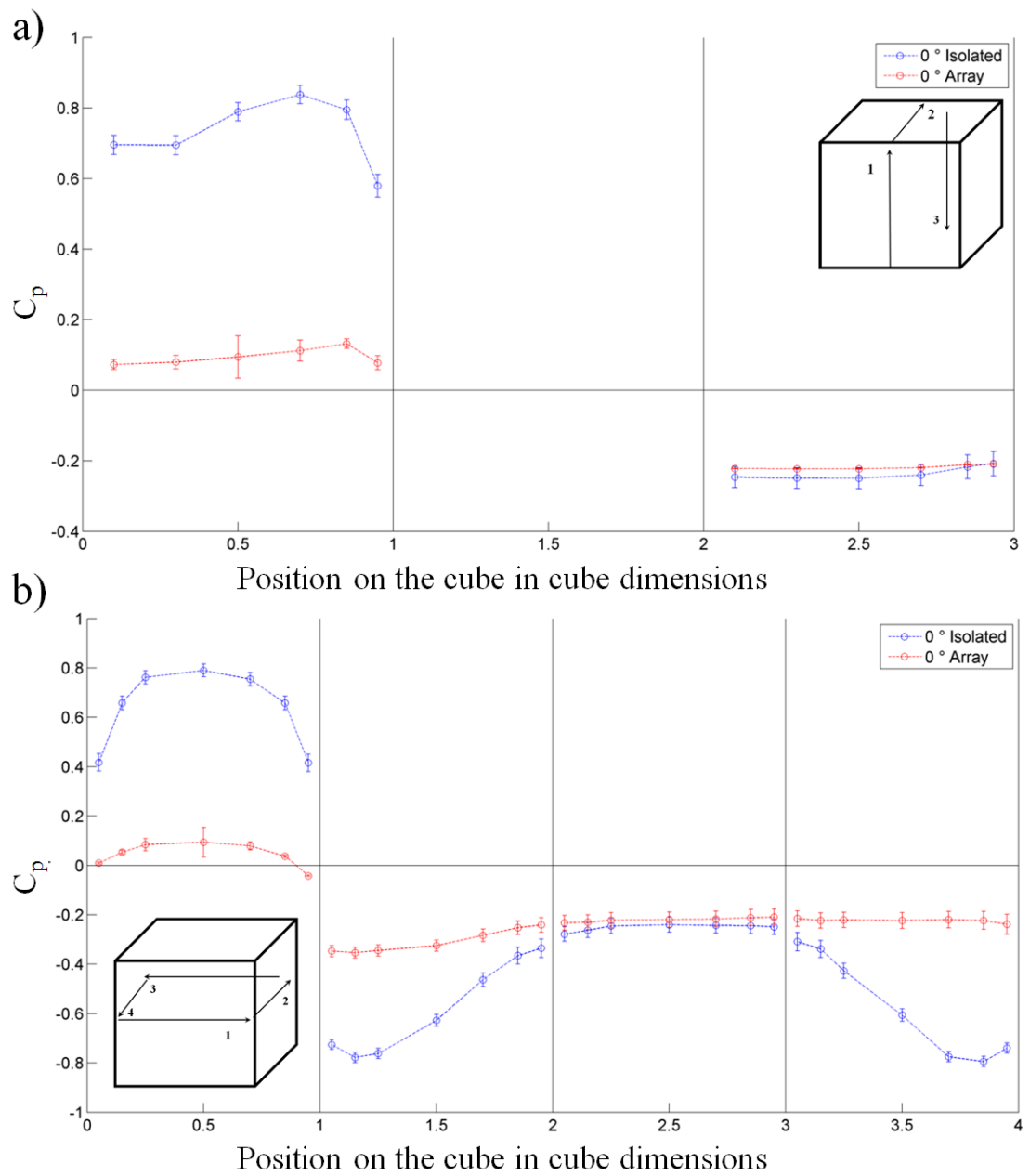


Figure 4.26: C_p of the a) vertical and b) horizontal traces around the instrumented cube for a $\theta_{ref} = 0^\circ$ for the Silsoe array (Figure 4.9a) and for an isolated cube (Table 4.2A).

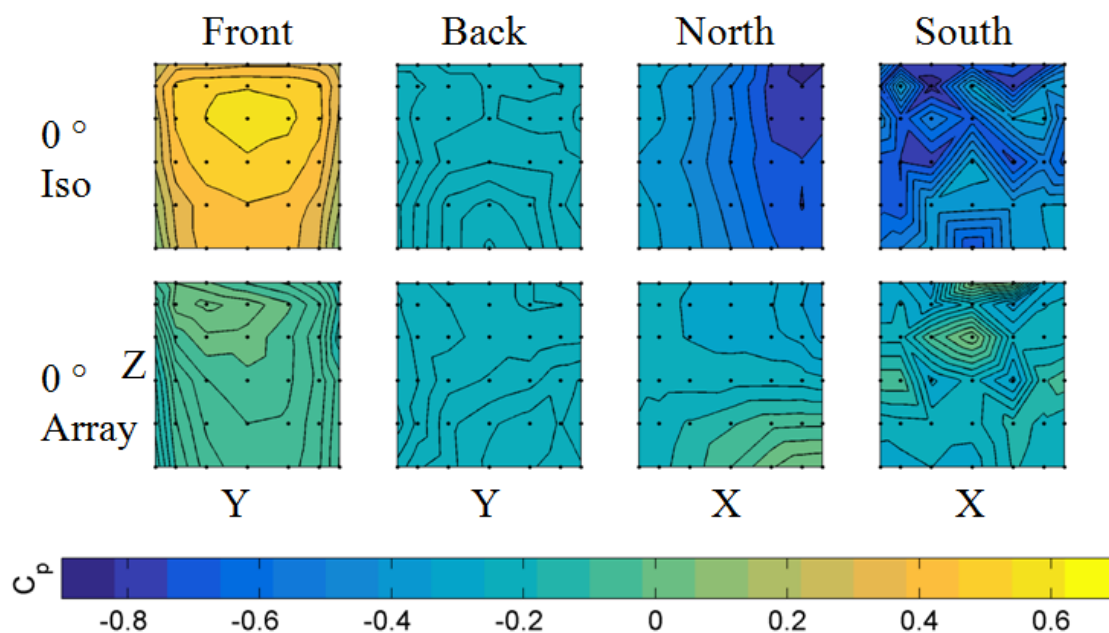


Figure 4.27: C_p contour plots of the isolated cube (Table 4.2A) and the Silsoe array (Figure 4.9a). Black dots denote measurement locations.

For the back face it is difficult to determine any notable differences, due to the magnitude of C_p being so similar (0.5 - 0.6). This probably reflects the unobstructed rear face of the cube in the Silsoe array. The effect of the array can clearly be seen to be non-linear over the whole cube due to the complex flow patterns caused by the array (Figure 4.28).

The north and south sides show some variation, potentially related to the array asymmetry. The south face suggests that there is a 40 % to 60 % decrease in C_p due to the presence of the array due to the shielded by the unaligned row in the centre of the array.

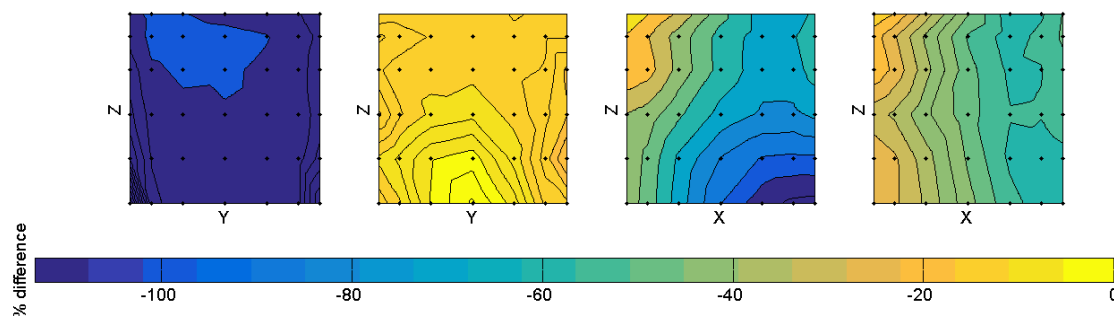


Figure 4.28: Percentage difference contour plot for the difference in C_p values measured for an isolated cube (Table 4.2A) and for a cube within the Silsoe array (Table 4.2B, Figure 4.9) for $\theta_{ref} = 0^\circ$. Black dots denote measurement locations.

Taking an average of all 42 taps on the front face allows for the face averaged difference to be determined, which depends on θ_{ref} (Figure 4.29). The largest differences occur

for $\theta_{ref} = 0^\circ$, where the sheltering of the array has the greatest effect.

For the street-aligned wind directions ($\theta_{ref} = \pm 90^\circ$), the array causes a difference in C_p of 0.4 to 0.6 ± 0.004 with the difference decreasing to 0.05 to 0.1 ± 0.004 for $\theta_{ref} = 180^\circ$. As the array is asymmetrical the effect of the array elements is non-uniform.

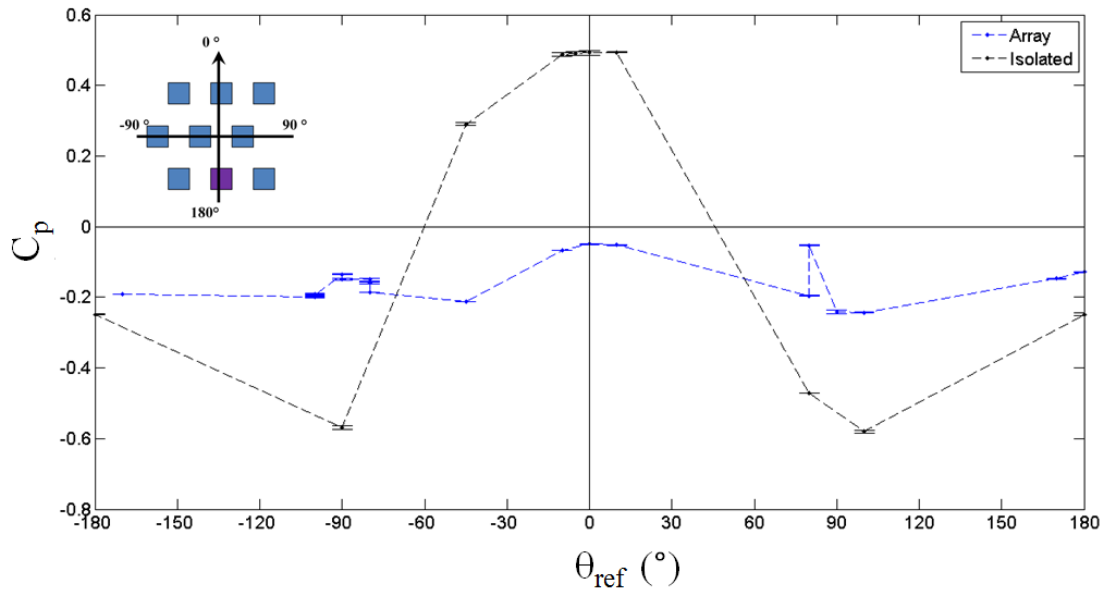


Figure 4.29: Front face averaged C_p values for the Silsoe array (Figure 4.9a) and the isolated cube (Table 4.2A) against θ_{ref} . Error bars are standard error. Points are joined for visual clarity.

Understanding the reduction in C_p caused by the array over a range of θ_{ref} is difficult as using a face average does not capture the change in pressure pattern across the face. Using individual taps fails to capture all the detail, as the effects captured are dependent on the tap location. In order to convey the effect of changing wind direction on C_p values, both face averaged C_p and contour plots should be considered, along with a description of the geometry of the surrounding array.

4.8 Effect of the storage shed on pressure distribution

Potential effects of the storage shed on the Silsoe full-scale site could not be ignored. For $\theta_{ref} = -90^\circ \pm 10^\circ$ the storage shed is positioned downwind of the isolated cube (Table 4.2G), implying that the shed is upstream for $\theta_{ref} = 80^\circ$ to 100° . The contour plots for $\theta_{ref} = 90^\circ$ (Figure 4.30) highlight the sheltering effect, especially on the north face, reducing C_p from 0.7 ± 0.004 to 0.3 ± 0.002 in the centre of the cube. The point of maximum C_p is also reduced by 0.2 from 0.7 to 0.5 and is moved upwards in the +x direction. For the full-scale experiment, this suggests that any winds coming from behind the storage shed will lead to a reduced C_p on the north side of the cube when compared to a fully isolated

cube.

When the storage shed is downstream of the isolated cube the effect is negligible with the north face C_p for the north face ($\theta_{ref} = 0^\circ$) being within error-bars of the isolated cube.

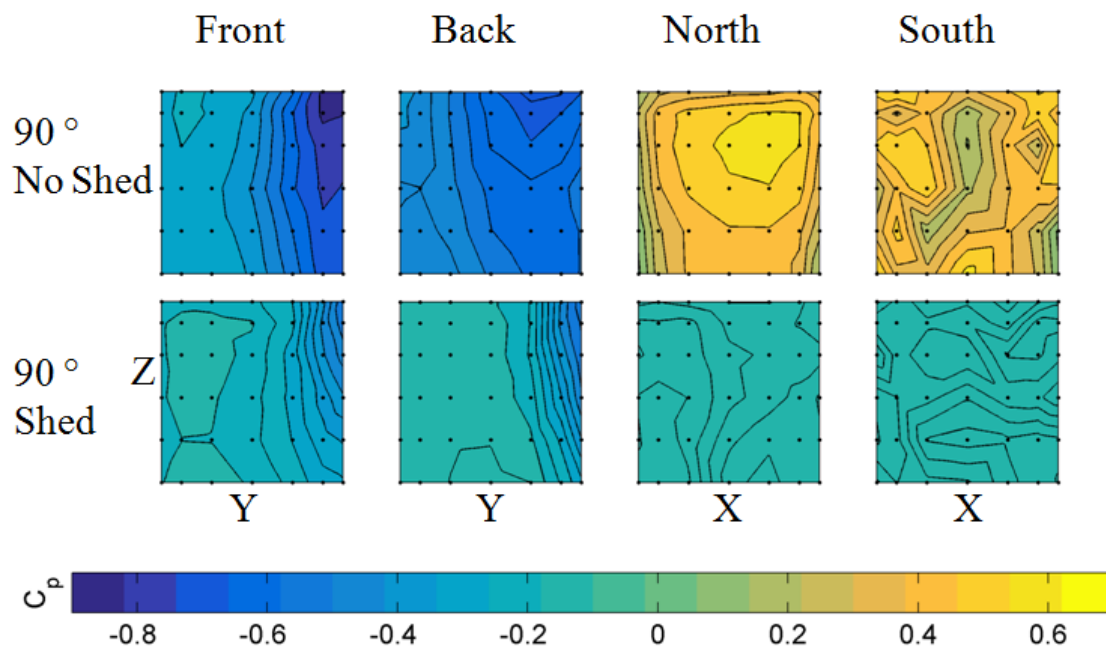


Figure 4.30: C_p Contour plots for the isolated cube (Table 4.2A) for $\theta_{ref} = 90^\circ$ with and without the storage shed present.

For the Silsoe array (Figure 4.9a), the effect of the storage shed is similar to that of the isolated cube, with the pressures on the north and south faces being reduced due to the storage shed (Figure 4.31). There is little change in the pressure distribution for the front and back faces due to the flow remaining parallel, which suggests that the wake of the storage shed does not affect the front and back faces. One possible effect of the storage shed is to cause the flow to lift and begin skimming over the array. The C_p values on the north face are reduced from 0.4 to -0.1 ± 0.1 , with a similar reduction occurring on the south face. Whilst the array elements either side of the pressure tapped cube act to reduce the C_p by an average of 0.2 ± 0.03 when compared to an isolated case, the introduction of the storage shed causes the C_p to become negative. This is likely to be due to the wake caused by the storage shed and the instrumented cube is now within a recirculation region, due to the estimated wake of the storage shed being several cube heights in length.

Like the isolated cube, there is little change when the storage shed is positioned downwind of the array or when there is a perpendicular wind.

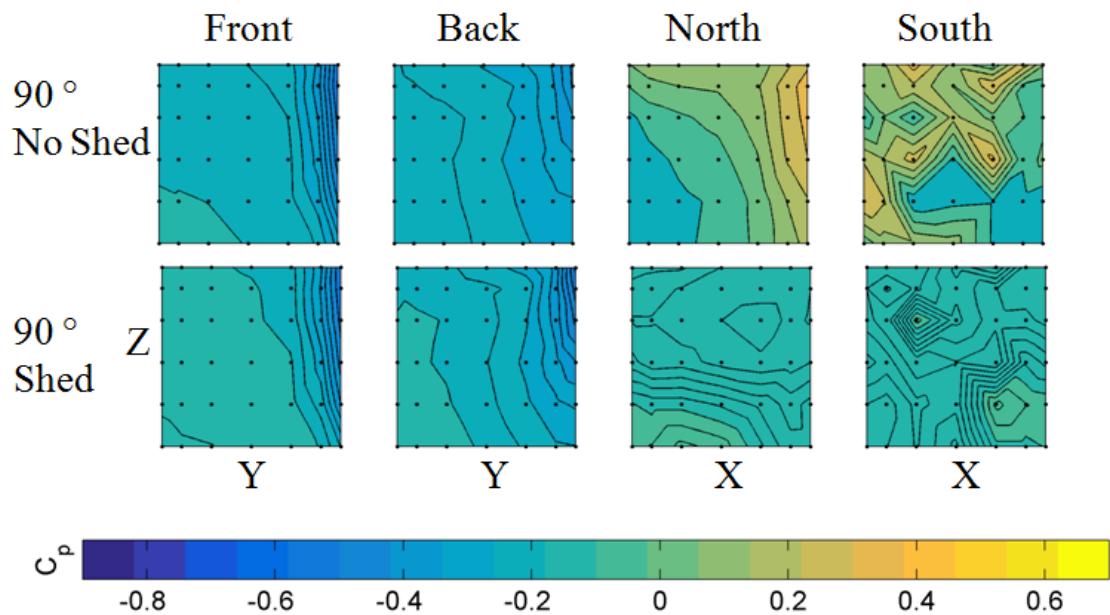


Figure 4.31: Contour plots of $\theta_{ref} = 90^\circ$ for the Silsoe array with and without the storage shed. Black dots denote measurement locations.

These findings suggest that for $\theta_{ref} = 90^\circ$ there may be little effect on the full-scale measured ventilation rates for both the isolated and array cases, due to the flow remaining aligned to the array and the front and back faces being less effected by the storage shed. The differences will only be most noticeable on the north and south faces, due to the storage sheds wake reducing the local flow velocity and creating a complex area where the wake of the storage shed interacts with the wakes of the cubes. The wind tunnel research was concentrated on $\theta_{ref} = 90 \pm 10^\circ$ directions due to concerns about the effects of the storage shed on the full-scale data. It is assumed that for all other wind angles the storage shed has little, if any measurable effect on the C_p for the array and isolated cases.

4.9 Differences between staggered and aligned nine-block arrays

To understand how the misalignment of the central row may effect the pressure field of the instrumented cube when flow is parallel to the array streets, the Silsoe array for $\theta_{ref} = \pm 90^\circ$ are compared to a true aligned array at $\theta_{ref} = 0^\circ$ and $\theta_{ref} = 90^\circ$ (Figure 4.32, Table 4.2H).

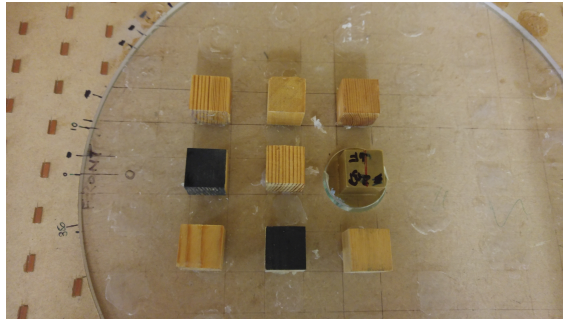


Figure 4.32: Photo of the aligned array. All array elements are 20 mm x 20 mm x 20 mm and are made of wood.

Differences in C_p (0.05 ± 0.004) are measured between the aligned (Figure 4.32) and Silsoe arrays (Figure 4.9a) for $\theta_{ref} = 90^\circ$ (Figure 4.33). Both the aligned and staggered cases show a 'quite similar' range of C_p values, probably due to θ_p being so high (25 %) that the oncoming flow cannot penetrate into the urban canopy layer regardless of θ_{ref} (Cheng *et al.*, 2007). Unlike a true aligned array (Figure 4.32) the central row in the Silsoe array is misaligned with the other two rows due to the staggered Silsoe array layout. This could be the cause of some of the difference, though the range of 0.05 is small and is not likely to be large enough to be of significance to designers.

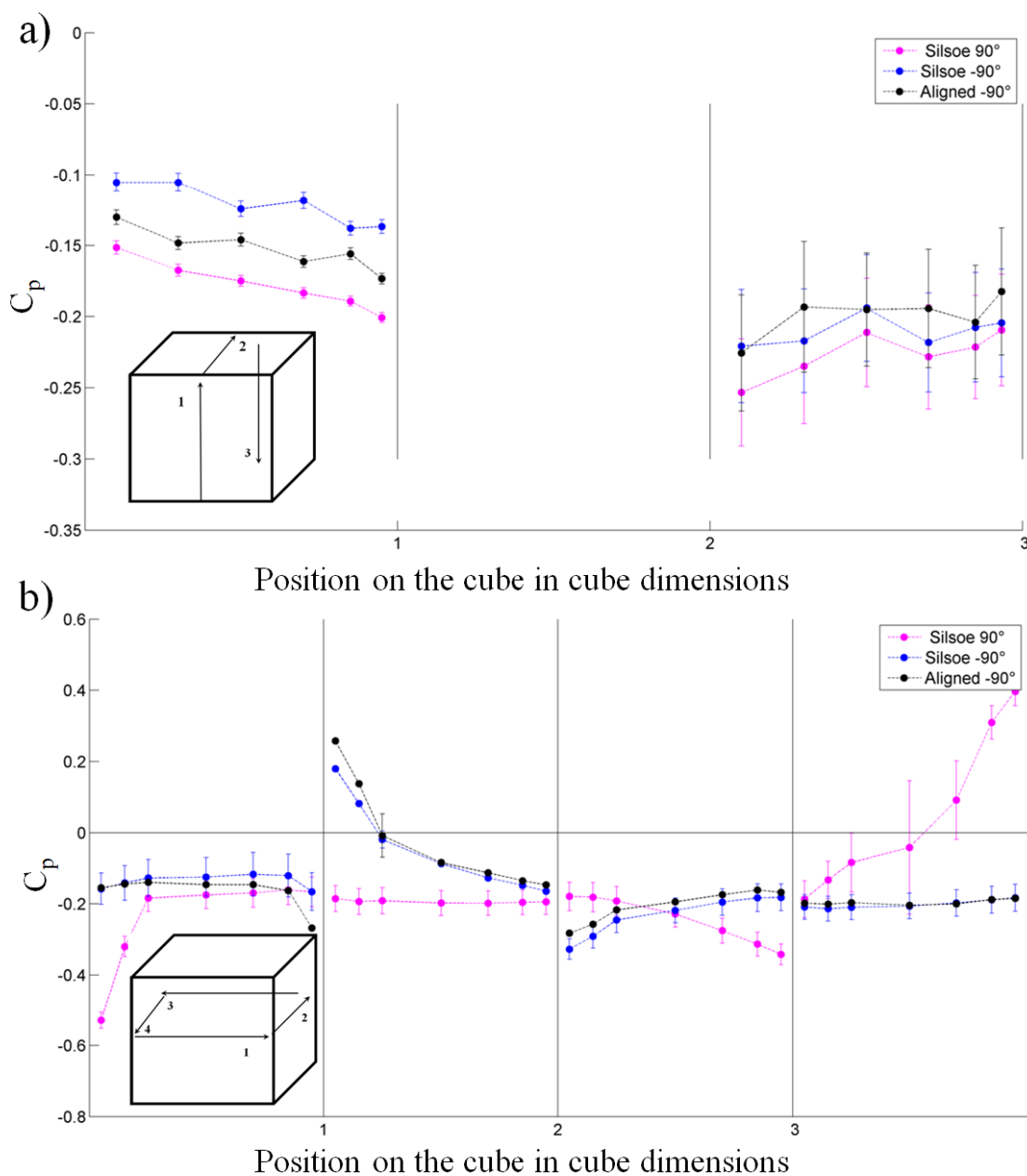


Figure 4.33: C_p comparison for the Silsoe array (Figure 4.9a) $\theta_{ref} = \pm 90^\circ$ to the aligned array $\theta_{ref} = 90^\circ$ for the a) vertical trace and b) horizontal trace.

For $\theta_{ref} = 0^\circ$, differences occur on the front face (Figure 4.34) because the test cube is shielded to a much greater degree in the aligned array. There are some differences on the north and south faces of the cube most likely due to the asymmetry of the Silsoe array. The high pressure at the bottom of the north face may be related to a recirculation region impacting on that corner due to a slight misalignment or could be due to the flow being deflected into the array. For larger aligned and staggered arrays ($\lambda_p = 25\%$) Hussain and Lee (1980) recorded front face C_p values as being near zero.

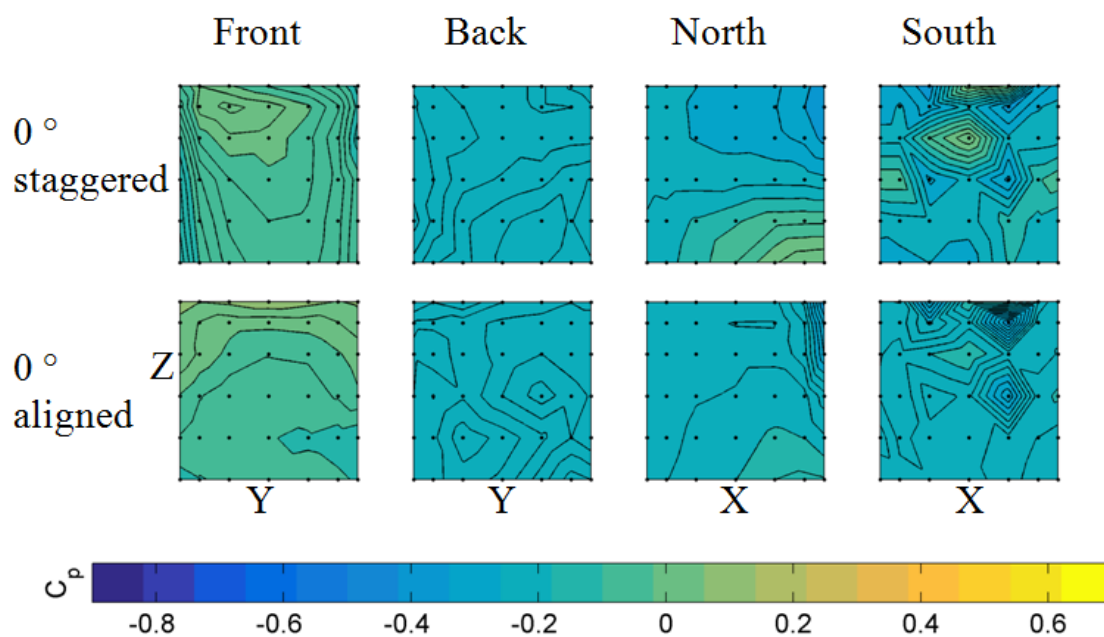


Figure 4.34: Contour plots for $\theta_{ref} = 0^\circ$ for the Silsoe array (staggered, Figure 4.9a) and the aligned array (Figure 4.32).

Large differences in the pressure distribution on the faces also occur for $\theta_{ref} = -45^\circ$ (Figure 4.35). The aligned array (Figure 4.32) has a positive C_p over a large fraction of the front face (-y) unlike the Silsoe array where the entire front face pressure is slightly negative. This positive pressure point is due to the aligned array not completely shielding the pressure tapped cube from the oncoming flow. Either the oncoming flow penetrates into the array, or it impacts the corner of the cube in front, causing eddies which impact on the pressure tapped cube. The misaligned central row in the staggered Silsoe array completely shields the pressure tapped cube from any oncoming flow, with a high pressure point of 0.05 to 0.1 forming on the bottom +y corner, likely a result of vortex shedding from the cubes in front or a cube misalignment.

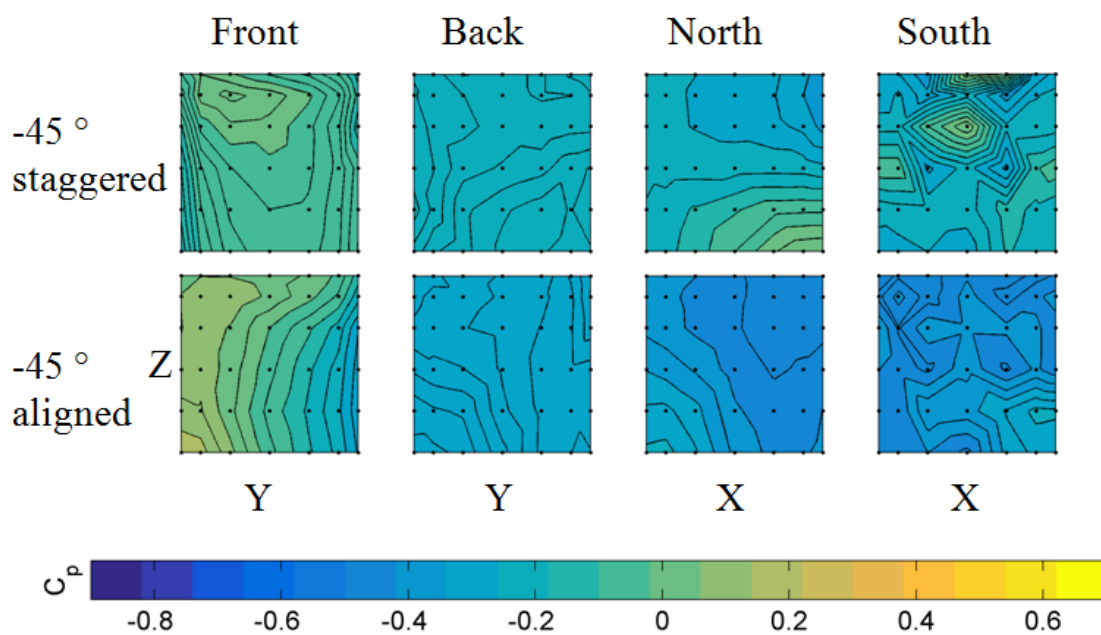


Figure 4.35: C_p contour plots of the pressure tapped cube within the Silsoe array (staggered, Figure 4.9a) and an aligned array (Figure 4.32) for $\theta_{ref} = -45^\circ$. Black dots denote measurement locations.

For $\theta_{ref} = 10^\circ$ the maximum pressures near the top of the front face on the aligned array move to the -y corner, similar to that seen in the staggered array (Section 4.10), though there is little difference measured on the other faces.

This shielding difference between aligned and staggered arrays has ramifications for the positioning of openings on buildings. Depending on the surroundings, the position of maximum pressure differences and thus likely positions of maximum air exchange will shift. Buildings in an aligned array can expect to experience more shielding for a perpendicular wind, due to other buildings completely blocking flow. For $\theta_{ref} = 45^\circ$ wind, the staggered layout has a more reduced flow, and thus a lower ventilation rate.

Regardless of array layout, if a building is fully exposed on one side, this will be the side which has the potential to achieve the largest ventilation rate. Staggered arrays provide more shielding for all angles other than $\theta_{ref} = 0^\circ$, though it is hypothesised that once the array expanse reaches a threshold for certain wind directions, there will be little, if any difference between the two layouts, due to the flow beginning to skim over the array elements (Cheng *et al.*, 2007). However, the staggered Silsoe array still offers more exposure for some θ_{ref} , where there is no building directly upwind.

4.10 Effect of increasing array size on C_p

Local flow conditions depend on the details of the roughness elements, being specific to each case (Yang *et al.*, 2016). The interactions between roughness elements are also likely to vary depending on the array size, shape and layout.

4.10.1 Effect of extra rows behind the Silsoe array on the pressure coefficient

Differences between the pressure coefficients measured in the extended Silsoe array (Figure 4.9b) and Silsoe array (Figure 4.9a) for $\theta_{ref} = 0^\circ$ are small (a range of 0.05 to 0.1 ± 0.005) and occur on all faces (Figure 4.36). The overall distributions are very similar, suggesting that the extra rows have little effect when positioned downwind of the instrumented cube.

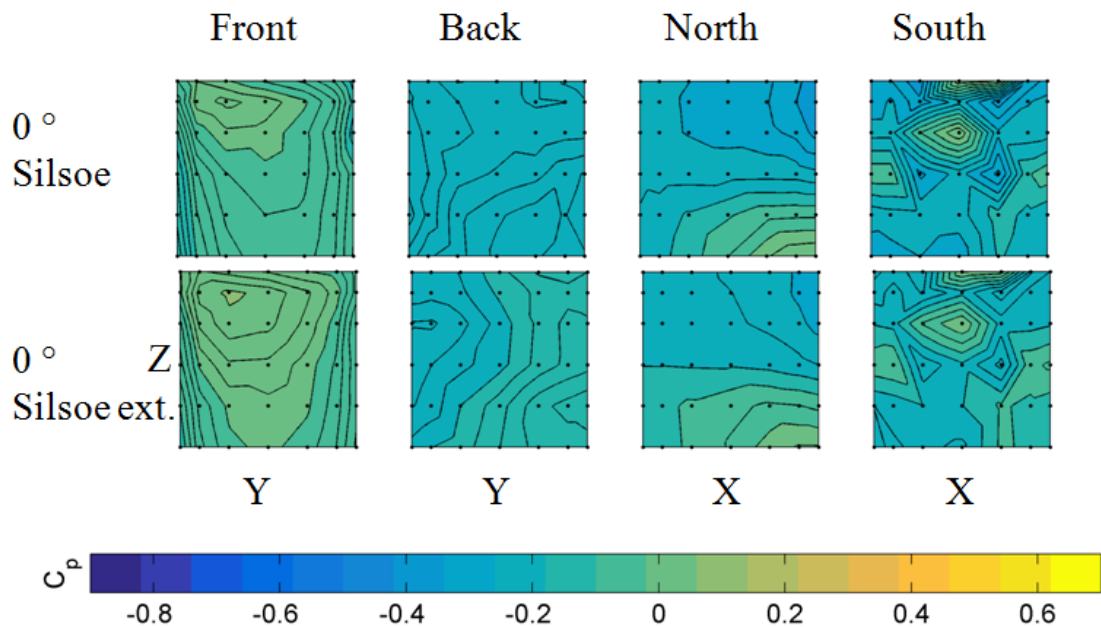


Figure 4.36: C_p contour plots of the Silsoe array (top row) and the extended Silsoe array (bottom row) for $\theta_{ref} = 0^\circ$. Black dots denote measurement locations.

However, a comparison between the two $\theta_{ref} = 180^\circ$ cases (Figure 4.37), when the extra rows are upstream of the instrumented cube, reveals major differences. The distribution on the back face behaves in a similar way to the $\theta_{ref} = 0^\circ$ front face (Figure 4.38). Differences are small for $\theta_{ref} = -70^\circ$ to 70° due to the two arrays being identical to the approaching flow. At $\theta_{ref} = 90^\circ \pm 10^\circ$ and $\theta_{ref} = -90^\circ \pm 10^\circ$ differences of 0.05 occur. This is due to the back face no longer being as exposed in the extended Silsoe array. At $\theta_{ref} = 180^\circ$ the difference is around 0.1 ± 0.005 due to the extra shielding provided by the added rows. The extended Silsoe array (Figure 4.9b), like the Silsoe array (Figure 4.9a), does not have a symmetrical distribution, due to the limited length of the cube rows (3

in each row).

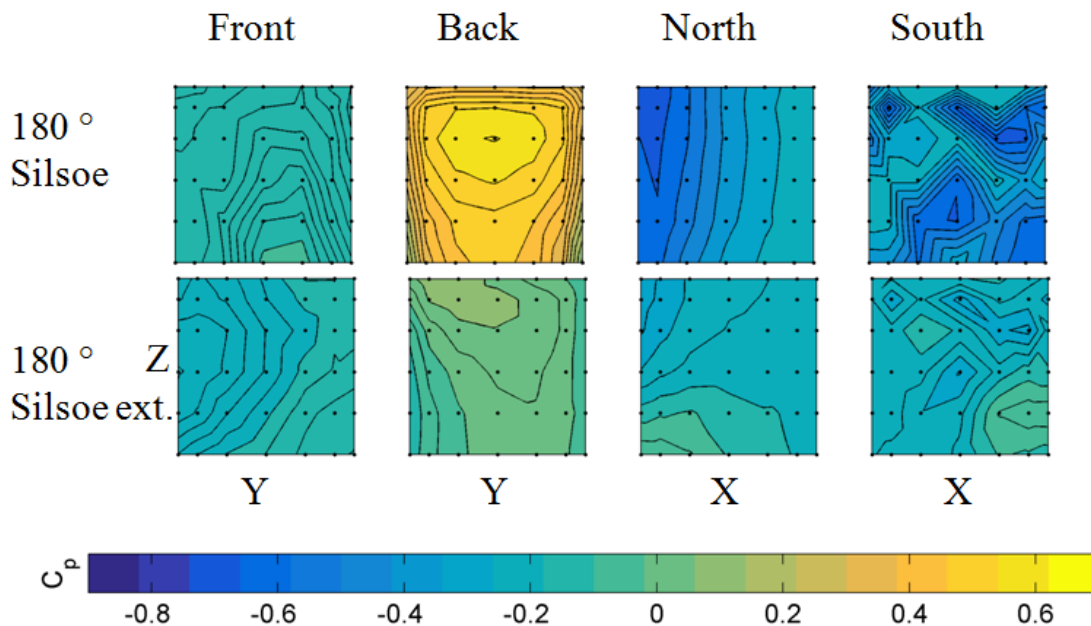


Figure 4.37: Contour plots of the Silsoe array (top row) and the extended Silsoe array (bottom row) for $\theta_{ref} = 180^\circ$. Black dots denote measurement locations.

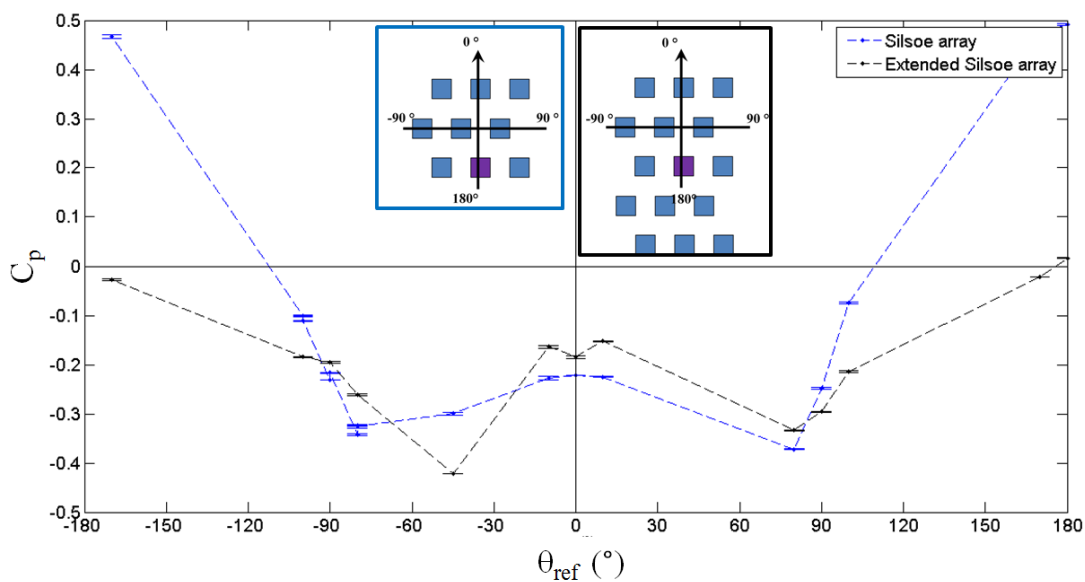


Figure 4.38: Back face averaged C_p against θ_{ref} for the Silsoe array and the extended Silsoe array. Points are joined for visual clarity.

This suggests that for the full-scale dataset the lack of obstacles behind the cube will lead to higher C_p values being recorded for $\theta_{ref} = -90^\circ$ to 180° and $\theta_{ref} = 90^\circ$ to 180° .

4.10.2 Symmetrical arrays

The small symmetrical (Figure 4.9c) and large symmetrical arrays (Figure 4.9d) increase both the number of rows in the array and the number of cubes in each row, maintaining a staggered pattern. The contour plots (Figure 4.39) highlight the limited effect of the extra rows behind the instrumented cube, with all back faces being similar in pattern and magnitude for the array cases. The front faces show a tendency for the peak pressure point to be shifted to the -y side of the instrumented cube and to around $z = 17$ mm, compared to the isolated instrumented cube where the peak C_p was located at $y = 0$ mm and $z = 14$ mm.

For $\theta_{ref} = 45^\circ$ and $\theta_{ref} = 90^\circ$ there is little difference between the two arrays (not shown).

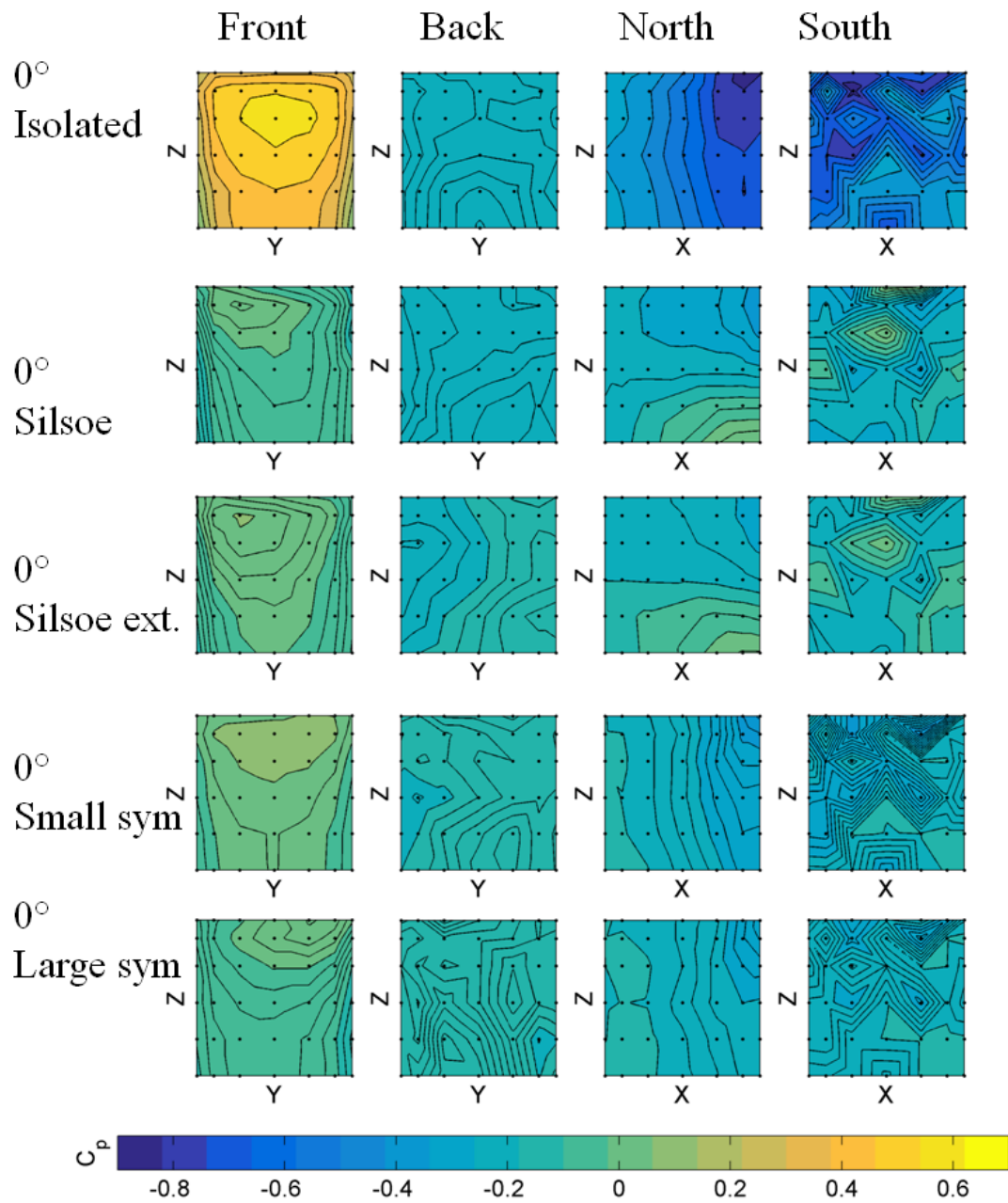


Figure 4.39: C_p contour plots for the isolated cube and all array cases (Figure 4.9) for $\theta_{ref} = 0^\circ$.

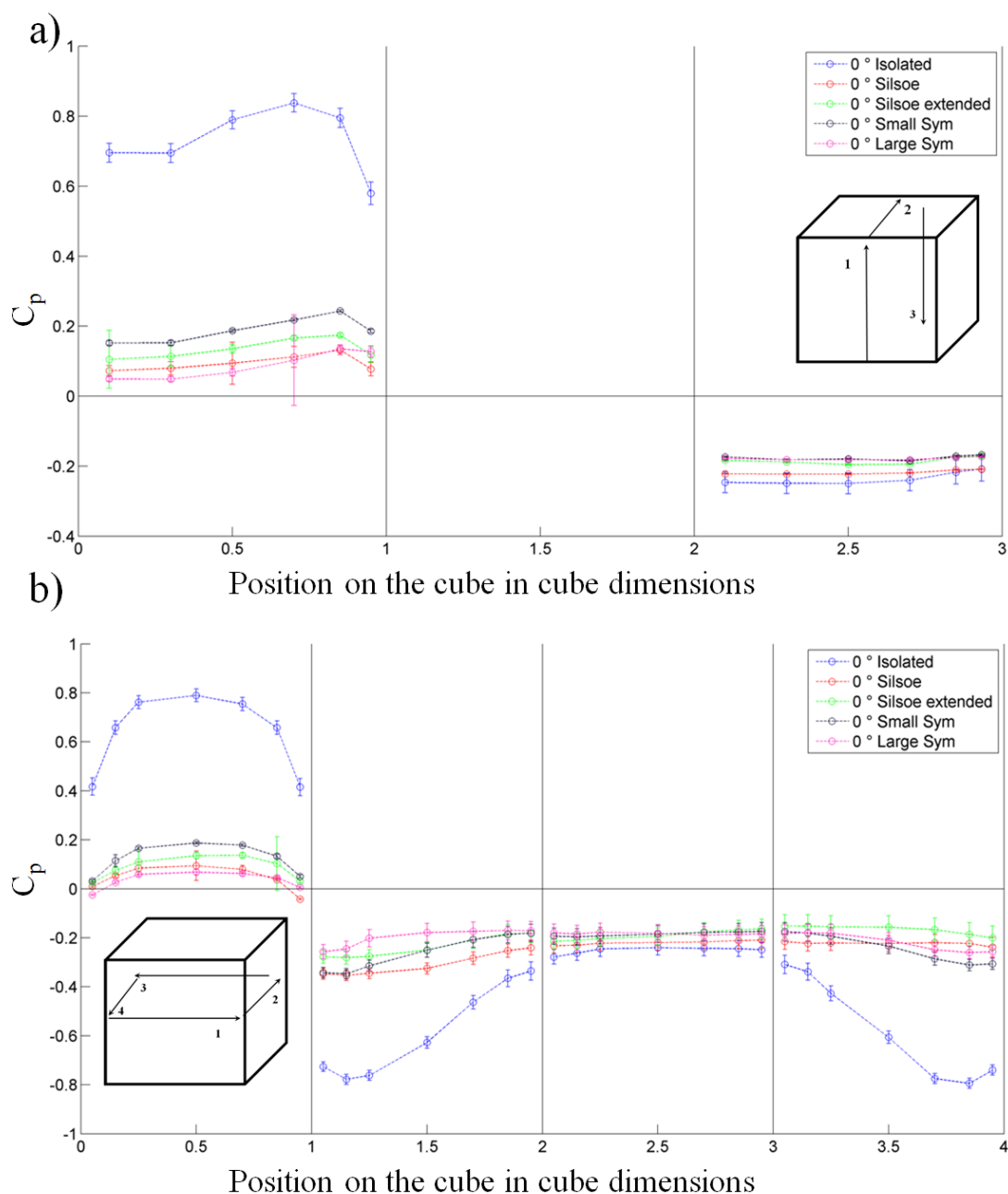


Figure 4.40: The a) vertical and b) horizontal traces of C_p for all of the staggered arrays (Figure 4.9) studied for $\theta_{ref} = 0^\circ$.

4.10.3 Comparison of the Silsoe array to the small symmetrical array

Of interest is an 0.05 increase on the front face C_p for the small symmetrical array (Figure 4.9c) compared to the Silsoe (Figure 4.9a) and extended Silsoe arrays (Figure 4.9b), as all have two rows upstream of the instrumented cube. This suggests that the longer rows of the small symmetrical array may greatly change the flow around the front face. This is hypothesised as being due to the extra cubes strengthening channelling effects and

the weakening of effects spreading in from the array edges. The tendency of the maximum pressure point to be towards the -y is reduced, with the maximum pressure point remaining central (Figure 4.39). The maximum pressure point for the large symmetrical array is shifted to the +y side, suggesting that the location of the maximum pressure is affected by the number of rows in front of the instrumented cube for a staggered array. This experiment has been repeated multiple (five) times, with each run returning the same results, which suggests that the results are not due to an error in set-up or due to instrument error.

Each row upwind has to be taken into account and the flow between the elements is an essential feature (Yang *et al.*, 2016). In these small arrays, the direct penetration of the approach flow into the array is probably dominant (Figure 4.15). The strength of the flow within the array then depends on simplicities of the pathways through the array, which is a function of θ_{ref} . Deep within an array, the driving force is the shear stress on the shear layer near roof level, rather than the direct penetration (i.e. from the upwind edges) of the approach flow. Edge effects generate mean flows into or from the array that, presumably, weaken as the array becomes wider.

4.11 Wind tunnel data comparison to the AIVC model

The wind tunnel array cases are directly compared to the AIVC (Air Infiltration and Ventilation Centre) (Liddament, 1986) sheltered building model in order to gain an understanding as to whether the asymmetry in the C_p values recorded for the full-scale array case is the cause of the differences between it and the model results. The AIVC sheltered model gives very similar C_p values to the CIBSE urban model due to both being derived from the same research and as such only one is used for comparison.

The AIVC model gives a higher C_p for $\theta_{ref} = 0^\circ$ on the front face (Figure 4.41a), related to the data being determined in a less turbulent boundary layer. The extended Silsoe array (Figure 4.9b) and the aligned array show similar front face average values of 0.07 to 0.09. The high value for the Silsoe array (Figure 4.9a) is due to the array not being extensive, meaning that sometimes flow can impact directly onto the front face at certain wind angles.

For $\theta_{ref} = \pm 45^\circ$ the C_p on the aligned array is 0.03 different from the AIVC sheltered values. All other arrays display lower values, with the Silsoe and extended Silsoe array being in good agreement for this θ_{ref} with a C_p value of -0.12. The small symmetrical array (Figure 4.9c) has a more positive C_p value of -0.03 compared to the large symmetrical array, again due to the addition of the extra rows and extended row length.

For $\theta_{ref} = \pm 90^\circ$, all arrays merge onto values between -0.07 and -0.1: this is due to channelling occurring in all arrays. It can be clearly seen that extending the length of the cube streets has no effect on the C_p of the front face for the parallel cases. The AIVC

model predicts a more negative pressure for $\theta_{ref} \pm 90^\circ$ than shown in the modelled arrays and continues this trend to $\theta_{ref} = 135^\circ$, with a difference of 0.2 between the AIVC model and the measured arrays.

For the back face (Figure 4.41b), the AIVC model shows a more negative C_p for $\theta_{ref} = 0^\circ$, but matches the trend seen for all arrays. The aligned and Silsoe array display more positive pressures for $\theta_{ref} = 180^\circ$, due to the pressure tapped cube being exposed on the edge of the array, rather than enclosed by other array elements.

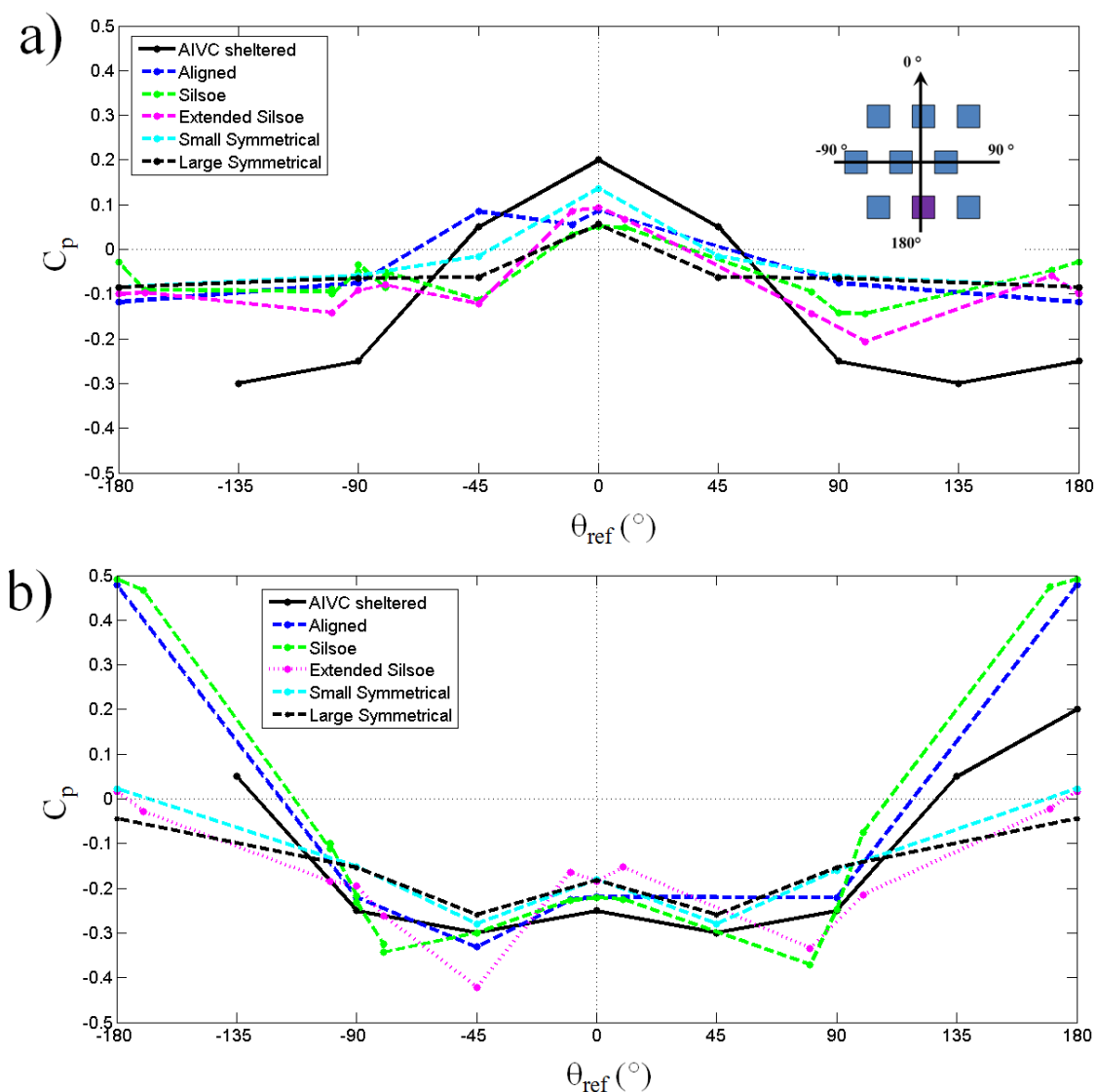


Figure 4.41: Comparison of the wind tunnel face-averaged C_p values as a function of θ_{ref} , measured for the Silsoe (Figure 4.9a), extended Silsoe (Figure 4.9b), Aligned, Small symmetrical (Figure 4.9c) and Large symmetrical arrays (Figure 4.9d) with the AIVC model (Liddament (1986)). a) front face and b) back face. Errors are too small to be plotted and are $\sim 5\%$. No errors were provided for the AIVC dataset. Points are joined for clarity.

The north (Figure 4.42) and south sides (not shown) display equal but opposite behaviour. The AIVC model (based on wind tunnel data) shows that for the sides of the

cube, there will be a peak pressure when the wind is perpendicular to that face, even if a surrounding array is acting to shield the building. For the unsymmetrical arrays this behaviour can be seen (Figure 4.42) with the extended Silsoe array, though the model over-estimates the face averaged C_p by 0.1.

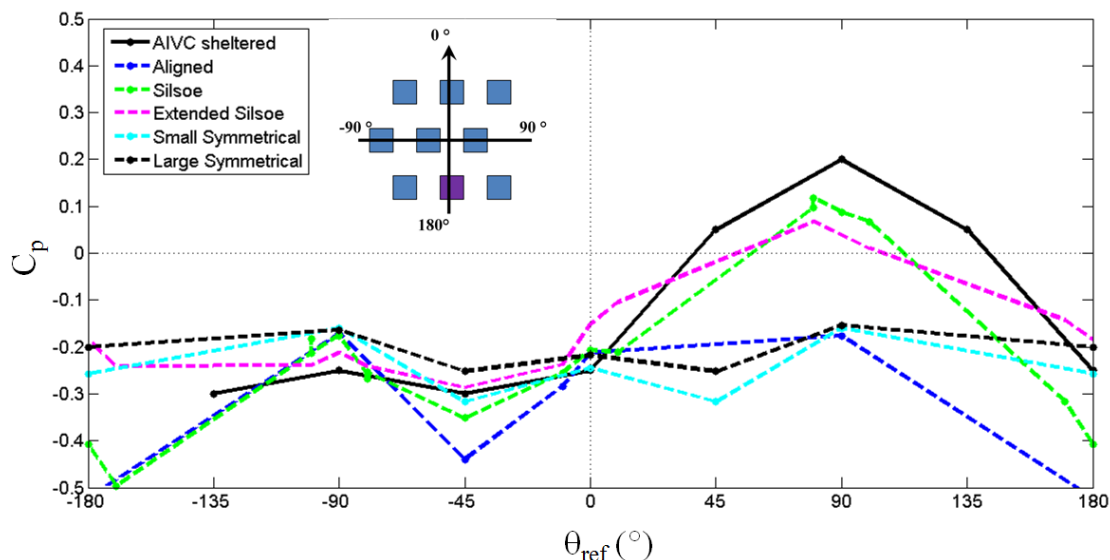


Figure 4.42: As Figure 4.41 but for the north face.

For the extensive symmetrical arrays (small and large) this tendency towards high values for $\theta_{ref} = 0^\circ$ is not seen. The peaks of 0.2 at $\theta_{ref} = \pm 90^\circ$ correspond to the perpendicular wind for the south side and the perpendicular wind for the north side respectively. An array generates a large amount of turbulence around the instrumented cube, leading to reduced pressures on the sides. The small and large symmetrical arrays are of sufficient depth to prevent any flow from directly impacting on the instrumented cube, even when the flow is perpendicular to the north face.

The AIVC model (and the CIBSE dataset) predicts the same trend for the small symmetrical array (Figure 4.9c) and the large symmetrical array (Figure 4.9d). The asymmetry of the north and south sides of the cube predicted by the AIVC is not seen in the extensive arrays due to the increased amount of shielding by added rows, but is seen in the Silsoe array and the extended Silsoe array. This dataset illustrates the uncertainties of using the AIVC dataset beyond its intended purpose, as differences can be seen for different cube arrays, let alone complex layouts of scaled building models.

4.12 Estimating ventilation rate

Scale modelling complex buildings is especially difficult due to the limited precision at such small scales: this especially affects ventilation and infiltration measurements, where the behaviour of the flow through the opening is likely to be changed due to the

scale of the opening. Scaled down openings may behave similarly to full-scale cracks, meaning that there could be some Reynolds Number dependency of the flow (Etheridge and Nolan, 1979). The relative size of the velocity instrumentation to the model can cause flow patterns to be disturbed, leading to problems during verification (Jiang *et al.*, 2003). For this reason, the cubes used in this wind tunnel experiment have no openings and are solid, with no velocity measurements being taken in the array to ensure that the flow is not disturbed.

Assuming that the pressure measurements and C_p are not influenced by the presence of openings it is possible to obtain an estimation of ventilation rate (Q_w) from the wind tunnel experiments (Straw, 2000). The time scale, like the length scale in the wind tunnel, was scaled by a factor of 300. It is assumed that the cube has one 'opening' on its front face and one opening on the back face, with an unobstructed stream connecting the two openings and that there are no temperature effects. The flow rate (Q_w) at tunnel scale is calculated (Awbi, 2003):

$$Q_w = C_d A \sqrt{\frac{2|\Delta P|}{\rho}} \quad (4.11)$$

where C_d is the discharge coefficient (0.61), A (m^2) is the area of the supposed opening, ΔP (Pa) is the pressure difference between the front and back faces and ρ (kg m^{-3}) is the density of the flow. The air change rate per hour (λ_{WT}) in the wind tunnel is:

$$\lambda_{WT} = \frac{12Q_w}{V} \quad (4.12)$$

where V is the volume of the cube (m^3). To allow for comparisons between different cases, Q_w is normalised using the mean flow speed (U_{ref}) multiplied by A :

$$Q_{Nw} = \frac{Q_w}{U_{ref} A} \quad (4.13)$$

Uncertainties in the flow rate are calculated using equation 3.6, which is used in the calculation of the error in λ_{WT} :

$$\sigma \lambda_{WT} = \lambda_{WT} \sqrt{\left(\frac{\sigma Q_w}{Q_w}\right)^2 + \left(\frac{\sigma V}{V}\right)^2} \quad (4.14)$$

where σ represents an error in the quantity. The error in the discharge coefficient C_d is assumed to be 10 % in line with the full-scale experiment, with errors in the volume of the cube and area of the window being based on measurement error (± 1 mm) (Appendix C). The error in the flow density is based on temperature and pressure measurements taken within the laboratory during the experiments. A and V are assumed values and are therefore exact.

The pressure difference was calculated from position of the front and back openings, referred to as the pressure difference method (Section 3.8.5). The pressure taps in the wind tunnel which were the closest match to the full-scale positions of the windows were (x, y, z) in (mm) (Figure 4.3):

- $(-10, 00, 10), (10, 00, 10)$
- $(-10, -04, 10), (10, -04, 10)$
- $(-10, 04, 10), (10, 04, 10)$
- $(-10, 00, 14), (10, 00, 14)$

where 'x' co-ordinates (-10) are positions on the front face of the cube and (10) the back face.

4.12.1 Results

Each wind tunnel run generates one Q_{Nw} (normalised wind tunnel ventilation rate) value (Figure 4.43). The trends captured in Q_w are similar to the face averaged C_p values, with the maximum air change rate occurring when the wind is perpendicular to the front or back faces ($\theta_{ref} = 0^\circ$ and 180°) and the minimum values occurring when the wind is parallel to the front and back faces ($\theta_{ref} = -90^\circ$ and 90°). Compared to the isolated cube, the Silsoe array (Figure 4.9a) reduces Q_{Nw} from 0.5 down to 0.25 for the perpendicular winds (a 50 % reduction). Similar levels of reduction are seen for all angles, though there is little difference for the parallel wind directions, with the Silsoe array recording a Q_{Nw} of 0.1, and the extended Silsoe array (Figure 4.9b) recording a value of 0.2. $\theta_{ref} = 180^\circ$ leads to a similar air change rate to that of an isolated cube. Like for C_p , the effect of the array is not symmetrical.

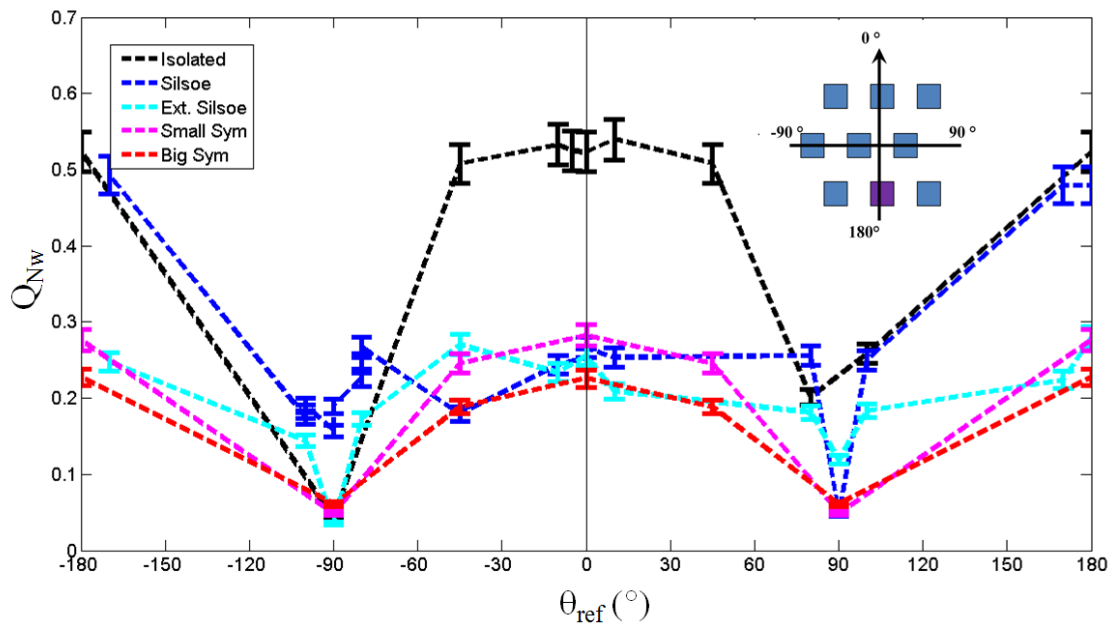


Figure 4.43: Q_{Nw} for the Silsoe, extended Silsoe, Small symmetrical and large symmetrical arrays (Figure 4.9) and the isolated cube with θ_{ref} . The 90° value for the isolated cube was not included due to concerns about misalignment, for this reason, the isolated cube plot appears asymmetrical.

The results for $\theta_{ref} \pm 90^\circ$ suggest that the impact on Q_w caused by extra rows is minimal for the parallel wind directions, and that the channelling behaviour is similar for all arrays. The small symmetrical array records slightly higher ventilation rates than the other arrays (Section 4.10.3). For $\theta_{ref} = 0^\circ$ the addition of an extra row (comparing small symmetrical to the large symmetrical array) causes the normalised air change rate to drop by 0.05 or by around 20 % to 25 %. The effect of the extra rows behind the instrumented cube for the extended Silsoe array (Figure 4.9b) is clear for $\theta_{ref} = 180^\circ$ with a decrease from $Q_{Nw} = 0.47$ for the Silsoe array (Figure 4.9a) to $Q_{Nw} = 0.3$. Values for the small symmetrical array (Figure 4.9c) are also similar to the extended Silsoe array for $\theta_{ref} = 180^\circ$. The Q_{Nw} for all arrays converges at $\theta_{ref} = 90^\circ$ due to the flow being parallel. Overall the large symmetrical array (Figure 4.9d) records the lowest values of Q_{Nw} for all values of θ_{ref} and the asymmetry of Q_{Nw} with θ_{ref} is reduced with Q_{Nw} being in the range of 0.2 to 0.25 for all angles besides $\theta_{ref} = 90^\circ$.

4.13 Conclusions

The wind tunnel study has allowed the array size to be expanded with controlled, constant wind directions, providing an enhanced dataset for the analysis of the full-scale data. As the wind tunnel model has a greater density of pressure taps it captured features not visible in the full-scale array data: such as the shift in the maximum pressure point when the cube is surrounded by an array (Section 4.7). The wind tunnel C_p values

are compared to the full-scale C_p values (Section 5.8) and ventilation rates (Section 6.5). Like the full-scale work, only the mean values are considered here.

The location of the maximum pressure on the front face of the isolated cube shifts with a $\pm 10^\circ$ change in θ_{ref} and this effect is visible within the array cases, although the shift is weakened for the Silsoe array, due to the natural tendency for flow to move towards the top -y corner of the front face (Figure 4.24). For the isolated cube a shift in maximum pressure location also occurs for a $\pm 5^\circ$ change in θ_{ref} (Figure 4.18), though this rotation was not tested for the Silsoe array (Table 4.2). These changes in θ_{ref} are relatively small for a realistic full-scale flow at building height, which suggests that for the full-scale experiment some of the features seen in the wind tunnel may not be observable because of the variable θ_{ref} during averaging periods leading to features being smeared. Note that the array drag scale is larger than the array dimensions so that direct penetration of the approach flow is the key factor driving flow within the array.

Tests comparing the Silsoe array to larger, symmetrical arrays highlight that the addition of cubes to pre-existing rows may cause a rise in C_p experienced by a cube central within the array due to edge effects of the previous rows becoming more remote. The addition of an extra row reduces the C_p experienced by the cube by 10 % to 50 % ± 5 % depending on the location of the pressure tap of interest. The higher C_p values for the small symmetrical array could be attributed to increased turbulence within the larger arrays (Hertig and Alexandrou, 1995).

Symmetrical arrays provide slightly less shielding than unsymmetrical arrays, with the large symmetrical array having a lower C_p across the front than the small symmetrical array (Figures 4.39, 4.40). This suggests that the addition of an extra row may have a greater shielding effect than the addition of extra elements to pre-existing rows. The effect of the width of the array on the results should also be considered as the effect is not negligible. It should also be noted that these observations are valid only for the Silsoe array and the arrays studied here, as there is not enough data to allow for a generalisation for all array types.

It is difficult to compare previous array work using due to the differences in boundary layer conditions, array elements, array size and packing density. Whilst increasing λ_p has been shown to decrease C_p as flow begins to skim over the array, there is little work on how the shape and structure of the array has an effect on C_p (Cheng *et al.*, 2007). The focus has predominately been large, expansive arrays, whereas this work focuses on limited arrays which display the characteristics of both flow within an array and flow directly impacting onto a building. If these difficulties occur for comparisons between wind tunnel experiments, experiments that are undertaken in controlled conditions, it is of no surprise that the results of the full-scale measurements undertaken under realistic atmospheric conditions are not being utilised by the design industry. There is little inter-comparison between data-sets, due to the complexity of each building or array and the differing research goals of each group. A way of improving comparisons between data

sets would be to ensure that all specifics of the wind tunnel set-up are included within published work, such as instrument error, boundary layer generation, instrument sensitivity and unique characteristics of a tunnel (Table 4.1).

The comparison of the wind tunnel results to the AIVC data for a shielded building highlight that the provided C_p values cannot be used beyond their intended purpose. This is especially true for the side walls (Figure 4.42) demonstrating that the instrumented cube does not behave as an isolated cube with a lower C_p due to shielding, but instead changes behaviour. The differences lie in the lack of symmetry and the variable shielding due to the surrounding elements, which would vary even if the array were vast. The AIVC model does not take into account different levels of shielding, with larger arrays having a greater effect for certain wind directions, due to a decreased penetration depth. The models do not take into account the layout of an array e.g. aligned vs staggered nor array expanse.

For $\theta_{ref} = \pm 90^\circ$, the addition of extra rows to the array had little or no effect, due to the flow being channelled down the streets of what appears to the flow as an aligned array. This suggests that currently used models do not take into account channelling within an array, leading to an underestimation of C_p for parallel wind directions.

The effect of increasing the array size and/or width is not well understood, though a comprehensive wind tunnel study which starts from an isolated cube and increases the array first in width, then in depth and then finally both, for a range of set boundary layer conditions would provide a useful guideline to those working in an urban area. C_p values derived from wind tunnel experiments should be listed alongside contour plots and a description of the surrounding array, such as the number of elements, type of array and the length and width of the array. This will allow for an understanding as to how the shape of an array influences the pressure pattern on faces of an array element. For the Silsoe array, the presence of the array causes a 60 % to 90 % decrease on the front face averaged C_p when compared to the results of the isolated cube, with the size of the decrease being dependent on the location of the tap of interest. The face averaged C_p masks the shift in peak pressure shown by the contour plots.

Another layer of complexity not considered here is heterogeneous building heights, which completely alter the flow patterns within an area depending on the location of the taller buildings. The layout of an array is also not considered here though has been considered in other work e.g. (Zaki *et al.*, 2010), as a true urban area is unlikely to have a repeating unit. In order to create a dataset which is of use to those working within urban areas, the effects of all variables need to be considered individually before being combined with one or two other variables in order to understand which variables dominate in an environment and what causes them to be dominant. However, creating a dataset of this size is easier said than done and may not be feasible, due to the need to repeat experiments in different experimental set-ups in order to understand the differences between wind tunnels.

Chapter 5

Flow structure and wind pressure for a full-scale idealised building within an array

5.1 Introduction

The full-scale pressure coefficient (C_p) results are analysed for the array and isolated cases, with the effects of boundary layer stability, reference wind speed (U_{ref}) and wind direction (θ_{ref}) being considered. The effect of the opening was found to be negligible in line with literature. The full-scale pressure coefficients are also compared to current models (Section 5.7) and the isolated and array case pressure coefficients are inter-compared (Section 5.6).

The data analysed in each section are indicated (e.g. $I(NN_H^{All})$). Dataset notation is shown in Figure 5.1 and is listed in Table 5.1.

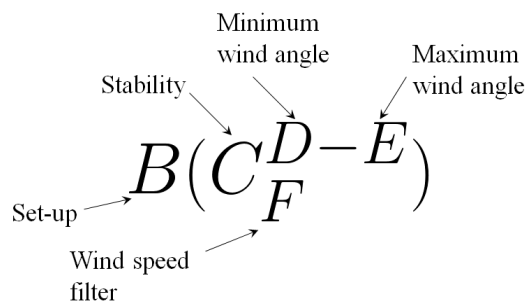


Figure 5.1: Notation for describing the data-set used.

Table 5.1: Examples of dataset labels used in Chapters 5 and 6.

Dataset	Set up (I/A/All)	Wind speed filter	Stability	θ min (°)	θ max (°)
$A(All_{All}^{-10-10})$	Array	All	All	-10	10
$A(All_{All}^{All})$	Array	All	All	All	All
$A(NN_M^{All})$	Array	$> 3 \text{ m s}^{-1}$	$-0.1 z/l < 0.1$	All	All
$All(All_{All}^{All})$	All	All	All	All	All
$All(All_M^{All})$	All	$> 3 \text{ m s}^{-1}$	All	All	All
$All(NN_{All}^{All})$	All	All	$-0.1 < z/l < 0.1$	All	All
$All(NN_M^{All})$	All	$> 3 \text{ m s}^{-1}$	$-0.1 z/l < 0.1$	All	All
$I(All_{All}^{-10-10})$	Isolated	All	All	-10	10
$I(All_{All}^{All})$	Isolated	All	All	All	All
$I(NN_H^{All})$	Isolated	$> 6 \text{ m s}^{-1}$	$-0.1 < z/l < 0.1$	All	All

5.2 External flow characteristics

5.2.1 Displacement height and roughness length

The friction velocities (u_*) measured at 6 m and 10 m were used to determine if the profile was logarithmic: if $\frac{u_{*6}}{u_{*10}} = 1$ it suggests the same level of shear at both heights, meaning both masts are within the same layer (Figure 5.2). For directions where the ratio is not 1, a roughness length and a displacement height cannot be calculated. For ratios close to 1 and near-neutral stability, the displacement height (d) can be calculated from the logarithmic wind speed equation (Section 4.2.3.2) (Kaimal and Finnigan, 1993). Below the displacement height, a different set of physical processes take over. The roughness length (z_0) is the height above the displacement plane at which the mean wind becomes zero when extrapolating the logarithmic wind speed profile downward through the surface layer (Stull, 1988).

The lack of consistency for z_0 and d make it difficult to accurately understand the profile of the site, especially over a range of θ_{ref} . The accuracy of a logarithmic profile applied to the site, especially for an array case, despite its greater amount of data, is contested. For this reason, the stabilities used throughout this chapter are calculated from z/L and not $(z - d)/L$ due to the difficulty and large error in calculating the displacement height for all wind directions.

By taking the ratio of wind speeds at two heights, and assuming that the friction

velocity is similar at both heights, d can be calculated (Rooney, 2001):

$$d = \frac{z_2 e^{-\frac{\kappa U_1}{u_*}} - z_1 e^{-\frac{\kappa U_2}{u_*}}}{e^{-U_1} - e^{-U_2}} \quad (5.1)$$

d is then used to obtain the corresponding z_0 (Figure 5.3):

$$U_Z = \frac{u_*}{\kappa} \ln\left(\frac{z-d}{z_0}\right) \quad (5.2)$$

Flow from $\theta_{ref} = 0^\circ, \pm 45^\circ, -180^\circ$ to -150° and 150° to 180° wind directions have a 1:1 ratio for u_* . Flows from $\theta_{ref} = -140^\circ$ to -50° and from $\theta_{ref} = 60^\circ$ to 120° show a reduced ratio, suggesting that u_* at 6 m is likely greater than that at 10 m. Flow in the -140° to 50° sector is likely to be influenced by the presence of buildings downstream, as well as the isolated cube itself. For $\theta_{ref} = 60^\circ$ to 90° , the smaller ratio is likely to be caused by the change in surface from grass to crop in this direction and is not likely to be caused by just the crop itself, due to $\theta_{ref} = -45^\circ$ to 45° having a ratio close to 1.

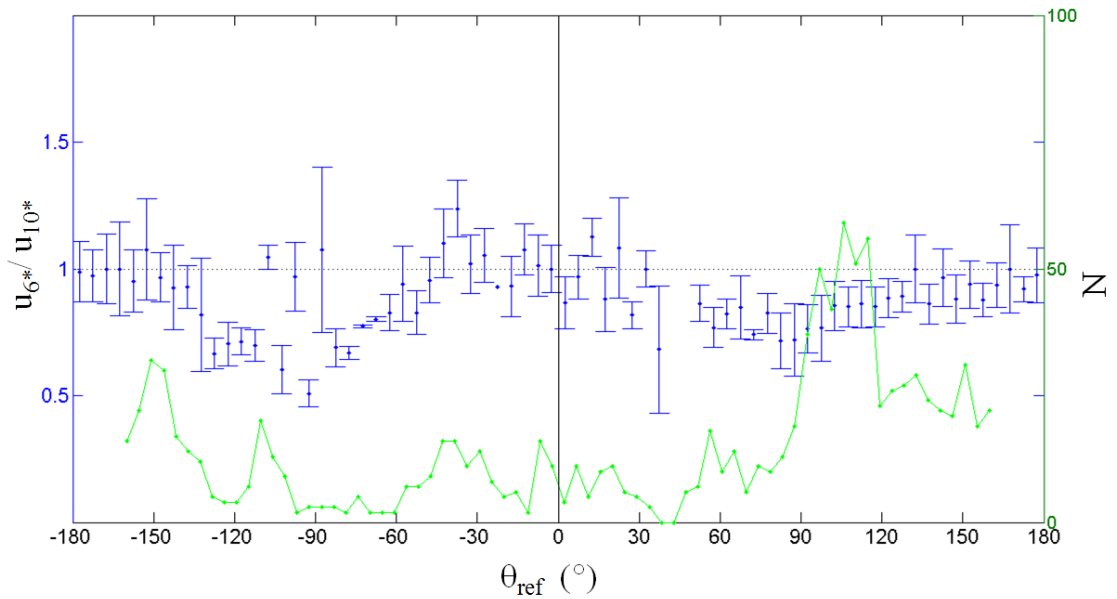


Figure 5.2: The ratio of the shear velocity u_* at 6 m and 10 m against θ_{ref} . Data are in 5° bins, with the median value for each bin shown. Error bars denote the interquartile range. Number of data points in each bin (right hand axis). Sections with < 3 data points are removed. Dataset: $I(NN_{All}^{All})$.

The peak of z_0 (0.2 m) between $\theta_{ref} = -30^\circ$ to 30° is due to the presence of the crop in the field adjacent to the mast being taller (approximately 1 m, there for the entire isolated cube dataset) than the grass on the field site for the isolated cube (Figure 5.3). The lack of a peak at around $\theta_{ref} = -150^\circ$ suggests that the 10 m is not influenced by the isolated cube

as values for z_0 of around 0.6 m would be expected for this direction. The peak at $\theta_{ref} = 90^\circ$ of $0.3 \text{ m} \pm 0.2 \text{ m}$ is not easily explained. One possible cause could be the presence of a fence in the field up wind in that direction, though this was 0.75 m tall and should not cause such a large change in roughness length. The displacement height for all wind directions is roughly between 6 m and 8 m with a smaller d of 5 m being recorded for the θ_{ref} bin 5° to 10° , likely due to this direction having a clearer fetch when compared to the other wind directions. The high displacement height could be caused by the large amounts of changes in surface type in the local area, with $\theta_{ref} = 100^\circ$ to 150° being influenced by the woodland area nearby. The peak of 8.75 m for $\theta_{ref} = -30^\circ$ is likely to be caused by the presence of the tree avenue upstream (Figure 3.2).

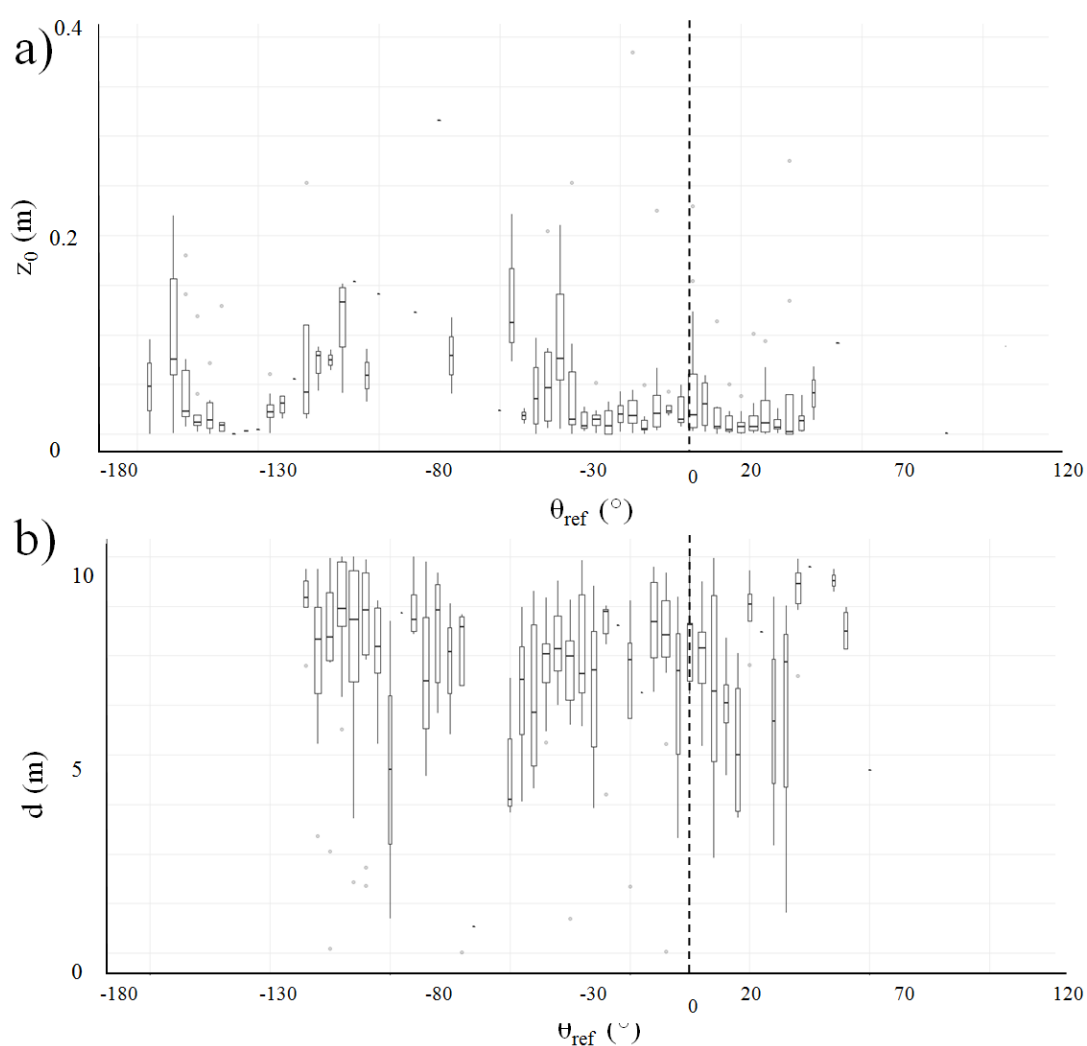


Figure 5.3: a) roughness length (z_0) and b) displacement height (d) for the isolated cube. Data are in θ_{ref} 5° bins, with the median value for each bin shown. Error bars denote the interquartile range. The width of the box plot is an indication of the number of values within the bin. Sections with < 3 data points have been removed. 0° is marked by the dashed line.

Taking the cases where the ratio of u_* at 6 m and 10 m is approximately one for the

array cases, the trends in the d for the isolated case are similar for $\theta_{ref} = -180^\circ$ to -120° . The lack of suitable data for the isolated cube makes it difficult to compare for all angles. For $\theta_{ref} = -30^\circ$ to 30° the array case has a larger displacement height, despite there being no changes to the upstream environment. For $\theta_{ref} = -120^\circ$ to -180° and $\theta_{ref} = 120^\circ$ to 180° there is little signal from the array. This suggests that due to the complexity of the area, the array has little effect on the oncoming flow. The measured z_0 for the array cases are symmetrical, with the longer roughness lengths occurring around $\theta_{ref} = -90^\circ$ and $\theta_{ref} = 90^\circ$, though there is no data for the isolated case for these wind directions. It could be assumed that the two roughness lengths would remain similar as the surrounding environment did not change over the field campaign. The large values may have been caused by the presence of the business park (Figure 3.2).

The 10 m sonic anemometer remains unaffected by the presence of both the isolated cube and the array, suggesting that the height of the cube's wake < 10 m.

5.2.1.1 Turbulence intensity and the Isolated cube

The turbulence intensities (Section 4.2.2) measured at 6 m and 10 m are similar over all wind directions for the isolated cube (Figure 5.4a, b). For $\theta_{ref} = 120^\circ$ to 180° the high turbulence intensities of 0.7 to 1 are likely to be caused by the woodland located in that direction, due to the tree height being around 10 m on average, meaning the reference mast may be in the wake of the woodland. The wake of the storage shed will be being affecting the reference mast for those directions. The large values of turbulence intensity for the isolated cube correlate with low wind speeds and cases where the oncoming flow is flowing over the instrumented cube ($\theta_{ref} = \pm 150^\circ$ to 180°) (measured at the reference mast). For wind speeds $> 5 \text{ m s}^{-1}$ the turbulence intensity can be seen to converge onto a value of 0.2 for the isolated case (Figure 5.4). The large range in turbulence intensity of 0.1 to 1 at $\theta_{ref} = -30^\circ$ to 60° could be due to wake of the tree avenue (Figure 3.2).

The range of 0.1 to 0.9 for $\theta_{ref} = 150^\circ$ to 180° and $\theta_{ref} = -150^\circ$ to -180° is caused by the oncoming flow impacting on the isolated cube, causing the reference mast to be downstream in the wake region (estimated to be ~ 85 m long using the geometrical methodology outlined by Millward-Hopkins *et al.* (2011)), leading to a higher turbulence intensity. The wake itself will be unsteady and will impact on the reference mast or either flow to either side, leading to a turbulence intensity value which is similar to that seen for other 'clean' wind directions. This effect can also be seen more strongly in the turbulence intensity values for the 3.5 m mast located in front of the cube (Figure 5.4c).

Unlike the 10 m and 6 m average turbulence intensities of 0.5 or less, the 3.5 m mast records values of 1 to 2.5 for $\theta_{ref} = -180^\circ$ to -120° . This higher averaged value is due to the 3.5 m mast being so close to the cube (3 m away) meaning it is consistently within the turbulent wake region of the isolated cube for these wind directions.

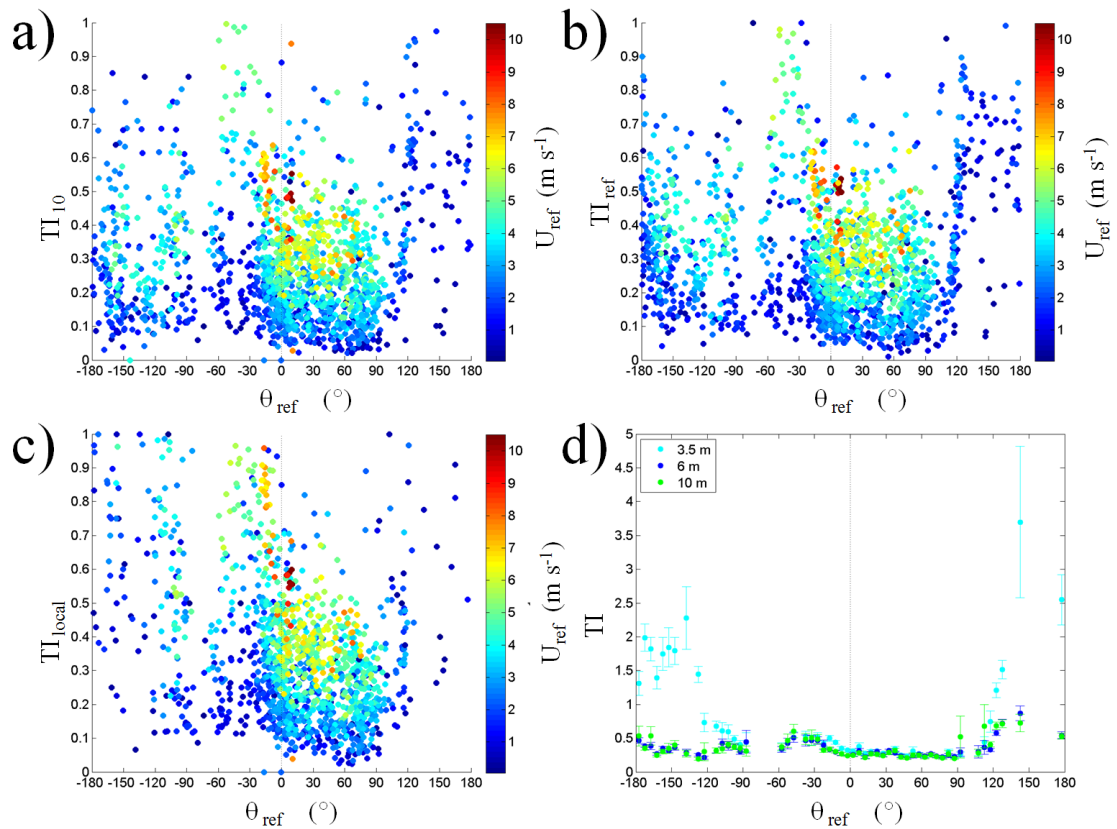


Figure 5.4: Turbulence intensity against θ_{ref} for the isolated cube cases with U_{ref} (colour). Turbulence intensity at a) 10 m b) 6 m c) at 3.5 m in front of the cube. d) is the data of a), b) and c) binned into 5° θ_{ref} bins, with the condition that $N > 10$ in order to be plotted. Mean values are plotted. Errors on d) are the standard errors of the bins.

There is agreement between all three mast averages for θ_{ref} values between $\theta_{ref} = -100^\circ$ and 120° , including the slight peak caused by the tree avenue (Figure 5.4d). The average turbulence intensity for this range of θ_{ref} was 0.3 to 0.4. The longitudinal turbulence intensity of the Silsoe cube at roof height (6 m) was 0.2, though these were taken in high winds with a direction perpendicular to the cube (Richards *et al.*, 2001). The higher values recorded here are likely to be due to the presence of the crop in the field in front of the site, which will increase the turbulence intensity for those directions. The storage shed has a similar effect on the local mast (3.5 m) as it does the reference (6 m) and 10 m mast, for $\theta_{ref} = 90^\circ$, due to local mast not being directly behind the storage shed.

5.2.1.2 Turbulence intensity within the array

There is good agreement between the 10 m and 6 m measurements for most θ_{ref} for the array (Figure 5.5). Differences occur at $\theta_{ref} = -150^\circ$ to -120° , with the 6 m mast range of turbulence intensities being 0.1 to 0.7 and the 10 m mast being 0.1 to 0.4 with a few points

around 0.6. This increase in range is due to the array wake reaching the reference mast height (6 m) but not consistently extending up to 10 m. The length of the array wake is estimated to be ~ 520 m (methodology outlined in Millward-Hopkins *et al.* (2011)). The decrease in the range of turbulence intensities for $\theta_{ref} = 90^\circ$ to 0.1 to 0.3 are equivalent to the isolated case turbulence intensity values for the 6 m mast, suggesting that the flow is being channelled down the array. Large amounts of scatter are present for low U_{local} values for both the isolated and array cases, though the array case has a larger range (0.1 to 5) due to the increased mechanical turbulence due to the array.

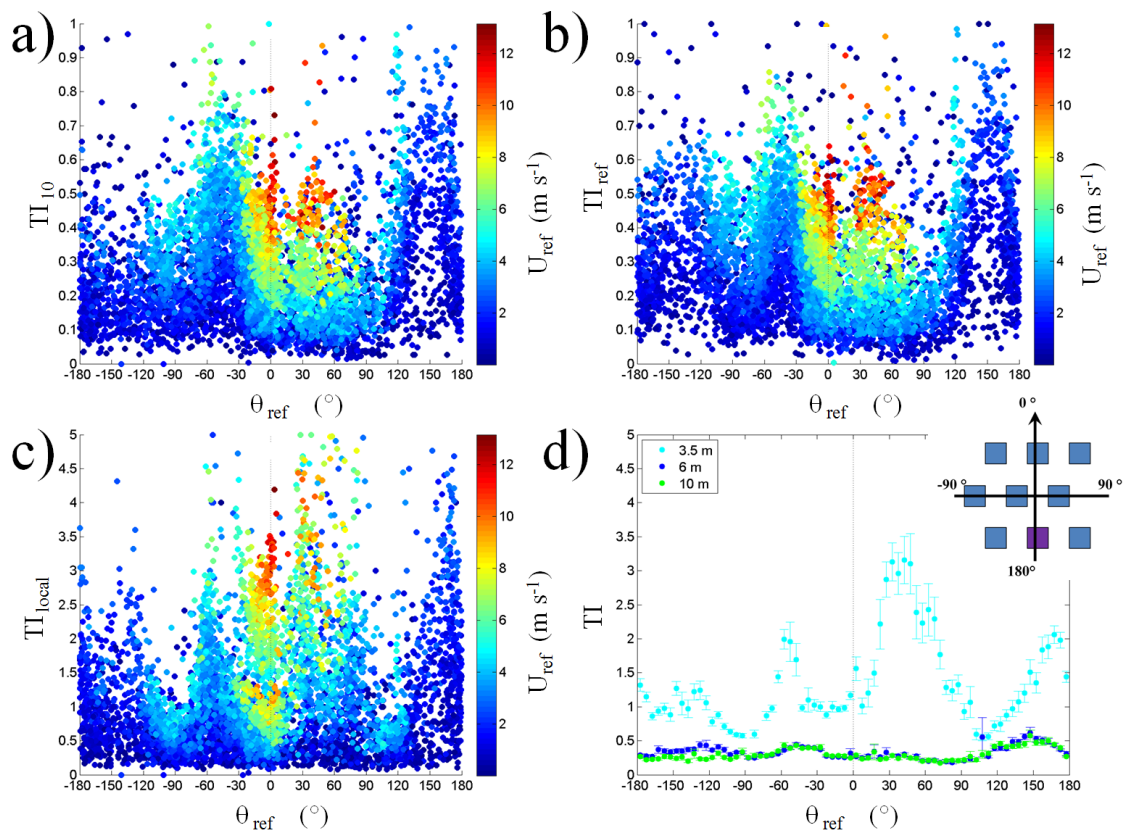


Figure 5.5: As Figure 5.4 but for the array case.

The wake of the storage shed is apparent for $\theta_{ref} = 150^\circ$ to 180° with a range of turbulence intensities of 0.1 to 1 for both the 6 m and 10 m measurements. For $\theta_{ref} = -60^\circ$ to 60° the turbulence intensity range is similar to the readings for the isolated cases, as the flow is approaching over similar conditions, suggesting that the changing height of the crop had little effect on the turbulence intensity of the oncoming flow. However there is an asymmetry in the average turbulence intensity between $\theta_{ref} = -60^\circ$ and $\theta_{ref} = 30^\circ$ to 60° , with $\theta_{ref} = -60^\circ$ having a peak of turbulence intensity of around 2 and $\theta_{ref} = 30^\circ$ to 60° having a turbulence intensity of 0.4 to 0.5.

The turbulence intensity within the array for θ_{ref} values such as $\theta_{ref} = 30^\circ$ are ten

times higher than in the upstream flow (Figure 5.5c). This result is similar to values obtained through CFD modelling: the presence of buildings can increase the turbulence intensity by up to 7 times the value for an isolated building (Lundquist and Chan, 2007).

Three peaks of turbulence intensity within the array can be identified from the data (Figure 5.5c). The first, at $\theta_{ref} = 0^\circ$ is due to the oncoming flow being forced to rise by the other upstream rows of the array, leading to a range of turbulence intensities of 0.1 to 3.5 due to the interaction of the cube wakes. The peaks at $\theta_{ref} = 60^\circ$ and $\theta_{ref} = -60^\circ$ are caused by the on-coming flow having to travel over two diagonally placed cubes and have a similar range to the 0° case, rising to five in some select cases. A reduction in turbulence intensity of 0.1 to 1 (a range similar to the isolated cube) occurs for $\theta_{ref} = -90^\circ$ due to the flow being channelled down the streets of the array. This suggests that the wakes of the cubes do not interact within the natural channels of the array and instead are aligned behind the cubes. Whilst $\theta_{ref} = 90^\circ$ shows a considerable decrease in turbulence levels, there is more scatter potentially caused by the storage shed, the woodland and the more variable terrain from that direction.

The array causes more turbulence for all wind directions, suggesting that the role of buoyant forcing on the turbulence is minimal as building induced turbulence dominates the turbulent kinetic energy budget (Figure 5.5d). The lack of buoyant forcing means that near-neutral boundary layer stability can be assumed, though not for all wind directions. Wind directions such as $\theta_{ref} = -150^\circ$ cause the reference mast to be within the array wake region, where the proportion of building induced turbulence will reduce, meaning that the near-neutral stability assumption is less valid for these wind directions (Lundquist and Chan, 2007).

5.2.2 Ratio of local wind speed to the 6 m reference wind speed

Datasets used: $All(NN_{All}^{All})$

Two unique trends differentiated by θ_{ref} can be identified between the 6 m reference speed (U_{ref}) and the local wind speed (U_{local}) for the isolated cube (Figure 5.7). A 1:1 ratio is not expected due to the height difference and distance between the measurements. For the majority of wind directions, there is linear agreement between the two wind speed measurements (marker **a**), suggesting that there are no low level obstacles which only effect the local mast. The deviations from this linear behaviour (marker **b**) occur at $\theta_{ref} = -180^\circ$ to -150° and $\theta_{ref} = 150^\circ$ to 180° (Figure 5.6d). This is caused by the oncoming flow impacting on the cube meaning the local mast is within the wake of the cube and not representative of the reference flow.

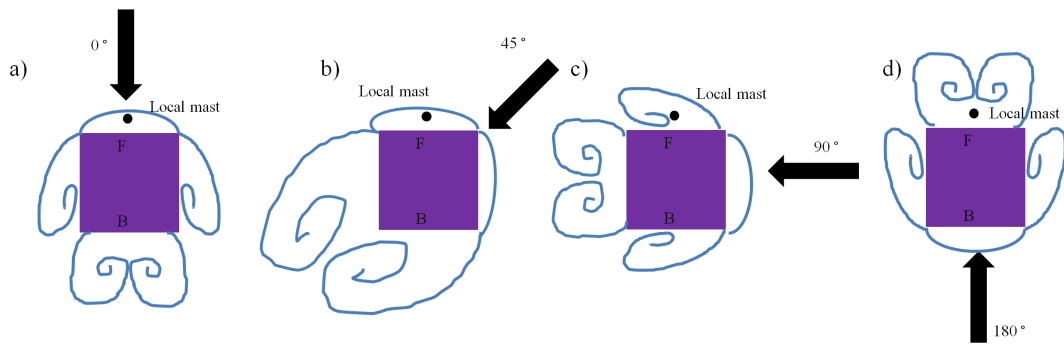


Figure 5.6: Plan view of the main flow features around an isolated cube when $\theta_{ref} =$ (a) 0° , (b) 45° , (c) 90° and (d) 180° . Side views for $\theta_{ref} = 0^\circ$ and 45° can be found in Figure 2.5.

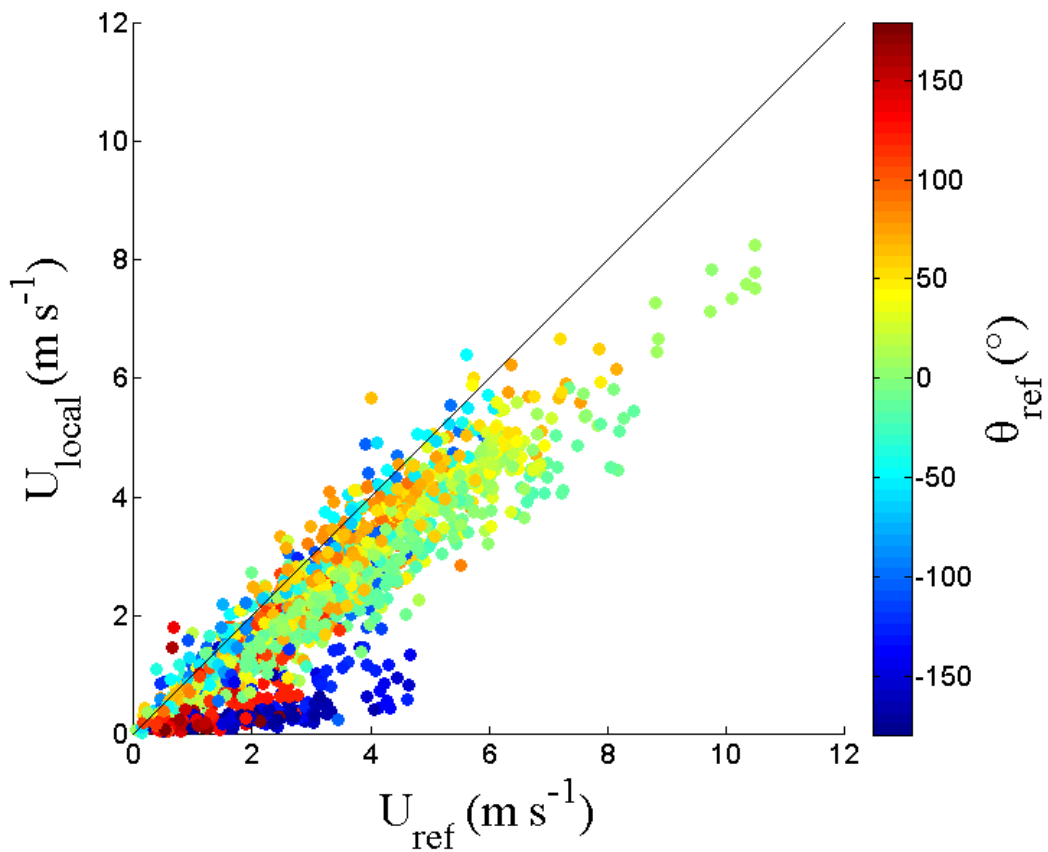


Figure 5.7: U_{local} and U_{ref} for the isolated cube with θ_{ref} (colour) and a 1:1 ratio (black line). Errors on the points are 0.01 m s^{-1} .

The behaviour of the two wind speed measurements for the array case is more complex and has three distinct trends, two of which cannot be distinguished by θ_{ref} (Figure 5.8 markers **b**, **c**). For $\theta_{ref} = -180^\circ$ to -150° and $\theta_{ref} = 150^\circ$ to 180° (a) the array case behaves similarly to the isolated case, with the local mast being in the wake of the instrumented cube. Also within this trend are $\theta_{ref} = \pm 90^\circ$, due to the oncoming flow

being parallel to the streets within the array. This trend is also seen in the ratio of U_{local} and U_{ref} , by the peak in the ratio values of around 1 (Figure 5.10).

Trends **b** ($\theta_{ref} = 0^\circ$ to 90°) and **c** ($\theta_{ref} = 0^\circ$ to -90°) suggest that there is a local feature within the array which is intermittent and has an impact for specific θ_{ref} values (Figure 5.9). These two trends are visible even when the θ_{ref} is limited between -10° to 10° , (Dataset: $A(All_{All}^{-10-10})$) (Figure 5.10). This effect does not disappear when the stability, U_{ref} , external temperature, temperature difference or opening type are taken into account.

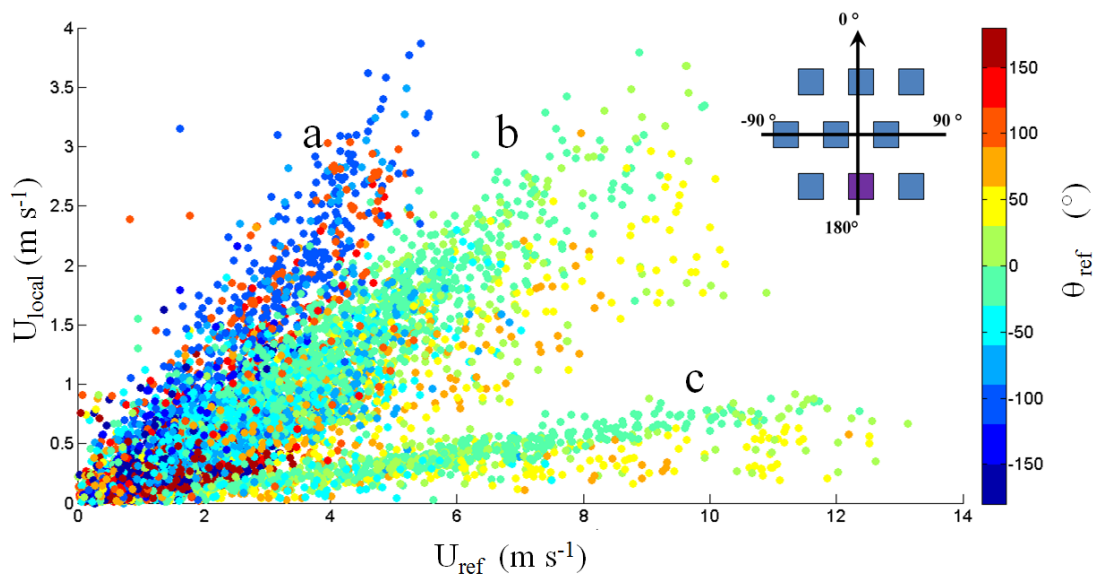


Figure 5.8: Same as Figure 5.7 but for the array data. Points **a**, **b** and **c** are commented on in the text.

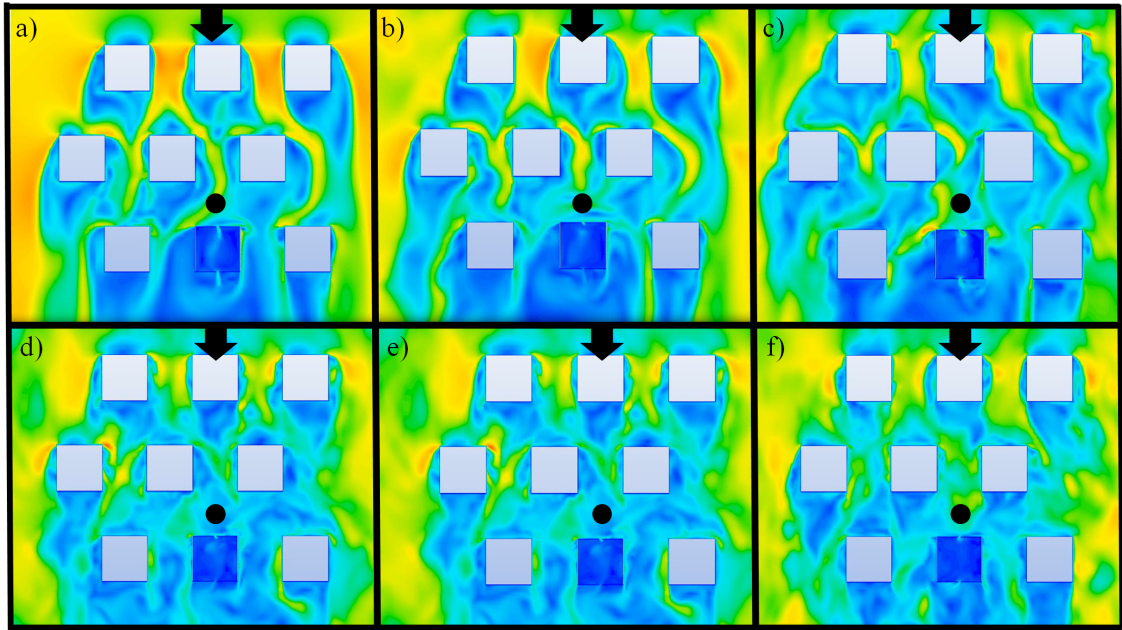


Figure 5.9: Instantaneous CFD flow schematic. Cases a-f highlight the different flow behaviours which may occur in front of the instrumented cube (blue cube) for $\theta_{ref} = 0^\circ$. Colour denotes the relative velocity, with greens and yellows being higher than blues. Black dots denote the approximate location of the local mast. The CFD set up is detailed in Appendix L. Image provided by King (2016).

One variable which changes between the two ratios (Dataset: $A(All_{All}^{-10-10})$) is the local turbulence intensity: the smaller wind speed ratios are associated with turbulence intensities above 1, meaning that the flow is fully dominated by turbulent effects close to the cube (Figure 5.9d, e, f).

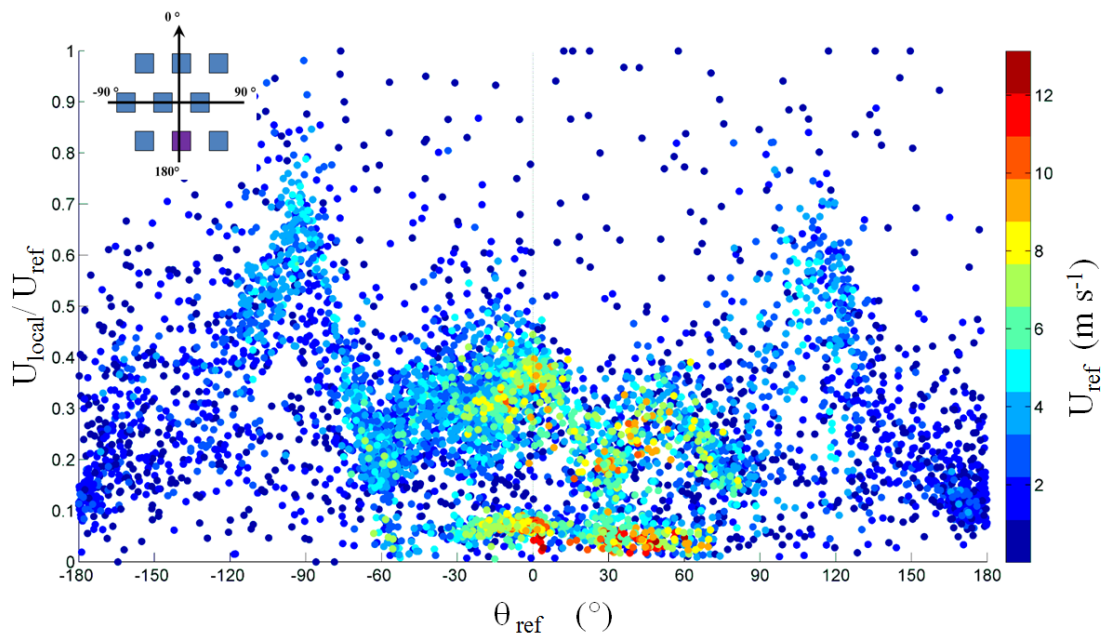


Figure 5.10: Ratio of U_{local} and U_{ref} against θ_{ref} , colour denotes U_{ref} .

Trends **b** and **c** (Figure 5.8) can also be differentiated by θ_{local} (Figure 5.11) with the ratios of less than 0.1 being for $\theta_{local} = 150^\circ$ to 180° , with the occasional -180° reading (Figure 5.9). This is a complete reversal of direction when compared to the θ_{ref} values of $0^\circ \pm 10^\circ$ (Figure 5.9b, f). The higher ratios (0.4 to 0.5) show that θ_{local} is between -50° and 50° , likely to be slightly skewed from θ_{ref} by the presence of the array elements (Figure 5.9a).

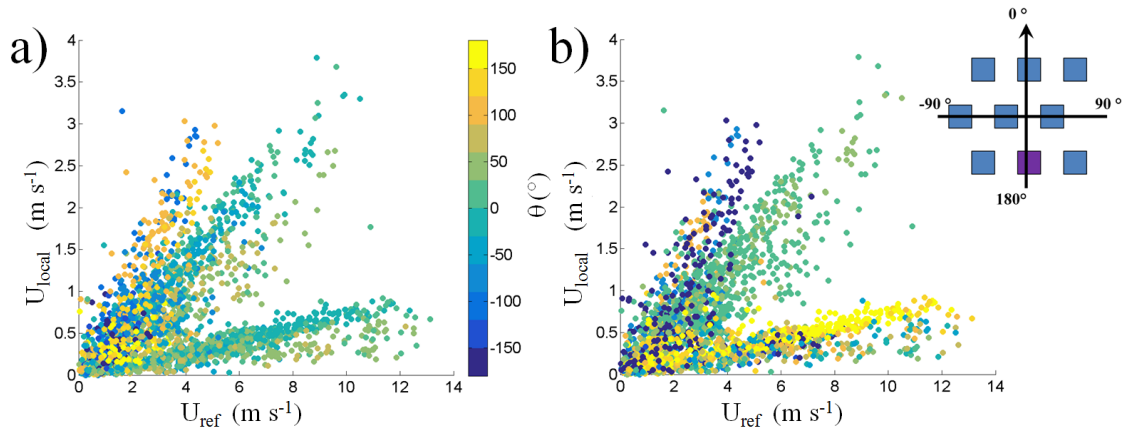


Figure 5.11: U_{ref} and U_{local} for array data colour coded for a) θ_{ref} reference wind direction and b) θ_{local} . The colour bar is applicable to both plots.

The reversal in flow direction for the smaller ratios suggests that the local mast is influenced by the recirculation regions of the adjacent cubes which will shift location with θ_{ref} (Figure 5.12). It is likely that the wakes themselves will encompass the side recirculation regions, though this is not illustrated here.

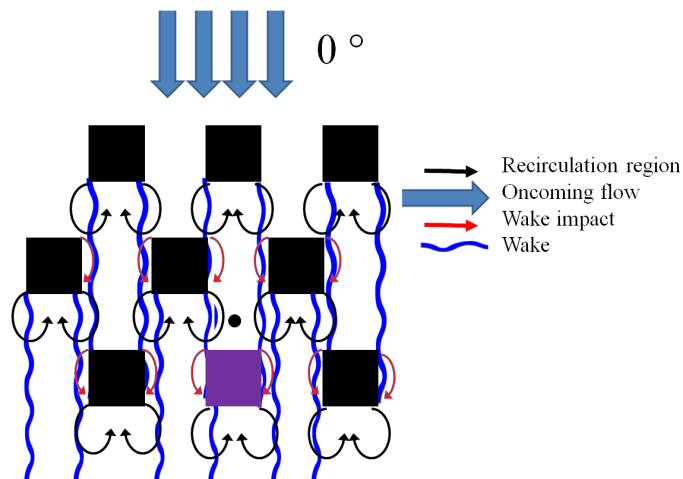


Figure 5.12: Plan view schematic of the wakes and recirculation regions present within the array for $\theta_{ref} = 0$. The black dot represents the location of the local sonic anemometer.

The dual trend is visible for 1, 5, 10, 30 and 60 minute averaging times for dataset $A(All_{All}^{-10-10})$ (Figure 5.13), therefore the behaviour is not an artefact of the averaging

time. The split of the half hourly data is $\sim 50:50$ (2260 half hour periods to 2085 for dataset A(All_{All}^{All})). This dual behaviour also occurs when U_{local} is compared to the 10 m wind speed (U_{10}).

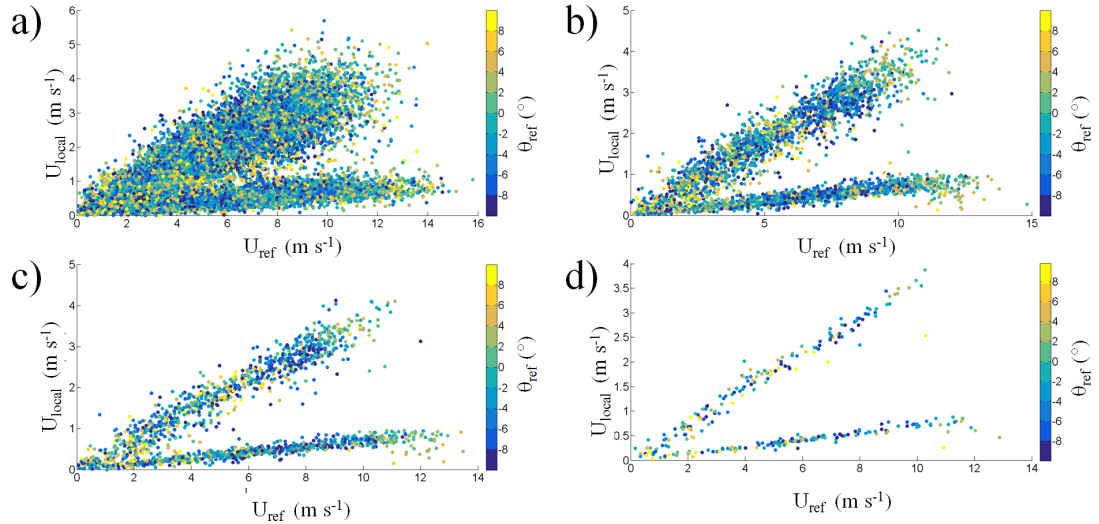


Figure 5.13: U_{local} and U_{ref} for the array case colour coded for θ_{ref} in the range 0° to $\pm 10^\circ$ for a) one minute averaged b) 5 minute averaged c) 10 minute averaged and d) 60 minute averaged data.

However, this dual behaviour cannot be seen in the ratio between U_{local} and $U_{channelling}$ (Figure 5.14). There is a channelling effect when $U_{local}/U_{channelling} = 1$ for $\theta_{ref} = -90^\circ$ (Figure 5.14). However this does not occur for 90° flow due to the influence of the storage shed (Figure 5.14). The ratio increases to 0.7 for $\theta_{ref} = 100^\circ$ to 120° due to the increased wind speed at the Channelling mast ($U_{channelling}$), possibly due to the down-flow from the wake of the storage shed.

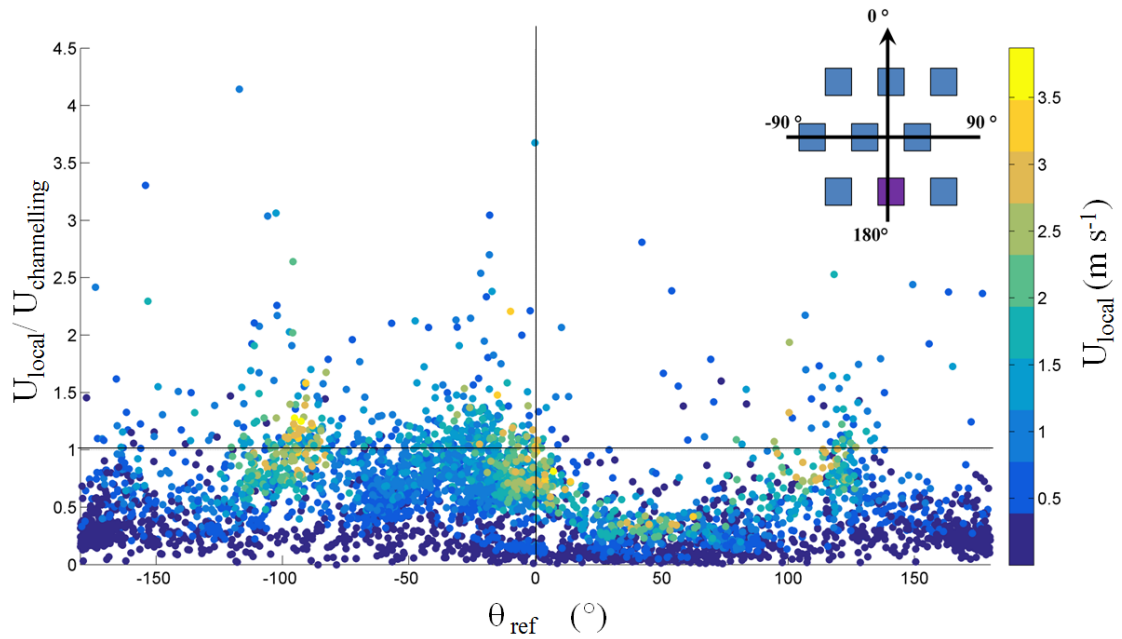


Figure 5.14: Ratio of U_{local} and $U_{channelling}$ against θ_{ref} for the array case. Colour denotes U_{local} . Dataset: $A(All_{All}^{All})$.

For $\theta_{ref} = -180^\circ$ to -150° and $\theta_{ref} = 150^\circ$ to 180° the flow to the local mast is completely blocked by the instrumented cube leading to a reduced ratio of 0.3, due the Channelling mast being positioned off centre. This behaviour is also seen in the isolated case, though the ratio is reduced to 0.1.

For $\theta_{ref} = 30^\circ$ the ratio is reduced to 0.2, due to the high amount of shielding affecting the local mast and only a small amount of shielding on the Channelling mast. The two trends visible in the ratio of the U_{local} to U_{ref} are visible in the U_{local} and $U_{channelling}$ ratio for $\pm 10^\circ$ and are not correlated with U_{ref} .

Comparing $U_{local}/U_{channelling}$ (Figure 5.14) with $U_{channelling}/U_{ref}$ (Figure 5.15) suggests that the dual behaviour is localised to the centre of the array where there is most blockage of the flow. The peak ratio occurs at $\theta_{ref} = 70^\circ$ to 90° along with the higher recorded values for the Channelling wind speed, suggesting that this is the effect of channelling down the streets of the array and that there is little shielding affecting the Channelling mast. Low U_{ref} values have more scatter, suggesting that in low wind speeds the features of the wakes are not as strong and are easily dispersed through interactions with neighbouring wakes.

Though the pattern of the ratios with θ_{ref} is symmetrical, the magnitudes of the ratios are not, with smaller ratios being correlated to the negative angles, which is due to more array elements being on that side, causing the flow to the Channelling mast to be reduced. One cause of the smaller ratio could be due to the length of the wake from the cube in the front row of the array. If the standard deviation of θ_{ref} is high, it could cause

this wake to shift depending on the mean θ_{ref} , meaning that the air in the centre of the array is not directly affected by the wake region.

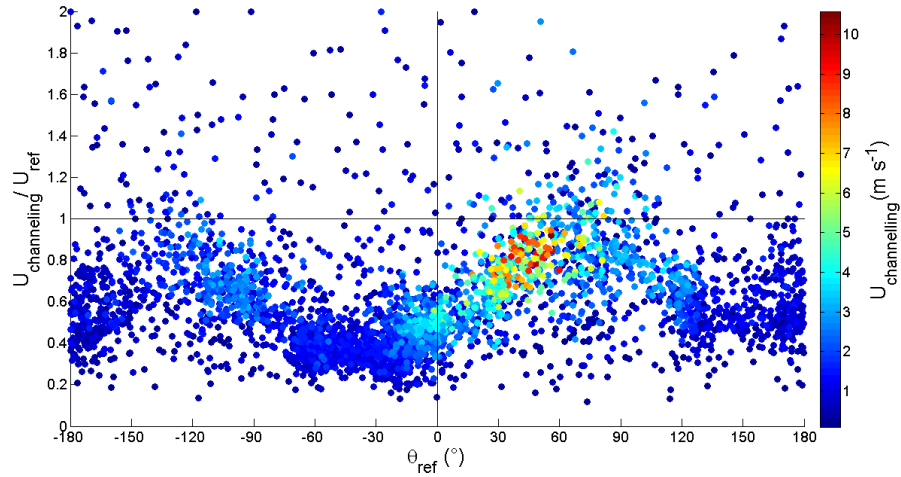


Figure 5.15: Ratio of $U_{channeling}$ and U_{ref} against θ_{ref} , colour denotes $U_{channeling}$. Dataset: $A(All_{All}^{All})$.

Two different ratios of U_{local} to U_{ref} lead to different θ_{local} values, which suggests a change in the structure of the flow within the array, especially in the region in front of the instrumented cube (Figure 5.11). Despite a θ_{ref} range of $\pm 10^\circ$ the smaller ratios suggest that θ_{local} is possibly within a recirculation region from the wakes of the neighbouring cubes. Also of note is the reduced scatter of the smaller ratios, suggesting that whatever is causing this feature is more dominant than the other influencing features.

The dual behaviour of the wind speeds cannot be linked to the standard deviation of θ_{ref} , even when limited to the angle range at which the array has maximum impact (Dataset: $A(All_{All}^{-10-10})$) (Figure 5.16). High variability in θ_{ref} is seen for $U_{ref} < 1 m s^{-1}$, where there is no dual behaviour, however when $U_{ref} > 1.5 m s^{-1}$, the split appears.

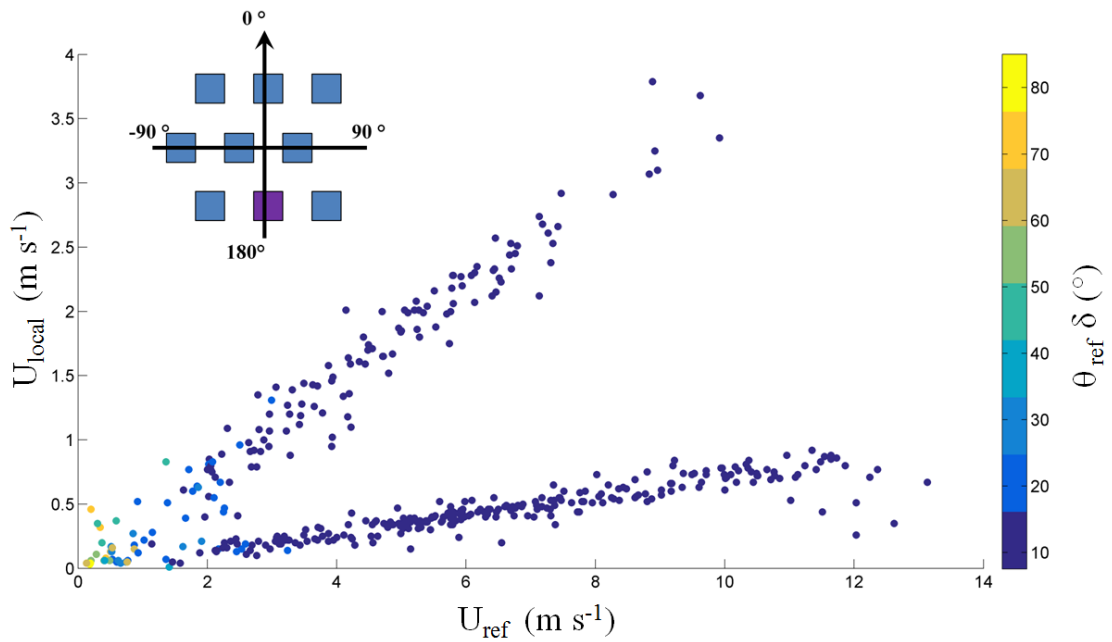


Figure 5.16: The relation of U_{local} and U_{ref} , colour coded for standard deviation (δ) of θ_{ref} for the array. Dataset: $A(All_{All}^{-10-10})$.

The turbulence intensity measured by the local mast show that these low U_{local} values for the smaller ratios of 0.1 also correlate with times when the flow is dominated by the mechanical turbulence generated by the cubes. This high value of turbulence intensity coupled with low U_{local} values suggests that the structures of the wakes are very weak, but cover a sufficient area to allow them to interact with each other, creating a flow that is low in wind speed due to conflicting flows and high in turbulence due to the nature of wakes (Figure 5.12). This only occurs over a small range of $\theta_{ref} = 0^\circ \pm 10^\circ$. θ_{local} is opposite to θ_{ref} for the smaller ratio cases, suggesting that it is caught in a recirculation region (Figure 5.19).

These results suggest that the wind speed within an array is difficult to understand and predict from U_{ref} , especially for a limited array. Even for limited θ_{ref} ranges (Figure 5.13), different behaviours may be experienced, making it difficult to predict the effect of the surroundings on the measured C_p and subsequently, the potential ventilation rate of a building. This dual behaviour may be a localised feature which occurs only in limited arrays, however, further research is needed to understand the driving variables and parameters behind it.

5.2.3 CIBSE wind prediction

Wind data for ventilation and C_p measurements are generally obtained from a meteorological station located away from the urban environment of interest (CIBSE, 2006). This

means that in general wind speed must be corrected for terrain conditions and for the height of the building. The equation suggested to do this is (CIBSE, 2006):

$$U_z = U_R k_c z^a \quad (5.3)$$

where U_z is the wind speed predicted at the height z , which is normally at building height. U_R is the reference wind speed measurement, often taken at 10 m. k_c and a are constants which vary depending on the terrain classification (Table 5.2).

Table 5.2:: Terrain coefficients k_c and a for equation 5.3.

Terrain	k_c	a	Source
Open, flat country	0.68	0.17	CIBSE (2006)
Country with scattered windbreaks	0.52	0.20	CIBSE (2006)
Urban	0.35	0.25	CIBSE (2006)
City	0.21	0.33	CIBSE (2006)
Sheltered City	0.03	0.45	This study

A measurement was not taken close to the building at building height so the 3.5 m ($z = 3.5$ m) measurement is used instead and assumes that the behaviour at 3.5 m will be representative of the flow at 6 m (building height). For the isolated cube (not shown), the open, flat country version of equation 5.3 produces values in excellent agreement with the measured data, but does not capture the scatter.

The open, flat country and country with scattered windbreaks coefficients over predict U_{local} for the array case (Figure 5.17). No version of equation 5.3 predicts the split of the array wind speeds, though the Urban form provides good agreement with results for $\theta_{ref} = 100^\circ$ to 150° , despite those wind directions not passing over an urban area. The City form captures trend **b** (Figure 5.8) well.

The CIBSE (2006) wind model gives a good prediction of the higher ratio trend (**b**) and the trend (**a**) which occurs when the oncoming flow is blocked by the instrumented cube using its city and urban set of coefficients respectively. However it does not predict the smaller ratios (**c**) which will lead to an overestimation of U_{local} and thus an overestimation of the ventilation rate for \sim half the time within the Silsoe array. This suggests that another set of coefficients is required for when the urban area completely shelters the building of interest. By extrapolating the values in Table 5.2 and comparing the result to the Silsoe data, a new set of coefficients for equation 5.3 was obtained. This set of coefficients is referred to as the 'Sheltered City' where $k_c = 0.03$ and $a = 0.45$ (Figure 5.17).

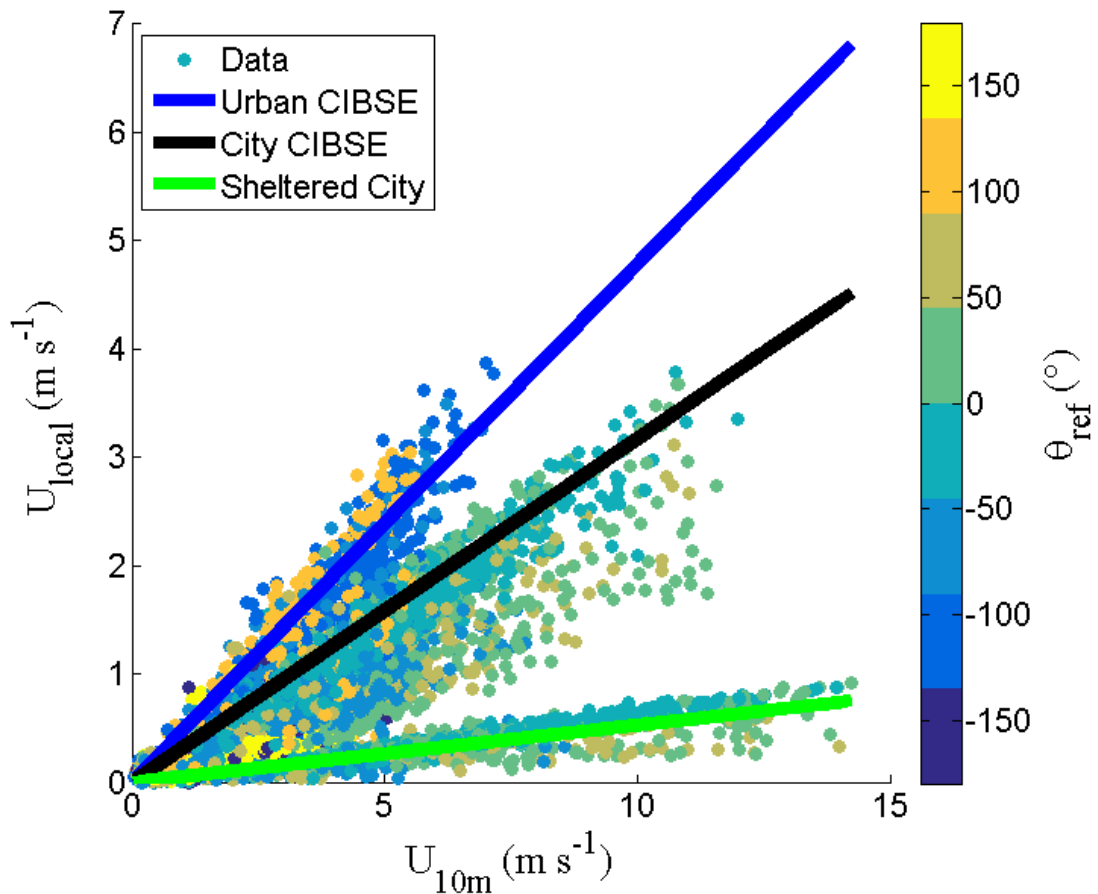


Figure 5.17: 30 minute averaged array data for all values of θ_{ref} , with the city (black) and urban (dark blue) CIBSE windspeed models being shown, along with a ‘Sheltered city’ (green) model to capture the smaller ratios between U_{local} and U_{10m} . Colour denotes reference wind angle.

The complexity occurs in knowing which model regime is the most representative for the current conditions, as the split between ratios is approximately even for the city and sheltered city cases and has not yet been linked to any variables (Section 5.2.2). Using a high estimate of U_{local} to estimate the wind driven component of the ventilation will lead to over predictions of 20-50 % for the Silsoe cube in the array

5.2.4 Comparing local wind directions to reference wind directions

Dataset used: $A(All_{All}^{All})$

The reference mast may be influenced by the array for θ_{ref} of between $\pm 90^\circ$ and $\pm 135^\circ$ where it is in the wake region (Figures 5.18, 5.6c). There is a linear relation between the θ_{local} and θ_{ref} for the isolated cube. The change in trend for θ_{ref} between -150° and -180° is due to the local mast being in the wake of the instrumented cube.

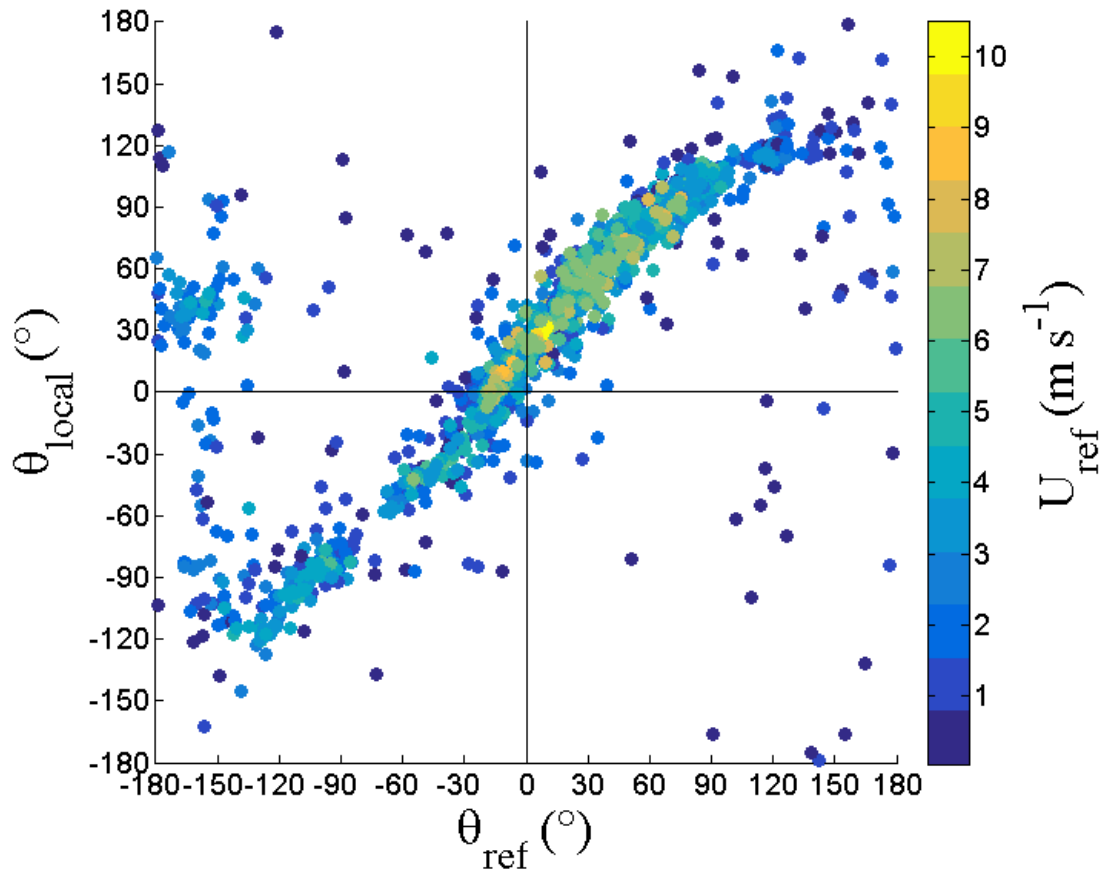


Figure 5.18: θ_{local} against θ_{ref} for all isolated cube cases (all opening configurations). Colours represent U_{ref} . Dataset: $I(All_{All}^{All})$.

The presence of the array leads to a complex relation between the two direction measurements (Figures 5.19, 5.9). The four clusters of points in each corner of the graph are due to the cyclic nature of wind direction. Starting with $\theta_{ref} = 0^\circ$, it is clear that there are two main trends present, one where θ_{local} is $\sim 30^\circ$ and one where $\theta_{local} = 120^\circ$ to 180° and $\theta_{local} = -150^\circ$ to -180° .

The second trend shows almost a complete reversal of the θ_{local} when compared to the θ_{ref} , suggesting that the recirculation regions behind the middle row of the array and perhaps the cube directly in front of the instrumented cube are having an effect on the local mast (Section 5.2.2). This behaviour is linked to a difference in turbulence intensity (Section 5.2.2), but is not linked to internal-external temperature differences, reference wind speed or atmospheric stability.

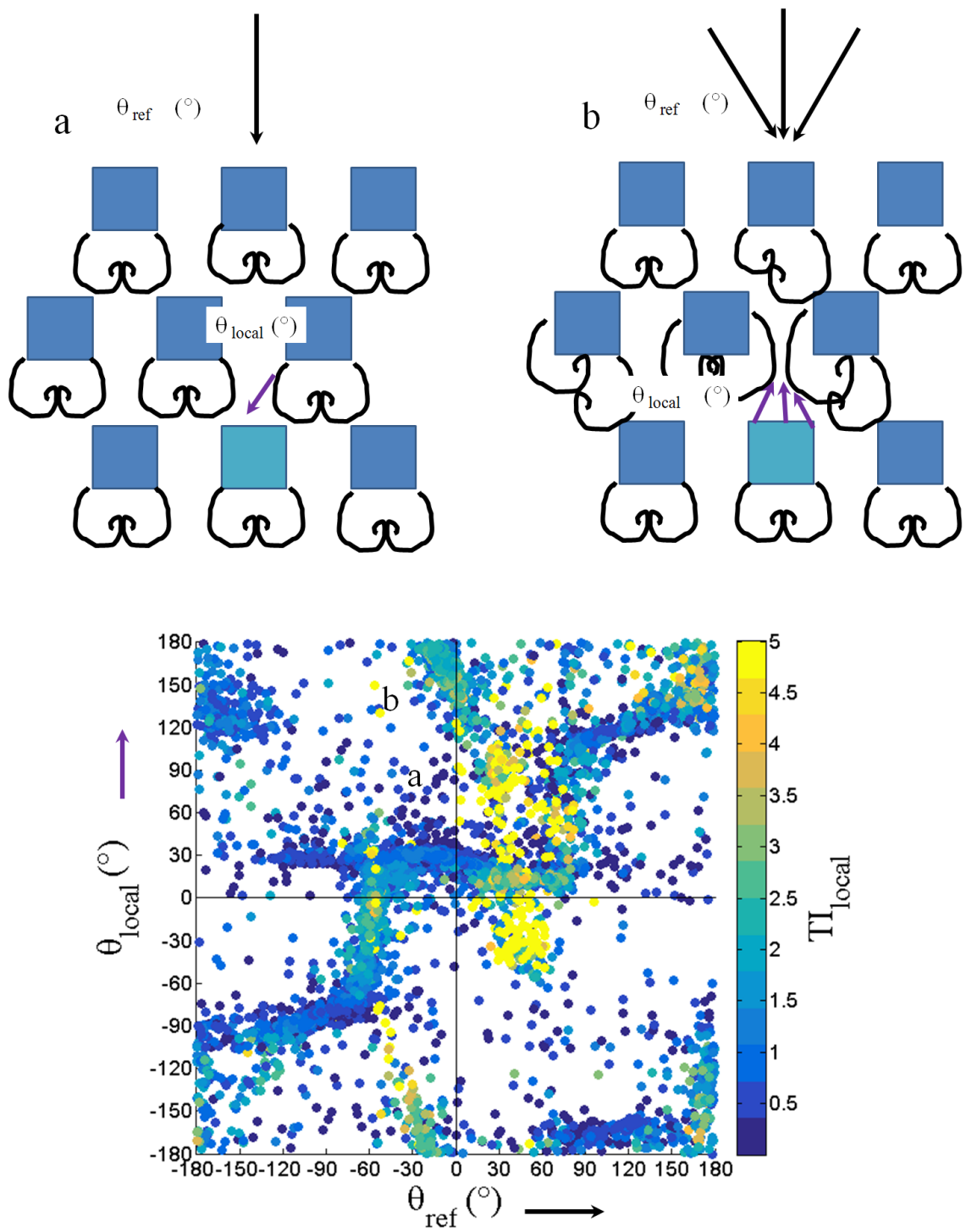


Figure 5.19: θ_{local} against θ_{ref} for dataset $A(All_{All}^{All})$ with the local turbulence intensity at 6 m (colour). Schematics are for points a and b on the graph.

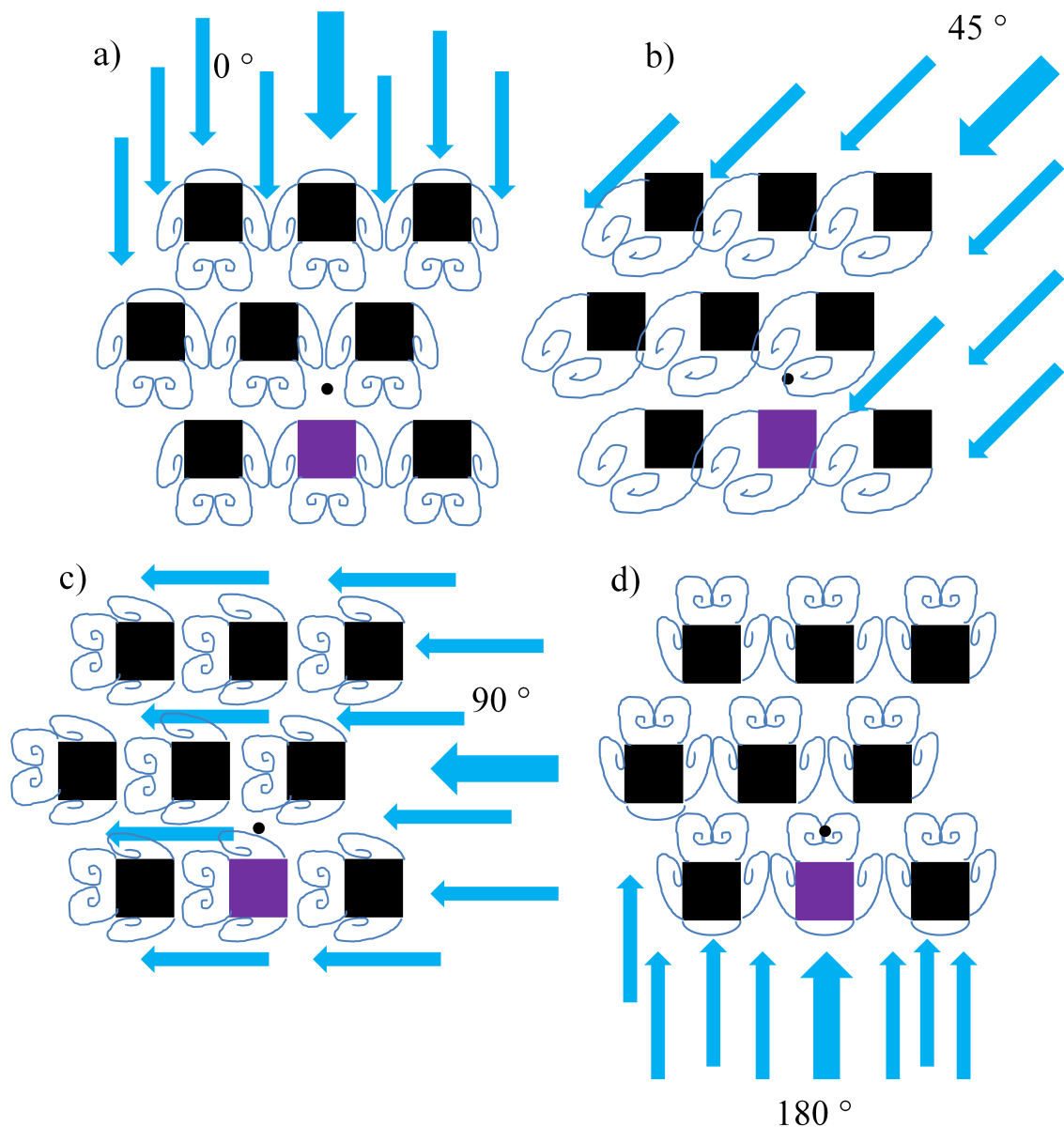


Figure 5.20: Plan view schematics of the main features of the flow around the array for $\theta_{ref} =$ a) 0° , b) 45° , c) 90° and d) 180° . Black dot denotes location of the local sonic anemometer.

For $\theta_{ref} = 30^\circ$ to 60° θ_{local} was mostly similar in direction, though there are two trends noticeable, which cause a change in θ_{local} of around 90° . It is not possible to distinguish the cause and effect of the two other trends due to a lack of data.

When $\theta_{ref} = \pm 90^\circ$ θ_{local} tends towards similar values, due to the flow being channelled down the streets of the array and being unimpeded by the array elements (Figure 5.20c). For $\theta_{ref} = 180^\circ$, similar behaviour is seen as for the isolated case, with the instrumented cube's wake affecting the mast in front of the cube (Figure 5.20d).

This variation between local and reference wind direction is also reported by Gao *et al.* (2012) for full-scale buildings located at the University of Reading campus. The

wind direction in the canyon studied was different to the observation station, which was representative of the local meteorological conditions in an open area (Gao *et al.*, 2012). This was also true for a courtyard area studied, where the turbulence created by the gaps in the neighbouring buildings caused ‘significant variations’ in local wind direction (Gao *et al.*, 2012). The two influential factors on wind direction and wind speed are the architectural layout and the local meteorology though the effects of the two factors vary for different wind directions and building set up (Gao *et al.*, 2012). For a more open case, such as the street canyon, the processes are mainly controlled by architectural factors, whereas for a semi-closed area: such as a built up area of buildings or a courtyard, the local meteorology is a large influence (Gao *et al.*, 2012).

The complexity of the flow pattern, even at half hour averaging times, demonstrates that even though the array set-up is relatively simple, there are variations with θ_{ref} , with some directions displaying dual behaviours, meaning θ_{local} cannot be accurately predicted from θ_{ref} . These dual behaviours have not been linked with any of the main variables, meaning that with the current dataset it is difficult to predict what is causing the change in behaviours. This suggests that the use of off-site meteorological datasets will lead to high errors in the local wind speed and wind direction predictions, leading to errors in C_p and ventilation rate calculations.

5.3 Influence of wind speed on pressure coefficient (C_p)

Dataset used: $I(All_{All}^{-5-5})$

Δp for use in C_p calculations is the difference between the measured pressure for each individual tap on the cube face and the reference pressure, taken on the 6 m mast using a pitot tube. Face averages are taken as the average of all taps on that face, with local C_p for the ventilation rate calculations being taken as the average of the four taps around the front and back openings minus the suitable internal pressure measurement.

The effect of turbulence intensity needs to be considered when measuring the C_p within the array, as the high levels of turbulence will influence the direction of the flow impacting the cube (Section 4.2.2), though this is more likely to be visible in the instantaneous values. It may be possible to correlate the instantaneous measurements of C_p with the gusts influencing the turbulence intensity, though this is beyond the scope of this thesis.

By comparing the results of the C_p of the Silsoe cube over a range of U_{ref} it can be determined whether or not low wind speeds should be discarded in line with the methodology used by Heijmans and Wouters (2002) and Richards and Hoxey (2012). Heijmans and Wouters (2002) and Richards and Hoxey (2012) neglected all C_p values measured under 4 m s^{-1} and 3 m s^{-1} respectively due to increased scattering, meaning there is little low wind speed C_p data for comparison.

The effect of U_{ref} will be considered for the C_p of the individual tap and the average C_p over the entire front face. There is a greater amount of scatter (a range of 1) for lower wind speeds ($< 4 \text{ m s}^{-1}$). The data were split into three categories of wind speeds: $U_{ref} < 3 \text{ m s}^{-1}$, $3 \text{ m s}^{-1} < U_{ref} < 4 \text{ m s}^{-1}$ and $U_{ref} > 4 \text{ m s}^{-1}$. The spread of data over wind direction is symmetrical with evidence of scatter for all three wind speed categories and the majority of C_p data being between 0.5 and 1.5 (Figure 5.21).

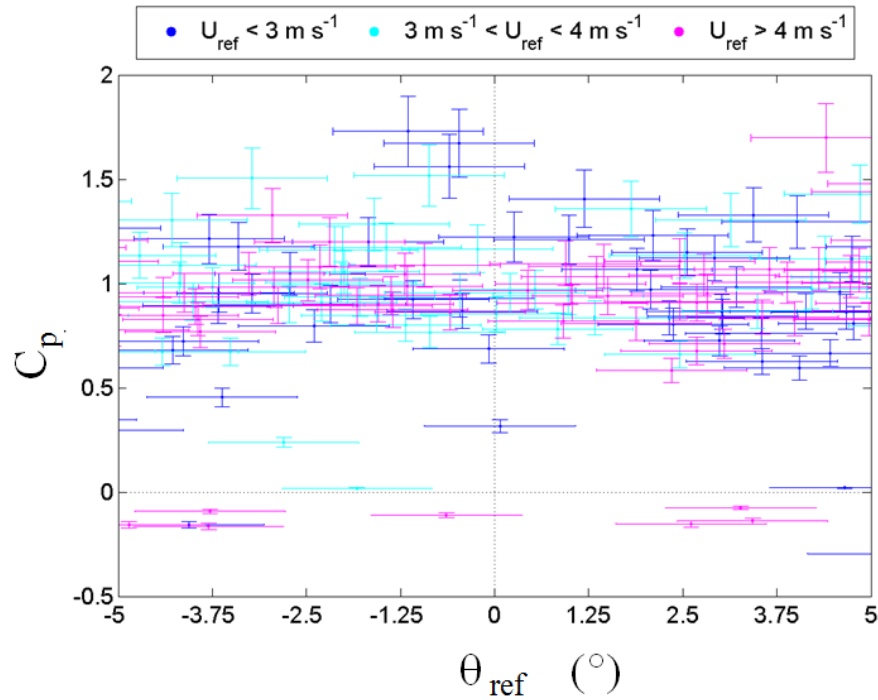


Figure 5.21: Variation of C_p for pressure tap 3 with U_{ref} and $\theta_{ref} = 0^\circ \pm 5^\circ$.

The C_p values measured for $U_{ref} < 3 \text{ m s}^{-1}$ had a larger interquartile range (IQR) (0.462) than the $U_{ref} < 4 \text{ m s}^{-1}$ (0.363) data, though all the $U_{ref} < 3 \text{ m s}^{-1}$ data were included in the set. Pressure coefficients measured for $U_{ref} > 4 \text{ m s}^{-1}$ had an IQR of 0.227, less than half that of the $U_{ref} < 3 \text{ m s}^{-1}$ data. The higher wind speeds have less variation in C_p than low wind speed cases (Table 5.3), in agreement with work undertaken by Heijmans and Wouters (2002).

To determine whether the three datasets are statistically similar or different, F and T tests are used (Appendix M) to compare the $U_{ref} < 3 \text{ m s}^{-1}$ with the $U_{ref} < 4 \text{ m s}^{-1}$ dataset, the $U_{ref} < 3 \text{ m s}^{-1}$ with the $U_{ref} > 4 \text{ m s}^{-1}$ dataset and the $U_{ref} < 4 \text{ m s}^{-1}$ with the $U_{ref} > 4 \text{ m s}^{-1}$ dataset. For all F-tests the null hypothesis cannot be rejected (95 % certainty), meaning that the variances of the data are likely to be equal, which can also be seen in the standard deviation values (Table 5.3). The two tail T-test results for equal variances also suggested that the null hypothesis (the means of the two datasets are equal), cannot be rejected (95 % certainty). These results also remain true when 97.5 % certainty is tested ($\alpha = 0.025$).

Table 5.3: Mean, standard deviation (σ), range and interquartile ranges (IQR) of the C_p values for the three different wind speed datasets for the front face average

	Mean	σ	Range	IQR
$< 3 \text{ m s}^{-1}$	0.477	0.230	1.297	0.242
$< 4 \text{ m s}^{-1}$	0.503	0.220	1.057	0.119
$> 6 \text{ m s}^{-1}$	0.519	0.207	1.297	0.209

The results of the F and T tests for the front face average suggest that there is little difference between the data for $U_{ref} < 4 \text{ m s}^{-1}$ and the $U_{ref} < 3 \text{ m s}^{-1}$ data. For this reason, $U_{ref} > 3 \text{ m s}^{-1}$ Dataset: $All(All_M^{All})$ will be used for the analysis of C_p unless the effects of stability are being considered. This lower wind speed threshold for U_{ref} allows for a larger, more meaningful dataset which covers a larger range of conditions. Lower U_{ref} values are also likely to be more representative of a building in an urban area.

For the isolated $U_{ref} < 3 \text{ m s}^{-1}$ data, C_p on the front face is 0.1 higher than for $U_{ref} > 3 \text{ m s}^{-1}$, due to U_{ref} being used to ‘normalise’ the pressure readings from the pressure tap (equation 2.28). However, the errors on the average C_p values for each tap overlap, suggesting that there is no meaningful difference between the two cases, with both showing the same trends and tendencies across the faces with little difference, especially for the back face. The horizontal path (Figure 5.22b) shows differences of 0.1 to 0.2 in C_p for the front face, possibly due to the positioning of the neutral pressure zone being approximately half cube height. High and low wind speed C_p averages are within standard error for the front and back faces.

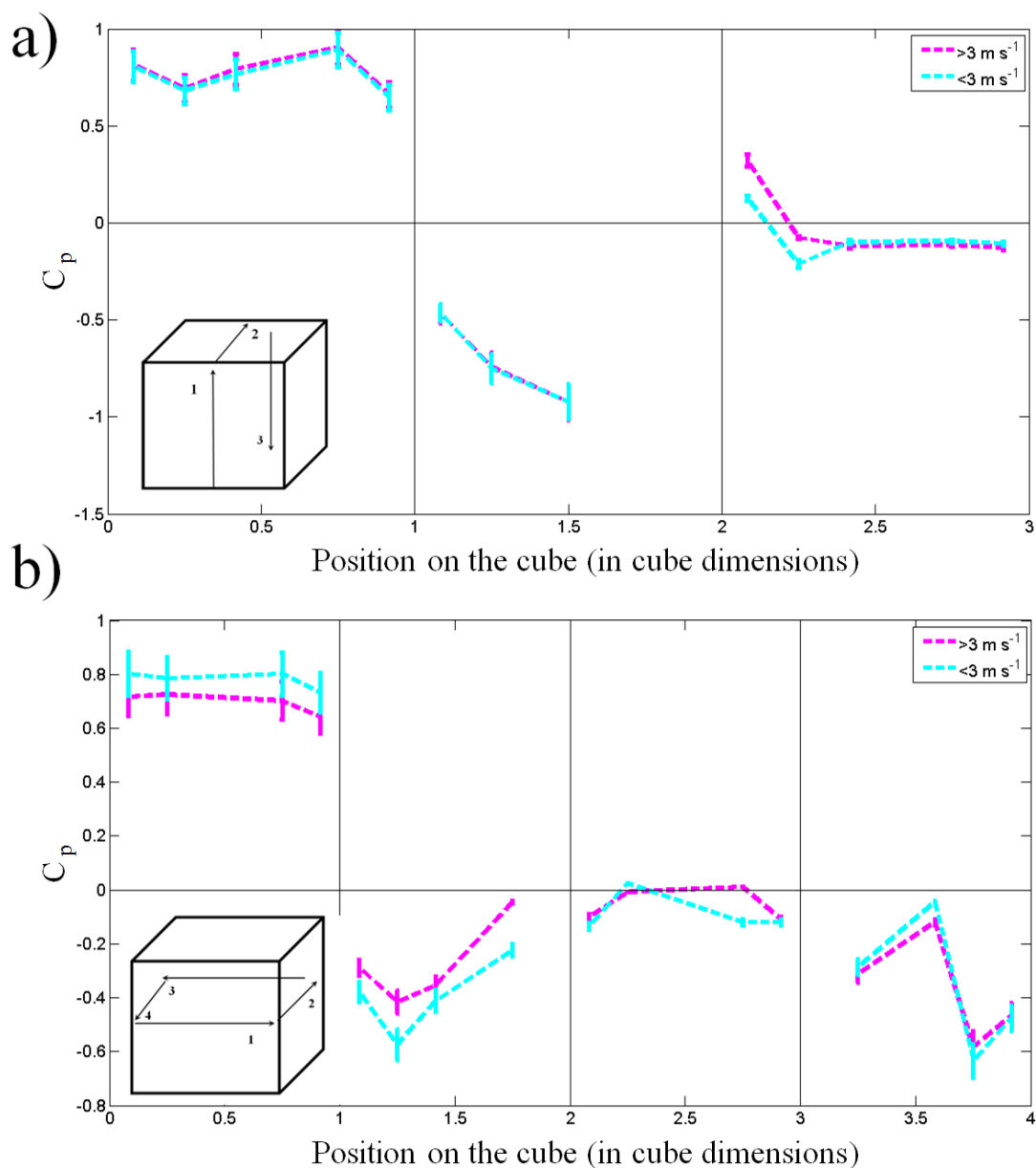


Figure 5.22: Average C_p at each pressure tap in the a) vertical array on the front face, roof and back face and b) horizontal array around the cube at half cube height split for high ($U_{ref} > 3 \text{ m s}^{-1}$) and low ($U_{ref} < 3 \text{ m s}^{-1}$) wind speeds for the isolated cube. The error bars on both plots denote the standard error of the C_p . Data are limited to $\theta_{ref} = 0^\circ \pm 10^\circ$ (Section 5.5).

There is a difference (0.1) between low and high U_{ref} cases for the vertical trace and for some points on the horizontal trace of C_p for the array case. Due to the low values of the average C_p for the array case it is difficult to draw any strong conclusions (Figure 5.23).

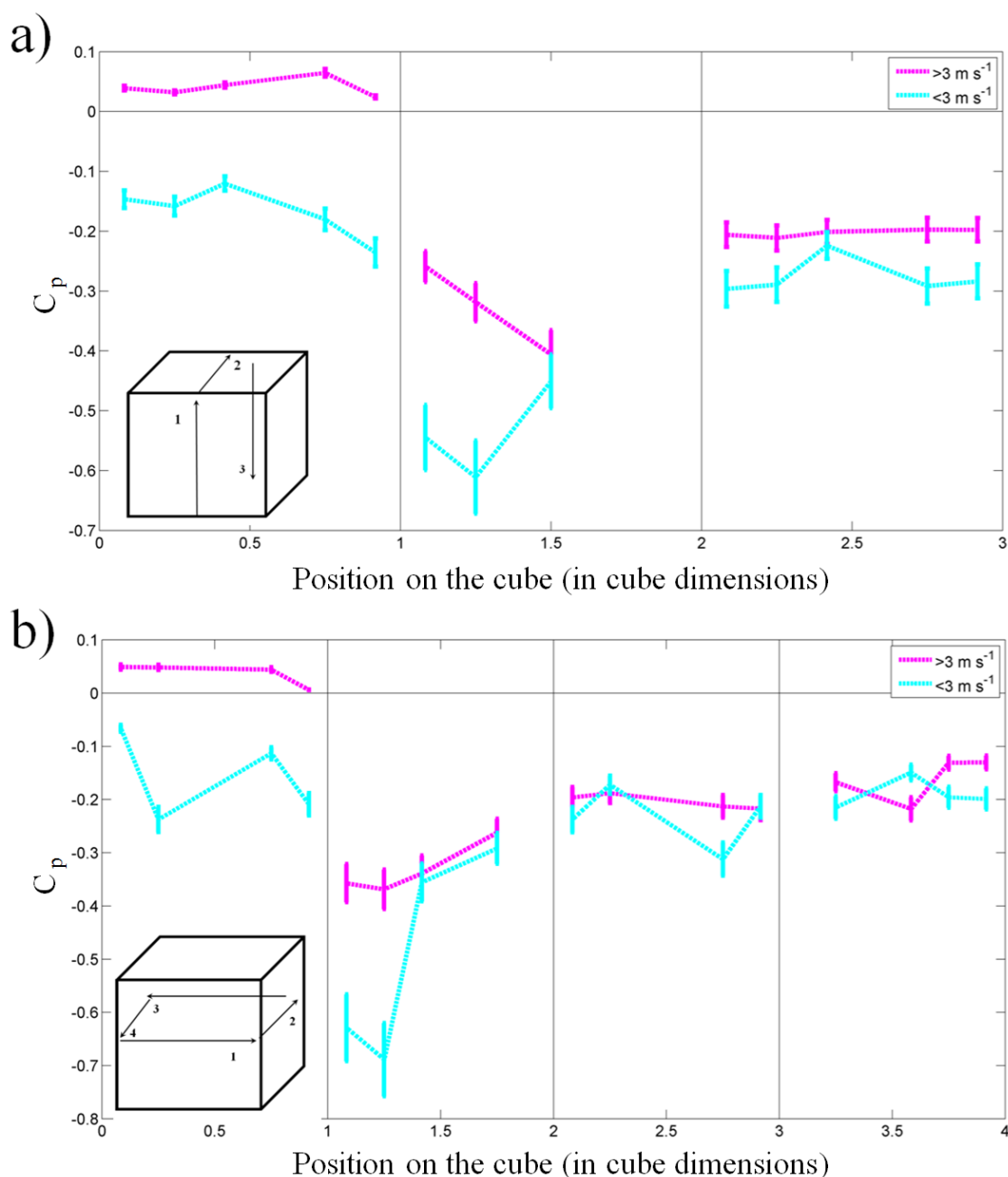


Figure 5.23: As Figure 5.22, but for the array case.

However, one cause of the much smaller C_p for $U_{ref} < 3 \text{ m s}^{-1}$ could be due to the effect of the array on U_{local} . There is not a 1:1 ratio between U_{ref} and U_{local} and even for $\theta_{ref} = 0^\circ$ to 10° , there are two clear relations (Figures 5.8, 5.13).

When $U_{ref} = 3 \text{ m s}^{-1}$, U_{local} is between 0.5 m s^{-1} and 1.5 m s^{-1} , causing lower surface pressure on the cube face due to the U^2 term being proportionally larger (leading to a reduced C_p). A difference of -0.2 can be seen across the roof of the cube, potentially due to a strong roof recirculation region forming that is not destroyed by high winds and thus increases suction on the roof. Like the isolated case there is good agreement

between low and high wind speed cases for the back face.

The horizontal path (Figure 5.23b) indicates a difference of 0.25 between $U_{ref} > 3 \text{ m s}^{-1}$ and $U_{ref} < 3 \text{ m s}^{-1}$ on the south cube face (1-2). This could be caused by a change in flow structure on the Front-South corner of the cube due to low wind speeds. The negative sign of the average C_p suggests suction or reverse flow occurs in this area for low wind speeds but not for high wind speeds. High and low U_{ref} C_p averages are within standard error of each other for the front and north faces.

In conclusion, the effect of low wind speeds ($U_{ref} < 3 \text{ m s}^{-1}$) is less pronounced for the isolated case for $\theta_{ref} = 0^\circ \pm 10^\circ$, due to the near 1:1 ratio between the U_{local} and the U_{ref} . Some differences may occur due to the pressure taps reaching sensitivity limits. However, low wind speed array cases are substantially different to high wind speed array cases, with more suction being present on the roof and a potentially altered structure on the south face, which appears to be caused by low wind speeds. The differences are due to the altered relation between U_{local} and U_{ref} (Figure 5.8).

For the array case the surface pressure is reduced due to reduced U_{local} , though C_p is still normalised by using U_{ref}^2 (equation 2.32), meaning that the overall value of C_p is reduced more so than for the isolated case.

Only high wind speed cases ($U_{ref} > 3 \text{ m s}^{-1}$) will be considered in the following chapters (Dataset: $All(All_M^{All})$). This difference also has implications for the use of wind tunnel data as reference data for buildings within an urban area; unless the relation between U_{ref} and U_{local} can be determined, C_p is likely to be overestimated by existing models. Low U_{ref} values are correlated with low U_{local} values within the array, which lead to a wide range of turbulence intensity values (0.1 - 5) within the local vicinity of the instrumented cube (Section 4.2.2).

5.4 The effect of stability on C_p

As C_p is sensitive to the oncoming flow structure, it is hypothesised that unstable conditions will lead to higher pressure coefficients when compared to equivalent near-neutral conditions, due to the higher wind speed impacting on the cube for the equivalent height and the change in the oncoming flow structure due to the presence of shear. Due to the Silsoe cube having a height to width ratio of 1 this research is applicable only to low rise buildings.

5.4.1 Isolated cases

Dataset used: $I(All_{All}^{-45-45})$

A ratio was taken of pressure tap 4, located just above the front opening and pressure tap 2, between the opening and the base (Figure 5.24). Taps 1 and 5 were not used due to

the influence of long grass (Tap 1) and the complex flow behaviour near the roof (Tap 5). By taking a ratio of two taps, it allows for an understanding as to how the stability of the atmosphere alters the vertical pressure distribution across the front face of the cube. A ratio under 1 means that the higher pressure occurs at tap 4, which would be associated with unstable conditions and over 1 suggests the higher pressure is positioned lower on the cube, at tap 2.

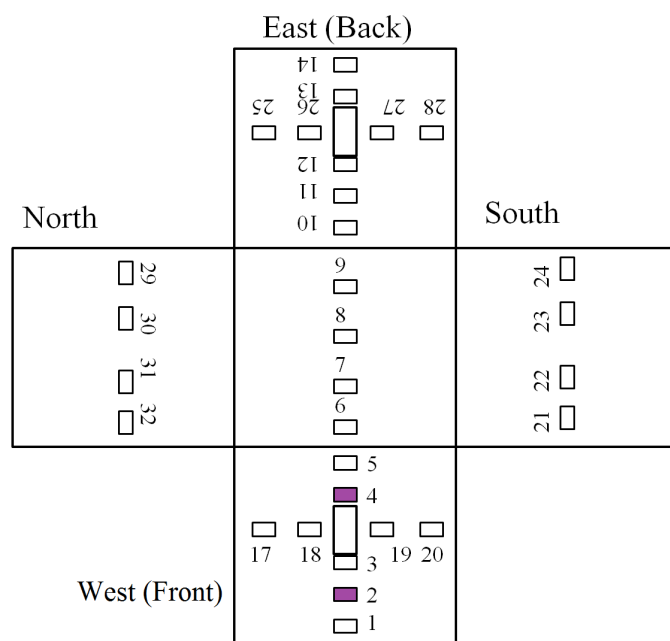


Figure 5.24: Location of the surface pressure taps. Taps 2 and 4 are highlighted (purple).

There is a large spread of pressure ratios for near-neutral conditions (1.1 to $1.6 \pm 5\%$) due to local effects. The ratio is larger for stable conditions, and smaller for unstable conditions with a linear relation between ratio and stability. The large amount of scatter could be attributed to the inclusion of low U_{ref} values (Section 5.3). There is very little difference in the distribution of near-neutral cases with high wind speeds (Figure 5.25a) and near-neutral cases with low wind speeds (Figure 5.25b). The low wind speed, stable pressure coefficients (Figure 5.25e) are $\sim 20\%$ smaller than the equivalent near-neutral cases (Figure 5.25b), though the distribution pattern is similar. Unstable high wind speed cases (Figure 5.25c) have larger pressure coefficients by 0.1 than the near-neutral high wind speed cases (Figure 5.25a). The distribution also appears more uniform, possibly due to the higher levels of turbulence being lost over the 30 minute averaging period. The low unstable case (Figure 5.25d) is somewhat anomalous, possibly due to a low number of cases (20). Also of note is the behaviour of the top pressure tap (tap 5), which remains at a similar value regardless of the stability type, suggesting that the flow separation which occurs close to the roof is not influenced by the stability of the atmosphere (correlation coefficient of 0.039).

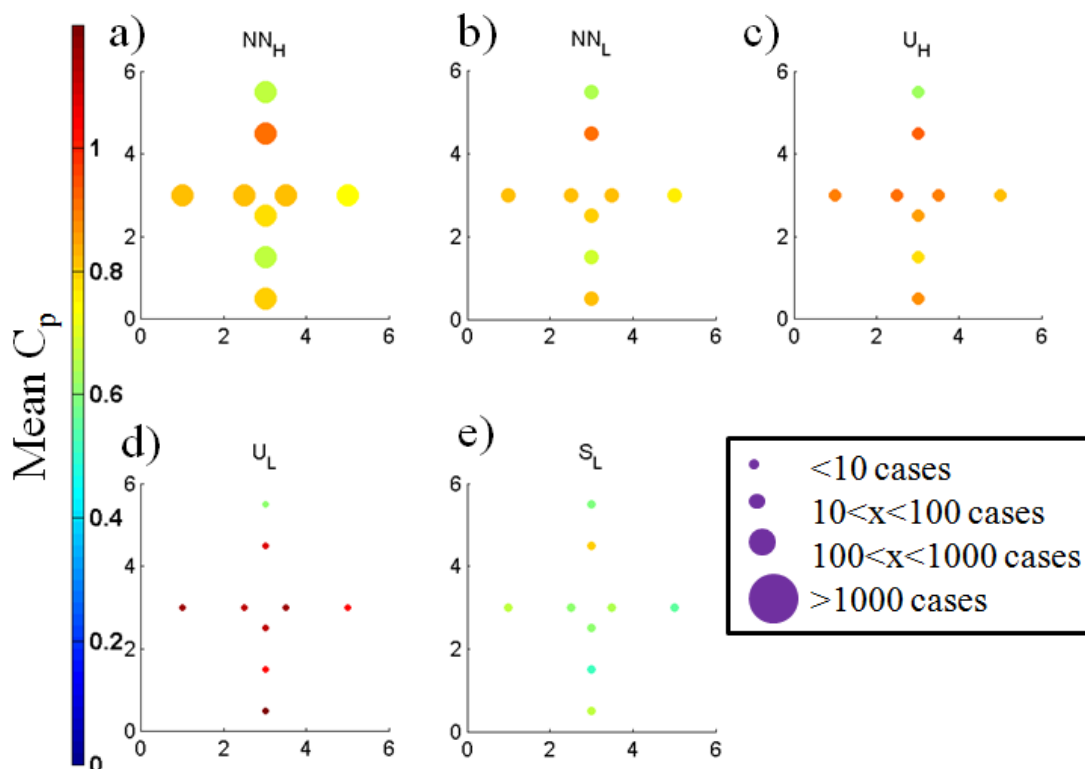


Figure 5.25: Mean C_p (colour bar) at each pressure tap on the front face for a range of atmospheric and wind speed conditions for the isolated cube. The points are positioned at the approximate location of the pressure taps on the front face of the cube. Near-neutral (NN), unstable (U) and stable (S). The subscript on these represent the category of U_{ref} : H ($U_{ref} > 3 \text{ m s}^{-1}$) and L ($U_{ref} < 3 \text{ m s}^{-1}$). The size of the dot is indicative of the relative amount of data points included in the average.

There is good agreement between all stabilities for the roof and north faces, with near-neutral and unstable cases showing agreement for all faces in the horizontal and vertical (Figure 5.26). However, the stable case deviates, despite large standard errors on the points. This deviation cannot be explained by the low U_{ref} values, as the opposite behaviour would be expected (Figure 5.23). This suggests that the effect of stability is only likely to be seen in the behaviour of individual taps or through the ratio of two vertical taps. Whilst it is clear that stability has an effect on the C_p distribution which can be seen through analysis of individual taps, C_p guidance such as that given by AIVC and ASHRAE is in the form of face averages often measured in near-neutral conditions (Swami and Chandra, 1987).

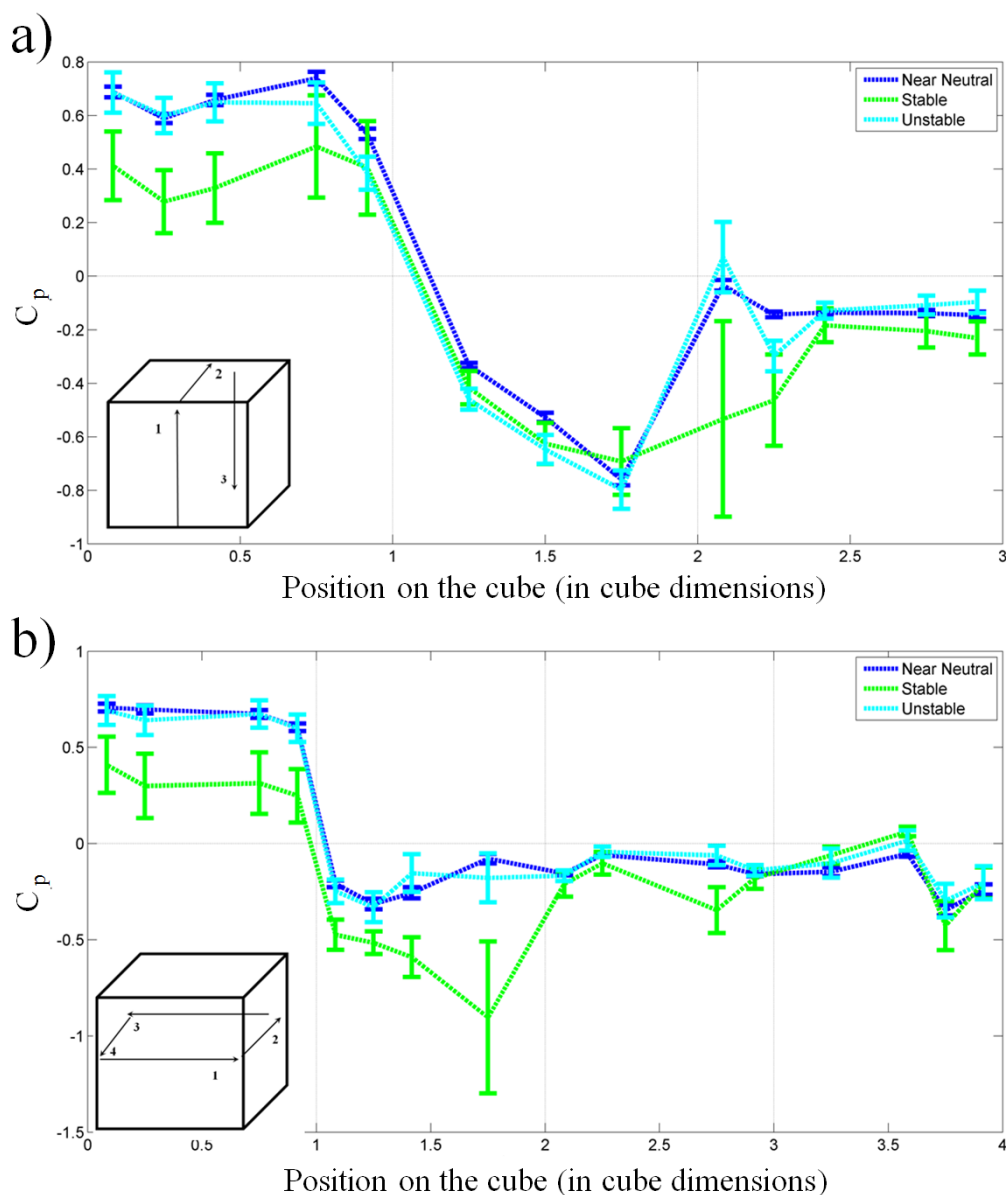


Figure 5.26: Average C_p for each tap a) up the front of the cube (0-1), along the roof (1-2) and down the back (2-3) split for different stabilities, b) on the horizontal path across the front face (0-1), along the south face (1-2), around the back face (2-3) and across the north face (3-4) at half cube height split for different stabilities. Standard error are shown as error bars. Dataset: $I(All_{All}^{-45-45})$.

An average of the nine pressure taps located on the front face of the cube for dataset $I(All_{All}^{-10-10})$ was taken. All were given equal weighting in the average. There is little trend with stability (Figure 5.27). F-Test results suggest that the variances in C_p for near-neutral, stable and unstable cases can be considered to be equal though, the means can not be considered similar, due to the small sample size of the stable and unstable cases (< 20) and the effect of low wind speed on the face averaged C_p .

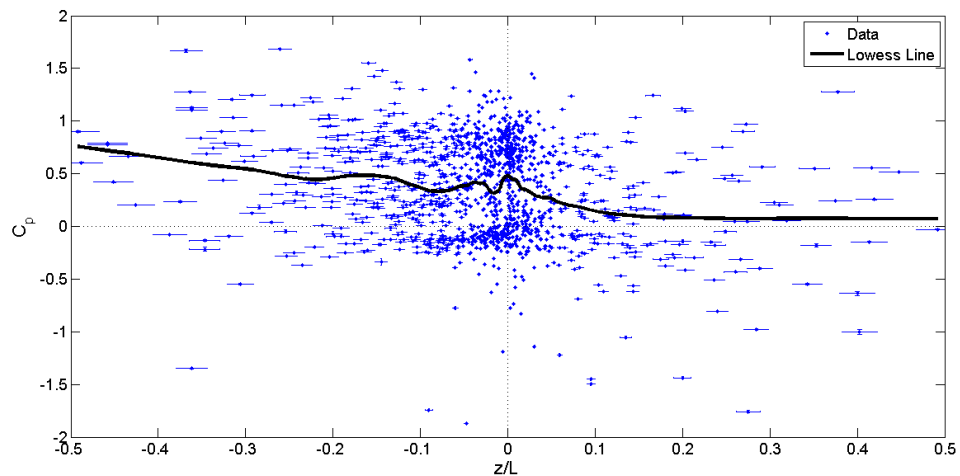


Figure 5.27: Front face averaged C_p over a range of stabilities. Error bars are 5 % for the stability measurements due to the difficulty quantifying the errors and the error on C_p is the standard error. A Lowess curve is shown. Dataset: $I(All_{All}^{-10-10})$.

5.4.2 Array cases

Dataset used: $A(A_{all}^{-45-45})$

There is a wide spread of values obtained for the ratio of pressure tap 2 to 4 for near-neutral stabilities for the array (0-5) (not shown). The large spread is likely related to the influence of the array and the difference in θ_{local} and θ_{ref} from outside the array. The array dataset is also larger, with some scatter caused by the inclusion of low wind speeds.

The reduced magnitude of C_p on the front face due to the array make it difficult to discern any patterns especially with the error on C_p being similar to the measured values (Figure 5.28). For the near-neutral high U_{ref} cases, the highest recorded C_p is positioned above the opening, with the top pressure tap (tap 5) being affected by the roof recirculation. There is little, if any, discernible difference between low wind speed near-neutral cases, low wind speed unstable cases and low wind speed stable cases. This suggests that if $U_{ref} < 3 \text{ m s}^{-1}$ for a $\theta_{ref} 0^\circ \pm 45^\circ$ to the perpendicular, the array reduces U_{local} further (Section 5.3) reducing the front face pressure.

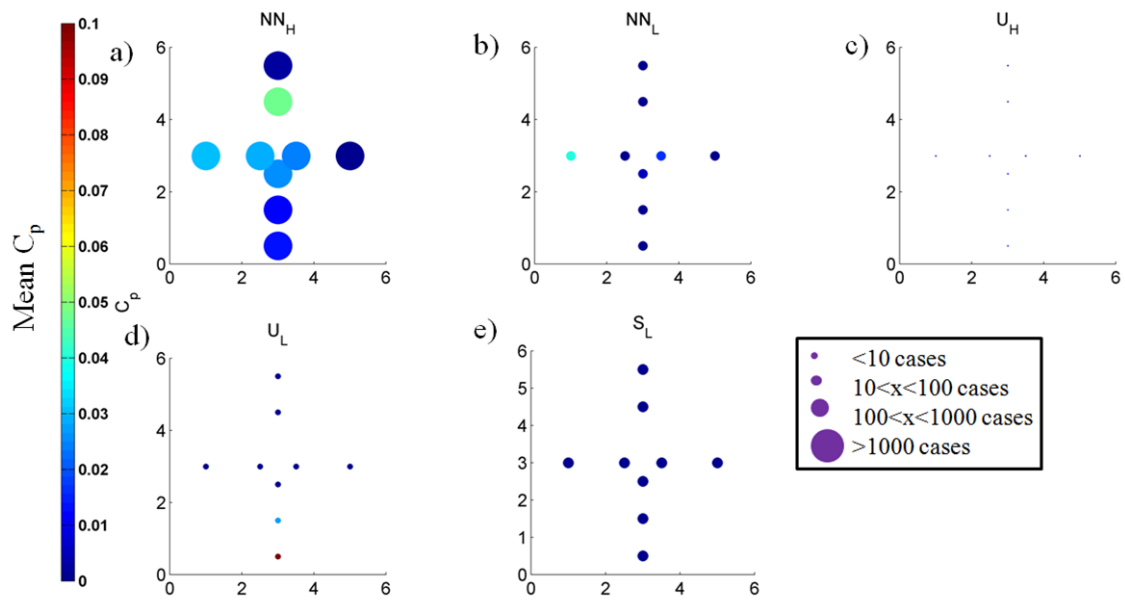


Figure 5.28: As Figure 5.25 but for the array.

Like for the isolated cube, there is no correlation between stability and the front face averaged C_p for dataset $A(All_{All}^{-10-10})$ (Figure 5.29). The values for unstable cases are also sparse, making it difficult to draw a trend line through the entire stability range. F and T tests reveal that the variance in near-neutral and stable cases, and the variance in near-neutral and unstable cases are likely to be unequal, with the variance in near-neutral and unstable cases being equal. The unequal variances could be due to wind speed effects on the cube. The means of the near-neutral and stable datasets and the means of the near-neutral and unstable datasets are unequal, with the means of the stable and unstable datasets likely to be equal. This is likely to be caused by the large spread in near-neutral values and the large range of U_{ref} to capture the three stabilities.

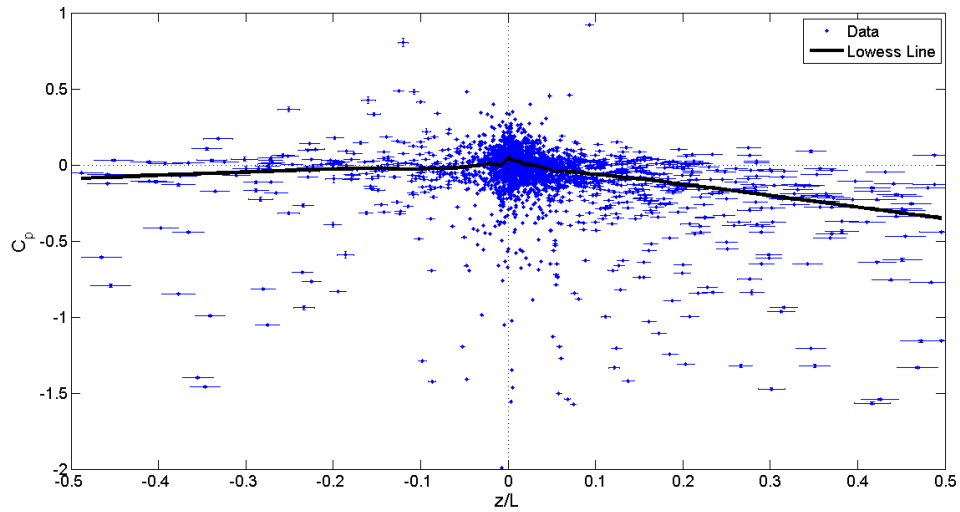


Figure 5.29: As Figure 5.27 but for the array. A Lowess curve is shown. Dataset: $A(All_{All}^{-10-10})$.

The array cases are filtered for θ_{ref} and not θ_{local} . For the isolated case there is little difference between the θ_{ref} and the θ_{local} , but this is not true for the array case. The number of unstable samples for $\theta_{local} = 0^\circ \pm 10^\circ$ is five. All variances are likely to be unequal, though the means of the near-neutral and unstable datasets are likely to be similar, as are the means of the stable and unstable dataset, though this is related to the low number of samples in the unstable dataset. The 30 minute average for θ_{local} has a large standard deviation (a range of 20° to 150° over the entire array dataset) which will affect the relevance of the data.

In conclusion, stability effects are not likely to be discernible for a front face average for both an isolated building and a building within the array, due to the comparatively stronger effects of the local flow, building shape and the averaging out of each individual taps unique behaviour. The reduction in measured C_p due to the presence of the array makes it difficult to draw any conclusions about the effect of stability, especially considering the instrument error which may occur when $U_{ref} < 3 \text{ m s}^{-1}$ and for low pressure readings. Whilst stabilities have an effect on the structure of the boundary layer, the effect on C_p is masked by other more dominant effects, such as θ_{ref} (Section 5.5) and U_{ref} (Section 5.3).

The assumption of near-neutral conditions within an urban area is valid due to the building induced turbulence dominating the flow, reducing the buoyancy effects in the local area (Lundquist and Chan, 2007). However, once downwind of the urban area, in the wake region, the building induced turbulence subsides, meaning that the assumption that near-neutral conditions can be assumed is less valid (Lundquist and Chan, 2007). The effect of the surrounding buildings on local external temperature should also not be neglected as this thermal effect may be stronger than the influence of the boundary layer stability.

5.5 Influence of wind direction on C_p

Whilst full-scale C_p data for the Silsoe site exists (e.g. Straw (2000), Yang (2004) and Richards *et al.* (2001)), the data are limited and cannot easily be compared to the large data-set gathered in this study. There are no full-scale data for the array available in the referenced literature.

5.5.1 Isolated case

For an isolated cube, the largest values of C_p occur when the oncoming flow is perpendicular to the front face, with values of 0.6 to 0.8 for $\theta_{ref} = 0^\circ \pm 60^\circ$ (Figure 5.30). The shape is roughly symmetrical with $\theta_{ref} = 0^\circ$ as the centre point, with C_p decreasing as the θ_{ref} moves away from perpendicular, turning negative for $\theta_{ref} = -90^\circ$ to -180° and at $\theta_{ref} = 100^\circ$ to 120° . It is unlikely that there will be complete symmetry, due to the presence of the storage shed in the positive wind directions (Figure 5.6). When the wind is parallel to the front face from the direction with the storage shed ($\theta_{ref} = 90^\circ$) the C_p is less than 0.1 whilst at $\theta_{ref} = -90^\circ$ it is around -0.2, though there are less data points for this wind direction.

LES modelling of an extensive staggered array (Ikegaya *et al.*, 2016) for $\theta_{ref} = 0^\circ$, shows similar values for the maximum C_p on the front face (0.28), though the location of the maximum C_p is not shifted to the side as seen in the wind tunnel data (Section 4.10). As the array modelled by Ikegaya *et al.* (2016) had a H_m/W ratio of 0.3, there was proportionally more space between the rows and the oncoming flow so they are unaffected by the wakes of the upwind array elements.

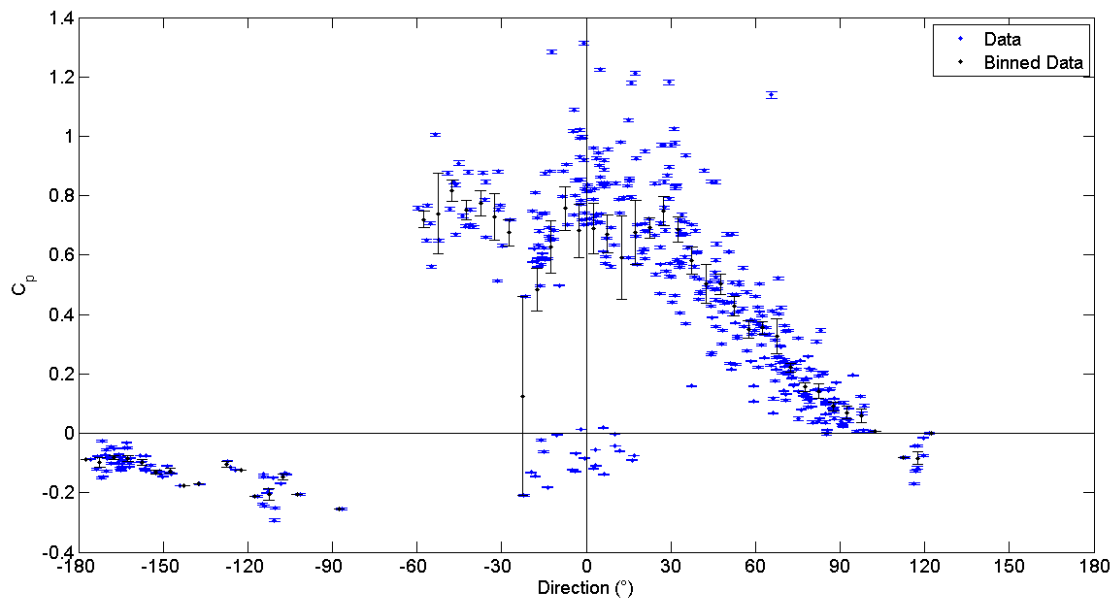


Figure 5.30: Front face average C_p with the error bars (instrument error) and the standard deviation away from the calculated mean (black) with the front face averaged C_p binned into $5^\circ \theta_{ref}$ bins with the error bars representing the standard error of each bin.

5.5.2 Low C_p values on the front face

A cluster of negative points (~ 30) of between 0 and $-0.2 C_p$ are visible, with apparently little error (Figure 5.30). Investigation into the relation between U_{ref} and U_{local} and θ_{ref} (Sections 5.2.2 and 5.2.4) confirms that there is no measurable difference in wind speeds or wind directions for these times. θ_{ref} varied between -22° to 17° during the periods of interest, suggesting that there is not a problem with averaging of the wind direction. All cases occurred on the 5th June 2015 (cross ventilated cube). No connection was found between the low front face averaged C_p and internal wind speed, wind direction, stability, atmospheric pressure, internal temperature or external temperature or temperature difference. No errors were reported on the day, though a power cut did occur at approximately 20:00 which caused all instruments to cease logging. There was no link between the synoptic conditions of the day and the behaviour observed.

5.6 Comparison of isolated and array C_p values

In general, the isolated cube C_p values are larger than those for the array, with the array acting to reduce the pressure difference between the front and back face (Figure 5.31). When the array is present and the $\theta_{ref} = 0^\circ$, the array reduces C_p to near zero, a difference of 0.8 to 1.2 from the isolated case (Figures 5.6, 5.20). Variations within the isolated case

are caused by stability and turbulence effects. The peak for the array cases at -45° is associated with the asymmetry of the array with the flow penetrating into the array from this angle (Figure 5.20b). The front face averaged C_p decreases at $\theta_{ref} = 45^\circ$ becoming negative suggesting suction is present.

For $\theta_{ref} = \pm 180^\circ$, there is little difference for the isolated and array cases, due to the back of the cube still being exposed, meaning that the back face records differences of 0.1 or less for these wind directions (Figure 5.20d). The effect of the array is also minimal for $\theta_{ref} = \pm 90^\circ$ for the front and back faces, as the oncoming wind is parallel (Figure 5.20c). The array reduces the C_p averaged over the front face by 0.3 to 0.6 for $\theta_{ref} = 0^\circ \pm 30^\circ$ as the shielding is greatest in this direction.

For the north face there is a reduction of 0.3 in the over all face averaged C_p with the south face seeing a reduction of around 0.4 when $\theta_{ref} = -90^\circ$. This shows that the cubes adjacent to the instrumented cube impact on the sides, with the wake region of those cubes, rather than the reference flow impacting on the North and South sides.

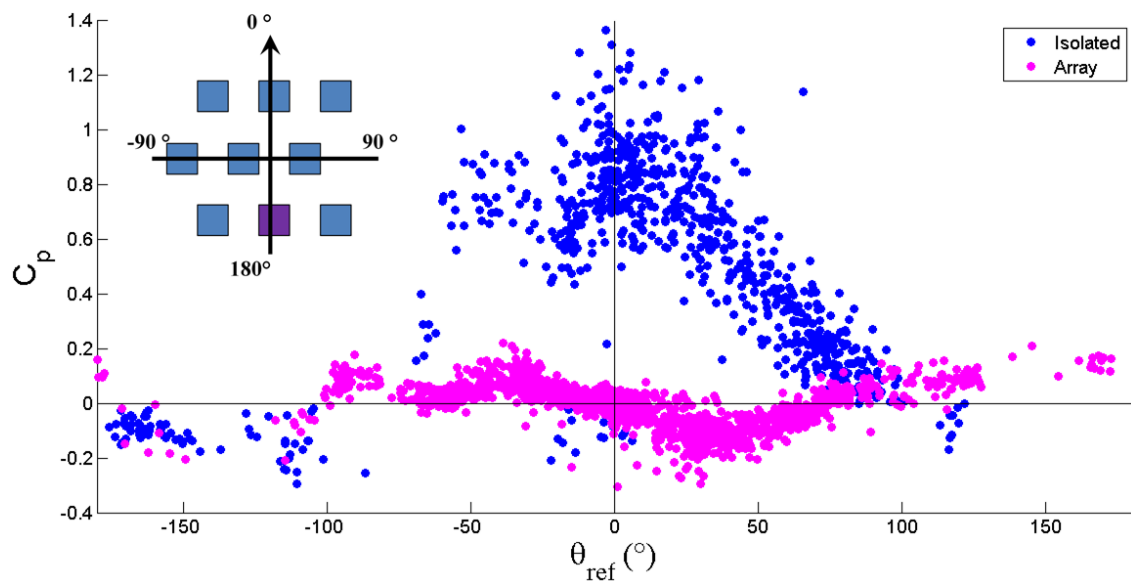


Figure 5.31: The front face averaged C_p for the isolated and array cases. Dataset: $All(All_M^{All})$.

This set of full-scale results shows the importance of not using a C_p dataset beyond its intended purpose, as inaccuracies occur due to the building layout not being uniform. It may contain features that will influence the C_p in unpredicted ways. Moving any cube within the array, even by a small amount is likely to alter the flow patterns, due to changes in channelling locations and shielding.

5.6.1 C_p differences between array and isolated cases for a range of wind directions in near-neutral conditions

Dataset: $All(NN_M^{All})$ (Number of 30 minute cases: 609 for the isolated cube and 2489 for the array).

The array has the greatest effect on the front face at $\theta_{ref} = 0^\circ$, due to the instrumented cube being fully shielded by the array from this wind direction (Figure 5.32a). The difference between the isolated and the array C_p values for this direction is 0.8. The difference between isolated and array decreases as θ_{ref} moves from 0° to 90° and 0° to -90° . Due to the lack of data for the negative arc, it is hard to determine whether the change in C_p with θ_{ref} is symmetrical for both sides. Close to $\theta_{ref} = 90^\circ$ the difference between array and isolated decreases to 0.1 - 0.2, due to the wind being parallel to the array (Figure 5.20c). This is also likely to be the case for $\theta_{ref} = -90^\circ$. For $\theta_{ref} = 90^\circ$ to 120° the difference becomes negative on the front face, suggesting that the array decreases the pressure difference across the instrumented cube due to the increased pressure on the front face.

For the back face, the large difference of 1.4 between isolated and array C_p is due to the array fully blocking the flow at $\theta_{ref} = 180^\circ$. Like the front face, the difference between isolated and array is at around 0 to 0.1 at $\theta_{ref} = 90^\circ$ and potentially $\theta_{ref} = -90^\circ$. The minimum difference at $\theta_{ref} -60^\circ$ is due to the array C_p being close to 0 and the isolated C_p being around -0.5. For $\theta_{ref} = 0^\circ$ to 90° there is little effect on the back face due to it being exposed.

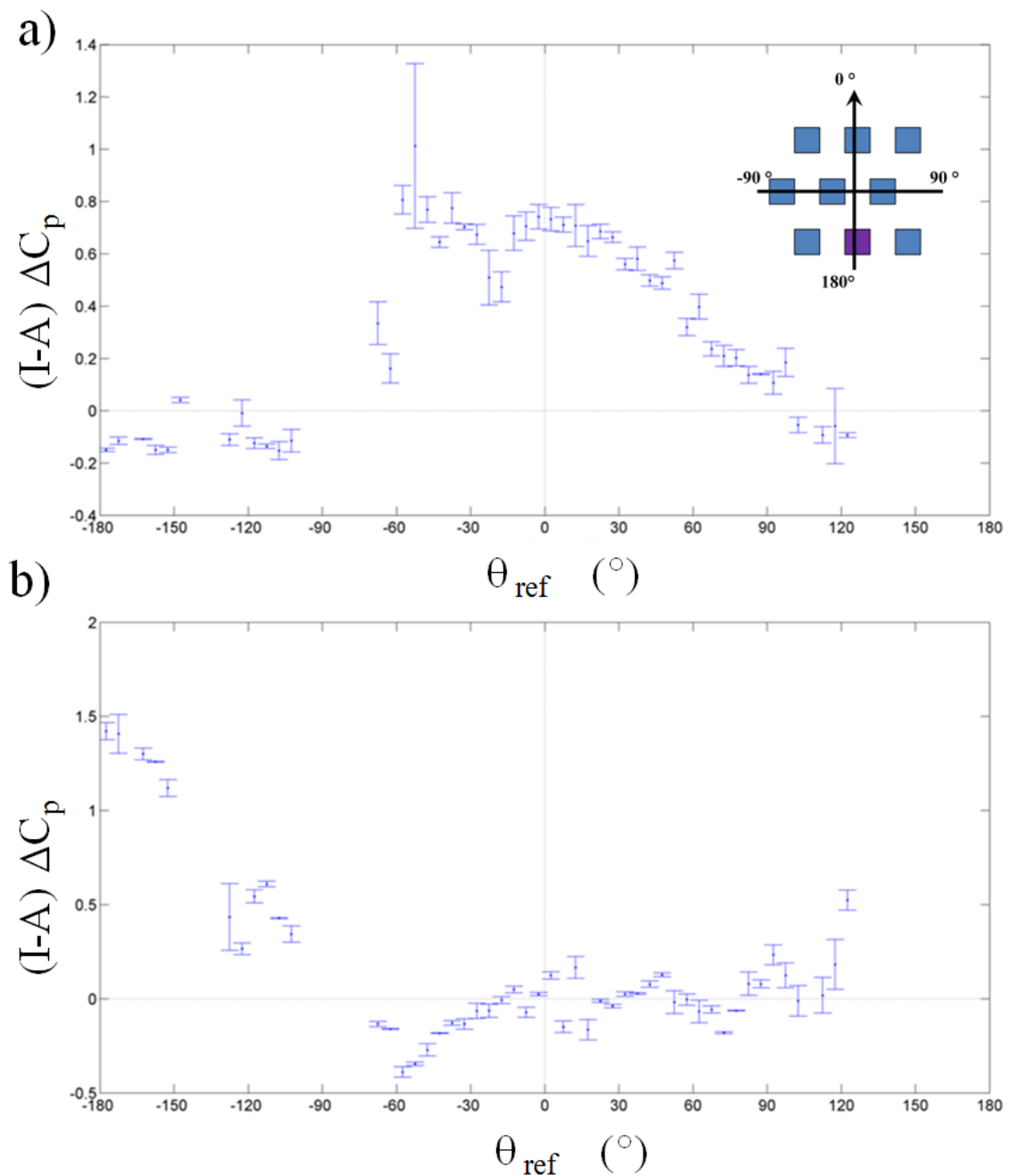


Figure 5.32: Comparison of the binned isolated (I) and array (A) C_p data for the (a) front face and (b) back face. Error bars are the error in the difference, based on the standard error of the isolated and array binned data. Data are binned into θ_{ref} 5° bins with the standard error being calculated for each bin. Then the difference between the isolated and array bins is found. Bins with less than 3 cases are omitted.

The side faces show a symmetry with their respective perpendicular θ_{ref} , with the maximum difference for the north face (Figure 5.33a) being at $\theta_{ref} = 90^\circ$ and at $\theta_{ref} = -90^\circ$ for the south face (Figure 5.33b), due to the adjacent cubes in the array. The north face records positive values when the south face records negative values of C_p .

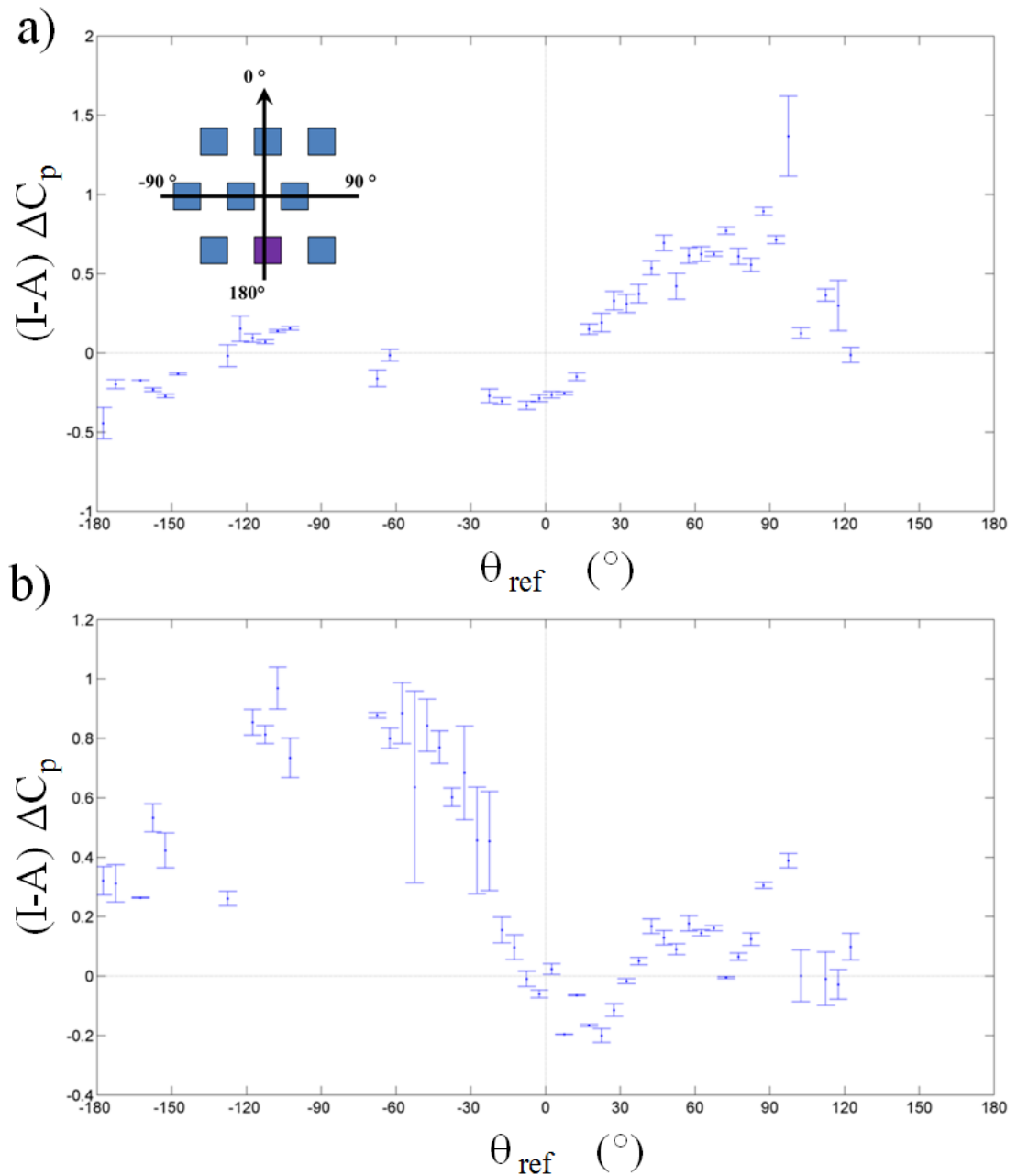


Figure 5.33: As Figure 5.32 but for the a) north and b) south faces.

To conclude, the array affects the instrumented cube only when the array is upwind. The presence of cubes either side of the isolated cube only appears to affect the north and south faces. The array, when providing maximum shielding, reduces C_p on the front face by 0.8, though the back face is not impacted due to it being on the edge of the array. The north and south faces act similarly with respect to their own perpendicular wind directions.

5.7 Comparisons to published C_p values

Dataset used: $All(NN_M^{All})$

Research into C_p has different aims meaning the results are reported in varying ways. Three commonly used C_p datasets are compared to the data obtained here for the isolated cube and (where possible) the array. The half hourly C_p values are averaged for each face, and are compared to the AIVC (Air Infiltration and Ventilation Centre) (Orme and Leksmono (2002)), ASHRAE (American Society of Heating, Refrigerating and Air-Conditioning Engineers) (Swami and Chandra (1987)) and CIBSE (Chartered Institution of Building Services Engineers) (CIBSE (2006)) model data.

5.7.1 ASHRAE

Swami and Chandra (1987) sought to combine all previous work on building C_p into one database. All but one of the datasets (8 in total) are for on low-rise buildings (< 3 stories high). Non linear regression behaviour with wind incidence angle and building side ratio is used to predict C_p data for the low rise datasets (correlation coefficient of 0.80) (Swami and Chandra, 1987). This dataset has become a standard within the ASHRAE community, it is based on near-neutral wind tunnel measurements in flow with little to no turbulence i.e not applicable to turbulent flows. The model has no surrounding roughness elements and assumes symmetrical behaviour across all reference wind directions.

Swami and Chandra (1987) note that ‘simplifications, modifications, and assumptions have to be made in order to get useful results from existing data’. The focus on face averaged C_p , reduces the amount of data and the variation e.g. 544 wall average data points are from several thousand local C_p data (Swami and Chandra, 1987).

The three main variables identified by Swami and Chandra (1987) to effect C_p are: wind angle, roof angle and height to width ratio of the building. These variables are used to create a normalised C_p for all of the datasets. However, some of the assumptions used to create normalised C_p , such as ‘irrespective of all other parameters the normalized C_p must always be equal to 1 for 0° wind angle’, mean that there will be differences between the full-scale data presented here and the model, as the roughness length and turbulence levels of the oncoming flow are not considered within this normalisation (Swami and Chandra, 1987). It is assumed that due to the symmetry of a building, the results can be mirrored to include -180° to 180° .

Within the amassed datasets, Swami and Chandra (1987) noted that for C_p values when the flow is perpendicular to a face there is no trend with respect to any variable studied. Cross comparison of open terrain data with suburban terrain revealed that depending on the dataset, some suburban C_p values can be larger than their open terrain counterparts, and vice versa. Due to the variation in research goals and experimental

configurations, it is not possible to correlate data for the 0° incidence angle (Swami and Chandra, 1987). They instead use a uniform value of C_p of 0.6 (the average across all the datasets for the 0° wind angle). Swami and Chandra (1987) also reference Wiren (1983) on the effect of sheltering on C_p for rectangular and hexagonal arrays, as well as the effect of one neighbouring building.

5.7.2 AIVC

AIVC provide guidance tables for surface averaged C_p for six different cases: a length to width ratio of 1:1 or 2:1 coupled with three shielding conditions: exposed, surrounded by obstructions equivalent to half the height of the building and surrounded by obstructions equivalent to the height of the building, based on wind tunnel experiments by Wiren (1983) and Bowen (1976). The C_p values are correlated to wind speed, measured at building height locally. They are given for the four façades of the building and for three different types of roof pitch ($< 10^\circ$, $11^\circ - 30^\circ$, $> 30^\circ$), and for each 45° sector (Heijmans and Wouters, 2002).

5.7.3 ASHRAE and AIVC for the isolated cube

The wind tunnel results of Swami and Chandra (1987) can be applied to all faces by changing the perpendicular wind angle. Heijmans and Wouters (2002) give values for all four faces simultaneously as well as for different sheltering effects, allowing the array data to be compared to the Silsoe array results (Section 5.7.4.2). These results are similar to those measured in the wind tunnel (Section 4.11).

Though all datasets have a similar trend, with the C_p becoming increasingly negative as the θ_{ref} moves away from 0° , the averaging applied by Swami and Chandra (1987) to the 0° C_p value means that the C_p values for the isolated Silsoe cube are 0.1 higher, but fall within the 80 % bounds (Figure 5.34). There is great similarity between Swami and Chandra (1987) and Heijmans and Wouters (2002), as both sets of data are based on Wiren (1983), but the AIVC data separates the sheltering effects into three categories, whereas Swami and Chandra (1987) averaged them all into one value. The modified values from Swami and Chandra (1987) treat the cube faces in isolation, whereas Heijmans and Wouters (2002) measure the front, back and sides simultaneously, capturing the effect of each face on the others (Figures 5.35, 5.36).

The resolution of the AIVC data causes differences between the mean C_p value predicted by the Swami and Chandra model, especially at $\theta_{ref} = 90^\circ$ (0.2 to 0.1 difference) though it still falls comfortably within the 80 % bounds of the data. Neither dataset provides errors on the face averages, making it difficult to accurately inter-compare in any detail. The minimum value of C_p is predicted by the AIVC data to occur at $\theta_{ref} = -90^\circ$ and 90° , when the oncoming flow is parallel to the cube, whereas the Swami and

Chadra model predicts the minimum value of C_p to occur at $\theta_{ref} = 115^\circ$, when the flow is impacting on the back face. The minimum binned value for the isolated Silsoe cube occurs in the range $\theta_{ref} = 90^\circ$ to 115° .

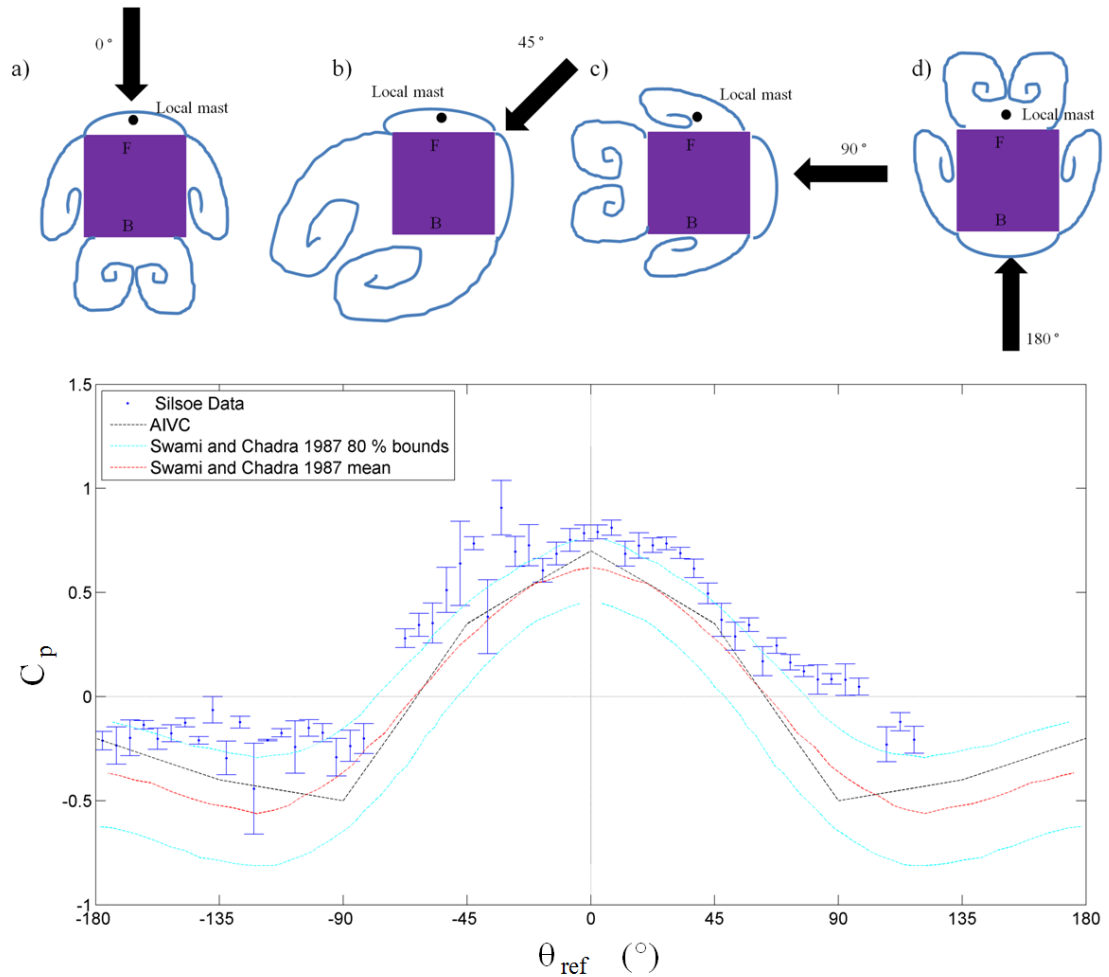


Figure 5.34: Binned front face averaged C_p for the isolated cube (Figure 5.30) and the digitised data (for this comparison) from Swami and Chandra (1987) and AIVC isolated cube data (Heijmans and Wouters, 2002). Error bars on the binned data are the standard error of the bin. Schematics are Figure 5.6.

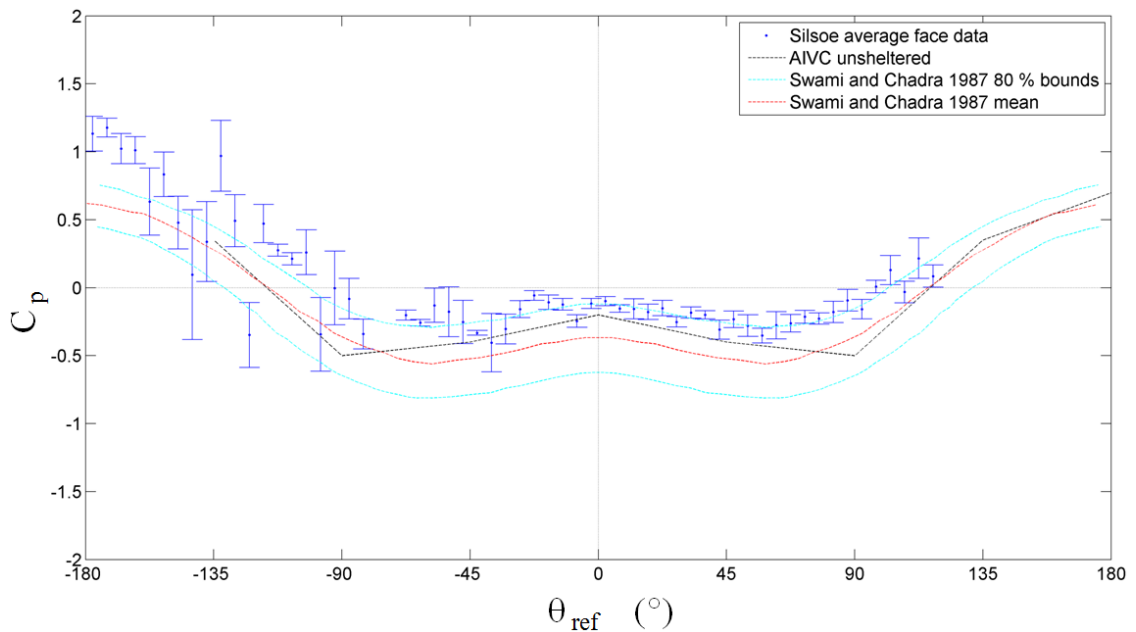


Figure 5.35: The C_p values for the back face of the Silsoe cube, binned into θ_{ref} 5° bins (dark blue). Error bars represent the standard error of each bin. The mean calculated by Swami and Chandra (1987) (red line), the 80 % bounds of the data (Cyan) and the AIVC unsheltered model (black line).

The back face experiences positive values for $\theta_{ref} = -90^\circ$ to 180° and $\theta_{ref} = 90^\circ$ to 180° , with the maximum C_p value at $\theta_{ref} = 180^\circ$, where the oncoming flow is perpendicular to the back face. Like the front face the values recorded for the Silsoe cube are slightly higher than the modelled data (0.1). The minimum value of C_p (-0.1) occurs when the wind is impacting on the front face: $\theta_{ref} = -45^\circ$ to 45° .

For the north face (Figure 5.36a) the Swami and Chandra (1987) estimate the C_p as having the the maximum C_p of 1 occurring when the wind is perpendicular to the face ($\theta_{ref} = 90^\circ$). When the wind is perpendicular to the south face (-90°), the north face pressure reduces to -0.1. For $\theta_{ref} = 45^\circ$ to 90° an increase in C_p of 0.5 occurs, due to the oncoming flow impacting on a larger surface of the north face. This pattern can also be seen for the south face (Figure 5.36b) with a peak at the perpendicular wind ($\theta_{ref} = -90^\circ$) and a value of between 0 and 0.1 for $\theta_{ref} = 90^\circ$. This difference in north and south faces matches the difference across the cube measured between the front and back faces. For $\theta_{ref} = -135^\circ$ to -45° there is larger variation recorded for the south face when compared to the north face. This is likely to be due to the influence of the sewage tanks on the south face and the change in roughness lengths as the flow travels across the buildings. Likewise the variation due to changing surfaces for the north face is smeared out by the storage shed which is upstream for $\theta_{ref} = 90^\circ$. As for the front and back faces, the models provide a good estimate of the magnitude of C_p with respect to θ_{ref} .

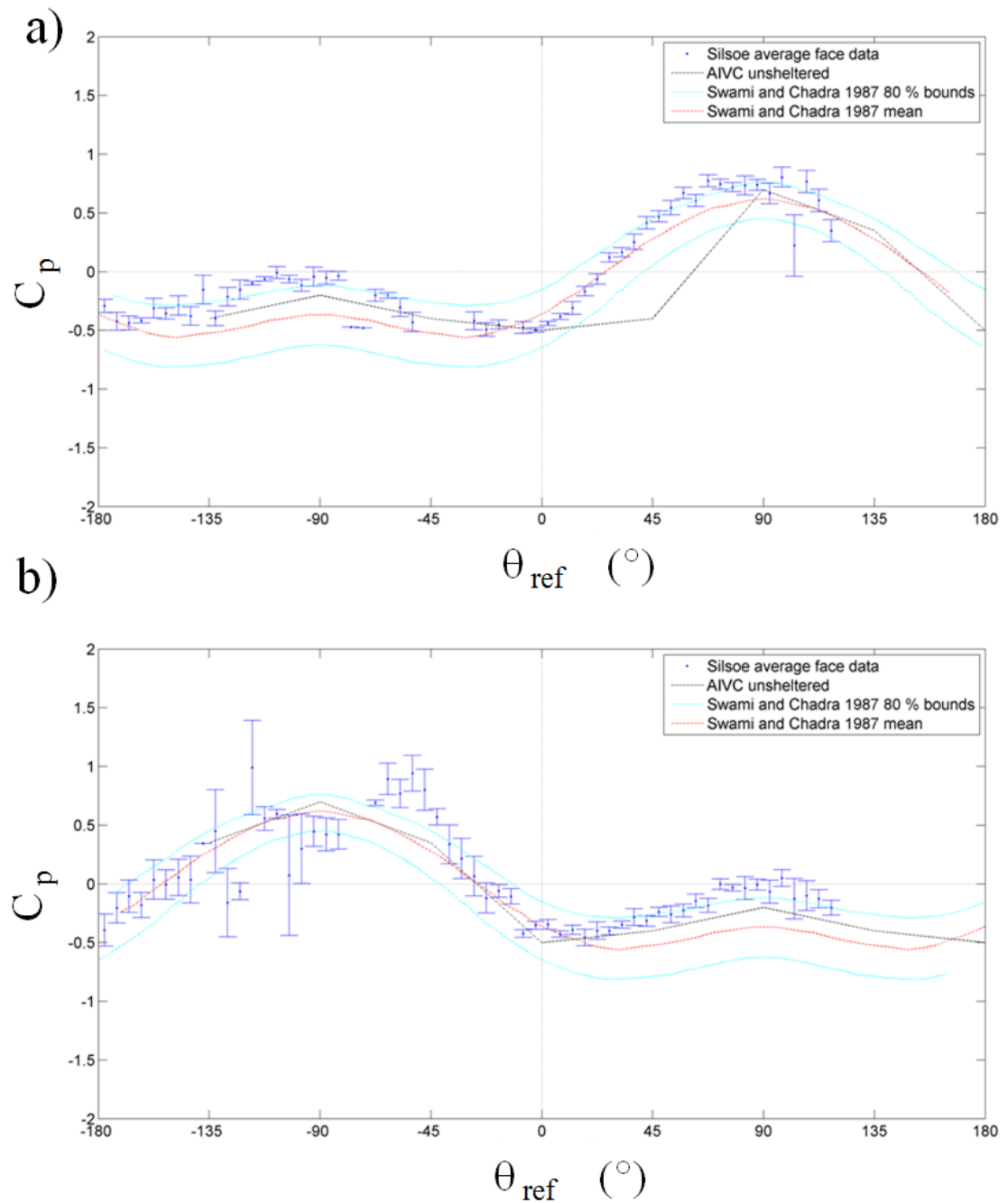


Figure 5.36: As Figure 5.35 but for the a) north and b) south faces.

5.7.4 CIBSE

CIBSE (2006) provide front face averaged C_p values for a square plan building less than three stories high. The complexities of a building's surroundings are not captured in the C_p values and refer the reader to Liddament (1996). Three types of surroundings are considered: isolated, in an open field with no obstacles, a building in open country with

scattered windbreaks and a building in urban location. Three roof pitches are given, but only impact the C_p on the roof so are not included in the analysis here. CIBSE (2006) give a procedure to determine the pressure coefficients of a building:

1. Determine the building height
2. Determine the nature of surrounding terrain
3. Find the correct meteorological wind speed data according to building height and terrain classification
4. Determine the approximate wind C_p for each face or for each opening in the building envelope or undertake wind tunnel studies if more accurate values of wind C_p are required.

5.7.4.1 Isolated

The isolated Silsoe cube (< 3 stories) is considered as being in an open field with some obstacles. The CIBSE data underestimates the front face averaged C_p but captures the trend with θ_{ref} well. The closest estimate of C_p is the 'open' measurements, though the Silsoe cube is known to be surrounded by roughness elements and a few scattered buildings. One cause of this difference could be related to the CIBSE data using a meteorological measurement of wind speed from a 10 m mast, whereas this work has used U_{ref} , located close to the site (Section 5.2.3). The proximity of the 10 m measurement used by CIBSE to the test building is unknown. The 10 m wind speed stated is 4 m s^{-1} so when the wind speed is normalised by the 'reference wind speed' for the CIBSE data, the resultant C_p will be lower.

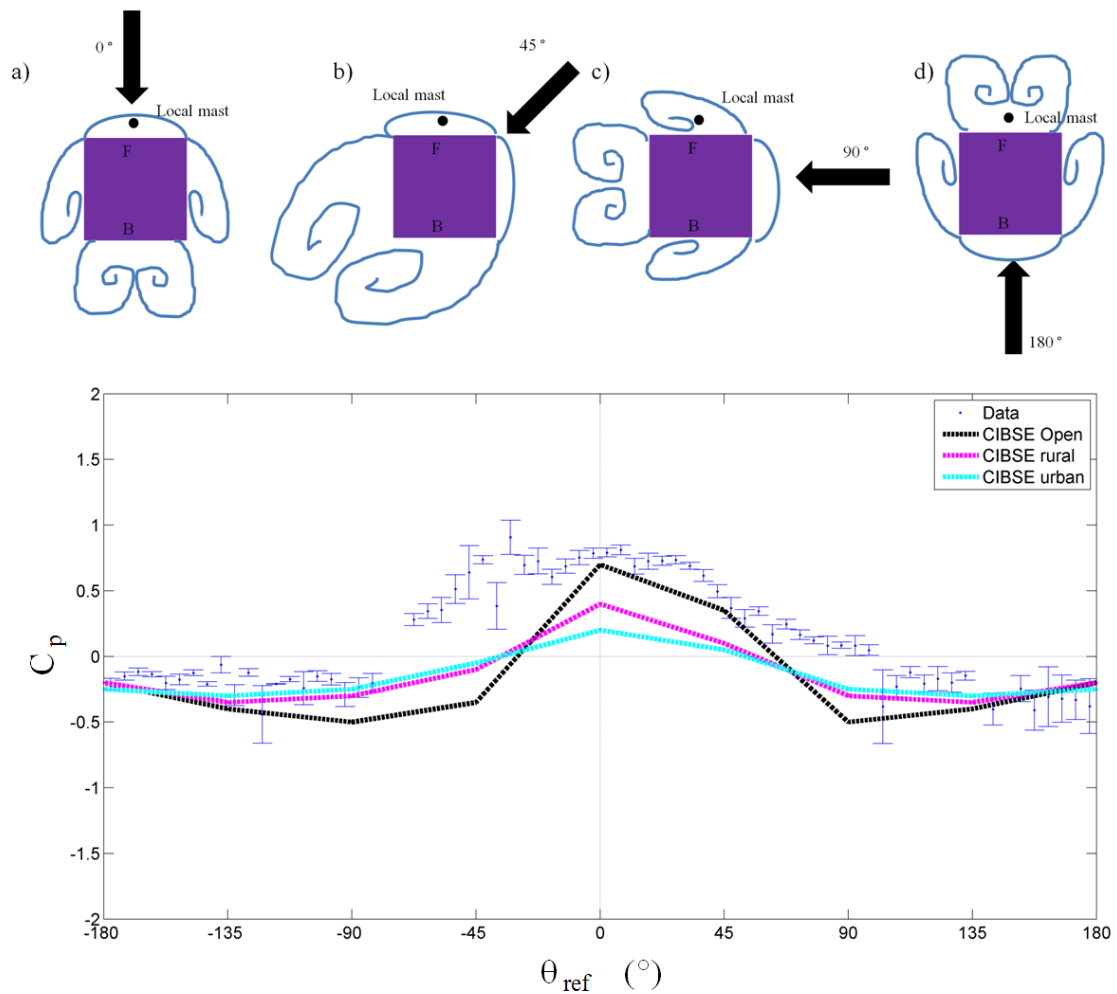


Figure 5.37: Averaged C_p from CIBSE (2006) for the front face of a square building of < 3 stories in height and full-scale data from the isolated cube binned into θ_{ref} 5° bins. Schematics are Figure 5.6.

The back (Figure 5.38), north (Figure 5.39) and south (not shown) face all have good agreement. Despite the influence of the storage shed on the North face, the ‘open’ model agrees well, capturing the change in C_p with θ_{ref} . The rural and urban models underestimate C_p due to overestimates of the shielding effects. This is also true for the back face for $\theta_{ref} = -90^\circ$ to 90° , though the model does not predict C_p well for a larger θ_{ref} , likely due to the complexity of the field site caused by changes in roughness.

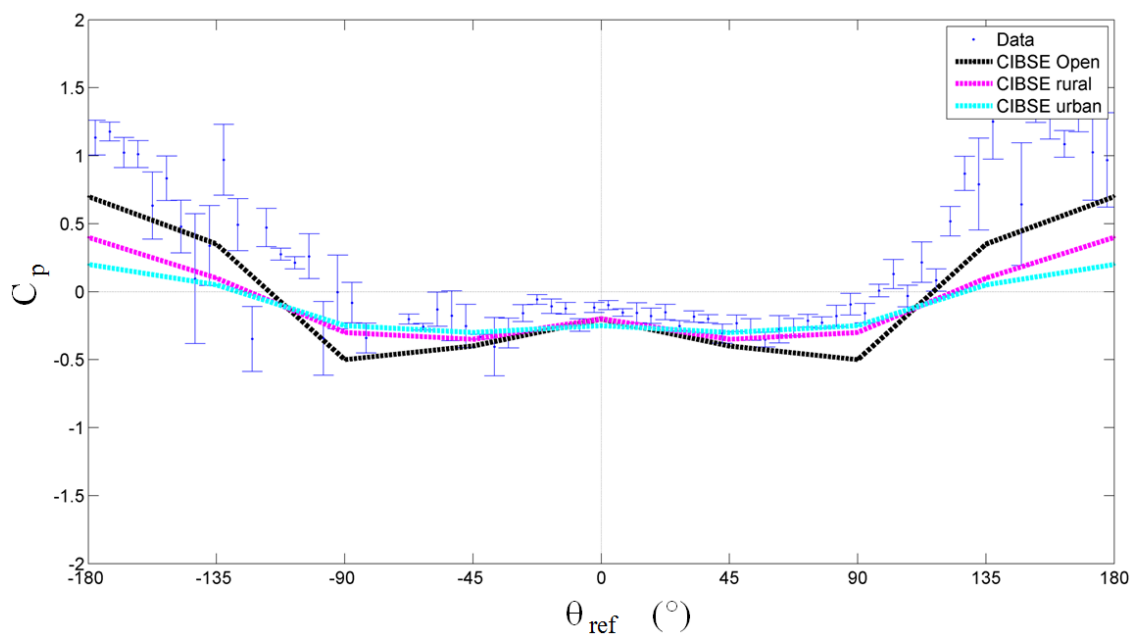


Figure 5.38: As Figure 5.37 but for the back face.

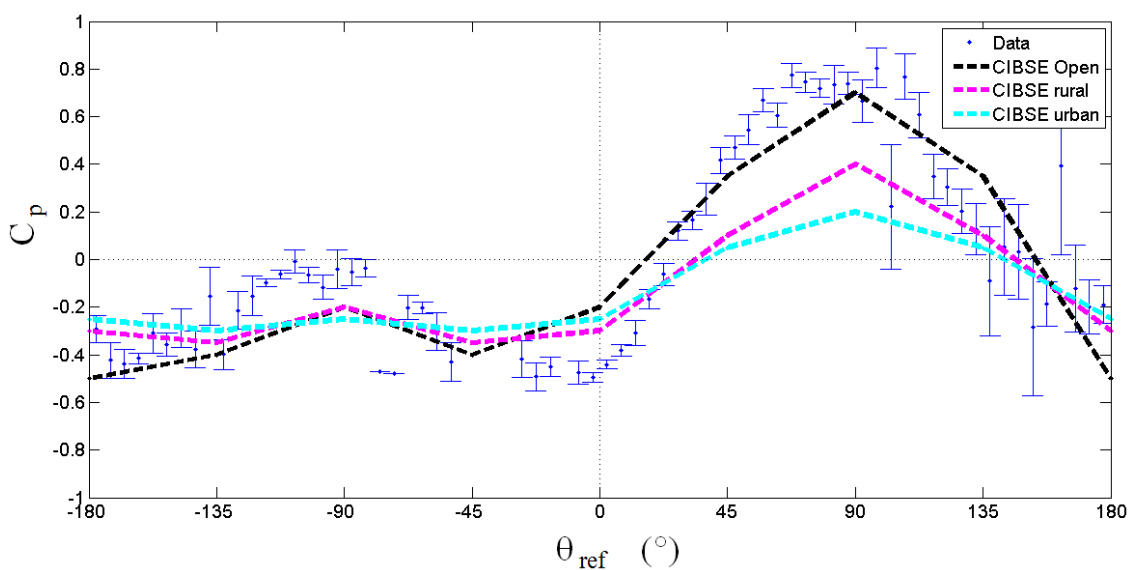


Figure 5.39: As Figure 5.37 but for the north face.

In summary, the estimations provided by CIBSE give a good estimate for the back, north and south sides, but underestimate front face C_p .

5.7.4.2 Array

As the Swami and Chandra (1987) model uses sheltered and unsheltered data, with a greater number of unsheltered models, only the AIVC (Heijmans and Wouters, 2002) is used to compare to the array. The CIBSE 'urban' sheltering data are the same as the AIVC

guidelines. Differences are to be expected due to the staggered array, and the Silsoe cube being on an external row.

The effect of the cube being on the outside of the array can clearly be seen (Figure 5.40), with C_p values of 0 being recorded when θ_{ref} is perpendicular to the front face (Figure 5.40a), due to the direct blockage by the two additional rows of the array and C_p values of 1 to 1.2 being recorded when the flow is perpendicular to the back face (Figure 5.40b), where the back face is exposed to the oncoming flow. These high C_p values for $\theta_{ref} = 180^\circ$ for the back face are equivalent to those recorded for similar conditions for the isolated case. This suggests that the array has no effect upstream.

The asymmetry of the array means that the C_p trends with θ_{ref} are no longer symmetrical, with the increased shielding in the anti clockwise direction (negative angles) causing a C_p of near 0 for $\theta_{ref} = -90^\circ$ to -45° for the front face. For $\theta_{ref} = 0^\circ$ to 45° , the front face displays a negative C_p of -0.2 - -0.3, which suggests suction is present on the face, though this decreases when $\theta_{ref} 90^\circ$. This could be caused by a vortex formed when flow impacts on the cube corner, as the effect is also visible on the north face (Figure 5.41a).

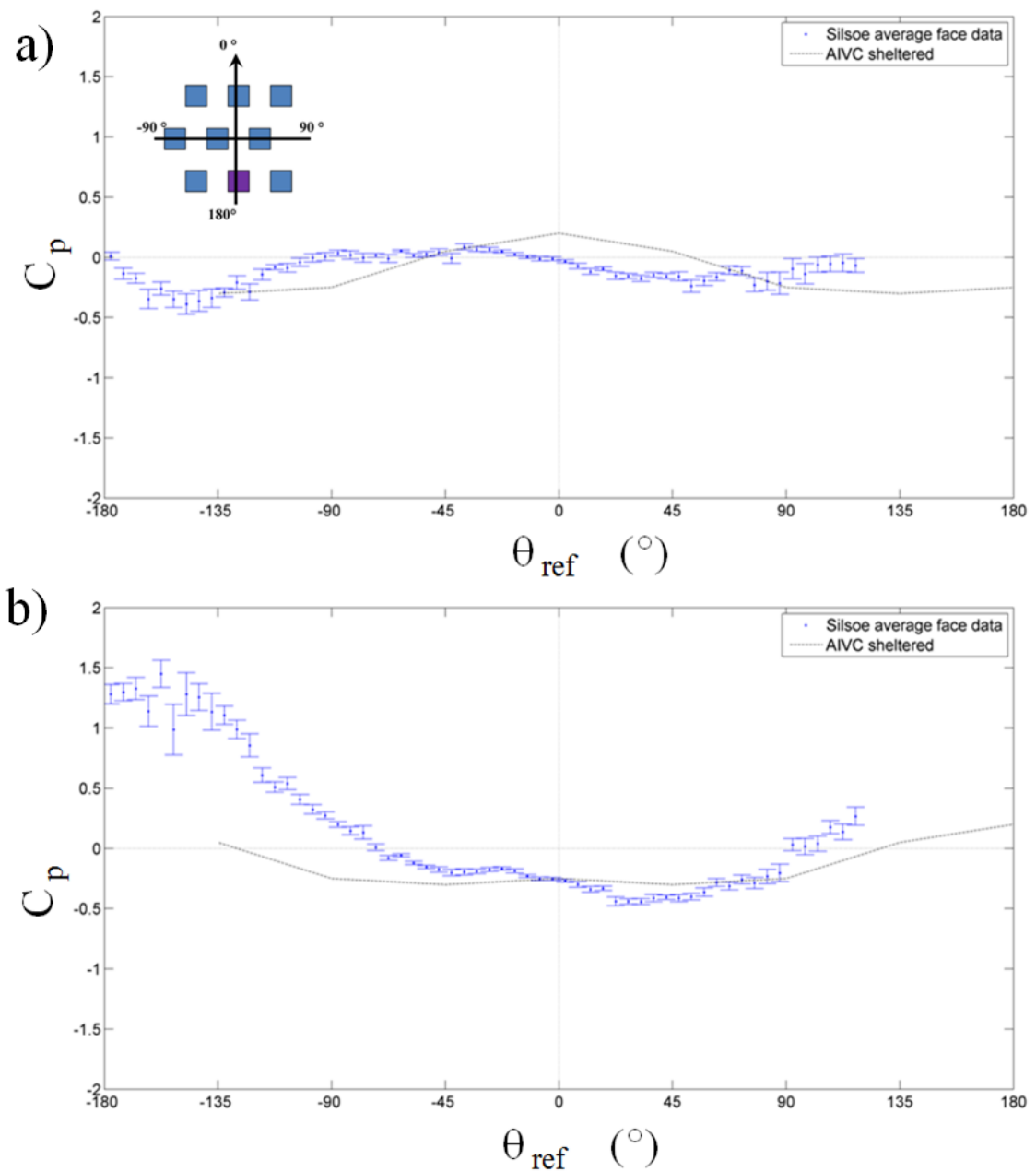


Figure 5.40: C_p values for the a) front and b) the back faces of the Silsoe cube, binned into θ_{ref} 5° mean and standard error bins for all array cases.

For the south face, the variation for $\theta_{ref} = -135^\circ$ to -90° is now no longer present, with the north and south face results being similar in magnitude for similar θ_{ref} values (Figure 5.41). The peaks for perpendicular wind directions ($\theta_{ref} = -90^\circ$ for south and 90° for north) are no longer as identifiable, due to the flow being blocked by a cube positioned directly in front of the face, meaning the wake from that cube is impacting on the face. The north face maximum C_p occurs at $\theta_{ref} = 120^\circ$ to 135° and is due to oncoming flow from that direction being unaffected by the array. The C_p values of 0.5 are similar to those for the isolated cube. This behaviour is also seen for the south face

at $\theta_{ref} = -135^\circ$.

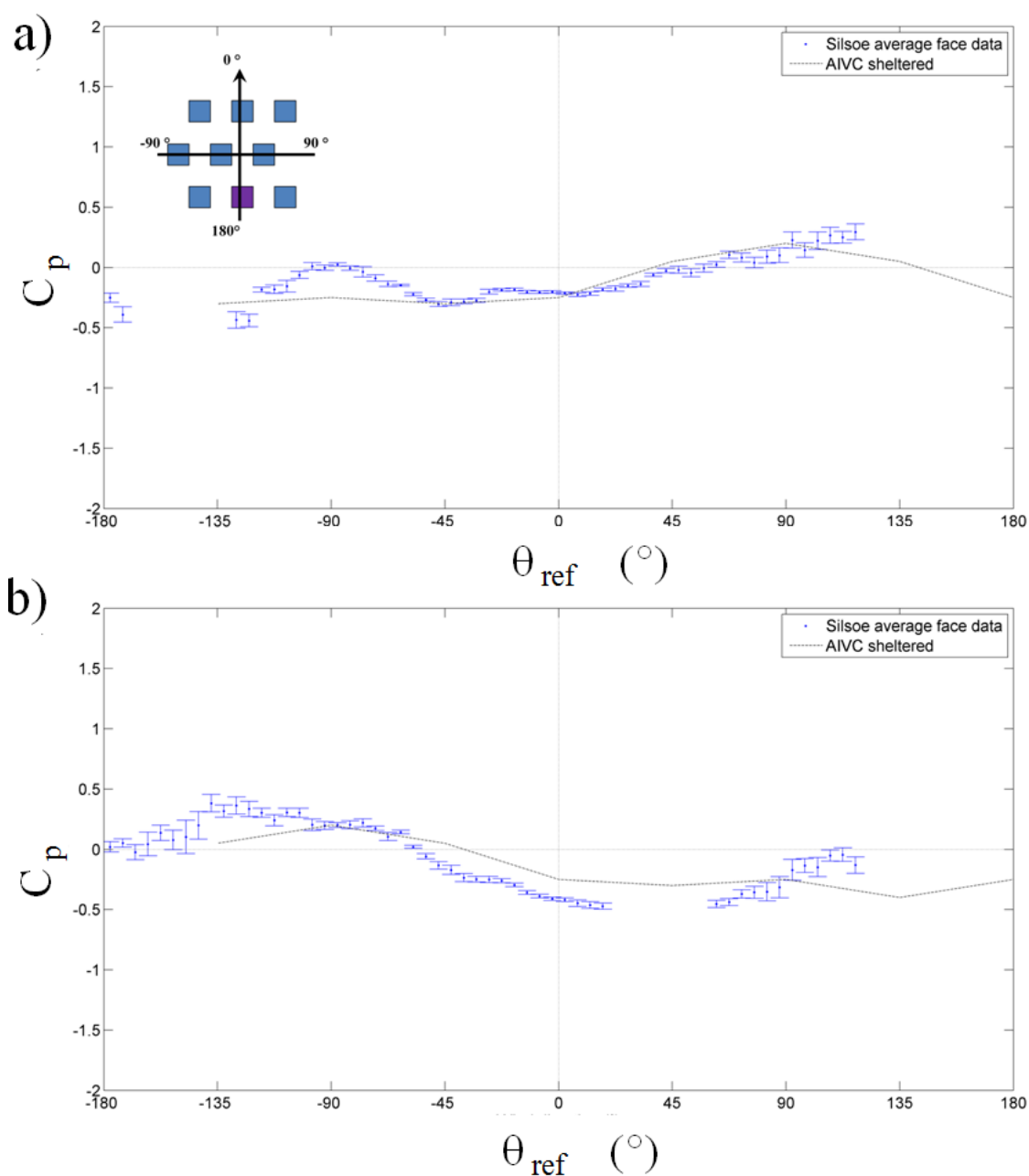


Figure 5.41: C_p values for the a) north and b) the south faces of the Silsoe cube, binned into θ_{ref} 5° mean and standard error bins for all array cases. Error bars represent the standard error of each bin.

For the front and back faces of the array case, the AIVC model does not accurately predict the trend of C_p with θ_{ref} , as the Silsoe array is neither extensive array or an aligned array. This can be seen in the wind tunnel C_p data (Section 4.11) with the models performing better for more extensive arrays. The north and south face trends in C_p are similar, with differences occurring due to the effect of the cube being on the edge of the

array. The perpendicular winds for the north and south faces also correspond to the directions with which the staggered array acts as an isolated array.

5.7.5 Conclusion

Whilst the pressure coefficients listed by Swami and Chandra (1987), Heijmans and Wouters (2002) and CIBSE (2006), provide a good estimate of the expected C_p for different wind directions for an isolated square building, the sheltered and urban area models by AIVC and CIBSE do not accurately predict the C_p for the Silsoe array. This is due to a differing reference wind speed height being used in the case of CIBSE (2006) and due to the array being limited in depth and asymmetrical in layout for the AIVC estimates. The model estimates should be used as estimates only, with wind tunnel or CFD modelling being undertaken in order to obtain more specific and accurate results.

5.8 Full-scale comparisons to the scale model

Dataset used: $All(NN_M^{All})$

Comparison of full-scale and scale model data requires the satisfaction of dynamic, kinetic and geometric similarity laws. The wind tunnel simulation of the Silsoe array (Chapter 4) uses a 1:300 scale model of the the full-scale array, making it geometrically similar (i.e. the H_m/W ratios being 1). Jensen (1958) first concluded that in order to obtain accurate results from a wind tunnel model, the wind and the building model need to match the full-scale characteristics. As noted in the Snyder (1981) review of the theory behind dynamical similarity, the equation of motion, continuity equation and the energy equation can be non-dimensionalised which yields the Rossby number, Froude number, Reynolds number and the Peclet number, as dimensionless parameters. Solutions to the equations of motion will be identical when the four dimensionless numbers and the non-dimensional boundary layer conditions are similar (Snyder, 1981). This applies to both laminar and turbulent flows. However, it is impossible to match all the dimensionless parameters when the ratio of the length scales is greater than about 10, therefore compromises are made (Snyder, 1981).

The Reynolds number (Re):

$$Re = \frac{U_{ref}L}{\nu} \quad (5.4)$$

where U_{ref} is the reference velocity, L is a characteristic length, in this case the height of the buildings, and ν is the kinematic viscosity of the air. The Reynolds number can be defined as the ratio of inertial forces to viscous forces. Reynolds numbers for the wind tunnel experiment were of the order of 10,000 and for the full-scale the Reynolds num-

ber varied between 31,000 and 5,000,000. The size of the largest eddies within the flow is controlled by the overall geometry of the flow whereas the smallest scales of eddies is set by the Reynolds number. Having a high Reynolds number indicates that the range of eddy sizes is larger within the flow, meaning that statistically all scales of motion are captured. Not matching the Reynolds number between the wind tunnel and the full-scale could lead to the wind tunnel model not modelling the smaller eddies correctly. The structure of turbulence is similar over a wide range of Reynolds numbers (not laminar flow). Reynolds number independence of the flow past sharp edged obstacles is satisfied when the Reynolds number is greater than 10^4 (Snyder, 1981).

In the full scale case, there are few data outside of the range $\theta_{ref} = 0^\circ \pm 60^\circ$ for both the isolated and array cases. The array case encompasses some of the less frequent wind directions, however, they cannot be compared to the wind tunnel measurements in a statically sound way. The spread of the full-scale wind directions emphasises the importance of the wind tunnel study, as a full-scale study would have to run for significantly longer in order to capture the full range of conditions. There were few recorded cases (< 10) of θ_{ref} 80° to 100° in dataset $All(NN_M^{All})$. As such the effect of the storage shed in the wind tunnel cannot be compared with the full-scale data.

Differences may occur between the two datasets, due to differences in longitudinal pressure gradients. At full-scale it can comfortably be assumed that as long as the reference pressure is not measured in the wake of the building or the array, it will be approximately the same wherever it is measured. For the wind tunnel this is not the case, with a systematic offset likely to be caused by the positioning of the reference pressure in the wind tunnel.

5.8.1 Isolated cube

The wind tunnel data (Figure 5.42a) suggests a maximum C_p of 0.6 for the front face, with a back C_p of -0.3, giving a difference of 0.9. The full-scale data has a maximum C_p difference between front and back of between 0.8 to 1.1, though this varied. For the horizontal trace around the cube, the effect of $\theta_{ref} 0^\circ \pm 10^\circ$ can be seen clearly in the wind tunnel data as $\theta_{ref} = 10^\circ$ and $\theta_{ref} = -10^\circ$ data, (black and green lines) behave in equal but opposite ways especially on the front face (Figure 5.42b). There is little variation in the vertical distribution of C_p for the isolated cube in the wind tunnel, with less than 0.05 difference between the three cases for the given angle range. Due to all the full-scale data being averaged into one box, the trend in the full-scale data matches that of the $\theta_{ref} = 0^\circ$ wind tunnel case.

For the north and south sides, the difference in magnitude of the C_p values could be due to the strength of the recirculation vortices. For the full-scale cube, the corners are not particularly sharp, due to weathering through outdoor use and the age of the structure. The wind tunnel model may also have imperfections due to the brass pressure

tapped cube being hand-made. This difference in sharpness may explain the deviations in C_p for the the north and south faces, due to the sharpness of the corners affecting the formation of vortices.

The full-scale face averaged C_p on the front face shows that the wind tunnel accurately represents the variation with θ_{ref} , with both datasets displaying similar trends: maximum for $\theta_{ref} = 0^\circ$, minimum for $\theta_{ref} \pm 90^\circ$ with a tendency to increase towards 0 as θ_{ref} moves to $\pm 180^\circ$ (Figures 5.43, 5.44). The wind tunnel distribution is affected by the lack of a 45° measurement which skews the line. The presence of the storage shed in the wind tunnel reduces the maximum value at $\theta_{ref} = 90^\circ$ to be within the range of the full-scale data (0 to 0.1), though there are few full-scale data for this direction making the trend difficult to discern. The low values of C_p for $\theta_{ref} = 0^\circ$ (Section 5.5.2) were not recorded within the wind tunnel.

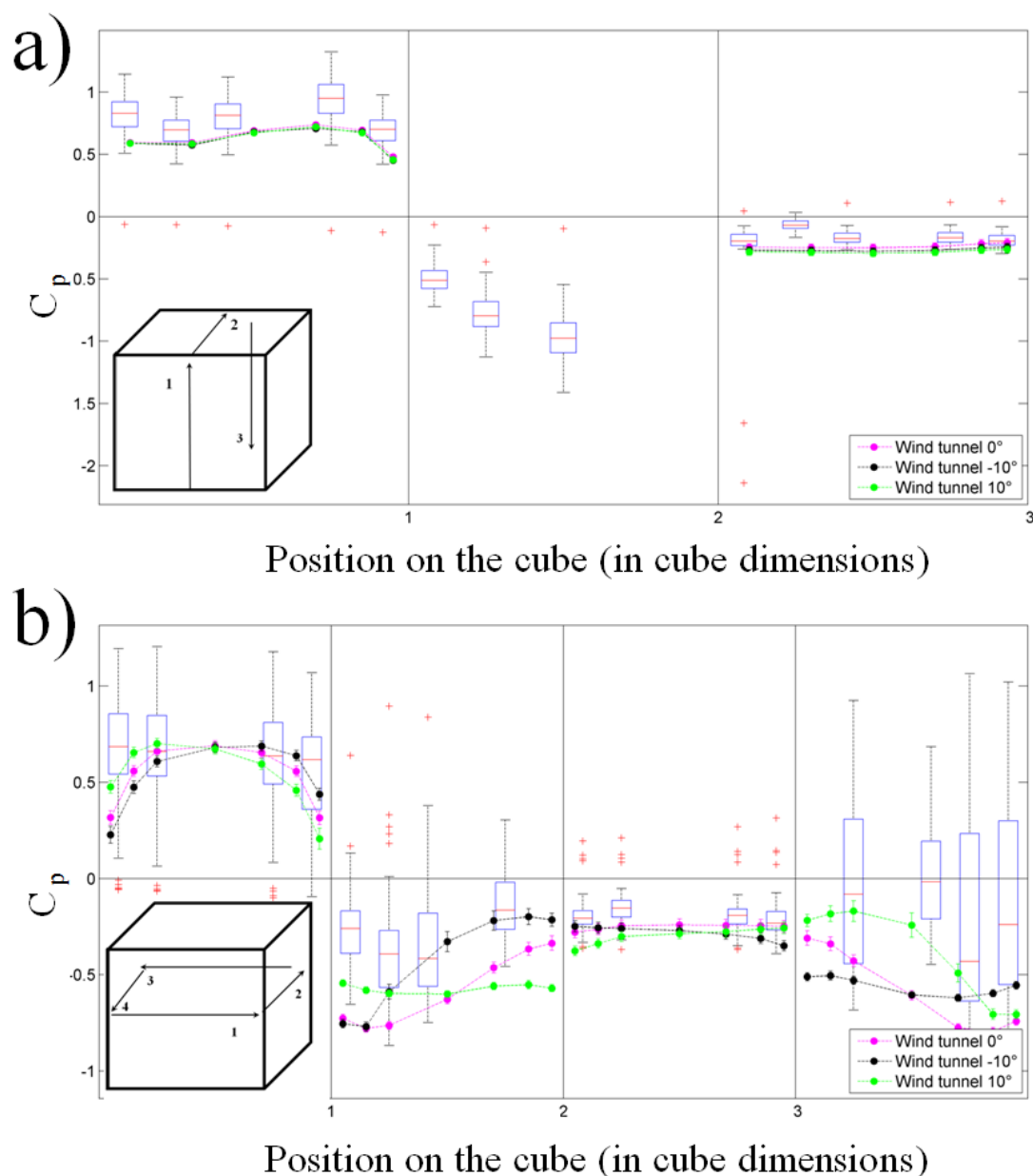


Figure 5.42: Comparison of wind tunnel and full-scale data $\theta_{ref} 0^\circ \pm 10^\circ$. Box plots (in blue) with the IQR of the full-scale data, with the the median (red). The black bars extend to 97.5 % of the data and the outliers (red crosses). Lines are wind tunnel data. Positions are given in cube heights. a) traces the path up the front of the cube (0-1) along the roof (1-2) and down the back face (2-3), with b) being path around the cube, beginning at the front -y corner and moving in an anticlockwise direction horizontally at the centre of the cube.

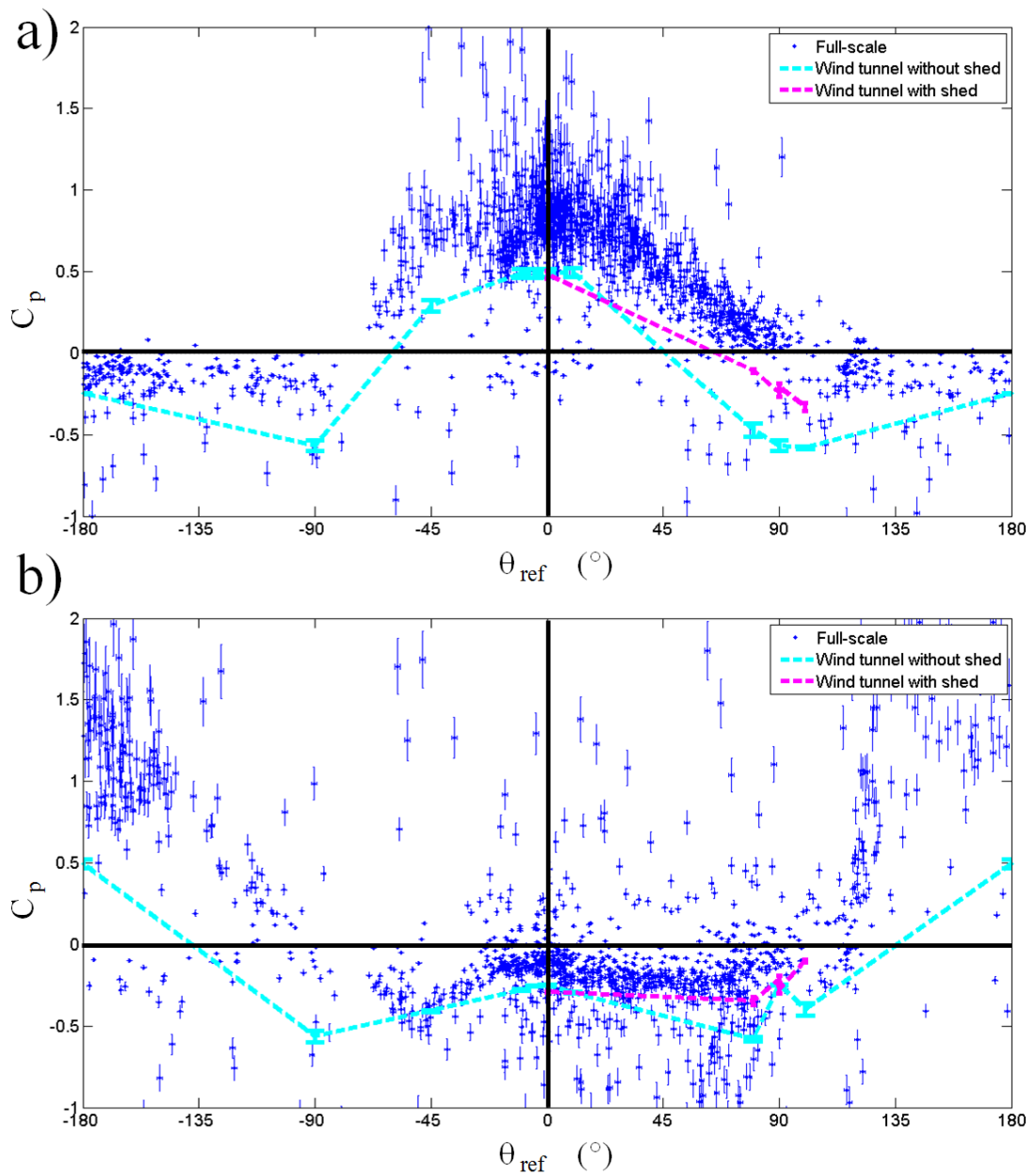


Figure 5.43: Comparison of dataset $I(NN_M^{All})$ to the wind tunnel data with (magenta line) and without (cyan line) a model of the storage shed included. C_p averaged over the a) front and b) back faces. 0° on both figures corresponds to the wind direction perpendicular to the front face.

The full-scale and wind tunnel results for the back face have agreement in trend but not in magnitude, perhaps due to the different positioning of the reference pressure (Figure 5.43). A more reduced pressure on the front face corresponds to a lower pressure on the back face, leading to this offset, which cannot be quantified due to it varying depending with θ_{ref} . The peak C_p for this face is when $\theta_{ref} = \pm 180^\circ$, displaying similar values to that of $\theta_{ref} = 0^\circ$ for the front face of an isolated cube (Figure 5.43). The maximum blockage occurs at $\theta_{ref} = 90^\circ$, while $\theta_{ref} = 0^\circ$ leads to a face averaged C_p of -0.25 to 0

in the full-scale flow and around -0.25 to 0.3 in the wind tunnel model. Including the storage shed in the wind tunnel model leads to a closer agreement for positive θ_{ref} , due to the sheltering effect of the storage shed being similar to that seen on the full-scale site.

The north and south faces display some asymmetry, with a peak in face averaged C_p occurring at $\theta_{ref} = 90^\circ$ for the north face and $\theta_{ref} = -90^\circ$ for the south face (Figure 5.44). For the north face, the addition of the storage shed in the wind tunnel model leads to lower C_p values at $\theta_{ref} = 90^\circ$ than seen in the full-scale data.

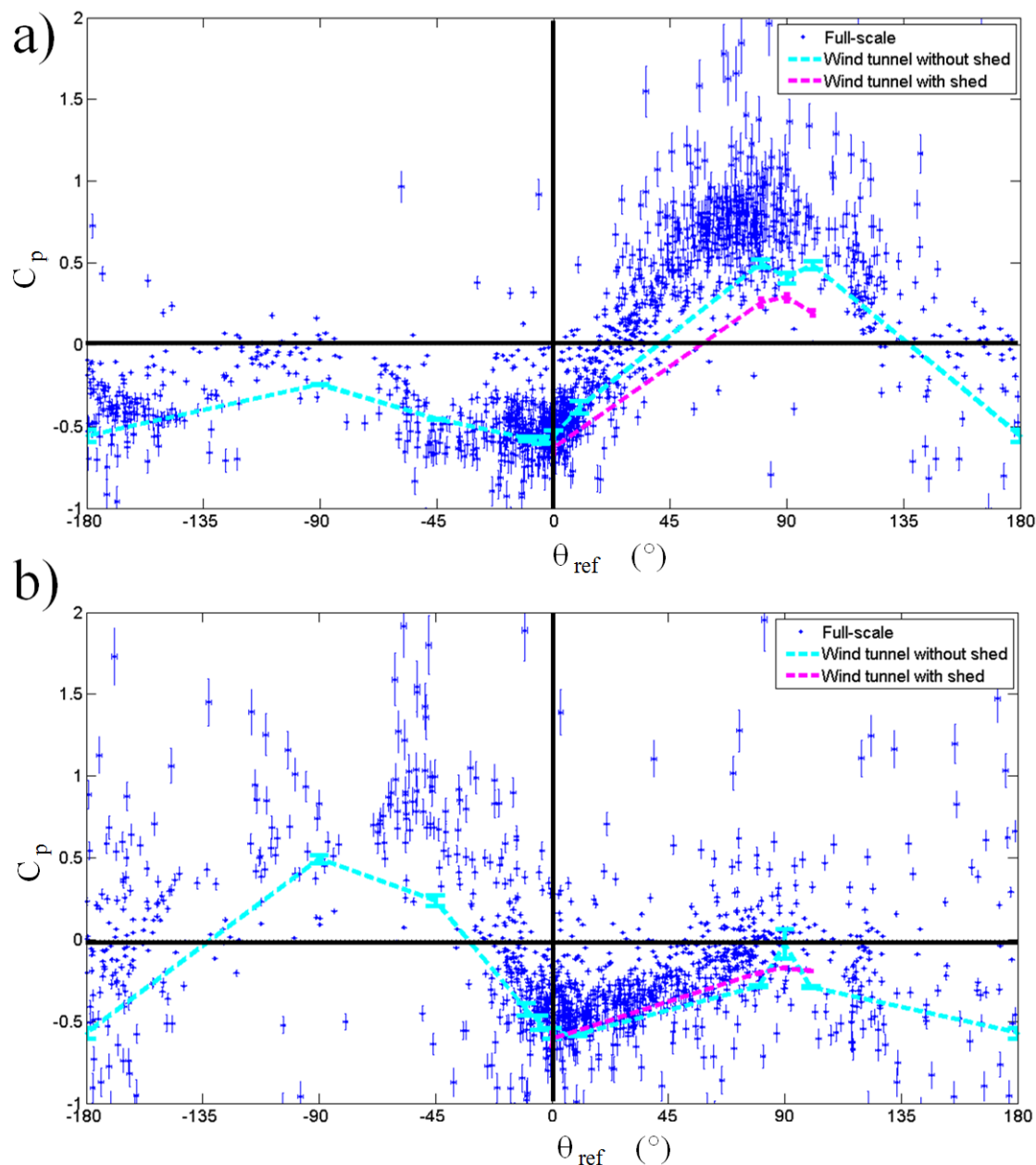


Figure 5.44: As Figure 5.43 but for the a) north and b) south faces.

For the south face (Figure 5.44b) there is little change with the inclusion of the stor-

age shed. The full-scale south side may also be influenced by the sewage tanks located upwind in these negative wind directions which was not modelled in the tunnel due to space limitations. The inclusion of the storage shed provides the wind tunnel model with better agreement than in the isolated cube case for positive wind angles, though like for the north face, the effects of the storage shed are overestimated in the wind tunnel.

5.8.2 Array

All pressure taps show a larger spread for the same angle range than for the isolated cube, due to the turbulent flow within the array (Figure 5.45). Of interest is the (very small) peak in positive pressure at the top of the front face, displayed by both wind tunnel and full-scale, though at slightly different heights, possibly due to the lesser number of pressure tap locations in the full-scale data. This peak in pressure is located closer to the cube roof than for an isolated cube, due to oncoming flow being displaced upwards by the array.

Both datasets show that the array significantly reduces the penetration of the oncoming flow, meaning that flow close to the cube is of low speed (Section 5.2.2), reducing the wind induced pressure on the cube. The pressure coefficients recorded for the back face are in good agreement with the wind tunnel data, being within the interquartile range of the full-scale data. There is less agreement in the horizontal trace on the back face, possibly due to the full-scale being effected by differing roughness types such as woodland, long grass and flat concrete surfaces, all within a 20° range (Figure 5.45b).

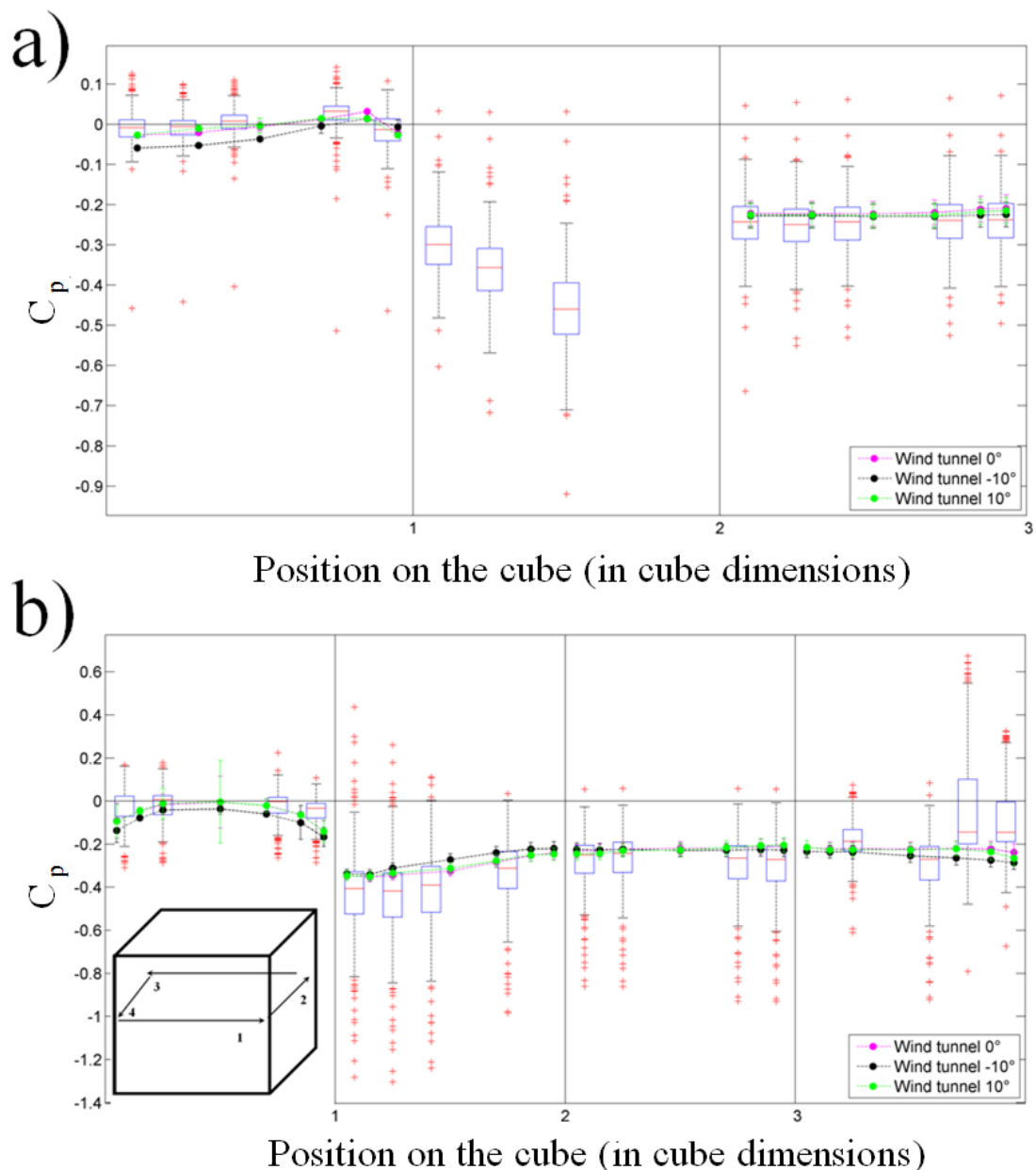


Figure 5.45: As Figure 5.42 but for the array data.

The front face C_p averages for the wind tunnel clearly show similar asymmetry with θ_{ref} compared to the full-scale flow (Figures 5.46, 5.47). The lack of a $\theta_{ref} = 45^\circ$ wind tunnel case misleads the eye, but it can be assumed that the result would be similar to that seen for $\theta_{ref} = -45^\circ$. However, within the wind tunnel, the trend is shifted slightly, suggesting the full-scale array is being influenced by fluctuating flow speeds. The fluctuating speeds will smear out the peaks seen in the wind tunnel due to steady mean flow speeds and turbulence intensities.

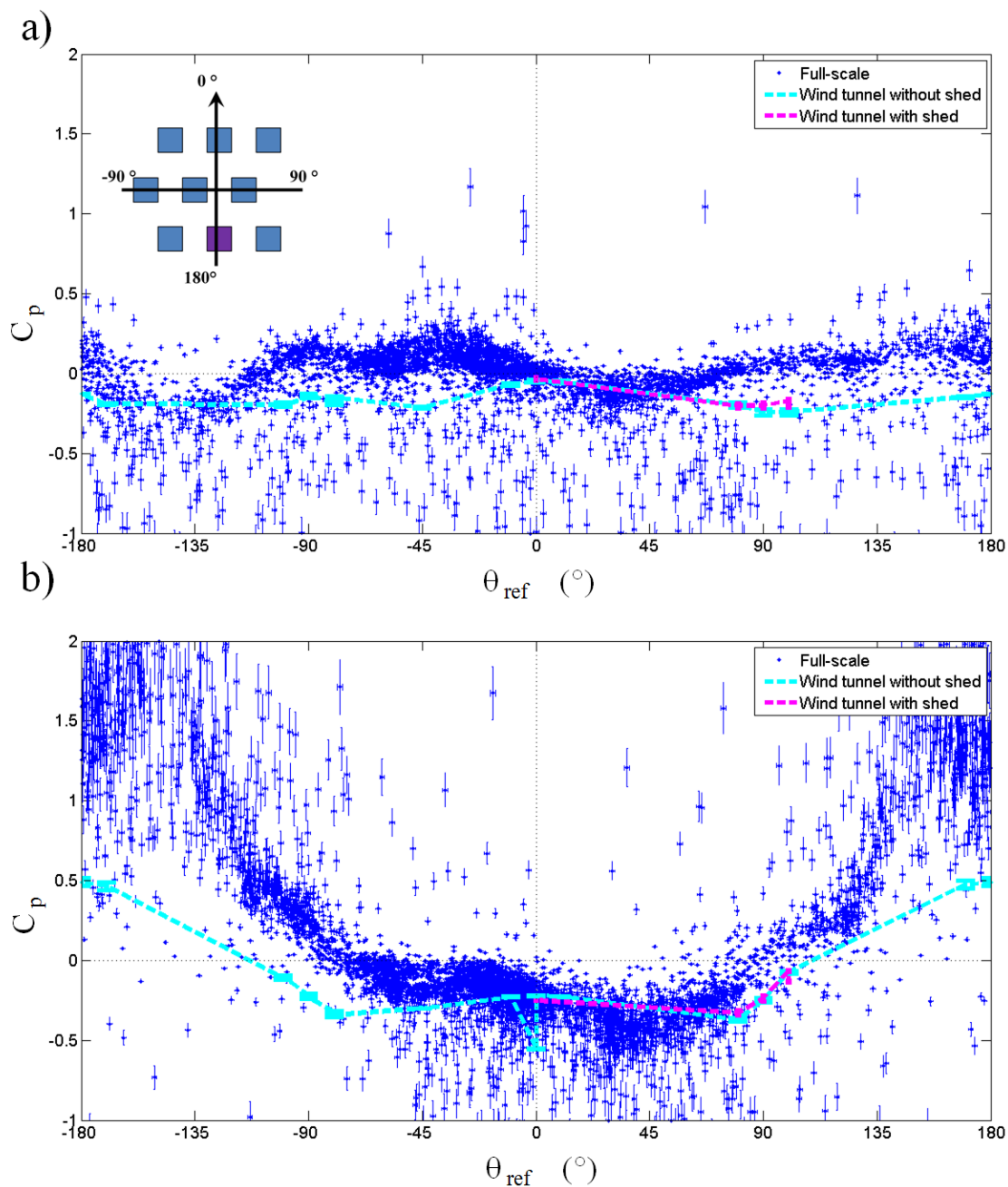


Figure 5.46: As Figure 5.43 but for the array data.

The wind tunnel over-predicts the average C_p on the front face by 0.1 for the perpendicular wind cases, possibly due to the full-scale array obstacles not being as sharp edged or as similar in height as the wind tunnel models (Figure 5.46a). It could also be due to the effect of the upstream roughness elements, such as the crop field which may reduce the pressure experienced by the instrumented cube due to it causing a small amount of shielding (Figure 3.2). The inclusion of the storage shed brings the front face wind tunnel C_p results in line with the full-scale C_p data for positive values of θ_{ref} , causing a change

of 0.1 to 0.2.

The back face is almost symmetrical, with values similar to the front face of an isolated cube for $\theta_{ref} = 180^\circ$ ($C_p = 0.4$ to 0.6). Like the front face, the back face shows asymmetry, following the same trends, though there are few high wind speed data for $\theta_{ref} = \pm 180^\circ$ (Figure 5.46b). For $\theta_{ref} = 0^\circ$ the wind tunnel model is similar to the full-scale case with values of between -0.4 and -0.1 . The wind tunnel predicts the trend on the back face to be symmetrical, which is not the case in the full-scale, due to varying obstacles and changes in roughness of nearby surfaces (not modelled in the wind tunnel).

Due to the instrumented cube being on the edge of the array, the north and south faces of the cube display peaks in similar positions to the isolated case, with the south peaking at $\theta_{ref} = -90^\circ$ and the north at $\theta_{ref} = 90^\circ$. For negative θ_{ref} values the average C_p is under-estimated by the wind tunnel model, possibly due a change in roughness at the full-scale site (Figure 5.47). The storage shed has little impact on the results for the array, due to the effects of the storage shed impacting on the edge of the array and not on the instrumented cube. The peak at $\theta_{ref} = -90^\circ$ for the south face is $\sim 50\%$ of the values recorded for the isolated case. This is due to the array acting as an aligned array for $\theta_{ref} = 0^\circ \pm 90^\circ$ (Figure 5.20c).

For the north face the C_p drop for $\theta_{ref} = 170^\circ$ to 180° is overestimated by the wind tunnel model, though there is very little field data, preventing any strong conclusions from being drawn. The peak at $\theta_{ref} = 90^\circ$ in the full-scale data for the array case is 60 to 70 % of that seen for an isolated cube, with the wind tunnel model also showing a similar 66 % drop in C_p .

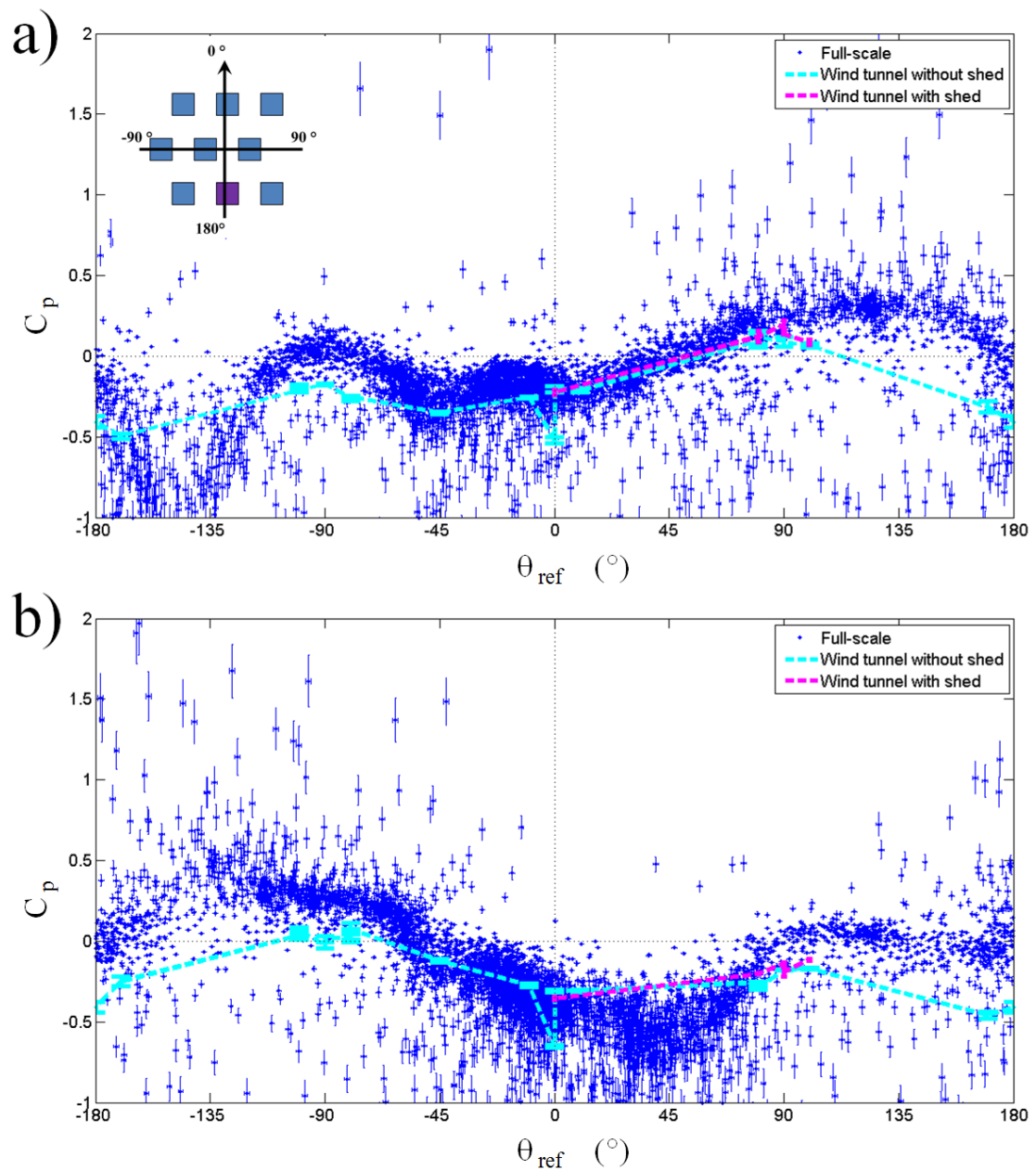


Figure 5.47: As Figure 5.44 but for the array case.

5.9 Conclusions

The effects of wind speed, wind direction and temperature difference on the C_p of an isolated cube and a cube surrounded by a limited asymmetrical array are explored in a rural area to reduce the complexity. It is evident that even here, there are complexities to be understood, especially when coupled with the presence of the simplified array.

5.9.1 Flow

The variation of wind speed with underlying surface and wind direction makes it difficult to position a reference wind measurement. In the simplified array case for $\theta_{ref} 0^\circ \pm 150^\circ$ the reference mast was in the wake of the array which undulates with time. Positioning a mast on, or near, to a building without proper consideration may influence the flow which the building is exposed to biasing the results.

The flow within the array was dominated by mechanical turbulence generated by the wakes of the array elements, with the turbulence intensity measured in front of the instrumented cube within the array being 7 to 10 times greater than for an isolated cube under similar wind conditions. This also suggests that the thermally driven turbulence is insignificant within this array of 6 m cubes, though may have a greater effect at smaller scales, such as over the opening of the cube and within the cube itself. Another consideration should be the thermal properties of the surrounding array, in this case, straw was used to create temporary cubes, but more realistic buildings will have greater heat capacities, altering the flow through thermal effects.

For $\theta_{ref} = \pm 90^\circ$ the turbulence intensity is lower than for other wind directions due to the oncoming flow being aligned down the channels in the array. This means that the wakes of the array elements are behind, in line with the other elements, meaning that the measurement points in the channel in front of the cube recorded lower turbulence intensities as a result. The effect of the wake on the reference mast means that the near-neutral stability assumption is less valid for those wind directions, due to the wake having a lower amount of mechanically generated turbulence (Lundquist and Chan, 2007).

The turbulence intensity of flow in and around the array is difficult to define, due to the effect of θ_{ref} on the flow path. This is also true for the boundary layer conditions, as despite the array being built in a field, there were still changes in surface roughness, for example crops in the adjacent field and pre-existing structures, which had an effect on the measurements. Especially in a heterogeneous urban area, it is likely that the boundary layer will not be fully adjusted to the underlying roughness and will display greater deviations than seen at this rural site due to the effects of varied building height and other street furniture. For the isolated case, only flows of $\theta_{ref} = 0^\circ \pm 45^\circ$ displayed a logarithmic profile, meaning that for all other directions a roughness length and displacement height could not be calculated accurately because measurements were not available at sufficient heights (Section 5.2.1).

The high levels of mechanical turbulence, sometimes as high as 5 means that even when the data are half hour averaged, the flow pattern even within a relatively simple and limited array is incredibly complex and sensitive to the external environment and wind direction. Certain flow directions, such as $\theta_{ref} = 0^\circ \pm 10^\circ$ demonstrated a dual behaviour visible in θ_{local} , meaning that θ_{local} cannot be accurately predicted from θ_{ref} for buildings within an array, especially as the dual behaviour could not be linked to

any other parameters. Low wind speeds within the array lead to an increase in local turbulence intensity as the oncoming flow has little structure, being completely dominated by the wakes of the array elements. Despite low wind speeds, the wake length of each array element was ~ 80 m, leading to a complex pattern of interactions dependent on θ_{ref} (Section 5.2.2). This caused cases where the recirculation region of the front row of array elements influenced the local mast and cases where, due to a slight change in wind angle, the wake of that array row did not influence the flow. The variation in U_{local} means that it will be difficult to estimate the ventilation rate of a building, due to the U_{ref} being much greater and less turbulent than flow within an array.

From the full-scale data it can be assumed that stability has little, if any measurable effect on C_p for an isolated cube, with the measured values on the array being too low to discern any differences (Section 5.4). Due to the lack of extremely stable and unstable cases in the dataset it is difficult to understand the effect of a strong instability on the instrumented cube. These results suggest that the near-neutral conditions commonly used in scale models are representative of full-scale data over a range of stabilities. More work is needed to demonstrate the effects of a strong instability on C_p values as it may alter the structure of the oncoming flow, but this is beyond the scope of this thesis.

5.9.2 Dual Behaviour

The cause of the switch between the two trends seen in the relations between local and reference wind speed for the array case remains unknown (Section 5.2.2) The impact of the limited array, staggered layout, packing density all need to be considered. Comparisons to other datasets with differing set-ups are required. To address this a wind tunnel dataset of sufficient scale to permit measurements of the local and reference wind speeds alongside pressures should be created for varying array layouts. Measurements could be taken at various locations throughout the array to determine whether specific interactions occur at the local measurement point or if this occurs throughout the array. Further work to understand whether the dual behaviour is localised to in front of the cube, or occurs in other places will include the use of DNS and LES models.

5.9.3 Pressure coefficient

The effect of wind speed on the measured C_p is as expected for the isolated cube. However, for the array case, C_p is reduced due to reduced U_{local} values. Although C_p is still normalised using U_{ref}^2 , the overall value of C_p is reduced more than for the isolated case. This difference in behaviour for the array case has implications for the use of wind tunnel data as reference data for buildings within an urban area; unless the relation between U_{ref} and U_{local} can be determined, C_p values are likely to be overestimated by existing wind speed based models, such as that suggested by CIBSE (2006).

The effects of different atmospheric stabilities are also not discernible from mean C_p , likely due to the building being low-rise. It is hypothesised that taller buildings will be more effected by changes in stability as they are exposed to greater wind speeds.

The array only influences the measured C_p when upwind of the instrumented cube, with the presence of cubes adjacent to the instrumented cube only appearing to effect the north and south faces. The array can be seen to reduce the front face averaged C_p by 80 % for perpendicular wind directions. There is good agreement with the wind tunnel and the full-scale, with the offset being due a difference in the location of the reference static pressure measurement.

5.9.4 Regulation Models

The AIVC, ASHRAE and wind tunnel models all agree for the isolated cube, despite different boundary conditions being used in each case. However, an isolated cube is a simplified building shape without awnings, intricate details, nor the material effects of a realistic building and care should be taken when applying results from simple models to full-scale buildings.

For the array case the small symmetrical array in the wind tunnel recorded higher values of C_p than the Silsoe array for $\theta_{ref} = 0^\circ$, despite all three of the arrays having two rows of cubes in front of the instrumented cube. The results suggest that symmetrical arrays should not be used to predict the pressure coefficients of asymmetrical arrays, especially for limited arrays, due to the edges of the arrays controlling a significant amount of the turbulence within the array. To improve the AIVC model and all other C_p models tested, a measure of the extent of the array, the organisation of the array and the uniformity of the array should be included.

The scale model of the isolated cube and the array captures the mean trends but does not capture the scatter in the full-scale data. This scatter is caused by varying reference wind conditions, differing scales of turbulence and a lack of detail of the full-scale surroundings within the wind tunnel due to space limitations. This suggests that whilst scale models can be used to provide an estimate of the C_p , the results show the associated scatter within realistic flow. All surrounding features of a building should be modelled within the array in order to capture a more realistic estimate of the C_p .

Chapter 6

The effect of an array on natural ventilation rates

6.1 Introduction

The ventilation rate of a cube is not completely comparable to that of a real building because of the simplicity of the set-up. The results of the different models are inter-compared between the different ventilation measurement methods: pressure difference (Section 3.8.5), tracer gas method (Section 3.8.1) and the volumetric flow rate (Section 3.8.6).

For the purposes of this chapter the tracer gas measurements are taken as the ‘true’ measurement of ventilation, as they consider both buoyancy and wind driven effects via a direct measurement of ventilation (Section 2.3). Results are compared to pre-existing models where possible. Only the half hour mean rates of ventilation are considered.

6.2 Overview of the ventilation rate data

The datasets were split into sealed, single sided and cross ventilated cases (Sections 2.3.7, 2.3.8, 2.3.10). Ventilation rates are reported as Q ($\text{m}^3 \text{s}^{-1}$) and may be normalised by dividing by the product of the opening area (A) and U_{ref} , (Q_N). The data analysed in each section are indicated (e.g. $I(NN_H^{All})$) and listed in Table 5.1. All data used is after the foam was put in place to reduce infiltration (Section 3.3).

6.2.1 Thermal effects in the Silsoe cube

Dataset used: $All(NN_{All}^{All})$.

A negative temperature difference (external - internal) represents a higher mean internal temperature (T_i), where T_i is the average of all internal thermocouple measurements.

The type of opening will affect the instrumented cube’s response to the external temperature (T_e) and solar irradiation, though all three cases show a diurnal cycle and simi-

lar ranges of T_e (0 °C to 8 °C), suggesting that heating within cube is predominately due to solar gains (Figure 6.1).

The internal temperature (T_i) is greatest when the cube is sealed, with cross ventilated and single sided cases having roughly similar trends, due to more air exchange between the internal and external environments (Figure 6.1). These trends occur independently of a change in T_e . For all cases, regardless of the cube being in the array or not, there is an increase in mean T_i with an increase in incoming short wave radiation.

For the isolated cube, there is no trend between U_{ref} and ΔT (internal - external). Whilst higher U_{local} values correspond to lower ΔT values (-4 °C to -6 °C), this range is also covered by the low U_{local} values (Figure 6.2a). The range of ΔT for all low U_{ref} values is -12 °C to 1.5 °C. A similar trend can be seen for the array (Figure 6.2b), though U_{local} is reduced by the array. Wind speeds $< 1 \text{ m s}^{-1}$ show a range of ΔT between -10.5 °C to 2 °C, with little data being available for $U_{local} > 3 \text{ m s}^{-1}$. For $U_{local} = 3 \text{ to } 4 \text{ m s}^{-1}$ the range of ΔT for the array case is -4 °C to 1 °C, with the isolated case range being larger: -9 °C to 1.5 °C due to it being undertaken in summer.

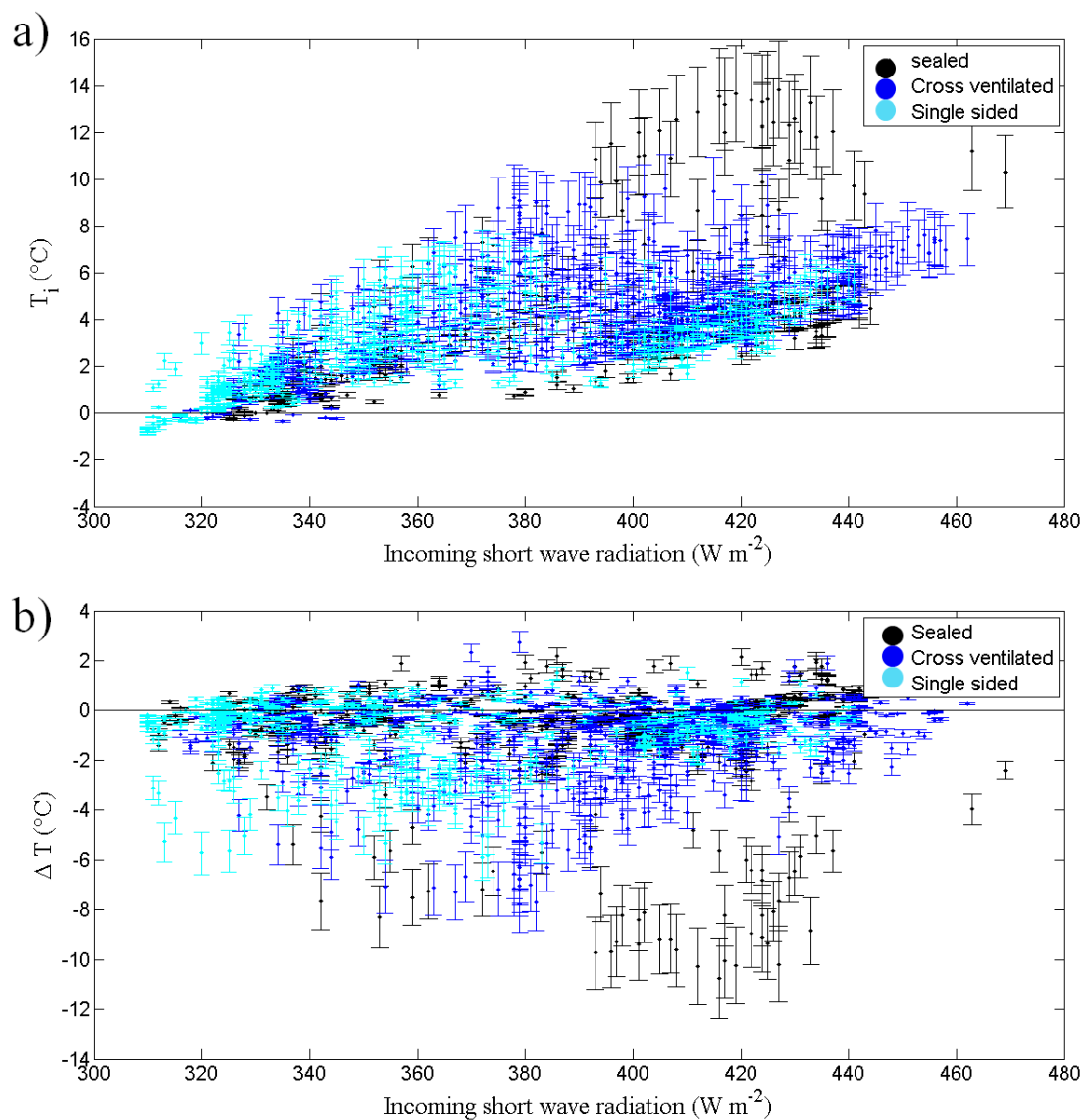


Figure 6.1: Daytime winter-time incoming short wave radiation thirty minute averages and the a) mean internal temperature and b) internal-external temperature difference (Section 3.5.4.1) for the cube within the array for the three different opening types: Sealed, single sided and cross ventilated (Section 2.3). Ideally the isolated dataset would have been used to display the relation between incoming short-wave radiation and internal temperature or temperature difference, but instrumentation issues did not permit this.

The effect of the shadowing by the array is clear, with the isolated cube having a median internal vertical temperature difference (difference between measurements at 4 m and 1 m) (ΔT_{iv}) of around 0 °C until 09:00, with the sunrise causing a larger spread (99.3 % of the data had a range of 4 °C or less, and an interquartile range of 2 °C). The median ΔT_{iv} rises to 1.5 °C at 15:00 and reduces to 0 to 0.5 °C after sunset. The low ΔT_{iv} during night-time hours cannot accurately be calculated due to instrument errors (Section 3.5.4.1).

For the horizontal temperature difference (ΔT_h) thermocouple sets 1 and 2 formed the 'front' measurement with sets 3 and 4 being the 'back' measurement. For the isolated cube 99.3 % of the data is between 0 °C to 0.8 °C difference (front - back). This difference is due to increased solar heating of the front face compared to the back, with higher ΔT_h values occurring in the evening between 16:00 and 20:00. For the array, 99.3 % of ΔT_h was within the range -0.25 °C to 1.5 °C. No diurnal trends were visible for the array case, however the array case had a larger amount of outliers of the range during daylight hours. This was due to the interaction of the weakened solar radiation due to the season and the shadows cast by the array. For cross ventilated cases, the horizontal thermocouple array could be influenced by sunlight shining through the openings, leading to an elevated internal temperature when compared to the vertical arrays.

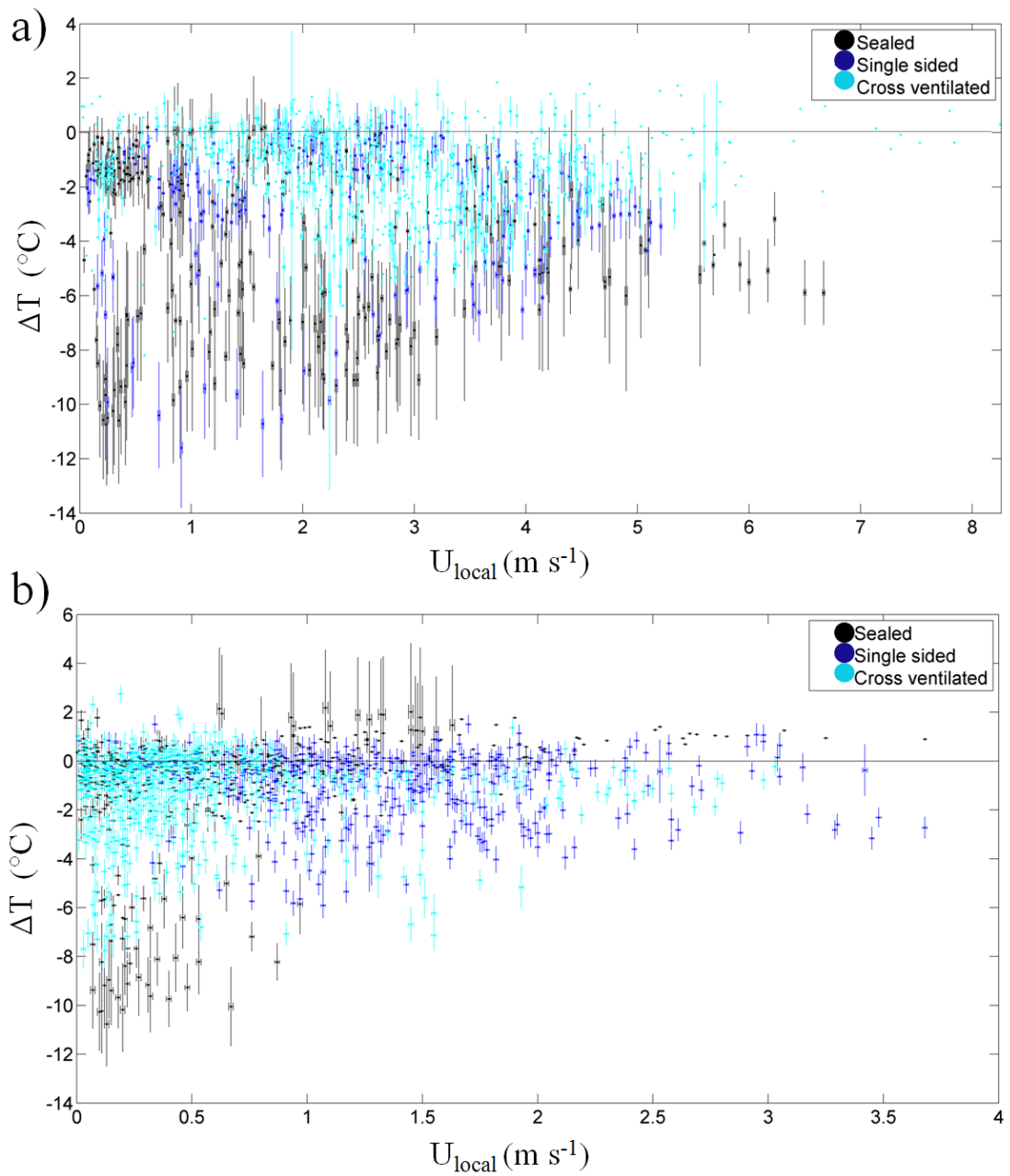


Figure 6.2: ΔT (external-internal) against U_{local} for a) isolated and b) array cases. T_i is taken as the mean of all the internal measurements with outliers removed. T_e is measured on the Channelling mast.

The instrumented cube has a complex temperature distribution which is affected by shadowing and solar gains. The presence of the array increases the horizontal variation of temperature across the cube, though has little effect on ΔT_{iv} with both isolated and array cases recording temperature differences of between 0 and 4 °C. To define “well mixed”, ΔT_{iv} and ΔT_h the thresholds used were < 2 °C per 5 m and < 2 °C over 3 m respectively. As expected, sealed cases are more prone to solar heating, while the temperature of cross ventilated and single sided cases being closer to external temperatures.

θ_{ref} has little, if any, effect on the ΔT . $U_{local} < 1 \text{ m s}^{-1}$ leads to a wide range of ΔT of $-12 \text{ }^\circ\text{C}$ to $1.5 \text{ }^\circ\text{C}$ for the isolated case and $-10.5 \text{ }^\circ\text{C}$ to $2 \text{ }^\circ\text{C}$ for the array case.

Coupled with the variations in θ_{ref} and opening type, the solar effects of the cube result in a complex temperature profile, with temperature gradients being present both vertically and horizontally within the cube, and across the opening (ΔT). The latter has to be considered for single sided ventilation, though the literature tends to neglect the thermal driven effects for cross ventilation.

6.2.2 Buoyancy driven ventilation

The methods used to obtain the buoyancy driven ventilation ($Q_{thermal}$) (equation 2.7) are discussed in detail in Section 2.3.4 (page 27). The total ventilation rate (Q_{all} , equation 2.12, page 31) is the combination of the buoyant and wind driven ventilation rates (the pressure difference method, Section 3.8.5, page 83). When a building is surrounded by an array and $U_{ref} < 3 \text{ m s}^{-1}$ cross ventilation driven by thermal effects can be up to 50 % of the total ventilation rate, and in some cases a higher proportion of the total ventilation rate (Figure 6.3). This is due to U_{local} being reduced by the presence of the array. Another contributing factor could be the scatter recorded in the pressure measurements under low U_{ref} values (Section 5.3).

For the isolated cube with cross ventilation, only a few instances of $U_{ref} < 2 \text{ m s}^{-1}$ are recorded. However, for $U_{ref} > 2 \text{ m s}^{-1}$, it is clear that the proportion of buoyant driven ventilation is low, with a median value of 2.3 % and a mean value of 3.4 %. For $U_{ref} > 4 \text{ m s}^{-1}$, the proportion of buoyant ventilation is $< 10 \%$ of the total ventilation rate (Figure 6.3). This suggests that for an isolated cube with $U_{ref} > 4 \text{ m s}^{-1}$ the buoyant effects are negligible, with errors on the wind driven ventilation rate being larger than the magnitude of the thermal component. This is also true for the array case.

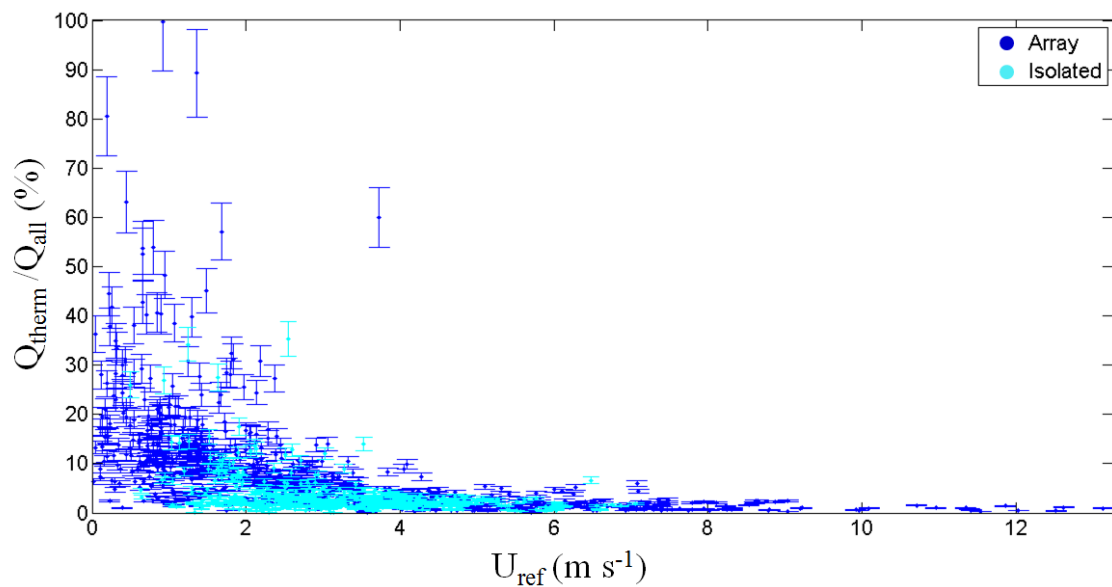


Figure 6.3: Proportion of $Q_{thermal}$ for the isolated and array cases. All data are for cross ventilated periods. Error bars are based on measurement errors. The ventilation rates are not normalised.

The proportion of thermally driven ventilation for single sided cases peaks for low U_{ref} values, with thermally driven ventilation (Q_{therm}) accounting for 5 % to 55 % of the total ventilation at $U_{ref} < 1 \text{ m s}^{-1}$ (Figure 6.4). For U_{ref} values between 1 and 3 m s^{-1} this range reduces to 5 % to 45 %, with the lower proportions likely to occur at night when there is no thermal heating of the cube. Unlike the cross ventilated results for the array (Figure 6.3), there are instances where there is a contribution from thermally driven flows that exceeds 10 % when $U_{ref} > 4 \text{ m s}^{-1}$. As U_{ref} increases, the percentage of thermally driven flow decreases which is likely to correlate to a decrease in turbulence intensity in the reference flow.

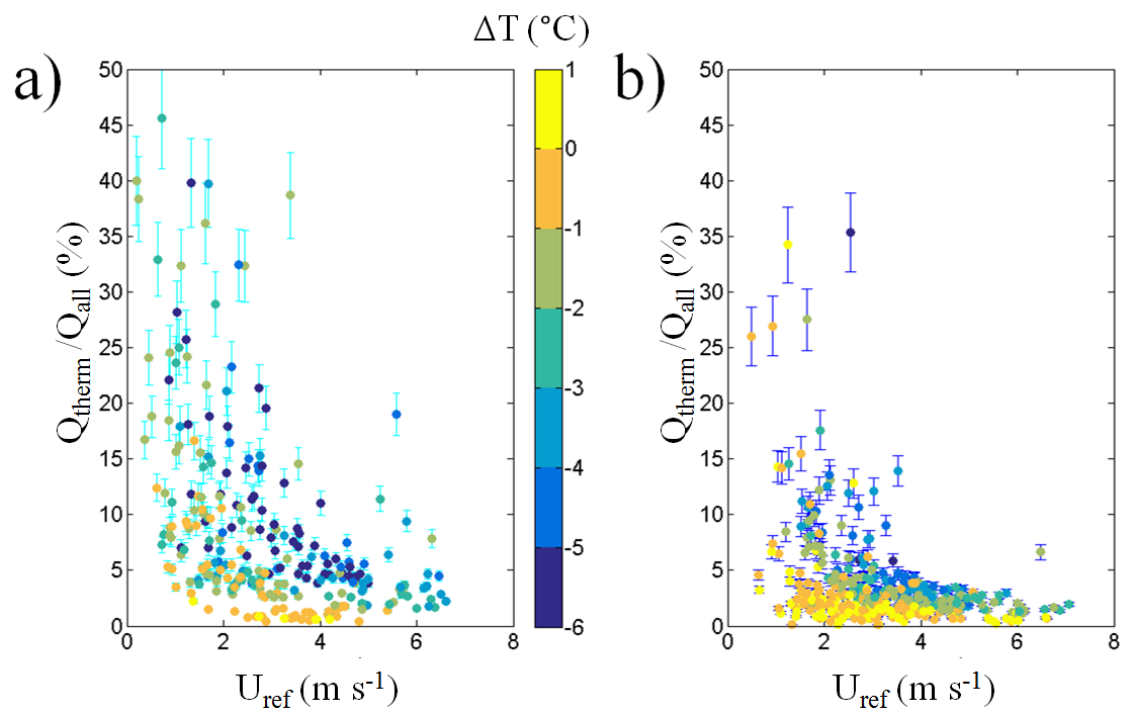


Figure 6.4: Proportion of single sided ventilation driven by buoyancy effects for the a) isolated and b) array cases. Colour represents ΔT (internal - external temperature difference). Errors are based on measurement error.

The array reduces the scatter seen during daylight hours due to the shielding effects, which reduce the magnitude of the thermal component of ventilation (Figure 6.5). However, large amounts of scatter occur after 20:00 for both the isolated and array cases, due to the cube being metal, though due to the lower ΔT values for the array case, there is less variation than for the isolated cube which will undergo rapid temperature changes.

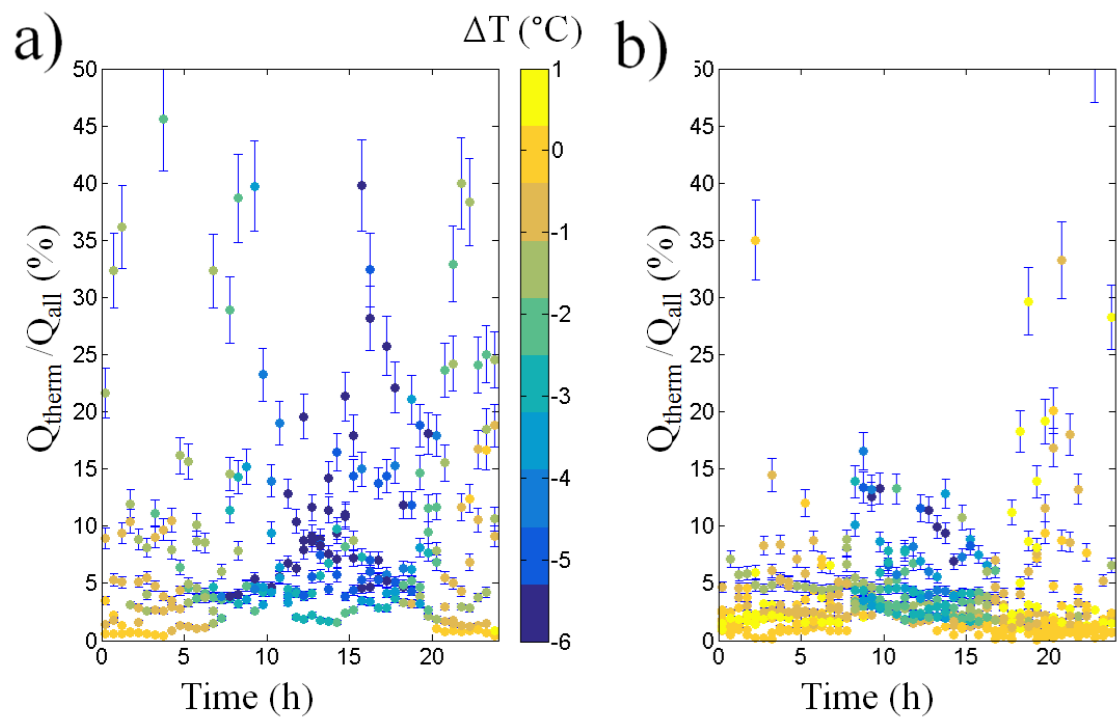


Figure 6.5: As Figure 6.4 but plotted against time of day rather than U_{ref} .

θ_{ref} also effects the percentage contribution of thermally driven wind ventilation. For single sided ventilation (Figure 6.6a) when θ_{ref} is not perpendicular to the opening, the thermally driven contribution increases for an isolated cube. For the array case (Figure 6.6b), this trend is dampened by reduced U_{local} values.

With the thermal contribution being dependent on wind direction, this suggests that it cannot easily be predicted for a building and will vary depending on the surroundings. For the array case the surroundings may act to damp this variation with wind direction, reducing the thermal driven ventilation to negligible levels, especially when ΔT is near 0°C and U_{ref} is low.

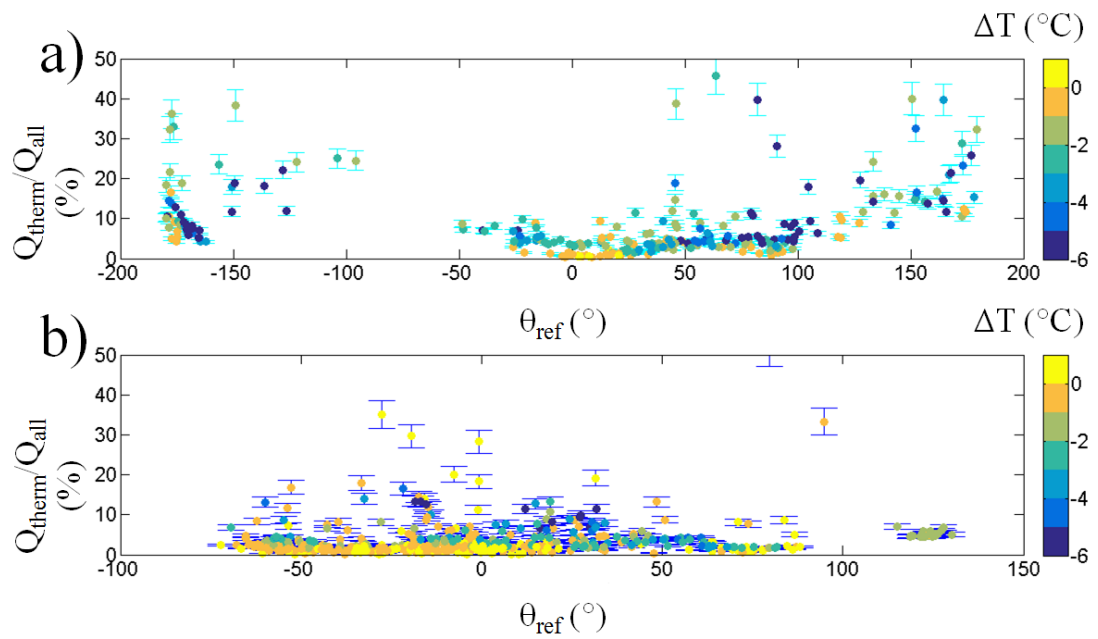


Figure 6.6: The average percentage of the total ventilation due to thermal effects for single sided ventilation cases against θ_{ref} for the a) isolated cube and b) array, colour coded for Δ . Error bars are measurement errors.

For the array cross ventilated case (Figure 6.7), the large amounts of mixing within the flows in the array and low U_{local} values lead to unpredictable spikes in the thermal contribution which are dependent on the specific conditions of the sampling time. This could be due to the openings acting as two separate single sided cases, especially on days with low U_{ref} , due to the thermal effects occurring around the cube.

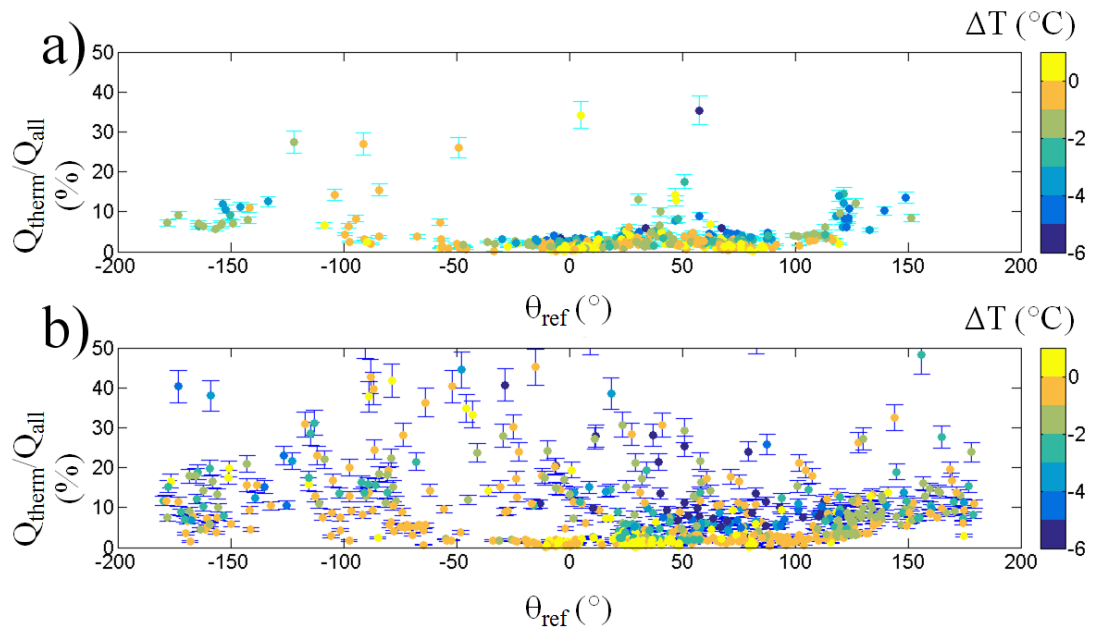


Figure 6.7: As Figure 6.6 but for cross ventilated cases.

In conclusion, the balance between thermal and wind driven natural ventilation cannot be simply quantified, due to the variation with ΔT , the effect of the surroundings and neighbouring buildings, U_{local} and θ_{local} . The buoyant and wind driven processes act both in alignment and against each other, with the conditions that decide this remaining unknown for the array case. For the array case the surrounding buildings also have an effect. However, when considering real buildings, these results may not be valid due to the different heat storage capacities of the surrounding buildings and the effect of the urban heat island, along with any effects due to surrounding vegetation.

6.2.3 Infiltration rates

Infiltration rates (Q_i) of the sealed cube were measured using the tracer gas decay method (Section 3.8.1). Q_i was calculated from the average of the three gas sensors within the cube. The opening around the base of the cube (0.05-0.1 m) contributes to large errors (Section 3.3). The time of year is assumed to not have an effect on the infiltration rate of the cube, as it is wind driven a majority of the time.

The infiltration rate for both the isolated and array case increase with larger U_{ref} values, regardless of θ_{ref} (Figure 6.8). For the isolated cube, Q_i increases as U_{local} increases, with differences being caused by flow approaching from the back of the instrumented cube. The internal wind speed (U_{intf}) also increases as Q_i increases for both set-ups. Q_i displays no correlation with T_i or ΔT for both the isolated and array cases.

Q_i is dependent on θ_{ref} for both isolated and array cases (Figure 6.8) in agreement with findings by Brocklehurst (2015). For $\theta_{\text{ref}} = 0$ °, the normalised Q_i (Q_{iN}) for the array

is larger, potentially due to the higher amounts of mixing in front of the cube. However, as θ_{ref} moves away from 0° , Q_i for the array decreases to levels below that of the isolated cube. This is due to the sheltering effect of the surrounding array elements.

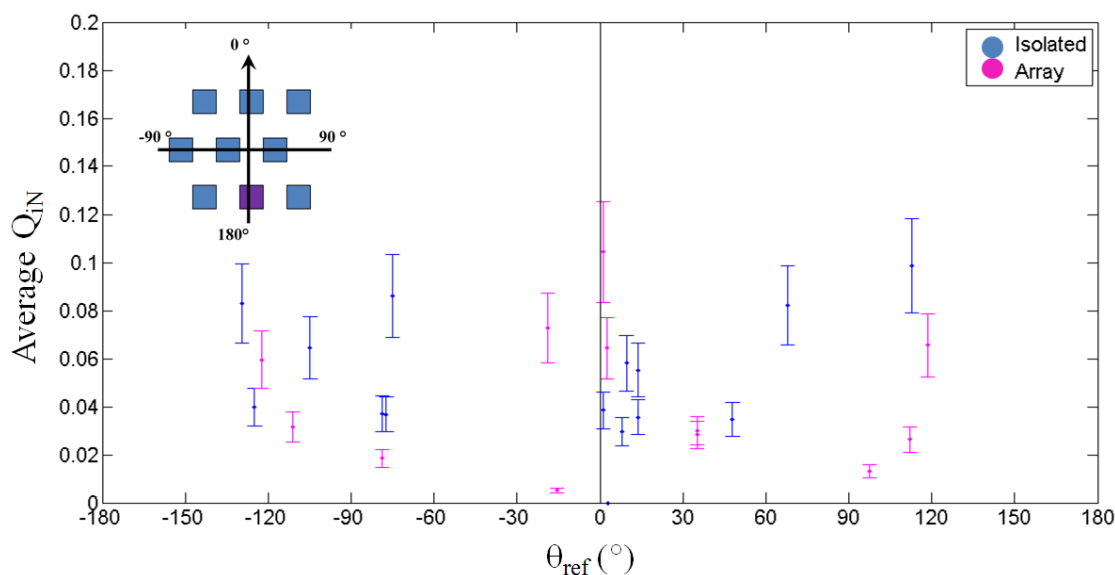


Figure 6.8: Average Q_{iN} results for the isolated and array cases. Error bars are the standard error of the measurement.

There are no data recorded for $\theta_{ref} = 180^\circ$, for both isolated and array cases, but it is assumed that it will behave in a similar way to the isolated cube when $\theta_{ref} = 0^\circ$ due to the lack of sheltering. The infiltration rate increases when $\theta_{ref} = \pm 120^\circ$ due to the largest gaps at the base of the cube being aligned with the oncoming wind. This may suggest that the internal flow is not well mixed and a jet may potentially form between the two largest gaps in the base of the cube. This behaviour was seen during smoke releases for this θ_{ref} .

To account for Q_i within the ventilation rate measurements for the isolated cube, ideally an infiltration measurement for each measured θ_{ref} should be taken. However, this was not practical during the observations and not likely to be possible when designing a building. Due to the lower number of infiltration measurements, a 'bulk' infiltration parameter will be applied, which does not consider θ_{ref} , unless a measurement is available for that direction. The most common measure of Q_{iN} over all θ_{ref} values was between 0.03 and 0.04.

The infiltration rate is only measured by the tracer gas decay method, as such, where possible the predicted infiltration rate may be deduced from the total ventilation rate measurement for the tracer gas results.

6.3 Choice of wind speed for the volumetric flow method

Little detail is given in the literature about the wind speed which should be used to calculate the ventilation rate (Section 3.8) if the speed directly in the opening is not available. For an isolated cube, any measured wind speed in the near vicinity is likely to be representative of the approaching flow, as long as the measurement is not positioned directly behind the cube or downstream (Section 5.2.2).

For the isolated case (Figure 6.9a) ventilation rates calculated using U_{local} and U_{intf} for $\theta_{ref} = 0^\circ$ overlap. However, U_{local} does not take into account the angle of the flow to the opening, causing it to predict high ventilation rates for $\theta_{ref} = 90^\circ$ when flow was parallel to the opening and thus Q decreases. The ventilation rate calculated using U_{intf} has a symmetrical trend centred around $\theta_{ref} = 0^\circ$, with the minimum Q_N (approximately 0.05) occurring when the flow is parallel to the opening ($\theta_{ref} = 90^\circ$). There is a slight increase to 0.2 for $\theta_{ref} = -120^\circ$ to 180° , due to the flow beginning to penetrate through the back opening.

For the sonic anemometer in the back opening (U_{intb}), Q_N remains constant for $\theta_{ref} = -60^\circ$ to 60° , suggesting that the internal behaviour of the cube remains similar for these wind angles. It may also suggest that there is no jet forming between the front and back openings, as the front and back predicted ventilation rates are not equal. Like the front internal sonic anemometer, when $\theta_{ref} = \pm 90^\circ$ Q_N is at its lowest (approximately 0.05). For $\theta_{ref} = -120^\circ$ to 180° , the Q_N calculated using U_{intb} peaks in the region of 0.6 to 0.8, similar values to the front opening at $\theta_{ref} = 0^\circ$. This behaviour is not seen in the U_{local} based ventilation rate for these angles as it is effected by the wake of the instrumented cube, and cannot be seen as representative of the flow through the opening.

For the array case, the results show a similar trend, despite being much lower than for the isolated cube, due to the normalisation by U_{ref} . There is greater scatter (range of 0.4) for the local external sonic anemometer for $\theta_{ref} = -60^\circ$ to -180° and $\theta_{ref} = 60^\circ$ to 180° . This is due to the local mast being positioned within a region of interacting wakes, and is sometimes in the recirculation region of the instrumented cube (Section 5.2.2).

For $\theta_{ref} = -60^\circ$ to 60° , Q_N predicted using U_{local} is between 0 and 0.1, suggesting that regardless of what direction of wake movement is captured in the mean value, Q_N remains approximately constant.

The U_{intf} and U_{intb} Q_N values are low, due to the normalisation, and show similar trends with θ_{ref} as the isolated cube. However, for $\theta_{ref} = -150^\circ$ to -180° and $\theta_{ref} = 150^\circ$ to 180° , U_{intb} may be higher or similar to U_{local} . This is due to the back face of the cube being fully exposed to the flow and not being influenced by the array. The values of 0.1 recorded are not as high as those recorded for the isolated cube (0.8), though this could be due to the reduced pressure difference across the cube, meaning there is less suction to draw flow into the cube.

Contrary to the isolated cube, there is a slight increase (0.01 to 0.03) in Q_N for $\theta_{ref} = 90^\circ$ when using the front internal sonic anemometer. This is likely due to the flow being parallel to the cube, but free from the array's influence. These values match those found for the isolated cube and highlight that the array does not have any influence when the obstacle rows are aligned with θ_{ref} ($\theta_{ref} = 90^\circ$).

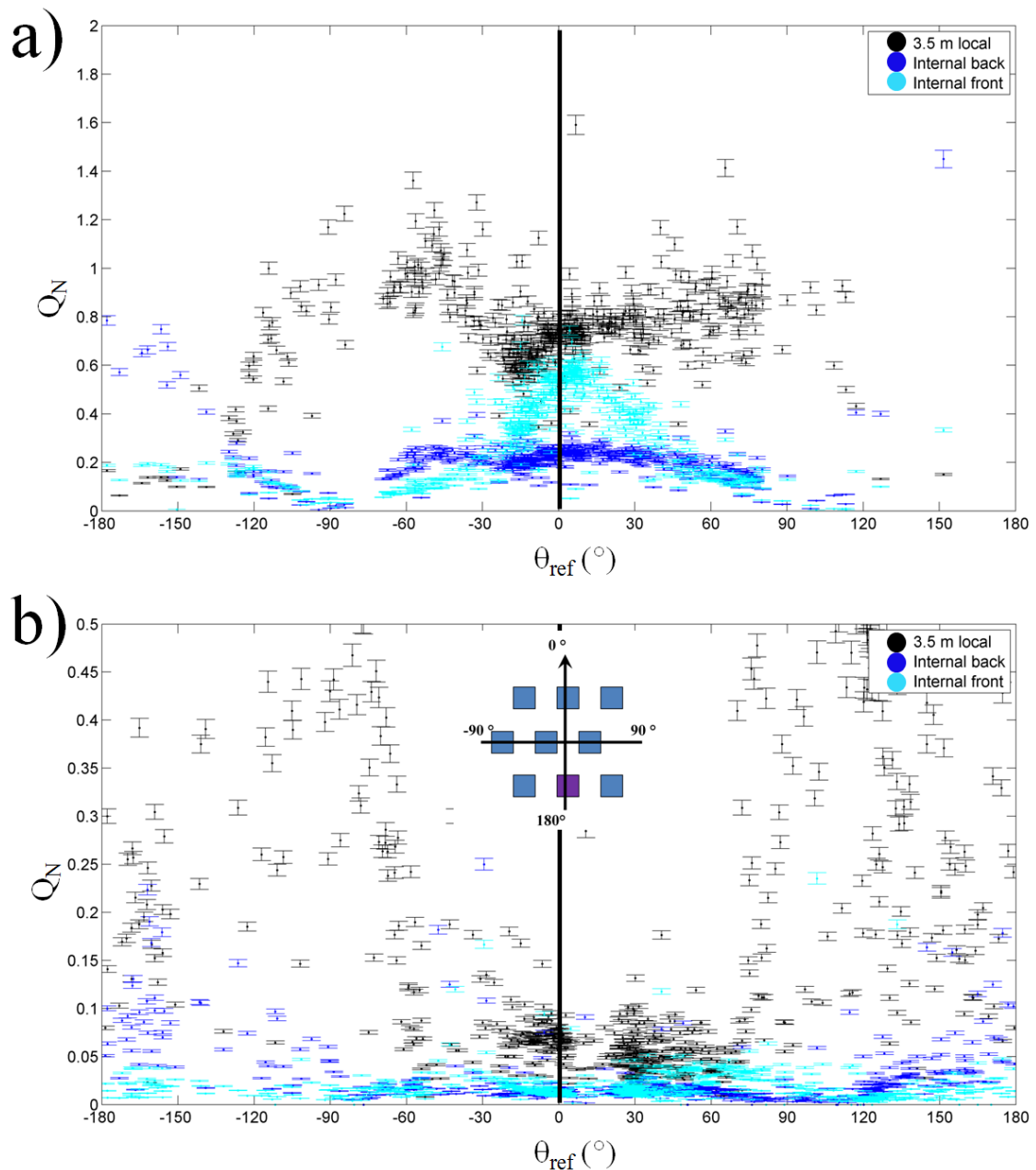


Figure 6.9: Normalised ventilation rate (Q_N) obtained by the volumetric flow method using the two internal sonic anemometers and the local sonic anemometer in front of the cube for the a) isolated cube and b) array case for cross ventilation.

For single sided ventilation, ventilation rates calculated using U_{intf} provide a better representation of the flow through the opening than using U_{local} and as such, will be

used to calculate the volumetric flow rate. For the cross ventilated case, the usefulness of the internal sonic anemometers depends on θ_{ref} and θ_{local} . For $\theta_{ref} = -60^\circ$ to 60° U_{intf} will be used and for θ_{ref} of -135° to -180° and 135° to 180° , U_{intb} . For $\theta_{ref} = -60^\circ$ to -135° and $\theta_{ref} = 60^\circ$ to 135° , the average of the ventilation rates calculated using U_{intb} and U_{intf} will be taken.

6.3.1 Internal wind speed (U_{int})

Dataset used: $All(All_{All}^{All})$.

One consideration is the position of the internal sonic anemometers. For $\theta_{ref} = 0^\circ$ the sonic anemometers will be in line with the peak in wind speed as it comes through the opening. As θ_{ref} shifts from 0° , it is likely that the peak flow speed will not impact on the sonic anemometer (Figure 6.11). This trend is clear for the isolated cube (Figure 6.10). The peak for the front sonic anemometer is more pronounced, with the back sonic anemometer being less sensitive for the single sided case (Figure 6.10a). However, when the cube is cross ventilated, the front and back sonic anemometers react in similar ways, with a peak also forming for the back sonic anemometer at $\theta_{ref} = 0^\circ$ (Figure 6.11a). U_{int} values are different for the single sided and the cross ventilated samples due to the data captured. Ideally both would cover a large range, however this was not possible to achieve with the current dataset.

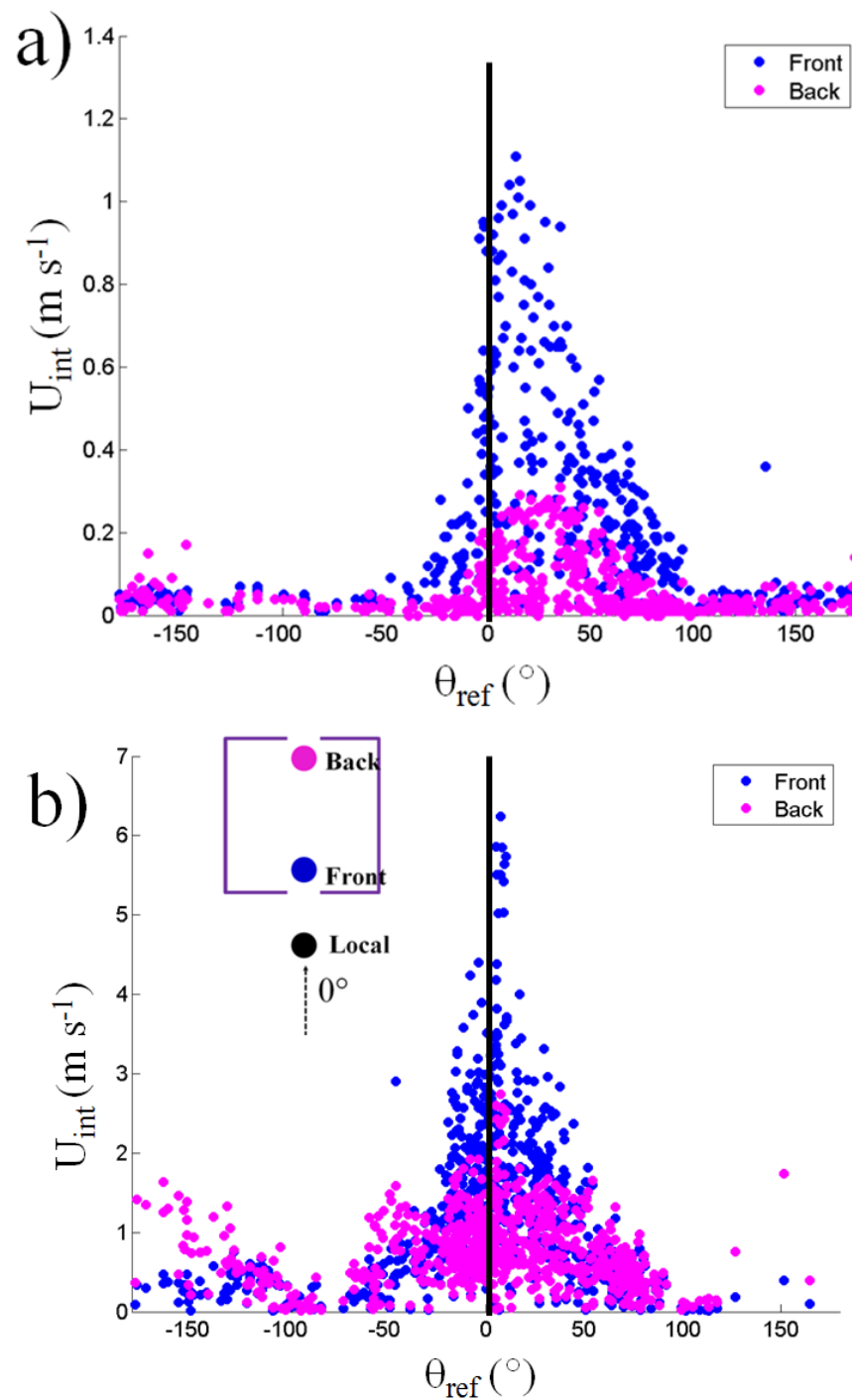


Figure 6.10: U_{intf} and U_{intb} against θ_{ref} for the isolated cube for a) single sided and b) cross ventilated cases. Schematic is valid for both plots. Dataset: $I(All_{All}^{All})$.

For both cross ventilation and single sided ventilation the trends in U_{intb} and U_{intf} are similar, though U_{intb} increases for a single sided set-up for $\theta_{ref} = 150^\circ$ to 180° and $\theta_{ref} = -150^\circ$ to -180° (Figure 6.12). This is due to the gaps in the bottom of the cube being focused on the back (east) face of the cube and thus the back sonic anemometer captures

the increase in infiltration rate. This occurs despite the majority of the gap around the base of the cube being filled with packing foam.

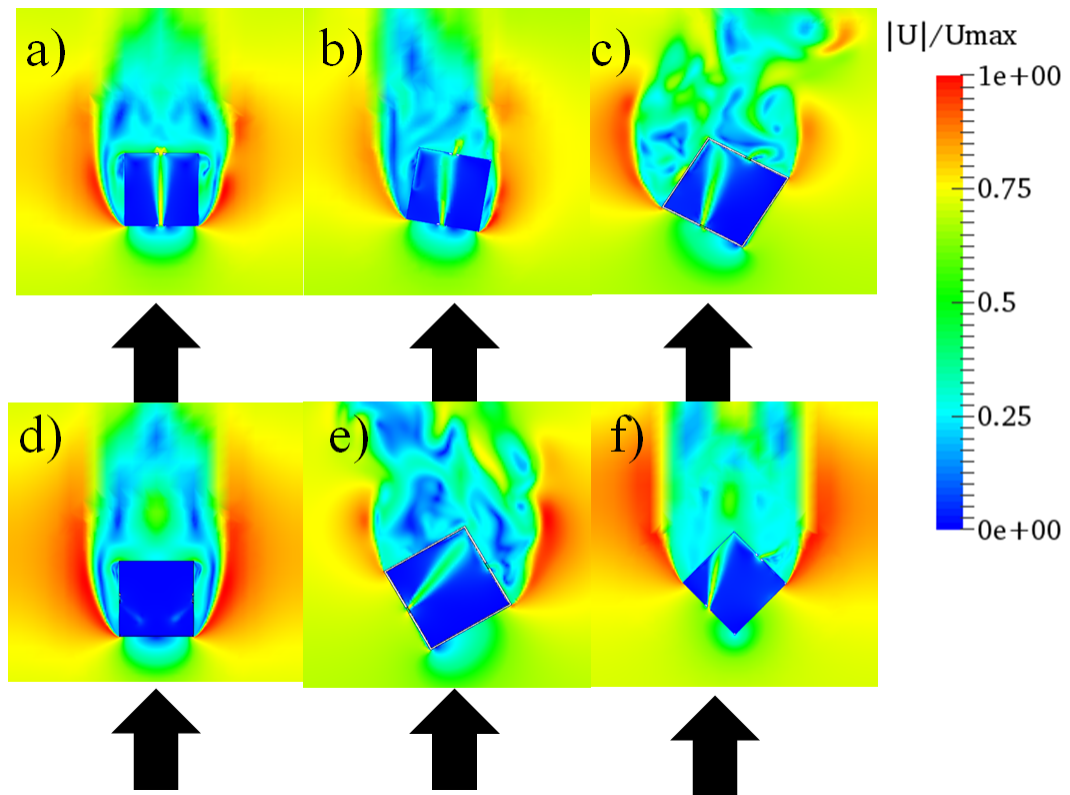


Figure 6.11: Schematic of the flow field around and inside the cross ventilated isolated cube caused by a) $\theta_{ref} = 0^\circ$ b) $\theta_{ref} = -10^\circ$ c) $\theta_{ref} = -30^\circ$ d) $\theta_{ref} = -90^\circ$ e) $\theta_{ref} = -60^\circ$ f) $\theta_{ref} = -45^\circ$. Colour denotes the relative velocity, with greens and yellows being higher than blues. The CFD set up is detailed in Appendix L. Image from King (2016).

For U_{ref} , there is more scatter with θ_{ref} , due to effect of the local roughness elements, though two trends, dependent on θ_{ref} are visible. These are caused by the local mast being within the wake of the cube for $\theta_{ref} = 150^\circ$ to 180° and $\theta_{ref} = -150^\circ$ to -180° . The reference mast is also likely to be affected by the wake of the storage shed from this wind direction. The lower trend occurs when the oncoming flow is roughly parallel to the openings and thus a lower U_{int} is recorded, due to the flow only entering the cube through turbulent processes.

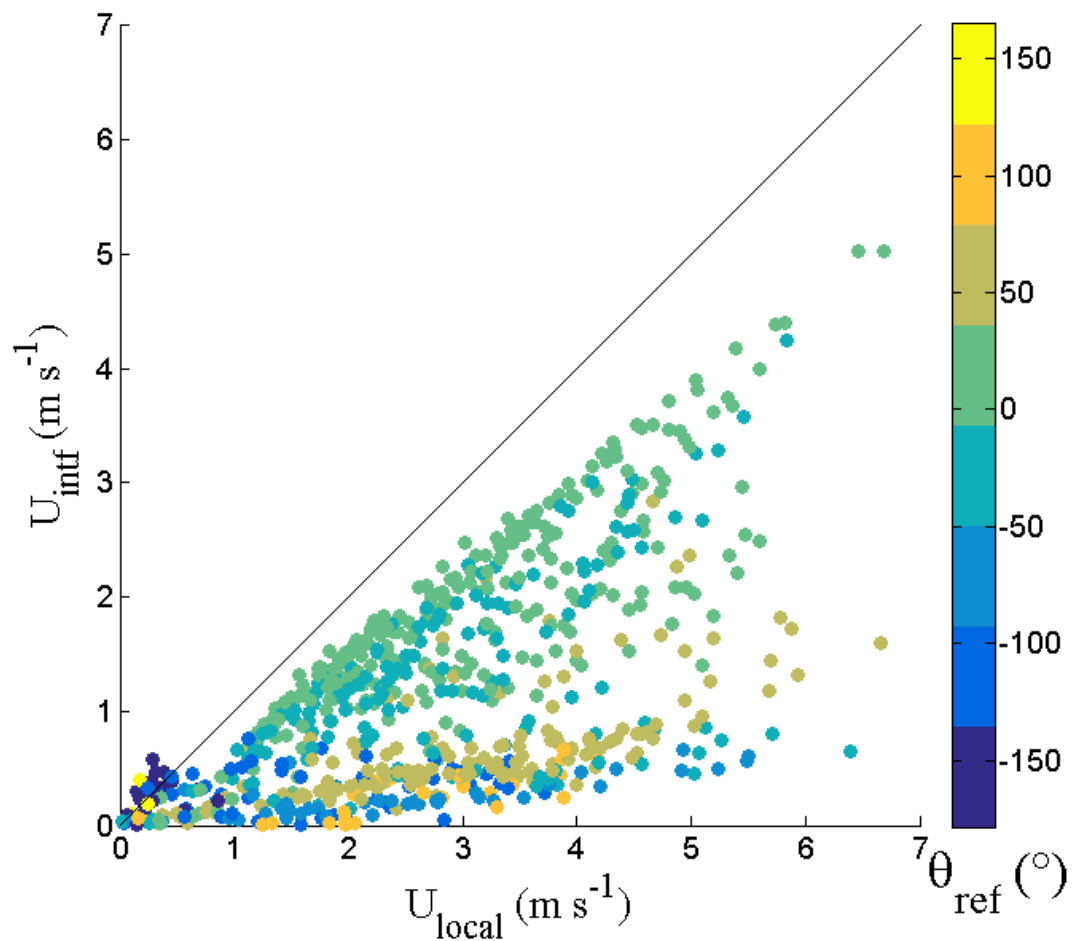


Figure 6.12: U_{local} and U_{intf} for a cross ventilated isolated cube, colour coded for θ_{ref} . The black line represents the 1:1 ratio.

A similar trend to that seen in Figure 6.10a can also be seen for the array, though the peak at $\theta_{ref} = 0^\circ$ for U_{intb} is less pronounced, likely due to the external flow being slowed by the array, thus preventing the incoming air from penetrating far into the room (Figure 6.13a). The flow is likely to be angled downwards towards the centre of the cube, meaning the back sonic anemometer only detects infiltration, rather than the flow through the opening. For a single sided opening within the array, $U_{intb} > 0.1 \text{ m s}^{-1}$ only once when compared to U_{intf} (Figure 6.12). The internal wind speeds are reduced by the array for single sided cases (Figure 6.14) and the result is similar for cross ventilated cases.

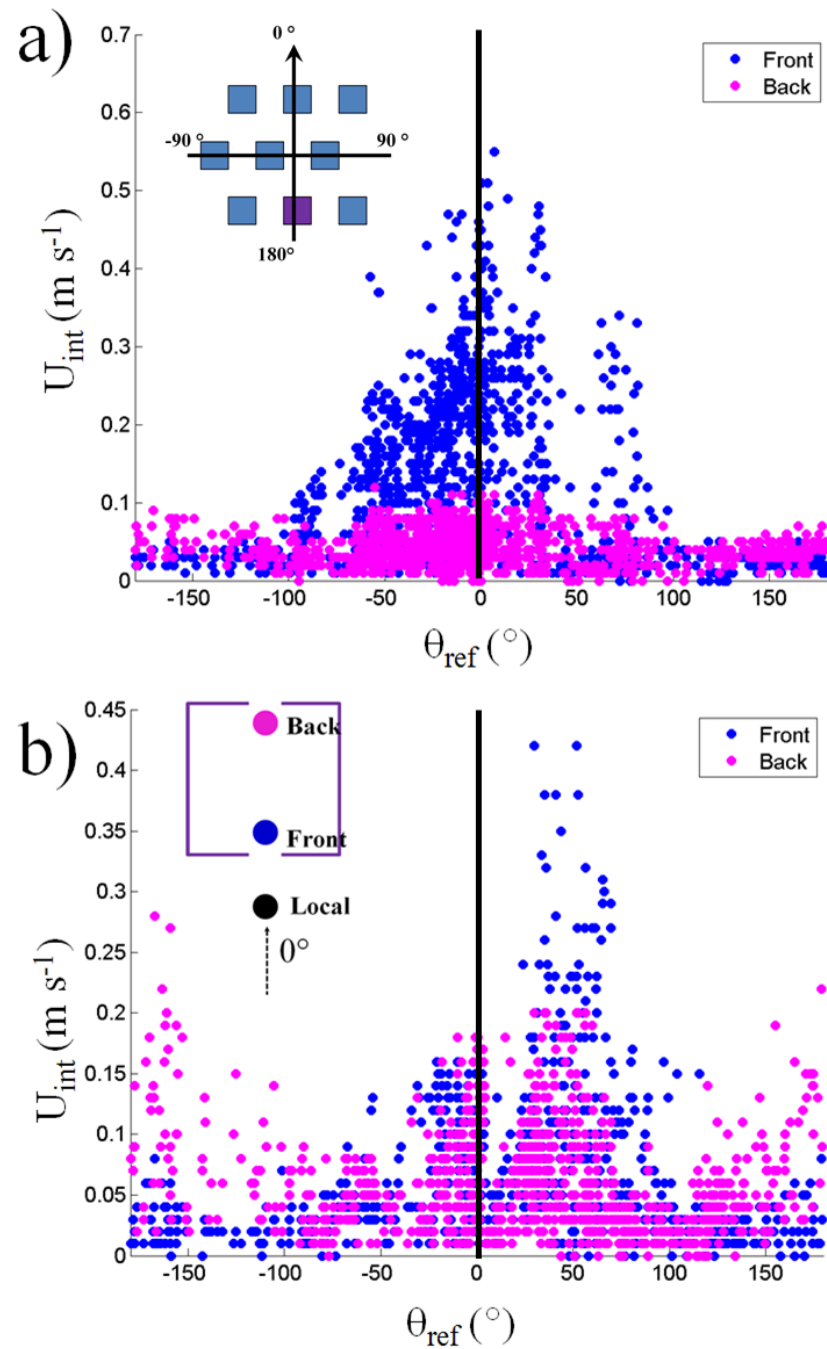


Figure 6.13: As Figure 6.10 but for the array cases. Dataset: $A(All_{All}^{All})$.

There is also a visible peak for the array case at $\theta_{ref} = 90^\circ$ (Figure 6.13) which is not present for the isolated cube. This is likely due to the channelling of the flow by the array elements, with both U_{int} values of 0.1 to 0.4 m s^{-1} being similar to that for the isolated cube. This is due to the array being parallel to the oncoming wind, leading to it not influencing U_{int} .

For the cross ventilated cube within the array (Figure 6.13b) it can be seen that like for

the isolated cube, the U_{intf} and U_{intb} become similar, suggesting that mixing is occurring within the cube, or that the jet is forming between the two openings. U_{intb} is higher for $\theta_{ref} = -150^\circ$ to 180° and 150° to 180° due to the back of the cube being completely exposed to the oncoming flow for these wind directions. The peak at $\theta_{ref} = 50^\circ$ is due to a higher U_{ref} being recorded for this direction.

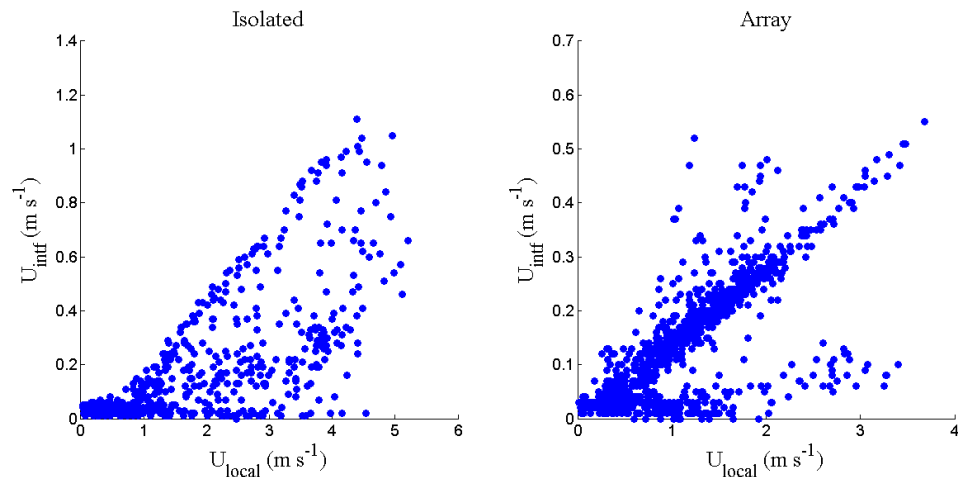


Figure 6.14: U_{intf} against U_{local} for both the isolated cube and a cube within the array for a single sided set-up. Black line denotes a 1:1 ratio.

U_{int} can be seen as a proxy of the mixing state of the cube and the presence of the jet between the two openings. When two openings are present, even in the array with lower U_{local} values, a jet can be seen for $\theta_{ref} = 0^\circ$. This jet is not as strong for $\theta_{ref} = \pm 180^\circ$ and cannot be seen in the single sided cases. Though the jet is present, it does not guarantee that the cube is well mixed, as if the jet is sufficiently strong mixing may not occur in the sides of the cube (Figure 2.14).

For the array case, the internal sonic anemometers are operating near the minimum measurement limits: 0.01 m s^{-1} which may lead to larger errors in U_{int} . Another consideration is that U_{int} will include Q_i for certain wind directions. An ideal internal set up would use a smaller instrument to allow for a greater resolution of measurements without disrupting the flow, in order to understand the effect of the opening on the flow structure as it passes into the array. A larger number of measurements should also be taken inside the cube, with perhaps a line of five instruments between the two openings and one on either side of the presumed jet area, in order to capture when the jet is forming and when the flow drops to the floor somewhere near the centre of the cube. The use of such delicate equipment, however, was not possible on the field site due to the excess moisture and spiders.

6.4 Effect of different variables on ventilation rate

The ventilation rate of a building is effected by thermal and wind driven processes, which suggest that it will also be affected by the turbulence intensity of the oncoming flow and the atmospheric stability. Ventilation rates will be compared to variations in wind direction, wind speed, turbulence intensity and stability. To ensure a large dataset, the pressure difference derived ventilation rate is mainly used, though where possible the tracer gas and volumetric flow methods are also included. For the ventilation rates derived from pressure differences across the opening, trends are likely to be similar for that seen for the pressure coefficient (Sections 5.3, 5.4 and 5.5).

6.4.1 Comparison of tracer gas and pressure difference methods

Dataset used: $All(All_{All}^{All})$

Where possible, the pressure difference has been calculated over the time of the tracer gas release, otherwise, the closest half hour average is used. There is greater agreement between the tracer gas and pressure difference methods when the cube is cross ventilated, likely due to the larger amounts of mixing which occur within the cube and the reduced impact of the internal thermal effects on the tracer gas measurements (Figure 6.15). There is also more agreement between the two methods for the array case, likely due to the shielding reducing the overall ventilation rate and preventing the tracer gas from being flushed. The relation between the two methods is not linear, and is likely to be effected by a wide range of variables, some of which may be unique to that half hour averaging period.

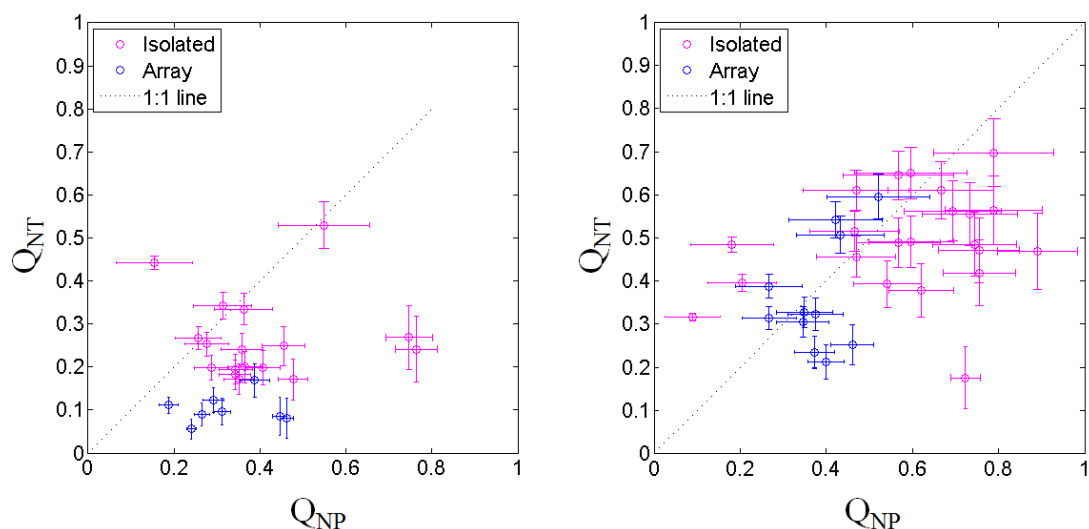


Figure 6.15: Comparison of the pressure difference method (Q_{NP}) and the tracer gas decay method (Q_{NT}) for (a) single sided and (b) cross ventilation.

6.4.2 Effect of wind direction on ventilation rate

The tracer gas dataset for single sided ventilation is lacking in measurements for $\theta_{ref} = 0^\circ$ to -120° , with the pressure difference dataset also being sparse for $\theta_{ref} = -90^\circ$ to -120° (Figure 6.16).

Despite being normalised by U_{ref} and opening area, both the single sided and the cross ventilation measurements highlight that even when θ_{ref} remains constant, there is a large spread of data. For $\theta_{ref} = 0^\circ \pm 30^\circ$ (Figure 6.11a, b and c) for the array case there is a range of 0.1 to 1.4 Q_{NP} for the single sided cases and a range of 0.1 to 3.275 Q_{NP} for the cross ventilated case (Figure 6.17). For the isolated cube the range of Q_{NP} is 0.7 to 2.9 for single sided, and 0.05 to 1.2 for the cross ventilated cases (Figure 6.16). This suggests that other factors are influencing the ventilation rate measured by pressure difference alongside the θ_{ref} . For both isolated and array cases, for $\theta_{ref} = \pm 180^\circ$, the single sided Q_{NP} becomes greater than that measured for $\theta_{ref} = 90^\circ$, despite being on the leeward wall.

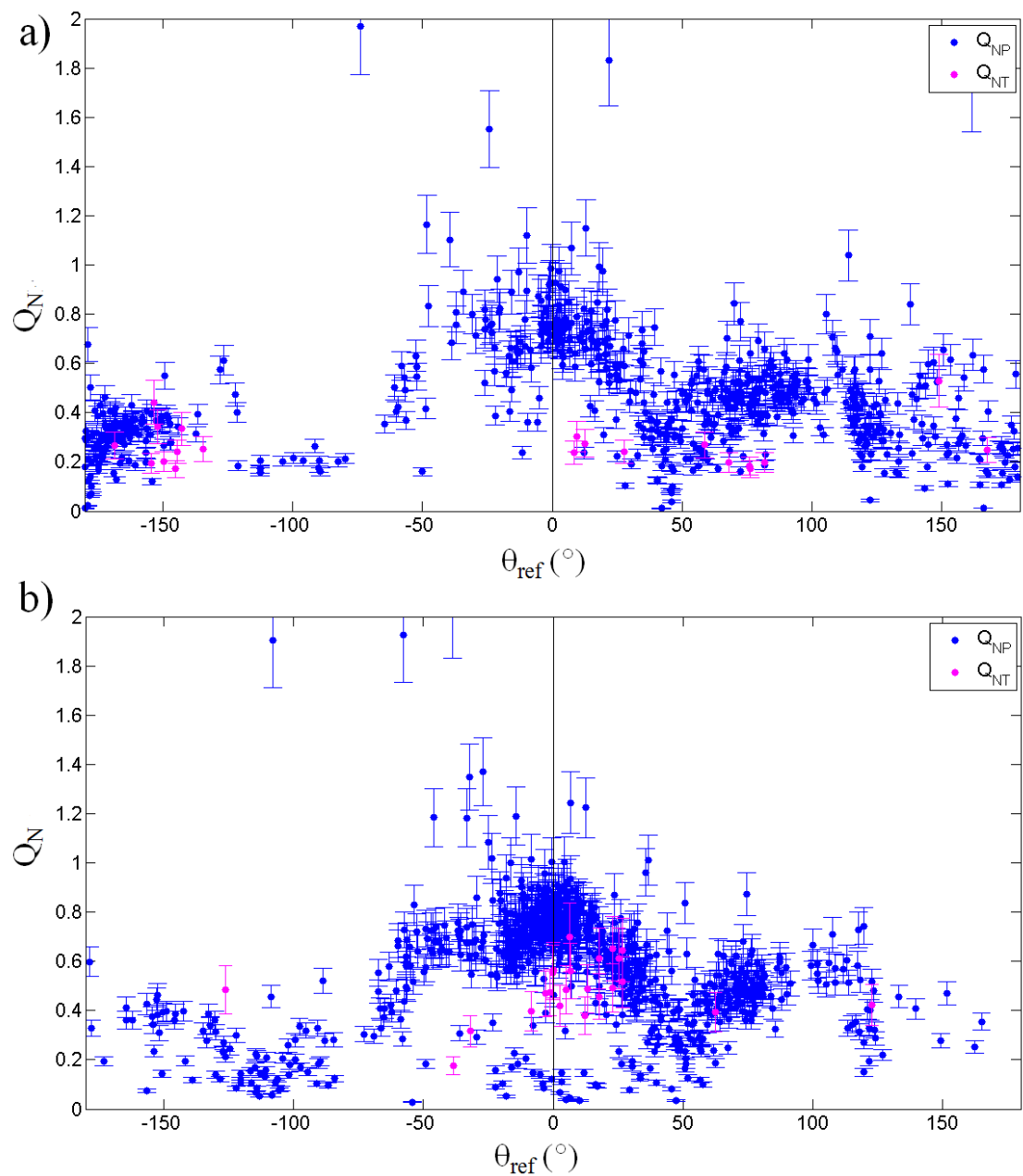


Figure 6.16: Q_N against θ_{ref} for the tracer gas measurements (Q_{NT}) and the pressure difference measurements (Q_{NP}) for the isolated cube for a) single sided and b) cross ventilation.

For the array case, a peak of $0.5 Q_{NP}$ occurs for $\theta_{ref} = \pm 45^\circ$ (Figure 6.17) due to the flow being able to penetrate the array diagonally. For the $\theta_{ref} = -100^\circ$ to -120° there is little ventilation recorded, due to flow being blocked by the aligned cubes (Figure 6.18f). Unlike for the isolated cube, the trend of Q_N with θ_{ref} for the array case is asymmetric, due to the array itself being asymmetrical (Figure 6.17). The pressure difference method (Q_{NP}) appears to predict a higher Q_N value for $\theta_{ref} = 0^\circ$ to -120° when compared to Q_{NT} , though this could be due to the thermal effects within the instrumented cube acting to reduce the ventilation rate measured by tracer gas (Figure 6.18a).

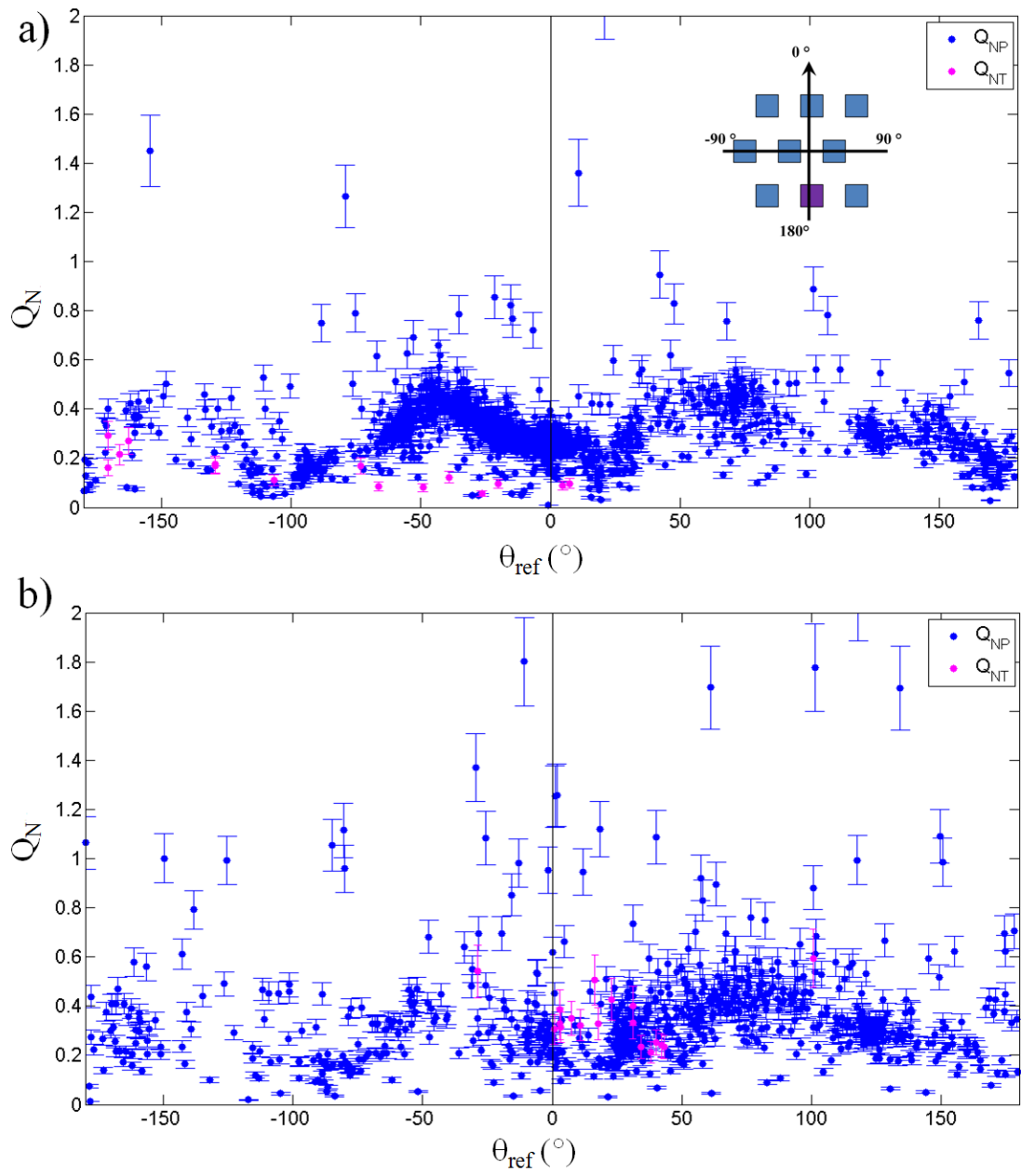


Figure 6.17: As Figure 6.16 but for the array case.

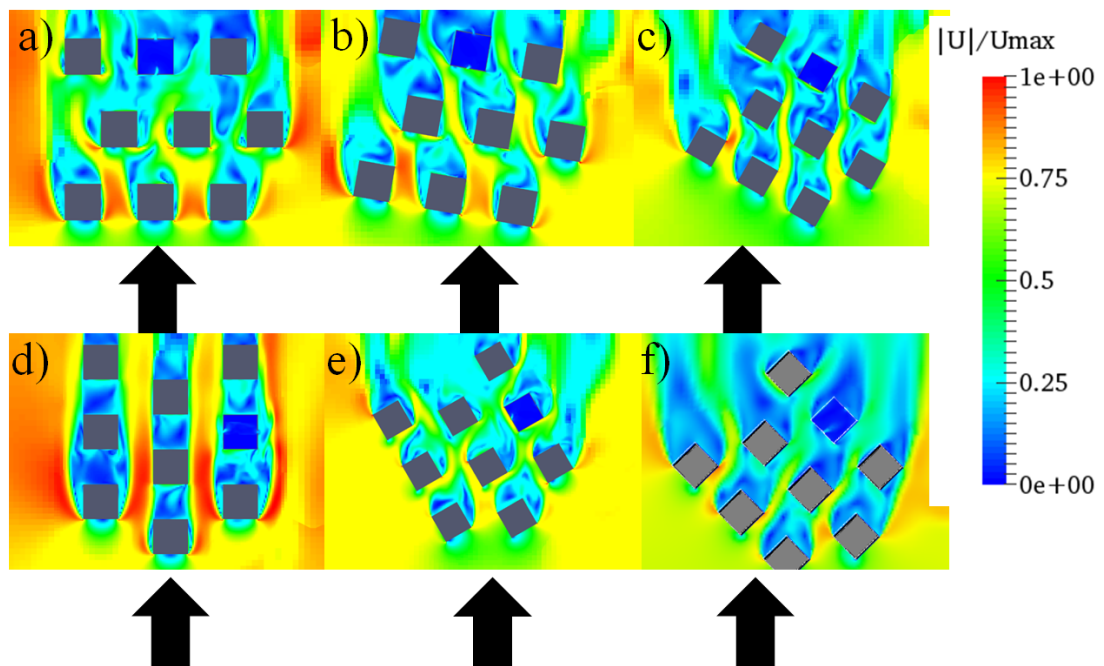


Figure 6.18: Schematic of the flow field caused by a) $\theta_{ref} = 0^\circ$ b) $\theta_{ref} = -10^\circ$ c) $\theta_{ref} = -30^\circ$ d) $\theta_{ref} = -90^\circ$ e) $\theta_{ref} = -60^\circ$ f) $\theta_{ref} = -45^\circ$. Colour denotes the relative velocity, with greens and yellows being higher than blues. The CFD set up is detailed in Appendix L. Image from King (2016).

The rapidly varying wind direction within the array suggests that the most simple design for cross ventilation (two openings in parallel) will be ineffective at providing a constant ventilation rate which matches thermal comfort and pollution criteria unless there is a strong, dominating prevailing wind direction at the site (e.g. a coastal area). An effective cross ventilation system for an urban area would have multiple openings and a system which responds to changing wind directions by opening and closing selected vents to control flow (CIBSE, 2005).

6.4.3 Effect of wind speed on ventilation rate

Dataset used: $All(NN_{All}^{All})$

Two wind speed measurements are used to understand the effect of differing wind speeds on Q : U_{ref} and U_{local} (Section 5.2.2). Ventilation rates will not be normalised by U_{ref} and will instead be given in air changes per hour (λ).

Q for the isolated cube is effected by both wind speed and wind direction (Section 6.4.2). The behaviour with wind speed can be split into three parts (Figure 6.19): part **a** which occurs for $\theta_{ref} = 0^\circ \pm 60^\circ$, part **b**, $\theta_{ref} = 60^\circ$ to 130° and **c** $\theta_{ref} = -130^\circ$ to -180° and 130° to 180° .

The behaviour of part **c** changes when λ is compared to U_{local} . When $\theta_{ref} = \pm 150^\circ$ to 180° the local sonic anemometer is within the wake region of the isolated cube, meaning

U_{local} is lower. For the isolated cases, the behaviour of single sided (Figure 6.19) and cross ventilated (not shown) cases are similar, with differences only occurring for $\theta_{ref} = \pm 150^\circ$ to 180° due to the back opening.

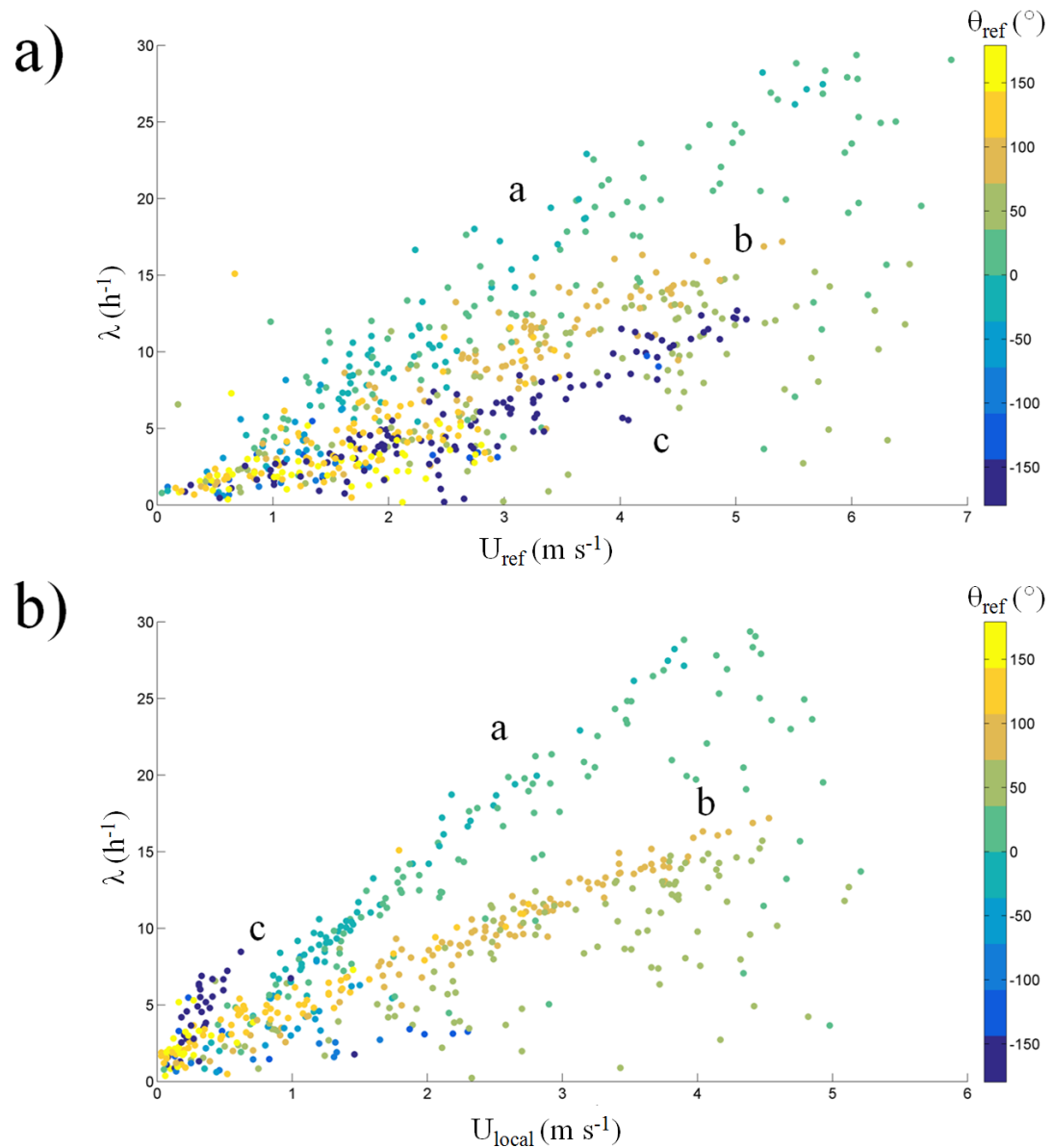


Figure 6.19: Air changes per hour (λ) calculated using the pressure difference method for a single sided opening state for the isolated cube against a) U_{ref} and b) U_{local} . Colour denotes θ_{ref} .

For a single sided building within an array, the relation with U_{ref} does not seem to depend as strongly on θ_{ref} (Figure 6.20), suggesting that local array effects dominate (Figure 6.20b). The difference in behaviour $\theta_{ref} = \pm 150^\circ$ to 180° is not noted for the array, due to the U_{local} measurement being influenced by recirculation regions and cube wakes regardless of θ_{ref} . The results of the cross ventilated cases (not shown), as with the isolated cube, are similar to the single sided cases, with slight changes for $\theta_{ref} = \pm$

150 ° to 180 ° due to flow passing through the instrumented cube.

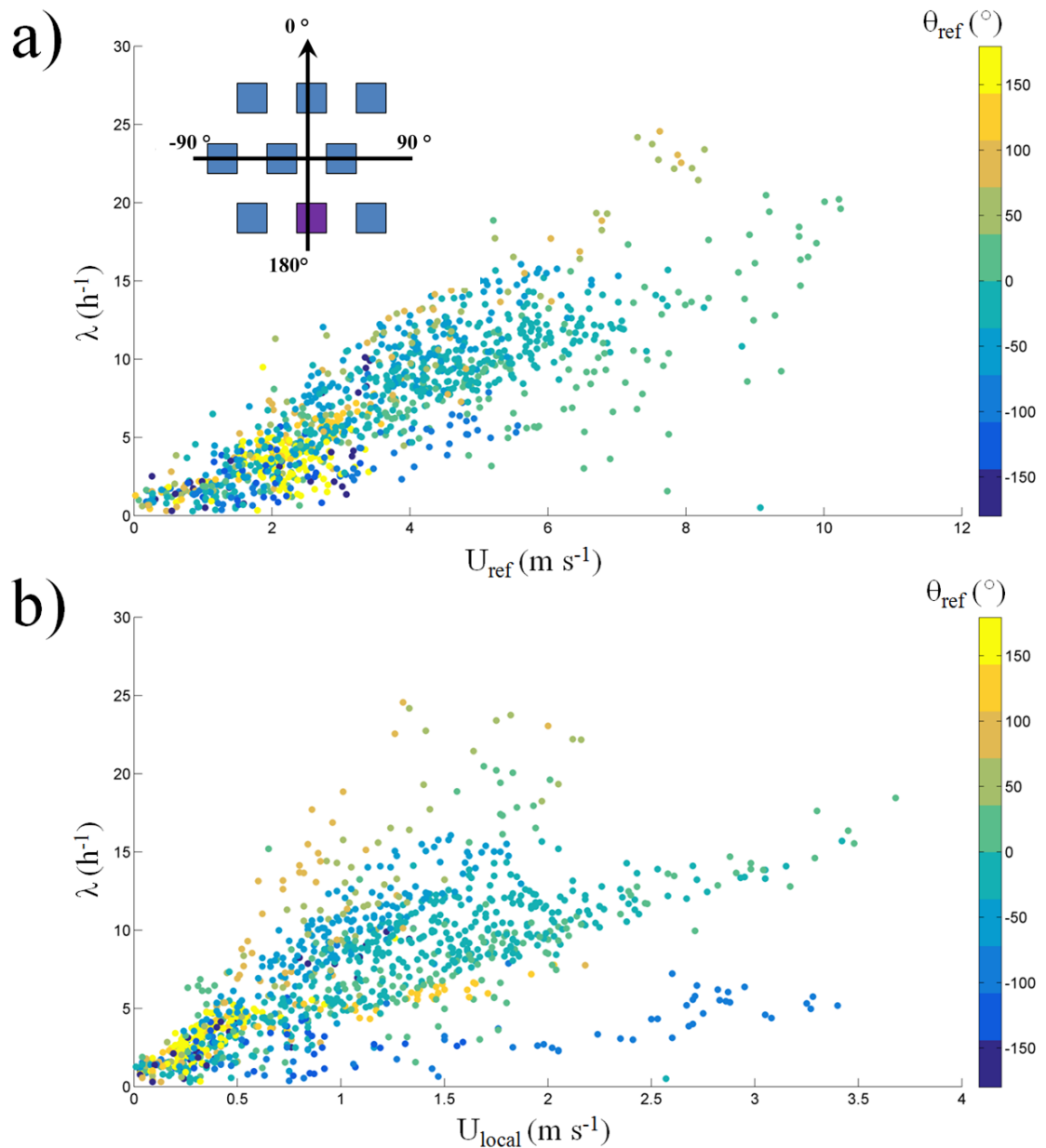


Figure 6.20: As Figure 6.19 but for the array data.

For λ plotted against U_{local} , the effects of θ_{ref} are more prominent, but cannot be split into three sections (Figure 6.20b). As expected for a single sided case, when $\theta_{ref} = -150^\circ$ to -180° low λ values are recorded, due to the back opening being closed. It can be seen that as θ_{ref} shifts from 0° to around $\pm 100^\circ$, λ increases, due to the flow being able to penetrate into the array and impact on the instrumented cube. For $\theta_{ref} = -90^\circ$ to -120° and 90° the array acts as an aligned array, with flow being roughly parallel to the instrumented cube (Figure 6.18d).

Using U_{local} instead of U_{ref} leads to a correlation coefficient of 0.61 for single sided ventilation and 0.16 for cross ventilation. This reduction in correlation coefficient for U_{local} suggests that the connection between U_{local} and λ is not linear (Section 5.2.2), and as such a model cannot be created based on U_{local} . The reduction could be caused by the complex non-linear interaction of the cube wakes, combined with changes in θ_{ref} and the thermal effects of the array.

It can be assumed that the higher U_{ref} or U_{local} , the greater the amount of wind driven ventilation, though the effects of thermal driven processes must also be considered. These will either increase λ , or act against the wind driven forces and reduce λ (Section 6.2.2). The results of this section suggest that an accurate model of ventilation rate cannot be created based on wind speed alone, due to the dependence on θ_{ref} and the thermal effects (Sections 5.2.2, 5.2.4).

6.4.4 Effect of turbulence intensity on mean ventilation rate

For both the isolated cube and the array there was no linear correlation found between turbulence intensity in the reference flow and Q_N . The pressure difference and volumetric methods will not detect the turbulent contribution to ventilation as only mean values are used, which may explain the large differences for the array case as the flow local to the cube is dominated by turbulent wakes and eddies (Straw, 2000). It can be seen that the greatest variation between the methods occur for single sided openings, likely due to the increased amount of thermally driven ventilation (Section 6.4.1). The tracer gas method will detect the changes in ventilation rate and the direction of the flow but the mean air change rate will not. The pressure derived ventilation rate (Q_P) is used for this comparison in order to ensure that there is a large dataset with less gaps, though the effects of low wind speeds on the pressure difference methods should be considered (Section 5.3).

Spearman's rank correlations were calculated between the percentage difference of the methods and θ_{ref} as well as the reference turbulence intensity (Table 6.1). For most cases there is no strong evidence of a correlation, suggesting multiple factors are contributing to the effect. For the difference between tracer gas and pressure difference methods there is moderate negative correlation (-0.59) with θ_{ref} for the cross ventilated cube within the array. This suggests as θ_{ref} increases, the difference between the two methods increases, with the pressure difference method over-predicting Q_N in comparison to the trace gas method.

The difference between the tracer gas predicted flow rate and the volumetric flow rate for a single sided case within the array has moderate positive correlation (0.55) with the turbulence intensity of the reference flow, suggesting that as the turbulence intensity increases, the volumetric flow method begins to under-predict Q_N . This may suggest that the large amounts of turbulence caused by the array elements actually increase sin-

gle sided Q_N , as more turbulence suggests more mixing, which will aid the transfer of flow through the opening.

Table 6.1: Spearmans rank correlation coefficients between the differences in ventilation rate predicted by the three different methods (Sections 3.8.1, 3.8.5, 3.8.6) for Q_N and θ_{ref} , θ_{local} and turbulence intensity recorded at 6 m (Ti_{ref}). Strong correlations are highlighted in bold. 'Iso' isolated cube, with 'Arr' array cases. 'XS' is cross ventilated and 'SS' is single sided ventilation. 'T' the tracer gas method, 'P' the pressure method and 'F' the volumetric flow method.

Case	Spearmans Rank	θ_{ref}	Ti_{ref}	θ_{local}
Iso XS T-P	0.20	-0.05	0.32	-0.24
Iso SS T-P	-0.09	-0.03	NaN	NaN
Arr XS T-P	-0.59	-0.19	0.11	-0.89
Arr SS T-P	-0.31	0.40	-0.40	-0.07
Iso XS T-F	0.07	-0.34	0.12	-0.20
Iso SS T-F	-0.22	0.13	0.03	0.87
Arr XS T-F	-0.03	-0.43	-0.29	0.29
Arr SS T-F	0.24	0.55	0.07	0.74

Looking at the θ_{local} and local turbulence intensity for the isolated single sided cube, there is a strong positive (0.87) correlation between the local turbulence intensity and the difference between the tracer gas and volumetric method. This also occurs for the single sided case within the array (0.74), suggesting that as the turbulence intensity increases, the flow through the opening method under-predicts the ventilation rate in comparison to the tracer gas measurements, again suggesting that the turbulence local to the cube increases mixing across the opening, ultimately increasing Q_N . However, for the cross ventilated cube within the array, there is a strong negative correlation (-0.89) between local turbulence intensity measurements and the difference between tracer gas and pressure difference ventilation measurements, suggesting that as the local turbulence intensity increases, the pressure difference method over-predicts the ventilation rate measured by the isolated cube.

These correlations suggest that for single sided ventilation, high levels of turbulence intensity increases the mixing occurring across the opening, though this effect does not occur for cross ventilation, likely due to the flow being driven by the mean flow rather than the turbulent fluctuations. There is correlation between low U_{local} values and high turbulence intensity for the single sided cube in array cases, though high turbulence intensity does not effect the Q_N for equivalent wind speed (Figure 6.21). The scatter in the ventilation rate is not entirely explained by θ_{ref} . For isolated case, low U_{local} also lead to higher local turbulence intensity, producing a range of Q_N between 0.1 and 0.5.

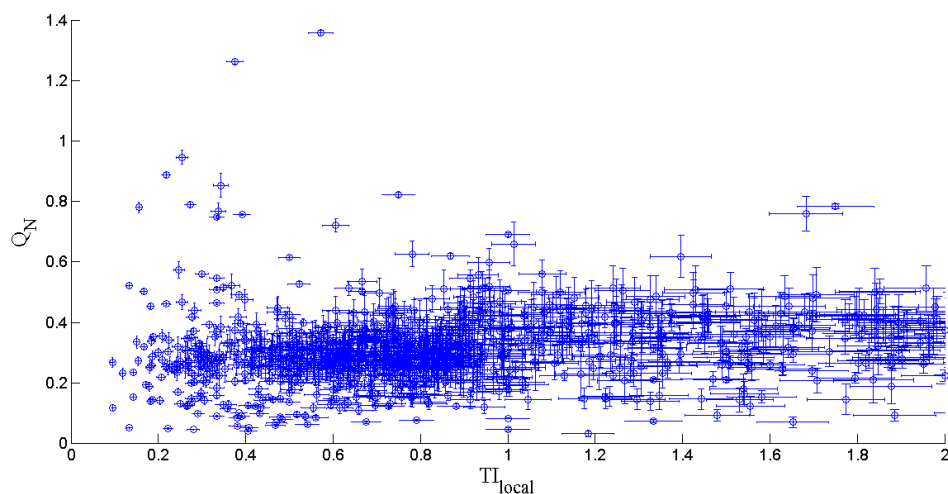


Figure 6.21: Q_N for single sided ventilation within the array and Ti_{local} . Dataset: $A(All_{All}^{All})$.

It is hypothesised that the effects of turbulence intensity cannot be seen in mean flows, but are likely to be seen in instantaneous flows where the time-scale is shorter and more similar to eddy size. A more turbulent flow would increase mixing within the cube, but would decrease the pressure felt on the external wall, due to the flow being less laminar. Higher turbulence intensities are also likely to disrupt the recirculation regions around the cube which will effect the ventilation rate on shorter time scales, due to the mean flow being briefly disrupted.

6.4.5 Effect of stability on ventilation rate

The effect of stability on Q was also considered for both the isolated and the array case, with the stability being measured at the reference mast. As for C_p , there is no correlation between Q and stability (Section 5.4). For both the isolated cube and the array case the Spearmans rank correlation coefficient for single sided and cross ventilated cases was within the range -0.09 to -0.03, suggesting no linear correlation between stability and ventilation rate.

6.4.6 Effect of the array on ventilation rate

Dataset: $All(NN_{All}^{All})$

As for for the pressure coefficient, the array elements will reduce the pressure on the instrumented cube, leading to reduced ventilation rates in comparison to the isolated cube. The reduced U_{ref} will also have an impact on the tracer gas and volumetric flow methods.

6.4.6.1 Single sided

For $\theta_{ref} = 0^\circ$ wind (Figure 6.11a), the isolated cube records $Q_N P$ values of 0.6 to 1 for single sided ventilation, whereas for the array case this is reduced to a range of 1.75 to 0.4 $Q_N P$, a decrease of over 50 %. When binned the difference is calculated to be 0.5 ($Q_N P$). Due to the channelling effect for $\theta_{ref} = 45^\circ$ (Figure 6.18f) the difference between isolated and array (Figure 6.22) becomes -0.2 $Q_N P$, suggesting that for this θ_{ref} , the single sided Q is greater within the array than for the isolated cube. This behaviour can also be seen for the cross ventilated cases (Figure 6.22b).

In contrast to the $\theta_{ref} = 45^\circ$ behaviour, the effect of the array on the measured ventilation rate for a single sided ventilated cube is minimal at $\theta_{ref} = 30^\circ$, suggesting at this angle, similar ventilation rates should be expected (Figure 6.18c). This is likely due to the channelling effect through the array combining with the recirculation region of the central cube within the array, which may accelerate flow towards the instrumented cube.

For $\theta_{ref} = 60^\circ$ to 90° the array begins to have a small but noticeable effect on Q_N , with a difference of 0.15 Q_N occurring at $\theta_{ref} = 90^\circ$, or parallel flow (Figure 6.22a). This is likely to be due to the presence of the storage shed upstream, which will reduce the wind speed flowing parallel to the instrumented cube and thus reduce Q as flow is not being forced through the opening.

For $\theta_{ref} = \pm 150^\circ$ to 180° the difference in Q_N is between 0.1 and 0, due to the array no longer shielding the instrumented cube from oncoming flow. There are few data for $\theta_{ref} = -60^\circ$ to -150° for the single sided set-up and as such cannot be compared.

6.4.6.2 Cross ventilated

For the cross ventilated cases (Figure 6.22b), the trends are similar to the single sided openings for $\theta_{ref} = 0^\circ$ to 60° , though the location of the negative values of the difference in Q_N is shifted from $\theta_{ref} = 45^\circ$ to $\theta_{ref} = 60^\circ$. This could be due to a complex interaction between the wakes of the neighbouring cubes and the instrumented cube which now has an opening on the back, which will change it's response to that type of flow. The behaviour is not as prevalent for $\theta_{ref} = -60^\circ$ (Figure 6.18e), likely due to the southernmost cube in the central row of the array blocking the flow, whereas this is not present for $\theta_{ref} = 60^\circ$. The array expanse is greatest for the negative θ_{ref} values due to the asymmetrical nature of the array, which leads to differences of $Q_N = 0.2 - 0.5$ between isolated and array measurements.

For $\theta_{ref} = 180^\circ$, there are no data available for the cross ventilated case. However, it is hypothesised that there will be little, if any, difference between the Q_N recorded for the isolated and array cases due to the lack of shielding in this direction. This can be seen in the cross ventilated datasets (Figure 6.22b). The low cross ventilation rates recorded for the isolated case (Figure 6.22b) are due to the low pressure measurements (Section 5.5.2).

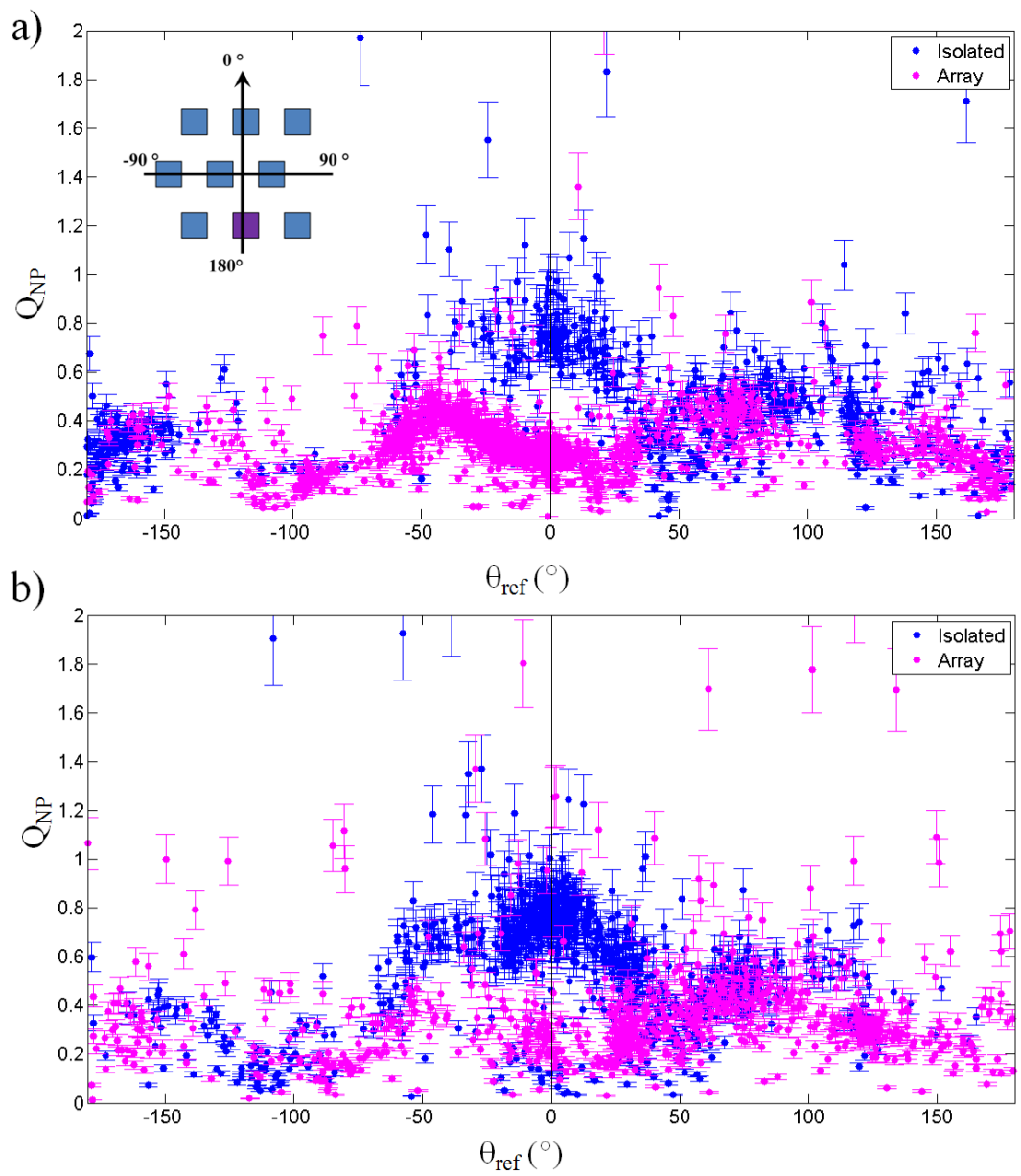


Figure 6.22: Q_{NP} for (a) single sided and (b) cross ventilation. Error bars are instrument error.

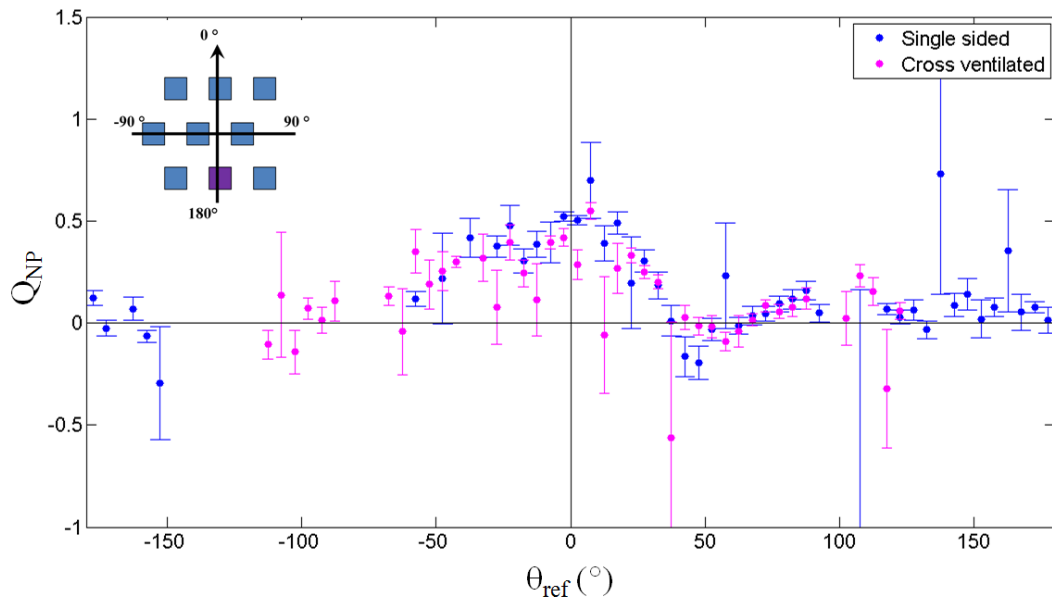


Figure 6.23: Q_{NP} values of Figure 6.22 binned into θ_{ref} 5° bins. Error bars are the standard error of each bin.

6.4.6.3 Frontal area density and ventilation rate

The frontal area density (λ_f) of the array was calculated using the methods outlined by Padhra (2010) for each θ_{ref} (Section 2.2, Figure 3.5). This method applies when the orientation of the obstacles is the same as that of the adjacent streets and all streets are aligned perpendicular and/or parallel to each other and is a sinusoidal function dependent on θ_{ref} (Figure 6.24) (Padhra, 2010). For an incident wind direction (θ_i) = 0 or $0 < \theta_i < \pi/2$:

$$\lambda_f(\theta_i) = \sqrt{(\lambda_f|_{\theta_i=0})^2 + (\lambda_f|_{\theta_i=\pi/2})^2} \sin(\theta_i + \gamma) \quad (6.1)$$

and for an incident wind direction (θ_i) = $\pi/2$ or $\pi/2 < \theta_i < \pi$:

$$\lambda_f(\theta_i) = \sqrt{(\lambda_f|_{\theta_i=0})^2 + (\lambda_f|_{\theta_i=\pi/2})^2} \sin(\theta_i - \gamma) \quad (6.2)$$

where

$$\gamma = \tan^{-1}\left(\frac{\lambda_f|_{\theta_i=0}}{\lambda_f|_{\theta_i=\pi/2}}\right) \quad (6.3)$$

More scatter occurs in Q_{NP} for higher λ_f values, partially due to the higher number of data points due to it corresponding to $\theta_{ref} = 0^\circ \pm 50^\circ$ (Figure 6.25). The amount of variation in the ventilation rate increases as the shielding effect of the cubes increases,

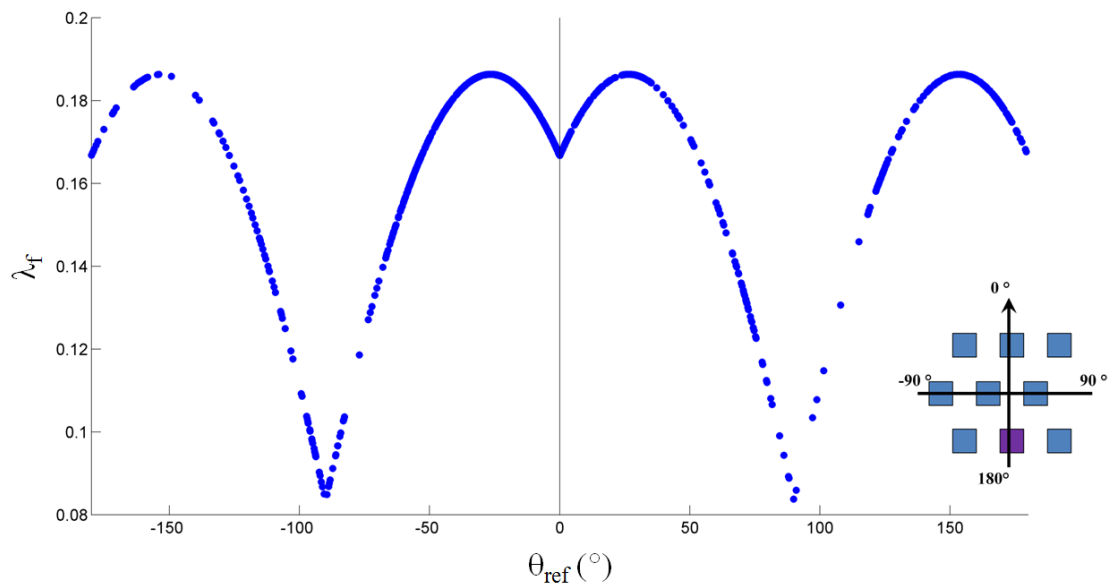


Figure 6.24: λ_f and $\theta_{ref} = 0^\circ \pm 180^\circ$ for the Silsoe data

possibly due to the variety of flow patterns which occur due to the wake interactions. A very similar trend is seen for the cross ventilated cases (not shown here). The large amount of scatter and lack of values for the lower regions of λ_f mean that a simple relation cannot be formed. Also, similar λ_f values can be caused by completely different building patterns, meaning that what works for this limited staggered array may not hold for an aligned array, or an realistic array of buildings.

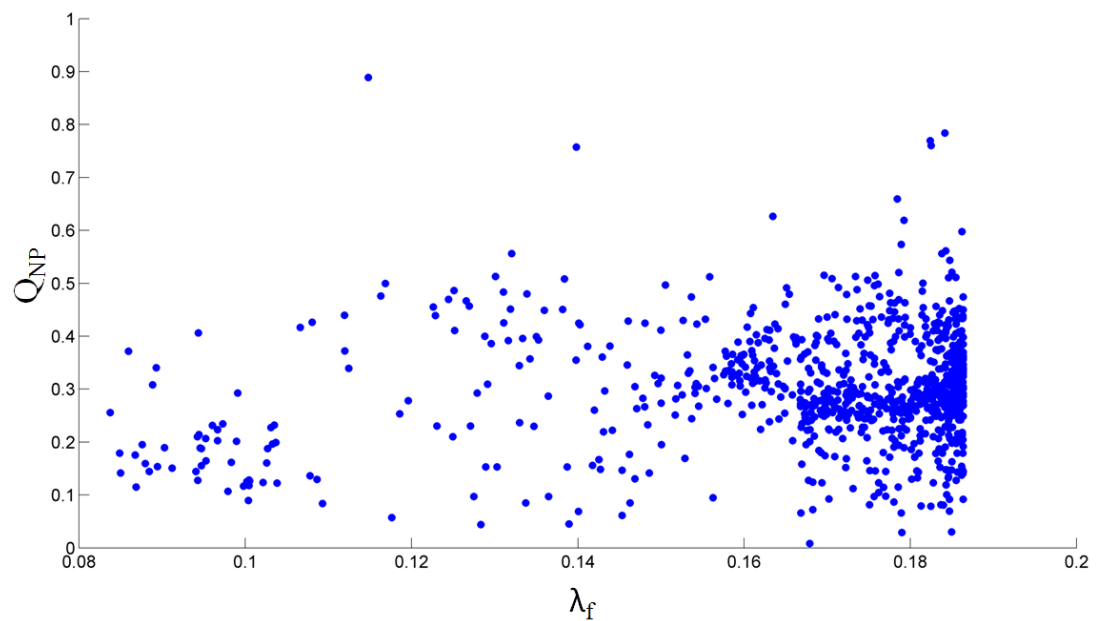


Figure 6.25: Relation between λ_f of the array exposed to the oncoming flow and Q_{NP} for the single sided opening case.

The range of θ_{local} within the array can be as great as 70° for a change of 20° in θ_{ref} (Figure 6.26). This suggests that Q_N cannot be correlated with λ_f due to the interactions of the wakes of the array obstacles, meaning λ_f and the θ_{ref} would not be representative of the local flow around the cube. As expected, a higher λ_f leads to lower U_{local} values due to a reduction of the flow penetrating into the array, however, it also leads to a larger spread of θ_{local} due to the number of obstacle wakes interacting.

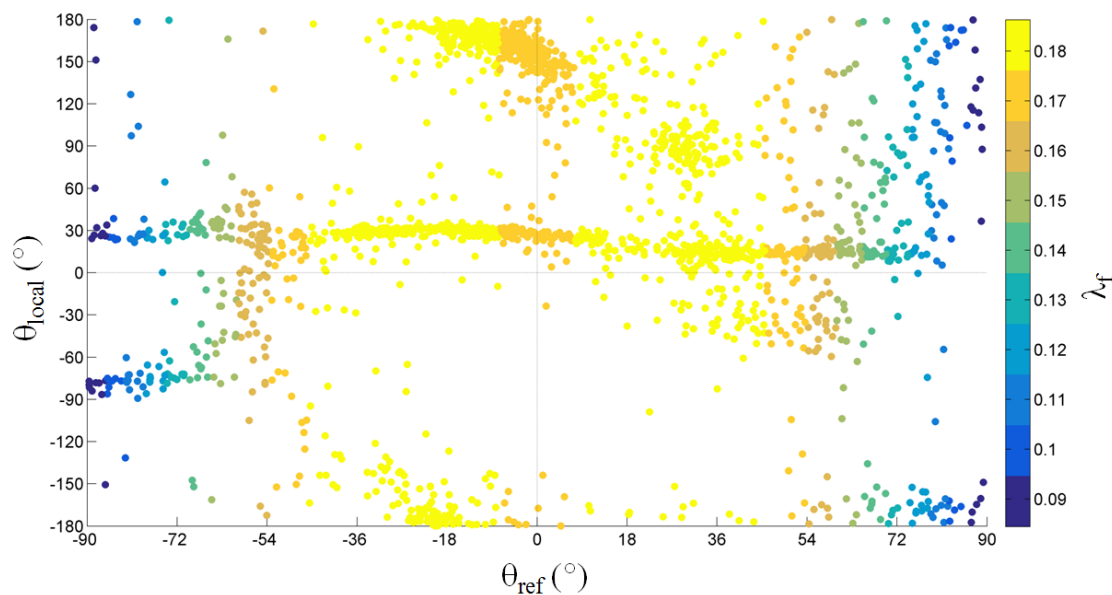


Figure 6.26: θ_{local} and θ_{ref} colour coded for λ_f . θ_{ref} is limited to $\pm 90^\circ$, the range at which the array has the greatest effect on U_{local} .

6.4.7 Summary

The results of this section suggest that for a 6 m cube, stability has no effect on the ventilation rate, though this should not be assumed for high rise buildings. λ_f also has no correlation with Q , though higher amounts of shielding lead to a larger scatter, likely due to the flow behaving in multiple ways. Of all variables tested, U_{ref} , U_{local} and θ_{ref} have the greatest measurable influence on Q . The array's asymmetry, as for the pressure coefficient (Section 5.6), causes an uneven reduction in Q when measured using all methods.

The choice of wind speed measurement used in the volumetric flow method will ultimately be dependent on what is available on the prospective construction site, but this section has highlighted that the volumetric flow rate may overestimate the ventilation rate if U_{ref} is used, and it may underestimate if U_{intf} or U_{intb} is used, due to the sonic anemometer not always capturing the peak wind speed, though this is dependent on wind direction and instrument position.

6.5 Comparisons to the wind tunnel dataset

Dataset: $All(NN_{All}^{All})$ cross ventilated cases.

The wind tunnel ventilation rate (Q_w) (Section 4.12) was calculated from the pressure difference across the cube, rather than the internal and external pressure difference, due to there being no openings in the wind tunnel cube model.

The wind tunnel data is also assumed to be entirely wind driven, with no thermal effects present. The volumetric flow rate for the full-scale data is calculated using the local external flow, due to an internal flow measurement not being possible in the wind tunnel.

For the isolated cube, the ventilation at $\theta_{ref} = 0^\circ$ (Figure 6.11a) is under predicted by the wind tunnel model, likely due to the location of the reference pressure measurement (Figure 6.27a). However the basic shape of the trend of ventilation rate and θ_{ref} is identified correctly. For $\theta_{ref} = 45^\circ$ there are differences between full-scale and wind tunnel of order $0.3 Q_N$ (Figure 6.27a). This is due to the full-scale having a change in surface type for the isolated cases, with $\theta_{ref} = 0^\circ$ to 45° having flow which approaches over a crop field, and flow from $\theta_{ref} > 45^\circ$ approaches from a well tended field of short grass (not modelled in the wind tunnel).

Q_N for $\theta_{ref} = 70^\circ$ to 90° is around 0.5 ± 0.06 for the full-scale isolated cube and 0.2 to 0.3 ± 0.009 for the wind tunnel model. This difference could be caused by the storage shed in the full-scale data, which will cause flow to descend and accelerate towards the instrumented cube. Also, θ_{ref} at full-scale will not be constant, which may lead to the average direction not correlating with the measured pressure due to the fluctuations of the flow. These small changes θ_{ref} mean that for the directions effected by the storage shed, the effect may not be as pronounced as expected.

For the array case, (Figure 6.27b), there is good agreement for $\theta_{ref} = 0^\circ$, which suggests that the wind tunnel captures the structures of the interacting wakes within the array adequately. Asymmetry is also captured by the wind tunnel model, though the peak $\theta_{ref} = -30^\circ$ (Figure 6.18c) is not, possibly due to it being caused by mainly fluctuating flow penetrating into the array. The wind tunnel model over estimates Q_N for $\theta_{ref} = \pm 180^\circ$, potentially due to the location of the reference pressure and the uniformity of the wind tunnel flow when compared to the real flow.

Results for $\theta_{ref} = -90^\circ$ (Figure 6.18d) also show good agreement, where flow is fully blocked by the two cubes either side of the instrumented cube. However, this does not occur for $\theta_{ref} = 90^\circ \pm 10^\circ$, perhaps due to slight misalignment of the wind tunnel model. Again, the effect of the storage shed may cause an increase in ventilation rate for this direction, as it accelerates flow down the array streets.

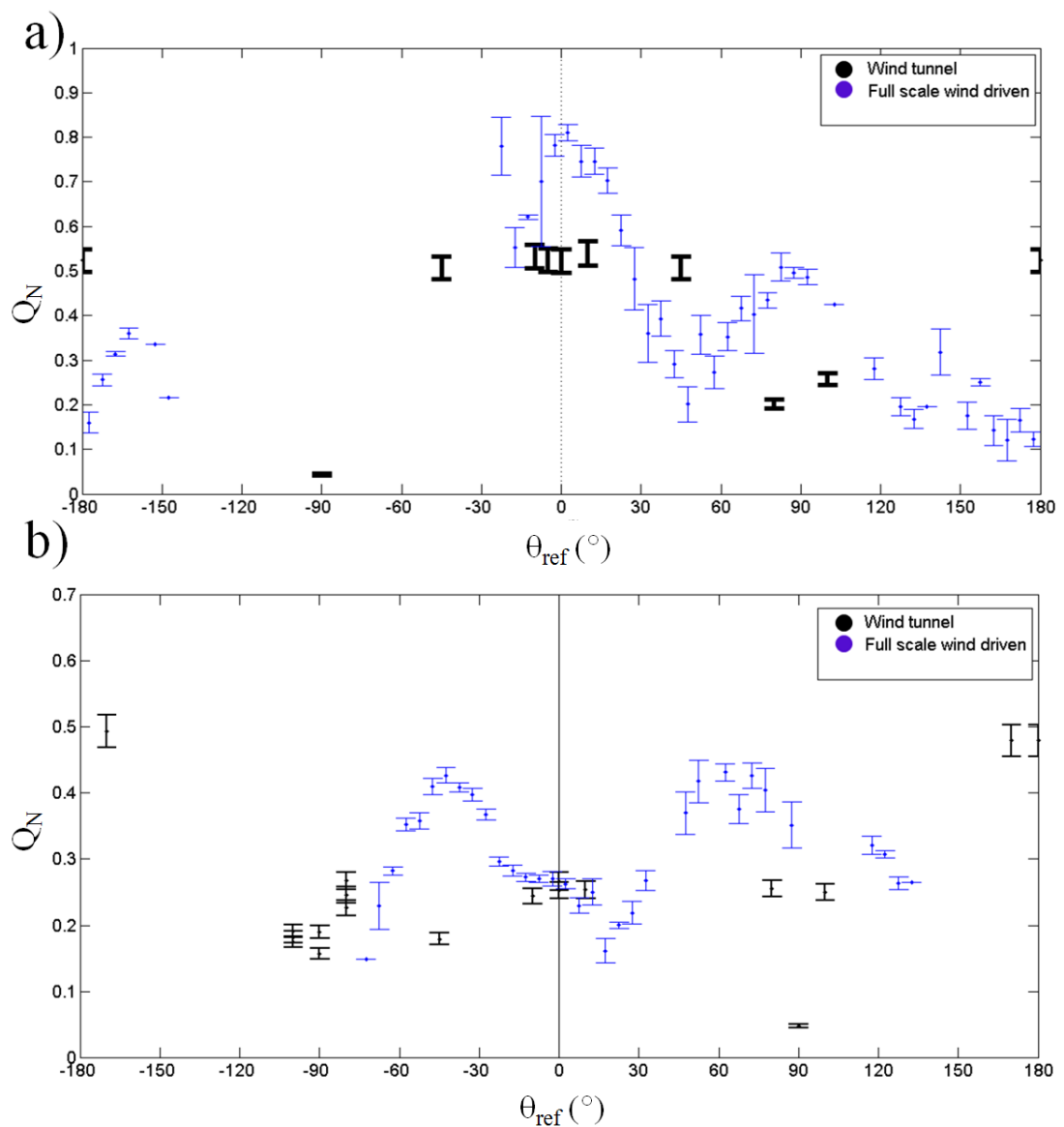


Figure 6.27: Comparison of the Q_N determined from the wind tunnel and full-scale pressure difference method for a cross ventilated cube a) isolated cube and b) array. Full-scale data are binned and results are included if >4 members.

6.5.1 Comparison to all full-scale ventilation measurement methods

For the isolated cube, the tracer gas measurements have greater agreement with the wind tunnel results, especially for $\theta_{ref} = 0^\circ \pm 30^\circ$ (Figure 6.28a). However, trace gas ventilation results carry large errors, due to incomplete mixing, sensor sensitivity and sensor response time. The error on the infiltration rate is also included in this measurement, as the infiltration rate has been subtracted from the tracer gas Q_N . The lack of tracer gas releases for $\theta_{ref} > 45^\circ$ also impedes comparisons, though the two cases for the isolated cube at $\theta_{ref} = 60^\circ$ and $\theta_{ref} = 120^\circ$ show agreement with both the volumetric method and the pressure difference method.

When comparing the pressure difference based method to the volumetric method, it can be seen that for $\theta_{ref} = 0^\circ \pm 20^\circ$ there is good agreement between the two for the binned data, which suggests that the flow measured by the local sonic anemometer is the flow which is impacting on the front face of the cube and thus is driving the ventilation rate. For $\theta_{ref} = -60^\circ$, there is a large difference between the volumetric and pressure difference methods, suggesting that U_{local} is not completely representative of the flow impacting on the cube (Figure 6.11e).

For the array case (Figure 6.28b), the differences in behaviour between the methods are not as clear. The volumetric flow rate predicts low values of Q_N (0.05 to 0.1) for $\theta_{ref} = 0^\circ$ (Figure 6.18a), whereas the pressure difference and tracer gas methods correlate with the wind tunnel results. This difference could be due to the flow being measured at the local sonic anemometer in front of the cube not being representative of the flow impacting on the cube, with the low Q_N suggesting that the sonic anemometer is in a region of slow moving air compared to that directly impacting on the instrumented cube. This also occurs for $\theta_{ref} = 0^\circ \pm 70^\circ$, before the volumetric ventilation rate begins to rise, due to the flow now being parallel to the cube and being channelled down the array streets.

For $\theta_{ref} = 120^\circ$ to 150° the volumetric and pressure difference methods are similar and show overlap, due to the low pressures on the front face. This is also true for $\theta_{ref} = -150^\circ$ to -180° , though there are few data available for this direction.

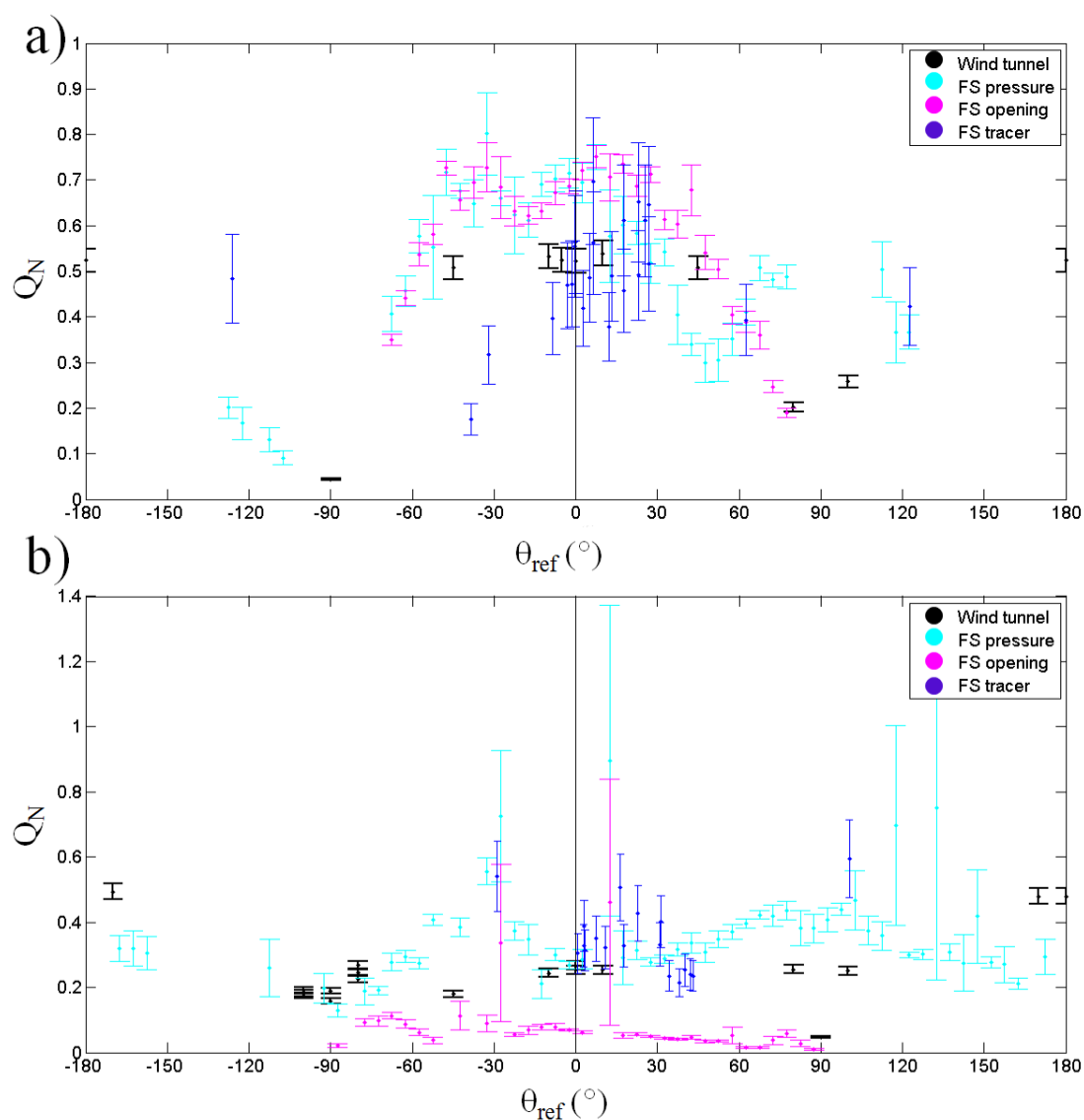


Figure 6.28: Comparison of the predicted Q_N for the cross ventilated cases for all three full-scale methods (tracer gas, pressure difference and volumetric flow using U_{local}) with the wind tunnel for the a) isolated cube and b) array. The tracer gas measurements, due to their small number are not binned, whereas the volumetric flow pressure difference derived ventilation rate are binned if >4 members.

The full-scale pressure difference derived results are under-predicted by the wind tunnel, due in part to the slight thermal effects experienced in the full-scale and possibly due to the lack of outflow being modelled in the wind tunnel model. This under-prediction, being constant in all measurements, may be due to the positioning of the reference pressure within the wind tunnel (Section 4.2.1). It is likely that, especially for the array case, the two openings in the cross ventilated set-up may not be linked by a jet, and may act as two independent single sided openings, increasing the thermal effects and implying that there is both inflow and outflow from each opening. Due to the lack

of physical openings in the wind tunnel model, this is not captured.

Another cause may be the changing roughness around the full-scale site, compared to the uniform boundary layer generated in the wind tunnel. This may cause the wind tunnel modelled flow to differ from the full-scale flow, with a rougher surface leading to lower windspeeds and ultimately lower pressures experienced by the instrumented cube. Also not modelled in the wind tunnel is the fluctuating wind direction, which will increase or decrease ventilation rates depending on the direction.

6.6 Comparisons to numerical models and pre-existing data

The full-scale data are compared to models of natural ventilation, mainly focusing on single sided ventilation (Sections 6.6.2 and 6.6.4). Stabat *et al.* (2012) reviews the progress of single sided ventilation modelling for a variety of window types and highlight the main correlations created for single sided ventilation and wind speed. These include Warren and Parkins (1985), De Gids and Phaff (1982), Larsen and Heiselberg (2008) and Caciolo (2010). These models are discussed in Section 6.6.6 on page 34. The models are explored individually and then compared to the results of the Silsoe dataset (Section 6.6.6). For this section, Q_E refers to the full-scale data.

6.6.1 Comparisons to data from Straw (2000)

Straw's (2000) full-scale ventilation study of the Silsoe cube, had two 1 m^2 openings in a cross ventilated configuration (C_d was assumed to be 0.61 (Straw, 2000)) and used all three ventilation rate measurement methods: tracer gas decay, pressure difference and volumetric flow. The dataset is limited, to one or two cases for $\theta_{ref} = 0^\circ$, 45° and 90° . Q_N can be compared to the isolated cases in this field campaign. There are no errors stated in the work.

Straw (2000) takes the tracer gas method as the 'true ventilation rate', as the method is a direct measurement of the flow entering and leaving the cube. For $\theta_{ref} = 0^\circ$, the pressure difference method does not capture 61 % of the flow rate (Straw, 2000). For $\theta_{ref} = 90^\circ$, the pressure difference method only predicted 21 % of the ventilation measured by the tracer gas method (Straw, 2000). This could be for two reasons: an inaccurate discharge coefficient of the openings and the fact that the pressure difference method is only a mean value, so the turbulent contributions to the ventilation rate are not quantified (Yang, 2004).

Straw (2000) used the pressure coefficient of the sealed cube to estimate the pressure driven ventilation rate. However there may have been some effect on the measured pressure coefficients by the opening due to the larger area (1 m^2 compared to the 0.4 m^2 used in this study) (Straw, 2000).

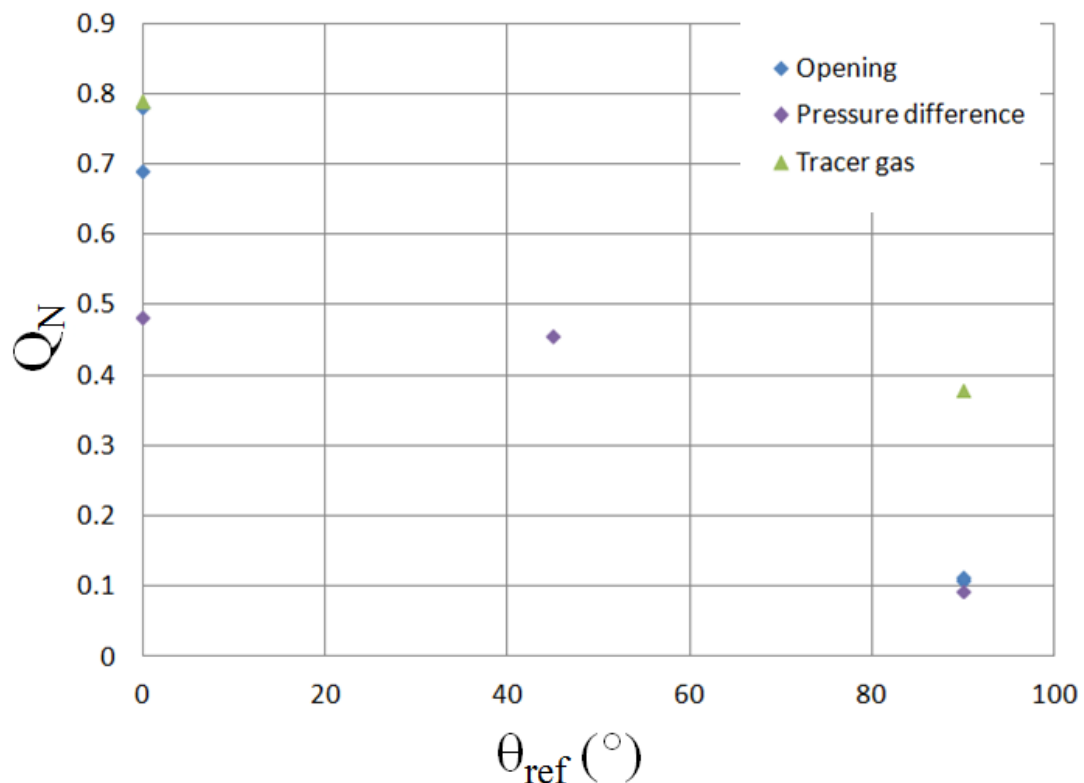


Figure 6.29: Q_N from Straw (2000) for a cross ventilated isolated cube with 1 m² openings.

The current field campaign suggests that the difference in the methods identified by Straw (2000) could be due to the large opening size of the windows (Figure 6.29). When converted from Q_N to λ , some of the air change rates (λ) were of magnitudes of 10 to 100 h⁻¹. One possible explanation of the large differences could be due to the tracer gas being rapidly flushed from the cube and not mixing completely with the air, despite a fan being used. Depending on the sampling rate of the gas sensor, there could only be a few measurements undertaken, with the concentration change occurring at time scales larger than that of the instrument's response time, leading to misleading readings. Some variance may also be caused by differing internal and external conditions, though these were not measured aside from U_{ref} and θ_{ref} (Straw, 2000).

6.6.2 Comparison to Warren and Parkins (1985)

For the isolated cube, equations 2.14 and 2.15 (Section 2.3.9.1 page 34) suggested by Warren and Parkins (1985) under-predict Q_E for $\theta_{ref} = 0^{\circ}$ to 60° when compared to the volumetric flow ventilation rate (using U_{local}), predicting Q_{Wref} and $Q_{Wlocal} = 0.1$ to 0.2 m³ s⁻¹ when $Q_E = 0.1$ to 0.45 m³ s⁻¹ (Figure 6.30). The use of the U_{local} with equation 2.14 to predict Q_E for $\theta_{ref} = 90^{\circ}$ leads to an over-prediction of 0.1 m³ s⁻¹ (Figure 6.30a). Q_E for $\theta_{ref} = \pm 120^{\circ}$ is also over predicted by 0.05 m³ s⁻¹. For $\theta_{ref} = \pm 180^{\circ}$ and $\theta_{ref} = \pm$

30° (Figure 6.18c), Q_{Wlocal} also over predicts Q_E , due to U_{local} being in the recirculation region of the wake of the instrumented cube.

For the array case (Figure 6.30b), the modelled results of Warren and Parkins (1985) match the trend of the observed data spread over θ_{ref} , though again both models under-predict Q_E by 0.05 to $0.1 \text{ m}^3 \text{ s}^{-1}$ for $\theta_{ref} = 0^\circ$ to 30° . Q_{Wlocal} over predicts Q_E by $0.1 \text{ m}^3 \text{ s}^{-1}$ for $\theta_{ref} = -90^\circ$ (Figure 6.18d). It can be assumed that this would also be true for $\theta_{ref} = 90^\circ$ if the storage shed was not present. The presence of the storage shed leads to a more turbulent environment with more flow features interacting in front of the cube, meaning that the wind is not parallel to the cube. For $\theta_{ref} = \pm 120^\circ$ to 180° the behaviour of the model is not as clear cut, due to the interaction of the instrumented cube's wake and the flow structures within the array. Q_{Wref} over predicts Q_E by $0.025 \text{ m}^3 \text{ s}^{-1}$ for this region. The peak at $\theta_{ref} = 120^\circ$ is likely due to flow directly impacting on the local mast, which will increase Q_{Wlocal} , but will not necessarily impact on the flow through the window. Caciolo *et al.* (2013) suggest that the Warren and Parkins (1985) models tend to over-predict ventilation rates when the opening is on the leeward side of the building (Figure 6.30).

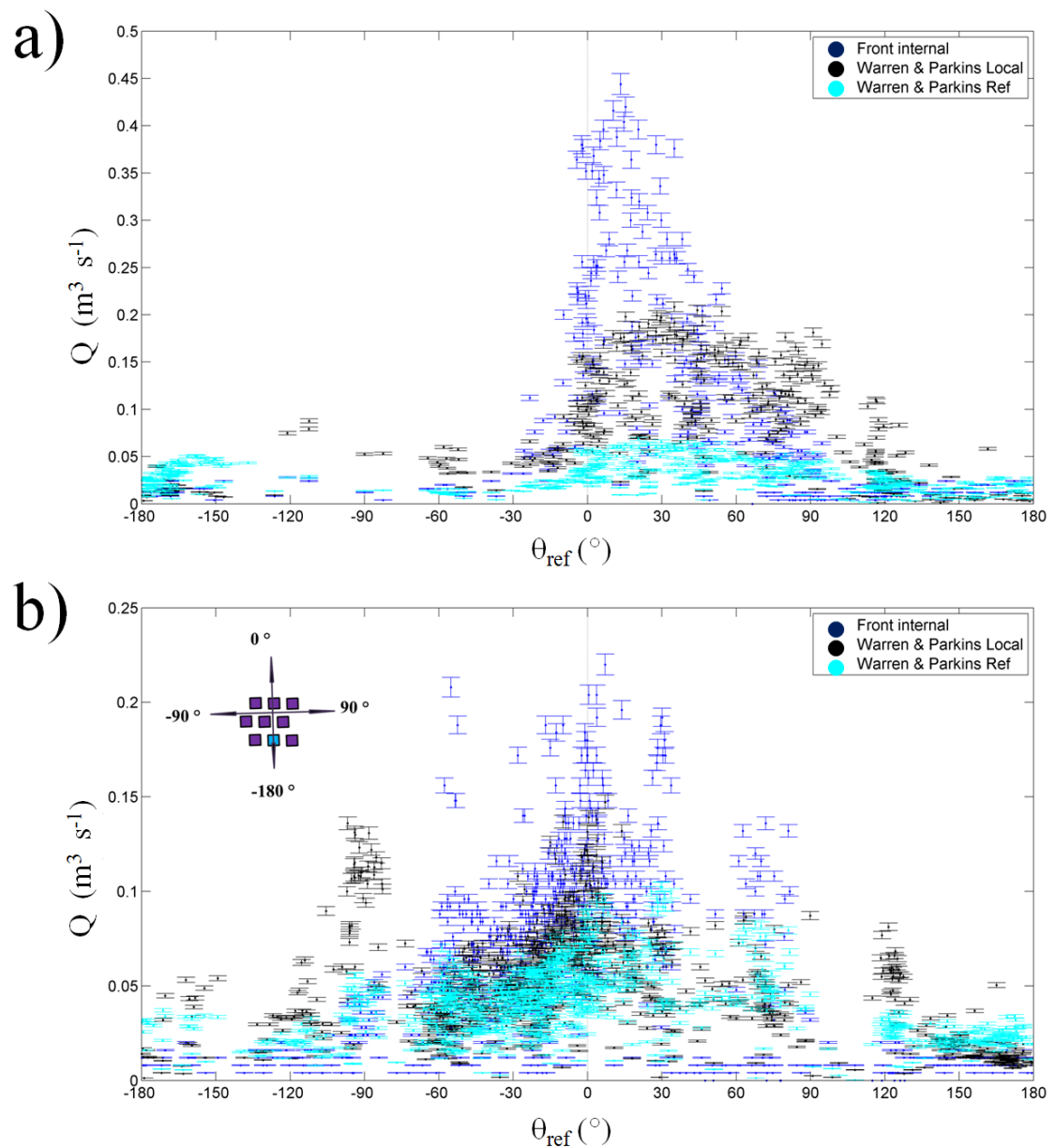


Figure 6.30: Q calculated from U_{int} compared to equations 2.14 and 2.15 by Warren and Parkins (1985) for single sided ventilation for the a) isolated cube and b) array. Dataset used: $All(NN_{All}^{All})$.

For both the isolated cube and the array case, the models proposed by Warren and Parkins (1985) are effective for $\theta_{ref} = \pm 60^\circ$ for the isolated case and $\theta_{ref} = -90^\circ$ for the array case, but have a tendency to under-predict Q for other wind directions. For the array case (Figure 6.30b), the U_{local} measurement is not always representative of the flow impacting on the isolated cube, leading to erroneous results.

6.6.3 Creating a wind speed model for the Silsoe array data

Dataset used: $A(All_{All}^{-10-10})$

Equations 6.4, 6.5 and 6.6 are of the same form as equations 2.14 and 2.15, suggested by Warren and Parkins (1985). Coefficients (to 3 significant figures) were determined using Matlab's 2010 polyfit function and have been fitted to the array case data with θ_{ref} limited to $0^\circ \pm 10^\circ$ to remove the data affected by the wake of the instrumented cube. The data has been further split for the high U_{local} to U_{ref} ratios (> 0.2 , equation 6.4, Figure 5.8 trend **b**) and for lower ratios (< 0.2 , equation 6.5, Figure 5.8 trend **c**) for the U_{local} equations, with equation 6.6 being applicable to all data. All coefficients are rounded to 1 s.f.

$$Q = 4U_{local}A \quad (6.4)$$

$$Q = 0.7U_{local}A \quad (6.5)$$

$$Q = 0.3U_{ref}A \quad (6.6)$$

The bi-modality in the relation between the U_{ref} and the U_{local} , makes it difficult to predict U_{local} from U_{ref} (Section 5.2.2), as this behaviour could not be linked to any other variable such as stability or wind direction.

R^2 values for the model fits were 0.83 for the low ratios, 0.85 for the high ratios (equations 6.4 and 6.5 respectively) and 0.76 for equation 6.6 using U_{ref} , due the larger amount of scatter in Q . These values are likely to only be applicable to the Silsoe array itself due to the unique interaction pattern of the cube wakes. These equations do not take into account θ_{ref} , thermal effects, turbulent contributions to the ventilation or measurement errors.

6.6.4 Comparison to work by Caciolo *et al.* (2013)

Due to the differences in temperature measurements available, only single-sided wind driven ventilation cases are compared (Section 2.3.9.2, page 35). Equation 2.16 under-predicts Q_E by between 0.4 and $1.4 \text{ m}^3 \text{ s}^{-1}$ (Figure 6.31). This is due to the coefficient reducing Q_{cac} to near 0 regardless of θ_{ref} . This also occurs when the U_{local} is used instead of U_{ref} . The cause of this difference could be the boundary layer in the full-scale flow, as the scaling of the CFD model is similar to that of a full-size building. Even when similar θ_{ref} values to Caciolo *et al.* (2013) are used ($\theta_{ref} = 30^\circ$ from perpendicular flow), the equation is dominated by the coefficient. This difference could be due to the location of the opening and the differences in size.

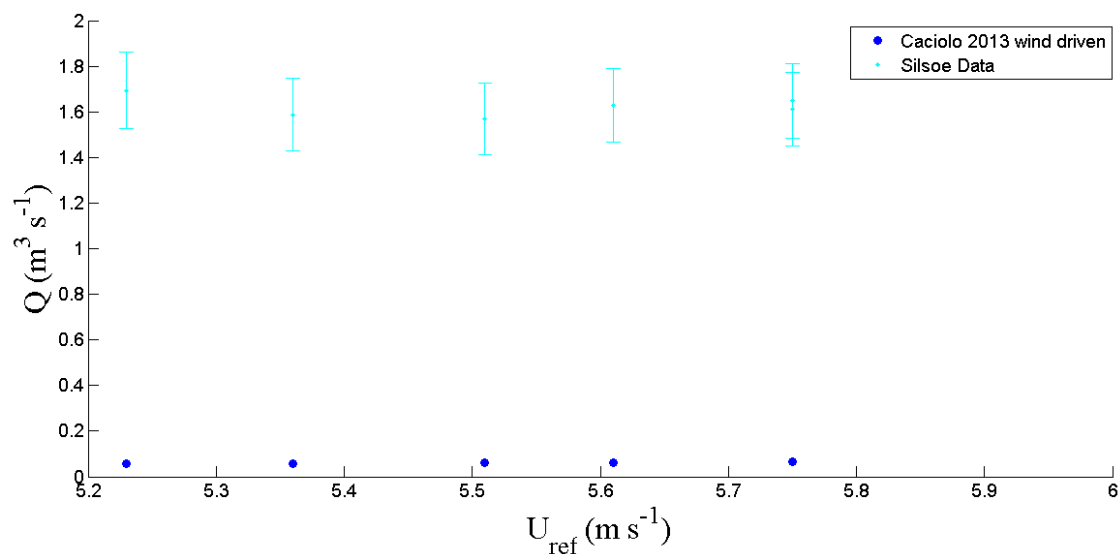


Figure 6.31: Comparison of Q_{cac} (equation 2.16) Caciolo *et al.* (2013) and Q_E for an isolated cube with single sided ventilation for $\theta_{ref} \pm 5^\circ$ and $U_{ref} > 5 \text{ m s}^{-1}$. U_{ref} is used as U_{wind} .

The opening used by Caciolo *et al.* (2013) was 1 m^2 positioned on the edge of the building. The shape of the opening may also have some effect, though this is beyond the scope of this thesis. One hypothesis is that the narrower opening (0.4 m^2) used in this study means that the turbulent flow on the opening edges has more impact on the centre of the opening compared to the 1 m^2 window. The model is designed to also fit data for top hung and bottom hung windows, where the calculation of the area of the opening is not as straight forward.

Caciolo *et al.* (2013) states that there is no need to change equations 2.14 and 2.15 for windward conditions as they provide a good estimate of the CFD. The best results were obtained with the Warren and Parkins (1985) correlation with almost all of the predicted values falling within the range of measurement accuracy ($\pm 25\%$) although the equation suggested by Larsen and Heiselberg (2008) (Section 2.3.9.4) also obtains ‘reasonably good results’ for the windward directions, but struggled with the leeward directions (Caciolo *et al.*, 2011).

For leeward conditions it is not possible to assess equation 2.19 as that wind direction is rare within the Silsoe dataset.

6.6.5 Flow number and Archimedes number

Caciolo *et al.* (2013) references the work by Warren (1977) and Warren (1986), in particular the graph of $\sqrt{F_{Arch}}$ against F , the flow number which is equivalent to a normalised ventilation rate (Q_N):

$$F = \frac{Q}{AU} \quad (6.7)$$

F is given as a function of the square root of the Archimedes number (F_{Arch}) (Warren, 1986). For a rectangular opening of area A, where air flowing in through one half of the opening must flow out through the other half at some point in time when mass conservation is assumed. F_{Arch} is related to the Richardson number (Ri), the Reynolds number (Re, Section 5.8) and the Grashof number (Gr) (Garratt, 1994). Gr is a special case of the F_{Arch} where density differences are caused by temperature differences. For a large F_{Arch} the stack effect will dominate and for a small F_{Arch} , the forced convection, or wind driven effects dominate.

$$F_{Arch} = RiRe^2 \quad (6.8)$$

This graph is created for the isolated and array datasets (Figure 6.32). Caciolo *et al.* (2013) identify three regions:

1. A zone close to the straight line, where the ventilation results mostly from the stack effect
2. A zone above the straight line, where the air change rate is higher than that due to the stack effect only. This means that the wind driven ventilation is reinforcing the stack effect, leading to increased ventilation rates
3. A zone below the straight line in which the air change is below that predicted with the stack effect only, which suggests that the wind driven component is acting against the thermal effects, leading to a diminished ventilation rate

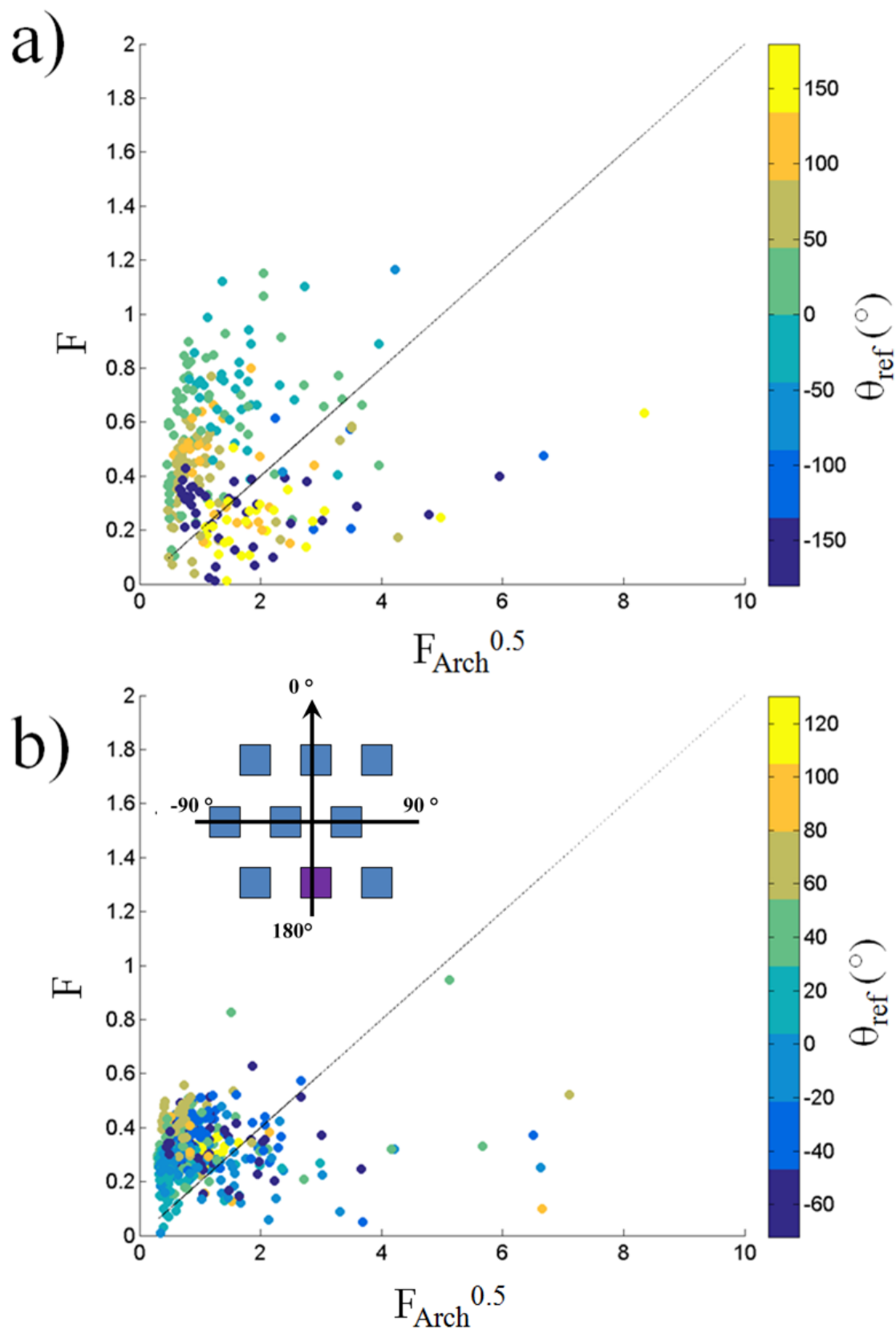


Figure 6.32: $\sqrt{F_{Arch}}$ against F for the single sided a) isolated cube b) array case. U_{ref} is used with colour denoting θ_{ref} . The 1:1 ratio line has the formula $F = 0.2 F_{Arch}^{0.5}$ and denotes the absence of any wind driven effects.

One cause for the Silsoe data not being correctly predicted by the models is that the range of the square root of the Archimedes number seen in the full-scale data is between 0 and 10, whereas the Caciolo *et al.* (2013) model has a range of only 0 to 0.4. A range difference also occurs for F , the flow number: Caciolo *et al.* (2013) (0 to 0.1), Silsoe data (0 to 1.2) due to the U_{ref} range. The values stated are for the isolated cube, but are also similar for the array case.

There is some directional dependence to the behaviour of the stack and wind driven effects. For $\theta_{ref} = 150^\circ$ to 135° it can be seen that the wake structures of the isolated cube act against the thermal effects, leading to reduced ventilation rates (Figure 6.32a). For $\theta_{ref} = -135^\circ$ to 180° there are cases close and on either side of the line. This difference between $\theta_{ref} = \pm 135^\circ$ and $\theta_{ref} = 180^\circ$ is likely to be caused by the presence of the woodland behind the site (Figure 3.2), with it only effecting positive θ_{ref} values. Flow over the woodland is likely to be more turbulent and will disrupt the thermal plumes close to the cube. For the negative θ_{ref} values, there is also some roughness from the wild field behind the site, though this is not likely to have as greater impact as the woodland, which may explain the spread for the negative wind directions. Cases close to the line suggest that low wind speeds and thermal effects are dominating in those conditions.

For the other wind directions, whilst there are some cases where the thermal and wind driven effects are in opposition, it is rarer than when they work in unison. These cases are likely to be when U_{ref} is low or when θ_{ref} deviates rapidly over the averaging period.

For the array case (Figure 6.32b), there is less directional dependence, with only around 50 of the 1104 cases being below the zero line. These 50 cases also show no directional dependence, suggesting that the thermal and wind driven effects within the array tend to act in unison. This means that for real buildings within an urban heat island, the stack and wind driven effects are likely to amplify the ventilation rate.

The origins of the chosen wind speed are not discussed, though for an isolated building there is likely to be little difference between reference and local wind speeds and directions. Using U_{local} instead of U_{ref} causes a greater spread in the flow number F , due to the denominator decreasing, otherwise, the distribution remains similar.

6.6.6 Inter-comparisons with the Silsoe full-scale data

Dataset: $I(All_{All}^{All})$

The models outlined (Sections 2.3.9, 6.6.2, 6.6.4, 2.3.9.3, 2.3.9.4) are used in conjunction with the measurements taken for the isolated and array cases to compare modelled ventilation rates to the measured ventilation rates (Figure 6.33). Caciolo (2010) has two entries, due to the lack of clarity about the location of the wind speed measurement, as such both U_{ref} and U_{local} are used.

6.6.6.1 Isolated cube

U_{local} used in equation 2.16 (Caciolo *et al.*, 2013) breaks the trend seen in the other models (Figure 6.33), leading to the conclusion that it is U_{ref} which should be used. Using U_{ref} in equation 2.16 gives the highest predicted Q value for all angles aside from $\theta_{ref} = 90^\circ$ to 135° , likely due to the different equation for T^* being used, regardless of wind speed (equation 2.16). For these θ_{ref} values the Caciolo model using U_{ref} gives the lowest prediction of Q , including being lower than using U_{local} . This suggests that it is underestimating the contribution of the wind driven component to the ventilation rate.

However, when compared to the measured Q_N at the Silsoe site (Figure 6.34) using U_{ref} in conjunction with the Caciolo model leads to a more realistic representation of the full-scale dataset, showing large overlap with the tracer gas measurements in the region $\theta_{ref} = 0^\circ$ to 90° and the ventilation rate predicted by the Warren model using U_{local} .

All models have a peak in Q at $\theta_{ref} = 0^\circ$ of 0.05 to $0.1 \text{ m}^3 \text{ s}^{-1}$ depending on the model (Figure 6.33). Interestingly there is also a peak at $\theta_{ref} = 90^\circ$, though this is due to the higher wind speeds occurring at that θ_{ref} (Figure 6.33).

Larsen and Heiselberg (2008) and De Gids and Phaff (1982) results are similar, with the Larsen model showing more scatter with θ_{ref} , as θ_{ref} is included in the model. Of interest is the $\theta_{ref} = 45^\circ$ to 90° region, where the model by Larsen and Heiselberg (2008) appears to capture two behaviours. This may be due to the coefficients changing, but it also may be due to the flow sometimes being thermally driven and sometimes being wind driven though it is not possible to tell from this data set.

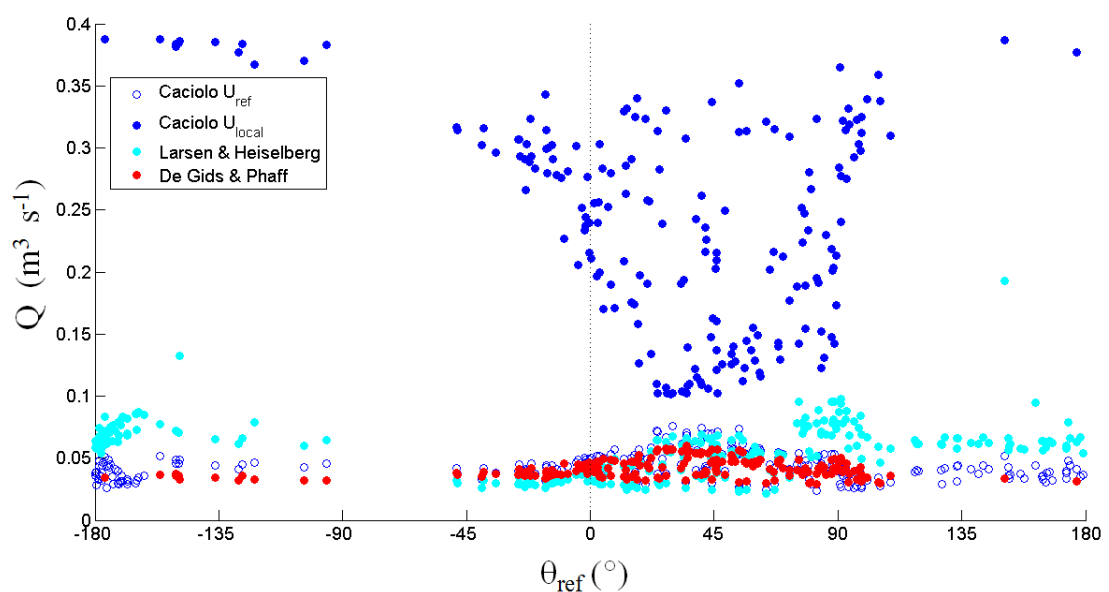


Figure 6.33: Comparison of the modelled ventilation rate from the calculations of Caciolo (2010), Larsen and Heiselberg (2008) and (De Gids and Phaff, 1982) for the isolated cube with single sided ventilation. Note that Q is not normalised on this plot.

Compared to the measured flow rate data none of the models perform well for wind directions behind the cube, where U_{local} is affected by the wake of the cube itself. The peak at $\theta_{ref} = 0^\circ$ for the pressure derived ventilation rate is not seen in any of the models, though the Warren model with U_{local} has a peak tending towards $\theta_{ref} = 45^\circ$. The highest R^2 values for the comparison to modelled and actual data were for the Warren models, with 0.44 for the U_{ref} and 0.39 for the U_{local} type. De Gids and Phaff (1982) also has an R^2 value of 0.42. The Spearman's rank correlation coefficients and R^2 values for the different models are listed in Table 6.2. The Warren and De Gidds models show a moderate correlation with the pressure derived ventilation. Using the U_{local} in the model by Caciolo (2010) causes a moderate negative correlation, likely due to the wind speed threshold within the equation. The lack of correlation with Larsen and Heiselberg (2008) is likely due to the difference in opening location and the modelled coefficients used in the equation. There are not enough complete data to compare the tracer gas results with the models.

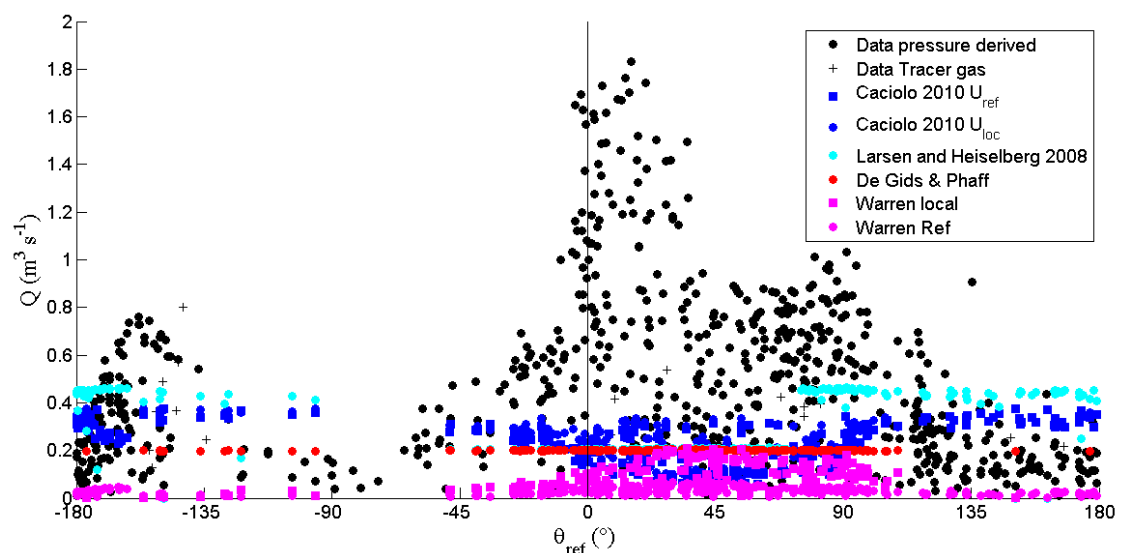


Figure 6.34: Comparison of modelled Q from the calculations of Caciolo (2010), Larsen and Heiselberg (2008) and (De Gids and Phaff, 1982) with the full-scale results for the isolated cube with single sided ventilation. Where possible pairs of models have been given similar colours. Errors that are included in the papers are from the Silsoe data, which are not representative of the models performance for any other dataset.

6.6.6.2 Array

The published models are compared to the array case, despite the models not being explicitly developed for sheltered buildings. As expected, the ventilation rate predicted by the model reduces, from a maximum of $Q = 0.4 \text{ m}^3 \text{ s}^{-1}$ for the isolated cube to a maximum of 0.14, due to the reduced pressure on the cube and U_{local} being reduced (Figures 6.35, 6.36). The use of the U_{local} in the Caciolo model leads to lower predictions

of the ventilation rate, though the shape becomes similar to the other models. All models are in good agreement for $\theta_{ref} = -60^\circ$ to 90° , though there is large variation for $\theta_{ref} = 90^\circ$ and 135° due to flow infiltrating into the array from behind. For this case the Caciolo model predicts the lowest ventilation.

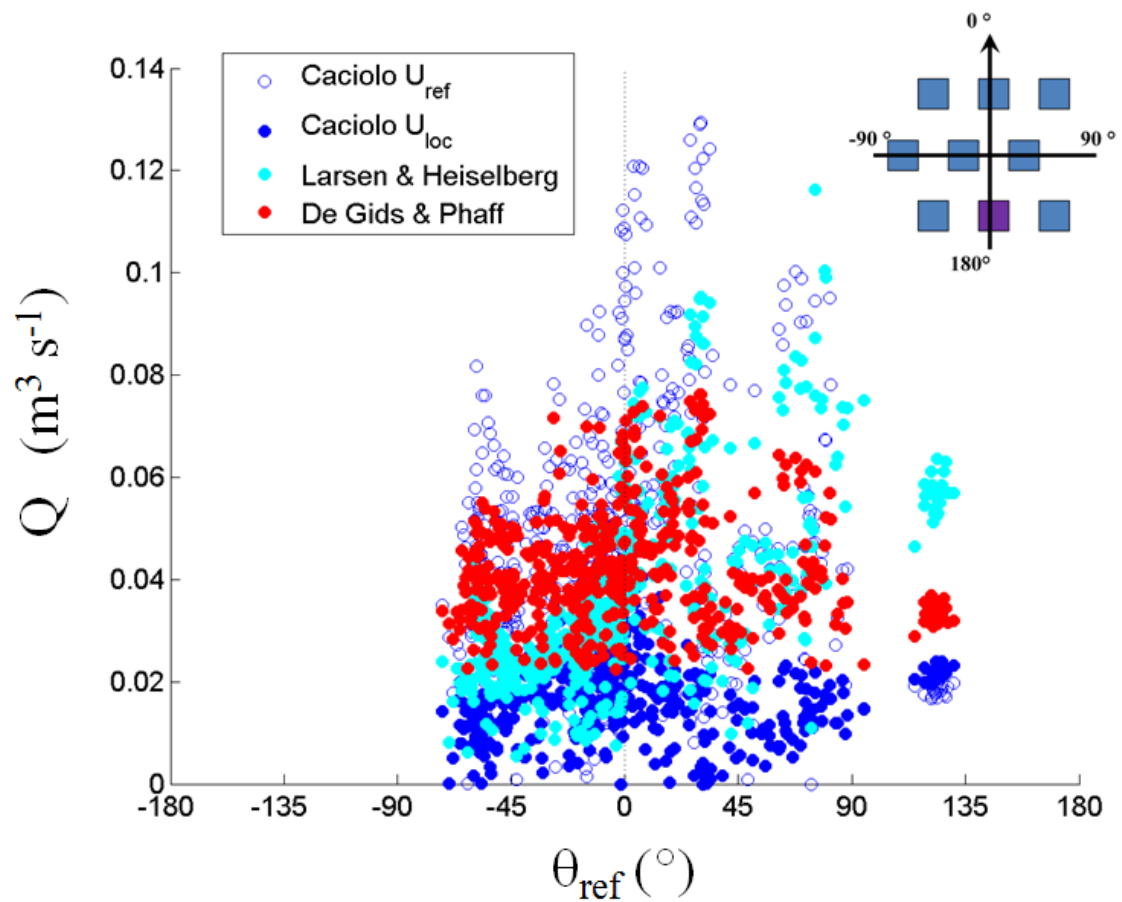


Figure 6.35: As Figure 6.33 but for the array.

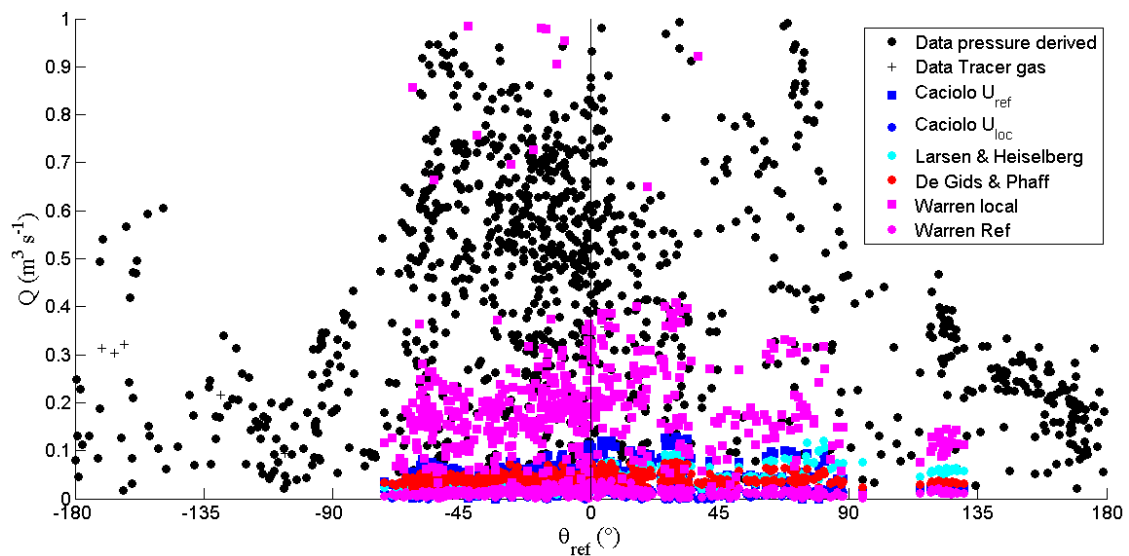


Figure 6.36: As Figure 6.34 but for the array.

The array data (Section 6.4.6) does not have a peak at $\theta_{ref} = 0^\circ$ due to the complex flow caused by the presence of the array. However, even with the shielding reducing Q_N , the models still under-predict the ventilation rate. This may be due to the models placing too much emphasis on the thermally driven ventilation and not the wind driven ventilation rate or it could be that the majority of the models were designed with real windows in mind and not the opening on the Silsoe cube.

The peaks at $\theta_{ref} = -45^\circ$ to -60° and $\theta_{ref} = 45^\circ$ to 60° are only identified by the Warren model, due to it being linked to U . The three different behaviours of the local flow within the array for similar U_{ref} mean that the values calculated by the Warren models will differ depending on the time of measurement (Section 5.2.2). The bi-modality needs to be quantified into something which can be used with these types of ventilation rate models in order to capture the range of potential ventilation rates.

As expected, the results for the array case (Figure 6.2) show little correlation between the measured ventilation rate and the models, due to the models not accounting for shielding, or varying θ_{local} compared to the θ_{ref} .

Table 6.2:: Spearmans rank correlation coefficient for the correlation between modelled ventilation rate and ventilation rate measured using the pressure difference method for the array. Number of cases: 648

Isolated		
Model	Spearmans rank	R^2
Warren (1977) U_{ref}	0.708	0.450
Warren (1977) U_{loc}	0.669	0.396
De Gids and Phaff (1982)	0.695	0.420
Larsen and Heiselberg (2008)	-0.039	0.003
Caciolo (2010) U_{loc}	-0.634	0.366
Caciolo (2010) U_{ref}	0.443	0.242
Array		
Model	Spearmans rank	R^2
Warren (1977) U_{ref}	0.595	0.023
Warren (1977) U_{loc}	0.466	0.016
De Gids and Phaff (1982)	0.801	0.603
Larsen and Heiselberg (2008)	0.439	0.272
Caciolo (2010) U_{loc}	0.548	0.287
Caciolo (2010) U_{ref}	0.764	0.554

A consideration is that these models were developed within the wind tunnel or in limited full-scale conditions, meaning the flow is likely to be uniform and not vary with direction over the averaging period or that only certain conditions were measured. The lack of roughness elements in the models will also alter the predicted ventilation rate. Some of the models such as that by Larsen and Heiselberg (2008), required detailed measurements in the opening, which may not be possible in the real environment, especially if the building is in the design phase and has not yet been built.

The implication of the differences between the models for both array and isolated cases is that the ventilation rate of a building tends to be under-predicted for most wind directions, which may lead to unwanted air-flow due to the actual ventilation rate being higher than predicted. The effect of a changing wind direction will not be captured within the models, leading to a more variable ventilation rate for the finished building. However, as long as the predicted ventilation rate matches the minimum requirements for the specific building type and occupant levels, it is likely that the building will exceed the minimum ventilation amount for thermal comfort for most wind directions.

6.7 Conclusions

A thorough understanding of the effect of the surroundings on ventilation rate requires a large dataset which covers all opening types, wind speeds, wind directions and temperature differences in order to provide accurate predictions as to the flow behaviour. Even with a nine month continuous dataset, there are insufficient data to truly capture the effect of wind direction and the surroundings for this specific case, let alone a broader dataset.

Care must be taken when creating a scale model of a building and its surroundings (Section 6.5) as the scale limits significant details which may alter the flow, especially with changing wind directions. For example, the boundary layer used in the wind tunnel was modelled to match the boundary layer present for $\theta_{ref} = 0$. However, despite the site being in a rural location, there are still large differences in the upstream make up of the flow, which lead to changes in turbulence intensities and flow structures. This ultimately leads to differences in pressure measurements and thus Q . A wind tunnel model can be used to understand the general trend of the Q with constant θ_{ref} , but does not provide an entirely accurate estimate of Q , especially when the model has been heavily simplified.

It can be concluded that the differences in ventilation rate measurements through the use of different methods varies and will have an effect if one particular method is used for modelling. The differences are likely to occur through a combination of factors: such as the presence of thermally driven ventilation, the direction of the ventilation, the location of the U_{local} measurement and the amount of turbulence within the flow. Each method is affected by different factors which cannot always be fully quantified, and whilst tracer gas measurements are a direct measurement of Q , they can be influenced by the position of sensors and whether the room is well mixed or not. An incorrectly positioned fan may alter the measured Q by impeding mixing rather than enhancing mixing.

Difficulty in separating out variables means that the variables which effect each different method cannot easily be identified from the mean data. It may be possible to identify them through the use of the instantaneous ventilation rate, though the instrument response time must also be considered due to the short time scale. The combined effect of all variables also means that the discussed empirical models (Section 6.6) are not representative of the full-scale mean ventilation rates obtained during this field campaign, likely due to the models being derived from wind tunnel data, which means variables such as the internal-external temperature difference, turbulence intensity, changes in wind direction and variable wind speeds throughout the averaging period are not considered. Too much emphasis is placed on the buoyant effects, which can be seen to be of less importance than the wind driven effects for this dataset, especially within the array, where the wind driven effects dominate. The effects of changing season, shadowing and time of day are also not considered explicitly in models. The current statistical

models only cover a small range of the potential conditions (e.g. small Archimedes numbers, specific wind speeds) in the full-scale environment.

The models consistently underestimate the ventilation rate of the isolated cube and as expected do not predict the ventilation rate of the cube in the array. This is due to the models putting too much emphasis on the thermally driven component of ventilation and not on the wind driven component, which itself affects the thermally driven component in either positive or negative ways depending on the wind direction and the background conditions. The statistical models do not include large scale thermal effects which will be essential for understanding how a building will behave in an urban environment. It could also be due to the opening types used, as the Silsoe openings are not realistic representations of windows.

To ensure simplicity, the current statistical ventilation models pay little attention to the internal environment, and seemingly assume that it is well mixed. Stratification in the inside of a building will lead to a change in flow behaviour around the opening and may cause the models to wrongly predict the resultant ventilation rate. A building may be between stratified and well mixed and this will affect the flow behaviour. Buildings of other materials should also be considered in order to ensure that the model is not just applicable to the specific building type.

The asymmetry of the array causes complex instantaneous wake patterns. U_{local} is coupled with ΔT , with higher U_{local} values leading to lower temperature differences, especially for cases where a window is open. However ΔT is also influenced by the incoming solar radiation and the atmospheric stability which may act in opposition to the local wind effects. The sensitivity of the internal temperature sensors means that the small temperature differences which occur in the higher U_{local} conditions cannot be determined.

There is also the issue of how to quantify T_i , especially if there is uneven heating due to shadowing from array elements. Both a mean and a single measurement close to the opening of interest may not be representative of the entire room and is something to consider when designing experiments. The statistical models (Section 6.6) focus on the buoyancy driven part of ventilation, which may be representative of a true brick building, but it is not true of the Silsoe cube, due to the increased leakiness and the simplicity of the openings. As the Silsoe set-up does not consider the heat caused by human activity or appliances within the cube, it should not be considered as representative of a residential building. Despite logging internal and external conditions simultaneously, there is not enough detail in the internal dataset to be able to couple the mean effects of the external environment to changes in the internal environment.

Another consideration is the direction of the flow through the opening, with uneven heating likely to lead to a shift in the neutral plane in an opening which will change the amount of the opening acting as an inlet and an outlet. A cross ventilated case in

sufficiently low local wind speeds may act as two single openings, with no connection due to the lack of a jet. This behaviour may be influenced by the internal environment, for example an obstacle in the centre of the room may block the jet and lead to inefficient ventilation. The flow through the openings themselves will influence the recirculation regions around the cube, for example a plume of warm air leaving through an outlet for a cross ventilated cube may disrupt the recirculation region behind the cube, altering the shape of the wake. For an array of buildings, each with an opening, this may lead to changes in the way the individual wakes interact, especially if some of the buildings are mechanically ventilated with exhaust vents being within recirculation regions. Again, a large amount of measurements is required within the opening itself in order to couple internal and external environments, though this was not possible in this study without disturbing the flow through the opening and due to the site conditions being unsuitable for the fragile instruments required.

The interaction between the oncoming wind speed and direction, local wind direction, local wind speed and local turbulence intensity is complex and difficult to model. λ_f can also not be used due as different layouts of buildings may have the same λ_f but local flow may behave completely differently for each case. The Silsoe data-set is the first step to addressing the effects of surrounding buildings on ventilation rate, changing seasons, time of day, opening type with data covering a much wider range of atmospheric conditions than that of previous work. The combined methodologies of meteorology and engineering create a unique dataset which can be built upon with more realistic models. The dataset highlights the effect of stability on ventilation rate and also demonstrates that buoyant flows also occur for cross ventilated cases, invalidating some of the commonly used assumptions in literature.

Chapter 7

Conclusions and Future Work

The aim of this thesis is to understand how a simplified urban area may affect the natural ventilation of a simplified building over a wide range of meteorological conditions. Part of this work involved creating a full-scale data set. This data set allowed for comparisons against previously created empirical models and industry standard values of pressure coefficient and ventilation rate (Chapters 5 and 6). The wind tunnel experiments with increasing array size allowed for the scope of the limited array to be determined (Chapter 4).

Despite the Silsoe array being a simplified representation of a group of buildings in both layout and building shape in a rural area it has highlighted that the 'Simple' case is incredibly complex, even for a site where the conditions have previously been studied. For example the dual behaviour of the ratio of local to reference wind speed for the array (Section 5.2.2) is approximately equal in data split, with one behaviour being well predicted by the CIBSE wind speed model, and the other requiring a new set of parameters in order to be modelled accurately (Section 5.2.3). Using the wrong coefficients within the wind model (equation 5.3) can cause over predictions of the wind driven ventilation rate of 20-50 % for the Silsoe cube within the array. Linked to this, the wind directions measured in the array demonstrated a dual behaviour, meaning that local wind directions and wind speeds cannot be accurately predicted from reference wind directions (Section 5.2.4). Low reference wind speeds also lead to local flows being dominated by the mechanical turbulence generated by the wakes of the neighbouring buildings and this is in an area with no obstacles such as street furniture. The Silsoe array does not consider the effect of an UHI on the ventilation rate, which would need to be considered for a building within a true urban area.

The presence of the array causes a 60 % to 90 % decrease on the front face averaged pressure coefficient when compared to the results of the isolated cube, with the size of the decrease being dependent on the location of the pressure tap (Section 5.6) and on the approaching flow. This suggests that ventilation rates will drop by a similar amount, a greater decrease than that predicted by CIBSE (2006) of 33 %. Pressure coefficient databases such as those provided by ASHRAE, CIBSE and AIVC (Section 5.7) did not predict the pressure coefficient trends well, especially for limited arrays for both the full-scale (Section 5.7) and wind tunnel (Section 4.11) models.

The turbulence intensity of flow within a staggered array is approximately ten times

that of an isolated building due to the increased mechanical turbulence generated by the array. Turbulence intensity is affected by the local features surrounding a site and will change with wind direction (Section 5.2.1.2). This suggests that the assumption made by CIBSE (2006) about turbulent effects not needing to be considered for estimations of ventilation rates may not be valid for all directions in an urban area.

Tracer gas methods (Section 3.8.1) are often treated as the ‘true’ methods of measured ventilation rate, as they are a direct measurement of the flow rather than by proxy. However the correlations to other methods, such as the volumetric flow method (Section 3.8.6) and the pressure difference method (Section 3.8.5) are not linear, due to each method being affected by different parameters. For example the pressure difference method does not pick up the turbulent fluctuations of the flow, causing a different estimate to that provided by the tracer gas method (Section 6.4.1). Errors and instrument specifications are not always reported within research, making it difficult to inter-compare different results as methods strengths and weaknesses are not considered.

Stability was found to have little impact on the pressure coefficients and ventilation rates for the instrumented cube, likely due to the building being a small obstacle to the flow (Section 5.4). It is hypothesised that for a tall building, the effects of stability would be more distinct. More detailed comments are given at the end of each chapter.

7.1 Implications for industry

Whilst there are models available to predict wind speed (CIBSE) (Section 5.2.3), pressure coefficient (Section 5.7) (ASHRAE, AIVC and CIBSE) and ventilation rate (Section 6.6), they do not consider all of the parameters which affect the measurement, leading to incorrect estimations. For example the ventilation rate statistical models (Section 6.6) tend to overestimate the buoyant component of single sided ventilation, even for the metal Silsoe cube, which leads to an underestimation of the total ventilation rate.

The comparison of the wind tunnel results to the AIVC data for a shielded building highlight that the provided pressure coefficients cannot be used beyond their intended purpose as the sheltered cube does not just have similar pressure coefficient distributions as an isolated cube, but instead changes behaviour completely, especially on the north or south walls, or in cases where the sheltering around the instrumented cube is not uniform. The AIVC model does not take into account different levels of shielding, with larger arrays having a greater effect for certain wind directions, due to a decreased penetration depth. The pressure coefficient estimates by AIVC are taken from results of an expansive array, which cannot be assumed to be representative of a limited array, showing better agreement with the small symmetrical and large symmetrical arrays (Section 4.10). However, the estimations by AIVC, CIBSE and ASHRAE are accurate and representative of the values obtained for the isolated cube in the full-scale data.

The commonly made assumption that the thermal component for cross ventilation can be neglected does not hold for the Silsoe cube (Section 6.2.2) leading to inaccurate predictions of ventilation rate. Current ventilation models (Section 6.6) do not consider the effects of the internal environment, for example, waste heating due to electrical components or human activity and assume that the internal environment is well mixed. However, this may not hold for an occupied building where stratification of the internal environment may occur. The thermal and wind driven effects within the array tend to act in unison, reinforcing each other, though the effect of an urban heat island is not considered (Section 6.6.5).

Due to the Silsoe cube being made of metal, the temperature results are likely only to be relevant to warehouse or storage buildings, with the height of the cube (6 m) limiting the applicability of the data to low rise buildings such as standard housing. The results are also likely to be more applicable to older housing stock due to the large amount of infiltration measured.

7.2 The wind tunnel dataset

The wind tunnel model allowed for the array size to be varied, in order to understand how the size of an array may effect the pressure coefficients measured (Chapter 4). This effect is not linear with array size and for limited arrays, may be linked to the length of the array rows as well as the depth of the array. This is hypothesised as being due to edge effects of the previous rows becoming more remote (Section 4.10) as row length increases. Generally, increasing the depth of the array leads to a reduction in pressure coefficients (10 to 50 % \pm 5 % depending on the location of the pressure tap) and thus ventilation experienced for the instrumented cube, though this is not the case for winds parallel to the building, where the ventilation rates and pressure coefficients remain constant.

Wind tunnel models, when set up specifically to model a certain area provide adequate estimates of the ventilation rate expected for the full scale building using a solid model (Section 6.5). However, the wind tunnel does not include the fluctuating wind direction over the averaging period or buoyancy effects which may effect the ventilation rate. Care must be taken to ensure that the wind tunnel set-up is as representative as the full-scale environment as much as possible for the best results. The wind tunnel model can be considered representative of the pressure coefficient data obtained in the full-scale, with offsets being due to the different reference static pressure measurement locations (Section 4.10).

Due to the greater density of pressure taps on the wind tunnel model, contour plots could be created for the pressure coefficient (Section 4.10). The point of maximum pressure shifts on the front face within the array when compared to the isolated cube for a perpendicular wind, tending towards one corner, due to the asymmetry of the flow

caused by the array (Section 4.7). However, once the array becomes symmetrical in both the x and y directions, this tendency is reduced (Section 4.10). This shift is enhanced when the wind direction is in line with the arrays natural tendency and is reduced if the wind direction opposes it (Section 4.7).

Inter-comparisons between wind tunnel data sets are rare, due to differing research aims and reporting of the needed parameters such as boundary layer conditions and turbulence intensity. To effectively compare wind tunnel measurements a table with the most important parameters (e.g. roughness elements, wind speed) should be considered to allow an instant understanding of whether or not data are directly comparable. An example is given in Table 4.1.

7.2.1 Future wind tunnel work

The wind tunnel experiment undertaken focused on the pressure coefficient, wind direction and array size. Other parameters which need to be considered are varying packing density, frontal area density, array layout (staggered, aligned or random), building heights, wind speeds and scale of model. A larger dataset needs to be created which includes these parameters to allow for more accurate predictions to be created, though this would be a time consuming endeavour. Pressure coefficients derived from wind tunnel experiments should also be listed alongside contour plots. This will allow for an understanding as to how the shape of an array influences the pressure pattern on faces of an array element as for array cases, due to the pressure coefficients being so small, sometimes the detail is lost when just numbers are reported.

Like the full-scale dataset the instantaneous pressure measurements are also available for the wind tunnel and these could be compared to the full-scale measurements in order to determine the effects of rapidly fluctuating wind direction on the pressure coefficient.

7.3 The full-scale dataset

To understand the coupling between the internal environment and the driving flow, measurements were simultaneously carried out inside the instrumented cube alongside measurements of the oncoming flow. This full-scale data set captured varied atmospheric stabilities, wind speeds, wind directions, weather conditions and flow behaviours for both an isolated cube and an array for a period of nine months. This makes it one of the largest full-scale ventilation rate measurement campaigns within the literature with all instrumentation, set-up and errors detailed (Chapter 3). The Silsoe array, unlike other full scale arrays (e.g. Biltoft (2001) and MacDonald *et al.* (1997)) is limited in depth, with the cube of interest being positioned on one of the external rows and not

in the centre of the array. This, in some aspects, means that it is more representative of a building on the edge of a neighbourhood, rather than in the centre.

7.3.1 Future work with the full-scale dataset

As the Silsoe site was decommissioned in April 2016, it is not possible to repeat the field campaign in order to obtain a larger data set and this limits the further work which can be undertaken.

The instantaneous ventilation rate and pressure coefficient can also be investigated from the Silsoe full-scale data to understand how the presence of the array alters the coupling between the wind speed, instantaneous pressure coefficient and ventilation. The effects of gusts on pressure coefficient and ventilation rates should also be considered on smaller time scales, in order to understand how better to design a building for gusts caused by its surroundings. The instantaneous pressure coefficient could also be related to the instantaneous changing of the wind direction and the standard deviation of the wind direction. The two sonic anemometers located in front and behind the instrumented cube could be correlated with the internal sonic anemometers to see if the fluctuating wind speeds and wind directions can be used to detect the pulsing of the flow for a cross ventilated cube. More research into the results of the internal sonic anemometer could also be done to determine internal flows in conjunction with the results of CFD simulations. The dataset will be compared to the results of the CFD model created as part of the Refresh project.

The effects of the diurnal cycle of the site could also be considered as could, to some extent, the effect of seasonal variation on ventilation rates. The dataset could also be tested against more existing models and empirical equations as part of a larger review of the methods available.

As part of the Refresh project the knowledge obtained from the Silsoe field campaign will be used to design an experiment which monitors people in a realistic office in order to understand how the local external flow effects the internal environment and thus the health and well-being of people.

7.3.2 Work beyond this dataset

More full-scale arrays, both limited and expansive, are required to ensure that the flow behaviours seen in the wind tunnel experiments are representative of the real world. They are also required for the verification of CFD models. Simplified full-scale structures may also be useful in understanding the effects of specific buildings on the flow environment. Linked to this the opening set ups considered in this set up are simple compared to actual opening designs and the effect of an array on the ventilation rate for shuttered or angled openings should also be considered at the full-scale. Research into

the most effective location for the openings for a building within the array should also be considered, as it may be possible to take advantage of the array effects in order to increase ventilation.

Most importantly, a method of relating the local flow to the reference flow for a building within an urban area would allow for better estimates of the local flow field in the urban environment to be obtained. Often, there is no local measurement of wind speed or direction available, and calculations have to be based on measurements taken kilometres away from the site of the building, normally at airports. However, these are not guaranteed to be representative of the urban environment, for example the meteorological station at Heathrow airport, UK has been used as a reference for the flow within London itself (Short *et al.*, 2004).

Appendix A

Appendices

A Structure of the Urban Boundary layer

Whilst the atmospheric boundary layer is difficult to precisely define, a working definition is given by Garratt (1994): “The atmospheric boundary layer is the lowest layer of the atmosphere in which the effects of the surface such as friction, heating and cooling are felt directly on time scales of less than a day. Within the boundary layer significant fluxes of momentum, heat or matter are carried by turbulent motions within the depth of the boundary layer”. The physical nature of the boundary layer is therefore highly dependent on the surface below, with urban boundary layers being different to rural boundary layers due to the significantly different underlying surface.

The boundary layer can be split into an outer and an inner layer, with the inertial sub-layer overlapping between the two. A schematic of this for urban areas is shown in Figure A.1.

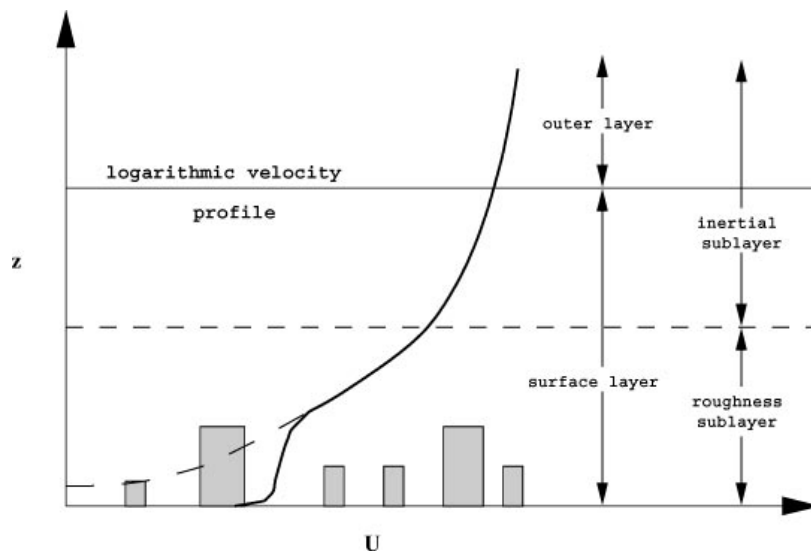


Figure A.1: Schematic of the boundary layer over an urban surface, with a log velocity profile (U) marked (thick black line). z represents height. Source: Britter and Hanna (2003).

The urban canopy layer (UCL), is the layer of air closest to the buildings in cities and extends upwards to roughly the mean roughness element height. A UCL is most easily

defined in a region of densely packed buildings of a near uniform height. Turbulence in this layer is dominated by the effects of individual buildings and other roughness elements. The UCL is often referred to as a subdivision of the roughness sub-layer.

Above the urban canopy layer is the roughness sub-layer (RSL), where the influence of individual buildings is less pronounced and the turbulence and velocity fields are not horizontally uniform (Barlow and Coceal, 2009). The roughness sub-layer is typically 2 to 5 times the mean height of the obstacles in depth, though this can rise to 10 to 15 times the mean obstacle height in unstable atmospheric conditions (Roth, 2000).

Above the roughness sub-layer is the inertial sub-layer (ISL), which may be referred to as the 'constant flux layer'. The inertial sub-layer contains flow that is spatially homogeneous and turbulent fluxes vary weakly with height. The inertial sub-layer is generally assumed to extend from the top of the roughness sub-layer to approximately one tenth of the total boundary layer depth. Rotach (1999) observed that a roughness sub-layer may be so deep that an inertial sub-layer cannot develop when the underlying roughness elements are extremely large. Within the ISL the velocity increases with height logarithmically with fluxes being roughly constant in this layer. This means that there is a downward transfer of momentum from the faster moving air at higher levels to the surface, which acts as a momentum sink.

Above the inertial sub-layer is the mixed or Ekman layer, known for large convective plumes which mix the fluxes efficiently, meaning they are horizontally homogeneous with uniform vertical profiles. It is assumed that the wind speed at the top of the atmospheric boundary layer is approximately geostrophic and that the time-averaged wind profile within a boundary layer is assumed from theory to increase logarithmically with height above the roughness sub-layer (Kaimal and Finnigan, 1993). The velocity profile can be seen in Figure A.1.

Due to the difficulty in building tall masts in urban areas to gather full-scale data, it is unclear as how far into an urban boundary layer that the logarithmic assumption holds. More data are available from scaled wind tunnel models, such as work by Castro *et al.* (2006) and Kastner-Klein and Rotach (2004). Direct Numerical Simulations (DNS) undertaken by Coceal *et al.* (2006) suggest the presence of shear layers directly above building height.

When the atmosphere encounters a surface of a different roughness such as the transition from a rural environment to an urban environment, an internal boundary layer develops, which can fill the entire boundary layer given sufficient urban fetch. The top of the so-called urban boundary layer is the height above which the profile is still adjusting to the upstream surface at which the conditions return to the previous profile.

B Flow across large openings for equation 2.7

Adapted from Awbi (1996): The pressure difference due to a temperature difference at height z (Figure A.2) across a large opening is given by:

$$\Delta p(z) = \Delta \rho g z \quad (\text{A.1})$$

where $\Delta \rho$ is the difference in density across the opening, z is the height in metres and g is gravitational acceleration. Also:

$$\Delta u(z) = \sqrt{\frac{2\Delta p(z)}{\rho}} \quad (\text{A.2})$$

where $u(z)$ is the wind speed at height z . Substituting equation A.1 into A.2 leads to equations A.3 and A.4.

$$u(z) \propto z^{\frac{1}{2}} \quad (\text{A.3})$$

$$\frac{u(z)}{u_{Max}} = \frac{z}{H} \quad (\text{A.4})$$

where u_{max} is the wind speed taken at the top of the opening, assuming a logarithmic wind profile and H is the height of the opening. The mean velocity (\bar{u}) through an opening of height H can be obtained using:

$$\bar{u} = \frac{u_{max}}{H^{\frac{1}{2}}} \int z^{\frac{1}{2}} dz \quad (\text{A.5})$$

This gives:

$$\bar{u} = \frac{u_{max}}{H^{\frac{1}{2}}} \frac{2}{3} H^{\frac{3}{2}} \quad (\text{A.6})$$

Which leads to:

$$\bar{u} = \frac{2}{3} H u_{max} \quad (\text{A.7})$$

The flow rate (Q) through the opening is determined by the effective area of the opening and the mean wind speed through the opening:

$$Q = C_d w \bar{u} \quad (\text{A.8})$$

Where C_d is the discharge coefficient of the opening and w is the width of the opening. Substituting equation A.7 into equation A.8 gives:

$$Q = \frac{2}{3} C_d A u_{max} \quad (\text{A.9})$$

where A is H multiplied by w . Equation A.9 gives the total volume flow rate through an opening, but in a buoyancy driven flow, it is assumed that equal masses of air enter and leave through the same opening, meaning the influx or efflux flow is given by Awbi (2003):

$$Q = \frac{C_d A}{3} u_{max} \quad (\text{A.10})$$

Using equation A.2 and substituting for u_{max} in equation A.10 gives:

$$Q = \frac{C_d A}{3} \sqrt{\frac{2\Delta p(H)}{\rho}} \quad (\text{A.11})$$

The pressure due to the stack effect is given by:

$$\Delta p = -\rho g H \frac{T_i - T_e}{T_i} \quad (\text{A.12})$$

By combining equation A.12 and A.11, it follows that:

$$Q = \frac{C_d A}{3} \sqrt{2gH \frac{T_i - T_e}{T_i}} \quad (\text{A.13})$$

Which is equation 2.7.

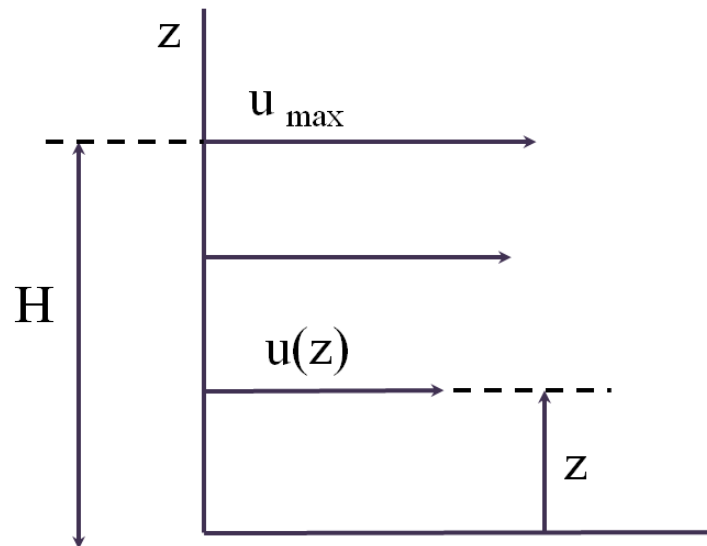


Figure A.2: Diagram of the components of the equations used to derive equations A.13 and 2.7. Adapted from Awbi (1996).

C Coefficient of discharge (C_d)

The experiments to determine the discharge coefficient of the Silsoe openings were carried out by Adam Robertson (University of Birmingham), Roger Hoxey (University of Birmingham) and Marco-Felipe King (University of Leeds) as part of the Refresh project using the facilities at Building Product Design, Nottingham NG16 6NS in the United Kingdom. Experiments were carried out using a test chamber in a purpose built open-ended wind tunnel (Figure A.3) to measure the C_d value for a window with a depth of 0.23 m made to the exact dimensions as the Silsoe openings (0.4 m by 1 m). The tunnel had a cross-section of 1.7 m x 1.7 m and exhausted directly into the ambient air. A lattice grid was installed to generate a uniform, homogeneous turbulent flow with a turbulence intensity of approximately 4 %.

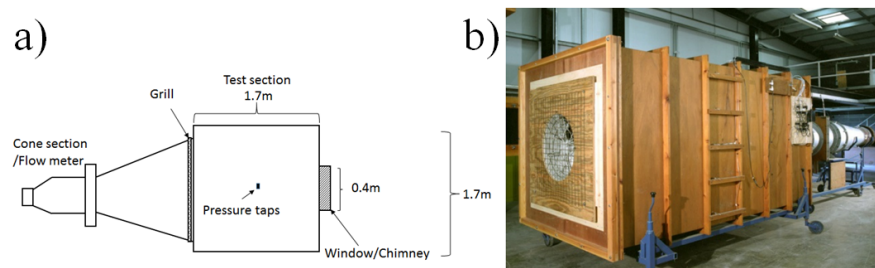


Figure A.3: The test chamber set up used. a) Schematic and b) a photo of the test chamber. Source: Robertson *et al.* (2004).

A fan within the rig draws air through the inlet cones which are calibrated to give flow rates from pressure at the conical outlet (Figure A.3). Pressures inside the settling chamber box at the downstream end are measured by micro-manometer (Robertson *et al.*, 2004). The test opening is mounted at the end of the settling box. Temperature, humidity and barometric pressure measurements are also taken to allow for an accurate calculation of the air density.

Two set-ups were studied: a rectangular window with a sill pointing inwards and a rectangular window with a sill pointing outwards (Figure A.4) to represent the the opening acting as an inlet and outlet respectively. For ease of handling, the openings were rotated horizontally.



Figure A.4: Image of the opening with the sill pointing outwards installed on the rig. Source: Personal communication King, (2016)

Figure A.5 shows the experimental results for the comparison between different flow rates and the resultant normalised pressured differences. Normalised pressure differences are calculated using:

$$P_n = \sqrt{\frac{2\Delta p}{\rho}} \quad (\text{A.14})$$

The gradient of the line on Figure A.5 is equal to C_d multiplied by the area of the opening. Robertson *et al.* (2004) states that for a carefully controlled experiment the trend line through the origin typically has an R^2 value of 0.999 or better, which is true for the experiment of the opening pointing into the box, though the opening pointing out of the box has a slightly lower rate. No errors were provided for the flow rate or pressure measurements. Errors on the area were assumed to be 0.01 m^2 . Errors in C_d were determined from the standard error of the fitted coefficients. The average C_d for the case of the windowsill pointing into the box was determined to be 0.616 ± 0.016 . Average C_d for the case of the windowsill pointing out of the box was 0.658 ± 0.0215 . Where possible in the thesis, these values have been used.

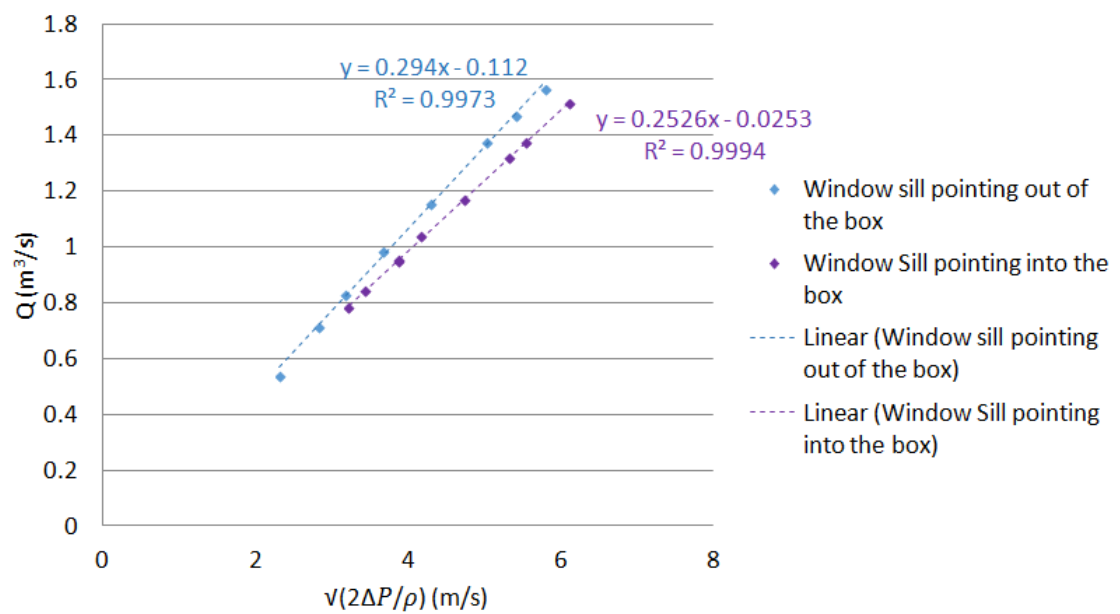


Figure A.5: Flow rate compared against normalised pressure for both window cases. Source: Personal communication King, (2016).

D Thermocouple image



Figure A.6: Photo of a Type-K thermocouple before deployment on site and a photo of the Picolog TC-08 thermocouple logging junctions and extension cabling used in the field work.

E Thermocouple Calibrations

An equation of the form $y = mx + c$ is calculated for each thermocouple for each calibration, providing that both the chamber and thermocouples have linear responses. The gradient of the line represents the sensitivity of the instrument, and the y-intercept the bias or offset of the instrument. The uncertainty of the fit is calculated using Matlab's statistical package, producing the standard errors with 95 % confidence intervals on the gradient and intercept. An example of this for a low to high temperature run (Run 1 repeat 2) for thermocouple 4 is shown:

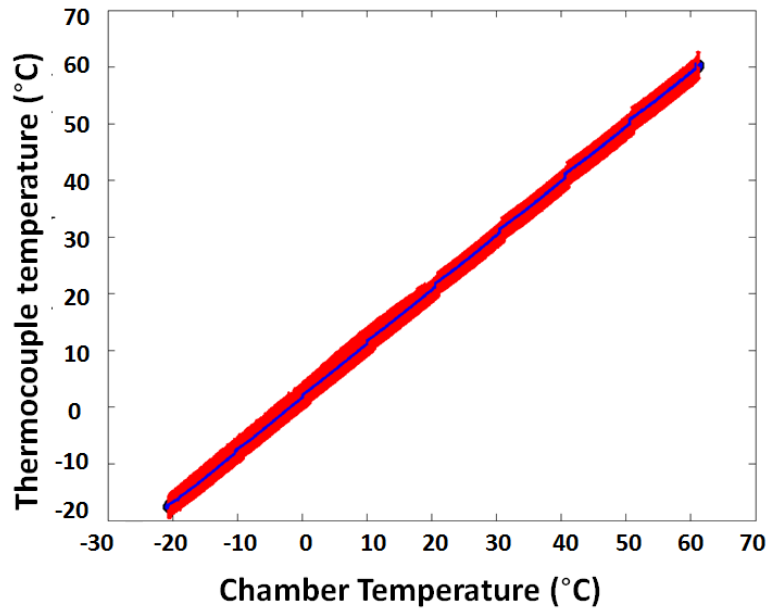


Figure A.7: An example of chamber temperature plotted against thermocouple temperature for thermocouple 9 of Set 1. Readings (blue), thermocouple reading error (red). The black visible at the start and end is the smaller error of ± 0.35 °C for the environmental chamber. The small undulations at the different staged temperatures are due to a greater amount of data at this point, as well as the slight shifts in temperature due to the environmental chamber temperature oscillating. Data were excluded when the thermocouples or the chamber was still adjusting to the change, with only data at stable temperatures being used.

Table A.1: Calibration and fit data for each thermocouple against the environmental chamber averaged over the repeats of calibration Runs 1 and 2 (Section 3.5.4.1).

Thermocouple	Gradient	Gradient error	Intercept (°C)	Intercept error (°C)	R^2
1	0.7162	0.0013	1.9601	0.0567	0.9993
2	0.9583	0.0015	2.3644	0.0486	0.9995
3	0.9537	0.0016	2.2045	0.0504	0.9994
4	0.9548	0.0016	1.9613	0.0490	0.9994
5	0.9520	0.0016	1.7469	0.0501	0.9994
6	0.9573	0.0015	2.0735	0.0481	0.9995
7	0.9567	0.0016	2.2776	0.0506	0.9994
8	0.9609	0.0013	2.5279	0.0410	0.9996
9	0.9557	0.0016	2.2632	0.0500	0.9994
10	0.9749	0.0023	2.0039	0.0724	0.9988
11	0.9576	0.0015	2.1574	0.0486	0.9994
12	0.9593	0.0016	1.9740	0.0491	0.9994
13	0.9614	0.0015	1.7179	0.0465	0.9995
14	0.9582	0.0015	1.9398	0.0477	0.9995
15	0.9561	0.0015	2.0536	0.0486	0.9995
16	0.9602	0.0015	2.1145	0.0467	0.9995
17	0.9852	0.0016	1.4570	0.0516	0.9994
18	0.9906	0.0014	1.5322	0.0446	0.9996
19	0.9882	0.0016	1.2861	0.0506	0.9994
20	0.9823	0.0016	1.5418	0.0500	0.9995
21	0.9876	0.0016	1.0727	0.0517	0.9994
22	0.9883	0.0016	1.3408	0.0507	0.9994
23	0.9855	0.0016	1.5282	0.0506	0.9994
24	0.9919	0.0016	1.4968	0.0495	0.9995

F Calibration of WXT520 temperature measurements

The temperature measurements of the WXT520 were calibrated by placing the WXT520 in the environmental chamber and varying the temperature between 5 °C and 45 °C, with stable 15 minute periods at set temperatures and 15 minute periods where the temperature has been programmed to decrease linearly. The external temperature range recorded by the WXT520 over the entire experiment was -2.5 °C to $33.9\text{ °C} \pm 0.3\text{ °C}$ with a relative humidity range of 22 % to $90\% \pm 3\%$.

The calibration cycle can be seen in Figure A.8 with the temperature range set to be similar to that observed over the course of the experiment (-2.5 °C to $33.9\text{ °C} \pm 0.3\text{ °C}$).

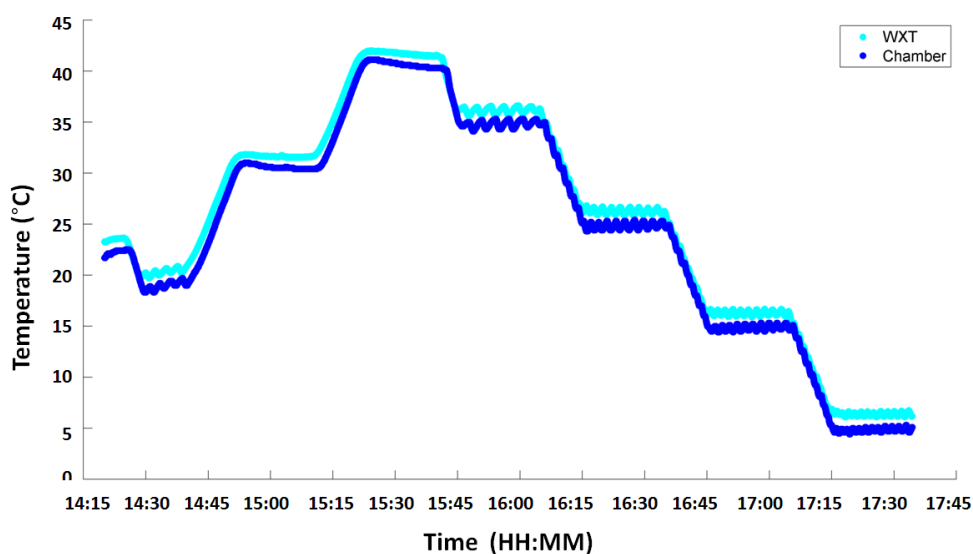


Figure A.8: Calibration cycle of the WXT520 in the environmental chamber. No errors are plotted.

Figure A.9 compares chamber temperature to the measured WXT520 temperature, with the green line being the line of best fit ($y = 0.99x + 1.437$). The standard errors of the fitted coefficients are 0.0004 and 0.012 respectively. The uncertainty of the fit was calculated using Matlab's statistical package, producing the standard errors with 95 % confidence intervals on the gradient and intercept. The R^2 value for the model fit was 0.997. The manufacturer stated error for the WXT520 was 0.3 °C.

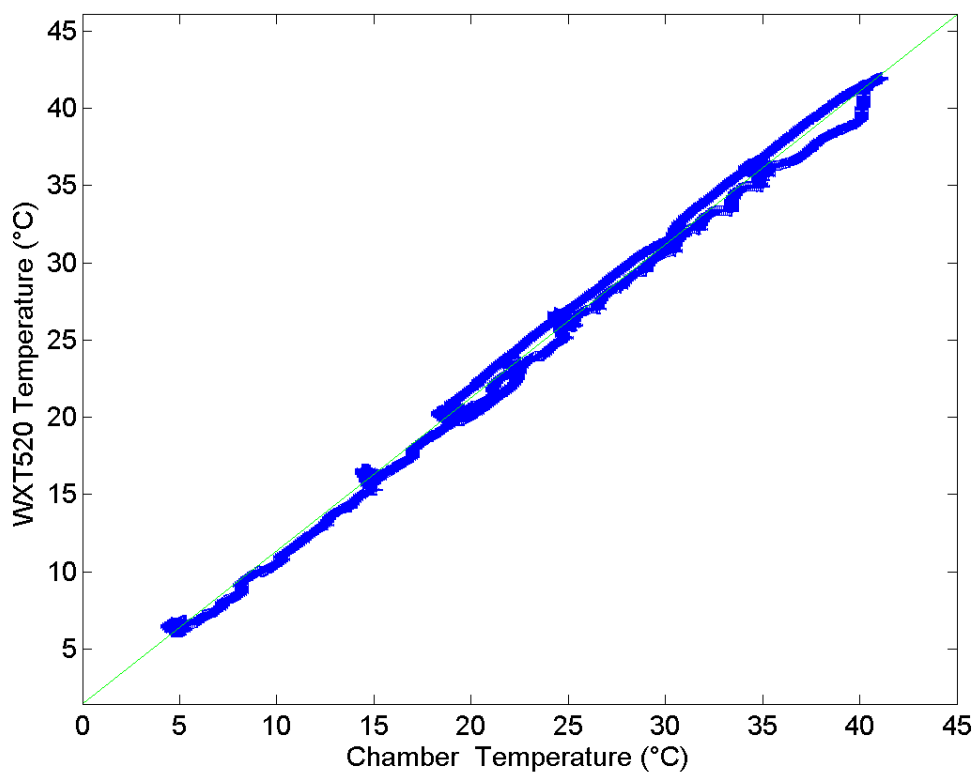


Figure A.9: Chamber recorded temperature and WXT520 recorded temperature. Error bars are plotted for both measurements, with the green line representing the line of best fit to the data.

G Pressure tap calibrations

Table A.2:: Pressure tap laboratory calibrations obtained by Solutions for Research. Calibration values are dimensionless and are used to correct the biases on the zero measurements in the pressure tap cycle by multiplying the raw pressure with the calibration value.

Pressure tap number	Calibration factor	Pressure tap number	Calibration factor	Pressure tap number	Calibration factor
1	-490.2	16	-492.6	31	-239.8
2	-492.6	17	-240.4	32	-241.5
3	-492.6	18	-242.1		
4	-495	19	-237		
5	-495	20	-239.8		
6	-495	21	-237.5		
7	-495	22	-245.7		
8	-495	23	-236.4		
9	-492.6	24	-238.7		
10	-492.6	25	-235.3		
11	-495	26	-239.2		
12	-485.4	27	-244.5		
13	-492.6	28	-248.1		
14	-492.6	29	-238.1		
15	-492.6	30	-234.7		

H K30 temperature tests

Table A.3:: Fitted coefficients for the effect of temperature on K30 concentration measurements at background concentration. m is the gradient and c is the y intercept.

K30 sensor	m	Error in m	c	Error in c	R^2
East	-0.004	0.000	412.873	1.654	0.469
Low	-0.008	0.000	328.499	0.698	0.468566
Mid	-0.005	0.000	257.602	0.834	0.839

I LI-COR calibration procedure

The zero values of the LI-COR 7500 are affected by temperature with the zero's response to temperature being typically 0.1 or 0.2 ppm per °C for CO₂ according to the operating manual. The gas analysers span for CO₂ is described as being independent of temperature fluctuations. A large pressure change (40 kPa) will affect the CO₂ spans by < 1 %, for ambient CO₂ concentrations (approximately 400 ppm) meaning that diurnal pressure fluctuations are not a concern.

The method for calibrating the LI-COR 7500 CO₂ zero and span were as follows:

1. Place the calibration tube into the sensor head, ensuring that it is correctly centred and connect the temperature sensor to the LI-COR 7500 control box. The calibration tube consists of a metal rod that lines the centre of the instrument, with three tubes coming off it; one for air input, one for an optional pressure sensor and one for air output.
2. Ensure that the temperature and pressure sensors are working as expected.
3. Attach the air in tube to a source of CO₂ free air and regulate the flow to 0.5 to 1 L min⁻¹.
4. Allow the CO₂ concentration to stabilise by waiting approximately 1 minute until the reading has settled. Make a note of the present zero value and reset the zero value using the software.
5. To set the span value, disconnect the CO₂ free air and attach a CO₂ span gas to the input tube, with a flow rate of at 0.5 to 1 L min⁻¹.
6. Enter the mole fraction in the target entry on the CO₂ calibration page.
7. Allow the reading to settle for 1 to 2 minutes, or longer if required and reset the span value.

J K30 fits to LI-COR data for background conditions

Table A.4: Fitted coefficients for the decay calibration of the LI-COR and K30 sensors for the background CO₂ condition calibrations in varying temperatures.

K30	m	Error on m	c	Error on c	R ²
East	2.083	0.084	-423.648	33.479	0.949
Low	1.470	0.143	-296.008	56.697	0.763
Mid	-2.662	0.684	1295.149	270.928	0.457

Table A.5: Fitted coefficients for the decay calibration of the K30 sensors against temperature.

K30 sensor	m	Error in m	c	Error in c	R^2
East	-0.609	0.132	422.977	4.028	0.392
Low	-0.684	0.060	309.120	1.830	0.797
Mid	-0.822	0.081	313.639	2.753	0.852

K K30 fits to LI-COR data for decay calibration

Table A.6: Fitted coefficients for the decay calibration of the LI-COR and K30 sensors.

K30 sensor	m	Error in m	c	Error in c	R^2
East	0.946	0.031	22.195	14.679	0.995
Low	0.692	0.028	-20.023	13.270	0.977
Mid	1.682	0.028	-397.790	39.713	0.980

L CFD modelling

As part of the Refresh project the Silsoe array and isolated cube were modelled by Marco-Felipe King from the University of Leeds. Full details of the set-up are not discussed here, see King *et al.* (2014). Two computational fluid dynamics (CFD) packages Openfoam and Ansys Fluent using the $k-\omega$ shear stress transport (SST) scale adaptive simulation (SAS) turbulence model are used to model the Silsoe site at full-scale. The $k-\omega$ SST SAS turbulent model was found to be a good balance between computational requirements and accuracy of surface pressure predictions. The internal flow of the cube is also modelled for the different ventilation set-ups and is coupled to the external flow.

A single representative wind speed is used of 10 m s^{-1} at a height of 6 m for the model, with ground roughness being assumed constant for all wind directions. The sides and top of the simulation were modelled as free-slip walls and are far enough way not to impact the flow around the cube, which was tested during a sensitivity analysis. A domain of (20 m x 50 m x 18 m) was modelled with approximately 3 H (building heights) upstream and 5H downstream from the isolated cube. For the array a bounding box of 6 H x 16.6 H x 3 H (72 m x 90 m x 18 m) was used.

Early results show that the predicted ventilation rates compare well with case studies of experimental values, with OpenFoam tending to give conservative estimates but with higher levels of variation. The CFD model will be used to gain further understanding into the potential behaviour of the flow field around the isolated cube and the array,

however it will not be used directly in this thesis.

M F-test and T-Test

F-tests test if two population variances are equal by comparing the ratio of the two variances. These were all carried out with $\alpha = 0.05$. Samples must be normally distributed and independent of each other (Snedecor and Cochran, 1989).

Variable 1 is always the case with the highest variance, meaning the F value is the ratio of the variance of case 1 to the variance of case 1 (Snedecor and Cochran, 1989). If the calculated F value is greater than the critical one tail value, the null hypothesis is rejected, meaning that the variances of case one and case two are unequal. If the calculated F value is less than the critical value, the null hypothesis is true. The results of the F-test are then used to decide which type of T-test to use: unequal variances or equal variances (Snedecor and Cochran, 1989).

The T-test is used to compare the actual difference of the means of two sets of data in relation to the variation of the data (Snedecor and Cochran, 1989). A T-tests statistical significance indicates whether or not the difference between two averages likely reflects a "real" difference in the population from which the groups were sampled. The null hypothesis used is that there is no difference between the two means for the open and closed cases. A two tail test is used: if the T value $< -$ critical T two tail or the T value $>$ T critical two tail, the null hypothesis is rejected and the means have a 95 % likelihood of being unequal. The tests assume that the data are normally distributed (Snedecor and Cochran, 1989).

References

- Ahmad, S., Hagishima, A., and Tanimoto, J. (2012). Experimental study of wind-induced ventilation in urban building of cube arrays with various layouts. *Jnl. of Wind Engineering and Industrial Aerodynamics*, **103**, 31–40.
- Allard, F. and Ghiaus, C. (2012). *Natural ventilation in the urban environment: assessment and design*. Routledge.
- Allegrini, J., Dorer, V., and Carmeliet, J. (2013). Wind tunnel measurements of buoyant flows in street canyons. *Building and Environment*, **59**, 315–326.
- Allen, G. and Hicks, J. (1999). A Century of Change: Trends in UK statistics since 1900 Research Paper 99/111 (available online). Technical report, House of Commons, London.
- Allocca, C., Chen, Q., and Glicksman, L. R. (2003). Design analysis of single-sided natural ventilation. *Energy and Buildings*, **35**(8), 785–795.
- Anderson Jr, J. D. (2010). *Fundamentals of aerodynamics*. Tata McGraw-Hill Education.
- Arnfield, A. (2003). Two decades of urban climate research: a review of turbulence, exchanges of energy and water, and the urban heat island. *International Journal of Climatology*, **26**, 1–26.
- Arnold, S. J., ApSimon, H., Barlow, J., Belcher, S., Bell, M., Boddy, J. W., Britter, R., Cheng, H., Clark, R., Colvile, R. N., Dimitroulopoulou, S., Dobre, a., Grealley, B., Kaur, S., Knights, a., Lawton, T., Makepeace, a., Martin, D., Neophytou, M., Neville, S., Nieuwenhuijsen, M., Nickless, G., Price, C., Robins, a., Shallcross, D., Simmonds, P., Smalley, R. J., Tate, J., Tomlin, a. S., Wang, H., and Walsh, P. (2004). Introduction to the DAPPLE Air Pollution Project. *The Science of the total environment*, **332**(1-3), 139–53.
- Atkinson, J., Chartier, Y., Silvia, C. L. P., Jensen, P., Li, Y., and Seto, W. H. (2009). *Natural ventilation for infection control in health-care settings*. World Health Organization.
- Awbi, H. (1996). Air movement in naturally-ventilated buildings. *Renewable Energy*, **8**(1-4), 241–247.
- Awbi, H. (2003). *Ventilation of Buildings*. Spon Press, 2nd editio edition.
- Bakó-Biró, Z. and Clements-Croome, D. (2012). Ventilation rates in schools and pupils' performance. *Building and Environment*, **48**, 215–223.
- Balogun, A. A., Tomlin, A. S., Wood, C. R., Barlow, J. F., Belcher, S. E., Smalley, R. J., Lingard, J. J., Arnold, S. J., Dobre, A., Robins, A. G., *et al.* (2010). In-street wind direction variability in the vicinity of a busy intersection in central london. *Boundary-layer meteorology*, **136**(3), 489–513.

- Barlow, J. and Coceal, O. (2009). A review of urban roughness sublayer turbulence. *Met Office Research and Development*, (527).
- Barlow, J. F. (2014). Progress in observing and modelling the urban boundary layer. *Urban Climate*, **10**, 216–240.
- Barlow, J. F., Halios, C. H., Lane, S. E., and Wood, C. R. (2014). Observations of urban boundary layer structure during a strong urban heat island event. *Environmental Fluid Mechanics*, **15**(2), 373–398.
- Belcher, S., Coceal, O., Hunt, J. C. R., Carruthers, D. J., and a.G. Robins (2012). A review of urban dispersion modelling. Technical Report Report ADMLC-R7, Annex B, Atmospheric Dispersion Modelling Liaison Committee.
- Belleri, A., Lollini, R., and Dutton, S. M. (2014). Natural ventilation design: An analysis of predicted and measured performance. *Building and Environment*, **81**, 123–138.
- Biltoft, C. A. (2001). Customer Report for Mock Urban Setting Test. Technical report, U.S. Army Developmental Test Command, Dugway.
- Blocken, B., Stathopoulos, T., and van Beeck, J. (2016). Pedestrian-level wind conditions around buildings: Review of wind-tunnel and cfd techniques and their accuracy for wind comfort assessment. *Building and Environment*, **100**, 50–81.
- Bowen, A. J. (1976). A wind tunnel investigation using simple building models to obtain mean surface wind pressure coefficients for air infiltration estimates. *Aero. Estab. Tech. Rep. LPR-LA-209*.
- BRECSU (2000). Energy Consumption Guide 19: Energy Use in Offices. Technical report, British Research Establishment Conservation Support Unit, Garston, Watford, UK.
- Britter, R. E. and Hanna, S. R. (2003). Flow and Dispersion in Urban Areas. *Annual Review of Fluid Mechanics*, **35**(1), 469–496.
- Brocklehurst, A. (2015). *The effect of the urban environment on wind driven infiltration of buildings*. Ph.D. thesis, University of Reading.
- Brown, M., Pol, S., Coirier, W., Kim, S., Huber, A., Nelson, M., Klein, P., Freeman, M., and Gowardhan, A. (2006). Experimental and model-computed area-averaged vertical profiles of wind speed for evaluation of mesoscale urban canopy schemes. In *Sixth Symposium on the Urban Environment AMS Forum: Managing our Physical and Natural Resources: Successes and Challenges*.
- Burge, P. S. (2004). Sick building syndrome. *Occupational and Environmental Medicine*, **61**(2), 185–190.
- Cable, J. (2004). Niosh report details dangers of carbon dioxide in confined spaces. *Occupational Hazards*, **12**(30), 2004.
- Caciolo, M. (2010). *Analyse expérimentale et simulation de la ventilation naturelle mono-façade pour le rafraîchissement des immeubles de bureaux*. Ph.D. thesis, École Nationale Supérieure des Mines de Paris.
- Caciolo, M., Stabat, P., and Marchio, D. (2011). Full scale experimental study of single-

- sided ventilation: Analysis of stack and wind effects. *Energy and Buildings*, **43**(7), 1765–1773.
- Caciolo, M., Cui, S., Stabat, P., and Marchio, D. (2013). Development of a new correlation for single-sided natural ventilation adapted to leeward conditions. *Energy and Buildings*, **60**, 372–382.
- Carey, P. and Etheridge, D. (1999). Direct wind tunnel modelling of natural ventilation for design purposes. *Building Services Engineering Research and Technology*, **20**(3), 131–142.
- Castro, I. (2003). Cfd for external aerodynamics in the built environment. *The QNET-CFD Network Newsletter*, **2**(2), 4–7.
- Castro, I. and Robins, A. G. (1977). The flow around a surface-mounted cube in uniform and turbulent flows. *J.Fluid.Mech*, **79**(Part 2), 307–335.
- Castro, I. P., Cheng, H., and Reynolds, R. (2006). Turbulence Over Urban-type Roughness: Deductions from Wind-tunnel Measurements. *Boundary-Layer Meteorology*, **118**(1), 109–131.
- Cheng, H. and Castro, I. (2002). Near wall flow over urban-like roughness. *Boundary-Layer Meteorology*, **0**, 229–259.
- Cheng, H., Hayden, P., Robins, A., and Castro, I. (2007). Flow over cube arrays of different packing densities. *Journal of Wind Engineering and Industrial Aerodynamics*, **95**(8), 715–740.
- Choinière, Y., Tanaka, H., Munroe, J., and Suchorski-Tremblay, A. (1992). Prediction of wind-induced ventilation for livestock housing. *Journal of Wind Engineering and Industrial Aerodynamics*, **44**(1-3), 2563–2574.
- Chu, C.-R. and Chiang, B.-F. (2013). Wind-driven cross ventilation with internal obstacles. *Energy and Buildings*, **67**, 201–209.
- CIBSE, A. (2005). Natural ventilation in non-domestic buildings. *London, UK*.
- CIBSE, G. A. (2006). Environmental design. *The Chartered Institution of Building Services Engineers, London*.
- Claus, J., Coceal, O., Thomas, T. G., Branford, S., Belcher, S. E., and Castro, I. P. (2011). Wind-Direction Effects on Urban-Type Flows. *Boundary-Layer Meteorology*, **142**(2), 265–287.
- Claus, J., Coceal, O., and Thomas, T. (2012). Wind-direction effects on urban-type flows. *Boundary-layer Meteorology*, pages 265–287.
- Coceal, O. and Belcher, S. E. (2004). A canopy model of mean winds through urban areas. *Quarterly Journal of the Royal Meteorological Society*, **130**(599), 1349–1372.
- Coceal, O., Thomas, T. G., Castro, I. P., and Belcher, S. E. (2006). Mean Flow and Turbulence Statistics Over Groups of Urban-like Cubical Obstacles. *Boundary-Layer Meteorology*, **121**(3), 491–519.
- Coceal, O., Thomas, T. G., and Belcher, S. E. (2007a). Spatial Variability of Flow Statistics within Regular Building Arrays. *Boundary-Layer Meteorology*, **125**(3), 537–552.

- Coceal, O., Dobre, A., and Thomas, T. (2007b). Unsteady dynamics and organized structures from DNS over an idealized building canopy. *International Journal of Climatology*, **19**(53)(July), 1943–1953.
- Cóstola, D., Blocken, B., and Hensen, J. (2009). Overview of pressure coefficient data in building energy simulation and airflow network programs. *Building and Environment*, **44**(10), 2027–2036.
- Counihan, J. (1969). An improved method of simulating an atmospheric boundary layer in a wind tunnel. *Atmospheric Environment (1967)*, **3**(2), Pages 197, Pages IN1, Pages 201–200–IN2–214.
- Da Graga, G. and Linden, P. (2003). Simplified modeling of cross-ventilation airflow. *ASHRAE Transactions*, **109**, 65–79.
- Dascalaki, E. (1996). Predicting single sided natural ventilation rates in buildings. *Fuel and Energy Abstracts*, **37**(3), 215.
- De Gids, W. and Phaff, H. (1982). Ventilation rates and energy consumption due to open windows: a brief overview of research in the netherlands. *Air infiltration review*, **4**(1), 4–5.
- Dobre, a., Arnold, S., Smalley, R., Boddy, J., Barlow, J., Tomlin, a., and Belcher, S. (2005). Flow field measurements in the proximity of an urban intersection in London, UK. *Atmospheric Environment*, **39**(26), 4647–4657.
- Drew, D. R., Barlow, J. F., and Lane, S. E. (2013). Observations of wind speed profiles over greater london, uk, using a doppler lidar. *Journal of Wind Engineering and Industrial Aerodynamics*, **121**, 98–105.
- Edwards, C. (1998). *Design rules of thumb for naturally ventilated office buildings in Canada*. Ph.D. thesis, University of Waterloo, School of Architecture.
- Eliasson, I., Offerle, B., Grimmond, C., and Lindqvist, S. (2006). Wind fields and turbulence statistics in an urban street canyon. *Atmospheric Environment*, **40**(1), 1–16.
- Etheridge, D. (2002). Nondimensional methods for natural ventilation design. *Building and Environment*, **37**(11), 1057–1072.
- Etheridge, D. (2015). A Perspective on Fifty Years of Natural Ventilation Research. *Building and Environment*, **91**(September 2015), 51–60.
- Etheridge, D. and Nolan, J. (1979). Ventilation measurements at model scale in a turbulent flow. *Building and environment*, **14**(1), 53–64.
- Etheridge, D. W. (2000). Unsteady flow effects due to fluctuating wind pressures in natural ventilation design - mean flow rates. *Building and Environment*, **35**, 111–133.
- Etheridge, D. W. and Sandberg, M. (1996). *Building ventilation: theory and measurement*. John Wiley & Sons.
- Farrou, I., Kolokotroni, M., and Santamouris, M. (2016). Building envelope design for climate change mitigation: a case study of hotels in greece. *International Journal of Sustainable Energy*, **35**(10), 944–967.
- Fedorovich, E. and Kaiser, R. (1998). Wind tunnel model study of turbulence regime

- in the atmospheric convective boundary layer. In *Buoyant Convection in Geophysical Flows*, pages 327–370. Springer.
- Freire, R. Z., Abadie, M. O., and Mendes, N. (2013). On the improvement of natural ventilation models. *Energy and Buildings*, **62**, 222–229.
- Gao, Y., Yao, R., Li, B., Turkbeyler, E., Luo, Q., and Short, A. (2012). Field studies on the effect of built forms on urban wind environments. *Renewable energy*, **46**, 148–154.
- Garratt, J. R. (1994). *The Atmospheric Boundary Layer*. Cambridge University Press, Cambridge, 2nd editio edition.
- Ghiaus, C., Allard, F., Santamouris, M., Georgakis, C., and Nicol, F. (2006). Urban environment influence on natural ventilation potential. *Building and Environment*, **41**(4), 395–406.
- Gilkeson, C., Camargo-Valero, M., Pickin, L., and Noakes, C. (2013). Measurement of ventilation and airborne infection risk in large naturally ventilated hospital wards. *Building and Environment*, **65**, 35–48.
- Grimmond, C. S. B. and Oke, T. R. (1999). Aerodynamic Properties of Urban Areas Derived from Analysis of Surface Form. *Journal of Applied Meteorology*, **38**(9), 1262–1292.
- Haghighat, F., Brohus, H., and Rao, J. (2000). Modelling air infiltration due to wind fluctuations-a review.
- Hall, D. J. and Spanton, A. M. (2012). Ingress of External Contaminants into Buildings A Review. Technical report, Envirobods Ltd., London.
- Hanna, S., Tehranian, S., Carissimo, B., Macdonald, R., and Lohner, R. (2002). Comparisons of model simulations with observations of mean flow and turbulence within simple obstacle arrays. *Atmospheric Environment*, **36**(32), 5067–5079.
- Heijmans, N. and Wouters, P. (2002). Impact of the uncertainties on wind pressures on the prediction of thermal comfort performances. *Principles of Hybrid Ventilation (ed. P. Heiselberg)*, IEA ECBCS Annex, **35**.
- Hertig, J.-A. and Alexandrou, C. (1995). The influence of surroundings on pressure distributions around buildings. In *Wind Climate in Cities*, pages 293–317. Springer.
- Högström, U. (1988). Non-dimensional wind and temperature profiles in the atmospheric surface layer: A re-evaluation. In *Topics in Micrometeorology. A Festschrift for Arch Dyer*, pages 55–78. Springer.
- Hölscher, N. and Niemann, H.-J. (1998). Towards quality assurance for wind tunnel tests: A comparative testing program of the windtechnologische gesellschaft. *Journal of Wind Engineering and Industrial Aerodynamics*, **74**, 599–608.
- Hoxey, R. and Parmentier, B. and Baker, C. (2012). The application of research on wind effects to design. Technical report, Silsoe Research Institute, Silsoe, Bedford, UK.
- Hoydysh, W. G. and Dabberdt, W. F. (1988). Kinematics and dispersion characteristics of flows in asymmetric street canyons. *Atmospheric Environment (1967)*, **22**(12), 2677–2689.

- Hussain, M. and Lee, B. (1980). A wind tunnel study of the mean pressure forces acting on large groups of low-rise buildings. *Journal of Wind Engineering and Industrial Aerodynamics*, **6**(3-4), 207–225.
- Ikegaya, N., Hirose, C., Hagishima, A., and Tanimoto, J. (2016). Effect of turbulent flow on wall pressure coefficients of block arrays within urban boundary layer. *Building and Environment*, **100**, 28–39.
- Inagaki, A. and Kanda, M. (2008). Turbulent flow similarity over an array of cubes in near-neutrally stratified atmospheric flow. *Journal of Fluid Mechanics*, **615**, 101.
- Inagaki, A. and Kanda, M. (2010). Organized structure of active turbulence over an array of cubes within the logarithmic layer of atmospheric flow. *Boundary-layer meteorology*, **135**(2), 209–228.
- Irtaza, H., Beale, R. G., Godley, M. H. R., and Jameel, a. (2013). Comparison of wind pressure measurements on Silsoe experimental building from full-scale observation, wind-tunnel experiments and various CFD techniques. *International Journal of Engineering, Science and Technology*, **5**(1), 28–41.
- Irwin, H. (1981). The design of spires for wind simulation. *Journal of Wind Engineering and Industrial Aerodynamics*, **7**(3), 361–366.
- Jensen, M. (1958). The model-law for phenomena in natural wind. *Ingenioren*, **2**(4), 121–128.
- Ji, L., Tan, H., Kato, S., Bu, Z., and Takahashi, T. (2011). Wind tunnel investigation on influence of fluctuating wind direction on cross natural ventilation. *Building and Environment*, **46**(12), 2490–2499.
- Jia, Y., Sill, B., and Reinhold, T. (1998). Effects of surface roughness element spacing on boundary-layer velocity profile parameters. *Journal of wind engineering and industrial aerodynamics*, **73**(3), 215–230.
- Jiang, Y. and Chen, Q. (2002). Effect of fluctuating wind direction on cross natural ventilation in buildings from large eddy simulation. *Building and Environment*, **37**, 379–386.
- Jiang, Y., Alexander, D., Jenkins, H., Arthur, R., and Chen, Q. (2003). Natural ventilation in buildings: measurement in a wind tunnel and numerical simulation with large-eddy simulation. *Journal of Wind Engineering and Industrial Aerodynamics*, **91**(3), 331–353.
- Kaimal, J. C. and Finnigan, J. J. (1993). *Atmospheric Boundary Layer Flows : Their Structure and Measurement: Their Structure and Measurement*, volume 1993. Oxford University Press.
- Kanda, M. (2006). Progress in the scale modeling of urban climate: Review. *Theoretical and Applied Climatology*, **84**(1-3), 23–33.
- Kanda, M., Inagaki, A., Miyamoto, T., Gryschka, M., and Raasch, S. (2013). A new aerodynamic parametrization for real urban surfaces. *Boundary-layer meteorology*, **148**(2), 357–377.
- Karava, P., Stathopoulos, T., and Athienitis, A. K. (2006). Impact of internal pressure co-

- efficients on wind-driven ventilation analysis. *International Journal of Ventilation*, **5**(1), 53–66.
- Karava, P., Stathopoulos, T., and a.K. Athienitis (2011). Airflow assessment in cross-ventilated buildings with operable façade elements. *Building and Environment*, **46**(1), 266–279.
- Kastner-Klein, P. and Rotach, M. W. (2004). Mean Flow and Turbulence Characteristics in an Urban Roughness Sublayer. *Boundary-Layer Meteorology*, **111**(1), 55–84.
- Kastner-Klein, P., Fedorovich, E., and Rotach, M. (2001). A wind tunnel study of organised and turbulent air motions in urban street canyons. *Journal of Wind Engineering and Industrial Aerodynamics*, **89**(9), 849–861.
- King, M., Gough, H., Noakes, C., and Barlow, J. (2014). Silsoe revisited: Benchmarking openfoam vs. fluent and a prospective full-scale study. In http://www.hembex.co.uk/wes2014/WES2014_Proceedings_Rev3_S.pdf, pages 93–96. Wind Engineering Society.
- Klepeis, N. E., Nelson, W. C., Ott, W. R., Robinson, J. P., Tsang, A. M., Switzer, P., Behar, J. V., Hern, S. C., Engelmann, W. H., *et al.* (2001). The national human activity pattern survey (nhaps): a resource for assessing exposure to environmental pollutants. *Journal of exposure analysis and environmental epidemiology*, **11**(3), 231–252.
- Knapp, G. A. (2007). *Improved methods for structural wind engineering*. Ph.D. thesis, University of Nottingham.
- Kolokotroni, M., Tassou, S. A., and Gowreesunker, B. L. (2015). Energy aspects and ventilation of food retail buildings. *Advances in Building Energy Research*, **9**(1), 1–19.
- Kukadia, V., Kolokotroni, M., and Perera, E. (1998). Barriers to natural ventilation design of office buildings. National report: United Kingdom. Technical Report 0, BRE.
- Lakehal, D. and Rodi, W. (1997). Calculation of the flow past a surface-mounted cube with two-layer turbulence models. *Journal of Wind Engineering and Industrial Aerodynamics*, **67**, 65–78.
- Larsen, T. S. and Heiselberg, P. (2008). Single-sided natural ventilation driven by wind pressure and temperature difference. *Energy and Buildings*, **40**(6), 1031–1040.
- Laussmann, D. and Helm, D. (2011). Air change measurements using tracer gases. In N. Mazzeo, editor, *Chemistry, Emission Control, Radioactive Pollution and Indoor Air Quality*, chapter 14, page 692 pages. InTech, 1 edition.
- Letzel, M. O., Krane, M., and Raasch, S. (2008). High resolution urban large-eddy simulation studies from street canyon to neighbourhood scale. *Atmospheric Environment*, **42**(38), 8770–8784.
- Li, H., Li, X., and Qi, M. (2014). Field testing of natural ventilation in college student dormitories (Beijing, China). *Building and Environment*, **78**(2), 36–43.
- Liddament, M. (1986). *Air infiltration calculation techniques: an applications guide*. Air infiltration and ventilation centre.
- Liddament, M. (1996). *A Guide to Energy Efficient Ventilation*. Technical report, Air Infiltration and Ventilation Centre.

- Lim, H. C., Castro, I. P., and Hoxey, R. P. (2007). Bluff bodies in deep turbulent boundary layers: Reynolds-number issues. *Journal of Fluid Mechanics*, **571**, 97.
- Linden, P. F. (1999). The fluid mechanics of Natural ventilation. *Annu. Rev. Fluid. Mech*, **31**, 201–38.
- Linden, P. F. and Carrilho da Graca, G. (2003). Simplified modelling of cross ventilation airflow. Technical report, ASHRAE, Chicago.
- Liu, C.-H., Barth, M. C., and Leung, D. Y. (2004). Large-eddy simulation of flow and pollutant transport in street canyons of different building-height-to-street-width ratios. *Journal of Applied Meteorology*, **43**(10), 1410–1424.
- Longley, I., Gallagher, M., Dorsey, J., Flynn, M., and Barlow, J. (2004). Short-term measurements of airflow and turbulence in two street canyons in manchester. *Atmospheric Environment*, **38**(1), 69–79.
- Lundquist, J. K. and Chan, S. T. (2007). Consequences of urban stability conditions for computational fluid dynamics simulations of urban dispersion. *Journal of applied meteorology and climatology*, **46**(7), 1080–1097.
- MacDonald, R., Griffiths, R., and Cheah, S. (1997). Field experiments of dispersion through regular arrays of cubic structures. *Atmospheric Environment*, **31**(6), 783–795.
- Macdonald, R., Griffiths, R., and Hall, D. (1998). A comparison of results from scaled field and wind tunnel modelling of dispersion in arrays of obstacles. *Atmospheric Environment*, **32**(22), 3845–3862.
- Millward-Hopkins, J., Tomlin, A., Ma, L., Ingham, D., and Pourkashanian, M. (2011). Estimating aerodynamic parameters of urban-like surfaces with heterogeneous building heights. *Boundary-layer meteorology*, **141**(3), 443–465.
- Mishra, A. K. and Ramgopal, M. (2015). A comparison of student performance between conditioned and naturally ventilated classrooms. *Building and Environment*, **84**, 181–188.
- Mochida, A., Yoshino, H., Takeda, T., Kakegawa, T., and Miyauchi, S. (2005). Methods for controlling airflow in and around a building under cross-ventilation to improve indoor thermal comfort. *Journal of Wind Engineering and Industrial Aerodynamics*, **93**(6), 437–449.
- Nakamura, Y. and Oke, T. (1988). Wind, temperature and stability conditions in an east-west oriented urban canyon. *Atmospheric Environment (1967)*, **22**(12), 2691–2700.
- Ng, E., Yuan, C., Chen, L., Ren, C., and Fung, J. C. (2011). Improving the wind environment in high-density cities by understanding urban morphology and surface roughness: A study in Hong Kong. *Landscape and Urban Planning*, **101**(1), 59–74.
- Offerle, B., Eliasson, I., Grimmond, C., and Holmer, B. (2007). Surface heating in relation to air temperature, wind and turbulence in an urban street canyon. *Boundary-Layer Meteorology*, **122**(2), 273–292.
- Ohba, M., Irie, K., and Kurabuchi, T. (2001). Study on airflow characteristics inside and outside a cross-ventilation model, and ventilation flow rates using wind tunnel

- experiments. *Journal of Wind Engineering and Industrial Aerodynamics*, **89**(14), 1513–1524.
- Oke, T. (1988). Street design and urban canopy layer climate. *Energy and Buildings*, **11**(1), 103–113.
- Olesen, B. W. (2015). Indoor environmental input parameters for the design and assessment of energy performance of buildings. *Rehva Journal*, pages 17–23.
- Orme, M. and Leksmono, N. (2002). Aivc guide 5: Ventilation modelling data guide. *International Energy Agency, Air Infiltration Ventilation Center. AIC-GUI*, **5**.
- Padhra, A. (2010). *Estimating the sensitivity of urban surface drag to building morphology*. Ph.D. thesis, University of Reading.
- Pardysak, E. R., Brown, M. J., Nelson, M. A., Zajic, D., Princevac, M., Biltoft, C., and Klewicki, J. C. (2002). Building effects on thermal stratification during the must trials. In *Proceedings, AMS 4th symposium on the urban environment, Norfolk, VA*.
- Park, J. (2013). Long-term field measurement on effects of wind speed and directional fluctuation on wind-driven cross ventilation in a mock-up building. *Building and Environment*, **62**, 1–8.
- Park, M., Hagishima, A., Tanimoto, J., and Narita, K.-i. (2012). Effect of urban vegetation on outdoor thermal environment: field measurement at a scale model site. *Building and Environment*, **56**, 38–46.
- Park, S.-B. and Baik, J.-J. (2013). A large-eddy simulation study of thermal effects on turbulence coherent structures in and above a building array. *Journal of applied meteorology and climatology*, **52**(6), 1348–1365.
- Pascheke, F., Barlow, J. F., and Robins, A. (2008). Wind-tunnel modelling of dispersion from a scalar area source in urban-like roughness. *Boundary-Layer Meteorology*, **126**(1), 103–124.
- Persily, A. and Levin, H. (2011). Ventilation measurements in iaq studies: problems and opportunities. In *Proceedings of Indoor Air 2011, 12th International Conference on Indoor Air Quality and Climate*.
- Raw, G. J., Roys, M. S., and Leaman, A. (1990). *Further Findings from the Office Environment Survey: Productivity*. Building Research Establishment.
- Reinhold, T. A. (1982). *Wind Tunnel Modeling for Civil Engineering Applications: Proceedings of the International Workshop on Wind Tunnel Modeling Criteria and Techniques in Civil Engineering Applications, Gaithersburg, Maryland, USA, April 1982*. Cambridge University Press.
- Richards, P. and Hoxey, R. (2002). Unsteady flow on the sides of a 6m cube. *Journal of Wind Engineering and Industrial Aerodynamics*, **90**, 1855–1866.
- Richards, P. and Hoxey, R. (2008). Wind loads on the roof of a 6m cube. *Journal of Wind Engineering and Industrial Aerodynamics*, **96**(6-7), 984–993.
- Richards, P. and Hoxey, R. (2012). Pressures on a cubic building Part 1: Full-scale results. *Journal of Wind Engineering and Industrial Aerodynamics*, **102**, 72–86.

- Richards, P., Hoxey, R., and Short, L. (2001). Wind pressures on a 6m cube. *Journal of Wind Engineering and Industrial Aerodynamics*, **89**, 1553–1564.
- Richards, P., Hoxey, R., Connell, B., and Lander, D. (2007). Wind-tunnel modelling of the silsoe cube. *Journal of Wind Engineering and Industrial Aerodynamics*, **95**(9), 1384–1399.
- Richardson, G. and Blackmore, P. (1995). The silsoe structures building: comparison of 1: 100 model-scale data with full-scale data. *Journal of wind engineering and industrial aerodynamics*, **57**(2), 191–201.
- Robertson, A., Highton, I., and Hedges, R. (2004). Translating ventilation research into meaningful design. In *Proceedings of the 11th UK conference on Wind Engineering*.
- Robins, A. and Macdonald, R. (2001). Review of Flow and Dispersion in the Vicinity of Groups of Buildings. Technical report, University of Surrey, UMIST and University of Waterloo.
- Robins, A., Castro, I., Hayden, P., Steggel, N., Contini, D., Heist, D., and Taylor, T. J. (2001). A wind tunnel study of dense gas dispersion in a stable boundary layer over a rough surface. *Atmospheric Environment*, **35**(13), 2253–2263.
- Robins, A., Savory, E., Scaperdas, A., and Grigoriadis, D. (2002). Spatial variability and source-receptor relations at a street intersection. *Water, Air and Soil Pollution: Focus*, **2**(5-6), 381–393.
- Rooney, G. (2001). Comparison of upwind land use and roughness length measured in the urban boundary layer. *Boundary-layer meteorology*, **100**(3), 469–485.
- Rotach, M. W. (1999). On the influence of the urban roughness sublayer on turbulence and dispersion. *Atmospheric Environment*, **33**(24), 4001–4008.
- Rotach, M. W., Vogt, R., Bernhofer, C., Batchvarova, E., Christen, a., Clappier, a., Feddersen, B., Gryning, S.-E., Martucci, G., Mayer, H., Mitev, V., Oke, T. R., Parlow, E., Richner, H., Roth, M., Roulet, Y.-a., Ruffieux, D., Salmond, J. a., Schatzmann, M., and Voogt, J. a. (2005). BUBBLE an Urban Boundary Layer Meteorology Project. *Theoretical and Applied Climatology*, **81**(3-4), 231–261.
- Roth, M. (2000). Review of atmospheric turbulence over cities. *Quarterly Journal of the Royal Meteorological Society*, **126**(564), 941–990.
- Santamouris, M. and Allard, F. (1998). *Natural ventilation in buildings: a design handbook*. Earthscan.
- Santamouris, M., Papanikolaou, N., Livada, I., Koronakis, I., Georgakis, C., Argiriou, a., and Assimakopoulos, D. (2001). On the impact of urban climate on the energy consumption of buildings. *Solar Energy*, **70**(3), 201–216.
- Santiago, J., Dejoan, A., Martilli, A., Martin, F., and Pinelli, A. (2010). Comparison between large-eddy simulation and reynolds-averaged navier–stokes computations for the must field experiment. part i: study of the flow for an incident wind directed perpendicularly to the front array of containers. *Boundary-layer meteorology*, **135**(1), 109–132.
- Sawachi, T., Ken-ichi, N., Kiyota, N., Seto, H., Nishizawa, S., and Ishikawa, Y. (2004).

- Wind pressure and air flow in a full-scale building model under cross ventilation. *International Journal of Ventilation*, **2**(4), 343–357.
- Schakib-Ekbatan, K., Çakici, F. Z., Schweiker, M., and Wagner, A. (2015). Does the occupant behavior match the energy concept of the building? Analysis of a German naturally ventilated office building. *Building and Environment*, **84**, 142–150.
- Sherman, M. (1990). Tracer-gas techniques for measuring ventilation in a single zone. *Building and Environment*, **25**(4), pp–365–374.
- Shetabivash, H. (2015). Investigation of opening position and shape on the natural cross ventilation. *Energy and Buildings*, **93**, 1–15.
- Short, C. A., Lomas, K. J., and Woods, A. (2004). Design strategy for low-energy ventilation and cooling within an urban heat island. *Building Research & Information*, **32**(3), 187–206.
- Short, C. A., Cook, M., and Lomas, K. J. (2009). Delivery and performance of a low-energy ventilation and cooling strategy. *Building Research & Information*, **37**(1), 1–30.
- Snedecor, G. W. and Cochran, W. G. (1989). *Statistical methods*. Iowa State University Press, 8th edition.
- Snow, S., Soska, A., Chatterjee, S. K., *et al.* (2016). Keep calm and carry on: Exploring the social determinants of indoor environment quality. In *Proceedings of the 2016 CHI Conference*, pages 1476–1482.
- Snyder, W. (1981). Guideline for fluid modeling of atmospheric diffusion. epa office of air quality, planning and standards, research triangle park. Technical report, EPA-600/8-81-009.
- Snyder, W. H. and Castro, I. P. (2002). The critical Reynolds number for rough-wall boundary layers. *Journal of Wind Engineering and Industrial Aerodynamics*, **90**(1), 41–54.
- Stabat, P., Caciolo, M., and Marchio, D. (2012). Progress on single-sided ventilation techniques for buildings. *Advances in Building Energy Research*, **6**(2), 212–241.
- Stathopoulos, T. (2006). Pedestrian level winds and outdoor human comfort. *Journal of Wind Engineering and Industrial Aerodynamics*, **94**(11), 769–780.
- Straw, M. (2000). *Computation and measurement of wind induced ventilation*. Ph.D. thesis, University of Nottingham.
- Stull, R. B. (1988). *An Introduction to Boundary Layer Meteorology*. Springer, first edition.
- Subudhi, S., Sreenivas, K., and Arakeri, J. H. (2013). Study of buoyant jets in natural ventilation of a model room. *International Journal of Heat and Mass Transfer*, **64**, 91–97.
- Suk, W. A., Murray, K., and Avakian, M. D. (2003). Environmental hazards to children's health in the modern world. *Mutation Research/Reviews in Mutation Research*, **544**(2), 235–242.
- Swami, M. V. and Chandra, S. (1987). Procedures for calculating natural ventilation airflow rates in buildings. *ASHRAE Final Report FSEC-CR-163-86, ASHRAE Research Project*.
- Tominaga, Y. and Blocken, B. (2015). Wind tunnel experiments on cross-ventilation flow

- of a generic building with contaminant dispersion in unsheltered and sheltered conditions. *Building and Environment*, **92**, 452–461.
- Uehara, K., Murakami, S., Oikawa, S., and Wakamatsu, S. (2000). Wind tunnel experiments on how thermal stratification affects flow in and above urban street canyons. *Atmospheric Environment*, **34**(10), 1553–1562.
- United Nations (2014). World Urbanization Prospects 2014 revision (highlights). Technical report, United Nations, Economic and social affairs, New York.
- Van Buggenhout, S., Van Brecht, A., Eren Özcan, S., Vranken, E., Van Malcot, W., and Berckmans, D. (2009). Influence of sampling positions on accuracy of tracer gas measurements in ventilated spaces. *Biosystems Engineering*, **104**(2), 216–223.
- Van Hooff, T. and Blocken, B. (2010). On the effect of wind direction and urban surroundings on natural ventilation of a large semi-enclosed stadium. *Computers and Fluids*, **39**(7), 1146–1155.
- Vardoulakis, S. and Heaviside, C. (2012). Health Effects of Climate Change in the UK 2012. Technical report, Health Protection Agency, London.
- Wackernagel, M., Onisto, L., Bello, P., Linares, A. C., Falfán, I. S. L., García, J. M., Guerrero, A. I. S., and Guerrero, M. G. S. (1999). National natural capital accounting with the ecological footprint concept. *Ecological economics*, **29**(3), 375–390.
- Walker, I. S., Wilson, D. J., and Sherman, M. H. (1998). A comparison of the power law to quadratic formulations for air infiltration calculations. *Energy and Buildings*, **27**(3), 293–299.
- Warren, P. (1977). Ventilation through openings on one wall only. In *International Conference Heat and Mass transfer in Buildings, Dubrovnik, Yugoslavia*.
- Warren, P. (1986). The analysis of single-sided ventilation measurements. *Air Infiltration Review*, **7**(2), 3–5.
- Warren, P. and Webb, B. (1980). The relationship between tracer gas and pressurization techniques in dwellings. In *Proc. First Air Infiltration Center Conference*, pages 245–276.
- Warren, P. R. and Parkins, L. M. (1985). Single-sided ventilation through open windows. In *Conf. proc. Thermal Performance of the Exterior Envelopes of Buildings, ASHRAE, Florida*, number 1, page 20.
- Watkins, R., Palmer, J., Kolokotroni, M., and Littlefair, P. (2002). The balance of the annual heating and cooling demand within the London urban heat island. *Building Services Engineering Research and Technology*, **23**(4), 207–213.
- Wilson, D. and Kiel, D. (1990). Gravity driven counterflow through an open door in a sealed room. *Building and Environment*, **25**(4), 379–388.
- Wiren, B. (1983). Effects of surrounding buildings on wind pressure distributions and ventilative heat losses for a single-family house. *Journal of Wind Engineering and Industrial Aerodynamics*, **15**(1), 15–26.
- Wood, C. R., Lacser, A., Barlow, J. F., Padhra, A., Belcher, S. E., Nemitz, E., Helfter, C., Famulari, D., and Grimmond, C. S. B. (2010). Turbulent flow at 190 m height above

-
- London during 2006–2008: a climatology and the applicability of similarity theory. *Boundary-layer meteorology*, **137**(1), 77–96.
- Xie, Z. and Castro, I. P. (2006). Les and rans for turbulent flow over arrays of wall-mounted obstacles. *Flow, Turbulence and Combustion*, **76**(3), 291–312.
- Xie, Z.-T. (2011). Modelling Street-Scale Flow and Dispersion in Realistic Winds Towards Coupling with Mesoscale Meteorological Models. *Boundary-Layer Meteorology*, **141**(1), 53–75.
- Yang, T. (2004). *CFD and Field Testing of a Naturally Ventilated Full-scale Building*. Ph.D. thesis, University of Nottingham.
- Yang, X. I., Sadique, J., Mittal, R., and Meneveau, C. (2016). Exponential roughness layer and analytical model for turbulent boundary layer flow over rectangular-prism roughness elements. *Journal of Fluid Mechanics*, **789**, 127–165.
- Yee, E. and Biltoft, C. A. (2004). Concentration Fluctuation Measurements in a Plume Dispersing Through a Regular Array of Obstacles. *Boundary-Layer Meteorology*, **111**(3), 363–415.
- Zaki, S., Hagishima, A., Tanimoto, J., and Ikegaya, N. (2010). Wind tunnel measurement of aerodynamic parameters of urban building arrays with random geometries. In *CWE2010 (Fifth International Symposium on Computational Wind Engineering)*.
- Zaki, S., Hagishima, A., and Tanimoto, J. (2012). Experimental study of wind-induced ventilation in urban building of cube arrays with various layouts. *Journal of Wind Engineering and Industrial Aerodynamics*, **103**, 31–40.